English Language Editor

RESEARCH ARTICLES

Title: Determination of Covid-19 Possible Cases by Using Deep Learning Techniques

Authors: Çinare OĞUZ, Mete YAĞANOĞLU

Determination of Covid-19 Possible Cases by Using Deep Learning Techniques

Çinare OĞUZ[*1], Mete YAĞANOĞLU[1]

Abstract

A large number of cases have been identified in the world with the emergence of COVID-19 and the rapid spread of the virus. Thousands of people have died due to COVID-19. This very spreading virus may result in serious consequnces including pneumonia, kidney failure acute respiratory infection. It can even cause death in severe cases. Therefore, early diagnosis is vital. Due to the limited number of COVID-19 test kits, one of the first diagnostic techniques in suspected COVID-19 patients is to have Thorax Computed Tomography (CT) applied to individuals with suspected COVID-19 cases when it is not possible to administer these test kits. In this study, it was aimed to analyze the CT images automatically and to direct probable COVID-19 cases to PCR test quickly in order to make quick controls and ease the burden of healthcare workers. ResNet-50 and Alexnet deep learning techniques were used in the extraction of deep features. Their performance was measured using Support Vector Machines (SVM), Nearest neighbor algorithm (KNN), Linear Discrimination Analysis (LDA), Decision trees, Random forest (RF) and Naive Bayes methods as the methods of classification. The best results were obtained with ResNet-50 and SVM classification methods. The success rate was found as 95.18%.

Keywords: ResNet-50, Alexnet, Deep Learning, COVID-19, Classification

[*] Corresponding Author: cinare.oguz.91@gmail.com
[1] Ataturk University, Department of Computer Engineering, Erzurum, Turkey, ORCID: https://orcid.org/0000-0003-0410-2429, E-mail: yaganoglu@atauni.edu.tr ORCID: https://orcid.org/0000-0003-3045-169X

1. INTRODUCTION

As stated by the World Health Organization (WHO), coronaviruses (CoV) are a one of the largest family at viruses are common in the community, such asthe common cold that can cause more severe infections than mild infections. Diseases, caused by COVID-19 virus are an inflammatory diseases that caused by a new viruses. The disease causes respiratory distress with symptoms including colds, coughs, fever, and respiratory problems in more serious cases [1].

According to data of WHO, it is stated that the interest for personal protective equipment and respirators. The usage of masks increased by 100 times compared to normal levels and prices of related materials increased by about 20 times during the process following the spread of the virus [2]. In the procerss until February 11, 2020, the spread of the new virus on the world and the threats posed at the global level will increase [3].

Since there is no gold standard test that can provide 100% definitive diagnosis yet for the detection of COVID-19, it is attempted to reach the diagnosis by performing rapid antigen test, Polymerase Chain Reaction (PCR) test and by taking Computerized Tomography (CT) image.

COVID-19 case definition evaluation is performed for incoming patients. Within the scope of this evaluation, those who meet the COVID-19 case definition are included in the designated area. It is then examined and vital signs are checked.

Due to the limited number of COVID-19 test kits, these test kits are not administered to all suspected COVID-19 patients. For this reason, one of the first diagnostic techniques for individuals with suspected COVID-19 cases is Thorax Computed Tomography. As a result of positive findings on computed tomography, PCR test can be performed on the patient. Thus, efficient use of test kits is provided. CT equipment is available in almost all hospitals and it may be possible to use CT images to investigate the COVID-19 cases without special test kits.

Since COVID-19 virus effects epithelial cells that can seal patient's airway, Computer Tomography can be used to examine the health of the patient's lungs. Doctors often use CT images to diagnose pneumonia, lung inflammation, abscesses and enlarged lymph nodes.

COVID-19 19 positive and negative lung CT images are shown in Figure 1.The figure shows a CT image of the lung of an individual infected with Covid 19 virus and a CT image of the lung of a healthy individual.

It is necessary to develop an automated diagnosis system to give medical professionals valuable advice so that the analysis of CT images does not require a radiologist and does not cause significant loss of time.

Common symptoms of this very spreading virus are respiratory symptoms, fever, cough and dyspnea. In more severe cases, it can result in severe consequences including pneumonia, kidney failure, acute respiratory infection. It can also cause death in serious cases. Therefore, early diagnosis is vital. In this article, it was aimed to analyze the CT images automatically and to direct probable COVID-19 cases to PCR test in order to ease the burden of healthcare workers.
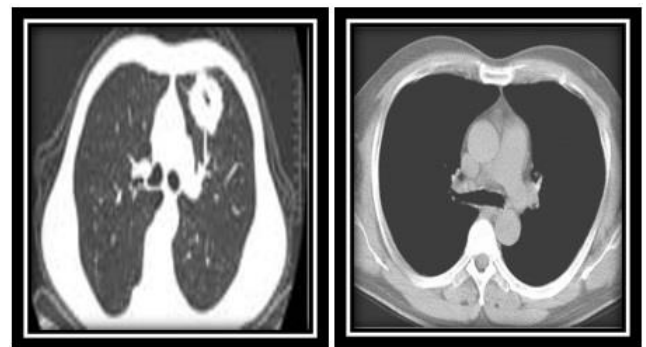
Figure 1. (Left) CT image of the lung of an individual infected with Covid 19 virus and (right) CT image of the lung of a healthy individual

Artificial intelligence (AI) is a tool used for estimation [4]. Deep learning, one of the sub-

branches of artificial intelligence, consists of steps involving the training process of many feed-forward neural networks. Deep learning architectureshave been created with the advances in hardware and the increasing number of layers of the Artificial Neural Network and these have been involved in the solution of more complex problems. Deep learning is one of the last techniques applied in the field of diagnostic medicine [5], [6]. It can help us address issues that should be raised by the COVID-19 outbreak. Deep learning, a kind of artificial intelligence, works by recognizing designs in chronic educational knowledge. Using our dynamic knowledge to do the best speculation of what works and what can happen, we can practice from a situation and apply them to new conditions. The outbreak requires real-time analysis of high-dimensional and heterogenous datasets. At this critical point, machine learning (ML) and deep learning have an important place for effective pandemic response.

The development of computer-assisted estimation and diagnostic tools has come to the fore with the development of medical image processing techniques[7].

Gu et al. [8] detected lung nodules with the model they developed with convolutional neural network and achieved a success rate of 79.67%.

Yadav et al. [9] used the SVM classification method for deep features obtained by InceptionV3 and VGG-16 models as a deep learning technique in the model they developed for the detection of pneumonia disease and achieved a success rate of 96.6%.

Talo [10] proposed an automatic recognition system for the diagnosis of pneumonia disease. ResNet-152 convolutional neural network was privatizeda recognition success of 97.4% was achieved in the detection of pneumonia disease without any pretreatment or manual feature extraction on radiography images.

Couhan et al. [11] achieved a success rate of 96.39% by performing a transfer learning with normal, virus pneumonia and bacterial pneumonia images for the diagnosis of pneumonia disease.

Abiyev et al. [12] achieved a success rate of 89.57% in diagnosing pneumonia disease by applying back propagation neural network and competitive neural network models using pneumonia and normal chest x-ray images.

Araujo et al. [13] classified the images at the patient level with a model similar to AlexNet for classification of cancer images. In this study, average accuracy of 90% and 85.6% with maximum fusion method was reported using different fusion techniques.

Pathak et al. [14] used a deep transfer learning technique to classify COVID- 19 infected patients and achieved a success rate of 93.0189%.

Toğaçar et al. [15] processed the feature sets obtained with deep learning techniques by using Social Mimic optimization method and COVİD 19, pneumonia and normal x-ray images and classified them with SVM in the model developed for the detection of COVID 19. Its success rate was 99.27%.

Ardakani et al. [16] evaluated performances using 10 well-known convo- lutional nerves to separate COVID-19 infection from non-COVID-19 groups. They achieved the best performance among all neural networks with ResNet 101 and Xception.

Sethy and Behara [17] did statistical analysis to choose the best classification model. They recorded this classification model as statistically superior compared to other ResNet-50 models. They obtained the proposed classification model for the detection of COVID-19 with an accuracy of 95.38%.

Xu et al. [18] divided the CT images of COVID-19 into three classes. The data set consisted of 618 images. They classified the images with a 3D deep learning model and achieved an overall classification accuracy of 87.6%.

2. METHODOLOGY

Deep learning is a sub-branch of machine learning related to algorithms inspired by the brain structure and functions. Deep learning models facilitate the detection of various diseases through images obtained using medical imaging techniques such as MRI and CT[19].

Basically, ML methods apply techniques such as various preprocesses, size reduction and feature selection to the untreated images, then manually extract features from the images obtained, or use the features extracted by other machine learning models. However, deep learning techniques perform automatic feature extraction without any preprocessing of images[20].

Therefore, we aim to determine whether patients are possible cases with CT images taken from suspicious COVID-19 patients by using deep learning models in the study to be conducted.

2.1. Dataset

Lung CT images used in this study were provided by the open source Kaggle[30] data set. The dataset used was divided into 1697 CT images as COVID-19 negative and 379 CT images as COVID-19 positive. In the study, 20% of 2076 CT images were used for testing.

2.2. Deep Learning Model

2.2.1 Alexnet

The winning of the alexnet model developed by Alex Krizhevskyin in the ImageNet Large Scale Visual Recognition Challenge 2012 (ILSVRC-2012) competition has led to an increased interest in deep learning. The classification has increased the accuracy rate from 74.3% to 83.6%.

Alexnet is the first model to run on a parallel dual GPU. Thus, the model is trained faster and memory problems are prevented.

It is a neural network containing 650000 neurons with 60 million parameters. It has a total of eight learned layers, five convolutional and three fully connected [25]. The main purpose of the convolutional layer is to extract features and maximum pooling performs feature matching [26].

The input size of Alexnet is 227*227*3 pixel. Normalization takes place after the first and second convolutional layer. Maximum pooling is applied both after normalization and after the fifth convolutional layer. RELU is used as the activation function. RELU is applied after each convolutional layer and to the output of the fully connected layer. It provides to reduce the training time. Each of the fully connected layers contains 4096 neurons. Dropout is applied in the first two fully linked layers to prevent the model from memorizing samples in training data [25].

The architecture of the Alexnet model is shown in figure 2.
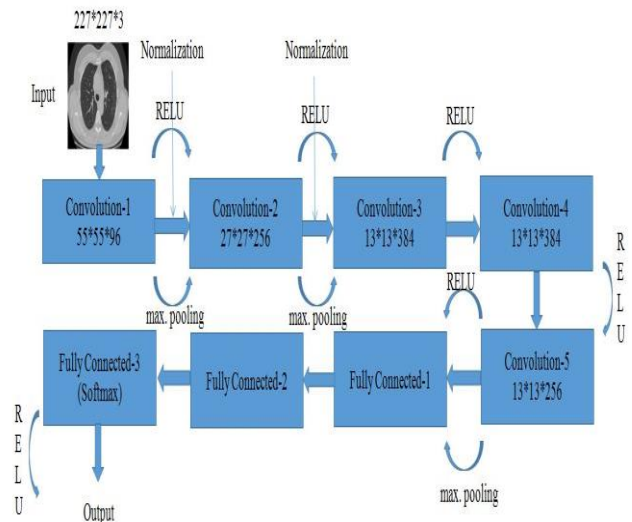
Figure 2. Architecture of Alexnet [25]

2.2.2 Resnet-50

Resnet-50 is a 50-layer network over the ImageNet dataset. Resnet-50 is an improved version of the Convolutional Neural Network (CNN). The Resnet model aims to solve the performance degradation problem of CNN

networks. As the depth of the network increases, loss of information occurs during parameter updates. To solve this problem, ResNet adds extra links between layers that connect the intermediate layers. Instead of creating a new network, using a trained models are more desirable [10].

Resnet-50 neural network consists of input, convolution, activation, pooling, normalization, fully connected, RELU, Softmax and classification layers as shown in Figure 3.
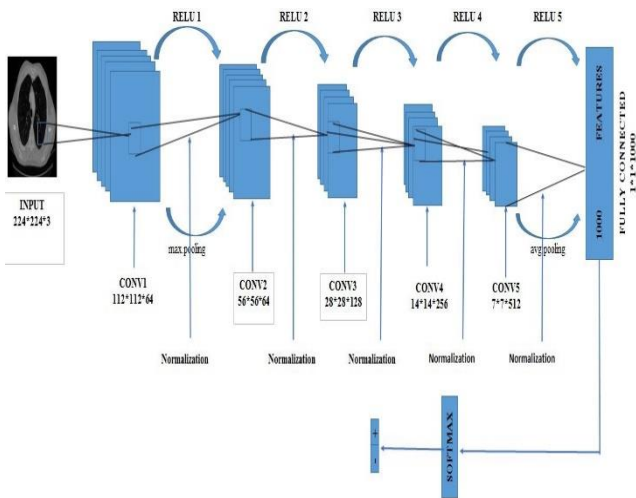
Figure 3. Architecture of Resnet-50[28]

The data is read in the input layer. The input size of Resnet is 224*224*3 pixel. In the convolution layers, activations from the previous layers are processed with various filters and the feature map is drawn for each filter.The convolution layer is the main building block of a CNN.The convolution layer does most of the computational dense elevation.Feature maps obtained from convolution layers are transmitted to the non-linear activation function.In addition, scaling is done on the image.To stabilize the training of the network in the normalization layer, standardization is performed based on the inputvalues in the neuron.The training of the network takes place faster thanks to this process[29].

The layer that follows the convolution layer and processes the output of neurons to nonlinear processing forms the activation layer. Nonlinear features are added to the network with the help of activation functions. The RELU activation function, which brings nonlinear features to the neural network, is often used in intermediate layers. After the activation process, each feature map can be reduced in size in the pool layer. Thus, the amount of calculation is reduced by reducing the number of parameters in the network. Average pooling and maximum pooling are the most common methods. The model to be used is available in both. No learning process takes place in this layer[29].

The data obtained from the previous layers in the fully connected layer is converted into a one-dimensional matrix in this layer. The Softmax activation function provides a categorical probability distribution using the neural network's output. The classification layer is the last layer of the network used after the Softmax layer. The output value of this layer is equal to the number of classes. In this study, there are two output values as COVID-19 positive and negative.

The block diagram of this study is shown in Figure 4. Deep feature extraction is based on the extraction of features from the pre-trained Resnet-50 neural network. Deep features are removed from the fully connected layer and the feature vector is obtained.

Deep features obtained from Resnet-50 and Alexnet networks are used by various classifiers (Knn, SVM, Naive Bayes, Decision Trees, RF and Discriminant Analysis) and the performance of all classification methods is measured.
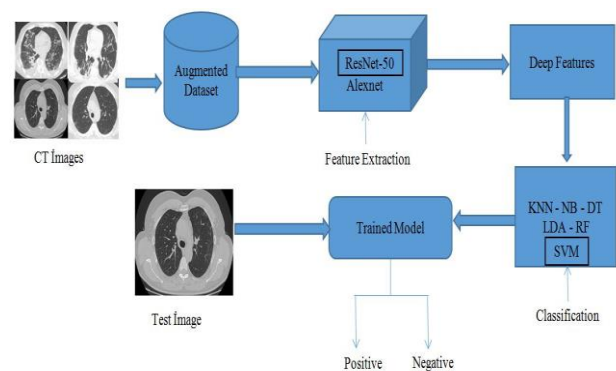
Figure 4. Block diagram

2.3. Classification Methods

2.3.1. K-Nearest Neigbors Algorithm (Knn)

Knn method is a widely used ML method to classify the test dataset according to the features obtained from the training set [22].

Cross Validation is a method used to estimate the ability of machine learning models. It is widely used in machine learning to compare and select a model for a given predictive modeling problem. The K value was determined using cross validation. The best k value was determined as 5.

The distance function is calculated between the samples in the training set and the test data. Euclidean method is used to calculate the distance between the data. Then, the distances obtained are listed and the closest k samples to the test data are selected in the training set. Among these examples, the most common class is considered to be the class of test data.

2.3.2. Support Vector Machine (SVM)

The SVM method is a statistical learning algorithm introduced by Vapnik, which has been widely used recently. Two hyperplanes are calculated: negativehyperplanes and positive hyperplanes belonging to the two classes obtained with the training dataset. An appropriate hyper plane is obtained which can make the best distinction between the two classes that are equidistant from these two hyperplanes. Support vectors closest to this hyperplane are called support vectors. The test data is then classified by the plane obtained [23]. In Figure 5, support vectors and separation plane are shown in SVM.
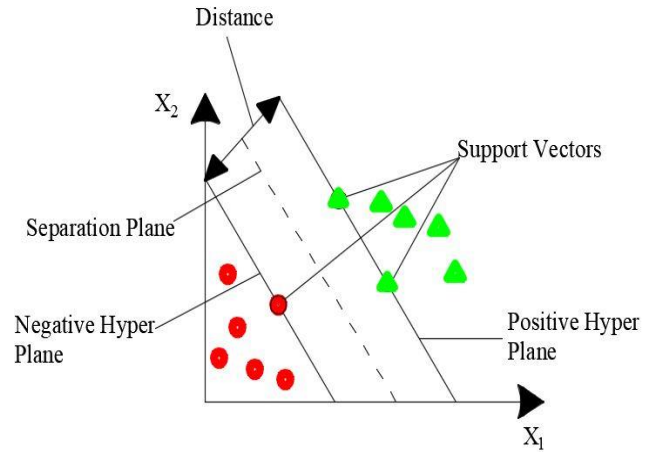
Figure 5. Support vectors and separation plane [27]

2.3.3. Decision Trees

The method of decision trees (DT) is an easy and common method unlike artificial neural networks in terms of classification [22]. The algorithm of decision trees takes place in two stages. First, a node of the tree is created using the features obtained from the training dataset, and then the process of dividing this data into two new nodes based on that feature takes place. The leaves of the tree are formed from these nodes. The division continues until each branch is labeled with only one classification. In the second stage, unnecessary branches of the tree are cut [22], [24]. Starting from the root node at the top of the Decision tree with test data, all possible outputs of the branch and the decision nodes are tested.

2.3.4. Random Forest (RF)

Random forest is a machine learning method that includes many decision trees, developed by Breiman [33] for regression and classification problems.

To train the classifier, multiple bootstrap training data sets are created from the original training data set with displacement, and a tree is generated for each bootstrap training data set. In while the original training set for currently tree is changed and sampled, approximately one third of the cases are excluded from the sample. This out-of-bag data is used to obtain an estimate of the classification error as the trees are insert to the forest. Incorrectly classified samples are

increased in weight to be more important in the next iteration [34].

2.3.5. Linear Discrinant Analysis (LDA)

The method of linear discriminant analysis is one of the widely used ML techniques based on statistical methods. This method aims to make the maximum in-group distance minimum[26]. It produces discriminant functions for all classes to separate classes. The discriminant function is given in equation 1.

$$f_i = \mu_i C^{-1} x_k^T - \frac{1}{2}\mu_i C^{-1}\mu_i^T + \ln(\frac{ni}{N}) \qquad (1)$$

N represents the total number of data. While ni is the number of data belonging to class i, μi refers to the average value of class i. C is the covariance matrix belonging to class i.

The test data is considered to belong to that class, whichever of the discriminant functions obtained for each class gives the highest results.

2.3.6. Naive Bayes

Naive Bayes (NB) method is a simple statistical approach classification method based on independent assumption. Basically, the Naive Bayes classifier accepts the fact that a class has a particular feature is irrelevant to having any other features. The advantage of the Naive Bayes method is that it requires few training data for classification.

In the Naive Bayes classification, a certain amount of taught data is presented to the system. The probability processes are applied on the taught data, the test data is evaluated according to the obtained probability values and it is tried to determine which class the test data belongs to.

In the NB method, X =$x_1,x_2,\ldots,x_n$ is an example of data whose class is unknown. Let $C_1, C_2,\ldots,C_m$ be the possible class values. The probabilities of the features of X by classes are calculated as in equation 2.

$$P(X|C_i) = \prod_{k=1}^{n} P(x_k |C_i) \qquad (2)$$

The probability of X belonging to each class is calculated in equation 3. In this case, it is decided which class X belongs to according to the biggest result.

$$P(C_i|X) = \frac{P(X|C_i)P(C_i)}{P(X)}$$
(3)

3. PERFORMANCE ANALYSIS

The detection of COVID-19 probable case was performed on MATLAB R2020a on a computer with Intel(R) Core (TM) i3-3220 CPU @ 3.30 GHz. 4 GB RAM using ResNet-50 and Alexnet architecture. The dataset used in the reported experimental results consists of 2076 CT images. Of this dataset, 80% was used for training and 20% for testing.

The confusion matrix is the summary of the educated network and it shows the performance of the network. A general confusion matrix is shown in Table 1 [31].

Table 1.
Confusion matrix

	Covid-19 Positive	Covid-19 Negative
Covid-19 Positive	TP	FP
Covid-19 Negative	FN	TN

TP: The image of COVID-19 is estimated to be positive and this image is positive.

TN: The image of COVID-19 is estimated to be negative and this image is negative.

FP: The image of COVID-19 is estimated to be negative, but this image is positive.

FN: The image of COVID-19 is estimated to be positive, but this image is negative.

Accuracy, Sensitivity and Specificity are calculated by equation 4,5,6 [32].

$$\text{Accuracy} = \frac{TP+TN}{TP+TN+FP+FN} \qquad (4)$$

$$\text{Sensitivity} = \frac{TP}{TP+FN} \qquad (5)$$

$$\text{Specificity} = \frac{TN}{TN+FP} \tag{6}$$

Resnet-50 and Alexnet deep learning techniques were used in the extraction of deep features. As classification methods, their performance was measured using SVM, KNN, LDA, Decision trees, RF and Naive Bayes methods. In Figure 6, the success rate of classification methods is given by using the deep features obtained with Resnet-50. As can be seen in Table 3, the best results were obtained with Resnet-50 and SVM classification methods. The confusion matrix obtained by using Resnet-50 and SVM methods together is given in Table 2. The success rate was recorded as 95.18%.

Table 2.
Comprehensive confusion matrix of Resnet-50 SVM methods

	Covid-19 Positive	Covid-19 Negative
Covid-19 Positive	67	9
Covid-19 Negative	11	328
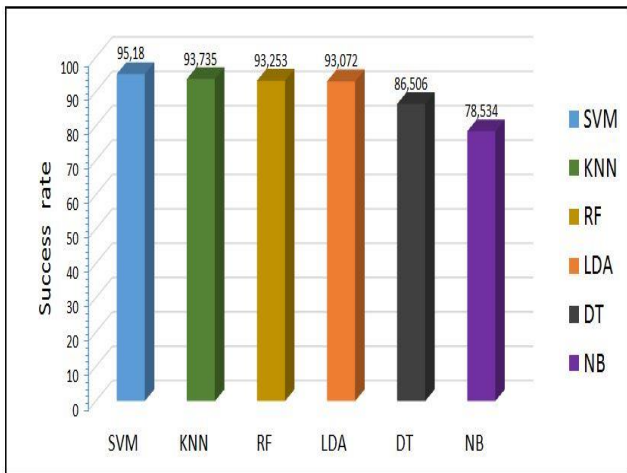
Figure 6. Success rate of classification methods with Resnet-50

Table 3.
Experimental results

		Accuracy (%)	Sensitivity (%)	Sensitivity (%)
ALEXNET	NB	75.904	72.861	89.473
	SVM	92.289	88.158	93.215
	KNN	91.566	84.211	93.215
	LDA	91.265	67.213	96.678
	DT	86.747	76.316	89.086
	RF	94.458	84.416	96.746
RESNET50	NB	78.534	75	79.351
	SVM	95.180	88.158	96.755
	KNN	93.735	85.526	95.575
	LDA	93.072	80	95.955
	DT	85.506	57.895	92.92
	RF	93.253	81.579	95.870

4. CONCLUSION

In this study, the performances of various classification methods were evaluated by using deep learning techniques for possible COVID-19 case detection from lung CT images. From the experimental results obtained, we see that the specificity values are higher than the sensitivity values in each classification method. Because more COVID-19 negative images in the dataset enabled the model to learn better the COVID-19 negative class type. It is planned to increase the success rate by increasing the number of insufficient COVID-19 positive images in the future. In addition, artificial neural network method can be considered as a classification method.

Intelligent algorithms focused on ML can provide effective responses and enhancements to the COVID-19 pandemic, while contributing to the development of various models, widely used in clinics around the world. This can help predict COVID-19 health outcomes in a variety of geographic and health systems environments. ML will help reduce diagnostic errors and unnecessary use of diagnostic tools through the development of rational algorithms. The model developed in this study can be used as an assistant decision support system by preventing unnecessary tests for COVID- 19 disease. The purpose of the developed system is not to replace a specialist, but only to support the decision to be made in the light of the information obtained from the experts working on the subject during the diagnostic phase.

The authors have no received any financial support for the research, authorship or publication of this study.

THE DECLARATİON OF CONFLİCT OF INTEREST

No potential conflict of interest was reported by the authors.

THE DECLARATİON OF ETHİCS COMMİTTEE APPROVAL

This study does not require ethics committee approval or any special permission.

THE DECLARATİON OF RESEARCH AND PUBLİCATION ETHİCS

In the writing process of this study, international scientific, ethical and citation rules were followed, and no falsification was made on the collected data. Sakarya University Journal of Science and its editorial board have no responsibility for all ethical violations. All responsibility belongs to the responsible author and this study has not been evaluated in any academic publication environment other than Sakarya University Journal of Science.

REFERENCES

[1] R. Sujath, J. M. Chatterjee and A. E. Hassanien, "A machine learning forecasting model for COVID-19 pandemic in India," Stochastic Environmental Research and Risk Assessment, 1, Springer, 2020.

[2] E. Mahase, "Coronavirus: global stocks of protective gear are depleted, with demand at 100 times normal level, WHO warns," British Medical Journal Publishing Group,2020.

[3] C. Columbus, K. B. Brust and A. C. Arroliga. "2019 novel coronavirus: an emerging global threat," Baylor University Medical Center Proceedings, vol. 33, no. 2, Taylor & Francis, 2020.

[4] Y. Mohamadou, A. Halidou and P. T. Kapen, "A review of mathematical modeling, artificial intelligence and datasets used in the study, prediction and management of COVID-19," Applied Intelligence, Springer, pp. 1-13, 2020.

[5] P. K. Shukla, P. K. Shukla, P. Sharma, P. Rawat, J. Samar, R. Moriwal and M. Kaur, "Efficient prediction of drug–drug interaction using deep learning models," IET Systems Biology, 2020.

[6] M. Kaur, H. K. Gianey, D. Singh and M. Sabharwal, "Multi-objective differential evolution based random forest for e-health applications," Modern Physics LettersB, World Scientific, 33, 05, 2019.

[7] M. Kaur and D. Singh, "Fusion of medical images using deep belief Networks," Cluster Computing, 1-15, 2019

[8] Y.Gu, X. Lu, L. Yang, B. Zhang, D. Yu, Y. Zhao and T. Zhou, "Automatic lung nodule detection using a 3D deep convolutional neural network combined with a multi-scale prediction strategy in chest CTs," Computers in biology and medicine, 103, pp. 220-231, 2018.

[9] S. S. Yadav and M. J. Shivajirao, "Deep convolutional neural network based medical image classification for disease diagnosis." Journal of Big Data 6.1, 113, 2019.

[10] M. Talo, "Pneumonia Detection from Radiography Images using Convolutional Neural Networks2019 27th Signal Processing and Communications Applications Conference (SIU), IEEE, pp. 1-4, 2019.

[11] V. Chouhan, S. K. Singh, A. Khamparia, D. Gupta, P. Tiwari, C. Moreira and V. H. C. De Albuquerque, "A novel transfer learning based approach for pneumonia detection in chest X-ray images," Applied Sciences, 10(2), 559, 2020.

[12] R. H. Abiyev and M. K. S. Ma'aitah, "Deep convolutional neural networks for chest diseases detection," Journal of healthcare engineering, Hindawi, 2018.

[13] T. Araújo, G. Aresta, E. Castro, J. Rouco, P. Aguiar, C. Eloy, A. Polonia and A. Campilho, "Classification of breast cancer histology images using convolutional neural networks," PloS one, Public Library of Science San Franscisco, CA USA, 12, 6 e0177544, 2017.

[14] Y. Pathak, P. K. Shukla, A. Tiwari, S. Stalin, S. Singh and P. K. Shukla, "Deep Transfer Learning based Classification Model for COVID-19 Disease," IRBM, Elsevier, 2020.

[15] M. Toğaçar, B. Ergen and Z. Cömert, "COVID-19 detection using deep learning models to exploit Social Mimic Optimization and structured chest X-ray images using fuzzy color and stacking approaches," Computers in Biology and Medicine, 103805, 2020.

[16] A. A. Ardakani, A. R. Kanafi, U. R. Acharya, N. Khadem and A. Mohammadi, "Application of deep learning technique to manage COVID-19 in routine clinical practice using CT images: Results of 10 convolutional neural Networks," Computers in Biology and Medicine, Elsevier, 103795,2020.

[17] P. K. Sethy and S. K. Behera "Detection of coronavirus disease (covid-19) based on deep features," Preprints, 2020030300, 2020.

[18] X. Xu, X. Jiang, C. Ma, P. Du, X. Li, S. Lv and G. Lang, "Deep learning system to screen coronavirus disease 2019 pneumonia," arXiv 2020, arXiv preprint arXiv:2002.09334, 2020.

[19] L. Liu, W. Ouyang, X. Wang, P. Fieguth, J. Chen, X. Liu and M. Pietikäinen, "Deep learning for generic object detection: A survey," International journal of computer vision, Springer, 128, 2, pp. 261-318, 2020.

[20] A. S. Lundervold and A. Lundervold, "An overview of deep learning in medical imaging focusing on MRI," Zeitschrift für Medizinische Physik,Elsevier, 29, 2, pp. 102-127, 2019.

[21] E. Alpaydin, Introduction to machine learning. MIT pres, 2020.

[22] P. Lubaib and K. A. Muneer, "The heart defect analysis based on PCG signals using pattern recognition techniques," Procedia Technology, Elsevier, 24, pp. 1024-1031, 2016.

[23] R. Nisbet, J. Elder and G. Miner, Handbook of statistical analysis and data mining applications, Academic Press, 2009.

[24] S. Balakrishnama and A. Ganapathiraju, "Linear discriminant analysis-a brief tutorial," Institute for Signal and information Processing, vol. 18, no. 1998, pp. 1-8, 1998.

[25] A. Krizhevsky, I. Sutskever and G.E. Hinton, "Imagenet classification with deep convolutional neural net works," Adv. Neural Inf. Process. Syst., pp. 1097–1105, 2012.

[26] X. Du, Y. Cai, S. Wang and L. Zhang, "Overview of deep learning", 31st Youth Acad. Annu. Conf. Chinese Assoc. Autom., pp. 159–164, 2016.

[27] H. Byun and S. W. Lee, "A survey on pattern recognition applications of support vector machines," International Journal of Pattern Recognition and Artificial Intelligence, 17,3, pp. 459-486, 2003.

[28] K. He, X. Zhang, S. Ren and J. Sun, "Deep residual learning for image recognition," Proceedings of the IEEE conference on computer vision and pattern recognition, pp. 770-778, 2016

[29] A. Çinar and M. Yıldırım, "Detection of tumors on brain MRI images using the hybrid convolutional neural network architecture," Medical Hypotheses, 109684.

[30] https://www.kaggle.com/luisblanche

[31] M. Yağanoğlu and C. Köse "Real-Time Detection of Important Sounds with a Wearable Vibration Based Device for Hearing-Impaired
People," Electronics, 7(4), 50, 2018.

[32] F. Bozkurt, C. Köse and A. Sarı, "An inverse approach for automatic segmentation of carotid and vertebral arteries in CTA," Expert Systems with Applications, 93, pp. 358-375, 2018.

[33] L. Breiman, "Random forests," Machine learning, 45(1), 5-32, 2001.

[34] L. Breiman and A. Cutler, Random Forests, 2004, Retrieved from: https://www.stat.berkeley.edu/~breiman/RandomForests/cc_home.htm#prox

Title: Molecular Characterization and Biofilm Formation of Escherichia coli from Vegetables

Authors: Fatma ÖZDEMİR, Seza ARSLAN

Molecular Characterization and Biofilm Formation of *Escherichia coli* from Vegetables

Fatma ÖZDEMİR[*1], Seza ARSLAN[1]

Abstract

Escherichia coli can cause diarrheal and extraintestinal illnesses in humans. Diarrheagenic *E. coli* can be transmit to human through consumption of contaminated food, including vegetables. Biofilm produced by *E. coli* during food processing plays a role in development of foodborne illnesses. Vegetables have often been involved in diarrheal *E. coli* infections. A total of 40 *E. coli* isolates from vegetables were tested to determine biofilm formation at 12°C, 25°C and 37°C by the crystal violet and MTT assays. All isolates were performed for the production of curli fimbriae and cellulose associated with biofilm formation on Congo red agar. Biofilm formation by the crystal violet assay at 37°C, 25°C and 12°C was detected in 87.5%, 70% and 70% of the isolates, respectively. The biomass and viability of *E. coli* biofilms were similar according to the results of crystal violet and MTT assays. Biofilm formation among the *E. coli* isolates using the crystal violet and MTT assays showed a statistically significant difference between 12°C and 25°C as well as 12°C and 37°C ($p < 0.05$). However, no significant difference between 25 and 37°C ($p > 0.05$) was obtained. Three different morhotypes (bdar, pdar and saw) were identified based on the expression of curli fimbriae and cellulose. The incidence of the bdar morhotype was 27.5% and 50% at 25°C and 37°C, respectively. Prevalence of the pdar morphotype was 50% and 70% at 25°C and 37°C, respectively. At 25°C, only one isolate (2.5%) showed the saw morphotype. All isolates tested expressed curli fimbriae or cellulose, only three of which were non-biofilm producer using the crystal violet assay. This study demonstrated that the presence of biofilm forming *E. coli* isolates in vegetables may cause a risk to human health and food safety.

Keywords: *Escherichia coli*, vegetables, biofilm formation, curli fimbriae, cellulose

---

[*] Corresponding Author: ozkardes_f@ibu.edu.tr
[1] Bolu İzzet Baysal University, Bolu, Turkey, ORCID: https://orcid.org/0000-0002-4804-936X,
E-mail: arslan_s3@ibu.edu.tr, ORCID: https://orcid.org/0000-0002-2478-6875

1. INTRODUCTION

Escherichia coli is a non-spore forming, Gram-negative and facultatively anaerobic bacterium. It is a widespread human and animal pathogen commonly found in the healthy human intestinal tract. Most strains of *E. coli* are harmless commensals, but some pathogenic strains are able to cause a variety of diseases such as gastrointestinal illness, urinary tract infections, pericarditis, septicemia, pneumonia, and meningitis [1]. *E. coli* strains linked to gastrointestinal diseases are classified into six pathotypes, including enteropathogenic, shiga toxin-producing, enterotoxigenic, enteroaggregative, enteroinvasive, and diffusely adhering *E. coli* [2]. These pathogenic *E. coli* strains causing human diarrhea of varying severity are well-known foodborne pathogens and pose human health problems worldwide. Transmission of diarrhea-associated *E. coli* strains to human often occurs through eating contaminated food, including raw milk, dairy products, raw or undercooked ground beef, raw fruits and vegetables [3]. Vegetables are important in human nutrition as sources of many nutrients. A diet rich in fresh vegetables can reduce the risk of long-term diseases such as cardiovascular diseases, cancer, diabetes, hypertension, and obesity including certain nutrient deficiencies [4]. The consumption of vegetables has increased substantially due to consumer demand for health promotion in the world. Vegetables can be a potential source of various foodborne infections and outbreaks as they are eaten raw or lightly cooked [4, 5]. Foodborne outbreaks of pathogenic *E. coli* which are caused by eating contaminated vegetables such as spinach [6], lettuce [7-9], cabbage [10] and fresh leafy vegetables [11, 12] have been increasingly reported.

A variety of bacterial pathogens are able to adhere, gather, and produce biofilms on both abiotic and biotic surfaces. Bacteria in biofilms are more resistant to pH and temperature changes, nutrient deprivation, disinfectants, antimicrobials and oxygen radicals better than planktonic organisms. Thus, it is extremely difficult to remove an established biofilm in food environment [13]. Biofilms in food processing environment might contribute the persistence of spoilage and pathogenic bacteria and contamination of foods. They are of important concern in food hygiene and create public health risks and economic losses [2, 13]. Several factors, including environmental conditions such as incubation temperature, growth medium, and surface material, strain origin and serovar effect the biofilm forming ability in *E. coli* strains [14, 15].

Curli fimbriae and cellulose are important biofilm matrix components in *E. coli* and other *Enterobacteriaceae* [16, 17]. Curli fimbria is a fibrous surface protein mainly associated with bacterial attachment, cell accumulation, and biofilm formation. The existence of cellulose in the biofilm matrix confers mechanical, chemical, and physiological protection and promotes bacterial adhesion to abiotic surfaces [1, 18]. Many researchers have been studied the expression of curli fimbriae and cellulose in *E. coli* strains [14, 17, 19].

Vegetables has been consumed increasingly worldwide due to healthy lifestyle recommendations. They can be contaminated with *E. coli* at any stage from production to consumption. *E. coli* presence and its biofilm formation ability in vegetables are important in terms of food safety and hygiene. Therefore, the aim of the present study was to determine the biofilm formation of the *E. coli* isolates originated from vegetables at different temperatures using the microtiter plate and MTT assays and detect the expression of biofilm matrix components (curli fimriae and cellulose) using the Congo red agar assay.

2. MATERIALS AND METHODS

2.1. Bacterial isolates

A total of 40 *E. coli* isolates from vegetables including spinach (n=15), lettuce (n=12), arugula (n=9), black cabbage (n=3) and lamb's lettuce (n=1) were used in this study. Vegetables collected from various supermarkets and public bazaars were fresh and not precooked or frozen. The isolates were maintained at −20°C in Brain Heart Infusion broth (Merck) with 20% (vol/vol) glycerol until use.

2.2. Phenotypic identification of *E. coli*

Colonies on Eosin Methylene Blue agar (Merck) seen as blue-black colonies, often with a green metallic sheen were counted as suspected *E. coli*. Phenotypic identification was performed using the conventional methods. For this, the following biochemical tests are used: Gram staining, catalase test, indole and H_2S production, citrate utilization, motility, Methyl red and Voges Proskauer test, urease test, and carbohydrate fermentation tests [1].

2.3. Molecular characterization

Genomic DNA extraction of the *E. coli* isolates was carried out using the cetyl trimethyl ammonium bromide (CTAB) method for PCR analysis according to Ausubel et al. [20]. The DNA was dissolved in Tris-EDTA (TE) buffer and stored at -20°C. Molecular characterization of the *E. coli* isolates was performed by amplification of the *E. coli*-specific universal stress protein A (*uspA*) gene. The *uspA* primers were F-5'-CCG ATA CGC TGC CAA TCA GT-3' and R-5'-ACG CAG ACC GTA GGC CAG AT-3', which were predicted to yield an 884 bp product [21]. PCR experiments were carried out using a thermal cycler (Bio-Rad T100). The PCR reaction mix (50 µl) contained 5 µl of 10X PCR buffer (Vivantis), 4 mM $MgCl_2$ (Vivantis), 0.2 mM dNTP mix (Thermo Fisher), 0.4 µM primer, 1.5 U Taq DNA polymerase (Vivantis), 4 µl (50 ng) extracted DNA and 31.7 µl nuclease free water (AppliChem). The cycling conditions were carried out with the following setup: 94°C for 5 min and 30 cycles of denaturation (2 min, 94°C), annealing (1 min, 60°C), extension (1 min, 72 °C), and final extension (5 min, 72°C). PCR products were analyzed by electrophoresis (Bio-Rad) in 1% agarose gels and visualized with UV transilluminator (DNR Minilumi Bioimaging Systems). *E. coli* ATCC 8739 was used as a reference strain in this study. Representative agarose gel photograph of the PCR products of the *uspA* gene is presented in Figure 1.
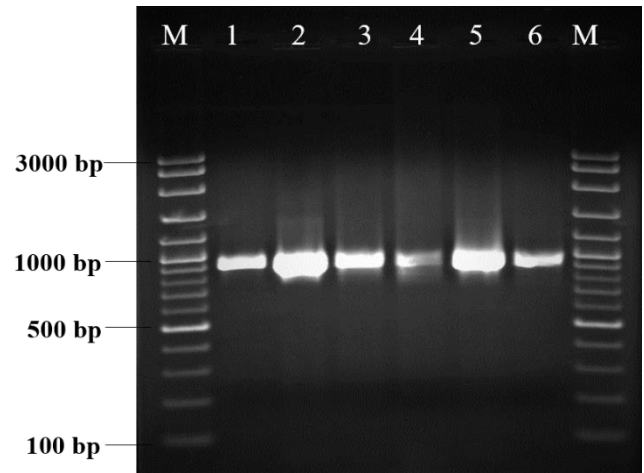
Figure 1. Gel electrophoresis of PCR product of the *uspA* (884 bp). M: 100 bp DNA ladder. Lane 1: positive control (*E. coli* ATCC 8739). Lanes 2-6: The *uspA* positive isolates from the spinach, lettuce, arugula, black cabbage, and lamb's lettuce samples, respectively.

2.4. Detection of biofilm by the microtiter

plate assay

Biofilm formation ability of the *E. coli* isolates on polystyrene plates was performed by the microtiter plate assay as described previously with some modifications [22, 23]. In brief, the turbidity of each isolate grown overnight in Tryptic Soy Broth (TSB) was adjusted to 0.5 McFarland. An aliquot of 200 µl of this suspension was inoculated into wells of a 96-well flat-bottom microplate and incubated for 24h at 12, 25 and 37°C. Following incubation, the plates were washed with sterile phosphate-buffered saline three times and fixed with 200 µl methanol (99%) (Merck) for 15 min. The wells were decanted to dry in the air and stained with 0.1% crystal violet solution for 15 min. The plates were washed with sterile distilled water, air-dried and then the adherent cells were resuspended in 160 µl of 33% (v/v) glacial acetic acid (Merck) per well. The optical density (OD) of each well was measured at OD_{570} nm using spectrophotometer. The experiments were made in triplicates. Sterile TSB was a negative control. The isolates were categorized as non-biofilm, weak, moderate and strong biofilm producers based on the OD values [22].

2.5. Detection of viability of cells in biofilm by the MTT assay

The MTT (3-(4, 5-dimethylthiazol-2-yl)-2, 5-diphenyltetrazolium bromide) tetrazolium assay to assess the metabolic activity of biofilm established by the *E. coli* isolates was performed as described in previous studies [24, 25]. All isolates of *E. coli* were grown overnight in TSB. Then, 200 µl of the adjusted suspension to 0.5 McFarland were added to each well in microtiter plate. After 24 h incubation at 37°C, the culture medium was removed and plate was washed with sterile phosphate-buffered saline (PBS) three times (200 µl per each well). After, 20 µl of pre-filter sterilized MTT solution (5 mg/ml in PBS) and 180 µl of TSB were added to individual well and incubated for 3 h at 37°C. The suspension was discarded and 150 µl of dimethyl sulfoxide (Sigma-Aldrich) were added to solubilize the formed formazan crystals. Viability of the cells was determined by measuring the optical density at OD_{570} nm using a microplate reader (Thermo Electron Corporation, Finland).

2.6. Detection of biofilm morphotypes

Biofilm morphotypes of the *E. coli* isolates were tested on Congo red agar (CRA) according to the method the previously described by Romling et al. [16] and Bokranz et al. [17]. CRA medium was prepared using Luria-Bertani agar without salt supplemented with Congo Red (40 µg/ml) and Coomassie brilliant blue (20 µg/ml). After overnight growing, 10µl of the culture were inoculated on the CRA plates and incubated at 25ºC and 37ºC for 96 h. The colonies were visualized and classified according to previous described four morphotypes: red, dry, and rough (rdar), which produce curli fimbriae and cellulose; pink, dry, and rough (pdar), which produce cellulose; brown, dry and rough (bdar), which produce curli fimbriae; smooth and white (saw), which do not produce both curli and cellulose [16, 17].

2.7. Statistical analysis

Statistical analysis were performed using the SigmaPlot 12.3 (Systat Software Inc.). The one-way analysis of variance (ANOVA) with Tukey's multiple comparison test was used to compare the results of biofilm formation at different temperatures. $p \leq 0.05$ was accepted to be significant.

3. RESULTS

3.1. Biofilm formation

This study investigated the ability of *E. coli* isolated from vegetables to form biofilm at three different temperatures. The results of biofilm formation of the *E. coli* isolates from vegetables are shown in Figure 2. Biofilm formation at 37°C, 25°C and 12°C was detected in 87.5%, 70% and 70% of the isolates, respectively (Tables 1 and 2). Under 37ºC condition, 11 (27.5%), 14 (35%), 10 (25%) and 5 (12.5%) of the isolates were strong, moderate, weak and non-biofilm producers, respectively. At 25ºC, 9 (22.5%) isolates were strong biofilm formers, 11 (27.5%) moderate, 8 (20%) weak, and 12 (30%) non-biofilm producers. At 12ºC, 2 (5%) isolates were classified as strong biofilm producers, 6 (15%) isolates as moderate producers, 20 (50%) isolates as weak biofilm producers, whereas 12 (30%) isolates did not produce biofilm. The findings showed that there was a statistically significant difference in biofilm formation using crystal violet staining at 12°C and 25°C ($p < 0.05$) as well as at 12°C and 37°C ($p < 0.05$). However, there was no significant difference between 25°C and 37°C ($p > 0.05$). We also assessed the viability of the *E. coli* cells in biofilm using the MTT assay (Figure 3). The results for the metabolic activity of *E. coli* at 12°C and 25°C ($p < 0.05$) as well as at 12°C and 37°C were statistically significant ($p < 0.05$), but there was no significant difference between 25 and 37°C ($p > 0.05$).

Table 1. Biofilm formation and morphotypes of *E. coli* isolates from vegetables

No	Isolate	Origin	Biofilm formation			Colony morphotypes	
			12°C	25°C	37°C	25°C	37°C
1	V1	Spinach	No biofilm	Weak	No biofilm	pdar	pdar
2	V2	Spinach	No biofilm	No biofilm	No biofilm	pdar	pdar
3	V3	Spinach	No biofilm	No biofilm	Moderate	pdar	pdar
4	V4	Spinach	No biofilm	No biofilm	No biofilm	pdar	pdar
5	V5	Spinach	Weak	No biofilm	No biofilm	pdar	pdar
16	V6	Spinach	Weak	Strong	Moderate	pdar	pdar
17	V7	Spinach	Weak	Strong	Weak	pdar	pdar
18	V8	Spinach	Weak	No biofilm	Weak	bdar	bdar
19	V9	Spinach	No biofilm	No biofilm	No biofilm	bdar	bdar
20	V10	Spinach	No biofilm	Weak	Moderate	pdar	bdar
21	V11	Spinach	Weak	Weak	Moderate	pdar	bdar
22	V12	Spinach	No biofilm	Moderate	Moderate	pdar	bdar
23	V13	Spinach	Weak	Strong	Strong	pdar	bdar
24	V14	Spinach	Weak	Moderate	Strong	pdar	bdar
25	V15	Spinach	Weak	Strong	Strong	pdar	bdar
6	V16	Lettuce	Weak	No biofilm	Weak	pdar	bdar
7	V17	Lettuce	Strong	Moderate	Strong	saw	bdar
8	V18	Lettuce	No biofilm	No biofilm	Weak	pdar	pdar
9	V19	Lettuce	Weak	No biofilm	Weak	bdar	bdar
10	V20	Lettuce	No biofilm	No biofilm	Weak	bdar	bdar
26	V21	Lettuce	Weak	Moderate	Weak	bdar	bdar
27	V22	Lettuce	Moderate	Strong	Strong	pdar	pdar
28	V23	Lettuce	Weak	Moderate	Strong	pdar	pdar
29	V24	Lettuce	Weak	Weak	Moderate	pdar	pdar
34	V25	Lettuce	Weak	Moderate	Weak	bdar	bdar
35	V26	Lettuce	No biofilm	Weak	Weak	bdar	bdar
36	V27	Lettuce	No biofilm	Weak	Weak	bdar	bdar
11	V28	Arugula	Weak	Moderate	Moderate	pdar	pdar
12	V29	Arugula	Moderate	Moderate	Moderate	pdar	pdar
13	V30	Arugula	Moderate	Moderate	Strong	pdar	pdar
14	V31	Arugula	Weak	Moderate	Moderate	pdar	pdar
15	V32	Arugula	Moderate	Weak	Moderate	pdar	pdar
30	V33	Arugula	No biofilm	No biofilm	Moderate	pdar	bdar
31	V34	Arugula	Moderate	Weak	Moderate	bdar	bdar
31	V35	Arugula	Moderate	No biofilm	Strong	pdar	pdar
33	V36	Arugula	Weak	Moderate	Moderate	bdar	bdar
37	V37	Black cabbage	Weak	Strong	Moderate	pdar	pdar
38	V38	Black cabbage	Strong	Strong	Strong	bdar	bdar
39	V39	Black cabbage	Weak	Strong	Strong	pdar	pdar
40	V40	Lamb's lettuce	Weak	Strong	Strong	pdar	pdar

Table 2. Biofilm formation categories of the *E. coli* isolates from vegetables at 12°C, 25°C and 37°C

Biofilm formation ability	12°C		25°C		37°C	
	No. (%)	OD$_{570}$[1]	No. (%)	OD$_{570}$	No. (%)	OD$_{570}$
Strong	2 (5)	0.257 ± 0.027	9 (22.5)	0.641 ± 0.086	11 (27.5)	0.332 ± 0.092
Moderate	6 (15)	0.101 ± 0.021	11 (27.5)	0.448 ± 0.084	14 (35)	0.200 ± 0.050
Weak	20 (50)	0.071 ± 0.007	8 (20)	0.169 ± 0.026	10 (25)	0.126 ± 0.018
Non-biofilm	12 (30)	0.053 ± 0.003	12 (30)	0.132 ± 0.017	5 (12.5)	0.065 ± 0.005

[1]OD$_{570}$: Optical density; values area expressed as mean ± standard deviation
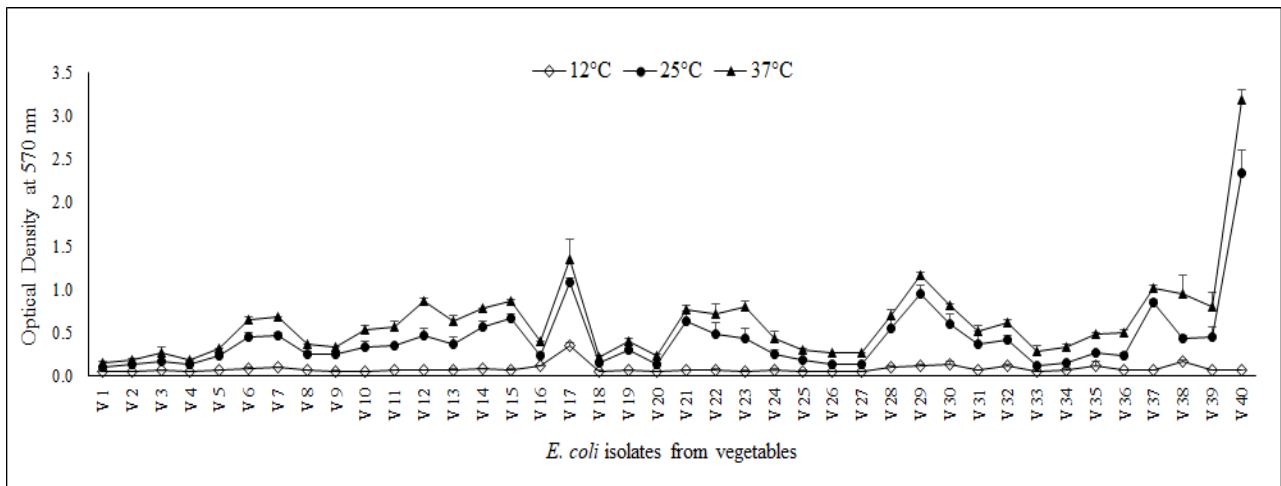
Figure 2. Biofilm formation of the 40 *E. coli* isolates from vegetables at 12ºC, 25ºC, and 37ºC by the crystal violet assay

Figure 3. The viability of the 40 *E. coli* isolates from vegetables at 12ºC, 25ºC, and 37ºC by the MTT assay

3.2. Biofilm morphotypes

In this study, representative morphotypes expressed at 37°C and 25°C by the *E. coli* isolates are presented in Figure 4. Three different morphotypes (bdar, pdar and saw) were detected (Table 1, Figure 4). However, colony morphotype at 12°C was not detected in none of the isolates. The occurrence of the bdar and pdar morphotypes at 37°C was 50%, but none of the isolates displayed saw morphology. Prevalence of the bdar and pdar morphotypes at 25°C was 27.5% and 70%, respectively. Under the same temperature, only one isolate (2.5%) showed the saw morphotype, indicating a lack of synthesis of both important biofilm components. All isolates were rdar negative at both temperature. The findings of this study revealed that there was no apparent association between the biofilm forming capabilities and morphotypes of the *E. coli* isolates from vegetables (Table 1).
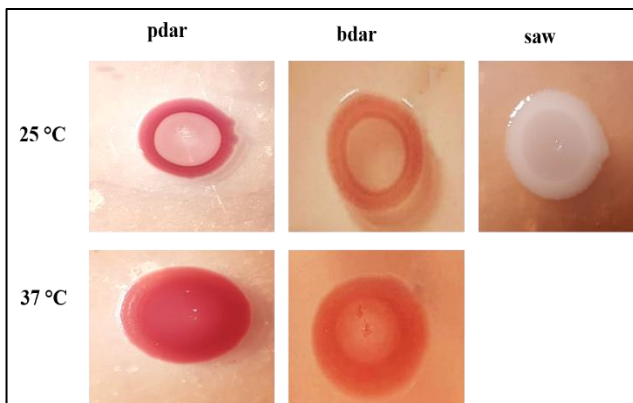
Figure 4. The identified morphotypes in the *E. coli* isolates from vegetables at 25ºC and 37ºC
pdar (pink, dry, and rough), bdar (brown, dry and rough), saw (smooth and white)

4. DISCUSSION

Biofilm produced by foodborne pathogens, including *E. coli* during food processing is involved in development of foodborne outbreaks [2, 13]. Leafy vegetables have often been implicated in *E. coli* outbreaks [4]. We investigated the ability of biofilm formation of the *E. coli* isolates from vegetables. It was detected that more than 70% of the isolates produced biofilm using crystal violet staining at three different temperatures. There was a statistically significant difference in biofilm formation at 12°C and 25°C ($p < 0.05$) as well as at 12°C and 37°C ($p < 0.05$). However, there was no significant difference between 25°C and 37°C ($p > 0.05$). The incidence of biofilm formation by *E. coli* isolates varied at different conditions [15, 19]. The ability of biofilm production was influenced by several factors such as incubation temperature and growth medium [15, 26, 27]. Nesse et al. [15] indicated that the *E. coli* isolates produced more biofilm at 25°C and 37°C than at 12°C, as we reported. Marti et al. [27] tested biofilm formation of *E. coli* isolates at 12, 28, and 37°C in different media. They reported that *E. coli* isolates showed the highest biofilm formation capacity at 28°C. The cultivation of *E. coli* isolates in nutrient rich medium (Tryptic Soy Broth) at lower temperature (20°C) exhibited a positive effect on biofilm formation [26].

In this study, three different morhotypes (bdar, pdar and saw) were identified based on curli fimbriae and cellulose production which are involved in attachment to surfaces and biofilm formation. As shown in Table 1, 27.5% and 50% of the isolates had the bdar morphotype, showing only curli fimbriae at 25°C and 37°C, respectively. Similarly, Schiebel et al. [19] found that the bdar morphotype was observed in 32.6% of the isolates at 28°C and in 38.5% of the isolates at 37°C. In other study, 83.3% and 77.7% of the isolates produced only curli fimbriae at 28°C and 37°C, respectively [14]. In contrast to our study, Dubravka et al. [26] documented that curli fimbriae were found in all *E. coli* isolates at 37°C. Cellulose, the second component of extracellular matrix, was expressed alone by some *E. coli* strains [18]. Silva et al. [14] documented the production of cellulose at 28°C (52.8%) and at 37°C (25%), similar to our results. At 25°C, most of our isolates (70%) from vegetables produced cellulose. In contrast, none of *E. coli* strains from mastitis milk samples produced cellulose [26]. In this study, the incidence of the saw morphotype (2.5%) was considerably lower than that (36%) obtained by Dubravka et al. [26]. Besides, we did not detect the rdar morhotype (expresses curli fimbria and cellulose) among the isolates. The production of both components at different

temperatures was observed in dairy isolates [27] and fecal isolates of *E. coli* [17]. The influence of environmental factors including low temperature, low osmolarity and poor carbon sources on expression of morphotypes has been reported [28].

In the present study, all isolates tested expressed curli fimbriae or cellulose, only three of which were not positive for biofilm formation using the crystal violet assay. Thus, this result may show a possible relationship between biofilm production and presence of curli fimbria and cellulose. A positive correlation was detected between cellulose production and biofilm production [27]. However, some studies demonstrated that there was no apparent association between the morphotype and biofilm formation [14, 17, 19].

5. CONCLUSION

The present study showed that most of the *E. coli* isolates from vegetables had biofilm formation ability at 12, 25, and 37°C. Three different morhotypes (bdar, pdar and saw) were identified based on the production of curli fimbriae and cellulose involved in biofilm formation. All isolates tested expressed curli fimbriae or cellulose, only three of which were not positive for biofilm formation using the crystal violet assay. In conclusion, biofilm formation by *E. coli* in leafy vegetables may be a primary source of food contamination and may cause a risk to human health and food safety.

The Declaration of Conflict of Interest/ Common Interest

No conflict of interest or common interest has been declared by the authors.

Authors' Contribution

All authors have contributed in experimental study and writing of the manuscript equally.

The Declaration of Ethics Committee Approval

The authors declare that this document does not require an ethics committee approval or any special permission.

The Declaration of Research and Publication Ethics

The authors of the paper declare that they comply with the scientific, ethical and quotation rules of SAUJS in all processes of the paper and that they do not make any falsification on the data collected. In addition, they declare that Sakarya University Journal of Science and its editorial board have no responsibility for any ethical violations that may be encountered, and that this study has not been evaluated in any academic publication environment other than Sakarya University Journal of Science.

REFERENCES

[1]   F. Scheutz and N. A. Strockbine, "Genus I *Escherichia*". In: Garrity, GM, Brenner DJ, Krieg NR, Staley JT. (Eds.), Bergey's manual of systematic bacteriology 2 (Part B). Springer, New York, pp. 607– 623, 2005.

[2]   A.K. Bhunia, "Foodborne microbial pathogens: mechanisms and pathogenesis," Springer, New York, 2008.

[3]   WHO, "Home/Newsroom/Fact sheets/Detail/E. coli, 7 February 2018,"https://www.who.int/news-room/fact-sheets/detail/e-coli2018, 2018.

[4]   G. I. Balali, D. Dekugmen, V. G. A. Dela, and P. Adjei-Kusi, "Microbial contamination, an increasing threat to the consumption of fresh fruits and vegetables in Today's world," International Journal of Microbiology, Article ID 3029295, 2020.

[5]   FAO, "Increasing fruit and vegetable consumption becomes a global priority," http://www.fao.org/english/newsroom/focus/2003/fruitveg1.htm, 2003.

[6]   M. T. Jay, M. Cooley, D. Carychao, G. W. Wiscomb, R. A. Sweitzer, and L. Crawford-

Miksza, "*Escherichia coli* O157:H7 in feral swine near spinach fields and cattle, central California coast," Emerging Infectious Diseases, vol. 13, pp. 1908–1911, 2007.

[7]   I. Friesema, G. Sigmundsdottir, K. van der Zwaluw, A. Heuvelink, B. Schimmer, C. de Jager, B. Rump, H. Briem, H. Hardardottir, A. Atladottir, E. Gudmundsdottir, and W. van Pelt, "An international outbreak of shiga toxin-producing *Escherichia coli* O157 infection due to lettuce, September–October 2007" Surveillance and outbreak reports, vol. 13, no. 50, pp. 1–5, 2008.

[8]   R. B. Slayton, G. Turabelidze, S. D. Bennett, C. A. Schwensohn, A. Q. Yaffee, F. Khan, C. Butler, E. Trees, T. L. Ayers, M. L. Davis, A. S. Laufer, S. Gladbach, I. Williams, and L. B. Gieraltowski, "Outbreak of shiga toxin-producing *Escherichia coli* (STEC) O157:H7 associated with romaine lettuce consumption, 2011," PLoS One vol. 8, no.2, e55300, 2013.

[9]   CDC, "Outbreak of *E. coli* Infections Linked to Romaine Lettuce Final Update," Available:

https://www.cdc.gov/ecoli/2019/o157h7-11-19/index.html, 2020.

[10]   CDC, "Multistate outbreak of shiga toxin-producing *Escherichia coli* O121 infections linked to raw clover sprouts (Final Update)," Available:

https://www.cdc.gov/ecoli/2014/o121-05-14/index.html, 2014.

[11]   K.M. Herman, A.J. Hall, and L. H. Gould, "Outbreaks attributed to fresh leafy vegetables, United States, 1973–2012," Epidemiology and Infection, vol. 20, pp. 1–11, 2015.

[12]   CDC, "Outbreak of *E. coli* Infections Linked to Romaine Lettuce," Available: https://www.cdc.gov/ecoli/2018/o157h7-11-18/index.html, 2018.

[13]   E. Giaouris, E. Heir, M. Desvaux, M. Hebraud, T. Moretro, S. Langsrud, A. Doulgeraki,

G-J. Nychas, M. Kacaniova, K. Czaczyk, H. Olmez, and M. Simoes, "Intra- and inter-species interactions within biofilms of important foodborne bacterial pathogens," Frontiers in Microbiology, vol. 6, no. 841, 2015.

[14]   G. I. Balali, D. Dekugmen, V. G. A. Dela, and P. Adjei-Kusi, "Microbial contamination, an increasing threat to the consumption of fresh fruits and vegetables in Today's world," International Journal of Microbiology, Article ID 3029295, 2020.

[15]   L. L. Nesse, C. Sekse, K. Berg, K.C. Johannesen, H. Solheim, L. K. Vestby, and A. M. Urdahlb, "Potentially pathogenic *Escherichia coli* can form a biofilm under conditions relevant to the food production chain," Applied and Environmental Microbiology, vol. 80, no. 7, pp. 2042–9, 2014.

[16]   U. Romling, W. D. Sierralta, K. Eriksson, and S. Normark, "Multicellular and aggregative behaviour of *Salmonella typhimurium* strains is controlled by mutations in the *agfD* promoter," Molecular Microbiology, vol. 28, pp. 249–264, 1998.

[17]   W. Bokranz, X. Wang, H. Tschape, and U. Römling, "Expression of cellulose and curli fimbriae by *Escherichia coli* isolated from the gastrointestinal tract," Journal of Medical Microbiology, vol. 54, pp. 1171–1182, 2005.

[18]   X. Zogaj, M. Nimtz, M. Rohde,W. Bokranz, and U. Romling, "The multicellular morphotypes of *Salmonella typhimurium* and *Escherichia coli* produce cellulose as the second component of the extracellular matrix," Molecular Microbiology, vol. 39, pp. 1452–1463, 2001.

[19]   J. Schiebel, A. Bohm, J. Nitschke, M. Burdukiewicz, J. Weinreich, A. Ali, D. Roggenbuck, S. Rödiger, and P. Schieracka, "Genotypic and phenotypic characteristics associated with biofilm formation by human clinical *Escherichia coli* isolates of different pathotypes," Applied and Environmental Microbiology, vol. 83, no. 24, e01660-17, 2017.

[20]   F.M. Ausubel, R.E. Kingston RE, R. Brent, D. D. Moore, J. Seidman , J.A. Smith, K.

Struhl, "Current protocols in molecular biology," Greene Publishing Associates & Wiley Interscience, New York, 1991.

[21] J. Chen and M.W. Griffiths, "PCR differentiation of *Escherichia coli* from other Gram negative bacteria using primers derived from the nucleotide sequences flanking the gene encoding the universal stress protein," Letters in Applied Microbiology, vol. 27, pp. 369–371, 1998.

[22] S. Stepanovic, D. Vukovic, I. Dakic, B. Savic, and M. Svabic-Vlahovic, "A modified microtiter-plate test for quantification of Staphylococcal biofilm formation," Journal of Microbiological Methods, vol. 40, pp. 175–179, 2000.

[23] S. Stepanovic, D. Vukovic, V. Hola, G. D. Bonaventura, S. Djukic, I. Cirkovic, and F. Ruzicka, "Quantification of biofilm in microtiter plates: overview of testing conditions and practical recommendations for assessment of biofilm production by staphylococci," APMIS, vol. 115, pp. 891–899, 2007.

[24] E. Walencka, S. Rozalska, B. Sadowska, and B. Rozalska, "The influence of *Lactobacillus acidophilus*-derived surfactants on Staphylococcal adhesion and biofilm formation," Folia Microbiology, vol. 53, pp. 61–66, 2008.

[25] Y.T Wu, H. Zhu, M. Willcox, and F. Stapleton, F, "Removal of biofilm from contact lens storage cases," Investigative Ophthalmology and Visual Science, vol. 51, pp. 6329-6333, 2010.

[26] M. Dubravka, P. Bojana, V. Maja, and T. Dalibor, and P. Vladimir, "Investigation of biofilm formation and phylogenetic typing of *Escherichia coli* strains isolated from milk of cows with mastitis," Acta Veterinaria-Beograd, vol. 65, no. 2, pp. 202–216, 2015.

[27] R. Marti, M. Schmid, S. Kulli, K. Schneeberger, J. Naskova, S. Knochel, C. H. Ahrens, J. Hummerjohanna, "Biofilm formation potential of heat-resistant *Escherichia coli* dairy isolates and the complete genome of multidrug-resistant, heat-resistant strain fam21845," Applied and Environmental Microbiology, vol. 83, no. 15, e00628-17, 2017.

[28] L.D. Sante, A. Pugnalonib, F. Biavascoa, E. Giovanettia, and C. Vignarolia, "Multicellular behavior of environmental *Escherichia coli* isolates grown under nutrient-poor and low-temperature conditions," Microbiological Research, vol. 210, pp. 43–50, 2018.

Title: Modelling the Effect Size of Microbial Fuel Cells Using Bernstein Polynomial Approach via Iterative Method

Authors: Mehmet GÜRCAN, Nurhan HALİSDEMİR, Yunus GÜRAL

Modelling the Effect Size of Microbial Fuel Cells Using Bernstein Polynomial Approach via Iterative Method

Mehmet GÜRCAN[*1], Nurhan HALİSDEMİR[1], Yunus GÜRAL[1]

Abstract

Microbial fuel cells are one of the most important issues in today's science. The studies in the literature on the subject are very limited. Nowadays, research on renewable energy sources brings scientists to the point of obtaining renewable energy sources from microbial fuel cells. In this study, we designed a battery using a microbial fuel cell. The four independent variables taken into account in the experiment are open-circuit voltage, short circuit current, measured voltage when loaded, the current measured when loaded, and dependent variable effect size. The numerical values of the effect size were obtained by using independent variables. Then, the obtained values from the effect size were modeled using Bernstein polynomial. Using the iterative calculations belonging to the Bernstein polynomial in calculations, the error of the model has been reduced to a minimum and thus the estimation model used has been made statistically significant for the effect size.

Keywords: microbial fuel cell, biosensor, organic materials, renewable energy, Bernstein polynom

1. INTRODUCTION

The amount of use of fossil-based fuel materials is increasing day by day. This situation has had negative consequences for the environment and human health. In addition, the emergence of the energy crisis has shown the need for more sustainable, lower-cost and environmentally friendly energy resources. Due to the increasing population and the risk of energy crisis, rapid urbanization and population growth, more comprehensive studies are required on both environment, health and renewable energy [1].

Various countries around the world have created large-scale energy production resources by

* Corresponding Author: mgurcan@firat.edu.tr
[1]Fırat University, Faculty of Science and Letters, Elazığ, Turkey.
ORCID: https://orcid.org/0000-0002-3641-8113,
E-Mail:halisdemir@firat.edu.tr, ORCID:https://orcid.org/0000-0003-2151-7917
E-Mail:ygural@firat.edu.tr, ORCID: https://orcid.org/0000-0002-0572-453X

GÜRCAN et al.

Modelling the Effect Size of Microbial Fuel Cells Using Bernstein Polynomial Approach via Iterative M...

making serious investment studies on renewable energy resources. In these resources, they generate energy from solar energy, wind energy and water. These efforts are very important breakthroughs to tackle the energy problem, in other words, the energy crisis. One of the renewable energy production sources is fuel cells. Fuel cells produce little or no gas emissions (such as SO_x, NO_x, CO_2 and CO) that pollute the environment. Therefore, fuel cells have a great advantage in terms of environmentalism. In addition, fuel cells have advantages such as high efficiency, no moving parts, and no noise pollution. Microbial fuel cells, one of the fuel cell types, are an emerging technology. Microbial fuel cells are bio-electrochemical devices that produce green energy by decomposing the waste biomass with bacteria [2].

Microbial fuel cell systems are a promising technology in terms of economy and environment. Full-scale applications in wastewater cleaning and electricity generation are still not possible due to difficulties such as biological contamination of electrodes and membrane surfaces, unstable and long-term performance, electrolyte resistance, reversible voltages and excessive potential increase [3].

Microbial fuel cells are electrical production systems that convert the chemical energy of organic substances directly into electricity by means of bacteria [4-6]. Organic matter and the bacteria that catalyze them are renewable energy systems, as long as there are anodes and cathode electrodes. Thus, it is possible to produce continuous electrical energy with microbial fuel cells [4-6]. Microbial fuel cells are mostly used in electricity generation, wastewater cleaning and biosensor applications [4-6]. The open-circuit voltage (Voc), short circuit current (Isc), voltage under load (V) and current (I) values of microbial fuel cells used in various applications do not correspond well with each other. This makes it difficult to predict future performance of applications for microbial fuel cells and therefore narrow the view of microbial fuel cells. This gives priority to the statistical modeling of microbial fuel cells. By performing statistical modeling, various parameters of microbial fuel cells and most importantly their performances will be obtained. Thus, calculations and visions related to microbial fuel cells will be generated more effectively.

2. SOME REMARKABLE NOTES ABOUT THE EXPERIMENT

In recent years, energy expenditure has tended to increase in the world. Energy resources are divided into three parts: fossil fuels, renewable resources and nuclear energy. Fossil fuels have an unfavorable influence on the environment due to carbon dioxide emissions. Expenditure of fossil fuels causes major problems such as global warming and atmospheric pollution. Therefore, it is stated that it will cause great problems for human life [7].

Since climate change is always a strong concern for the world, various efforts are never enough to resolve it. The International Energy Agency (IEA) proposed the 2 °C scenario (2DS) to deal with this problem. The 2DS has been widely examined by many researchers. According to this scenario, carbon dioxide (CO_2) emissions in 2060 should be reduced by 70% compared to 2014. 23% of the total CO_2 emissions come from the transportation sector. To achieve this goal, CO_2 consumption in transportation should be reduced. Nowadays, electric vehicles have become a hopeful option in transportation. However, biofuels are expected to be a key alternative energy source for CO_2 reduction in the transport sector. According to the results of the mobility model for 2DS published by the IEA, the biofuel and electricity share of total transport-fuel consumption by 2060 is estimated to be 30.7% and 27% respectively. To achieve these goals, biofuel production must be increased 10 times. Unfortunately, several major barriers to the realization of biofuels' implementation goal currently exist [8].

Despite all these, biomass-derived biofuels are used to directly generate energy. Biomass is used as a source of biofuels in microbial fuel cells (MFCs) and direct electricity is produced. MFCs are environmentally friendly electricity generation systems [9].

GÜRCAN et al.

Modelling the Effect Size of Microbial Fuel Cells Using Bernstein Polynomial Approach via Iterative M...

The chemical energy from the renewable carbohydrate structure of biomass and other organic wastes such as wastewater is an interesting alternative compared to the existing large fossil fuels. MFCs simultaneously produce both wastewater treatment and electrical energy [10].

MFCs have received great interest in recent years as a new renewable energy source. MFCs, which are regarded as direct bio-electrochemical reactors, use the redox reaction to produce direct electricity with microorganisms in the chemical energy in the biomass [9, 11].

In the literature, the principle of electrical energy production in MFCs has been examined in detail. Bacteria catalyze organic matter in biomass and release electrons (e-) and protons (H+). The released electrons go to the anode electrode. After, the electrons then travel from the anode electrode to the cathode electrode by an external circuit. The released protons go through the electrolyte to the cathode electrode. Oxygen (O_2) in the air, electrons (e^-) and protons (H^+) form water (H_2O) in the cathode. This ensures the electrical load balance of the MFC. As a result, oxidation reaction for anode and reduction reaction for cathode take place. Thus, the microbial fuel cell produces electrical energy as follows in Figure 1 [4-5].
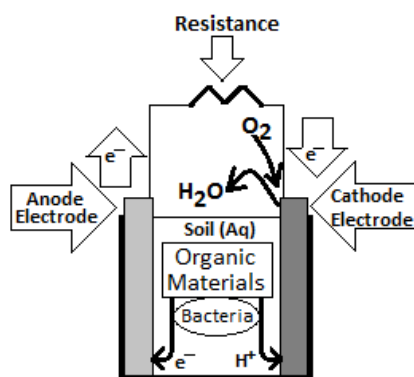
Figure 1 Operating principle of MFC at example study [4]

Biochemical and electrochemical reactions in MFCs are a complex and hybrid system. It is difficult to control and optimize the electrical power generation of MFCs. It is useful to establish a mathematical model to observe the power generation performance of MFCs [11].

3. STATISTICAL INFORMATION

Statistical methods are important scientific tools that provide a more effective and understandable presentation of the observed data. It is very important that the observed data is observed depending on time. The fact that the observed data varies over time and the character of this change is more accurate. Accordingly, it is important for the regression models whether the data are time-dependent or not. Regression models differ according to this situation.

Assuming that the time-dependent data generally comes from the same distribution, it is considered to be the realization of an appropriate stochastic process. It is important to create a stochastic process with continuous parameters that can represent the data. In many physical experiments, the creation of the stochastic process depending on the nature of the experiment allows more accurate interpretation of the observed experiment.

Let X_t be the observation value at time $t \geq 0$. Then, $X_1, \cdots, X_n$ are the realization of continuous parameter stochastic process $\{X_t : t \geq 0\}$. Discrete parameter stochastic process $\{X_n : n = 0, 1, \cdots\}$ is called the embedding process in $\{X_t : t \geq 0\}$.

4. METHOD

In experimental studies, modeling of the observations made in equal time periods is very important in evaluating the data obtained from the study. In general, this type of observation is examined in two groups. When data have an increasing structure due to observation order, observation values are considered as growth data and growth models are used in data analysis. On the contrary, time series models are used when data does not have an increasing structure. Depending on the type of methods used in examining time series, the model cannot always give the optimal estimate.

GÜRCAN et al.

Modelling the Effect Size of Microbial Fuel Cells Using Bernstein Polynomial Approach via Iterative M...

The model that shows the best fit among the equally spaced regression models is generally the Bernstein polynomial. Bernstein polynomial as follows [12],

$$B_n(y) = \sum_{k=0}^{n} \binom{n}{k} y_k x^k (1-x)^{n-k} \qquad (1)$$

where $y_0, \cdots, y_n$ are observation values.

Since the kernel structure of the polynomial is similar to the binomial distribution, the Bernstein polynomial can also be expressed as the expected value of the binomial distribution. The convergence characteristics of Bernstein polynomial have been studied by many researchers such as Voronovskaya [13], Butzer [14] and Phillips [15] in the literature. Kelisky and Rivlin [16], Sahai [17] who researched the iterative calculation process in the Bernstein model are the major authors in the literature related to the subject.

The method used for the iterative calculation is based on the formation of a new Bernstein polynomial by using the error terms obtained from the polynomial formed with the help of observation values. The iterative calculation formula, after estimating the error in the first step, the estimation values of the errors are subtracted from the estimated values of the data and new estimation values are generated for the data. As follows,

$$B_n^{(r+1)}(y) = B_n^{(r)}(y) - B_n\left(B_n^{(r)}(y) - y\right) \qquad (2)$$

5. INVESTIGATION OF DATA

The observation values obtained from the experiment are shown in the table 1 (Appendix). The correlation calculated between the measured short-circuit current and the measured current when loaded is 0.84. In this case, there is an 84% relationship between them. The linear equation of the open-circuit voltage according to time is obtained as follows when three median methods are used,

$$V_{oc} = 0.516 - 0.007t \qquad (3)$$

In the analysis of decrease of open-circuit voltage according to time, the use of three median methods instead of the least squares estimation method is more useful in terms of obtaining linear equation. Three median methods can minimize errors due to measurement.

The effect size (fill factor) of MFC was evaluated by $f = P_{max}/(I_{sc} * V_{oc})$, where $P_{max} = VR * IR$ [18].

Effect size is defined as the ratio of real maximum power to theoretical maximum power. The closer the real power is to the maximum power, the more efficient the system. Measurement and estimation values of the effect size values obtained from the data in table 1 (Appendix) and their graphs are available below
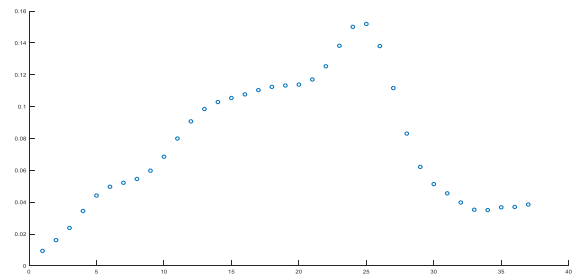
Figure 2 Graph of observed effect size values according to time
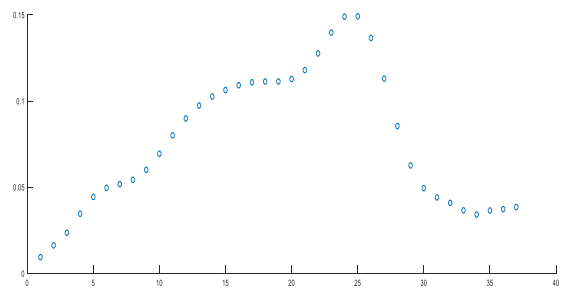
Figure 3 Graph of estimated effect size values according to time

6. CONCLUSIONS

The need for renewable energy sources is increasing day by day. Undoubtedly, today's science stands sensitively on this subject with all

GÜRCAN et al.

Modelling the Effect Size of Microbial Fuel Cells Using Bernstein Polynomial Approach via Iterative M...

its resources. Investigation of different renewable energy sources is one of the most important issues of modern science. Examining the performance of a renewable energy source is very important for identifying where it can be used and for the development of the energy source.

Since effect size is designed as the ratio of maximum power to theoretical power, it is an important indicator for energy generators. The performances of energy generators can be evaluated in real terms according to this parameter. The reason for this is related to the biofilm formation process in the anode electrode of the bacteria in the structure of the MFC and the catalysis reactions of the bacteria. When the MFC is at maximum efficiency, the effect size also reaches its maximum value. Maintaining efficiency varies depending on the surface

structure of the electrode and the state of bacteria sustaining the catalysis reaction.

In this study, the performance of microbial fuel cells which is a renewable energy source has been tried to be analyzed statistically. In the experiment, the effect sizes obtained from the battery produced by using microbial fuel cells were modeled according to time and the effect size plot was formed. Change of effect size according to time can be examined easily with this model.

APPENDİX

Table 1
Obtained measurement values

Day	VOC (V)	ISC (µA)	VR (V)	IR (µA)	Effect Size	Estimated Effect Size
1	0.75	14	0.009	11	0.0094	0.0094
2	0.6875	21	0.01475	15.75	0.0162	0.0163
3	0.625	28	0.0205	20.5	0.0238	0.0236
4	0.5625	35	0.02625	25.25	0.0345	0.0346
5	0.50	42	0.032	30	0.0442	0.0444
6	0.495	40.5	0.032	30.5	0.0497	0.0497
7	0.49	39	0.032	31	0.0522	0.0518
8	0.485	27.5	0.032	31.5	0.0546	0.0543
9	0.48	36	0.032	32	0.0598	0.0601
10	0.48	45.75	0.039	39	0.0685	0.0694
11	0.48	55.5	0.046	46	0.0800	0.0802
12	0.48	65.25	0.053	53	0.0908	0.0899
13	0.48	75	0.060	60	0.0985	0.0974
14	0.48	77.75	0.062	61.75	0.1029	0.1027
15	0.48	80.5	0.064	63.5	0.1054	0.1064
16	0.48	83.25	0.066	65.25	0.1077	0.1092
17	0.48	86	0.068	67	0.1104	0.1109
18	0.4825	89.5	0.06975	69.25	0.1124	0.1114
19	0.485	93	0.0715	71.5	0.1133	0.1114
20	0.4875	96.5	0.07325	73.75	0.1139	0.1128
21	0.49	100	0.075	76	0.1170	0.1180
22	0.4775	109.25	0.08075	81.5	0.1253	0.1277
23	0.465	118.5	0.08650	87	0.1382	0.1398
24	0.4525	127.75	0.09225	92.5	0.1501	0.1490
25	0.44	137	0.098	98	0.1519	0.1492
26	0.44	121.5	0.08475	84.75	0.1380	0.1366
27	0.44	106	0.0715	71.5	0.1116	0.1131
28	0.44	90.5	0.05825	58.25	0.0831	0.0855
29	0.44	75	0.045	45	0.0621	0.0627
30	0.45	86.25	0.045	45	0.0514	0.0494
31	0.46	97.5	0.045	45	0.0456	0.0441
32	0.47	108.75	0.045	45	0.0398	0.0409
33	0.48	120	0.045	45	0.0353	0.0366
34	0.47	108	0.042	43	0.0350	0.0342
35	0.46	96	0.039	41	0.0368	0.0365
36	0.45	84	0.036	39	0.0370	0.0373
37	0.44	72	0.033	37	0.0385	0.0385

GÜRCAN et al.

Modelling the Effect Size of Microbial Fuel Cells Using Bernstein Polynomial Approach via Iterative M...

The Declaration of Conflict of Interest/ Common Interest

No potential conflict of interest was reported by the authors.

The Declaration of Ethics Committee Approval

Ethics Committee Approval is not required.

The Declaration of Research and Publicatıon Ethics

In the writing process of this study, international scientific, ethical and citation rules have been followed.

Authors' Contribution

The authors contributed equally to the study.

The Declaration of Research and Publication Ethics

The authors of the paper declare that they comply with the scientific, ethical and quotation rules of SAUJS in all processes of the paper and that they do not make any falsification on the data collected. In addition, they declare that Sakarya University Journal of Science and its editorial board have no responsibility for any ethical violations that may be encountered, and that this study has not been evaluated in any academic publication environment other than Sakarya University Journal of Science.

REFERENCES

[1] G. Palanisamy, H. Jung, T. Sadhasivam, M. D. Kurkuri, S. C. Kim, S. Roh, "A comprehensive review on microbial fuel cell technologies: Processes, utilization, and advanced developments in electrodes and membranes", Journal of Cleaner Production, vol. 221, pp. 598-621, 2019.

[2] M. Rahimnejad, A. Adhami, S. Darvari, A. Zirepour, S. Oh, "Microbial fuel cell as new technology for bioelectricity generation: A review," Alexandria Engineering Journal, vol. 54, no. 3, pp. 745-756, 2015.

[3] M. Abdallah, S. Feroz, S. Alani, E. T. Sayed, A. Shanableh, "Continuous and scalable applications of microbial fuel cells: a critical review," Rev Environ Sci Biotechnol, vol. 18, pp. 543–578, 2019.

[4] N. Çek, "Examination of Zinc Electrode Performance in Microbial Fuel," Gazi University Journal of Science, 30, pp. 395–402, 2017.

[5] N. Çek, "Parçacıklar ve Enerji Kaynakları," Lambert Academic, pp. 348, 2016.

[6] S. B. Velasquez-Orta, D. Werner, J. C. Varia, S., Mgana, "Microbial fuel cells for inexpensive continuous in-situ monitoring of groundwater quality," Water Research, vol. 117, pp. 9-17, 2017.

GÜRCAN et al.

Modelling the Effect Size of Microbial Fuel Cells Using Bernstein Polynomial Approach via Iterative M...

[7] M. Rahimnejad, A. Adhami, G. Najafpour, S. Darvari, A. Zirepour and S. Oh, "Microbial fuel cell as new technology for bioelectricity generation: A review," Alexandria Engineering Journal, vol. 54, pp. 745–756, 2015.

[8] Y. K. Oh, K. R. Hwang, C. Kim, J. R. Kim, J. S. Lee, "Recent developments and key barriers to advanced biofuels: A short review," Bioresource Technology, vol. 257, pp. 320-333, 2018.

[9] A. Erensoy, N. Çek, "Alternative Biofuel Materials for Microbial Fuel Cells from Poplar Wood," Chemistry Select, vol. 3, pp. 11251–11257, 2018.

[10] E. T. Sayed, M. A. Abdelkareem, "Yeast as a Biocatalyst in Microbial Fuel Cell," Old yeasts-new questions, Intech, 2017.

[11] C. Xia, D. Zhang, W. Pedrycz, Y. Zhu, Y. Guo, "Models for Microbial Fuel Cells: A critical review," Journal of Power Sources, vol. 373, pp. 119–131, 2018.

[12] O. Szasz, "Generalization of S. Bernstein's polynomials to infinite interval," Journal of Research of the National Bureau of Standards, vol. 45, pp. 239–244, 1950.

[13] E. Voronovskaya, "D´etermination de la forme asymptotique d'approximation des fonctions par les polyn^omes de M. Bernstein," Doklady Akademii Nauk SSSR, pp. 79-85, 1932.

[14] P. L. Butzer, "Linear combinations of Bernstein polynomials," Canadian J. Math., vol. 5, pp. 559-567, 1953.

[15] G. M. Phillips, "On generalized Bernstein polynomials," In Approximation and optimization, vol. 1, pp. 335-340, 1996.

[16] R. P. Kelisky and T. J. Rivlin, "Iterates of Bernstein polynomials," Pacific J. Math., vol. 21, pp. 511–520, 1967.

[17] A. Sahai, "An iterative algorithm for improved approximation by Bernstein's operator using statistical perspective," Appl. Math. Comput., vol. 149, pp. 327-335, 2004.

[18] Z. He, N. Wagner, D. S. Minteer, and L. T. Angenent, "An Upflow Microbial Fuel Cell an Interior Cathode: Assessment of the Internal Resistance by Impedance Spectroscopy," Environ. Sci. Technol., vol. 40, pp. 5212-5217, 2006.

Sakarya University Journal of Science
SAUJS

Title: Interaction and Characterization of The Triarylmethane Dye Bromophenol Blue with CdSeTe Quantum Dots

Authors: Erdem ELİBOL,Tuna DEMİRCİ

Interaction and Characterization of The Triarylmethane Dye Bromophenol Blue with CdSeTe Quantum Dots

Erdem ELİBOL [*1], Tuna DEMİRCİ [2]

Abstract

The use of hybrid associates in biological, optoelectronics and energy fields are increasing day by day. In this context, in this study, CdSeTe Quantum dots (QD): Bromophenol Blue (BPB) hybrid associates were studied for the first time in the literature and their spectroscopic characterizations were examined. In the study, CdSeTe QDs were synthesized with trioctylphosphine (TOP) ligands by hot injection method, and it was planned that the BPB would passivate the surface of the QD by interacting with the TOP ligand of the CdSeTe QDs. CdSeTe QD: BPB hybrid associates were prepared in different concentrations, and the effects of QD: BPB ratios on absorbance and emission characterizations were examined. Structures have been characterized using Uv-vis, PL, ICP-OES and FTIR. With the results found, the predictive mechanism has been put forward.

Keywords: CdSeTe QDs; bromophenol Blue; hybrid associate; emission; absorption

1. INTRODUCTION

Organic dyes have become an indispensable part of industrial applications, especially in many areas of daily life. They have a lot of advantages with their bright colours, easy applicability and colour sensitivity [1]. The main factor that determines the usage areas of organic dyes is their optical properties. In recent years, it has been shown that using hybrid associates can be beneficial both in order to increase the optical properties of organic dyes and to increase the areas of use [2,3]. For this reason, studies on hybrid associates of semiconductor nanocrystals (QDs) and organic dyes are increasing rapidly. These hybrid associates are highly related not only to the optical properties of their components, QD and dye, but also to the new characterization results resulting from the resulting composition [4]. So much so that hybrid associates can find application areas in many fields such as optoelectronic [5], biological imaging [6] and energy [7]. Stimulated electron transfer in hybrid associates plays an important role in the formation of these structures. In hybrid associates, QDs often act as donors, especially in associations in the aquatic environment. On the other hand,

---

* Corresponding Author: tunademirci@duzce.edu.tr
[1] Duzce University, Faculty of Engineering, Department of Electrical Electronics Engineering, Duzce, Turkey, ORCID: https://orcid.org/0000-0001-8933-4944
[2] Duzce University, Scientific and Technological Research on Application and Research Center, Duzce, Turkey, E-mail: erdemelibol@duzce.edu.tr, ORCID: https://orcid.org/0000-0003-0328-5534

Erdem ELİBOL,Tuna DEMİRCİ

Interaction and Characterization of The Triarylmethane Dye Bromophenol Blue with CdSeTe Quantum Dots...

organic dyes mostly take the role of acceptor [8]. At this process photon-induced charge transfer or irradiated energy transfers play a fundamental role.

Quantum dots have many advantages over bulk semiconductor materials with their unique optical and electronic properties. The energy levels of QDs, which are under the influence of quantum confinement in all three dimensions, turns from continuous to discrete [9]. This ensures that the QDs have adjustable energy band gap according to their size [10]. This feature paves the way for the quantum dots to be synthesized in the required absorbance and emission properties [11]. QDs have also started to be used in many fields with their multiple exciton production, easy and cheap production capacities, stability and high stability [12–14]. One of the main reasons for QDs to create hybrid associates with organic dyes is due to their long PL lifetime times and their ability to donor and adjust their absorbance and emission characteristics [15].

The optical properties of QD/organic dye hybrid associates have been investigated in many studies in the literature. Smirnow et al studied on CdS, passivized with TGA and Europium 1, 3-Diketonate, and methylene blue dye (MB) hybrid associate. In their study, it was observed that the maximum point of the absorbance peak did not shift with the addition of MB, but there was a 10-15% increase at the Full Width at Half Maximum (FWHM). In addition, nonradiative excitation energy transfer has been determined from Eu3+ and CdS QD to MB [16]. Rakovich et al. also worked on hybrid associates consisting of methylene blue and TGA capped CdTe QDs. As the amount of MB added to a fixed amount of CdTe solution increased, a decrease in absorbance was observed. They also showed that there was a certain electrostatic interaction between MB and QD while dimerization processes were observed due to the addition of MB. With their study, it has been shown that the efficiency of a light sensitive dye can be increased by using QDs. Orlova et al worked on hybrid associates consisting of CdTe QD / Sulfophthalocyanine molecule and similar luminescence quenching was detected. In this study, it was stated that PL quenching resulted

from FRET mechanism [17]. Ovchinnikov et al found that in their study for CdS QD / methylene blue hybrid associates, CdSQDs behave as donors. However, it was found that dimerization increases as MB increases in the mixture formed with QD [18].

Bromophenol blue (BPB), which is one of these anionic dyes, is an acid organic dye, but it is used for especially in textile products [19], biological applications [20], and cosmetics [21], monitoring electrophoresis processes. However, it has recently been used as a photosensitizer material in dye-sensitive solar cells [22]. Bromophenol blue (BPB), is used in polyacrylamide gel electrophoresis and agarose gel electrophoresis processes due to its most commonly used electrophoretic colour marker feature. The main reason for this is that, since the structure contains a low density negative charge in the neutral close pH, it performs linear progress with DNA during the electrophoresis process. In addition to this feature, many drugs are used as colour markers in the UV analysis of the active substance [23]. If it is necessary to give examples, examples such as Atorvastatin Calcium [23], Ofloxacin [24], Levetiracetam [25] can be given. Still exploiting this property Beryllium [26], Calcium/Magnesium [27] being used in quantitative analysis of structures.

However, a study in which BPB is studied as QD/BPB hybrid associates is not available in the literature. For the QD/Dye hybrid associate, alloy CdSeTe QDs were preferred specifically for this study. Alloy CdSeTe QDs have the potential to be synthesized more precisely with their 3-component structures in a wider absorbance range to other QDs. However, according to many QDs, it is possible to synthesize them to cover the entire spectrum of the sunlight [28]. In this study, optical properties of CdSeTe QD / BPB hybrid associates were tested. Absorbance characterization and PL characterizations were studied depending on both QD and BPB. In the study, FT-IR analyses were done to make sense of the interactions of the mixes.

Erdem ELİBOL, Tuna DEMİRCİ

Interaction and Characterization of The Triarylmethane Dye Bromophenol Blue with CdSeTe Quantum Dots...

2. MATERİALS AND METHOD

2.1. Materials

Technical-grade trioctylphosphine (TOP, 90 %), trioctylphosphine oxide (TOPO, 99 %), cadmium oxide (CdO, 99 %), selenium powder (Se, 99 %), tellurium powder (Te, 99 %), 1-tetradecyl phosphonic acid (TDPA, 99 %), 1-Octadecene technical grade (ODE, 90 %), Bromophenol blue (BPB, 99 %).

2.2. Synthesis of CdSeTe QDs

In this study, alloy CdSeTe QDs were performed based on the method proposed by Debnath et al [29]. Minor changes were made in the applied method.

For synthesising the alloy CdSeTe firstly Cd, TOP-Se and TOP-Te precursors must be ready in at three different 3-neck flasks. For TOP-Se precursors Se (0.019 g, 0.25 mmol), TOP (0.57 ml) and ODE (1.25 ml) were mixed in 3-neck flasks while Te (0.011 g, 0.085 mmol), TOP (0.57 ml) and ODE (1.25 ml) were mixing for have TOP-Te precursors. After TOP-Se and TOP-Te were heated to 70°C and 200°C respectively. When precursors were ready TOP-Se was ınjected to TOP-Te precursors fastly for have TOP-Se-Te precursors. At the same time for prepare the Cd precursors, CdO (0.013g, 0.095 mmol), TDPA (0.075 g, 0.27 mmol), TOPO (1 g, 2.098 mmol) were mixed in ODE (2.5 ml). The solution was heated to 300°C and kept at this temperature until the clear solution had seen. When all precursors were ready, TOP-Se-Te precursors were injected in Cd precursors and the solution kept at the 260°C. At this temperature CdSeTe QDs were growing with time and solutions were taken at different grown times. Alloy CdSeTe QDs were washed with methanol and centrifuged and dissolved in chloroform for using. Synthesized steps of CdSeTe QDs are showed at Figure 1 and images of synthesized CdSeTe QDs in daylight and fluorescent light are shown in Figure 2.
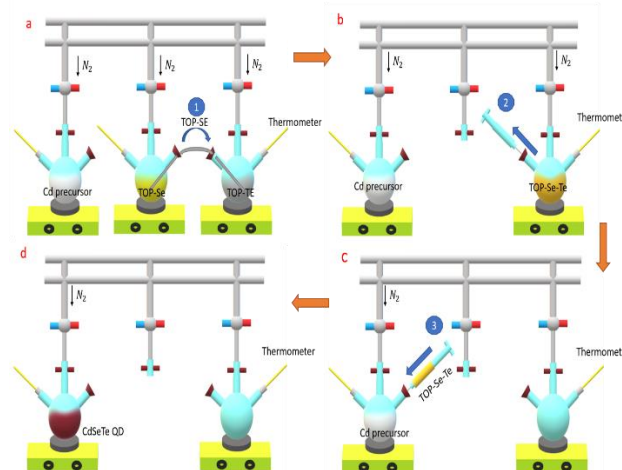
Figure 1 Synthesized steps of CdSeTe QDs.

2.3. Preparing Bromophenol Blue

Bromo phenol blue 0.669 g (0.01 mmol) is taken as main stock and completed with 50.0 ml of chloroform. The prepared main stock solution displays a colourless appearance.
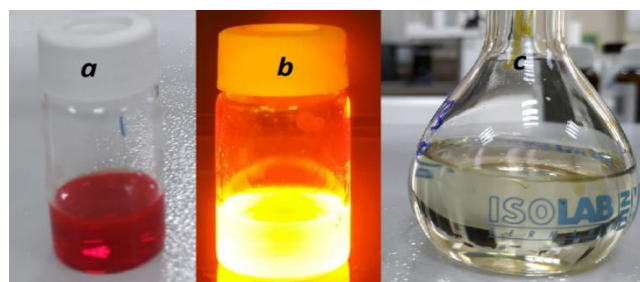
Figure 2 a) Image of CdSeTe QD under sunlight, b) image of CdSeTe QDs under florescent light, c) bromophenol blue solution in chloroform.

2.4. Sample Preparation

Bromophenol blue colourless solution was mixed with 100 ul withdrawn CdSeTe QD solution in various concentrations. The final concentration was used as about 1.0×10^{-4} M. CdSeTe QD solution molarity calculation by ICP-OES analysis. This result was shown CdSeTe QD concentration 2.0×10^{-6} M.

Erdem ELİBOL, Tuna DEMİRCİ

Interaction and Characterization of The Triarylmethane Dye Bromophenol Blue with CdSeTe Quantum Dots...

Table 1.
Concentrations and mixing ratios in CdSeTe QD: BPB hybrid associate.

QD:BPB ratio	CdSeTe QD concentration (M)	BMB concentration (M)
0:1	-	1.0×10^{-4} M
0.5:1	2.0×10^{-6}	1.0×10^{-4} M
1:1	4.0×10^{-6}	1.0×10^{-4} M
2:1	8.0×10^{-6}	1.0×10^{-4} M
3:1	16.0×10^{-6}	1.0×10^{-4} M
4:1	64.0×10^{-6}	1.0×10^{-4} M
1:0	4.0×10^{-6}	-
1:0.25	4.0×10^{-6}	2.5×10^{-5} M
1:0.5	4.0×10^{-6}	5.0×10^{-5} M
1:1	4.0×10^{-6}	1.0×10^{-4} M
1:2	4.0×10^{-6}	2.0×10^{-4} M
1:3	4.0×10^{-6}	3.0×10^{-4} M

Images of CdSeTe QD/BPB hybrid associates prepared at different concentration ratios are shown in Figure 3 under daylight (Figure 3-A) and fluorescent light (Figure 3-B).

Figure 3 Image of CdSeTe QD/ BPB hybrid associates samples A) under sunlight, B) under florescent light. a-h shows the different ratio of hybrid associates QD: BPB , a) 100:0, b) 1:0, c) 1:0.25, d)1: 0,5, e) 1: 1, f)1:2, g) 1:3, h) 0:3.

2.5. Characterization

Absorption spectra of hybrid associates prepared in the study were tested using UV-1800 Shimadzu UV Spectrometer. It was chosen as the scanning range between 230-800 nm. It is known that bromophenol blue can give absorbance peaks in the range of 230-600 nm [30]. Absorption spectra scans for CdSeTe QD/BPB hybrid associates were performed based on their mixtures in different concentrations given in Table 1. Similarly, emission spectra scans of QD/BPB hybrid associates prepared with freshly synthesized CdSeTe QDs throughout the study were performed with Edinburgh Instruments FLS1000 Spectrometer. Emission scanning was performed in the range of 300-800 nm and excitation wavelength was preferred as 380 nm. The absorption and emission characteristic curves obtained were drawn with Origin Pro 8 and FWHM values were calculated again with this program.

Fourier transform infrared (FTIR) spectra of bromophenol blue and CdSeTe QD were recorded with ATR Attached Shimadzu IR Prestige 21 spectrometer. Spectrum was performed between 400-4000 nm and 32 scans. Metal contents of bromophenol blue and CdSeTe QD were measured on a Perkin Elmer 200 Avio ICP OES.

Erdem ELİBOL, Tuna DEMİRCİ

Interaction and Characterization of The Triarylmethane Dye Bromophenol Blue with CdSeTe Quantum Dots...

3. RESULTS and DISCUSSION

3.1. Absorption Spectra

Absorption analyses for the prepared QD / BPB hybrid associates were evaluated in two parts. In the first part, while the BPB concentrations in the hybrid associates were kept constant, the amount of QD added was gradually increased and changes in the absorption spectrum were followed. In the second part, the amount of BPB added was gradually increased by keeping the QD concentrations in the hybrid associates constant. With the study, the role of QD, which is usually a donor in the literature [31], and the absorption characterizations of the hybrid associate have been investigated. Remarkable results were obtained in both stages.

The absorption characteristic obtained in the first stage, where the BPB concentration in the hybrid associates is constant, is shown in Figure 4. The initial absorption peak of CdSeTe QDs, which were also added to hybrid associates, was calculated as 584 nm as shown in the bottom right figure in Figure 4. On the other hand, although the absorption of BPB used in hybrid associate comes at 410 nm levels (up right figure in Figure 4), it is not possible to obtain a clear absorption value of BPB which is very transparent in chloroform. With the addition of QDs into the hybrid associate, there was a marked increase in the BPB absorption peak. While the amount of BPB in the hybrid associates is constant, the addition of QDs showed a marked increase at the point where the absorbance peak of the BPB was present. Thus, while the maximum absorbance point of the reference BPB (0:1) was 0.1, the absorbance point increased 22.5 times and was observed as 2.25 with the addition of CdSeTe QD (half the concentration of BPB (0.5:1)) into the hybrid associate. Similarly, as the amount of QD added was increased, the increase in absorbance continued and the absorbance peak reached its maximum (2.6) with a mixture of 3:1. The QDs added (4:1) to the hybrid associate after this stage did not cause a change in the BPB peak at 408 nm, even though the absorbance peak of QD at 584 nm continued to increase minimally. Even if the ratio of QD: BPB in the hybrid associates varies, no

obvious changes were observed in the wavelengths of the absorbance peak. This is an indication that there are no major chemical changes with the mixture. However, it is thought that there may be electrostatic attraction between QD and BPB [32], and the obvious increase in the absorbance peak is due to this interaction. It is also deducted that the QDs added to the hybrid associate cause dimerization in BPB and cause a marked increase in the maximum point at the peak [33].

Figure 4 Absorbance spectra for hybrid associates prepared at different QD: BPB ratios where the BPB concentration is constant.

In the second stage, the absorbance characterization of hybrid associates prepared with different ratio of QD:BPB at constant CdSeTe QD concentration is shown in Figure 5. The absorbance spectra images for the reference samples with QD: BPB ratios 1:0 and 0:1 are given in the upright figure in Figure 4 and bottom right at Figure 5 respectively, since the absorbance maximum peak points were quite small. As can be understood from the figure at the upright in Figure 5, the absorbance peak of CdSeTe QDs with a QD: BPB ratio of 1:0 has reached 584 nm. With the increase in the BPB rate in the hybrid associate, it started to increase at the maximum peak point. When the QD: BPB ratio was 1:3, the maximum peak of the hybrid associate increased to 40 times the absorbance maximum peak of the BPB reference sample. An increase in the FWHM values of the absorbance peaks was observed, equivalent to an increase in the absorbance peak points. Although the amount

Erdem ELİBOL, Tuna DEMİRCİ

Interaction and Characterization of The Triarylmethane Dye Bromophenol Blue with CdSeTe Quantum Dots...

of QDs in the hybrid associate is constant, minimal increases were observed in the absorbance peak of QD, as seen in the lower right corner of Figure 5. This is thought to be caused by the fact that QDs increase the absorbance feature by the interaction of TOPO ligands present on the surfaces of CdSeTe QDs and Br ions in BPB. There are case studies in the literature where ions such as Cl, Br and I have been used to treat surface ligands of QDs [34]. Here, although surface treatment is not applied with Br ions on its own, it can be considered that Br ions interact with the surface of the QD.

While the amount of QDs in the CdSeTe QD:BPB hybrid associate is constant, it is expected that the absorbance will increase depending on the amount of BPB [17]. However, when comparing both absorbance graphs (Figure 4 and Figure 5), the QD: BPB hybrid associate has an absorbance value much higher than the BPB and QD's individual absorbance values.

Figure 5 Absorbance spectra for hybrid associates prepared at different QD: BPB ratios where the CdSeTe QD concentration is constant.

3.2. Emission Spectra

The as in the absorbance study, emission characterization studies were also carried out in two stages. Similarly, emission studies were carried out due to keeping the QD and BPB amounts in the hybrid associate constant, respectively. The normalized emission characterization for the hybrid associates obtained in the first stage, namely by keeping the BPB constant and increasing the amount of CdSeTe QDs, is shown in Figure 6. The emission characterization for the hybrid associates obtained in the first stage, namely by keeping the BPB constant and increasing the amount of CdSeTe QDs, is shown in Figure 6. As can be seen from the bottom left of Figure 6, the QD:BPB ratio is 0:1, that is, the emission value for BPB is shown. On the contrary, for the 1:0 ratio, the emission peak of CdSeTe QD is shown in Figure 6. The increase in the amount of CdSeTe QD in the hybrid associate naturally caused an increase in the luminescence peak [30]. When the hybrid associate is 1:0, the emission peak of QD is close to around 605 nm. As the ratio of QD in it decreased, the emission peak of QD shifted to 601 nm as seen at Figure 5. The 4 nm blue shift in the emission peak can be associated with the measurement sensitivity errors in the emission peak, and the continuity of this blue shift process has been determined by repeated analysis. This situation can be interpreted as that the long TOPO ligands of the QDs interact with the BPB, causing the QD to be partially passivated and the emission peak to blue. Another remarkable factor in Figure 6 is the decreasing amount of CdSeTe QDs, causing a noticeable change in the FWHM of the luminescence peak. Such that while the FWHM value of the emission peak of QD at 1:0 was 37.89 nm, the FHWM increased up to 38.28 nm with a ratio of 0.5:1. Partial increases in the emission peak of the BPB were observed with increasing QD in the hybrid associate ratio. This situation can be interpreted as the increase in the amount of QD present in the hybrid associate as a donor in the mixture causes an increase in the emission peak of the acceptor BPB [31][32].
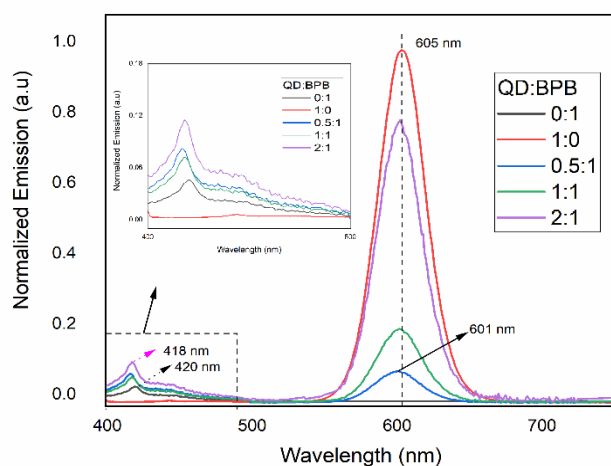
Erdem ELİBOL, Tuna DEMİRCİ

Interaction and Characterization of The Triarylmethane Dye Bromophenol Blue with CdSeTe Quantum Dots...
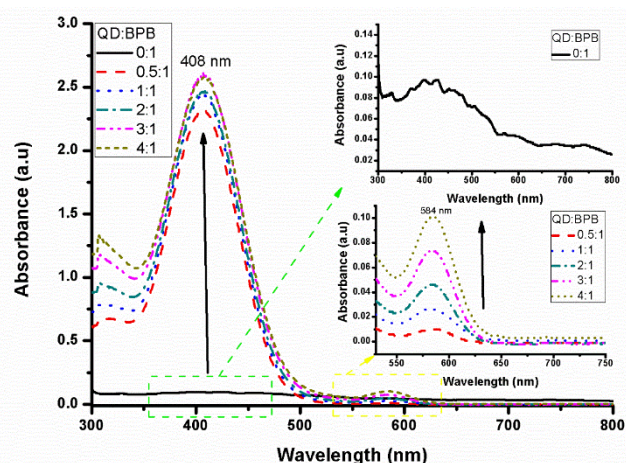

Figure 6 Normalized *Emission spectra for hybrid associates prepared at different QD: BPB ratios where the BPB concentration is constant.*

In the second stage of the emission characterization study, while the amount of QD in the CdSeTe QD:BPB hybrid associate was kept constant, the amount of BPB was gradually increased and the emission graph obtained is given in Figure 7. In the study, quenching in luminescence started to appear with the increase amount of BPB in the hybrid associates. With the luminescent quenching process the peak length, 1 for QD:BPB ratio was 1:0, started to be minimalized. However, with the increase in the amount of BPB, the wavelength of the luminescence peak shifted towards blue up to 6 nm, while the luminescence peak FWHM values increased in proportion to the increase in BPB. In fact, while the FWHM value for 1:0 was 37.28 nm, this value increased to 45.72 nm for 1:3.

Although bromophenol blue has not been used in any hybrid associate studies before, it is known that when different types of hybrid associates are examined in the literature [3,18,31], such quenching occurring in luminescence is mainly caused by Forster resonance energy transfer (FRET) or charge transfer. In the emission spectrum, quenching at the luminescence peak of CdSeTe QD suggests that CdSeTe QDs function as donors in the hybrid associate. Similarly, a partial increase in the luminescence peak of BPB can be expected, as can be seen at Figure 6 and Figure 7. This indicates that the quenching mechanism in CdSeTe QD:BPB hybrid associate is due to FRET. The data obtained indicate that

the CdSeTe QD:BPB hybrid associate can be used in solar energy systems, applications where electrochemical processes are required, in sensors and imaging areas. In fact, load transfer transitions between components are very important in terms of efficiency of these mechanisms.
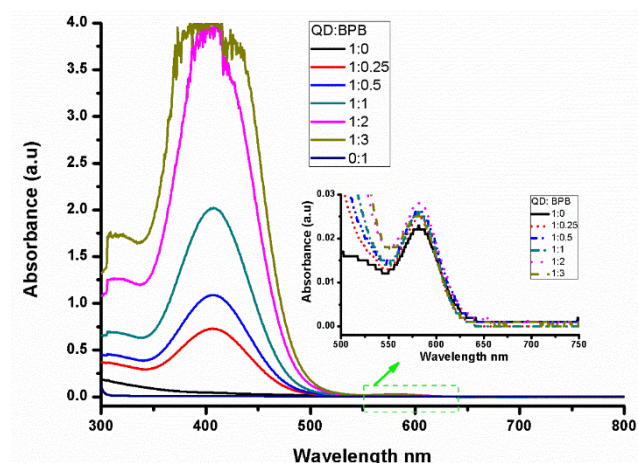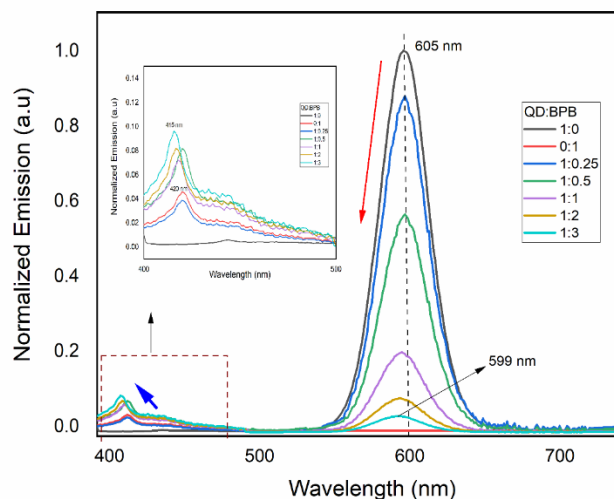

Figure 7 Normalized *Emission spectra for hybrid associates prepared at different QD:BPB ratios where the CdSeTe QD concentration is constant.*

3.3. FT-IR Spectra

FT-IR spectra of the CdSeTe QD structure synthesized into the TOPO substrate are shown in Figure 8. Firstly, when the structure was examined against the trioctylphosphine oxide (TOPO) spectrum, CH_2 vibrations at 2945 cm^{-1} showed a progress towards a lower frequency thanks to the coated layer surface. Similarly, when the vibrations at 1450 cm^{-1} were examined, the asymmetric and symmetrical vibrations of the P=O were also observed. This observation shows that the TOP structure enters the structure by interacting with Cd^{+2} ions located on the outer surfaces of CdSeTe QD. The shear vibration of the methylene (CH_2) shear vibration of the CdSeTe QD structure was observed at 750 cm^{-1} and 735 cm^{-1} between Cd^{+2} and the Se^{+2} and Te^{+2} ions, confirming the realization of CdSeTe QDs. Looking at the Bromo Phenol blue and CdSeTe spectrum, it corresponds to the C-H release and tensile vibration of the Bromo phenol blue groups at 1190 cm^{-1} and 1225 cm^{-1}. S-O stretching

Erdem ELİBOL,Tuna DEMİRCİ

Interaction and Characterization of The Triarylmethane Dye Bromophenol Blue with CdSeTe Quantum Dots...

vibration and S=O symmetrical stretching vibrations within the bromophenol blue structure of the QD's structure of the peaks coming around approximately 750 cm^{-1} and 1194 cm^{-1} increased. This has shown that the interaction is stronger with the QD and sulphate groups, but low level interaction with the hydrogen of the ring.
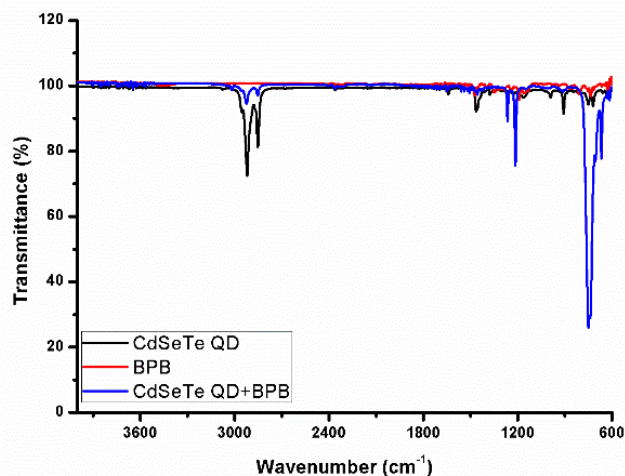
Figure 8 *FT-IR spectra for hybrid associates prepared at different QD:BPB (1:1) ratios*

The main reason for the transformation of yellow colour is the interaction between bromophenol blue and quantum dots. When viewed in FT-IR spectra, it is thought that the strength of S-O and S=O and 750 cm^{-1} and 1184 cm^{-1} vibrations, the intensity of the C-H peak coming around 1190 cm^{-1} and the visually the colour shift from yellow to low pH. Looking at the Uv-Vis spectra, Bromophenol blue appears to show a very low 425 nm in dichloromethane, while a QDs are added to a high absorbance of about 408 nm. In other words, it is thought that the way of interaction is estimated.
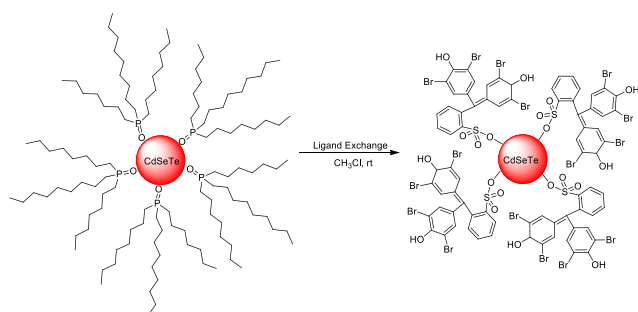
Figure 9 Q.dot-BPB interaction in QD:BPB (1:1) ratios

4. CONCLUSION

The spectroscopic characterization of CdSeTe:BPB hybrid associates has been studied in this study. The study has been examined in two basic stages. In the first stage, QD: BPB concentration was kept constant in the BPB hybrid associate and the amount of QD concentration in the solution was gradually increased and its spectroscopic characterizations were examined. The remarkable factor at this stage is the increase in BPB absorbance peak length with the addition of minimal QD. In the second stage, this time QD concentration was kept constant while the amount of BPB was changed. As a result of the study, it was determined that quenching occurred in the luminescence peak according to the amount of BPB added to the constant QD concentration. This led to the conclusion that while CdSeTe QDs act as donors in the associate, BPB acts as an acceptor and the FRET mechanism is active. As a result, CdSeTe QD:BPB shows that hybrid associate can be used especially in solar cells, biosensors and optoelectronic devices based on electron transfer. The enormous increase in absorbance peak, however, promises that CdSeTe QD: BPB can be used in the textile and cosmetic industries.

REFERENCES

[1] K. Hunger, Industrial Dyes: Chemistry, Properties. 2003.

[2] H. Xu, X. Huang, W. Zhang, G. Chen, W. Zhu, and X. Zhong, "Quantum dots acting as energy acceptors with organic dyes as donors in solution," ChemPhysChem, 2010.

[3] A. R. Clapp, I. L. Medintz, J. M. Mauro, B. R. Fisher, M. G. Bawendi, and H. Mattoussi, "Fluorescence Resonance Energy Transfer between Quantum Dot Donors and Dye-Labeled Protein Acceptors," J. Am. Chem. Soc., 2004.

[4] M. S. Smirnov et al., "Control of direction of nonradiative resonance energy transfer in hybrid associates of colloidal Ag2S/TGA

Erdem ELİBOL,Tuna DEMİRCİ

Interaction and Characterization of The Triarylmethane Dye Bromophenol Blue with CdSeTe Quantum Dots...

QDs with thionine molecules," J. Nanoparticle Res., 2019.

[5] M. F. Frasco, V. Vamvakaki, and N. Chaniotakis, "Porphyrin decorated CdSe quantum dots for direct fluorescent sensing of metal ions," J. Nanoparticle Res., 2010.

[6] H. Jang et al., "In vivo magnetic resonance and fluorescence dual imaging of tumor sites by using dye-doped silica-coated iron oxide nanoparticles," J. Nanoparticle Res., 2016.

[7] M. Shalom, J. Albero, Z. Tachan, E. Martínez-Ferrero, A. Zaban, and E. Palomares, "Quantum dot-dye bilayer-sensitized solar cells: Breaking the limits imposed by the low absorbance of dye monolayers," J. Phys. Chem. Lett., vol. 1, no. 7, pp. 1134–1138, 2010.

[8] O. Adegoke and T. Nyokong, "Effects of analytes on the fluorescence properties of CdTe@ZnS quantum dots decorated with cobalt tetraamino-phthalocyanine," J. Lumin., 2014.

[9] T. Takagahara and K. Takeda, "Theory of the quantum confinement effect on excitons in quantum dots of indirect-gap materials," Phys. Rev. B, 1992.

[10] D. Bera, L. Qian, T. K. Tseng, and P. H. Holloway, "Quantum dots and their multimodal applications: A review," Materials. 2010.

[11] E. Elibol and N. Tutkun, "Improving CdTe QDSSC's performance by Cannula synthesis method of CdTe QD," Mater. Sci. Semicond. Process., 2019.

[12] D. Sharma, R. Jha, and S. Kumar, "Quantum dot sensitized solar cell: Recent advances and future perspectives in photoanode," Sol. Energy Mater. Sol. Cells, vol. 155, pp. 294–322, 2016.

[13] F. Li et al., "Emission tunable CdZnS/ZnSe core/shell quantum dots for white light emitting diodes," J. Lumin., vol. 192, pp. 867–874, 2017.

[14] O. V Salata, "Journal of Nanobiotechnology," J. Nanobiotechnology, vol. 6, no. 3, pp. 1–6, 2004.

[15] A. Baride, D. Engebretson, M. T. Berry, and P. Stanley May, "Quenching of coumarin emission by CdSe and CdSe/ZnS quantum dots: Implications for fluorescence reporting," J. Lumin., 2013.

[16] M. S. Smirnov et al., "Luminescent Properties of Hybrid Nanostructures Based on Quantum Dots of CdS, Europium 1,3-Diketonate, and Methylene Blue Molecules," Opt. Spectrosc., vol. 125, no. 2, pp. 249–255, Aug. 2018.

[17] A. O. Orlova, V. G. Maslov, A. V. Baranov, I. Gounko, and S. Byrne, "Spectral-luminescence study of the formation of QD-sulfophthalocyanine molecule complexes in an aqueous solution," Opt. Spectrosc. (English Transl. Opt. i Spektrosk., 2008.

[18] O. V. Ovchinnikov et al., "Spectroscopic investigation of colloidal CdS quantum dots-methylene blue hybrid associates," J. Nanoparticle Res., 2014.

[19] A. Nezamzadeh-Ejhieh and H. Zabihi-Mobarakeh, "Heterogeneous photodecolorization of mixture of methylene blue and bromophenol blue using CuO-nano-clinoptilolite," J. Ind. Eng. Chem., 2014.

[20] R. Flores, "A rapid and reproducible assay for quantitative estimation of proteins using bromophenol blue," Anal. Biochem., 1978.

[21] J. Hong, N. Ta, S. gui Yang, Y. zi Liu, and C. Sun, "Microwave-assisted direct photolysis of bromophenol blue using electrodeless discharge lamps," Desalination, 2007.

[22] S. Kushwaha and L. Bahadur, "Enhancement of power conversion efficiency of dye-sensitized solar cells by co-sensitization of

Erdem ELİBOL,Tuna DEMİRCİ

Interaction and Characterization of The Triarylmethane Dye Bromophenol Blue with CdSeTe Quantum Dots...

Phloxine B and Bromophenol blue dyes on ZnO photoanode," J. Lumin., 2015.

[23] A. V. Kalvelytė, A. Imbrasaitė, N. Krestnikova, and A. Stulpinas, "Adult Stem Cells and Anticancer Therapy," 2017, pp. 123–202.

[24] M. A. Al-Omar, "Ofloxacin," 2009, pp. 265–298.

[25] H. Alrabiah, "Levetiracetam," 2019, pp. 167–204.

[26] P. G. JEFFERY and D. HUTCHISON, "Beryllium," in Chemical Methods of Rock Analysis, Elsevier, 1981, pp. 102–106.

[27] V. Nand and M. J. Ellwood, "A simple colorimetric method for determining seawater alkalinity using bromophenol blue," Limnol. Oceanogr. Methods, vol. 16, no. 7, pp. 401–410, Jul. 2018.

[28] L. He, L. Li, W. Wang, E. S. Abdel-Halim, J. Zhang, and J. J. Zhu, "Highly luminescent and biocompatible near-infrared core-shell CdSeTe/CdS/C quantum dots for probe labeling tumor cells," Talanta, 2016.

[29] T. Debnath, S. Maiti, and H. N. Ghosh, "Unusually Slow Electron Cooling to Charge-Transfer State in Gradient CdTeSe Alloy Nanocrystals Mediated through Mn Atom," J. Phys. Chem. Lett., 2016.

[30] E. Simonenko, A. Gomonov, N. Rolle, and L. Molodkina, "Modeling of H2O2 and UV oxidation of organic pollutants at wastewater post-treatment," in Procedia Engineering, 2015.

[31] M. S. Smirnov, O. V. Ovchinnikov, A. O. Dedikova, B. I. Shapiro, A. G. Vitukhnovsky, and T. S. Shatskikh, "Luminescence properties of hybrid associates of colloidal CdS quantum dots with J-aggregates of thiatrimethine cyanine dye," J. Lumin., vol. 176, pp. 77–85, Aug. 2016.

[32] A. Rakovich et al., "Photosensitizer methylene blue-semiconductor nanocrystals hybrid system for photodynamic therapy," in Journal of Nanoscience and Nanotechnology, 2010.

[33] D. Severino, H. C. Junqueira, M. Gugliotti, D. S. Gabrielli, and M. S. Baptista, "Influence of Negatively Charged Interfaces on the Ground and Excited State Properties of Methylene Blue¶," Photochem. Photobiol., 2003.

[34] R. C. Page et al., "Near-Unity Quantum Yields from Chloride Treated CdTe Colloidal Quantum Dots," Small, vol. 11, no. 13, pp. 1548–1554, 2015.

[35] M. Amelia, C. Lincheneau, S. Silvi, and A. Credi, "Electrochemical properties of CdSe and CdTe quantum dots," Chem. Soc. Rev., vol. 41, no. 17, p. 5728, 2012.

[36] A. Rakovich, Y. P. Rakovich, and J. F. Donegan, "Optical studies of the methylene blue-semiconductor nanocrystals hybrid system," in e-Journal of Surface Science and Nanotechnology, 2009.

[37] O. Mashinchian, M. Johari-Ahar, B. Ghaemi, M. Rashidi, J. Barar, and Y. Omidi, "Impacts of quantum dots in molecular detection and bioimaging of cancer," BioImpacts, vol. 4, no. 3, pp. 149–166, 2014.

Title: Pollen morphology in the genus Bolanthus (Ser.) Reichb. (Caryophyllaceae) in Turkey

Authors: Yağmur CÖMERT, Mevlüde Nur TOPAL, Murat KOÇ

Pollen morphology in the genus *Bolanthus* (Ser.) Reichb. (Caryophyllaceae) in Turkey

Yağmur CÖMERT[*1], Mevlüde Nur TOPAL[1], Murat KOÇ[1]

Abstract

Bolanthus including 11 species and all endemic in Turkey. Pollen morphology that belong to the genus *Bolanthus* were investigated using light microscopy (LM) and scanning electron microscopy (SEM). In this study, all of 11 species in *Bolanthus* were studied. Pollen of seven species were determined from Turkey and reported for the first time. Pollen shape has two different ornamentation at genus *Bolanthus* as prolate-spheroidal and oblate-spheroidal. Pollen grains are polipantoporate and isopolar symmetrical. The pollen ornamentation is scabrate-perforate. Pollen diameter, pore diameter, pore numbers, exine thickness, operculum diameter, distance between two pores, spinule numbers, punctum numbers are varying characters between *Bolanthus* species. The taxonomic separations of the species have been demonstrated with SPSS analysis as dendrogram.

Keywords: *Bolanthus*, Caryophyllaceae, LM, pollen, SEM

---

[*] Corresponding Author: yagmurcomert1@gmail.com

[1] Ankara Yildirim Beyazit University, Faculty of Science and Letters ,Ankara, Turkey , ORCID: https://orcid.org/0000-0001-7517-2833, E-mail: nurtopal92@gmail.com , ORCID: https://orcid.org/0000-0002-9720-8662, , E-mail: aybumuratkoc@hotmail.com , ORCID: https://orcid.org/0000-0002-0829-4571

CÖMERT et al.

Pollen morphology in the genus Bolanthus (Ser.) Reichb. (Caryophyllaceae) in Turkey

1. INTRODUCTION

Caryophyllaceae is a large family in terms of the number of species and genus for Turkey [1-2-3]. The Caryophyllaceae family contains about 86 genera and about 2200 species. This family is generally common in temperate regions [4]. The tribe Caryophylleae includes 17 genera, namely *Acanthophyllum* C. A. Mey., *Dianthus* L., *Gypsophila* L., *Petrorhagia* (Ser. ex DC.) Link, *Saponaria* L., *Vaccaria* Medic., *Allochrusa* Bunge ex Boiss., *Ankyropetalum* Fenzl, *Bolanthus* (Ser.) Reichb., *Cyathophylla* Bocquet et Strid, *Diaphanoptera* Rech. f., *Kohlrauschia* Kunth, *Ochotonophila* Gilli, *Phrynella* Pax et K. Hoffm., *Pleioneura* Rech. f., Scleranthopsis Rech. f. and *Velezia* L. and about 600 species [4].

The family Caryophyllaceae of genus *Bolanthus* is located in the Caryophylleae tribes in the subfamily Caryophylloideae. It is perennial plants in the form of slants or pillows. The leaves are small, stripy and flowers dicazium. The genus *Bolanthus* comprising 29 species, mostly occurring in the Mediterranean region in the world. The genus is represented by six taxa found in Syria, Palestine, Israel and Lebanon [5-7]. The eight taxa growing in Europe are known from Greece or the East Aegean Islands [8]. The flora of Turkey includes five *Bolanthus* taxa. As a result of recent studies, six additional taxa were added to *Bolanthus,* of which one is an overlooked species (*B. huber-morathii* C. Simon) and five are new species (*B. stenopetalus* Hartvig & Strid, *B. mevlaneae* Aytaç, *B. turcicus* Koç & Hamzaoğlu, *B. sandrasicus* Hamzaoğlu & Koç, *B. aziz-sancarii* Koç & Hamzaoğlu) [9-10-11-12]. Together with these additions, the number of taxa belonging to the genus *Bolanthus* that occur in Turkey increased to 11, all of which are endemic.

There are many studies on pollen morphology of Caryophylleae [15-16-17-18-19-20-21]. Palynological characteristics of Caryophyllaceae such as pore shape, number of pores and ornamentation are proved to have taxonomical importance [22-23-24-25-26-27-28]. Using palynological features, scientists identified new species and also distinguished new species from other similar species [29-30-31-32-33].

The aim of this study is determined the pollen morphology of the genus *Bolanthus* and contributing to taxonomy. For this purpose, the pollen morphology of 11 endemic species of *Bolanthus* have studied by using scanning electron microscopy (SEM) and light microscopy (LM). In addition, taxonomic relationships between species have been revealed.

2. MATERIALS AND METHODS

The pollen of 11 taxa of genus *Bolanthus* were examined with light microscopy (LM) and scanning electron microscopy (SEM) (Figure 1 and 2).

The localities of the specimens are given below Table 1. After the plants were diagnosed and pollen materials the plants were left in the Gazi University Herbarium (GAZI) for storage. Saffron with glycerine-gelatin was used for staining pollen. Pollen grains were prepared for light microscopy (LM) using [34].

The pollens were photographed with a spot insight colour digital camera on a LEICA DM1000 microscope with digital imaging system which is Leica Application Suit program equipped with an apochromatic 100x oil immersion objective [34]. Morphological observations were carried out in microscope in the LM of Ankara University.

For scanning electron microscopy, each of the pollen was attached on stubs applying double-sided adhesive tape. Every sample was coated with a 100-Å-thick layer of gold in a Polaron SC7620 rotating and tilting vacuum coating apparatus for 60 s and scanned using a JEOL 5600 LV SEM (Scanning Electron Microscopy) with 20-kV accelerating voltage [35-36]. Morphological observations were carried out in a Jeol 5600 electron microscope in the Electron Microscopy Laboratory of Gazi University.

CÖMERT et al.

Pollen morphology in the genus Bolanthus (Ser.) Reichb. (Caryophyllaceae) in Turkey

Pollen ornamentation, operculum ornamentation, pollen diameter, pore diameter, pollen shape, distance between two pore, operculum diameter, pore numbers, spinule numbers, number of spinules on operculum, punctum numbers, punctum diameter, exine and intine thickness measurements were made with 20 to 30 pollen grains. Measurements were made with AlaMet 0.06 program. The average of the measured samples was calculated with Microsoft Office Excel Programme. Pollen morphologies were determined by using glossary of pollen and spore terminology [37]. The taxonomic separation of the species has been demonstrated with SPSS software analysis as dendrogram (Figure 3).

3. RESULTS AND DISCUSSION

Bolanthus including 11 species and all endemic in Turkey. Pollen morphology of four species from this genus was reported from Turkey [38]. Pollen morphology of the other seven species was determined for the first time in this study. Pollen in the Caryophyllaceae family are generally radially symmetrical, apolar or isopolar, spheroidal, polygonal or polygonal spheroidal, oblate-spheroidal, prolate spheroidal, periporate or pantopoliporate [13-18-38-39-23-40-41]. The findings of the study shows, *Bolanthus* taxa pollens are isopolar symmetry, shape of pollen is oblate-spheroidal (9 species) and prolate-spheroidal (2 species). The pollen ornamentation have been observed scabrate-perforate.

Our results are consistent with those reported by Pınar [38] who worked on *B. minuartioides, B. spergulifolius, B. thymoides, B. frankenioides* var. *fasciculatus* and *B. turcicus.* Likewise, in the species, pollen shape is polipantoporate. Pollen and pore diameters are similar average. Pınar's of the study [38], pollen is spheroidal. In our study, pollen is prolate-spheroidal and oblate-spheroidal. However, in this study, exine thickness was measured about 1.3 μm while Pınar's of the study as 2 μm in this species [38]. When our study was compared to Pınar's study, the exine thickness was measured as thinner. In addition, in this study, it was determined that *B. minuartioides* taxa have a fewer number of

pores. Pore numbers of the others taxa are similar average.

The pollen characteristics of *Bolanthus* taxa in 11 species were listed in detail in Table 2. All characters were evaluated under the separate titles. In addition, the pollen morphologies of *Bolanthus* taxa were compared with related genera. Moreover, the taxonomic separations of the species were demonstrated as dendrogram (Figure 3).

Cluster analysis divided the taxa into 2 groups: clusters as number of pores which is A and B. Cluster A was divided into 2 subgroups according to the distance between the pores: A1 (*B. turcicus, B. stenopetalus, B. cherlierioides, B. aziz-sancarii* and A2 (*B. minuartioides*). Cluster B was divided into 2 subgroups according to the spinule number: B2 (*B. frankenioides*) and B1, which B1 was further divided C1 and C2 according to punctum number. C1 are *B. frankenioides* var. *fasciculatus, B. thymoides, B. huber-morathii* and *B. mevlanae* C2 is *B. spergulifolius* (Figure 3). The data obtained and the cluster analysis results are consistent with each other.

3.1. Evaluation of the findings of *Bolanthus* taxa

3.1.1. Pollen shape

The findings of the study shows, pollen shape have 2 different at genus *Bolanthus.* prolate-spheroidal (*B. spergulifolius, B. huber-morathii*) and oblate-spheroidal (*B. thymoides, B. aziz-sancarii, B. frankenioides, B. frankenioides* var. *fasciculatus, B. cherlerioides, B. stenopetalus, B. minuartioides, B. turcicus, B. mevlanae*). All the species are isopolar symmetrical. Another study, pollen grains of *Bolanthus* taxa in 4 species (*B. minuartioides, B. spergulifolius, B. thymoides and B. frankenioides* var. *fasciculatus*) were determined as spheroidal [38]. In additon to the pollen grains of *Acanthophyllum, Dianthus, Gysophila, Bolanthus* have spheroidal [44]. In the literature, *B. filicaulis* species pollen is radially symmetrical and spheroidal [16]. *Bolanthus* is isopolar symmetrical.

CÖMERT et al.

Pollen morphology in the genus Bolanthus (Ser.) Reichb. (Caryophyllaceae) in Turkey

3.1.2. Pollen ornamentation

The findings demonstrated that, pollen grains ornamentation have scabrate-perforate (Figure 2, Table 2). However, another study, pollen grains of four Turkish endemic *Bolanthus* taxa belong to *B. minuartioides*, *B. spergulifolius*, *B. thymoides* and *B. frankenioides* var. *fasciculatus* were detected tectate-perforate [38].

The pollen ornamentation was observed scabrate, scabrate-perforate ve scabrate-perforate-foveolate for *Dianthus* taxa [45]. Silenoideae, a subgroup of the Caryophyllaceae family, is usually characterized by polypantoporate [15]. Likewise *Bolanthus* taxa pollen aperture type are polypantoporate.

3.1.3. Pollen diameter

The largest pollen diameter has been observed in *Bolanthus turcicus* as 30.33±1.14 μm (mean±standard deviation), the smallest in *Bolanthus frankenioides.* var. *fasciculatus* as 22.30±0.30 μm (mean±standard deviation) (Table 2). The pollen grains of *Acanthophyllum*, *Dianthus*, *Gysophila*, *Bolanthus* are spheroidal. The pollen grains of *Acanthophyllum* with a diameter of 28.65–30.87 μm, *Dianthus* 30.05–40.22 μm and *Gypsophila* 16.95–27.77 μm [44]. The pollen grains of *Bolanthus* has been measured as 22.23-30.33 μm. In terms of pollen diameter, *Bolanthus* is generally smaller than *Acanthophyllum* and *Dianthus*, larger than *Gypsophila.*

3.1.4. Pore diameter

The largest pore diameter has been observed in *B. thymoides* as 4.25±0.63 μm (mean ± standard deviation), the smallest in *B. mevlanae* as 2.31±0.40 μm (mean ± standard deviation) (Table 2). The pore diameter was measured as 2.2-9.3 μm for *Dianthus* taxa [45]. The biggest species *Silene bupleuroides* subsp. *bupleuroides* with 6.96±1.65 μm whereas the smallest species *Silene cartilaginea* with 3.54±0.66 μm of the pore diameter [42]. Pore diameter of *Bolanthus* taxa is smaller than *Silene and Dianthus.*

3.1.5. Distance between two pores (μm²)

The findings shows that the largest species *B. minuartioides* with 6.75±2.01 μm (mean±standard deviation) while the smallest species *B. turcicus* with 3.90±1.07 μm (mean±standard deviation) of the distance between two pores. In the literature, *Gypsopila* and *Dianthus* have been measured as 4.69-9.86, 9.42-13.07 μm respectively [44]. Comparing the distance between pores, *Bolanthus* is different from *Dianthus*, similar to *Gypsophila*. Therefore, the distance between pores of *Dianthus* are more than *Bolanthus*.

3.1.6. Pore numbers

The results demonstrated that the highest species *B. spergulifolius* with 22±3 while the lowest species *B. minuartioides* with 10±3 (Table 2) of the pore numbers. In another study, pore numbers have been detected as 21-22 in *B. minuartioides* and *B. spergulifolius* 19-22 [38]. Therefore, in this study, it was determined that *B. minuartioides* taxa have a fewer number of pores. In the literature, pore numbers are determined as 10-16 in *Acanthophyllum, Dianthus, Gysophila* [44]. Likewise, *Bolanthus* pollen is 10-22 pores.

3.1.7. Operculum diameter

The largest operculum diameter has been observed in *Bolanthus thymoides* as 3.33±0.53 μm, the smallest in *Bolanthus turcicus* as 1.19±0.22 μm (Table 2). The operculum diameter was measured as 1.2-5.2 μm for *Dianthus* taxa [45]. *Saponaria karapinarensis* (Caryophyllaceae) have operculum diameter 2 μm [43] Similarly, *Bolanthus* taxa have been measured as approximately 2 μm.

3.1.8. Exine thickness

The findings indicated that, the largest species *B. stenopetalus* with 1.47±0.14 μm (mean±standard deviation) while the smallest species *B. turcicus* with 0.94±0.11 μm (mean±standard deviation) (Table 2) of the exine thickness. In the literature, *Bolanthus filicaulis* was measured 2 μm [16]. In our study, exine thickness have determined as more thinner compered to other studies. *Petrorhagia*, which is close to the *Bolanthus*

CÖMERT et al.

Pollen morphology in the genus Bolanthus (Ser.) Reichb. (Caryophyllaceae) in Turkey

genus, have been measured from 1.73 µm to 3.78 µm [25]. In another study, exine thickness was determined as above 2 for all studied taxa [38]. In our study, exine thickness have been detected as about 1.3.

3.1.9. Intine thickness

The largest intine thickness has been observed in *B. thymoides* as 0.66±0.10 µm (mean±standard deviation), the smallest in *B. frankenioides* as 0.47±0.07 µm (mean±standard deviation) (Table 2). In another study, the intine thickness was measured as 0.4-1.1 µm for *Dianthus* taxa [45].

3.1.10. Spinule and punctum numbers

The most spinule numbers have been observed in *B. frankenioides* as 24-26, the least species *B. minuartioides as* 8-10.

The most punctum numbers have been determined in *B. spergulifolius* as 15-17, the least in *B. frankenioides* as 3-5 (Table 2). All species have differed when compared within themselves. In the literature, the spinule and punctum numbers have been measured as 9-28 and 1-23 µm for *Dianthus* taxa [45].

3.2. Description:

3.2.1. *B. spergulifolius* pollen features: Pollen shape is prolate-spheroidal (P/E=1.06). In general aspect pollen is isopolar. Polar axis is 26.44±0.77 µm, equatorial axis is 24.93±1.98 µm. Pollen type is polipantoporate. Pollen ornamentation is scabrate-perforate. Pore numbers are 19-25. Pore diameter is 2.59±0.27 µm. The distance between two pores are 3.94±1.81 µm. Operculum diameter is 1.31±0.15 µm. Number of spinules on operculum are 5-7. Number of spinule is 13-16. Number of punctum is 15-17. Exine thickness is 1.39±0.09 µm. Intine thickness is 0.60±0.08 µm (Table 2, Figure 1, 1 a-b-c, Figure 2, 1 a-b).

3.2.2. *B. huber-morathii* pollen features: Pollen shape is prolate-spheroidal (P/E=1.04). In

general aspect pollen is isopolar. Polar axis is 25.32±0.51 µm, equatorial axis is 24.25±0.71 µm. Pollen type is polipantoporate. Pollen ornamentation is scabrate-perforate. Pore numbers are 13-19. Pore diameter is 3.22±2.65 µm. The distance between two pores are 4.83±1.42 µm.

Operculum diameter is 1.72±0.31 µm. Number of spinules on operculum are 6-8. Number of spinule is 13-16. Number of punctum is 11-13. Exine thickness is
1.33±0.07 µm. Intine thickness is 0.56±0.10 µm (Table 2, Figure 1, 2 a-b-c, Figure 2, 2 a-b).

3.2.3. *B. frankenioides* pollen features: Pollen shape is oblate-spheroidal (P/E=0.95). In general aspect pollen is isopolar. Polar axis is 22.91±0.28 µm, equatorial axis is 23.99±0.23 µm. Pollen type is polipantoporate. Pollen ornamentation is scabrate-perforate. Pore numbers are 17-23. Pore diameter is 2.81±0.25 µm. The distance between two pores are 4.02±1.43 µm. Operculum diameter is 1.67±0.20 µm. Number of spinules on operculum are 4-6. Number of spinule is 24-26. Number of punctum is 3-5. Exine thickness is 1.30± 0.10 µm. Intine thickness is 0.47±0.07 µm (Table 2, Figure 1, 3 a-b-c, Figure 2, 3 a-b).

3.2.4. *B. frankenioides* var. *fasciculatus* pollen features: Pollen shape is oblate-spheroidal (P/E=0.97).). In general aspect pollen is isopolar. Polar axis is 23.71±0.56 µm, equatorial axis is 24.23±0.80 µm. Pollen type is polipantoporate. Pollen ornamentation is scabrate- perforate. Pore numbers are 15-21. Pore diameter is 3.51±0.40 µm. The distance between two pores are 4.17±1.78 µm. Operculum diameter is 2.65±0.32 µm. Number of spinules on operculum are 4-6. Number of spinule is 16-18. Number of punctum is 7-9. Exine thickness is 1.35±0.09 µm. Intine thickness is 0.66±0.08 µm (Table 2, Figure 1, 4 a-b-c, Figure 2, 4 a-b).

3.2.5. *B. minuartioides* pollen features: Pollen shape is oblate-spheroidal (P/E=0.97). In general aspect pollen is isopolar. Polar axis is 25.86±0.64 µm, equatorial axis is 26.43±0.68 µm. Pollen type is polipantoporate. Pollen

CÖMERT et al.

Pollen morphology in the genus Bolanthus (Ser.) Reichb. (Caryophyllaceae) in Turkey

ornamentation is scabrate- perforate. Pore numbers are 7-13. Pore diameter is 3.75±0.87 µm. The distance between two pores are 6.75±2.01 µm. Operculum diameter is 1.89±0.35 µm. Number of spinules on operculum are 5-7. Number of spinule is 8-10. Number of punctum is 10-12. Exine thickness is 1.31±0.07 µm. Intine thickness is 0.55±0.07 µm (Table 2, Figure 1, 5 a-b-c, Figure 2, 5 a-b).

3.2.6. *B. cherlierioides* **pollen features:** Pollen shape is oblate-spheroidal (P/E=0.91). In general aspect pollen is isopolar. Polar axis is 21.74±0.29 µm, equatorial axis is 23.86±0.29 µm. Pollen type is polipantoporate. Pollen ornamentation is scabrate-perforate. Pore numbers are 11-17. Pore diameter is 3.02±1.64 µm. The distance between two pores are 4.21±1.41 µm. Operculum diameter is 1.39±0.30 µm. Number of spinules on operculum are 4-6. Number of spinule is 15-18. Number of punctum is 4-6. Exine thickness is 0.96±0.12 µm. Intine thickness is 0.57±0.07 µm (Table 2, Figure 1, 6 a-b-c, Figure 2, 6 a-b).

3.2.7. *B. turcicus* **pollen features:** Pollen shape is oblate-spheroidal (P/E=0.95). In general aspect pollen is isopolar. Polar axis is 27.11±0.62 µm, equatorial axis is 28.47±0.34 µm. Pollen type is polipantoporate. Pollen ornamentation is scabrate- perforate. Pore

diameter is 4.25±0.63 µm. The distance between two pores are 4.83±1.12 µm.Operculum diameter is 3.33±0.53 µm. Number of spinules on operculum are 7-9. Number of spinule is 16-18. Number of punctum is 9-11. Exine thickness is 0.94±0.06 µm. Intine thickness is 0.66±0.10 µm (Table 2, Figure 1, 9 a-b-c, Figure 2, 9 a-b).

3.2.10. *B. aziz-sancarii* **pollen features:** Pollen shape is oblate-spheroidal (P/E=0.92). In general aspect pollen is isopolar. Polar axis is 23.36±0.45 µm, equatorial axis is 25.14±0.35 µm. Pollen type is polipantoporate. Pollen ornamentation is scabrate- perforate. Pore numbers are 13-19. Pore diameter is 3.91±0.35 µm. The distance between two pores are 5.19±1.56 µm. Operculum diameter is 2.48±0.52 µm. Number of spinules on operculum are 7-9. Number of spinule is 10-12.

numbers are 11-17. Pore diameter is 2.78±0.31 µm. The distance between two pores are 3.90±1.07 µm. Operculum diameter is 1.19±0.22 µm. Number of spinules on operculum are 5-7. Number of spinule is 12-15. Number of punctum is 4-6. Exine thickness is 0.94±0.11 µm. Intine thickness is 0.50±0.11 µm (Table 2, Figure 1, 7 a-b-c, Figure 2, 7 a-b).

3.2.8. *B. mevlanae* **pollen features:** Pollen shape is oblate-spheroidal (P/E=0.97). In general aspect pollen is isopolar. Polar axis is 23.26±0.24 µm, equatorial axis is 23.79±0.72 µm. Pollen type is polipantoporate. Pollen ornamentation is scabrate- perforate. Pore numbers are 15-21. Pore diameter is 2.31±0.40 µm. The distance between two pores are 3.98±1.42 µm. Operculum diameter is 1.60±0.39 µm. Number of spinules on operculum are 4-6. Number of spinule is 13-15. Number of punctum is 9-11. Exine thickness is 1.25±0.09 µm. Intine thickness is 0.59±0.10 µm (Table 2, Figure 1, 8 a-b-c, Figure 2, 8 a-b).

3.2.9. *B. thymoides* **pollen features:** Pollen shape is oblate-spheroidal (P/E=0.99). In general aspect pollen is isopolar. Polar axis is 23.32±0.49 µm, equatorial axis is 23.53±0.43 µm. Pollen type is polipantoporate. Pollen ornamentation is scabrate- perforate. Pore numbers are 13-19. Pore

Number of punctum is 4-6. Exine thickness is 1.13±0.12 µm. Intine thickness is 0.65±0.06 µm (Table 2, Figure 1, 10 a-b-c, Figure 2, 10 a-b).

3.2.11. *B. stenopetalus* **pollen features:** Pollen shape is oblate-spheroidal (P/E=0.92). In general aspect pollen is isopolar. Polar axis is 20.84±0.38 µm, equatorial axis is 22.56±0.65 µm. Pollen type is polipantoporate. Pollen ornamentation is scabrate-perforate. Pore numbers are 11-17. Pore diameter is 3.06±0.31 µm. The distance between two pores are 6.03±1.79 µm. Operculum diameter is 2.39±0.32 µm. Number of spinules on operculum are 5-7. Number of spinule is 13-15. Number of punctum is 4-6. Exine thickness is 1.47±0.14 µm. Intine thickness is 0.54±0.28 µm (Table 2, Figure 1, 11 a-b-c, Figure 2, 11 a-b).

CÖMERT et al.

Pollen morphology in the genus Bolanthus (Ser.) Reichb. (Caryophyllaceae) in Turkey

Specimens examined

Table 1
 List of the studied *Bolanthus* taxa and localities

Taxa	Collector Name and Number	Localities
B. spergulifolius	Koç 2043	B2 Kütahya: Gediz, Murat Mountain, Kaplıcalar road, serpentine soils, grassy levels, 1495 m, 25.06.2016
B. huber-morathii	Koç 2352	A2 Bursa: Between Soğukpınar and Keles, on the way out Soğukpınar, 40°30'80" K – 29°70'20", 930 m, 19.07.2016
B.frankenioides	Koç 2167	C3 Burdur: Altınyayla southwestern, Akpınar yaylası around limestone slopes, 1865 m, 04.08.2016
B.frankenioides var. fasciculatus	Koç 2188	C2 Muğla: Köyceğiz, Yayla village, Gökçeova lake around, Sandras Mountain, serpentine rocky, 2030 m, 05.08.2017
B. minuartioides	Koç 2006	B2 Kütahya: Aslantepe, between Çavdar and Hisar, calcareous rocks, 1090 m, 24.06.2015
B. cherlerioides	Koç 3054	B4 Between Akşehir and Şarkikaraağaç, Yellibel gateway around, slopes around, 38°14'06" K- 031°19'36" D, 1550 m, 14.07.2017
B. turcicus	Koç 2226	B4 Aksaray: Karkın Beldesi, Karbeyaz Hotel around, Hasan Mountain to the south, 2760 m, 07.08.2016
B. mevlanaea	Koç 3365	C3 Antalya: Between Akseki and Bozkır, 60. km, Gölcük kuruçay tableland, 1200 m, 23.07.2017
B. thymoides	Koç 1848	C3 Burdur: Between Yeşilova and Salda Village, Eşeler Mountain, watchtower around, serpantine, stony places, 37°27'50" K – 29°39'30" D, 2000 m, 18.08.2016
B. aziz-sancarii	Koç 1209	B3 Afyonkarahisar: between Bayat and Iscehisar, 1500 m, 02.07.2010
B. stenopetalus	Koç 2196	C2 Muğla: Köyceğiz, Yayla village, Gökçeova lake around, Sandras Mountain, 2030 m, 05.08.2017

CÖMERT et al.

Pollen morphology in the genus Bolanthus (Ser.) Reichb. (Caryophyllaceae) in Turkey

Table 2
Pollen morphological characters of the *Bolanthus* taxa analyzed

	B.spergulifolius	*B.huber-morathii*	*B.frankenioides*	*B. frankenioides var. fasciculatus*	*B.minuartioides*
Pollen diameter (M±SD)	26.50±0.31	23.56±0.32	23.68±0.48	22.23±0.30	26.42±0,23
Polar axes (M±SD)	26.44±0.77	25.32±0.51	22.91±0.28	23.71±0.56	25.86±0.64
Equatorial axes (M±SD)	24.93±0.70	24.25±0.71	23.99±0.23	24.23±0.80	26.43±0.68
Pollen shape	Prolate-spheroidal	Prolate-spheroidal	Oblate-spheroidal	Oblate-spheroidal	Oblate-spheroidal
Pollen ornamentation	Scabrate-Perforate	Scabrate-Perforate	Scabrate-Perforate	Scabrate-Perforate	Scabrate-Perforate
Exine thickness (M±SD)	1.39±0.09	1.33±0.07	1.30± 0.10	1.35±0.09	1.31±0.07
Intine thickness (M±SD)	0.60±0.08	0.56±0.10	0.47± 0.07	0.66±0.08	0.55±0.07
Pore diameter (M±SD)	2.59±0.27	3.22±2.65	2.81±0.25	3.51±0.40	3.75±0.87
Number of pore	22±3	16±3	20±3	18±3	10±3
Distance between two pores (M±SD)	3.94±1.81	4.83±1.42	4.02±1.43	4.17±1.78	6.75±2.01
Operculum diameter (M±SD)	1.31±0.15	1.72±0.31	1.67±0.20	2.65±0.32	1.89±0.35
Number of spinule ($10\mu m^2$)	13-16	13-16	24-26	16-18	8-10
Number of spinules on operculum	5-7	6-8	4-6	4-6	5-7
Number of punctum ($10\mu m^2$)	15-17	11-13	3-5	7-9	10-12

CÖMERT et al.

Pollen morphology in the genus Bolanthus (Ser.) Reichb. (Caryophyllaceae) in Turkey

	B.cherlierioides	*B.turcicus*	*B.mevlanae*	*B.thymoides*	*B.aziz-sancarii*	*B.stenopetalus*
Pollen diameter (M±SD)	23.06±0.43	30.33±1.14	25.71±0.93	24.76±0.38	24.25±0.39	23.86±0.36
Polar axes (M±SD)	21.74±0.29	27.11±0.62	23.26±0.24	23.32±0.49	23.36±0.45	20.84±0.38
Equatorial axes (M±SD)	23.86±0.29	28.47±0.34	23.79±0.72	23.53±0.43	25.14±0.35	22.56±0.65
Pollen shape	Oblate-spheroidal	Oblate-spheroidal	Oblate-spheroidal	Oblate-spheroidal	Oblate-spheroidal	Oblate-spheroidal
Pollen ornamentation	Scabrate – Perforate	Scabrate – Perforate	Scabrate – Perforate	Scabrate – Perforate	Scabrate – Perforate	Scabrate – Perforate
Exine thickness (M±SD)	0.96±0.12	0.94±0.11	1.25±0.09	0.94±0.06	1.13±0.12	1.47±0.14
Intine thickness (M±SD)	0.57±0.07	0.50±0.11	0.59±0.10	0.66±0.10	0.65±0.06	0.54±0.28
Pore diameter (M±SD)	3.02±1.64	2.78±0.31	2.31±0.40	4.25±0.63	3.91±0.35	3.06±0.31
Number of pore	14±3	14±3	18±3	16±3	16±3	14±3
Distance between two pores (M±SD)	4.21±1.41	3.90±1.07	3.98±1.42	4.83±1.12	5.19±1.56	6.03±1.79
Operculum diameter (M±SD)	1.39±0.30	1.19±0.22	1.60±0.39	3.33±0.53	2.48±0.52	2.39±0.32
Number of spinule ($10\mu m^2$)	15-18	12-15	13-15	16-18	10-12	13-15
Number of spinules on operculum	4-6	5-7	4-6	7-9	7-9	5-7
Number of punctum ($10\mu m^2$)	4-6	4-6	9-11	9-11	4-6	4-6

Abbreviations: M – mean value; SD – standard deviation

CÖMERT et al.

Pollen morphology in the genus Bolanthus (Ser.) Reichb. (Caryophyllaceae) in Turkey
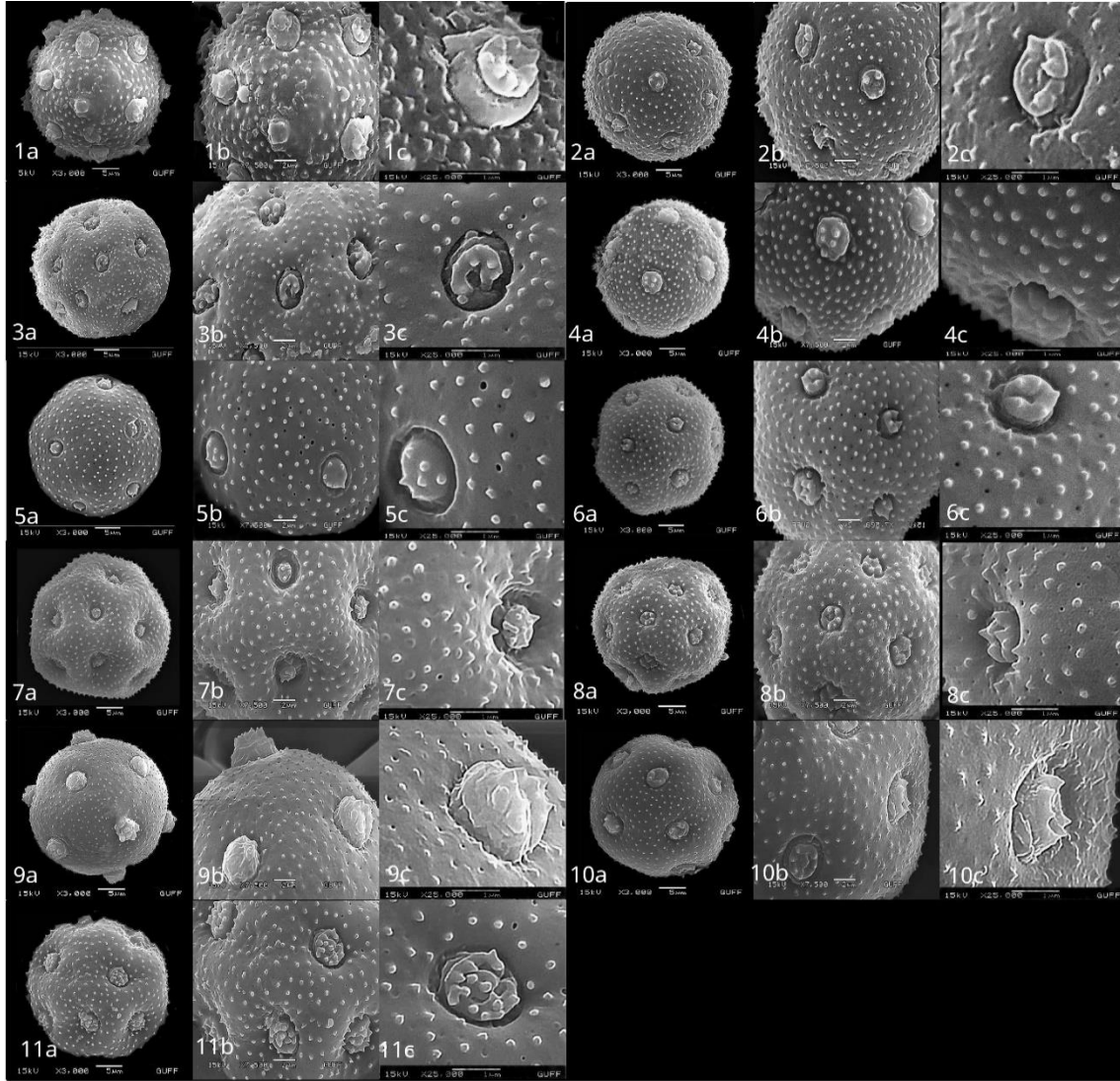
Figure 1 SEM photos of pollen grains of studied *Bolanthus* taxa: 1a-1b-1c: *B. spergulifolius,* 2a-2b-2c: *B. huber-morathii*, 3a-3b-3c: *B. frankenioides*, 4a-4b-4c: *B. frankenioides* var. *fasciculatus*, 5a-5b-5c: *B. minuartioides,* 6a-6b-6c: *B. cherlerioides*, 7a-7b-7c: *B. turcicus,* 8a-8b-8c: *B. mevlanae,* 9a-9b-9c: *B. thymoides,* 10a-10b-10c: *B. aziz-sancarii,* 11a-11b-11c: *B. stenopetalus*

CÖMERT et al.

Pollen morphology in the genus Bolanthus (Ser.) Reichb. (Caryophyllaceae) in Turkey
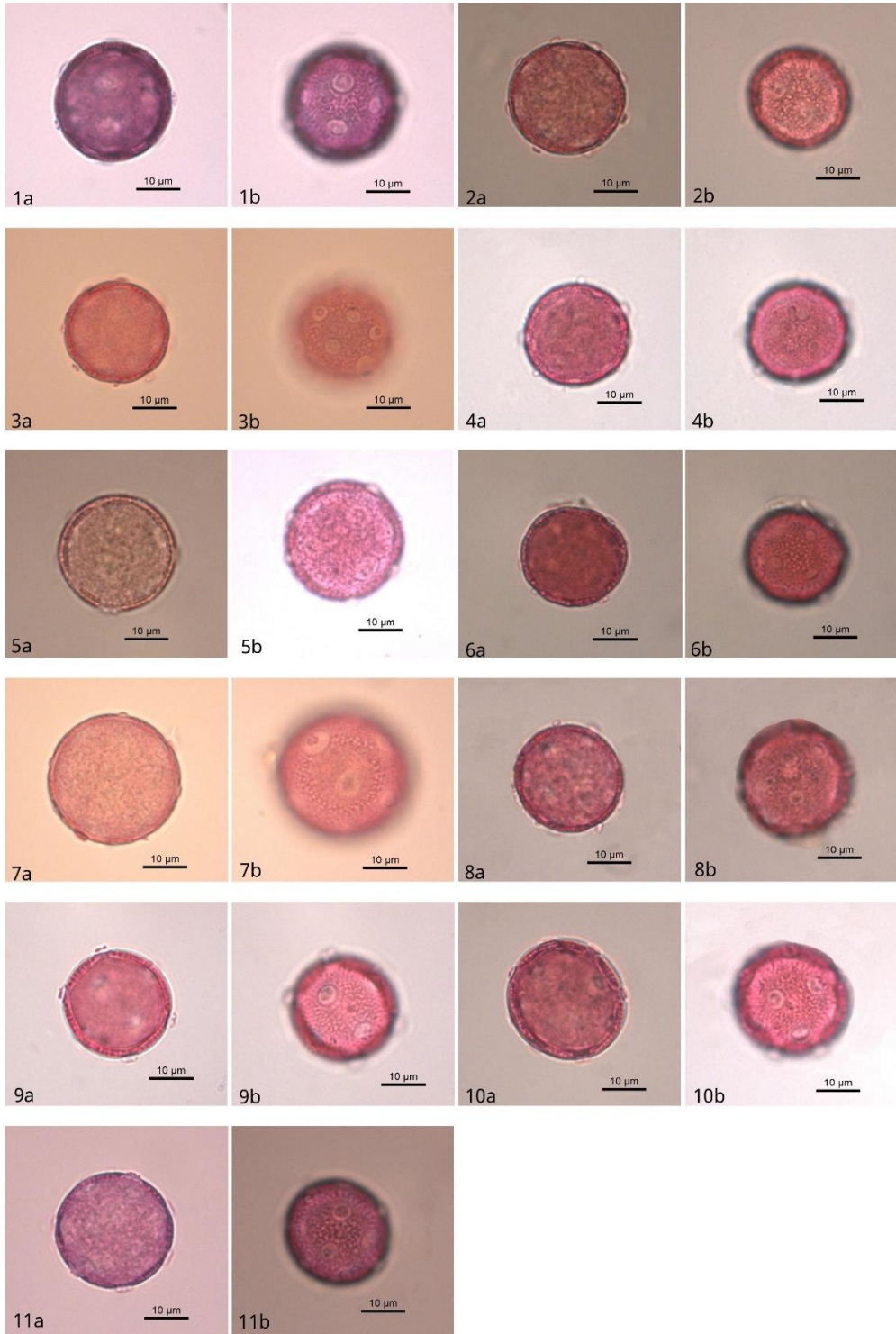
Figure 2 LM photos of pollen grains of studied *Bolanthus* taxa: 1a-1b: *B. spergulifolius,* 2a-2b: *B. huber-morathii*, 3a-3b: *B. frankenioides*, 4a-4b: *B. frankenioides* var. *fasciculatus,* 5a-5b: *B. minuartioides,* 6a-6b: *B. cherlerioides,* 7a-7b: *B. turcicus*, 8a-8b: *B. mevlanae,* 9a-9b: *B. thymoides,* 10a-10b: *B. aziz-sancarii*, 11a-11b: *B. stenopetalus*

CÖMERT et al.

Pollen morphology in the genus Bolanthus (Ser.) Reichb. (Caryophyllaceae) in Turkey
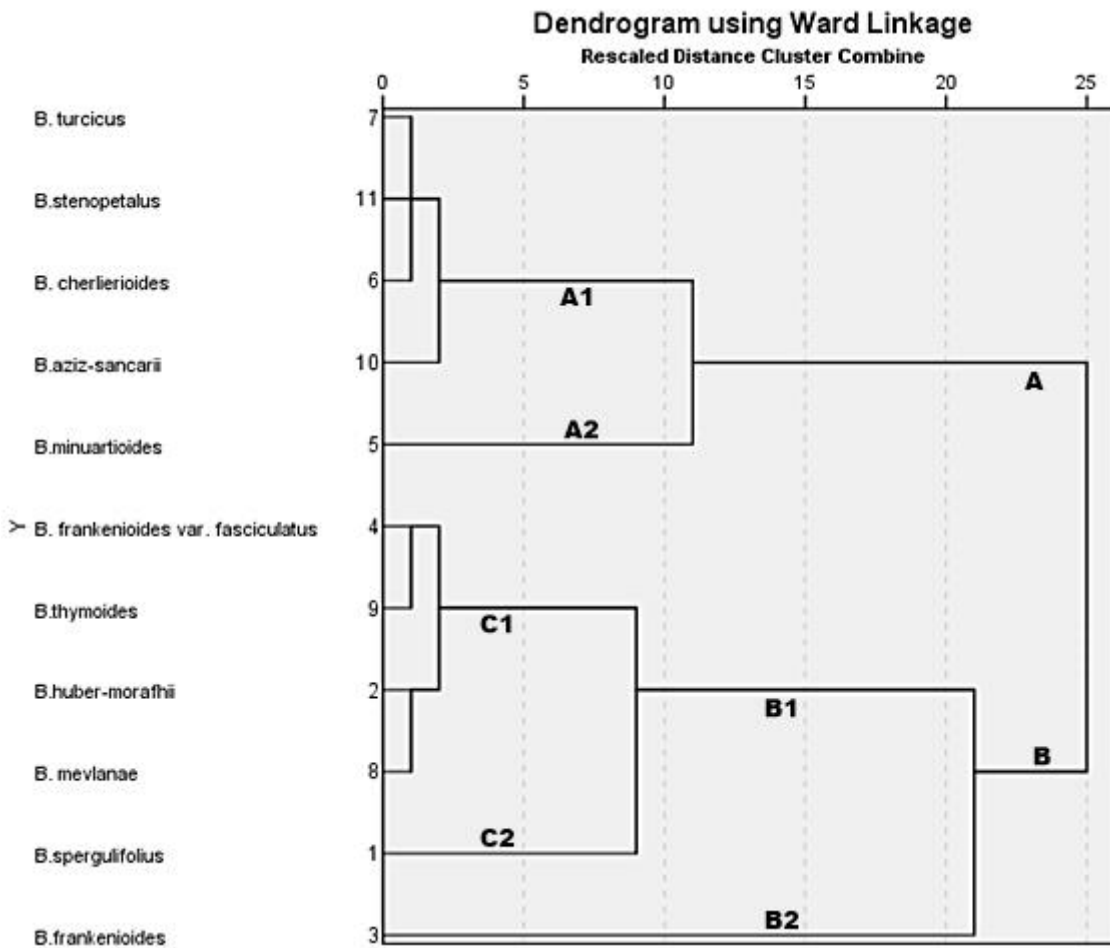
Figure 3 Cluster dendrogram showing species similarities based on pollen micro-morphological data

4. CONCLUSION

The findings of the study shows, pollen ornamentations and pollen shape to be important morphological characteristics for the systematics of the taxa. Pollen grains are isopolar symmetrical. The pollen grains of the *Bolanthus* taxa are oblate spheroidal and prolate spheroidal. The pollen grains are polipantoporate. The pollen ornamentation of all taxa is scabrate-perforate. Morphological structures of pollen seem to be useful for distinguish taxa. The outcomes of the study could be benefited in taxonomical studies.

The Declaration of Conflict of Interest/ Common Interest

No conflict of interest or common interest has been declared by the authors.

Authors' Contribution

Y.C: Literature research, data collection, organize the execution of the study, contribution

CÖMERT et al.

Pollen morphology in the genus Bolanthus (Ser.) Reichb. (Caryophyllaceae) in Turkey

to article writing and study, data entry and measurement, create an idea.

M.N.T: Contribution to article writing and study, data entry and measurement.

M.K: Provision of the plant material, provide a working environment and tools, create an idea.

The Declaration of Ethics Committee Approval

The authors declare that this document does not require an ethics committee approval or any special permission.

The Declaration of Research and Publication Ethics

The authors of the paper declare that they comply with the scientific, ethical and quotation rules of SAUJS in all processes of the paper and that they do not make any falsification on the data collected. In addition, they declare that Sakarya University Journal of Science and its editorial board have no responsibility for any ethical violations that may be encountered, and that this study has not been evaluated in any academic publication environment other than Sakarya University Journal of Science.

REFERENCES

[1] A. Guner, Ozhatay, T. Ekim and K.H.C. Baser, "Flora of Turkey and the East Aegean Islands," Vol. 11, Edinburg University Press, Edinburgh, 2000.

[2] M. Korkmaz and H. Özçelik, "Economic importance of *Gypsophila* L., *Ankyropetalum* Fenzl and *Saponaria* L. (Caryophyllaceae) taxa of Turkey." Afr. J. Biotechnol., 10: 9533-9541, 2011.

[3] O. Seçmen, Y. Gemici, G. Gork, L. Bekat and E. Leblebici, "Systematic of Seed Plants," Ege University Publishing., Izmir, Turkey, 2004.

[4] V. Bittrich Caryophyllaceae., In: K. Kubitzki, JG. Rohwer, Bittrich V, editors, "The families and genera of vascular plants," Vol. 2. Berlin (Germany): Springer; p. 206–236, 1993.

[5] YI. Barkoudah, "A revision of *Gypsophila, Bolanthus, Ankyropetalum* and *Phryna,*" Wentia 9:1–203, 1962.

[6] M. Zohary, *Bolanthus* (Ser.) Reichenb. P. 102 in Flora Palaestina, vol. 1, eds. M. Zohary and N. Feinbrun-Dothan Jerusalem: Israel Academy of Sciences and Humanities., 1966.

[7] YI. Barkoudah and JR. Akeroyd, *Bolanthus* (Ser.) Reichenb. Pp. 222–223 in Flora Europaea, vol. 1, eds. T. G. Tutin, V. H. Heywood, N. A. Burges, D. H. Valentine, S. M. Walters, and D. A. Webb, Cambridge, UK: Cambridge University Press, 1993.

[8] D. Phitos, *Bolanthus* (Ser.) Reichenb. Pp. 325–329 in Flora Hellenica, vol. 1, eds. A. Strid and K. Tan. Koenigstein: Koeltz Scientific Books., 1997.

[9] N. Özhatay, Ş. Kültür & N. Aksoy, "Checklist of additional taxa to the Supplement Flora of Turkey II. Turk," J Bot., 23: 151-169, 1999.

[10] Z. Aytaç & H. Duman, "Six new taxa (Caryophyllaceae) from Turkey," Ann. Bot. Fennici 41: 213-221, 2004.

[11] M. Koç, E. Hamzaoğlu, "*Bolanthus turcicus* (Caryophyllaceae), a new species from Turkey, " PhytoKeys., 52: 81-88, 2005.

[12] E. Hamzaoğlu, M, Koc, "*Bolanthus sandrasicus* sp. nov. (Caryophyllaceae) from Turkey," Nord J Bot 35: 563-568, 2017a.

[13] S. Chanda, "On the pollen morphology of some Scandinavian Caryophyllaceae," Grana Palynol. 3:67–89, 1962.

[14] JW. Nowicke, "Pollen morphology in the order Centrospermae," Grana., 15:51–77, 1975.

[15] PD. Moore, JA. Webb, ME. Collinson, "An illustrated guide to pollen analysis," London (UK): Hodder and Stoughton., 1977.

[16] D. Al-Eisawi, "Pollen morphology of Caryophyllaceae in Jordan," Mitteilungen (aus)

CÖMERT et al.

Pollen morphology in the genus Bolanthus (Ser.) Reichb. (Caryophyllaceae) in Turkey

der Botanischen Staatssammlung Munchen., 28:599 –614, 1989.

[17] WK Taia, "On the pollen morphology of some Egyptian Caryophyllaceae," J King Saud Univ. 6:149–165, 1994.

[18] W. Punt, PP, Hoen, "The Northwest European pollen Flora: 56," Caryophyllaceae. Rev Palaeobot Palynol. 88:83–272, 1995.

[19] FX Wang, NF Qian, YL Zhang, HQ. Yang, "Pollen flora of China," Beijing (China): Science Press, 1997.

[20] K. Yildiz, "Pollen morphology of Caryophyllaceae species from Turkey," Pak J Bot., 33:329–355, 2001.

[21] A. Perveen, M. Qaiser, "Pollen flora of Pakistan-LI –Caryophyllaceae," Pak J Bot., 38:901–915, 2001.

[22] S. Sahreen, MA. Khan, AA. Meo, A. Jabeen, "Studies on the pollen morphology of the genus Dianthus (Caryophyllaceae) from Pakistan," Biol Divers Cons., 1:89–98, 2008.

[23] E. Ataşlar, I. Potoglu Erkara, S. Tokur, "Pollen morphology of some Gypsophila L. (Caryophyllaceae) species and its taxonomic value," Turk J Bot., 33:335–351, 2009.

[24] LX. Dong, XL. Guan, "Pollen morphology of eight species of Dianthus from Xinjiang," Bull Bot Res. 29:647–650, 2009.

[25] K. Aktaş, Y. Altan, C. Ozdemir, P. Baran, T. Garnatje, "Comparative pollen morphology of Turkish species of Petrorhagia (Caryophyllaceae) and its systematic implications," Biologia. 65:444–450, 2010.

[26] İ. Kızılpınar, B. Özüdoğru, E. Özmen, S. Erik, C. Doğan, "Morphological, palynological and ecological features of Dianthus engleri Hausskn. & Bornm.," Hacettepe J Biol Chem., 38:139–147, 2010.

[27] A. Nejad Falatoury, F. Ghahremaninejad, M. Assadi, "Palynological study of the genus Gypsophila in Iran," Rostaniha. 18:16–32, 2017.

[28] F. Ullah, M. Zafar, M. Ahmad, S. Dilbar, SN. Shah, A. Sohail, W. Zaman, M. Iqbal, S. Bahadur, A. Tariq, "Pollen morphology of subfamily Caryophylloideae (Caryophyllaceae) and its taxonomic significance," Microscop Res Tech., 81:704–715, 2018.

[29] LX. Dong, CY. Yang, MX. Wang, MR. Huang, YM. Cai, "A new speciesm of the genus Dianthus from Xinjiang, China," Bull Bot Res., 28:644–647, 2008.

[30] C. Vural, "A new species of Dianthus (Caryophyllaceae) from Mount Erciyes, Central Anatolia, Turkey," Bot J Linn Soc., 158:55–61, 2008.

[31] MP. Macukanovic-Jocic, SV. Jaric, MA. Mladenovic, "Palynomorphological study of Dianthus petraeus Waldst. Et Kit. (Caryophyllaceae)," Arch Biol Sci., 67:973–980, 2015.

[32] A. Nejad Falatoury, M. Assadi, F. Ghahremaninejad, "A new species of Gypsophila (Caryophylloideae, Caryophyllaceae) from Iran," Phytotaxa., 222:276–282, 2015.

[33] A. Nejad Falatoury, M. Assadi, F. Ghahremaninejad, "New species and new synonymy in the genus Gypsophila L. subgenus Pseudosaponaria Williams (Caryophyllaceae)," Adansonia. 38:257–265, 2016.

[34] Wodehouse, "R.R. Pollen grains," McGraw-Hill, New York, 574 pp, 1935.

[35] JW Walker, "Evolution of exine structure in the pollen of primitive Angiosperms," Am J Bot., 61: 891-902, 1974a.

[36] JW. Walker, "Aperture evolution in the pollen of primitive Angiosperms," Am J Bot., 61: 1112-1137, 1974b.

[37] W. Punt, PP. Hoen, S. Blackmore, S. Nilsson, A. Le Thomas, "Review of Palaeobotany and Palynology," Volume 143, Issues 1–2, 2007, Pages 1-81, 2007.

CÖMERT et al.

Pollen morphology in the genus Bolanthus (Ser.) Reichb. (Caryophyllaceae) in Turkey

[38] NM. Pınar and E. Oybak, "Pollen Morphology of Turkish Endemic *Bolanthus* (Ser.) Reichb. (Caryophyllaceae)," Hacettepe Bulletin of Natural Sciences and Engineering., 26, 1-9.

[39] A. Kaplan, "Pollen morphology of some *Paronychia* species (Caryophyllaceae) from Turkey," Biologia, 63(1), 53-60, 1997, 2008.

[40] E.İ. Poyraz and Ataşlar, E. "Pollen and seed morphology of *Velezia* L. (Caryophyllaceae) genus in Turkey," Turk J Bot., 34, 179-190, 2010.

[41] G. Mostafavi and I. Mehregan, "Pollen Micro-morphology of the Minuartia Species (Caryophyllaceae) in Iran," International Journal of Modern Botany., 4(1), 8-21, 201, 2014.

[42] K. Yıldız, A. Çırpıcı and M. Y. Dadandı, "Pollen morphology of Silene taxa (Caryophyllaceae) in four sections from Turkey," Phytologia Balcanica., 16 (1), 85–95, 2010.

[43] D. Ulukuş, "Morphology, anatomy and palynology study on Turkish endemic species *Saponaria karapinarensis* (Caryophyllaceae)," Phytotaxa., 374(1), 080–086, 2018.

[44] X. Cui, M. Wang, L. Gu, JX. Liu, "Pollen morphology of Chinese Caryophylleae and its systematic significance. Palynology," 43 (4), 574– 584, 2019.

[45] D. Mete, "Türkiye *Dianthus* L. (Caryophyllaceae) taksonları üzerinde palinolojik araştırma," Ankara University, Institute of Science, Ph.D Thesis, Thesis No: 568365, 2019.

Title: The Importance in Phylogenetic Relationships of The Regions Belonging to Nuclear and Plastid DNA among Crocus Biflorus Subspecies

Authors: Aykut YILMAZ

The Importance in Phylogenetic Relationships of The Regions Belonging to Nuclear and Plastid DNA among *Crocus biflorus* Subspecies

Aykut YILMAZ[*1]

Abstract

The genus *Crocus* L. (Iridaceae) composed of about 200 species is taxonomically very problematic, because of introgression and backcrossing observed among closely related species. Furthermore, determination of new taxa and variable characters observed in these new taxa are other important reasons of the taxonomic problems. Recently, many molecular based studies to understand the phylogenetic relationships of the *Crocus* taxa show the presence of the problems among the taxa, especially in *C. biflorus* subspecies. As a result of this, some researchers state that the term of subspecies must be changed in the genus and the most of subspecies must be categorized as species. For these reasons, in this study, the four regions belonging to nuclear and plastid DNA (*ITS1-5.8S rRNA-ITS2*, *psbA-trnH IGS*, *rpoC1* and *trnL-trnF IGS*) were used to understand the identification and separation abilities of taxa studied, in addition to understanding the taxonomy of *C. biflorus* subspecies.

Keywords: *Crocus*, introgression, backcrossing, *C. biflorus*

---

[*] Corresponding Author: aykut.yilmaz@usak.edu.tr
[1] Usak University, Usak, Turkey, ORCID: https://orcid.org/0000-0002-0327-8388

Aykut YILMAZ

The Importance in Phylogenetic Relationships of The Regions Belonging to Nuclear and Plastid DNA amon...

1. INTRODUCTION

The genus *Crocus* L. belonging to the family Iridaceae consists of about 200 recognized species distributed from western Europe and north west Africa to western China. Balkan Peninsula and Turkey are considered as the center of species diversity for the genus [1, 2, 3, 4].

The genus *Crocus* is famous with their flowers in different colours and popular ornamentals. However, *C. sativus* is the best popular species of the genus because of the Saffron known as the world's most expensive spices [5].

The genus is very complicated and hard to understand as taxonomic and phylogenetic. In addition to intermediate or variable characters observed in closely related species caused by introgression and backcrossing [6, 7], especially the continuously determination of new taxa and not assigned to any series [8] are the main reasons of taxonomic problems and doubtful species identification within the genus. Furthermore, recent phylogenetic analyses clearly show that subspecies of *C. biflorus* occur in distinct clades even in different series on the dendrogram prepared for phylogenetic relationships [9, 10]. This situation reveal that subspecies status of the genus for *C. biflorus* is incorrect. In other words, the term "subspecies" which was brought into the genus taxonomy by Mathew (1982) [1] can not be maintained any more [2].

Molecular studies such as PCR-based and especially in last years the studies on DNA sequence informations accelerated understanding of the genus taxonomy. As a result of these studies, taxonomical situation of the genus *Crocus* changed [9, 10, 11, 12] and many taxonomic classifications belonging to the genus were revised because of incorrect phylogenetic relationships.

Furthermore, two new series named as *Isauri* and *Lyciotauri* for section *Nudiscapus* were described by Kerndorff et al. (2014; 2015) [13, 14] and some subspecies of *C. biflorus* were grouped into these series [15].

For these reasons stated, determination of phylogenetic relationships among *Crocus biflorus* subspecies and grouped according to their genetic similarity of subspecies is necessary.

In this study, different regions containing *ITS1-5.8S rRNA-ITS2*, *psbA-trnH IGS*, *rpoC1* and *trnL-trnF IGS* belonging to nuclear and plastid DNA were used to understand the taxonomy of *C. biflorus* subspecies and to contribute the solution of the still existing problems.

2. MATERIAL AND METHODS

Sequence informations of four different regions containing *ITS1-5.8S rRNA-ITS2*, *psbA-trnH IGS*, *rpoC1* and *trnL-trnF IGS* belonging to nuclear and plastid DNA were provided from National Centre of Biotechnology Information [16]. Sequence informations belonging to *Crocus biflorus* subspecies for each regions were separately examined to evaluate discrimination ability of each regions studied and to understand the taxonomy and phylogenetic relationships of *C. biflorus* subspecies. For this aim; 16 subspecies of *C. biflorus* for *ITS1-5.8S rRNA-ITS2*, 9 subspecies of *C. biflorus* for *psbA-trnH IGS*, 16 subspecies of *C. biflorus* for *rpoC1*, 17 subspecies of *C. biflorus* for *trnL-trnF IGS* and their sequence informations were performed by using Molecular Evolutionary Genetics Analysis (MEGA).

After the sequence informations for *C. biflorus* subspecies were obtained, multiple sequence alignments for each regions were seperately performed by using MEGA X [17].

After that, the alignment sequence informations for each barcoding regions studied were used to assign the variable sites, probabilities of substitution from one base to another base, transitional substitutions (%), transversional substitutions (%), transition/transversion rates for purines-pyrimidines and nucleotide frequencies (Table 5).

Moreover, the tables showing the variable sites were prepared for each regions separately (Table 1, 2, 3, 4).

Aykut YILMAZ

The Importance in Phylogenetic Relationships of The Regions Belonging to Nuclear and Plastid DNA amon...

Neighbour-joining dendrograms showing bootstrap values on branches were provided for each regions examined to determine the species identification abilities and phylogenetic relations among *C. biflorus* subspecies.

All positions containing gaps and missing data for each regions were eliminated with the complete deletion option of the program for effective analyses.

3. RESULTS AND DISCUSSIONS

3.1. Analysis results for ITS1-5.8S rRNA gene-ITS2

Sequence informations belonging to 16 subspecies of *C. biflorus* were provided from NCBI [8, 10]. These DNA regions containing sequence informations of *ITS1-5.8S rRNA gene-ITS2* were aligned by using Molecular Evolutionary Genetics Analysis (MEGA X). The sites with missing/ambiguous data and gaps were excluded for effective analyses in the determination of alignment length and variable sites. After the exclution of these regions, alignment length for taxa studied was established as 604 bp. Totally 62 variable sites for taxa examined were determined (Table 1).

Furthermore, the probabilities of substitutions from one base to another base were computed as transitional and transversional substitutions (Table 5). It was observed that rate of transitional substitutions with 75.72 % is higher than the transversional substitutions. In other words, it can be said that the variable sites among the *C. biflorus* taxa are highly caused by the substitutions between same base groups (purines; A ↔ G or pyrimidines; C ↔ T).

In addition to the rate of base substitutions, transition/transversion rate for purines (k_1), pyrimidines (k_2) and overall transition/transversion rate (R) were assigned as 3.73, 8.84 and 2.89, respectively.

The nucleotide frequencies for *ITS1-5.8S rRNA gene-ITS2* of *C. biflorus subspecies* were analysed as 37.42 % (A+T/U) and 62.58 % (C+G) (Table 5). In other words, it can be said that the DNA region examined consists of highly G and C bases.

Finally, Neighbor-Joining (NJ) dendrogram based on the sequence informations of *ITS1-5.8S rRNA gene-ITS2* for *C. biflorus* subspecies was drawn to evaluate the phylogenetic relationships of taxa studied (Figure 1). Furhermore, the separation ability of *ITS1-5.8S rRNA gene-ITS2* was evaluated for the taxa studied. Branch lengths in dendrogram infer the evolutionary distances. The evolutionary distances in dendrogram were computed using the Maximum Composite Likelihood method [18].

Table 1

Subspecies of *C.biflorus* and variable sites belonging to *ITS1-5.8S rRNA-ITS2* (The numbers show variable nucleotides)

Subspecies	42	43	47	52	53	57	59	61	64	65	67	71	74	78	84	90
fibroannulatus	T	C	T	C	T	G	C	C	G	T	C	C	C	T	C	G
pulchricolor	.	T	C	A	A	.	.	T	.	.	.	.	.	C	.	.
albocoronatus	.	.	.	.	.	.	A	.	.	.	.	.	T	.	T	A
wattiorum	C	T	.	A	A	A	.	T	.	.	.	.	.	C	.	.
atrospermus	.	T	.	A	A	A	.	T	.	.	.	T	C	.	.	.
artvinensis	.	.	.	.	.	.	.	.	.	.	.	.	.	.	.	.
isauricus	.	T	.	A	A	A	.	T	.	C	.	.	.	C	.	.
tauri	.	.	.	.	.	.	.	.	.	.	.	.	.	.	.	.
punctatus	.	T	C	A	A	.	.	T	.	C	.	.	C	.	.	.
nubigena	.	T	C	A	A	.	T	.	.	.	.	T	C	.	.	.
yataganensis	.	T	.	A	A	.	.	T	T	.	.	.	C	.	.	.
caricus	.	T	.	A	A	A	.	T	.	.	.	.	C	.	.	.
ionopharynx	.	T	.	A	A	A	.	T	.	.	.	T	C	.	.	.
leucostylosus	.	T	C	A	A	.	.	T	.	C	.	.	C	.	.	.
crewei	.	T	.	A	A	A	.	T	.	.	T	T	.	C	.	.
pseudonubigena	.	.	.	.	.	.	.	.	.	.	.	.	.	.	.	.

Subspecies	96	98	101	103	117	127	158	166	173	228	230	244	259	295	442
fibroannulatus	T	A	A	A	A	G	C	G	C	C	A	T	C	C	G
pulchricolor	.	G	.	.	.	.	.	.	.	G	.	.	T	T	C
albocoronatus	.	.	.	.	.	A	.	A	.	.	.	.	.	.	.
wattiorum	.	G	.	.	.	.	.	.	G	.	C	T	.	.	C
atrospermus	.	G	.	.	.	T	.	.	G	.	.	T	.	.	C
artvinensis	.	.	.	G	.	.	.	.	.	.	.	.	.	.	.
isauricus	.	G	G	.	C	.	.	.	T	G	.	.	T	T	C
tauri	.	.	.	.	.	.	.	.	.	.	.	.	.	.	.

punctatus	. G . . . . . . G . . T T C
nubigena	. G . . . . . . G . . T T C
yataganensis	. G . . C . . . G . . T . C
caricus	. G . . C . . T G . . T T C
ionopharynx	C G . . . . . . G G . T T C
leucostylosus	. G . . . . . . G . C T T C
crewei	. G . . . . . . G . . T . C
pseudonubigena	. . . . . A . . . .

```
                4 4 4 5 5 5 5 5 5 5 6 6 6 6 6 6
                7 7 8 0 4 5 7 8 9 9 0 1 2 2 2 2
                6 7 3 9 3 3 8 9 1 4 8 4 6 7 8 9
```

fibroannulatus	C T G T A T C C C T G C T C C
pulchricolor	. . . T . . T . . A T C . G
albocoronatus	. . A . . . T . . . . C T .
wattiorum	T . . C T . T . T . . A T . . G
atrospermus	T . . T . . T T . A T . . G
artvinensis	. . . . C T .
isauricus	. C . . T . . T . . A T C . G
tauri	. . . . T C . .
punctatus	. C . . T . . T . . A T C . G
nubigena	. . A . T C . . T . . A T . . G
yataganensis	T . . . T . . T . . A T . . G
caricus	. C . . T . . T . . A T . . G
ionopharynx	. C . . T C . . T . . A T . . G
leucostylosus	. C . . T . . T . . A T C . G
crewei	T . . . T . . T . . C A T . . G
pseudonubigena	. . A . . . . T C . .

```
                6 6 6 6 6 6 6 6 6 6 6 6 6 6 6 6
                3 3 3 3 3 4 7 7 8 8 8 8 9 9 9
                2 4 7 8 0 2 3 1 3 4 5 1 2 4
```

fibroannulatus	T G T C T T G G A G T G T G
pulchricolor	. . . T C G C A . G A G C A .
albocoronatus	. . . . A . . G A . .
wattiorum	. . . T C G C A . G A G . C .
atrospermus	. . . T C G T A . G A G . C .
artvinensis	. . . . . C . . . . . A . .
isauricus	. . . . C G C A . G A G . C .
tauri	. T C T . G . . A . . G A . .
punctatus	. . . T C G C A . G A G C C .
nubigena	. . . T C G C A . G A G C C .
yataganensis	. . . T C G T A . G A G . C .
caricus	. . . T C G C A . G A G . C .
ionopharynx	. . . T C G C A . G A G C C .
leucostylosus	. . . T C G C A . G A G C C .
crewei	. . . T C G C A . G A G C C A
pseudonubigena	C T C T . G . . A . . G A . .

```
  90 ┌ Crocus biflorus subsp. punctatus
  61 └ Crocus biflorus subsp. leucostylosus
  29   Crocus biflorus subsp. pulchricolor
       Crocus biflorus subsp. nubigena
  40 71 Crocus biflorus subsp. ionopharynx
        Crocus biflorus subsp. isauricus
  100 78 Crocus biflorus subsp. caricus
  41   Crocus biflorus subsp. wattiorum
       Crocus biflorus subsp. crewei
  43   Crocus biflorus subsp. atrospermus
  43   Crocus biflorus subsp. yataganensis
  71  Crocus cf. biflorus subsp. tauri
      Crocus biflorus subsp. pseudonubigena
      Crocus biflorus subsp. fibroannulatus
  50  Crocus biflorus subsp. albocoronatus
  46  Crocus biflorus subsp. artvinensis

  0.0050
```

Figure 1 Neighbor-Joining dendrogram provided from *ITS1-5.8S rRNA-ITS2*

3.2. Analysis results for psbA-trnH IGS

Sequence informations belonging to 9 subspecies of *C. biflorus* were provided from NCBI [9]. These DNA regions containing sequence informations of *psbA-trnH IGS* were aligned by using Molecular Evolutionary Genetics Analysis (MEGA X). The sites with missing/ambiguous data and gaps were excluded for effective analyses in the determination of alignment length and variable sites.

Alignment length for taxa studied was established as 603 bp. Variable sites showing the phylogenetic relationships among the taxa examined were determined in 6 nucleotides (Table 2).

Transitional and transversional substitutions expressing the substitutions between same or different base groups were determined as 70.39 % and 29.61 %, respectively. Moreover, transition/transversion rate for purines (k_1), pyrimidines (k_2) and overall transition/transversion rate (R) were assigned as 2.30, 7.12 and 2.22, respectively (Table 5).

The nucleotide frequencies for psbA-trnH IGS of *C. biflorus subspecies* were analysed as 62.41 % (A+T/U) and 37.59 % (C+G) (Table 5).

Finally, Neighbor-Joining (NJ) dendrogram based on the sequence informations of *psbA-trnH IGS* for *C. biflorus* subspecies was drawn to evaluate the phylogenetic relationships of taxa studied and to understand the discrimination ability of *psbA-trnH IGS* for the taxa studied (Figure 2).

Table 2

Subspecies of *C.biflorus* and variable sites belonging to *psbA-trnH IGS* (The numbers show variable nucleotides)

	29	71	111	112	113	170
Crocus biflorus subsp. weldenii	C	A	T	C	T	C
Crocus biflorus subsp. leucostylosus	T	.	.	.	.	.
Crocus biflorus subsp. adamii	.	.	A	G	A	.
Crocus biflorus subsp. pseudonubigena	.	G	.	.	.	.
Crocus biflorus subsp. artvinensis	.	G	.	.	.	A
Crocus biflorus subsp. melantherus	.	.	.	.	.	.
Crocus biflorus subsp. pulchricolor	T	.	.	.	.	.
Crocus biflorus subsp. punctatus	T	.	.	.	.	.
Crocus biflorus subsp. stridii	T	.	A	G	A	.
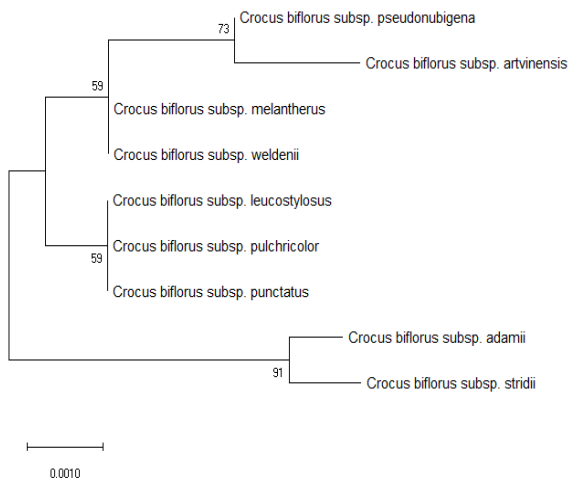
Figure 2 Neighbor-Joining dendrogram provided from *psbA-trnH IGS*

3.3. Analysis results for rpoC1

The DNA sequences belonging to 16 subspecies of *C. biflorus* for *rpoC1* were provided from NCBI [9] and than these sequence informations were aligned by MEGA X for further analysis.

Alignment length for 16 taxa belonging to *C.biflorus* subspecies was established as 575 bp, after the exclution of the positions containing gaps and missing data for effective analyses. Totally 8 variable sites were determined among the taxa studied (Table 3).

The rate of transitional substitutions for *rpoC1* sequence is higher with 91.83 % than transversional substitution. In addition to transitional and transversional substitutions, transition/transversion rates were assigned as 30.85 for purines (k_1) and 13.60 for pyrimidines (k_2). The overall transition/transversion rate (R) was 11.13. The nucleotide frequencies of A+T/U and G+C were determined as 58.03 % and 41.97, respectively (Table 5).

Finally, Neighbor-Joining (NJ) dendrogram based on the sequence informations of *rpoC1* for *C. biflorus* subspecies was drawn to evaluate the phylogenetic relationships of taxa studied and to understand the discrimination ability of rpoC1 for the taxa studied (Figure 3).

Table 3

Subspecies of *C.biflorus* and variable sites belonging to *rpoC1* (The numbers show variable nucleotides)

	292	270	287	316	407	437	506	566
Crocus biflorus subsp. wattiorum	A	A	A	T	T	G	G	C
Crocus biflorus subsp. weldenii	G	.	G	C	.	.	.	.
Crocus biflorus subsp. leucostylosus	G	.	G	.	.	.	.	.
Crocus biflorus subsp. adamii	G	.	.	.	.	.	.	.
Crocus biflorus subsp. pseudonubigena	G	.	.	.	.	.	.	.
Crocus biflorus subsp. artvinensis	G	.	.	.	.	.	A	.
Crocus biflorus subsp. melantherus	G	C	.	.	C	.	.	.
Crocus biflorus subsp. pulchricolor	G	.	G	.	.	.	.	.
Crocus biflorus subsp. punctatus	G	.	G	.	.	.	.	.
Crocus biflorus subsp. stridii	G	.	G	.	.	.	.	.

Aykut YILMAZ

The Importance in Phylogenetic Relationships of The Regions Belonging to Nuclear and Plastid DNA amon...

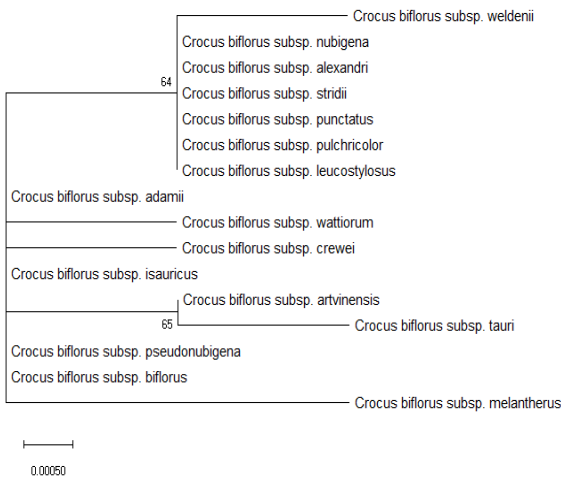| Crocus biflorus subsp. alexandri	G	.	G	.	.	.	.
Crocus biflorus subsp. isauricus	G	.	.	.	.	.	.
Crocus biflorus subsp. crewei	G	.	.	.	A	.	.
Crocus biflorus subsp. biflorus	G	.	.	.	.	.	.
Crocus biflorus subsp. nubigena	G	.	G	.	.	.	.
Crocus biflorus subsp. tauri	G	.	.	.	.	A	T

Figure 3 Neighbor-Joining dendrogram provided from *rpoC1*

3.4. Analysis results for trnL-trnF IGS

Sequence informations belonging to 17 subspecies of *C. biflorus* for *trnL-trnF IGS* were provided from NCBI [10]. After that, these DNA sequences for *C. biflorus* subspecies were aligned by using Molecular Evolutionary Genetics Analysis (MEGA X). The sites with missing/ambiguous data and gaps were excluded in the analysis of alignment length and variable sites.

Alignment length was established as 670 bp for taxa studied. Variable sites which were very important in species identifications and phylogenetic relationships among the taxa were determined in 9 nucleotides (Table 4).

The rates of transitional and transversional substitutions were determined as 79.77 % and 20.23 %, respectively. In other words, it can be said that the most of variable sites among the taxa

were caused by the substitutions between same base groups.

Furthermore, transition/transversion rate for purines (k_1), pyrimidines (k_2) and overall transition/transversion rate (R) were assigned as 8.45, 7.21 and 3.65, respectively (Table 5).

The nucleotide frequencies belonging to trnL-trnF IGS sequences of *C. biflorus subspecies* were analysed as 65.08 % (A+T/U) and 34.92 % (C+G) (Table 5).

Finally, Neighbor-Joining (NJ) dendrogram was drawn to evaluate the phylogenetic relationships of *C. biflorus* taxa and to understand the discrimination ability of *trnL-trnF IGS* for the taxa studied (Figure 4).

Table 4

Subspecies of *C.biflorus* and variable sites belonging to *trnL-trnF IGS* (The numbers show variable nucleotides)

	129	248	286	362	566	580	603	652	658
Crocus biflorus subsp. stridii	G	C	G	G	A	G	T	T	G
Crocus biflorus subsp. weldenii	.	.	.	.	.	.	.	.	.
Crocus biflorus subsp. melantherus	.	.	.	.	.	.	.	.	.
Crocus biflorus subsp. biflorus	.	A	.	.	.	.	.	.	.
Crocus biflorus subsp. fibroannulatus	A	.	.	A	G	.	C	.	.
Crocus biflorus subsp. albocoronatus	.	A	.	A	.	.	C	.	.
Crocus biflorus subsp. wattiorum	.	.	.	.	.	.	.	.	.
Crocus biflorus subsp. atrospermus	.	.	.	.	.	.	.	.	.
Crocus biflorus subsp. artvinensis	.	.	.	A	.	T	C	.	.
Crocus cf. biflorus subsp. tauri	.	.	A	A	G	.	C	.	.
Crocus biflorus subsp. nubigena	.	.	.	.	.	.	.	.	.
Crocus biflorus subsp. caelestis	.	.	.	.	.	.	C	.	.
Crocus biflorus subsp. yataganensis	.	.	.	.	.	.	.	.	.
Crocus biflorus subsp. caricus	.	.	.	.	.	.	.	C	.
Crocus biflorus subsp. crewei	.	.	.	.	.	.	.	.	.
Crocus biflorus subsp. pseudonubigena	.	.	.	A	.	.	C	.	T
Crocus biflorus subsp. adamii	.	.	.	A	G	.	C	.	.

Aykut YILMAZ

The Importance in Phylogenetic Relationships of The Regions Belonging to Nuclear and Plastid DNA amon...

Figure 4 Neighbor-Joining dendrogram provided from *trnL-trnF IGS*

Table 5

The comparisons of all studied DNA regions.

DNA regions	Taxon (number)	Alignment lenght [bp]	Variable site	Transitional substitutions (%)	Transversional substitutions (%)	(k_1)	Pyrimidines (k_2)	Purines Overall (R)	Nucleotide freq. (%) A+T/U	G+C
ITS1-5.8S rRNA-ITS2	16	604	62	75.72	24.28	3.73	8.84	2.89	37.42	62.58
psbA-trnH IGS	9	603	6	70.39	29.61	2.30	7.12	2.22	62.41	37.59
rpoC1	16	575	8	91.83	8.17	30.85	13.60	11.13	58.03	41.97
trnL-trnF IGS	17	670	9	79.77	20.23	8.45	7.21	3.65	65.08	34.92
Total	58									

4. CONCLUSIONS

In the comparisons of sequence informations according to species identification abilities, it can be said that the region belonging to *ITS1-5.8S rRNA gene-ITS2* is more efficient among the DNA regions examined for *Crocus* taxa. This region phylogenetically separated the taxa in two groups, besides it identified all taxa studied. Furthermore, variable sites that was important in species identification and phylogenetic relationships among taxa was observed in highest rate on *ITS1-5.8S rRNA gene-ITS2*.

It can be stated that although other DNA regions examined (*psbA-trnH IGS*, *rpoC1* and *trnL-trnF IGS*) clearly separated some taxa from each other, these regions were insufficient in the separation and identification of all taxa studied. Variable sites expressing the substitutions based on the sequence informations are the most important characters in the evaluation of taxa phylogenetically. However, these regions showing the sequence changes among the taxa were observed on several nucleotides. In other words, it can be stated that the sequence informations belonging to *psbA-trnH IGS*, *rpoC1* and *trnL-trnF IGS* were highly preserved for *C. biflorus* taxa.

Recent molecular studies show that taxa belonging to *C. biflorus subspecies* were not grouped together, even occur in distinct clades [9, 10]. In other words, it is observed that subspecies status of the genus for *C. biflorus* is incorrect and can not be maintained any more [2].

Harpke et al. (2016) [2] updated the Mathew's study (1982) [1] which present the nineteen subspecies of *Crocus biflorus* in Turkey and they stated as a result of this study that all subspecies of *C. biflorus* ranged from Balkan Peninsula to Caucasus and Iran represent the independent lineages and should be treated at species level. Similarly, Addam et al. (2019) [19] states as a result of the studies based on morphological and molecular genetic in the *Crocus* genus that the most of the subspecies must be categorized as species because of their genetic divergences. This opinion is still controversial among scientists and
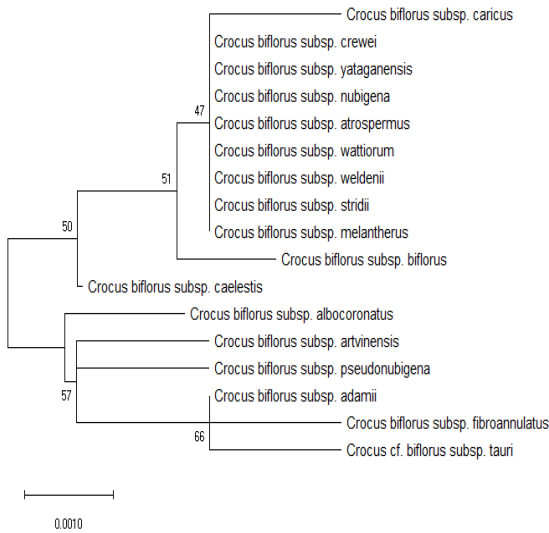
Aykut YILMAZ

The Importance in Phylogenetic Relationships of The Regions Belonging to Nuclear and Plastid DNA amon...

it has not completely resolved as in the number of taxa.

All of them make necessary the phylogenetically evaluation of *C. biflorus* taxa and the examination of their subspecies status in more detail.

For these reasons, in this study, *ITS1-5.8S rRNA-ITS2* belonging to nuclear DNA and three regions (*psbA-trnH IGS*, *rpoC1* and *trnL-trnF IGS*) belonging to plastid DNA were used to understand the taxonomy of *C. biflorus subspecies* and to contribute the solution of the still existing problems. Moreover, the discrimination abilities of each DNA regions examined and nucleotide substitutions were analysed for *C .biflorus* taxa. Although the different DNA regions and their combinations are very important for effective phylogenetic analysis, some barcoding regions are not enough for species identification and discrimination on the dendrogram prepared to show phlogenetic relationships. This study results could provide important data for further studies in the selection of usefull regions, in addition to undestanding of taxonomic relationships of *C. biflorus subspecies*.

Appendix

ITS1-5.8S rRNA-ITS2:

HE663991, HE663973, HE664018, HE663980, HE663975, HE664004, HE663976, HE664016, HE663972, HE664014, HE663978, HE664003, HE663969, LN864707, HE664017, HE664013

psbA-trnH IGS:

EU110184, EU110183, EU110150, EU110202, EU110195, EU110140, EU110134, EU110185, EU110129

rpoC1:

EU110612, EU110523, EU110533, EU110539, EU110544, EU110550, EU110605, EU110595, EU110637, EU110527, EU110530, EU110593, EU110522, EU110594, EU110524, EU110560

trnL-trnF IGS:

HE864180, HE864177, HE864182, HE864185, HE864208, HE864210, HE864257, HE864275, HE864227, HE864220, HE864183, HE864211, HE864207, HE864174, HE864165, HE864212, HE864198

The Declaration of Conflict of Interest/ Common Interest

No conflict of interest or common interest has been declared by the authors.

The Declaration of Ethics Committee Approval

This study does not require ethics committee permission or any special permission.

The Declaration of Research and Publication Ethics

The authors of the paper declare that they comply with the scientific, ethical and quotation rules of SAUJS in all processes of the paper and that they do not make any falsification on the data collected. In addition, they declare that Sakarya University Journal of Science and its editorial board have no responsibility for any ethical violations that may be encountered, and that this study has not been evaluated in any academic publication environment other than Sakarya University Journal of Science.

REFERENCES

[1] B. Mathew, ''The *Crocus*. A revision of the genus *Crocus*,'' Timber Press, London, 224 pp, 1982.

[2] D. Harpke, H. Kerndorff, E. Pasche, and L. Peruzzi, ''Neotypification of the name *Crocus biflorus* Mill. (Iridaceae) and its consequences in the taxonomy of the genus,'' Phytotaxa, vol. 260, no. 2, pp. 131–143, 2016.

[3] R.B. Saxena, ''Botany taxonomy and cytology of *Crocus* series *Reticulati*,'' World Journal of Pharmaceutical and Medical Research, vol. 2, no. 3, pp. 53–73, 2016.

[4] F. Roma-Marzio, D. Harpke, and L. Peruzzi, ''Rediscovery of *Crocus biflorus* var. *estriatus* (Iridaceae) and its taxonomic characterisation,'' Italian Botanist, vol. 6, pp. 23‒30, 2018.

[5] M.J. Bagur, G.L.A. Salinas, A.M. Jiménez-Monreal, S. Chaouqi, S. Llorens, M. Martínez-Tomé, and G.L. Alonso, ''Saffron: An Old Medicinal Plant and a Potential Novel Functional Food,'' Molecules, vol. 23, no. 1, 2018.

[6] R.G. Harrison and E.L. Larson, ''Hybridization, introgression, and the nature of species boundaries,'' J. Hered., vol. 105, pp. 795‒809, 2014.

[7] H. Kerndorff, E. Pasche, and D. Harpke, ''The Genus *Crocus* (Liliiflorae, Iridaceae): Taxonomical Problems and How to Determine a Species Nowadays?'' Stapfia, vol. 105, pp. 42‒50, 2016.

[8] O. Erol, D. Harpke, and H. Yıldırım, ''A new *Crocus* L. (Iridaceae) species from SE Turkey, based on morphological and molecular data,'' Phytotaxa, vol. 239, pp. 223–232, 2015.

[9] G. Petersen, O. Seberg, S. Thorsøe, T. Jørgensen, and B. Mathew, ''A phylogeny of the genus *Crocus* (Iridaceae) based on sequence data from five plastid regions,'' Taxon, vol. 57, no. 2, pp. 487–499, 2008.

[10] D. Harpke, S. Meng, T. Rutten, H. Kerndorff, and F.R. Blattner, ''Phylogeny of *Crocus* (Iridaceae) based on one chloroplast and two nuclear loci: ancient hybridization and chromosome number evolution,'' Molecular Phylogenetics and Evolution, vol. 66, pp. 617–627, 2013.

[11] D. Harpke, L. Peruzzi, H. Kerndorff, T. Karamplianis, T. Constantinides, N. Ranđelović, V. Ranđelović, M. Jušković, E. Pasche, and F.R. Blattner, ''Phylogeny, geographic distribution and new taxonomic circumscription of the crocus reticulatus species group (Iridaceae),'' Turk. J. Bot., vol. 38, no. 5, 2014.

[12] D. Harpke, A. Carta, G. Tomović, V. Ranđelović, N. Ranđelović, F.R. Blattner, and L. Peruzzi, ''Phylogeny, karyotype evolution and taxonomy of Crocus series Verni (Iridaceae),'' Plant Syst Evol., vol. 301, no. 1, pp. 309‒325, 2015.

[13] H. Kerndorff, E. Pasche, and D. Harpke, ''*Crocus isauricus* Siehe ex Bowles (Liliiflorae, Iridaceae) and its relatives,'' Stapfia, vol. 101, pp. 3–14, 2014.

[14] H. Kerndorff, E. Pasche, and D. Harpke, ''*Crocus lyciotauricus* Kerndorff & Pasche (Liliiflorae, Iridaceae) and its relatives,'' Stapfia, vol. 103, pp. 67–80, 2015.

[15] O. Erol, D. Harpke, and A. Çiftçi, ''*Crocus heilbronniorum*, a new Turkish species of Series *Lyciotauri* (Iridaceae),'' Phytotaxa, vol. 298, no. 2, pp. 173‒180, 2017.

[16] NCBI, National Centre of Biotechnology Information,
https://www.ncbi.nlm.nih.gov/genbank.

[17] S. Kumar, G. Stecher, M. Li, C. Knyaz, and K. Tamura, ''MEGA X: Molecular Evolutionary Genetics Analysis across computing platforms,'' Molecular Biology and Evolution, vol. 35, pp. 1547‒1549, 2018.

[18] K. Tamura, M. Nei, and S. Kumar, ''Prospects for inferring very large phylogenies by using the neighbor-joining method,'' Proceedings of the National Academy

Aykut YILMAZ

The Importance in Phylogenetic Relationships of The Regions Belonging to Nuclear and Plastid DNA amon...

of Sciences (USA), vol. 101, pp. 11030–11035, 2004.

[19] K. Addam, M. Bou-Hamdan, N. Sabbagh, J. Takkoush, and K. Hout, ''*Crocus baalbekensis* K. Addam & M. Bou Hamdan sp. Nov and its three forms (IRIDACEAE), new endemic species and forms from Lebanon, joined the Lebanese Flora,'' MOJ Ecology & Environmental Sciences, vol. 4, no. 2, pp. 75–83, 2019.

Sakarya University Journal of Science
SAUJS

Title: Handwritten Digit Recognition Using Machine Learning

Authors: Rabia KARAKAYA, Serap KAZAN

Handwritten Digit Recognition Using Machine Learning

Rabia KARAKAYA[1], Serap CAKAR[1*]

Abstract

Technology is getting more and more involved in our lives, and so are algorithms. These algorithms speed up work and reduce workload. Especially machine learning algorithms are improving day by day by imitating human behaviours. Handwriting recognition systems are also stand out on this field. In this study, handwriting digit recognition process has been done with algorithms having different working methods. These algorithms are Support Vector Machine (SVM), Decision Tree, Random Forest, Artificial Neural Networks (ANN), K-Nearest Neighbor (KNN) and K- Means Algorithm. The working logic of the handwriting digit recognition process was examined, and the efficiency of different algorithms on the same database was measured. A report was presented by making comparisons on the accuracy.

Keywords: handwriting digit recognition, machine learning

1. INTRODUCTION

Today, handwriting recognition systems are used in many areas. For example, there is a need for handwriting recognition systems for reading and archiving old documents, bank checks and letters. In addition to these examples, online handwriting recognition applications are also widely used. Especially in the field of education, there are educational applications that support handwriting

recognition in electronic devices such as tablets. There are customized applications supported by handwriting recognition for individuals with

physical or mental disabilities as well as children [2].

Some smartphone applications that we use in our daily lives also have handwriting recognition systems. Handwritten texts in the surrounding area can be quickly scanned and processed via the phone camera. The scanned texts can be translated into different languages or searches can be made over the internet.

The text recognition area has a very large scope. Handwriting recognition and typewriter / computer writing recognition are subfields of the

---

* Corresponding Author: scakar@sakarya.edu.tr
[1] Sakarya University, Department of Computer Engineering, Sakarya, Turkey, E-mail:
rabia.kara2@ogr.sakarya.edu.tr , ORCID: https://orcid.org/0000-0003-2704-3708, ORCID:
https://orcid.org/0000-0002-3682-0831

handwriting recognition area. Computer or typewriter recognition field can produce faster and more accurate results. Unlike handwriting recognition; It is expected to see higher success rates as there are no characteristic patterns and lines in letters or digits, such as spaces between letters and words.

There are many studies on handwriting recognition. Engin Dagdeviren, in his handwritten number recognition studies with Modified National Institute of Standarts and Technology (MNIST) data set; SVM and ANN compared to the obtained accuracy rates. In his tests on MATLAB, he reached a success rate of 99.97% in a data set of 10000 data for SVM. In the handwriting recognition system developed using ANN, he again achieved an 80.39% success in a data set of 10000 data [3].

Murat Sekerci used the correlation method for Turkish handwritten character recognition and strengthened his systems with the KNN algorithm. The data set was created with text samples taken from 172 different people. With this study, recognition rates of 93% in digits, 90.4% in lowercase letters and 91.2% in capital letters were achieved. These rates decreased by 10% in the words and digits written in combination. 100% success was achieved in text which is a mix of letters and digits. In addition, recognition system has been strengthened by using dictionary [1].

Tsehay Admassu Assegie has developed a digit recognition application with a Decision Tree algorithm on a data set consisting of 42000 rows and 720 columns. A success of 83.4% was achieved [4].

In this study, tests were performed on the MNIST handwritten digit data set with SVM, Decision Trees, Random Forests, ANN, KNN, K-Means Algorithm. The success rates of the algorithms in the field of handwriting recognition were compared. In the methods section of this article, brief information is given about handwriting recognition and compared machine learning methods. In the third section, the values obtained as a result of the study were compared.

Evaluations were made on the compared machine learning algorithms.

2. METHODS

Handwriting recognition has some general steps. These are; pre-processing, segmentation, feature extraction, classification and recognition, post processing.
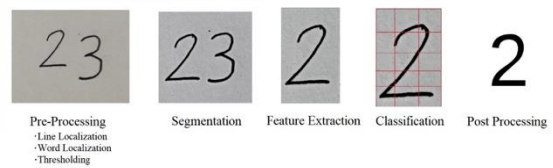
Figure 1. Handwriting digit recognition steps

In the pre-processing step, operations such as line localization, word localization, thresholding are performed [1].

In the segmentation step, words are divided into parts corresponding to letters or digits. Even this is the explanation in the literature, since the MNIST data set was used in this study, the segmentation step was not performed.

In the feature extraction step, the data is processed and defined in a more limited space and prepared for the recognition step.

In general, the classification and recognition step consists of only matching the character's symbolic class. There are many methods that can be used in this step. ANN, classification algorithms are some of them. The data set to be used at this step is so important. The diversity and richness of the data set in which the algorithm is trained will increase the success rate [5].

In post processing step, it is aimed to eliminate possible errors after recognition. Some systems use dictionaries at this stage. Thus, the recognized text after the recognition process is checked again by comparing it with possible words in the dictionary [6].

In this study, a data set that is suitable to be studied was used. Therefore, the results obtained in this study may be very different in another study. It is clear that handwriting digit recognition is affected by many situations.

Figure 3. Sample images of MNIST data [13]
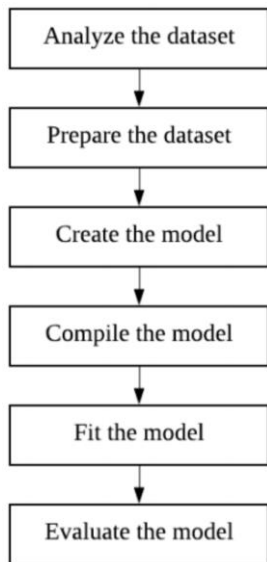
Figure 2. Handwriting recognition processing steps

In this study, MNIST data set was used for the training and tests of the system. MNIST database is widely used internationally. It consists of handwritten numbers. The MNIST database contains 60,000 training data and 10,000 test data. The black and white images from MNIST were normalized to fit into a 28x28 pixel bounding box and anti-aliased, which introduced grayscale levels [12].

All tests within the scope of this study were performed on the PyCharm (v2020.1 community edition), which is an integrated development environment used in programming, specially for the Python language.

Figure 4. Representation of the digit 1 on matrix form in MNIST [14]

A Python library called Scikit Learn (v0.22.2.post1) was used in the study. It offers the opportunity to effectively implement many machine learning algorithms. It enables the rapid training and testing of machine learning algorithms with high level languages.

The definitions of the values in the reports provided by the Scikit Learn's Metrics module are as follows:

Precision: TP / (TP + FP) It is the accuracy rate of positive predictions.

Recall: TP / (TP + FN) is the sensitivity or true positive rate (TPR).

F1 Score: This value is the harmonic mean of precision and recall values.

Accuracy: This value, which can also be called accuracy, shows the accuracy rate. It is calculated

by the ratio of correct predictions to all predictions made.

While determining the algorithms to be compared within the scope of the study, algorithms belonging to different sub-branches of machine learning were chosen.

2.1. Support Vector Machine

SVM, a supervised classification method, starts with a previously created training set. During the training, SVM learns the relationship of each data and tag in the existing training set. Creates SVM with these relationships [3].

SVM is successful in solving classification problems compared to many other techniques. This is one of the reasons why this technique is chosed as one of the algorithms to be tested in this study. Kernel function selection is an important step in the process of SVM to solve a problem [7].

Polynomial kernel function was used in the tests performed on the MNIST data set on Scikit Learn. In tests performed on other kernel functions, the highest accuracy was obtained in this function. The test results are given on Table 1.

Table 1. SVM tests for choosing kernel function

Kernel Function	Training Time (s)	Test Time (s)	Accuracy (%)
Polynomiyal	0.7	6.3	90
RBF	0.8	7.7	89
Linear	0.4	5.8	87
Sigmoid	0.6	7.8	84

2.2. Decision Tree

Decision trees form a classification model as a tree structure for the solution of a problem. The tree structure and rules are easy to understand. This simplifies the implementation of the algorithm. Decision trees method consists of simple sequential decision making operations [8].

One of the most important steps in creating the tree structure is choosing the attribute value for which the branching in the tree will be determined [8].

The division criterion for decision trees in the Scikit Learn library is the Gini Index. The decision tree method provided by the Scikit Learn library was used in the tests. Scikit Learn library uses CART algorithm that creates binary trees. In this algorithm, each node has only two sub-nodes or end leaves. Tree structures with more sub-nodes can be created using different algorithms such as ID3 [9].

2.3. Random Forest

Random forest algorithm can be used in both classification and regression problems like decision trees. The logic of work is to create more than one decision tree and produce average results with the help of these trees.

The reason why this algorithm is called randomly is that it offers extra randomness during the creation of the tree structure. When splitting a node, instead of looking for the best attribute directly, it looks for the best attribute in a subset of random attributes. This situation creates more diverse trees [9].

In this test, the Gini index was used as the branching factor like the decision trees. The number of trees is determined as 150.

2.4. Artifical Neural Network

ANN model is modeled on the transmission model of human nervous system and parallel computing ability of human brain instead of computer architecture. Neurons, which are the basic units in the human nervous system, take certain data and produce a binary output. Similar logic is also valid for ANNs [3].

When designing a handwritten character recognition application with ANN, the first step is to create a matrix of a character in the text expected to be recognized in accordance with the input for the neural network. In this way, artificial neural network can be trained. Outputs are created for each character's matrix. In the learning process, the excess number of neurons in the hidden layers causes the training process to take too much time and increases the remembering

ability of the network at the same rate. After learning, verification is done. This process can be done in many ways. One of these methods is to use databases that contain combinations of two or three letters. Thus, the letter sequence will not contain impossible combinations. (eg 'fdr') Another way is to use a word dictionary. Thus, it can be understood whether the string is a real word [1].

MLPClassifier stands for Multi Layer Perceptron. Unlike other classification algorithms such as SVM machines or Naive Bayes, MLPClassifier has a neural network to perform its classification task.

After the MLPClassifier model was created, it was trained with MNIST data and then tested. While creating the MLPClassifier, the 'batch_size' value was set to 200 as default. And the 'learning_rate' value is constant. It was set to '0.001'. Lastly as the activation function 'relu' was chosen.

2.5. K-Nearest Neighbor

KNN is one of the classification methods. The KNN algorithm is used to determine which class a new observation to be included in the sample from the observation values in a sample set with certain classes [10].

In this method, first of all, the similarity of the test data to be classified with the education data is calculated. Classification is made according to the threshold value determined with the average of the k data that appears to be the closest. The performance of the method is influenced by the closest neighbor number, threshold value, similarity measurement and sufficient number of normal behaviors in the learning cluster [11]. It was trained with MNIST data and then tested. While creating the KNN classifier with Scikit Learn, the number of neighbor was set to 5. And all points in each neighborhood are weighted equally as 'weight' parameter was set to 'uniform'.

2.6. K-Means Algorithm

This algorithm is one of the most preferred unsupervised learning algorithms. Clusters are created by looking at the similarity rates of the data. The number of clusters to be created in the algorithm is determined in advance. The number of clusters is expressed by "k". Among the algorithms compared within the scope of the study, the only algorithm that is an unsupervised learning algorithm is the K-means algorithm. While creating K-Means clustering with Scikit Learn, the number of clusters was set to 10. In the tests performed with Scikit Learn on the MNIST data set, it was observed that the accuracy of the clusters was high. Accuracy scores are given in table 3.

3. RESULTS AND DISCUSSION

In this study, handwriting digit recognition was made with six different machine learning algorithms. MNIST handwritten digits dataset was used in all tests.

Table 2 lists the values obtained from the algorithms tested. The definitions of the listed values are defined in the methods title. All values are average.

Table 2. Report values of compared algorithms

Algorithm	Precision	Recall	F1-Score
Support Vector Machine	0.97	0.98	0.97
Decision Tree	0.85	0.90	0.86
Random Forest	0.97	0.97	0.96
Artifical Neural Network	0.98	0.98	0.97
K-Nearest Neighbor	0.96	0.98	0.96

The accuracies of the compared algorithms are given in Table 3. The goal of this study and the table; to guide the people who will work in the field of handwriting digit recognition in the field

in which they will advance and in the method of machine learning they choose.

Table 3. Accuracies of compared algorithms

Algorithm	Accuracy	Training Time	Test Time
Support Vector Machine	%90	372.294 s	97.769 s
Decision Tree	%87	21.142 s	0.645 s
Random Forest	%97	63.055 s	1.106 s
Artifical Neural Network	%97	178.390 s	1.014 s
K-Nearest Neighbor	%98	36.396 s	865.93 s
K-Means Algorithm	%98	8.350 s	0.569 s

The use of SVM in the field of handwriting digit recognition is quite common. SVM based on statistical learning method have some advantages when compared with other classification algorithms. They can also work strongly and efficiently in situations where educational data are small. The ability to produce and generalize better classifiers is also high. Within the scope of this study, it has been observed that the SVM is widely used in the field of handwriting digit recognition and are suitable for use in the field of handwriting digit recognition, as evidenced by its values such as speed and efficiency.

Decision trees and random forest algorithms are actually built on the same basis. Random forest algorithms consist of trained decision trees algorithms. These two algorithms are well suited for use in handwriting digit recognition. Decision trees make inferences from the existing data set and form the tree structure. A little more prediction and randomness predominate in random forests. As can be seen in random forests, random forests provide higher accuracies, although they are trained much slower. Despite the low accuracy, a fast training period is in the decision trees.

ANN are used in many fields other than handwriting digit recognition today, and they are getting more and more popular. It is among the algorithms that give the best results with its high accuracy. It gives good results in problems aimed at imitating more people's decision-making mechanism, such as handwriting digit recognition.

KNN algorithm is one of the most preferred classification algorithms. Although it has a simple structure, it worked fast and gave high-accuracy results.

The only algorithm that is unattended among the algorithms compared in the study is the K-Means algorithm. It provided a very high efficiency in the tests and made very little mistakes in clustering.

In this thesis study, only one data set was studied. The working conditions of the algorithms can be examined by performing tests on different data sets. In this way, studies can be expanded and clearer results can be obtained.

Acknowledgements

Funding

The Declaration of Conflict of Interest/ Common Interest

No conflict of interest or common interest has been declared by the authors.

Authors' Contribution

R. K: Literature research, data collection, data processing, organize the execution of the study, contribution to article writing and study.

S. C: Contribution to article writing and study, literature research, create an idea.

The Declaration of Ethics Committee Approval

The authors declare that this document does not require an ethics committee approval or any special permission.

The Declaration of Research and Publication Ethics

The authors of the paper declare that they comply with the scientific, ethical and quotation rules of SAUJS in all processes of the paper and that they do not make any falsification on the data collected. In addition, they declare that Sakarya University Journal of Science and its editorial board have no responsibility for any ethical violations that may be encountered, and that this study has not been evaluated in any academic publication environment other than Sakarya University Journal of Science.

REFERENCES

[1] Sekerci, M., "Birlesik ve egik Turkce el yazisi tanima sistemi," Trakya University, Master's Thesis, 2007.

[2] Yilmaz, B., "Ogrenme guclugu ceken cocuklar icin el yazisi tanima ile ogrenmeyi kolaylastirici bir mobil ogrenme uygulamasi tasarimi," Maltepe University, Master's Thesis, 2014.

[3] Dagdeviren, E., "El yazisi rakam tanima icin destek vektor makinelerinin ve yapay sinir aglarinin karsilastirmasi," Istanbul University, Master's Thesis, 2013.

[4] Assegie, T. A., Nair, P. S., "Handwritten digits recognition with decision tree classification: a machine learning approach," International Journal of Electrical and Computer Engineering (IJECE), Indonesia, 446-4451, 2019.

[5] Arica, N., Vural, Y., F.T., "An overview of character recognition focused on offline handwriting," IEE Transactions on Systems Man and Cybernetics, 2001.

[6] MacKenzie, S., Tanaka-Ishii, K., "Text entry systems," Morgan Kaufmann Publishing, 123-137, 2007.

[7] Gunn, S.R., "Support vector machines for classification and regression," 1998.

[8] Safavian, S.R., Landgrebe, D., "A survey of decision tree classifier methodology," IEE Transactions on Systems Man and Cybernetics, 1991.

[9] Géron, A., "Hands-On machine learning with Scikit-Learn and TensorFlow concepts," O'Reilly Publishing, 2017.

[10] Arya, S., Mount, D.M., Netanyahu, N.S., Silverman, R. Wu, A.Y., "An optimal algorithm for approximate nearest neighbor searching in fixed dimension," Journal of the ACM, 2017.

[11] Kirmizigul Caliskan, S., Sogukpinar, I., KxKNN : "K-ortalama ve K-en yakin komsu yontemleri ile aglarda nufuz tespiti," Electronic Journal of Vocational Colleges (Ejovoc) , Kırklareli , 2015.

[12] Gunes, A., Yigit, T., "Hizlandirilmis destek vektor makineleri ile el yazisi rakamlarin taninmasi," 20th Signal Processing and Communications Applications Conference, Mugla, 2012.

[13] Liu, C, Fujisawa, H., "Handwritten digit recognition: Benchmarking of state-of-the-art techniques," Pattern Recognition, 2003.

[14] Fialoke, S., "Predicting Digits from their handwritten images, (16.10.2020), http://suruchifialoke.com/2017-06-15-predicting-digits_tensorflow.

Sakarya University Journal of Science
SAUJS

Title: Development of a Data Clustering System for 2DOF Robotic Ball Balancer Using Laser Scanning RangeFinder

Authors: Gokhan BAYAR

Development of a Data Clustering System for 2DOF Robotic Ball Balancer Using Laser Scanning RangeFinder

Gokhan BAYAR[1*]

Abstract

In this study, a new perspective for developing laser scanner rangefinder based data clustering system for a 2DOF robotic ball balancer was proposed. The study focused on detecting an object (i.e., ball) on the tilt-table robotic platform using the sensor fusion and data clustering systems proposed. Clustering system was modeled by following the principles of hierarchical clustering method. The developed system involving the clustering and sensor fusion algorithms was embedded in Matlab-Simulink environment to be able to run in real-time applications. The system was tested using an experimental platform including a 2DOF robotic ball balancer equipped with high resolution encoders and a laser scanner rangefinder. In the experiments, the goal was to detect the ball and its position not only on the flat but also on the tilted platform. A camera was also attached to the top of the experimental setup and used to monitor the location of the ball on the platform. By this way the results obtained using the proposed system could be verified for accuracy, performance and repeatability issues.

Keywords: Robotic ball balancer, laser scanner rangefinder, identification, object detection, sensor fusion, hierarchical clustering.

1. INTRODUCTION

Balancing systems are commonly used in automobile, space, aviation, maritime and manufacturing industries. They are utilized to adjust the systems which are under the effects of disturbances. The use of them gives ability to regulate the systems running in real-time operations. They are also used in the research &

development applications of the robotic systems. In the control, automation, robotics, mechatronics, electronics and mechanical engineering education, such systems are placed in the education plans as well.

As well as using robotic balancers in research and industrial applications, they give opportunities to students to test the data mining and control algorithms and observe the results. For example,

---
* Corresponding Author: bayar@beun.edu.tr
[1] Zonguldak Bulent Ecevit University, Department of Mechanical Engineering, Zonguldak,Turkey, ORCID: https://orcid.org/0000-0002-6344-3621

Gokhan BAYAR

Development of a Data Clustering System for 2DOF Robotic Ball Balancer Using Laser Scanning RangeFind...

a robotic ball balancer system gives a chance to engineering students to adapt their theoretical knowledge to a real system and conduct some real experiments. Such systems whereby new methodologies like system dynamics, controller design, data clustering, object recognition, etc. can be tested.

Robotic balancers are designed to track desired reference inputs so the algorithms running inside the control block gain importance. In order to adapt control algorithms and mathematical expressions describing the motion of the system, accurate feedback information is needed and a robust data mining and sensor fusion system should be constructed to be able to handle this information.

In this study, a new characterization and data clustering system for a 2DOF robotic ball balancer integrated with a laser scanner rangefinder was proposed. The data clustering system was developed by using the principles of hierarchical clustering technique. It was used to obtain the ball position in two directions on the tilt-table. The system developed was tested using an experimental platform, which involved a 2DOF robotic ball balancer and a laser scanner rangefinder. 2DOF ball balancer was constructed using 2 sets of driving systems. Driving systems were built with gear couples and high resolution encoders. The use of encoders was able to give tilt angle information of the platform in two directions. The laser rangefinder sensor has ability to scan its surrounding in a range of 240^0. It can achieve a full scan with 0.36^0 angular resolutions in 0.1 s. The measurement capability of the laser scanner used in this study is between 60 mm and 4095 mm. As the computational and communication platform, Matlab-Simulink was used. In Matlab - Simulink, there is no available data clustering function that can be used in real-time operations. As one of the main contributions of this study, the clustering algorithm, developed based on the hierarchical clustering technique, was prepared using C/C++ programming language and embedded in Matlab-Simulink environment. The data coming from the high resolution encoders mounted on the balancing system were also acquired in the same

computational system. In order to verify the accuracy and performance of the proposed system, a camera was attached to the top of the experimental platform.

This paper is organized as follows. In Section 2 relevant literature studies are reviewed. In Section 3 general information about clustering methods are presented. Hierarchical clustering is also explained in this section. In Section 4 the experimental setup constructed for this study is introduced in detail. In Section 5 experimental studies and their results are presented. The paper is concluded in Section 6 with an analysis of results.

2. LITERATURE STUDIES

Literature studies are given in the groups of balancing systems, laser scanner rangefinder based systems and clustering algorithms and their usage.

In [1], the balancing performance of an automatic ball balancer was taken into account. The study focused on investigating the performance of the system. Kinematic and dynamic modeling of the ball balancer was studied. In [2], analytical and experimental investigation of automatic balancing systems was studied. A dynamic balancer was designed and a monitoring system was created to observe the dynamics of the system. In [3], a laser scanner rangefinder based detection and tracking system was proposed. The system developed focused on tracking people. It also investigated the use of the system in mobile robotic and intelligent surveillance applications. The proposed system was constructed by using laser point clustering method to extract object locations. In [4], an agglomerative hierarchical clustering system was used to create a real-time plane extraction in point clouds. The sensor data was clustered to be able to detect the multiple planes. In [5], a laser scanner rangefinder was used together with a CCD color camera. To segment the flat areas and detect the planes, RANSAC search engine was adopted to the system. The use of proposed system gave ability to create a 3D space scene and merge the data coming from laser scanner and camera. In [6], a

Gokhan BAYAR

Development of a Data Clustering System for 2DOF Robotic Ball Balancer Using Laser Scanning RangeFind...

stepwise cluster technique was used to classify individual trees. The system used laser scanning rangefinder data as the data source. The unsupervised stepwise cluster algorithm was used to create groupings of similar objects at consecutive steps by adapting the k-medoid algorithm. In [7], laser scanner rangefinder was used to create an intelligent space algorithm. A position estimation methodology that was constructed based on the target shape information was proposed. To extract the target object, background subtraction and a basic clustering method were adapted to the system. In [8], Gaussian mixture model and robust structural matching were integrated to create a clustering system related to change detection in 3D environments. A hierarchical cluster system was built to create a binary tree based on splitting each region. The objective of this study was to adapt the proposed system for autonomous robotic applications. In [9], to achieve high speed rendering, hierarchical face cluster partitioning system was introduced. The study intended to reduce the computational time during rendering since a computer's rendering capability is generally not enough when the data load is high and high-quality rendering is expected. To solve such problems, a recursive clustering method was presented. In [10], a feedback system involving a laser scanner and monocular camera was presented. The objective was to create a data grouping system for improving robustness and precision in mobile robotic applications. In [11], a data clustering system for detecting, classifying and tracking of moving objects was proposed. The idea of the system was to use an octree model constructed using the principles of occupancy grid representation. The proposed method aimed to model the objects placed in the surroundings of the laser scanner. In [12], a data filtering system based on morphological methods was developed. The system was coupled with a laser scanner.

This paper addresses a laser scanner based clustering system for characterization of a tilt-table ball balancer. It looks for the solutions that use easy-to-use and easy-to-find computational platforms like Matlab-Simulink. The methodology introduced combines mathematical modeling, sensor data integration with the computational platform, sensor fusion, data decoding and clustering, and successful experiments with verification.

3. CLUSTERING METHODS

In data mining, many clustering methods have been developed. The reason of why there are many clustering methods is that each method has been created to achieve a special goal. Besides the goals, the mathematical backgrounds used to develop the clustering algorithms have also different principles. In [13], it is suggested that clustering methods can be specified into two groups; hierarchical and partitioning methods. The study [14] offers to categorize the clustering methods into three groups; density based, model based clustering and grid based methods. The details about the groups of clustering methods can be seen in [14, 15].

3.1. Hierarchical clustering

Hierarchical clustering is a commonly used data analysis approach in data mining applications. The main principle of this approach is that the method searches for creating linkages between data based on hierarchy of the data clusters. There are two groups of hierarchical clustering; agglomerative and divisive techniques. The first technique seeks to build a clustering system in which each object initially represents a cluster of its own. Once the clustering algorithm is initiated, the clusters built are connected until the ultimate data grouping operations is achieved. The latter technique offers an approach proposing that all the objects are located in a unique cluster. Then the cluster is divided into sub groups. This process continuous until the desired data grouping is achieved. To build desired clusters, operations of merging or dividing clusters should be performed by following some optimization constraints. There are three commonly used operations. They do similarity measurements called single-link, complete-link and average-link clustering methods. Single-link clustering is the nearest neighborhood method. It searches the distance between two clusters or one cluster and one member or two members. The method looks for the minimum distance to build similarity groups

Gokhan BAYAR

Development of a Data Clustering System for 2DOF Robotic Ball Balancer Using Laser Scanning RangeFind...

[15, 16]. The similarity criteria are defined according to the types of objective. Complete-link clustering is known as furthest neighborhood method. It tries to find the maximum distance between two clusters or one member and a cluster [15]. Same as with single-link clustering, searching criteria are defined to meet the aim of the data clustering. Average-link clustering technique uses the principles of minimum variance approach. The method considers the average distance between two clusters or one member and one cluster or one cluster and any member of other clusters [15].

In this study, single-link hierarchical clustering algorithm is adapted to the experimental system. As mentioned above, this technique is known as the minimum distance clustering or nearest neighborhood clustering. In real-time data mining applications, this method is commonly preferred since a standard personal computer would be enough to construct and run it. It does not require using of high capacity of RAM, number of processors, high volume storage for hard-disc, etc. The main idea of the single-link hierarchical clustering is represented in Figure 1-a. The minimum distance between two clusters specified by (d) should be obtained using the algorithm constructed. This process should continue until the last member of the data set is included in a cluster.
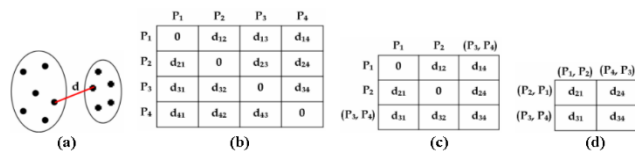

Figure 1. (a) Main idea of the clustering, (b, c, d) Distance matrices of the clusters.

The methodology of the single-link hierarchical clustering technique adapted to this study is explained by using a simple data set. Suppose that we have 4 members (P_1, P_2, P_3, P_4) in the data set. In the first step, the distances between each point are calculated (d_{12}, d_{13}, d14, d_{23}, d_{24}, d_{34}). Then, a 4 by 4 input distance matrix is created as shown in Figure 1-b. Now we have a big cluster.

In the second step, the smallest value should be found. Assume that the minimum distance

information is d_{43}. In this case, two members should be merged. This merge operation is shown in Figure 1-c. In the next step, one more merging operation should be performed. Assuming the smallest value is d_{12}. The merge operation is resulted as shown in Figure 1-d. In the last step, the minimum distance can easily be found and clustering is completed. By using the information obtained above, a tree diagram can be drawn as shown in Figure 2-a. The clustering hierarchy can also be plotted as given in Figure 2-b.
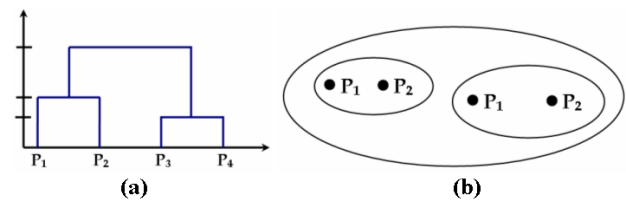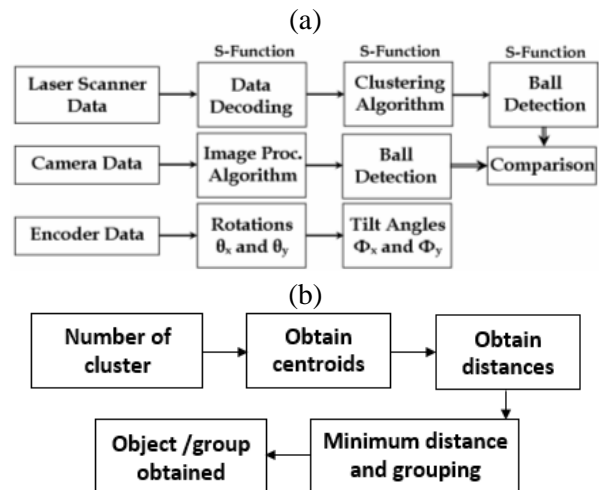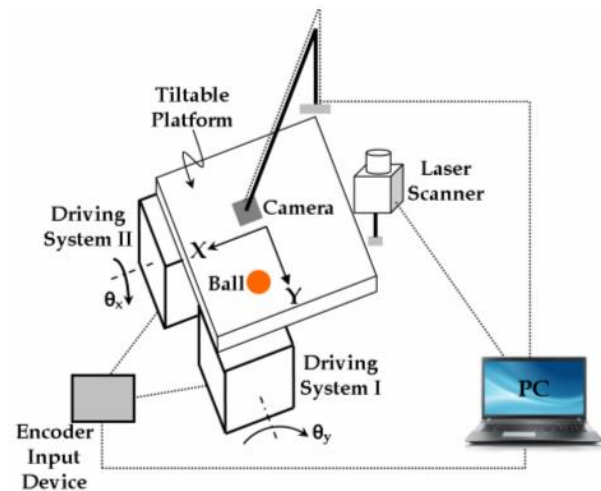

Figure 2. (a) Data tree showing data clustering steps, (b) Clustering hierarchy.

4. EXPERIMENTAL SETUP

Gokhan BAYAR

Development of a Data Clustering System for 2DOF Robotic Ball Balancer Using Laser Scanning RangeFind...

(c)

Figure 3. (a) Experimental set-up, (b) Block diagram of the proposed system, (c) Flow chart of the clustering algorithm.

In this study, an experimental setup shown in Figure 3-a was constructed. It involves a robotic balancer, a laser scanner rangefinder and a camera attached to the top of the platform. Robotic balancer includes two driving systems manufactured by Quanser Company (SRV02) and high resolution quadrature encoders mounted to the driving units. The angular resolution of the encoders is 4096 pulses per revolution. In order to communicate with the encoders and count their pulses, an encoder input card, manufactured by Quanser Company (Q2-USB), was also added to the system. The platform (table) can be tilted in two (X, Y) directions (Figure 3-a). The block diagram used for data processing tasks is illustrated in Figure 3-b. Flow diagram of the clustering algorithm developed is demonstrated in Figure 3-c as well. The tilt angles are obtained using the kinematics of the system and information coming from the encoders (mounted at point O – Figure 4). The kinematic model of the driving units and the tilted platform is shown in Figure 4. In this schematic, the link lengths are specified by L_1, L_2, L_3 and the radius of driving unit is shown by R. Angular rotation and tilt angle are specified by θ and Φ, respectively. This schematic is given to represent one DOF of the balancing system. The other DOF system is identical, so the second tilt angle can also be obtained using the rotation information from the second high resolution encoder.
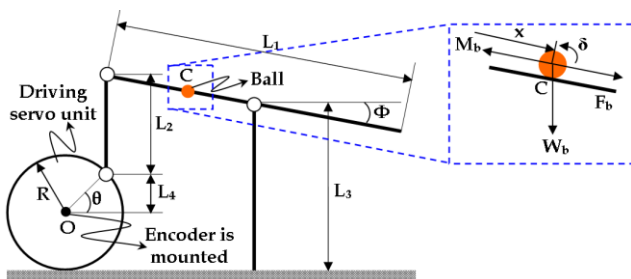

Figure 4. Geometric model of the balancing system.

Considering the balancing system (Figure 4) and the ball (highlighted by the dashed-line-rectangle in Figure 4), equation of motion of the system can

be built in the following order (Equations 1 through 6) [17]. This modeling strategy is used for the control, sensor fusion and data mining purposes.

$$m_{ball}a_{ball} = F_{sum} = F_I + F_G \qquad (1)$$

where forces caused from the inertia of the ball and gravitational acceleration are indicated by F_I and F_G, respectively. Mass and acceleration of the ball are specified by m_{ball} and a_{ball}, respectively. The forces caused by gravity in x and y directions can be written as:

$$F_G = m_{ball}g\sin(\Phi) \qquad (2)$$

The force created by the ball rotation is constructed as:

$$F_I = \frac{J_{ball}X}{r^2_{ball}} \qquad (3)$$

where r_{ball} indicates the radius of ball used in this study. Combining the equations above yields the following relationship:

$$\ddot{x} = \frac{m_{ball}g\sin(\Phi)r^2_{ball}}{m_{ball}r^2_{ball} + J_{ball}} \qquad (4)$$

From the geometry given in Figure 4, one can find:

$$\sin(\Phi) = \frac{2R\sin(\theta)}{L_1} \qquad (5)$$

Inserting Equation (5) into Equation (4) gives the following equation of motion for the ball:

$$\ddot{x} = \frac{2\theta m_{ball}gRr^2_{ball}}{L_1\left(m_{ball}r^2_{ball} + J_{ball}\right)} \qquad (6)$$

To feed the developed data clustering system and obtain the ball position on the platform, a laser scanner rangefinder sensor (Hokuyo URG-04LX - Figure 5-a) was attached to the balancing system. The baud rate speed of the laser scanner can be set to 19.2, 57.6, 115.2 and 500 Kbps. In this study, the speed was adjusted to 19.2 Kbps and the communication was achieved through

Gokhan BAYAR

Development of a Data Clustering System for 2DOF Robotic Ball Balancer Using Laser Scanning RangeFind...

RS232 serial protocol. The angular resolution of the laser scanner is about 0.36^0 (360^0 / 1024) and the scanner is able to scan its surroundings from 0^0 to 240^0 (Figure 5-b) in 0.1 s. The minimum and maximum measurement distances, and the resolution are 60 mm, 4095 mm and 1 mm, respectively. The mounting tool designed to locate the laser scanner range finder in the experimental system is also illustrated in Figure 5-c.
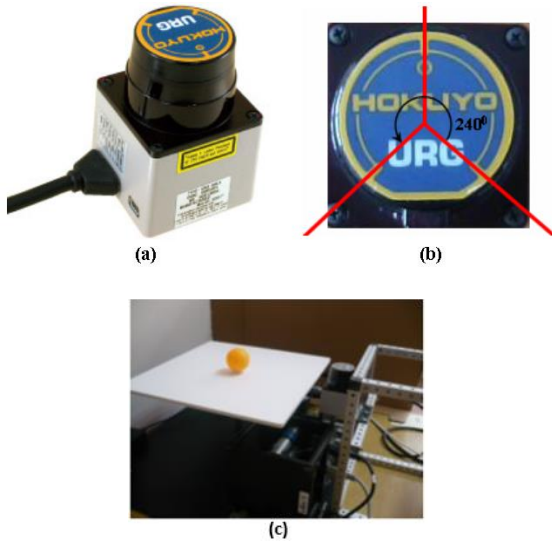

Figure 5. (a) Hokuyo URG-04LX laser scanner rangefinder, (b) Scanning range, (c) Installing laser scanner rangefinder sensor to the system.

The real-time Workshop toolbox of Matlab-Simulink was used for all experimental studies. The block diagram of the system is presented in Figure 3-b. The encoder input card, laser rangefinder and camera were run together inside Simulink block. The data coming from the laser scanner rangefinder was decoded by the use of S-function feature of Matlab (Figure 3-b) for real-time use. The laser scanner sends a packet containing 1435 bytes with 683 equal intervals. The data package content is shown in Figure 6-a. Each distance value having length of 12 bytes is represented with two parts specified by D_A and D_B. An example for decoding process of the sensor data is shown in Figure 6-b. The placement of the laser scanner in the experimental area is illustrated in Figure 7-a. Using the distance (shown by d) between the laser scanner and the platform, the angle δ is obtained. By this way data clustering is performed from the angle δ to the

angle (1800 - δ). This reduces the data size and processing time.
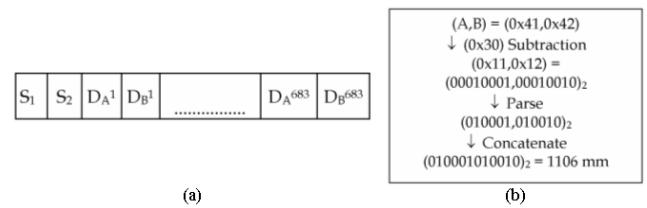

Figure 6. (a) Data packet sent by the laser scanner, (b) Data decoding process.

The other unit of the experimental platform is the camera located at the top (Figure 3-a). It was exactly placed at the point which was coincident with the geometric center of the tilt-table. The camera was used to detect the ball and find its location on the platform so that the results obtained using the developed clustering system could be verified.
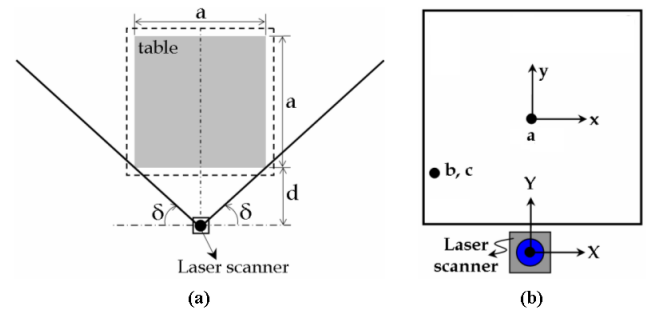
Figure 7. (a) The placement of the laser rangefinder sensor. (b) 3 different test cases. Each letter indicates a different ball position on the platform. The cases specified by a and b are tested on the flat platform whereas the experiments of the case shown by c are performed on the tilted platform.

5. EXPERIMENTAL STUDIES

The clustering algorithm developed was tested using the experimental set-up introduced above. The objective of using the experimental set-up was to detect the ball position on the platform for different cases. The geometric representation of the platform and the test locations are shown in Figure 7-b. The placement of the laser scanner rangefinder is also illustrated in this figure. Two coordinate axes, (x, y) and (X, Y), were located at the geometric center of the platform and the laser

Gokhan BAYAR

Development of a Data Clustering System for 2DOF Robotic Ball Balancer Using Laser Scanning RangeFind...

scanner's mounting point, respectively. Different test cases were considered. Each case was thought to create a different characteristic so that the behavior of the proposed system could be evaluated. The test cases are specified by the letters of a, b and c (Figure 7-b). As well as conducting experiments on the flat positioned table (cases a and b), the ball positions were detected on the table which was tilted (case c). The experiment results were verified by using the camera + image processing algorithm.

The data coming from the laser scanner and the clustering results for the case (a) are presented in Figure 8. In this case study, number of clusters are created and specified by different colored points. The cluster indicating the ball position on the table is highlighted with the red points inside the dashed square shape. The detected ball center is also shown via the asterisk (*). In order to provide a clear presentation, the data of the ball cluster is given in a zoomed view. The results indicate that the ball is placed at -15 mm and 174 mm in X and Y directions, respectively. Note that this test was performed on the flat positioned table (i.e., $\Phi_x = 0^0$ and $\Phi_y = 0^0$).

Three different test cases are presented in Figure 9. In Figure 9-a, the ball is placed at the geometric center of the platform (case a). The tilt angles in X and Y directions are zero. In the right image of Figure 9-a, the results obtained using the clustering system is presented. The image processing results are also shown in this figure. The location of the laser scanner is specified with the black colored square. The detected ball position is also given in a zoomed view. The clustered laser and camera data are specified with red and green points, respectively. The ball center obtained is highlighted via black-diamond (laser data) and blue-square (camera data) filled shapes. The position values in X-direction are found as $X_b = 166.24$ and $^C X_b = 163.80$ mm by the use of (laser scanner + clustering system) and (camera + image processing), respectively. In Y-direction, the position values are detected as $Y_b = -3.02$ and $^C Y_b = 0.33$ mm, respectively. Note that the laser scanner was located at (0, 0) position showing the center of the coordinate axes.

In the second case study (case b), the platform is still flat however the ball is moved from the center. The results are presented in Figure 9-b. The data showing the ball and its center are also exhibited in a zoomed view. In this test, the ball center is detected as -116.49 mm (laser scanner + clustering system) and -114.74 mm (camera + image processing) in X-direction, and 123.96 mm (laser scanner + clustering system) and 125.34 mm (camera + image processing) in Y-direction. In the third case (case c), the ball position is nearly same as with the case given in Figure 9-b, however the platform is tilted in both X and Y directions about 29^0 (Figure 9-c). The clustering system gives the ball center position as (-118.61, 125.74). These values are found as (-118.93, 133.56) by the use of camera. To show the variations in the ball position results obtained, Table 1 is prepared for the cases (a), (b) and (c). As seen in this table, minimum, maximum, mean and standard deviation values are given. (The speed of the data flow is determined by the slowest unit of the experimental system, which is the laser scanning range finder. It works with 10 Hz running frequency, which has the meaning of that 10 samples are taken from the sensors in each second. In the experiments, the data is taken for more than one second and the clustering algorithm is run for this time instances. By this way, minimum, maximum and mean values are obtained. Standard deviation values are also obtained in order to show the measure of the amount of variation of the data collected and analyzed in this time interval). Locational outputs in Case (a) are obtained in the range of 166.61 mm to 168.44 mm in X-direction. The average value of the experiments (in X-direction for Case (a)) is 166.24 mm. The camera output gives the location information as 163.80 mm. This means that the location in X-direction is obtained with 1.49% estimation error. Clustering system yields nearly 6% estimation error in Y-direction for Case (a). Errors in X-direction are obtained as rougly 1% and 0.2% for Case (b) and (c), respectively. Those values are calculated as 1.1% and 5.8% in Y-direction.

Gokhan BAYAR

Development of a Data Clustering System for 2DOF Robotic Ball Balancer Using Laser Scanning RangeFind...

Table 1.
Ball position results obtained for the Case (a), (b) and (c) specified in Figure 7-b. Flat platform positioning are the cases of (a) and (b). Case (c) specifies the tilted platform.

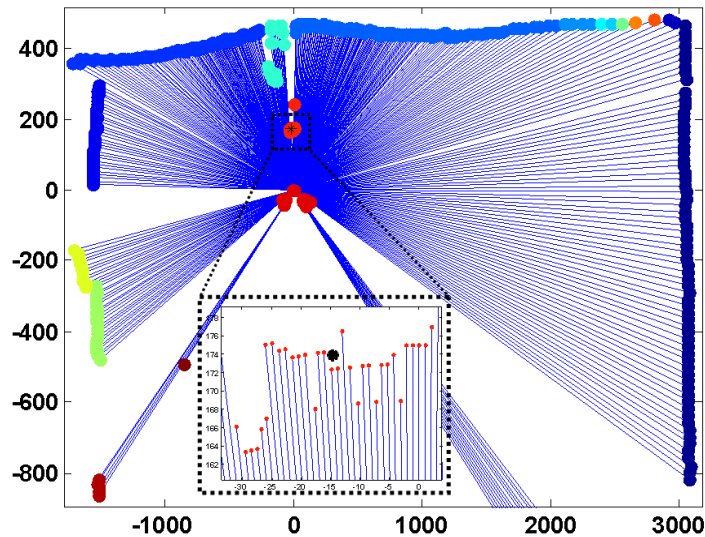|		Camera	Min	Max	Mean	Std
Case (a)	X_b	163.80	166.61	168.44	166.24	0.99
	Y_b	0.33	-3.21	2.58	-0.31	0.07
Case (b)	X_b	-114.74	-117.70	-115.35	-116.49	0.62
	Y_b	125.34	122.50	125.75	123.96	0.74
Case (c)	X_b	-118.93	-119.83	-117.56	-118.61	0.62
	Y_b	133.56	124.65	127.03	125.74	0.63

Figure 8. Scanned data of the laser scanner for the case (a). The colored points show the data clusters obtained using the proposed clustering system. The ball center is also specified by the asterisk (*). Dimensions are in mm.

Gokhan BAYAR

Development of a Data Clustering System for 2DOF Robotic Ball Balancer Using Laser Scanning RangeFind...
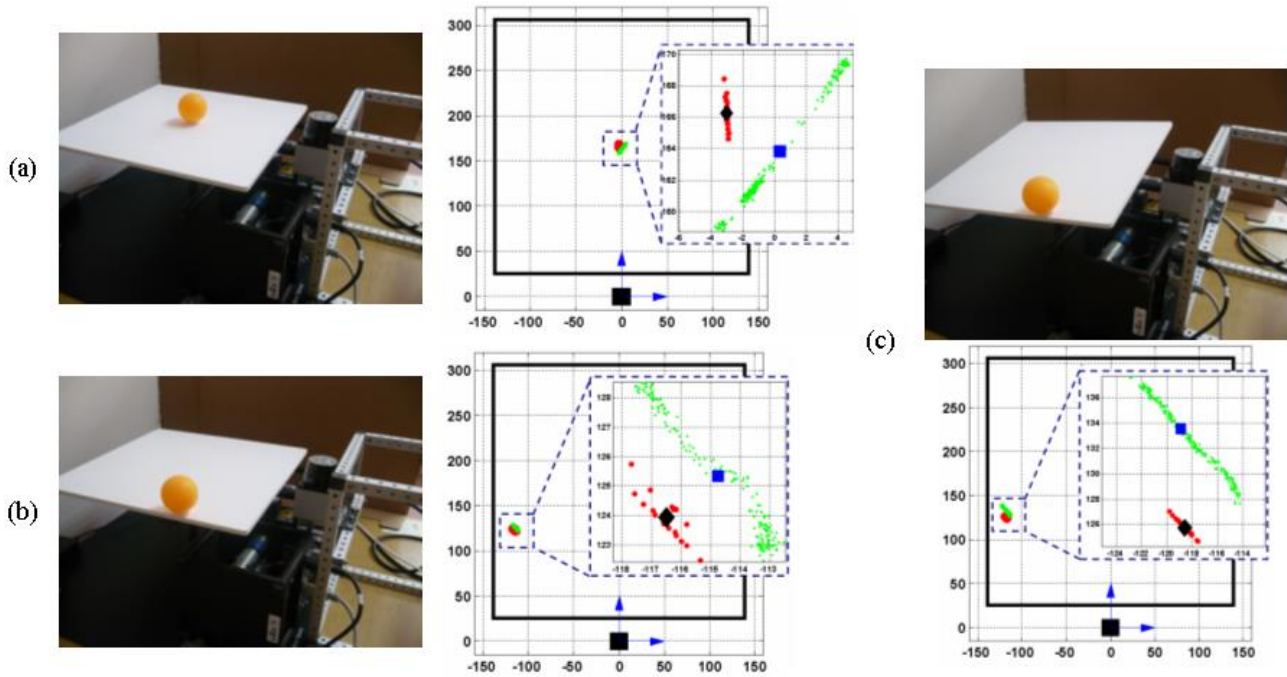
Figure 9. Data clustering experiments for the cases a, b and c. Laser scanner position is represented via black-colored square. The results obtained by using the proposed clustering system (X_b, Y_b) and camera (^cX_b, ^cY_b) are shown by red and green points. Black-diamond and blue-square shapes specify the ball center positions detected.

6. ANALYSIS AND CONCLUSION

Balancing systems are commonly used for the research and educational purposes. New approaches focused on developing models and control systems for balancing platforms are also continuously carried out by the scientists and research engineers. In this study, a new data clustering procedure for a 2DOF ball balancing system, designed for small-scale research activities and educational purposes, was taken into account. The ball balancer has a configuration that it can be tilted in two rotational directions. A laser rangefinder sensor was integrated with this system. To get the tilt information of the platform, two high resolution encoders were mounted on the system. To verify the results obtained using the proposed system, a camera was attached to the top the platform. The clustering system based on the hierarchical clustering technique was developed in order to detect the ball and its position on the platform. The whole system was implemented in Matlab-Simulink for real-time use. The clustering system was tested in the flat and tilted positions of the platform. Different scenarios were tested to see the performance, accuracy and repeatability of the

system introduced. The results indicate that the proposed system involving the sensor fusion and data clustering algorithms would be used for further research activities like mathematical modeling, robust and intelligent control of the robotic balancing platforms. The system including clustering algorithm and a laser scanning range finder can be integrated into any balancing platform on which the object should be detected. It can be able to detect the object's location without interesting the lighting conditions of the working environment. This provides an advantage over using camera based solutions. It also gives opportunities than using ultrasonic sensor based, radar & sonar based and mechanical & digital switches based solutions. The algorithm proposed does not also require high capacity of processing equipment like ram, hard disk, processing unit, DAQ card, etc. Professional experience about installing and using mechatronic systems is not needed as well to be able use the system proposed in this paper.

Gokhan BAYAR

Development of a Data Clustering System for 2DOF Robotic Ball Balancer Using Laser Scanning RangeFind...

Zonguldak Bulent Ecevit University (Zonguldak, Turkey) numbered 2013-77654622-03 for providing the equipment of 2DOF robotic ball balancer and laser scanner rangefinder used in this research.

The Declaration of Conflict of Interest/ Common Interest

No conflict of interest or common interest has been declared by the author.

The Declaration of Ethics Committee Approval

The author declares that this document does not require any ethics committee approval or any special permission.

The Declaration of Research and Publication Ethics

The author of this paper declares that he complies with the scientific, ethical and quotation rules of SAUJS in all processes of the paper and that he does not make any falsification on the data collected. In addition, he declares that Sakarya University Journal of Science and its editorial board have no responsibility for any ethical violations that may be encountered, and that this study has not been evaluated in any academic publication environment other than Sakarya University Journal of Science.

REFERENCES

[1] N. Wouw, M. N. Heuvel, H. Nijmeijer, J. A. Rooij, "Performance of an automatic ball balancer with dry friction", International Journal of Bifurcation and Chaos, 15(1), 65-82, 2005.

[2] K. Green, A. R. Champneys, M. I. Friswelland, A. M. Munoz, "Investigation of a multi-ball, automatic dynamic balancing mechanism for eccentric rotors", Phil. Trans. R. Soc. A, 366, 705–728, 2008.

[3] J. Cui, H. Zha, H. Zhao, R. Shibasaki, "Laser-based detection and tracking of multiple people in crowds", Computer Vision and Image Understanding, 106, 300–312, 2007.

[4] C. Feng, Y. Taguchi, V. R. Kamat, "Fast plane extraction in organized point clouds using agglomerative hierarchical clustering", In: Proceedings of the IEEE International Conference on Robotics and Automation (ICRA), Hong Kong, 6218-6225, 2014.

[5] A. Lipnickas, K. Rimkus, S. Sinkevicius, "Design of 3D scene scanner for slat surface detection", Issues and Challenges in Artificial Intelligence, Switzerland: Springer International Publishing, 2014.

[6] S. Kim, T. Hinckley, D. Briggs, "Classifying individual tree genera using stepwise cluster analysis based on height and intensity metrics derived from airborne laser scanner data", Remote Sensing of Environment, 115, 3329–3342, 2011.

[7] T. Sasaki, H. Tamura, H. Hashimoto, F. Inoue, "Position estimation based on the target shape information using laser range finders for intelligent space", In: Proceedings of the IEEE/ASME International Conference on Advanced Intelligent Mechatronics, Montreal, Canada, 605-610, 2010.

[8] P. Nunez, P. Drews, A. Bandera, R. Rocha, M. Campos, J. Dias, "Change detection in 3D environments based on Gaussian mixture model and robust structural matching for autonomous robotic applications", In: Proceedings of the IEEE/RSJ International Conference on Intelligent Robots and Systems, Taipei, Taiwan, 2633-2638, 2010.

[9] T. Tsuji, H. Zha, T. Hasegawa, R. Kur, "Hierarchical face cluster partitioning of polygonal surfaces and high-speed rendering", Systems and Computers in Japan, 38(8), 1205–1215, 2007.

[10] K. O. Arras, N. Tomatis, "Improving robustness and precision in mobile robot localization by using laser range finding and monocular vision", In: Proceedings of the Third European Workshop on Advanced Mobile Robots (Eurobot99), Zurich, 177-185, 1999.

[11] A. Azim, O. Aycard, "Detection, classification and tracking of moving objects in a 3D environment", In: Proceedings of the

Gokhan BAYAR

Development of a Data Clustering System for 2DOF Robotic Ball Balancer Using Laser Scanning RangeFind...

IEEE Intelligent Vehicles Symposium (IV), Alcala de Henares, 802-807, 2012.

[12] Q. Chen, P. Gong, D. Baldocchi, G. Xie, "Filtering airborne laser scanning data with morphological methods", Photogrammetric Engineering & Remote Sensing, 73(2), 175–185, 2007.

[13] C. Fraley, A. E. Raftery, "How many clusters? which clustering method? answers via model-based cluster analysis", Technical Report No. 329, Department of Statistics University of Washington, 1998.

[14] J. Han, M. Kamber, "Data mining: concepts and techniques", USA: Morgan Kaufmann Publishers, 2001.

[15] L. Rokach, O. Maimon, "Clustering methods: data mining and knowledge discovery handbook, USA: Springer, 2005.

[16] P. Sneath, R. Sokal, "Numerical taxonomy", San Francisco, CA, USA: W.H. Freeman Co., 1973.

[17] 2-DOF ball balancer Workbook and User Manual, Quanser Inc., 2013.

Title: 5,6,7-Trimethoxy-2-(methylthio)quinoline with Different Anchoring Groups: Synthesis and dye-sensitized Solar Cell Applications

Authors: Barış Seçkin ARSLAN

5,6,7-Trimethoxy-2-(Methylthio)Quinoline with Different Anchoring Groups: Synthesis And Dye-Sensitized Solar Cell Applications

Barış Seçkin ARSLAN[*1]

Abstract

Two new metal-free organic dyes in D-π-A structure, containing a quinoline π-bridge and malononitrile (**4a**) and cyanoacrylic acid (**4b**) as acceptors, were synthesized for the first time to apply dye-sensitized solar cell (DSSC). The structures of these compounds were elucidated by FT-IR, ^{1}H NMR, ^{13}C NMR techniques. The photophysical and photovoltaic properties of the obtained compounds were investigated and compared by current density–voltage (J–V) graphs. Compound **4b** containing cyanoacrylic acid as an acceptor reached an open–circuit voltage (Voc) of 0.645 V, short–circuit current density (Jsc) of 6.66 mA cm^{-2} and fill factor (FF) of 0.70 in the presence of chenodeoxycholic acid (CDCA), showing a power conversion efficiency (PCE) of 3.01%. It is also observed that the incorporation of thiomethyl group to the structure instead of methoxy group increases the PCE.

Keywords: Dye-sensitized solar cells, metal free dyes, quinoline, thiomethyl group.

1. INTRODUCTION

Metal-free dye sensitized solar cells (DSSCs) are a good alternative to silicon-based solar cells thanks to their low manufacture cost, easy production, environment friendly, easily adjustable electrochemical properties [1-5]. A conventional organic dye contains a system (D-π-A) that carries electrons from donor (D) to acceptor (A) via π-bridge (π) [6]. The main component in these dyes is the aromatic π-bridge that affects absorption capability and intra-molecular charge transfer (ICT) [7]. As the π-bridge, especially focused on fused, rigid and planar aromatic structures [8].

Quinolines containing a fused and rigid structure are important compounds of the dye class. The quinoline derivatives found in the structure of natural compounds have applications in various fields such as medicine, organic optoelectronics,

---

[*] Corresponding Author: barisseckin@gmail.com

[1] Sakarya University, Faculty of Science and Letters ,Sakarya, Turkey, ORCID: https://orcid.org/0000-0003-0022-4701

electronics and polymer chemistry. Besides being used as a light emitting layer in OLEDs owing to their exciting optoelectronic features, they can be used as corrosion inhibitors as they are easily absorbed into metal surfaces. These compounds are promising in DSSC applications due to their described properties [8, 9-14].

In this study, novel two dyes (**4a** and **4b**) containing three methoxy (-OCH$_3$) and one thiomethyl (-SCH$_3$) groups as donors, quinoline ring as π-bridge, malononitrile and cyanoacrylic acid as acceptor were synthesized (**Figure 1**). The structures of the obtained compounds were confirmed by FT-IR, ^{1}H and ^{13}C NMR spectra. In addition, DSSC applications of these compounds in D-π-A structure were carried out and their photophysical properties and photovoltaic performances were investigated.
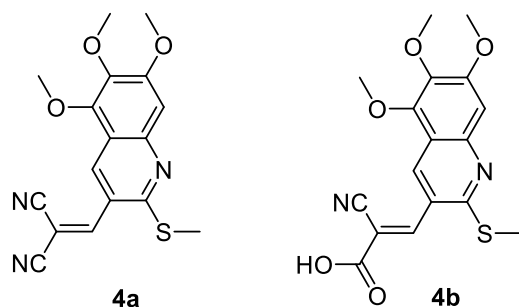

Figure 1. Chemical structures of **4a** and **4b**

2. EXPERIMENTAL

2.1. Materials

Fluorine-doped SnO$_2$ conducting, TiO$_2$ paste, platinum paste, sealing film, N719 and redox electrolyte (iodide/triiodide) were purchased from Solaronix. Chenodeoxycholic acid (CDCA), 3,4,5-trimethoxyaniline, dichloromethane (DCM), acetic anhydride, sodium carbonate, *N,N*-dimethylformamide (DMF), phosphoryl chloride, sodium sulfide nonahydrate (Na$_2$S.9H$_2$O), methyl iodide, acetonitrile, piperidine, malononitril, cyanoacetic acid were purchased from Sigma-Aldrich. Solvents were highly purified by applying standard methods.

2.2. Synthesis

Compounds **1** and **2** were synthesized in 92% and 87% yields according to the literature, respectively [8]. Synthesis procedure and spectroscopic data of the original compounds (**3**, **4a** and **4b**) are expressed below.

2.2.1. Synthesis of 5,6,7-trimethoxy-2-(methylthio)quinoline-3-carbaldehyde, 3

DMF (20 mL), sodium sulfide nonahydrate (3.60 g, 15 mmol) and 2-chloro-5,6,7-trimethoxyquinoline-3-carbaldehyde (**2**) (2.82 g, 10 mmol) were added to a 100 mL flask and the mixture was stirred at room temperature for 6 hours. Then, methyl iodide (0.62 mL, 10 mmol) was added to the mixture and the reaction was continued for 12 hours at room temperature. After completion of the reaction, the mixture was extracted with ethyl acetate-water. The organic portion was dried over sodium sulfate and the solvent was removed. It was purified by column chromatography (SiO$_2$) using hexane/ethyl acetate (19: 1). Beige solid (2.23 g, 76% yield). M.P.: 100-101 °C. IR (cm^{-1}): 3038 (aromatic C-H), 2943 (aliphatic C-H), 2831-2769 (aldehyde C-H), 1682 (C=O), 1609 (C=N), 1586 (C=C), 1114 (C-O-C). ^{1}H NMR (300 MHz, CDCl$_3$) δ 10.25 (s, 1H, aldehyde-H), 8.65 (s, 1H, aromatic-H), 7.13 (s, 1H, aromatic-H), 4.12 (s, 3H, -OC$\underline{H}_3$), 4.05 (s, 3H, -OC$\underline{H}_3$), 3.96 (s, 3H, -OC$\underline{H}_3$), 2.68 (s, 3H, -SC$\underline{H}_3$). ^{13}C NMR (75 MHz, DMSO) δ 191.77, 159.81, 158.87, 148.31, 147.27, 140.17, 139.80, 125.46, 115.17, 103.76, 62.44, 61.63, 57.05, 13.16.

2.2.2. Synthesis of 2-((5,6,7-trimethoxy-2-(methylthio)quinolin-3-yl)methylene) malononitrile, 4a

The mixture of compound **3** (0.293 g, 1 mmol), malononitrile (0.132 g, 2 mmol) and piperidine (0.2 mL) in acetonitrile (20 mL) was refluxed for 6 hours. After the reaction was completed, the mixture was poured into ice water. The precipitate was filtered off, washed with cold ethanol and finally dried. Orange solid (0.314 g, 92% yield). M.P.: 153-154 °C. IR (cm^{-1}): 3000 (aromatic C-H), 2949 (aliphatic C-H), 2226 (C≡N), 1606

Barış Seçkin ARSLAN

5,6,7-Trimethoxy-2-(methylthio)quinoline with Different Anchoring Groups: Synthesis and dye-sensitize...

(C=N), 1568 (C=C), 1117 (C-O-C). ^{1}H NMR (300 MHz, CDCl$_3$) δ 9.01 (s, 1H, alkenyl-H), 8.22 (s, 1H, aromatic-H), 7.10 (s, 1H, aromatic-H), 4.10 (s, 3H, -OC$\underline{H}_3$), 4.05 (s, 3H, -OC$\underline{H}_3$), 3.97 (s, 3H, -OC$\underline{H}_3$), 2.73 (s, 3H, -SC$\underline{H}_3$). ^{13}C NMR (75 MHz, DMSO) δ 159.83, 158.62, 156.16, 148.29, 147.28, 140.78, 131.90, 121.79, 115.43, 114.40, 113.65, 104.03, 85.41, 62.78, 61.67, 57.17, 13.63.

2.2.3. Synthesis of 2-cyano-3-(5,6,7-trimethoxy-2-(methylthio)quinolin-3-yl)acrylic acid, 4b

Compound **4b** was synthesized according to the method used in the synthesis of compound **4a** using cyanoacetic acid (0.170 g) instead of malononitrile. Dark-yellow solid (0.292 g, 81% yield). M.P.: 227-228 °C. IR (cm^{-1}): 3035-2500 (carboxylic acid, O-H), 2994 (aromatic C-H), 2946 (aliphatic C-H), 2225 (C≡N), 1711 (C=O), 1605 (C=N), 1582 (C=C), 1248 (carboxylic acid, C-O), 1116 (C-O-C). ^{1}H NMR (300 MHz, CDCl$_3$) δ 8.86 (s, 1H, alkenyl-H), 8.47 (s, 1H, aromatic-H), 6.97 (s, 1H, aromatic-H), 3.94 (s, 3H, -OC$\underline{H}_3$), 3.90 (s, 3H, -OC$\underline{H}_3$), 3.82 (s, 3H, -OC$\underline{H}_3$), 2.57 (s, 3H, -SC$\underline{H}_3$). ^{13}C NMR (75 MHz, DMSO) δ 163.42, 159.25, 158.97, 148.53, 148.17, 146.87, 140.67, 131.11, 121.70, 116.36, 115.55, 106.85, 103.96, 62.66, 61.62, 57.05, 13.56.

2.3. Instruments

^{1}H, ^{13}C NMR measurements were performed on an VARIAN Infinity Plus 300 MHz. The melting points of the compounds were observed using the Schorpp MPM-H1 device. FT-IR spectra were recorded on a Perkin–Elmer FT-IR spectrophotometer. Absorption and fluorescence spectra were obtained in DMSO solution using Shimadzu UV-2600 UV–VIS spectrophotometer and Hitachi F-7000 Fluorescence spectrophotometer, respectively. The J–V features were studied by utilization the potentiostat/galvanostat under AM 1.5 global one sun lighting (100 mW cm^{-2}) from a solar simulator (96000, Newport).
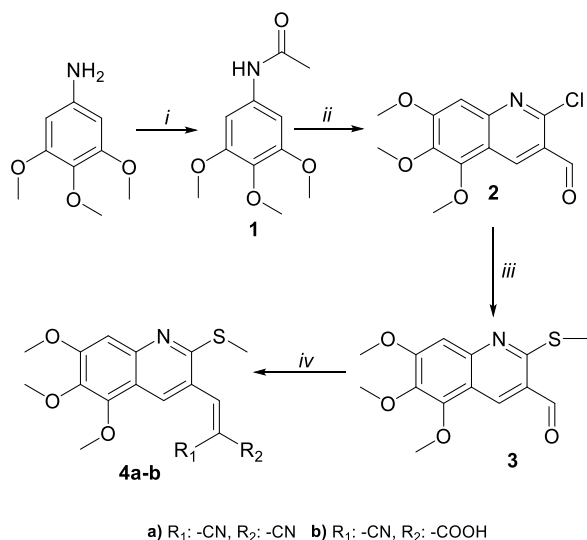
2.4. Production and characterization of DSSCs

DSSCs were prepared pursuant to the Doctor Blade method by applying TiO$_2$ paste on the FTO substrate [15]. To prepare dye-sensitized photoanodes, FTO substrates were immersed (24 hours for **4a** and 6 hours for **4b**) into a 0.3 mM dye solution in MeOH (both without CDCA and with 5mM CDCA). Platinum counter electrodes were prepared by pouring the platinum paste solution over FTO substrates [16]. Photoanote and counter electrode were combined and sealed with Surlyn and redox electrolyte (I$^-$/I$_3^-$) was added through the hole opened in the counter electrode.

3. RESULTS AND DISCUSSIONS

3.1. Synthesis of compounds

Synthesis pathways of compounds **4a** and **4b** are indicated in **Scheme 1**. Primarily, purchased 3,4,5-trimethoxyaniline compound was acetylated with acetic anhydride to obtain the acetanilide derivative (**1**). The acetanilide was converted into the 2-chloro-5,6,7-trimethoxyquinoline-3-carbaldehyde compound (**2**) by the Vilsmeier-Haack reaction [17,18]. Compound **2** was reacted with Na$_2$S.9H$_2$O and then methyl iodide to obtain 5,6,7-trimethoxy-2-(methylthio) quinoline-3-carbaldehyde (**3**) compound [19]. Ultimately, **4a** and **4b** dyes were obtained by Knoevenagel reaction of compound **3** with malononitril and cyanoacetic acid, respectively [15].

Barış Seçkin ARSLAN

5,6,7-Trimethoxy-2-(methylthio)quinoline with Different Anchoring Groups: Synthesis and dye-sensitize...

Scheme 1. Synthetic route for compounds **4a** and **4b**

(*i*): DCM, Na$_2$CO$_3$, 0°C, Ac$_2$O, rt, 3 h; (*ii*): DMF, 0°C, POCl$_3$, 80 °C, 16 h; (*iii*): Na$_2$S.9H$_2$O, DMF, rt, 6 h, MeI, rt, 12 h; (*iv*): R$_1$CH$_2$R$_2$, piperidine, MeCN, reflux, 6 h.

3.2. Structural Characterization

Compounds **1** and **2** were synthesized according to the literature and their structure was verified by FT-IR, ^{1}H and ^{13}C NMR techniques [8].

FT-IR spectra of the compounds were recorded and compared (**Figure 2**). In FT-IR spectrum of **3**, aromatic C-H, aliphatic C-H, aldehyde C-H, aldehyde C=O, aromatic C=N, aromatic C=C and ether C-O-C stretching vibrations appeared at 3038, 2943, 2831-2769, 1682, 1609, 1586 and 1114 cm^{-1}, respectively. In the **4a** and **4b** FT-IR spectra, aldehyde group stretching vibrations of **3** disappeared. Differently, sharp nitrile stretching vibrations (2226 cm^{-1} for **4a** and 2225 cm^{-1} for **4b**) and stretching vibrations belonging to the carboxylic acid group (3035-2500, 1711 and 1248 cm^{-1} for **4b**) are observed. Other bands are similar for all compounds.
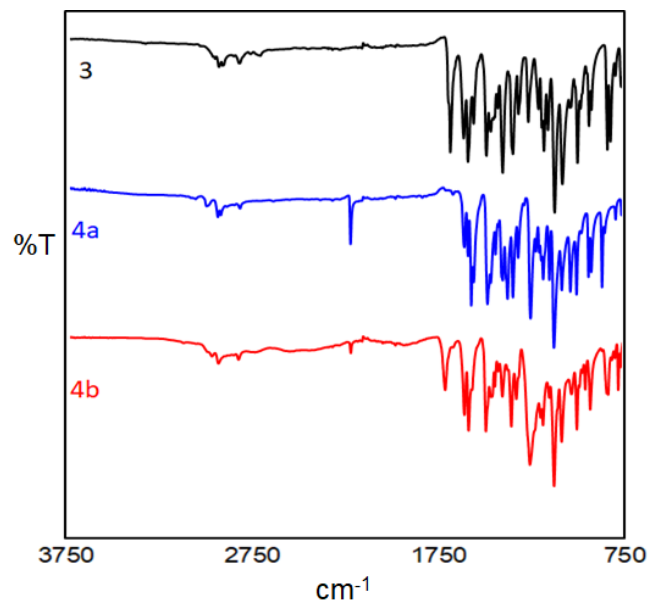
Figure 2. FT-IR spectra of **3**, **4a** and **4b**

^{1}H NMR spectra (**Figure 3**) of **3**, **4a** and **4b** were taken in CDCl$_3$ and compared with each other. In ^{1}H NMR spectrum of compound **3**, one proton of aldehyde group was observed as singlet at 10.25 ppm. Two aromatic protons of the quinoline ring resonated as two singlets at 8.65 and 7.13 ppm. Hydrogens of three different methoxy groups and one thiomethyl group were observed as four singlets of three protons at 4.12, 4.05, 3.96 and 2.68 ppm, respectively. In ^{1}H NMR spectra of compounds **4a** and **4b**, the aldehyde proton of compound **3** disappeared, replaced by the singlet signals (9.01 ppm for **4a** and 8.86 ppm for **4b**) of alkenyl protons. In addition, two singlets in the aromatic region and four singlet signals in the aliphatic region are observed separately for the two compounds.

Barış Seçkin ARSLAN

5,6,7-Trimethoxy-2-(methylthio)quinoline with Different Anchoring Groups: Synthesis and dye-sensitize...

Figure 3. ^{1}H NMR spectra of **3**, **4a** and **4b**
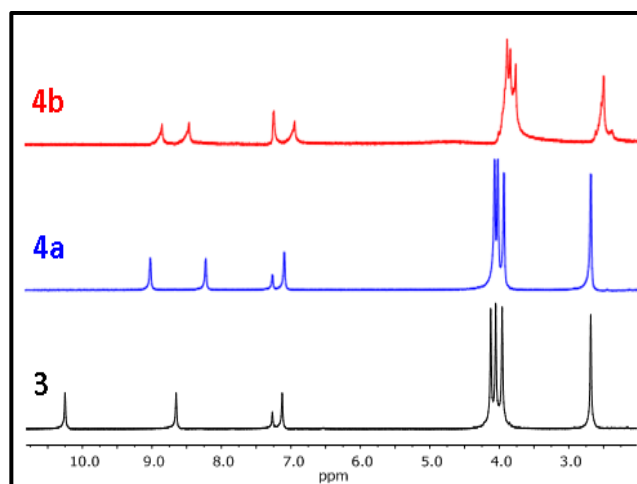(300 MHz, CDCl$_3$)
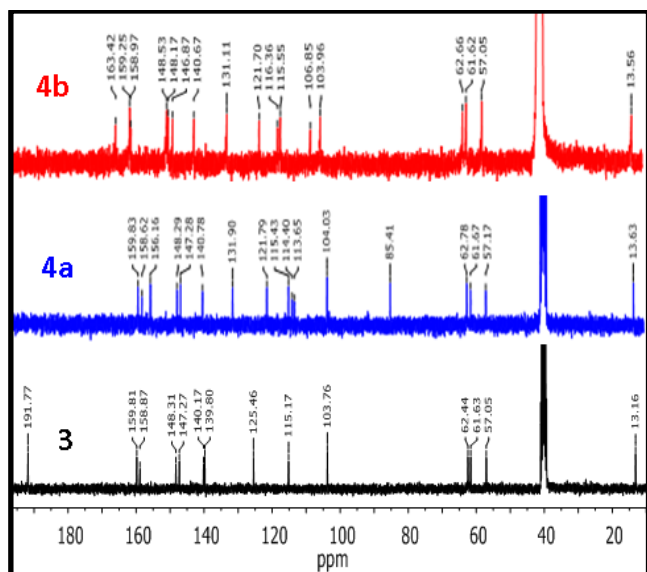
Figure 4. ^{13}C NMR spectra of **3**, **4a** and **4b**
(75 MHz, DMSO-d$_6$)

^{13}C NMR spectra (**Figure 4**) of **3**, **4a** and **4b** were taken in DMSO-d$_6$ and compared with each other. In ^{13}C NMR spectrum of **3**, carbon signal of the aldehyde group is observed at 191.77 ppm. Nine different aromatic carbons appeared at 159.81, 158.87, 148.31, 147.27, 140.17, 139.80, 125.46, 115.17 and 103.76 ppm. Methoxy groups and thiomethyl group carbon peaks are detected at 62.44, 61.63, 57.05 and 13.16 ppm, respectively. In ^{13}C NMR spectrum of **4a**, the signal of the aldehyde carbon has disappeared, instead, signals of two alkenyl carbons and two nitrile carbons are observed. As well as signals of nine aromatic, three methoxy and one thiomethyl carbons are seen. In ^{13}C NMR spectrum of **4b**, one carboxylic acid carbon (163.42 ppm), two alkenyl carbons and one nitrile carbon are observed instead of the aldehyde carbon. As well as signals of nine aromatic, three methoxy and one thiomethyl carbons are seen.

When the FT-IR, ^{1}H NMR and ^{13}C NMR spectra of the compounds **3**, **4a** and **4b** are examined, it is observed that the proposed compound structures are compatible with the results obtained.

3.3. Photophysical characteristics

The UV−Vis absorption spectra of compounds **3**, **4a** and **4b** in DMSO solution are displayed in **Figure 5** and the relevant data are given in **Table 1**. The λ_{abs} for compounds **3**, **4a** and **4b** are 334, 397 and 380 nm for the intramolecular charge transfer (ICT) band, respectively. As expected, the lowest absorption band belongs to compound **3** with relatively lower conjugation. When compound **4a** containing malononitrile unit and compound **4b** containing cyanoacrylic acid unit were compared, it was observed that the absorption band of **4a** is red shifted (17 nm) [20].

The fluorescence spectra in DMSO solution (**Figure 6**) were recorded by exciting at the absorption maxima of the compounds. The emission maxima (λ_{em}) for all compounds are parallel to the absorption maxima (λ_{abs}). It demonstrates that the malononitrile moiety similarly affects both light absorption and emission.
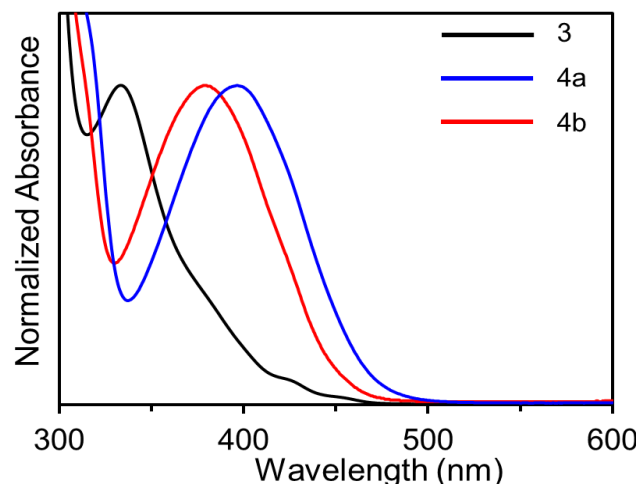

Figure 5. Normalized absorption spectra of **3**, **4a** and **4b** in DMSO solution
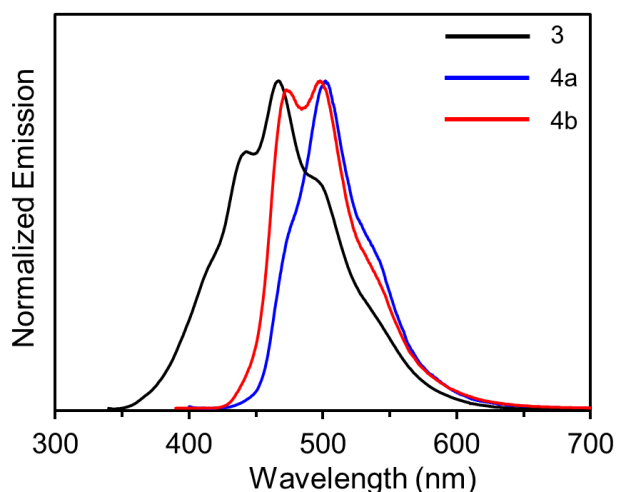
Barış Seçkin ARSLAN

5,6,7-Trimethoxy-2-(methylthio)quinoline with Different Anchoring Groups: Synthesis and dye-sensitize...

Figure 6. Normalized emission spectra of **3**, **4a** and **4b** in DMSO solution

Table 1.
Optical properties of the compounds

Compound	λ_{abs} [nm][a]	λ_{onset} [nm][b]	λ_{em} [nm][c]	E_{0-0} [eV][d]
3	334	390	443, 467	3.18
4a	397	470	502	2.64
4b	380	450	473, 498	2.76

[a] λ_{abs}: absorption maximum wavelength.

[b] λ_{onset}: absorption onset wavelength.

[c] λ_{em}: emission maximum wavelength

[d] E_{0-0}: band gap, calculated using the equation
$E_{0-0} = 1240/\lambda_{onset}$.

3.4. Photovoltaic properties of DSSCs

Due to the low absorption band (334 nm) of compound **3**, only the photovoltaic properties of compounds **4a** and **4b** were investigated. Firstly, the prepared photoanodes were immersed in dye solutions for 6 hours. Because of the weak bonding on TiO_2 surface of the malononitrile group in compound **4a**, there was hardly any coating during this time. Therefore, the immersion time for **4a** was determined as 24 hours.

The current density–voltage (J–V) graph of the DSSCs obtained from dyes **4a** and **4b** are shown in **Figure 7** and the photovoltaic parameters (Jsc, Voc, FF and PCE) are given in **Table 2**. When the PCE of the dyes (0.28% for **4a** < 2.73% for **4b**)

are compared, an increase is observed in parallel with the Jsc values. There was a more red shift of compound **4a** (397 nm) than **4b** (380 nm) in the absorption spectra. Although this is expected to have an effect on light harvesting ability, it does not appear to be compatible with PCEs [20]. The reason for this is the carboxyl group forms a strong ester bond with the TiO_2 surface, which increases electron conduction [21]. Compound **4b** containing cyanoacrylic acid as an acceptor forms a stronger bond with TiO_2 than compound **4a** containing malononitrile. This results in a higher power conversion efficiency of compound **4b**.

CDCA, which is commonly used as a coadsorbent in DSSC production, prevents aggregation as well as recombination, leading to an increase in Jsc and Voc [22]. The J-V curves of the DSSCs of the two dyes containing 5 mM CDCA are shown in **Figure 7** and the associated data in **Table 2**. Two dyes show 0.22–0.40 mA cm^{-2} of Jsc increase and 12–13 mV of Voc increase. It shows the utility effect of CDCA on performance, the final PCEs lie of **4b** (3.01%) > **4a** (0.44%). When compared to the efficiency of the N719-based device (7.81%) measured under the same conditions, it was determined that compound **4b** (with CDCA) reached approximately 39% of the N719.
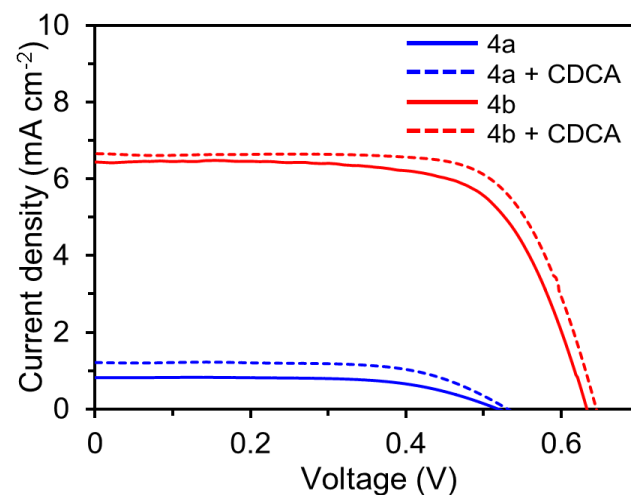

Figure 7. *J-V* curves of DSSCs based on the dyes in the absence and presence of CDCA

Table 2.
Photovoltaic parameters of the DSSCs

Dye	J_{SC} (mA cm^{-2})	V_{OC} (V)	FF	PCE (%)
4a	0.82	0.518	0.66	0.28
4a+CDCA	1.22	0.531	0.68	0.44
4b	6.44	0.633	0.67	2.73
4b+CDCA	6.66	0.645	0.70	3.01
N719+CDCA	15.16	0.736	0.70	7.81

To understand the effect of the thiomethyl group on PCE, compound **4b** can be compared with structurally similar compound **5b** which is previously synthesized for application in DSSC by our study group [8]. Higher PCE was obtained when the thiomethyl group is incorporation (**Figure 8**) instead of only one methoxy group. The PCEs for the two compounds are 2.62% for **5b** and 3.01% for **4b** in the presence of CDCA. Although the maximum absorbances (380 nm) of these two compounds were the same, due to the different λ_{onset} values (432 nm for **5b** and 450 nm for **4b**), the band gaps (2.87 eV for **5b** and 2.76 eV for **4b**) were changed. This explains why the PCE of compound **4b** is higher than that of compound **5b**.
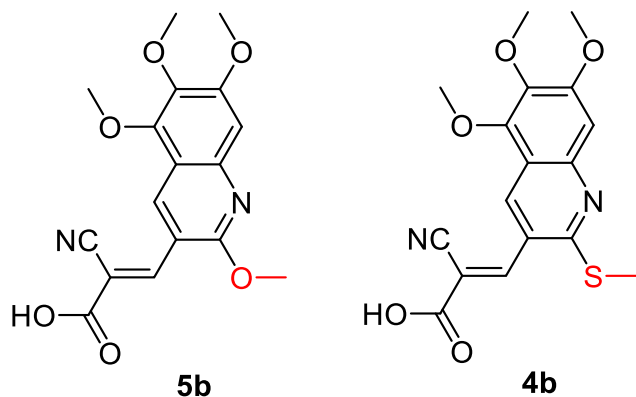

Figure 8. Molecular structures of **5b** in previous work and **4b** in this study

4. CONCLUSIONS

In this study, two novel D-π-A dyes (**4a** and **4b**) containing three methoxy (-OCH$_3$) and one thiomethyl (-SCH$_3$) groups as donors, quinoline ring as π-bridge, malononitrile or cyanoacrylic acid as acceptors were synthesized. The compounds obtained were structurally characterized by FT-IR, ^{1}H NMR and ^{13}C NMR techniques. Two dyes (**4a** and **4b**) were applied on DSSC and the effects of anchoring groups on PCEs were investigated. Compound **4b** demonstrated (Jsc = 6.66 mA cm^{-2}, Voc = 0.645 V and FF = 0.70) the highest power conversion efficiency of 3.01% in the presence of CDCA as a coadsorbent. It also caused a narrowing of the band gap with the introduction of the thiomethyl group into the structure, which positively affects the power conversion efficiency. To sum up, it is determined that the presence of thiomethyl group instead of methoxy group and the better anchoring of cyanoacrylic acid, which forms an ester bond with the TiO$_2$ surface, increases the PCE.

The Declaration of Conflict of Interest/Common Interest

No conflict of interest or common interest has been declared by the author.

The Declaration of Ethics Committee Approval

The author declares that this document does not require an ethics committee approval or any special permission.

The Declaration of Research and Publication Ethics

The author of the paper declares that she complies with the scientific, ethical and quotation rules of SAUJS in all processes of the paper and that she does not make any falsification on the data collected. In addition, she declares that Sakarya University Journal of Science and its editorial board have no responsibility for any ethical violations that may be encountered, and that this study has not been evaluated in any academic

Barış Seçkin ARSLAN

5,6,7-Trimethoxy-2-(methylthio)quinoline with Different Anchoring Groups: Synthesis and dye-sensitize...

publication environment other than Sakarya University Journal of Science.

REFERENCES

[1]   B. O'Regan and M. Gratzel, "A low-cost, high-efficiency solar cell based on dye-sensitized colloidal TiO2 films," Nature, vol. 353, pp. 737-740, 1991.

[2]   P. Li, Z. Wang, C. Song, and H. Zhang, "Rigid fused π-spacers in D-π-A type molecules for dye-sensitized solar cells: A computational investigation," Journal of Materials Chemistry C, vol. 5, pp. 11454-11465, 2017.

[3]   H. Huang, H. Chen, J. Long, G. Wang, and S. Tan, "Novel D-A-p-A organic dyes based on 3-dimensional triarylamine and benzothiadiazole derivatives for high-performance dye-sensitized solar cells," Journal of Power Sources, vol. 326, pp. 438–446, 2016.

[4]   M. M. Jadhav, J. V. Vaghasiya, D. Patil, S. S. Soni, and N. Sekar, "Synthesis of novel colorants for DSSC to study effect of alkyl chain length alteration of auxiliary donor on light to current conversion efficiency," Journal of Photochemistry and Photobiology A, vol. 377, pp. 119-129, 2019.

[5]   J. Zhang, Y. H. Kan, H. B. Li, Y. Geng, Y. Wu, and Z. M. Su, "How to design proper π-spacer order of the D-π-A dyes for DSSCs? A density functional response," Dyes Pigments, vol. 95, pp. 313-321, 2012.

[6]   Y. S. Yen, J. S. Ni, W. I Hung, C. Y. Hsu, H. H. Chou, and J. T. Lin, "Naphtho[2,3-c][1,2,5]thiadiazole and 2H-Naphtho[2,3-d][1,2,3]triazole-containing D-A-π-A conjugated organic dyes for dye-sensitized solar cells," ACS Applied Materials & Interfaces, vol. 8, pp. 6117-6126, 2016.

[7]   N. Zhou, K. Prabakaran, B. Lee, S. H. Chang, B. Harutyunyan, P. Guo, M. R. Butler, A. Timalsina, M. J. Bedzyk, M. A. Ratner, S. Vegiraju, S. Yau, C. G. Wu, R. P. H. Chang, A. Facchetti, M. C. Chen, and T. J. Marks, "Metal-free tetrathienoacene sensitizers for high-performance dye-sensitized solar cells," Journal of the American Chemical Society, vol. 137, pp. 4414-4423, 2015.

[8]   B. S. Arslan, S. N. Ülüş, M. Gezgin, B. Arkan, E. Güzel, D. Avcı, M. Nebioğlu, and İ. Şişman, "Insight into the effects of the donors and pi-spacers on the photovoltaic performance of quinoline and pyridocarbazole based DSSCs," Optical Materials, vol. 106, pp. 109974, 2020.

[9]   O. O. Ajani, K. T. Iyaye, O. Y. Audu, S. J. Olorunshola, A. O. Kuye, and I. O. Olanrewaju, "Microwave assisted synthesis and antimicrobial potential of quinoline based 4-hydrazide-hydrazone derivatives," Journal of Heterocyclic Chemistry, vol. 55, pp. 302-312, 2017.

[10] P. Pounraj, V. Mohankumar, M. S. Pandian, and P. Ramasamy, "Donor functionalized quinoline based organic sensitizers for dye sensitized solar cell (DSSC) applications: DFT and TD-DFT investigations," Journal of Molecular Modeling, vol. 24, pp. 343, 2018.

[11] G. C. dos Santos, E. F. Oliveira, F. C. Lavarda, and L. C. da Silva-Filho, "Designing new quinoline-based organic photosensitizers for dye-sensitized solar cells (DSSC): a theoretical investigation," Journal of Molecular Modeling, vol. 25, pp. 75, 2019.

[12] A. Slodek, M. Matussek, M. Filapek, G. Szafraniec-Gorol, A. Szlapa, I. Grudzka-Flak, M. Szczurek, J. G. Malecki, A. Maron, E. Schab-Balcerzak, E. M. Nowak, J. Sanetra, M. Olejnik, W. Danikiewicz, and S. Krompiec, "Small donor–acceptor molecules based on a

Barış Seçkin ARSLAN

5,6,7-Trimethoxy-2-(methylthio)quinoline with Different Anchoring Groups: Synthesis and dye-sensitize...

quinoline–fluorene system with promising photovoltaic properties," European Journal of Organic Chemistry, vol. 14, pp. 2500-2508, 2016.

[13] P. Singh, V. Srivastava, and M. A. Quraishi, "Novel quinoline derivatives as green corrosion inhibitors for mild steel in acidic medium: Electrochemical, SEM, AFM, and XPS studies," Journal of Molecular Liquids, vol. 216, pp. 164-173, 2016.

[14] M. Mao, X. Zhang, B. Zhu, J. Wang, G. Wu, Y. Yin, and Q. Song, "Comparative studies of organic dyes with a quinazoline or quinoline chromophore as π-conjugated bridges for dye-sensitized solar cells," Dyes Pigments, vol. 124, pp. 72-81, 2016.

[15] B. S. Arslan, E. Güzel, T. Kaya, V. Durmaz, M. Keskin, D. Avcı, M. Nebioğlu, and İ. Şişman, "Novel D-π-A organic dyes for DSSCs based on dibenzo[b,h][1,6] naphthyridine as a π-bridge," Dyes Pigments, vol. 164, pp. 188-197, 2019.

[16] B.S. Arslan, B. Arkan, M. Gezgin, Y. Derin, D. Avcı, A. Tutar, M. Nebioğlu, and İ. Şişman, "The improvement of photovoltaic performance of quinoline-based dye-sensitized solar cells by modification of the auxiliary acceptors," Journal of Photochemistry and Photobiology A: Chemistry, vol. 404, pp. 112936, 2021.

[17] B. Cheng, and J. Xu, "Mechanistic insight into the thermal 1,3-chlorine migrations of N-chloroacetanilides under neutral conditions," Phosphorus, Sulfur, and Silicon and the Related Elements, vol. 192 pp. 518–525, 2017.

[18] O. Meth-Cohn, B. Narine, and B. Tarnowski, "A versatile new synthesis of quinolines and related fused pyridines. Part 5. The synthesis of 2-chloroquinoline-3-carbaldehydes,"

Journal of the Chemical Society Perkin Transactions 1, pp. 1520–1530, 1981.

[19] A. D. Sonawane, D. R. Garud, T. Udagawa, and M. Koketsu, "Synthesis of thieno [2, 3-b] quinoline and selenopheno [2, 3-b] quinoline derivatives via iodocyclization reaction and a DFT mechanistic study," Organic & Biomolecular Chemistry, vol. 16, pp. 245-255, 2018.

[20] A. Kathiravan, M. Panneerselvam, K. Sundaravel, N. Pavithra, V. Srinivasan, S. Anandan, and M. Jaccob, "Unravelling the effect of anchoring groups on the ground and excited state properties of pyrene using computational and spectroscopic methods," Physical Chemistry Chemical Physics, vol. 18, pp. 13332-13345, 2016.

[21] Y. Ooyama and Y. Harima, "Molecular designs and syntheses of organic dyes for dye-sensitized solar cells," European Journal of Organic Chemistry, vol. 18, pp. 2903-2934, 2009.

[22] N. Prachumrak, T. Sudyoadsuk, A. Thangthong, P. Nalaoh, S. Jungsuttiwong, R. Daengngern, S. Namuangruk, P. Pattanasattayavong, and V. Promarak, "Improvement of D–π–A organic dye-based dye-sensitized solar cell performance by simple triphenylamine donor substitutions on the π-linker of the dye" Materials Chemistry Frontiers, vol. 1, pp. 1059-1072, 2017.

Sakarya University Journal of Science
SAUJS

Title: Temperature Dependence of Ferromagnetic Resonance in Double Perovskite La2NiMnO6 Thin Films

Authors: Sinan KAZAN

Temperature dependence of ferromagnetic resonance in double perovskite La$_2$NiMnO$_6$ thin films

Sinan KAZAN[*1]

Abstract

The results of the linewidth analysis of ferromagnetic resonance (FMR) spectra of epitaxial La$_2$NiMnO$_6$ (LNMO) thin films on (100) oriented SrTiO$_3$ and (110) oriented NdGaO$_3$ substrates at different temperature have been presented. Observed two well resolved FMR signals have been attributed to the coexistence two magnetic phases with different easy and hard axis in the film plane of LNMO. The line shape and the linewidth of the ferromagnetic resonance spectra were measured as a function of temperature. Asymmetry ratio of field derivative FMR absorption curve shows unusual behavior with decreasing temperature. This unusual temperature dependency of the FMR linewidth confirms the presence of magnetoelectric effect in epitaxial LNMO thin films grown by pulse laser deposition technique.

Keywords: Ferromagnetic Resonance, Double perovskite, Magnetodielectric, La$_2$NiMnO$_6$

1. INTRODUCTION

Multiferroic materials have been studied intensively due to their wide applications in the fields of magnetoelectronics and spintronics [1–6]. Recently, the semiconducting materials with double perovskite structure has drawn more attention due to the presence of charge and magnetic order simultaneously at near-room temperature [7]. Even though most oxides doped with transition metal ions are antiferromagnet, La$_2$NiMnO$_6$ (LNMO) is a ferromagnet due to the superexchange interaction and the nature of this interaction is explained by some rules [7-8]. In LNMO crystal structure, NiO$_6$ and MnO$_6$ octahedrons are organized in order to produce double perovskite with a pseudo cubic structure. In LNMO, 3d ions (Ni^{2+} and Mn^{4+}) are distributed randomly at B site of ABO$_3$ perovskite unit cell resulting Ni-O-Mn, Ni-O-Ni and Mn-O-Mn chemical bonds with different superexchange interaction. Ni-O-Ni and Mn-O-Mn are expected to result antiferromagnetic phase [8-10]. High temperature ferromagnetic order is caused by only Ni-O-Mn bonds.

Magnetic properties of bulk and thin film structured double perovskite sample have been studied intensively for the past decades to understand the nature of interaction mechanism between the magnetic ions in this materials. It is well known that LNMO is a ferromagnetic at near-room temperature compared to

* Corresponding Author: kazan@gtu.edu.tr
[1] Gebze Technical University, Faculty of Science and Letters, Kocaeli, Turkey, ORCID: https://orcid.org/0000-0002-8183-5733

antiferromagnetic and paramagnetic properties of perovskites $LaMnO_3$ and $LaNiO_3$ [11-18]. It was recently reported that the LNMO exhibits remarkable magnetodielectric effects, which is very useful for spintronic devices, at room temperature [8]. Furthermore, considerable increase in the electronic properties with the external magnetic field have been observed in LNMO at a temperature of 280 K which is the suitable temperature for the magnetoelectric devices [8].

Ferromagnetic LNMO thin films were fabricated epitaxially on different substrates by the pulsed laser deposition (PLD) technique [19]. On the other hand, the fabrication technique, growth temperature, and substrate related mismatch mechanism cause considerable influence on the magnetic and magnetoelectric properties of the thin films.

It was reported that the ferromagnetic resonance (FMR) is a very informative technique for the investigation of structural, magnetic, and transport properties of perovskite materials [19, 25]. By this point of view the investigation of the temperature dependent FMR spectra, as well as the linewidth analysis of the spectra and subsequent study of magnetic anisotropy in these films gains much interest. This paper presents mainly the results of the linewidth analysis of the temperature dependent FMR spectra of double perovskite LNMO thin films growth on different substrates.

2. MATERIALS AND METHODS

A ferromagnetic semiconductor La_2NiMnO_6 (LNMO) double perovskite thin films were grown on (100)-oriented cubic $SrTiO_3$ (STO) and (110)-oriented $NdGaO_3$ (NGO) substrates using pulsed laser deposition (PLD) technique. The substrate temperature and the background oxygen pressure were maintained 750 ºC and 28-800 mTorr. A KrF excimer laser (248 nm) source was used. After 5000 laser pulses the thickness of deposited films of about 170 nm were measured by small angle X-Ray reflectometry [9].

Ferromagnetic resonance spectra (FMR) were recorded with Bruker EMX electron spin resonance spectrometer which operates at X band frequency (9.8 GHz) at two conventional
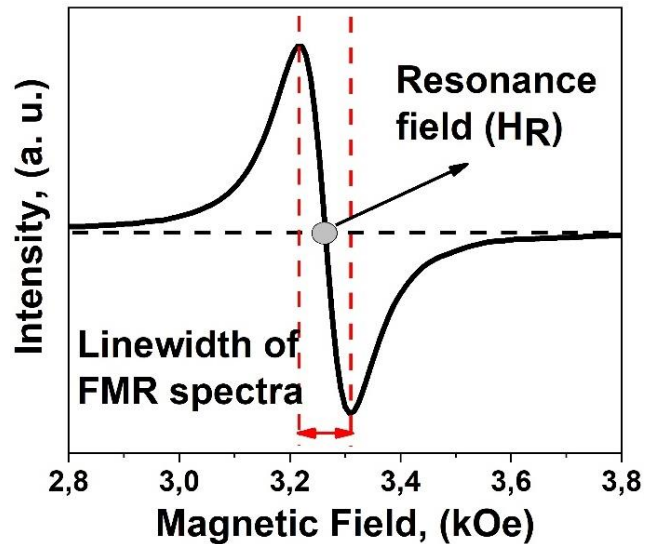
Figure 1 Characteristics of a FMR spectra (Resonance field and linewidth)

measurement geometries. The first geometry is known as the in-plane geometry. In this geometry, external dc magnetic field lies in the plane of the sample and magnetic field component of the microwave is always perpendicular to the surface of the film during rotation of the sample. Second one is known as the out of plane geometry. In this geometry, magnetic field component of microwave always lies in the film plane during the rotation of the sample. The characteristics of the FMR spectra used in this study are illustrated in Figure 1. The details of ferromagnetic resonance measurement at different geometries were provided elsewhere [19]. Low temperature FMR measurements were performed by using the continuous He gas flow cryostat of Oxford Instruments between the temperature of 10 K and 300 K.

3. EXPERIMENTAL RESULTS AND DISCUSSION

In out of plane ferromagnetic resonance (FMR) measurements, two distinct well resolved FMR peaks were observed at room temperature for the La_2NiMnO_6 (LNMO) double perovskite thin films on (100)-oriented $SrTiO_3$ (STO) and (110)-oriented $NdGaO_3$ (NGO) substrates as seen in Figure 2. These two signals have been attributed to the two different magnetic phases [16, 19-20] with different magnetocrystalline anisotropy. Angular variation of these two resonance fields at
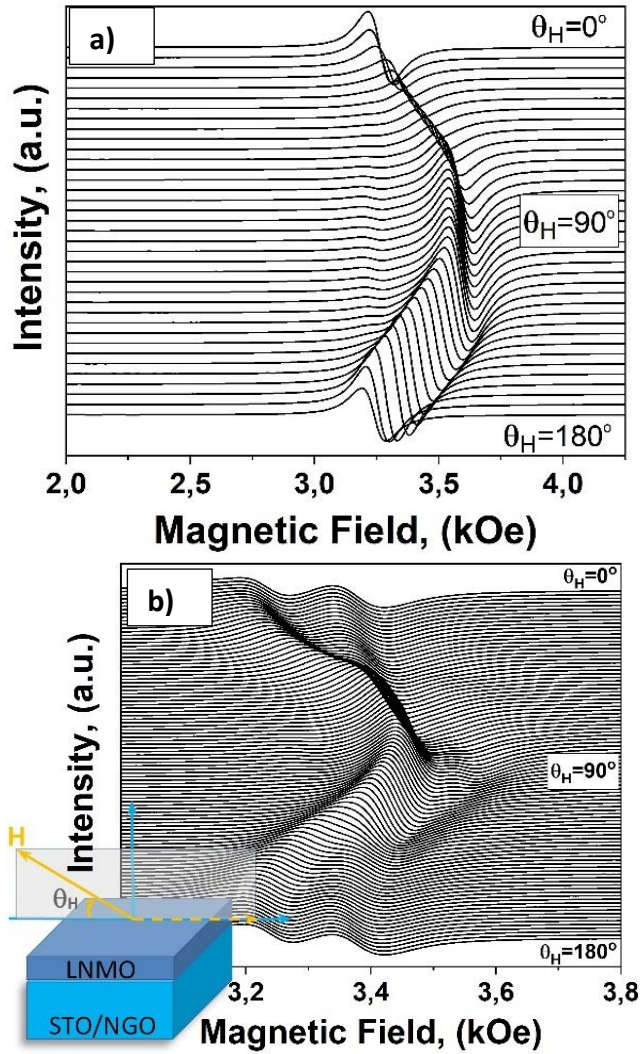
Figure 2 Out of plane FMR spectra of LNMO thin films on a) STO and b) NGO substrate

out of plane FMR spectrum show opposite angular response that is the minimum resonance field of the first mode correspond to the maximum resonance field of second mode for LNMO/NGO in contrast to the LNMO/STO sample. The reason of these two different magnetic phases lies in the nature of magnetic superexchange interaction between different spin configurations of Mn and Ni ions in different compound in LNMO sample. The effective magnetization which is the distance between the maximum and the minimum resonance fields on the spectra for both sample have been considered as low due to the measurement temperature which is close to the Curie temperature. The intensity ratio of the two observed FMR signals which belong to the

different phase gives very strong evidence of site ordering and coexistence of two crystallographic form in La_2NiMnO_6 thin film samples. The FMR spectra at in-plane geometry as a mirror of magnetocrystalline anisotropy show four-fold cubic anisotropy for LNMO/STO sample and two-fold uniaxial anisotropy for the LNMO/NGO sample due to the mismatch mechanism between the lattice and the substrate [19]. The peak-to-peak ferromagnetic resonance linewidth denoted as ΔH_{pp} presents the rate of relaxation of the magnetization back to relaxed position when the external static magnetic field is zero. The linewidth of the observed FMR spectra, ΔH_{pp} is affected by two mechanisms. The First one is the intrinsic damping of magnetization (ΔH_{hom}, Gilbert damping) which depends on the frequency of applied microwave and the second one is the magnetic inhomogeneity of the ferromagnetic sample (ΔH_{inhom}) and it is independent from the frequency. The inhomogeneity in ferromagnetic sample may be originated from the distribution of demagnetizing field in the sample, randomly distributed defects, exchange-conductivity mechanism and two magnon scattering from the spatially localized magnetic inhomogeneities [21]. The magnetic inhomogeneities cause FMR line broadening due to the distribution of different local resonance frequencies. The frequency dependent damping term (ΔH_{hom}) manifests itself by the way of dissipation of absorbed microwave energy from the spin system into the lattice generating phonons. Therefore it reflects the anisotropy via spin orbit coupling and generally ΔH_{hom} damping term is explained by the following formula [22],

$$\Delta H_{hom}(\theta, \emptyset) = \frac{2}{\sqrt{3}} \frac{1}{\left|\frac{\partial \omega_R}{\partial H}\right|} \frac{G}{M^2} \left(F_{\theta\theta} + \frac{F_{\emptyset\emptyset}}{sin^2\theta} \right)$$

$$\approx 1.16 \frac{G}{\gamma^2 M(T, H)} \omega$$

where θ and $\emptyset$ denotes to the angular position of the magnetization M. $F_{\theta\theta}$ and $F_{\emptyset\emptyset}$ are second derivatives of the total magnetic free energy. G is the Gilbert damping constant at given temperature T. γ is the gyromagnetic ratio. ΔH_{hom} has a minimum (hard axis) at a special direction of magnetization and has a maximum where magnetization varies strongly (easy axis). Also
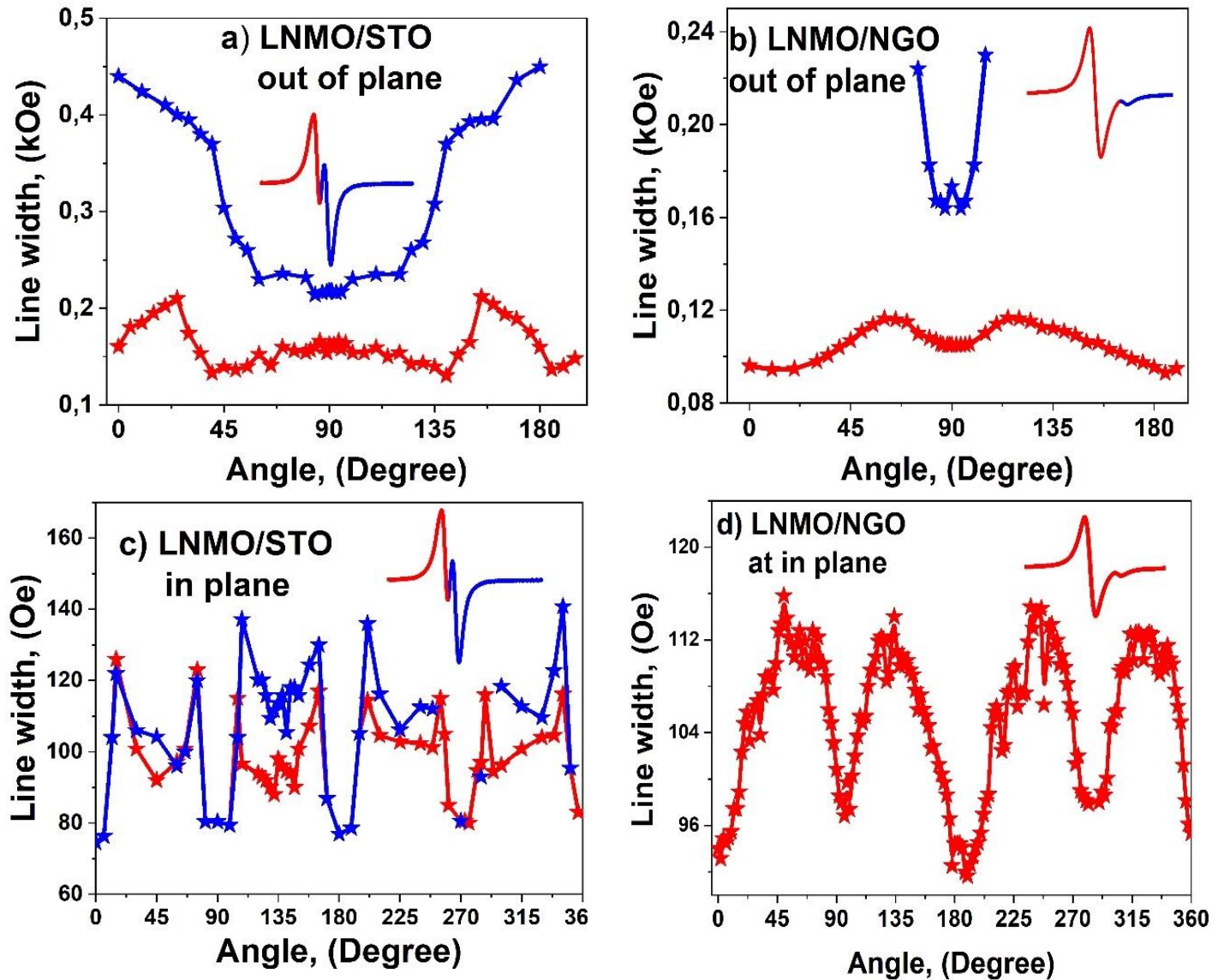
Figure 3 Angular variation of FMR linewidth at out of plane and in-plane geometry at room temperature belong to samples growth on NGO and STO substrate

there is another important contribution to the FMR line broadening due to the exchange conductivity mechanism. Microwave can penetrate a few nm into the surface of conductive ferromagnet producing inhomogeneous dynamic magnetization. The Spatial variation of magnetization exert a torque on M is given as $\left(\frac{2A\gamma}{M^2}\right)\left(\vec{M}x\nabla^2\vec{M}\right)$ [23] where A is the exchange stiffness constant. Therefore this term must be included in equation for the dynamic of magnetization. In conductive ferromagnetic spin system the exchange term causes a net contribution to linewidth. However, if the conductivity of sample is very low or exchange

stiffness is very small this contribution is negligible as in our sample system. It is well known that La_2NiMnO_6 (LNMO) double perovskite thin film is ferromagnetic semiconductor and its dielectric constant is very large [8]. The angular variation of the FMR linewidth of the LNMO sample grown on two different substrates at room temperature is shown in Figure 3. Figures 3a and 3b show anisotropic FMR linewidth of two well resolved signals (peak) at out of plane geometry. According to the figure, the linewidth of signals has a minimum at perpendicular orientation where applied static magnetic field is parallel to the film normal as expected. The variation of linewidth near 90
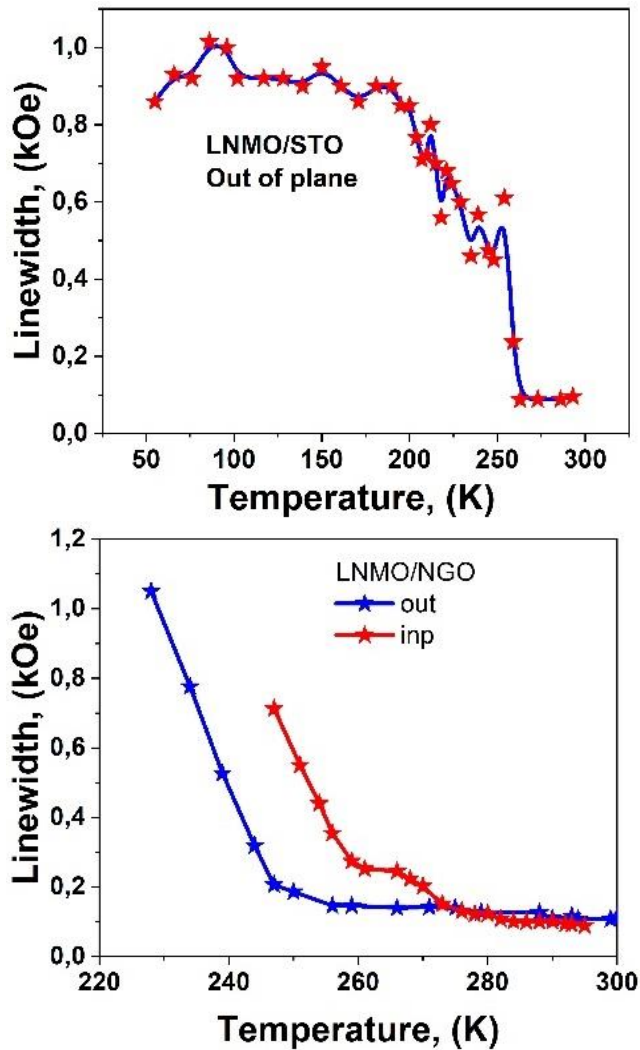
Figure 4 Temperature variation of FMR linewidth at out of plane and in-plane geometry of the sample La_2NiMnO_6 thin film

degree is very large since the measurements have been made at ferromagnetic-paramagnetic phase transition temperature and the magnetic exchange interaction between the cation ions is very small. Figures 3c and 3d show FMR linewidth of two well resolved signals (peak) at in-plane geometry showing four-fold anisotropy. This anisotropic behavior have been attributed to the two magnon scattering [22]. As a result the microscopic origin of the damping mechanism base on the spin orbit coupling and quantitative analyzing to the angular variation of linewidth was very difficult due to the various contribution to the angular dependent linewidth.

The results can be interpreted using the previously reported results of the magnetodielectric effect in

La_2NiMnO_6 presented by N. S. Rogada and Co-workes [8] who presented the temperature dependency of the dielectric constant (ε) at the frequency of 10 kHz at external magnetic field. It was observed that the dielectric constant ε has a value of approximately 600 at zero magnetic field and at room temperature. It decreases gradually with decrease of the temperature until it reach 220 K. At this temperature a sharp drop of dielectric constant value exists. When an external magnetic field (0.1 T) was applied, this sharp transition shift to the room temperature region resulting a very large magnetodielectric response of La_2NiMnO_6. This remarkable change in dielectric constant by external magnetic field makes ferromagnetic semiconductor La_2NiMnO_6 (LNMO) a magnetoelectric material suitable for spintronic applications. Analyzing of temperature dependent FMR linewidth of the sample LNMO growth on STO/NGO substrates leads to some interesting results in accordance with the magnetodielectric effect observed in the mentioned temperature dependency of the dielectric constant.

The FMR linewidth of the both samples growth on different substrates at different temperatures are shown in Figure 4. The temperature dependency of linewidths shows similar variation of magnetization with temperature (M-T graph). The asymmetric FMR spectrum which is the field derivative of absorption curve, is shown in Figure 5a. The spectrum was divided into two parts assigned as A and B as shown in Figure 5a for presenting the asymmetry in FMR spectrum. The variation of the parameters of A, B and the asymmetry ratio (A/B) of FMR line shape with the temperature are shown on Figures 5b and 5c. According to the Dyson theory this ratio is related with conductivity of the samples [24].

At in-plane geometry and at room temperature the asymmetry parameter (A/B) is nearly one showing the paramagnetic phase or referring to the charge ordering in LNMO sample. A and B parts of the spectrum show different responses with degrease of the temperature. B part decreases faster than the A part Therefore the ratio of A/B decreases from 1 to 0.6 between the temperatures of 300 K and 265 K. This asymmetric response of the line shape coincides with the magnetodielectric effect given in Ref. [8]. The appearance of asymmetric line shape between the
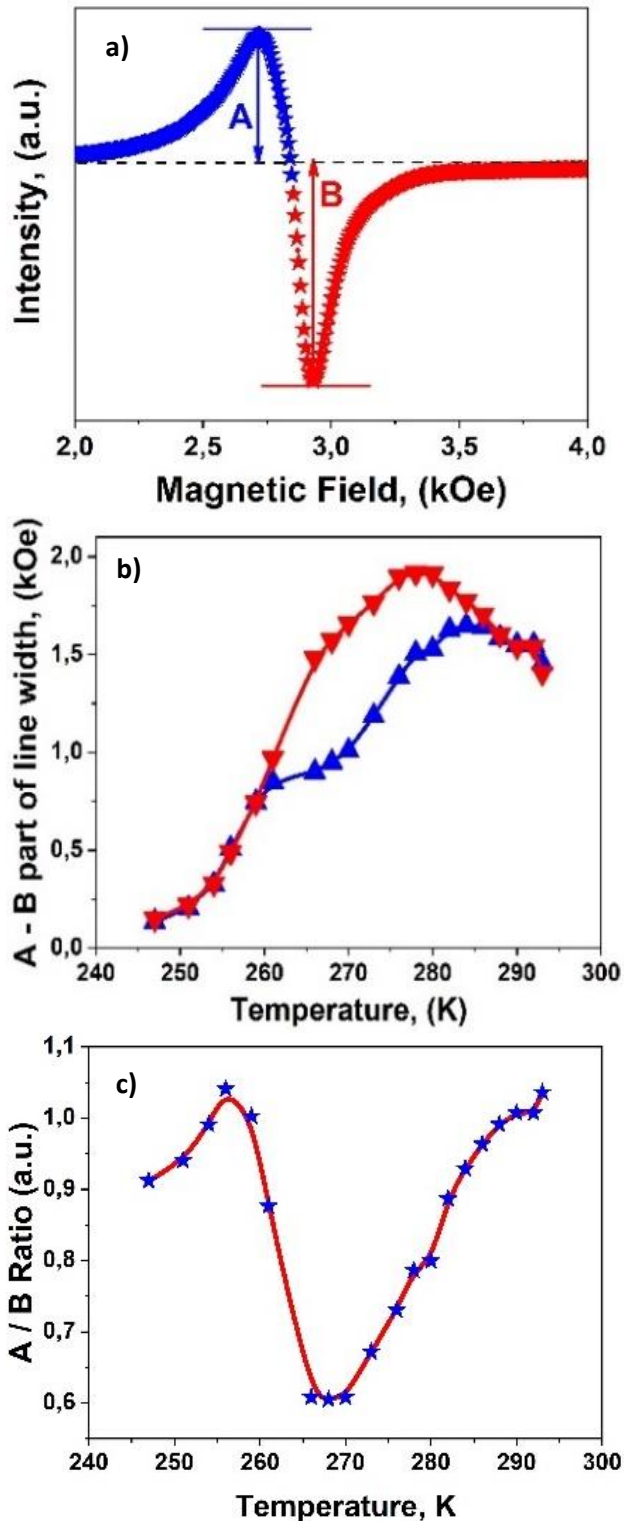
Figure 5 Temperature dependency of the asymmetry parameter at in-plane geometry. a) Asymmetric FMR spectrum of the LNMO/ NGO at 274 K. b) Temperature dependency of A and B part of the spectrum. c) Variation of the A/B ratio with the temperature

temperature of 280 and 250 K in ferromagnetic semiconductor compound La_2NiMnO_6 indicates a coupling between magnetic and electric properties of the films. The magnetoelectric coupling in the form of $\gamma P^2 M^2$ where P and M are the polarization and magnetization respectively and γ is the coupling constant. This coupling causes a net changing in the dielectric susceptibility below the Curie temperature by applying the magnetic field.

4. CONCLUSIONS

In conclusion, the linewidth analysis of the temperature dependent FMR spectra of ferromagnetic La_2NiMnO_6 double perovskite thin films synthesized on STO and NGO substrates by using laser pulse deposition technique has been performed. The observed peculiarities in the angular and temperature dependences of FMR linewidth have been interpreted on the base of the existence of previously reported magnetoelectric effect in this material.

The Declaration of Conflict of Interest/ Common Interest

No conflict of interest or common interest has been declared by the author.

The Declaration of Ethics Committee Approval

The author declares that this document does not require an ethics committee approval or any special permission.

The Declaration of Research and Publicatıon Ethics

The author of the paper declares that she complies with the scientific, ethical and quotation rules of SAUJS in all processes of the paper and that he does not make any falsification on the data collected. In addition, he declares that Sakarya University Journal of Science and its editorial board have no responsibility for any ethical violations that may be encountered, and that this study has not been evaluated in any academic publication environment other than Sakarya University Journal of Science.

REFERENCES

[1] M. Fiebig, "TOPICAL REVIEW: Revival of the magnetoelectric effect," Journal of Physics D: Applied Physics, vol. 38, no. 8, pp. R123-R152, 2005.

[2] N. A. Hill, "Why are there so few magnetic ferroelectrics?," Journal of Physical Chemistry B, vol. 104, no. 29, pp. 6694-6709, 2000.

[3] W. Eerenstein, N. Mathur and J. Scott, "Multiferroic and magnetoelectric materials," Nature, vol. 442, pp. 759–765, 2006.

[4] G. Lawes, A. P. Ramirez, C. M. Varma and M. A. Subramanian, "Magnetodielectric effects from spin fluctuations in isostructural ferromagnetic and antiferromagnetic systems," Physical Review Letters, vol. 91, no. 25, pp. 257208, 2003.

[5] J. S. Moodera, X. Hao, G. A. Gibson and R. Meservey, "Electron-spin polarization in tunnel junctions in zero applied field with ferromagnetic EuS barriers,"

Physical Review Letters, vol. 61, no. 5, pp. 637-640, 1988.

[6] M. Gajek, M. Bibes, A. Barthèlèmy, K. Bouzehouane, S. Fusil, M. Varela, "Spin filtering through ferromagnetic $BiMnO_3$ tunnel barriers," Physical Review B, vol. 72, no. 2, pp. 020406(R), 2005

[7] R. I. Dass, J. Q. Yan and J. B. Goodenough, "Oxygen stoichiometry, ferromagnetism, and transport properties of $La_{2-x}NiMnO_{6+\delta}$," Physical Review B, vol. 68, no. 6, pp. 064415, 2003.

[8] N. S. Rogada, J. Li, A. W. Sleight, M. A. Subramanian, "Magnetocapacitance and magnetoresistance near room temperature in a ferromagnetic semiconductor La_2NiMnO_6," Advanced Materials, vol. 17, no. 18, pp. 2225-2227, 2005.

[9] H. Guo, J. Burgess, S. Street, A. Gupta, T. G. Calvarese and M. A. Subramanian, "Growth of epitaxial thin films of the ordered double perovskite La_2NiMnO_6 on different substrates," Applied Physics Letters, vol. 89, no. 2, pp. 022509, 2006.

[10] A. Wold, R. J. Arnott and J. B. Goodenough, "Some magnetic and crystallographic properties of the system $LaMn_{1-x}Ni_xO_{3+\lambda}$," Journal of Applied Physics, vol. 29, no. 3, pp. 387-389, 1958.

[11] J. B. Goodenough, A. Wold, R. J. Arnott and N. Menyuk, "Relationship between crystal symmetry and magnetic properties of ionic compounds containing Mn^{3+}," Physical Review, vol. 124, no. 2, pp. 373-384, 1961.

[12] G. Blasse, "Ferromagnetic interactions in non-metallic perovskites," Journal of Physics and Chemistry of Solids, vol. 26, no. 12, pp. 1969-1971, 1965.

[13] K. Asai, H. Sekizawa, and S. Iida, "Magnetization measurements and ^{55}Mn NMR studies of $LaNi_{0.5}Mn_{0.5}O_3$," Journal

of the Physical Society of Japan, vol. (47), no. 4, pp. 1054-1060, 1979.

[14] M. Sonobe and K. Asai, "Magnetization measurement and ^{55}Mn NMR study of La(Ni$_{1-x}$Mg$_x$)$_{0.5}$Mn$_{0.5}$O$_3$," Journal of the Physical Society of Japan, vol. 61, no. 11, pp. 4193-4203, 1992.

[15] N. Y. Vasanthacharya, P. Ganguly, J. B. Goodenough and C. N. R. Rao, "Valence states and magnetic properties of LaNi$_{1-x}$Mn$_x$O$_3$ (for 0≤x≤0.2 and x=0.5)," Journal of Physics C: Solid State Physics, vol. 17, no. 15, pp 2745-2760, 1984.

[16] V. L. Joseph Joly, P. A. Joy, S. K. Date and C. S. Gopinath, "Two ferromagnetic phases with different spin states of Mn and Ni in LaMn$_{0.5}$Ni$_{0.5}$O$_3$," Physical Review B, vol. 65, no. 18, pp. 184416, 2002.

[17] CL Bull, D Gleeson and KS Knight, "Determination of B-site ordering and structural transformations in the mixed transition metal perovskites La$_2$CoMnO$_6$ and La$_2$NiMnO$_6$," Journal of Physics: Condensed Matter, vol. 15, no. 19, pp. 4927-4936, 2003.

[18] J. Blasco, M. C. Sánchez, J. Pérez-Cocho, J. García, G. Subía and J. Campo. "Synthesis and structural study of LaNi$_{1-x}$Mn$_x$O$_{3+\delta}$ perovskites," Journal of Physics and Chemistry of Solids, vol. 63 no. 5, pp. 781-792, 2002.

[19] S. Kazan, F. A. Mikailzade, M. Özdemir, B. Aktaş, B. Rameev, A. Intepe, A. Gupta. "Ferromagnetic resonance in double perovskite epitaxial thin films of La$_2$NiMnO$_6$ on SrTiO$_3$ and NdGaO$_3$ substrates," Applied Physics Letters, vol. 97, no. 7, pp. 072511, 2010.

[20] M. Belmeguenai, S. Mercone, C. Adamo, L. Méchin, C. Fur, P. Monod, P. Moch and D. G. Schlom, "Temperature dependence of magnetic properties of La$_{0.7}$Sr$_{0.3}$MnO$_3$/SrTiO$_3$ thin films on silicon substrates," Physical Review B, vol. 81, no. 5, pp. 054410, 2010.

[21] M. L. Spano and S. M. Bhagat, "Ferromagnetic resonance in amorphous alloys," Journal of Magnetism and Magnetic Materials, vol. 24, no. 2, pp. 143-156, 1981.

[22] M. J. Hurben and C. E. Patton, "Theory of two magnon scattering microwave relaxation and ferromagnetic resonance linewidth in magnetic thin films," Journal of Applied Physics, vol. 83, no. 8, pp. 4344-4365, 1998.

[23] Z. Zhi-Dong, "Spin waves in thin films, superlattices and multilayers in Handbook of thin film materials: Nanomaterials and magnetic thin films," vol. 5, Academic Press, 2002.

[24] F. J. Dyson, "Electron spin resonance absorption in metals. II. Theory of electron diffusion and the skin effect," Physical Review, vol. 98, no. 2, pp. 349–359, 1955.

[25] S. E. Lofland, T. Scabarozi, S. Kale, S. M. Bhagat, S. B. Ogale, T. Venkatesan et al. "Ferromagnetic resonance and magnetization studies on ferrimagnetic double perovskites A$_2$FeReO$_6$ (A=Ca, Sr, Ba)," IEEE Transactions on Magnetics, vol. 37, no. 4, pp. 2153-2155, 2001.

Authors: Sevgi POLAT ALTİNTAS

Structural and Microhardness Studies of

Rare-Earth Doped Ruddlesden−Popper Manganites

Sevgi POLAT ALTİNTAS[1*]

Abstract

We investigate the explicit role of the A-site doping by Pr and Sm on the mechanical and structural features of the lanthanum based double-layered manganites. The polycrystalline samples of the Ruddlesden-Popper $(La_{1-y}RE_y)_{1.4}Ca_{1.6}Mn_2O_7$ phase with RE: Pr and Sm are elaborated by the solid-state synthesis route. Powder X-ray analysis reveal that the samples structure is tetragonal (I4/mmm space group) and the lattice parameters do not change significantly with the rare-earth substitution. However, the scanning electron microscopy analyses demonstrate that the substitution with Pr and Sm affects the microstructure, significantly. Vickers micro-hardness measurements are performed on both samples to evaluate several structural parameters such as the stiffness, creep, micro-hardness, etc. We compare and construct the mechanical and microstructural changes due to the Sm and Pr doping with La site. The detailed explanations for the observed mechanical changes by Pr and Sm doping is given.

Keywords: Ruddlesden-Popper phase, rare-earth substitution, microhardness, IIC and HK models

1. INTRODUCTION

Due to the potential applications in technology and exotic physical properties, perovskite manganites have been devoted much attention, recently. For instance, magnetic manganite materials have been used as the key ingredient for building some technological devices such as magnetic recording and readout equipment, highly sensitive magnetic-field sensors, solid oxide fuel cells, and refrigerators [1-3]. The general formula of the chemical compound given as $(RE, A)_{n+1}Mn_nO_{3n+1}$ is the well-known rare earth-doped perovskite manganite of the Ruddlesden–Popper series [4]. Here RE denotes a trivalent rare earth ion, while A represents the divalent alkaline earth ion, and n is the number of MnO_2 layers per unit cell. The simple perovskite manganites with n = ∞ have been deeply investigated which have a three-dimensional Mn-O networks and exhibit several novel physical phenomena [5-7]. The double layered manganite series with n=2, the MnO_2 sheets are isolated by

---
* Corresponding Author: sevgialtintas@ibu.edu.tr
[1] Abant İzzet Baysal University,,Bolu, Turkey, ORCID: https://orcid.org/0000-0002-3133-5693

two (RE, A)O planes which keeps the bilayer slices of MnO_6 octahedra. The reduced dimensionality and structural anisotropy introduce great effect on the physical properties of these manganites. The double layered manganite series have been found to exhibit an anisotropic reduction in the one-electron (e_g) bandwidth. The magnetic, electronic and structural features of the double layered manganite series are very interesting and apparently different from the those of exhibited by cubic perovskites [8-12]. In general, the mixed Mn^{3+}/Mn^{4+} valence state causes magneto-transport phenomena. One may expect interesting magneto-transport properties exhibited by the manganites in terms of anisotropic transport and exchange interactions [13,14].

Application of strong magnetic fields during magnetoresistance (MR) measurements is shown to induce large stresses in colossal magnetoresistance materials. Recent studies showed that determining the elastic moduli of the polycrystalline materials is crucial to reveal the binding forces and to understand thermodynamic features of the solid materials [15-20]. Beside the magnetic and the electric property investigations, exploration the elastic properties are also important to find the convenient material in the use of polycrystalline materials applications in technology.

Recent studies have been mainly focused on the transport, electrical and structural properties or the technological applicational area of the mixed valence manganites. On the other hand, there are few studies that investigates the elastic features of the layered manganites [15-17,21]. Specifically, a recent study [21] have been shown that the Nd and Gd rare earth doping with La site have prominent effects on the mechanical and structural features of $LaCaMnO_7$ compound. In this study [21], the apparent micro-hardness values of the Nd and Gd doped samples shows an enhancement with increasing the external load (an effect known as reverse indentation size effect which will be elaborated later in the text). In the present contribution, we investigate the role of Pr and Sm substitution with La on the mechanical and structural properties of the double layered

manganites with chemical formula $(La_{1-y}RE_y)_{1.4}Ca_{1.6}Mn_2O_7$ (y: 0.857, 0.5). The explicit role of the external load force on the apparent micro-hardness values for the Pr and Sm doped compounds have been revealed. The true micro-hardness values under different external loads for the considered rare-earth substitution elements have also been investigated.

2. EXPERIMENTAL DETAILS

We used the standard solid-state reaction technique to prepare the polycrystalline bulk samples which are formulated as $(La_{0.142}Pr_{0.857})_{1.4}Ca_{1.6}Mn_2O_7$ (LPCMO) and $(La_{0.5}Sm_{0.5})_{1.4}Ca_{1.6}Mn_2O_7$ (LSCMO). In the formulation, the A-site average ionic radius is kept constant at $<r_A>\approx 1.32$ Å. The average ionic radii for rare earth and calcium ions are computed according to Shannon's ionic radii with twelve-coordination number (La^{3+} (1.36 Å), Sm^{3+} (1.24 Å), Pr^{3+} (1.49 Å) and Ca^{2+} (1.34 Å)). The precursor powders were first heated 2 hours at 800 °C. The stoichiometric amounts of La_2O_3, Pr_2O_3, Sm_2O_3, $CaCO_3$ and Mn_2O_3 (Alfa Aesar, >99.9%) were thoroughly mixed for 4 hours with acetone to homogenize the mixture preliminary to the solid-state formation of manganite. Then they are calcined at 1150 °C for 24 hours with two intermediate grindings. The powders were consolidated into pellets of approximate dimensions 13 mm (diameter)×1.5 mm (thickness) by using a hydraulic press with an applied pressure of 3000 psi at room temperature. The final sintering was done at the temperature 1250 °C for 24 hours by slowly heating and cooling rate.

X-ray diffraction was used to carry out the structural characterization. The XRD instrument uses CuKα radiation at 1.5418 Å wavelength (Rikagu D/Max – IIIC diffractometer). The diffraction angle (2θ) was changed from 20º to 80º with 0.01° step size. The count time for each step was 1 s. Rietveld method in Jana2007 software package was used to analyze the experimental outputs [22]. Scanning electron microscope (Jeol 6390-LV) was used to investigate the role of the rare earth doping on the changes in the grain size, growth and morphology. 10 measurements (in

average) at random points were performed by the energy dispersive X-ray (EDX) spectrometer inside the scanning electron microscope in order to make a good prediction on the La, Pr, Sm, Ca and Mn contents. The indentation measurements were performed with a UMT–Bruker SYS2 coded mechanical tester which uses a Vickers type indenter. We aim to elucidate the effect of the applied loading force during the indentation. Therefore, an increasing loading force, such as (800, 1200, 1600, 2000) mN, was implemented during 10 seconds at room temperature (approximately 300 K).

3. RESULTS AND DISCUSSIONS

3.1. XRD and SEM Analysis

The powder XRD patterns for the polycrystalline $(La_{0.142}Pr_{0.857})_{1.4}Ca_{1.6}Mn_2O_7$ and $(La_{0.5}Sm_{0.5})_{1.4}Ca_{1.6}Mn_2O_7$ recorded at room temperature are demonstrated in Fig. 1. XRD data were analyzed using Rietveld refinement in Jana2006 program. Refinements were carried out in the $Sr_3Ti_2O_7$-type with a body-centered tetragonal unit cell (space group I4/mmm, JCPDS card no. 41–1488). Legendre polynomials consisting of 36 terms were used to model the background. Here the peak shape is identified by the pseudo-Voight function. Fig. 2 demonstrates the X-ray diffraction patterns which includes the fitted profile, the raw data as well as the difference profile for the rare earth doped samples. We observe an agreement between the observed and calculated intensities and positions of the lines which suggest that the considered samples have $Sr_3Ti_2O_7$-type perovskite structure [23]. We would like to remark here that a small amount of ABO_3-type structure is found in X-ray pattern which can be considered as an additional phase in the multiphase refinement (see the phase 2 in Fig. 2). Table 1 summarizes the relevant structural parameters and the quality factors obtained from Rietveld analysis.
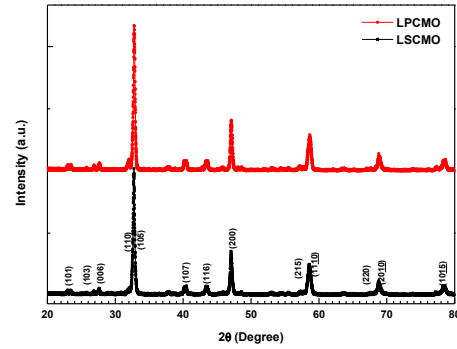
Figure 1 Powder X-ray diffraction pattern of the LPCMO and LSCMO samples.
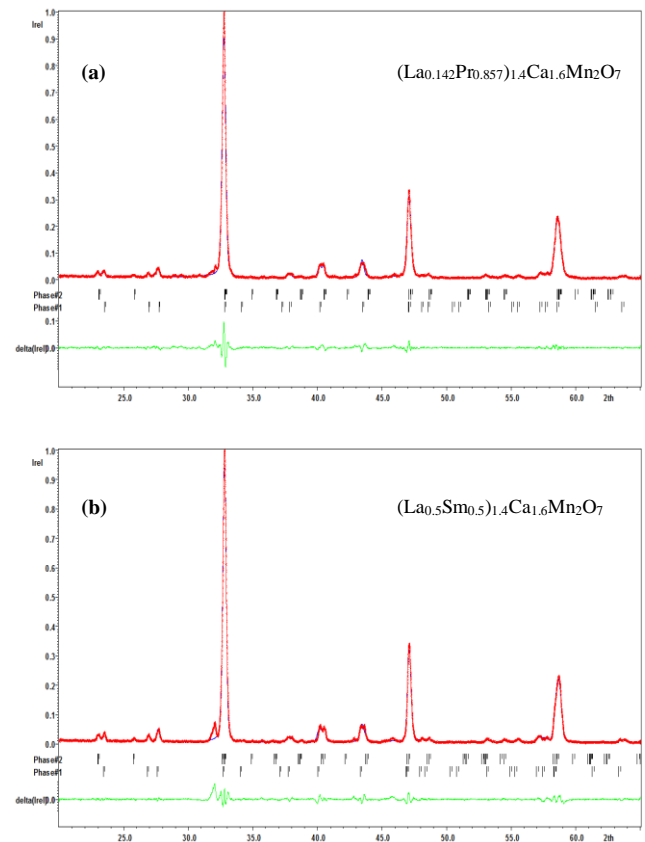
Figure 2. (Color online.) Rietveld profiles considering I4/mmm space group for the samples (a) LPCMO and (b) LSCMO. Here the red line corresponds to the observed XRD pattern, while blue line indicates the calculated XRD pattern. The black vertical bars represent the Bragg positions, and the green line (at the bottom) shows the difference between the calculated and the observed XRD diagram.

Table 1
Refined structural parameters, unit cell volume, R-factors and average crystallite size of bilayered manganites.

Structure		
T e t r a g o n a l e		
Space Group I4 / m m m		
$<r_A> = 1.3213$ Å		
	LPCMO	LSCMO
a(Å)	3.869816	3.857851
Δa	0.000509	0.000347
c(Å)	19.38771	19.29455
Δc	0.00287	0.00166
V(Å³)	290.3403	287.1611
ΔV	0.0687	0.0338
GOF	1.44	1.14
R_p	9.53	9.21
R_wp	15.65	12.89
<D>(nm)	61	53

We calculate the average crystallite size by using the Scherrer formula through measuring the full width at half maximum of the diffraction line in the XRD patterns. The Scherrer formula is given by $D = k\lambda/\beta \cos\theta$. Here D is the measure of the average crystallite size, k is the shape factor (which is 0.89), $\lambda = 1.5418$ Å is the wavelength of X-ray source, θ is the diffraction angle for the highest intense peak (with Miller index (106) on the Bragg angle $2\theta=32.79°$) and β is the full-width at half maximum of each diffraction peak in the radian unit [24, 25]. The refinement values are tabulated in Table 1.

The SEM micro-graphs shown in Fig.3 explicitly demonstrate that the surface morphology and the grain size are uniform, homogenous and also dense for the Pr and Sm doped samples. The measurements of the average grain sizes of the samples were performed from several SEM micrographs by using the ImageJ software. Based on Gaussian fitting method, average grain size is obtained to be 1.61 μm for LPCMO and 1.43 μm for LSCMO samples. The energy dispersive analysis of EDX spectrums of both samples are presented in the below of the SEM pictures in Fig. 3. The elemental concentrations of the considered samples are checked by using EDX analysis and no impurity peaks are observed.
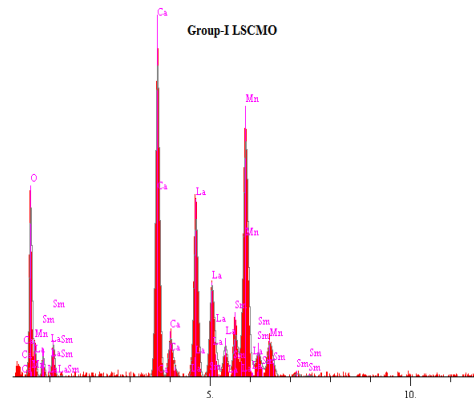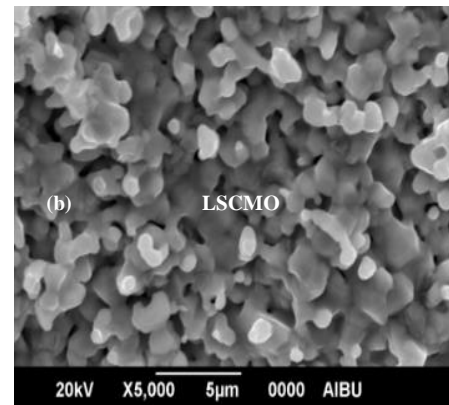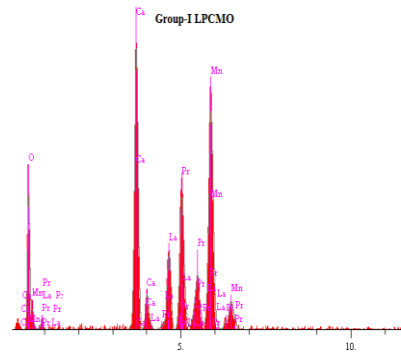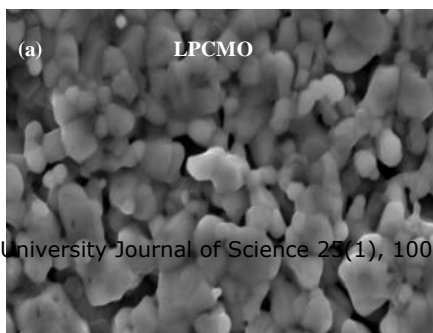
Figure 3 SEM micrographs for **(a)** LPCMO and **(b)** LSCMO bilayered manganites revealing surface morphologies.

3.2. Dynamic micro-hardness measurements

The aim of the present contribution is to investigate the changes in the mechanical properties of LPCMO and LSCMO composite samples via the Pr and Sm substitution. Along this aim, we measure the load dependent contact length. Using the Vickers hardness tester, micro-hardness measurements are performed for the applied loads between 400 mN and 2000 mN values. The dynamic indentation measurements

give the loading and unloading penetration depth relation [26, 27]. It is well known that during the loading and unloading stages, the materials are subject to a process where plastic and elastic deformations occur. In a similar way, we expose our samples to elastic and plastic deformation processes during the loading and unloading stages. The mechanical properties of the samples are calculated by using techniques introduced by the Oliver and Pharr in Ref. [28].

Figs. 4 and 5 show the applied load and unload forces as a function of the contact depth for LPCMO and LSCMO samples, respectively. In addition, we present a contact depth, hc, extracted from the unloading curve for Pr substituted sample in the inset of Fig. 4. The same method is used to evaluate the value of hc for the LSCMO sample for each load and tabulated in Table 2. We calculate the values of hc for the LPCMO sample as 8.8992 μm and 22.469 μm at applied unloading force 400 mN and 2000 mN, respectively. Morover, the similar values for LSCMO sample are 10.9221 μm and 17.9106 μm at the unloading force 400 mN and 2000 mN, respectively. The variation in the hc for the LPCMO sample is obviously greater than that of the LSCMO sample. This result indicates that the Pr substituted sample has more plastic deformation and less elastic recovery than that of the Sm substituted sample.

Figure 5 Loading/unloading versus depth curve for the LSCMO sample.

Now we investigate the area of the indent imprint which describes the cross-sectional area of the indenter in a given distance at the back of its tip. The area can be calculated as [28],

$$A_c = \pi h_c^2 \tan^2 \alpha \qquad (1)$$

where α is 70.3° for a Vickers or Berkovich indenter. Therefore, the area A_c is given as $24.5 h_c^2$. The A_c values are calculated by using Eq. (1) for the Pr and Sm substituted samples and are tabulated in Table 2. It is seen here that the A_c values for the both samples are monotous with the applied loads. In other words, A_c decreases with the decreasing loads.

Figure 4 Loading/unloading versus depth curve for the LPCMO sample. Inset shows the contact depth, h_c, extracted from the unloading curve.

Table 2

h_c, h_{max}, A_c, Creep, S, H and E_r values as a function of applied load for the samples LSCMO and LPCMO. All parameters are defined in the text.

Sample	P_{max} (N)	h_c (μm)	h_{max} (μm)	A_c (m²)	Creep (μm)	S (MN/m)	H (G Pa)	E_r (GPa/m)
LPCMO	0.4	8.89	10.64	1.93E-09	1.97	0.229	0.206	4.619
LPCMO	0.8	15.07	17.00	5.56E-09	2.89	0.413	0.144	4.913
LPCMO	1.2	19.0	21.04	8.84E-09	2.53	0.589	0.136	5.549
LPCMO	1.6	22.68	24.9	1.26E-08	2.15	0.723	0.127	5.706
LPCMO	2.0	22.46	24.33	1.23E-08	1.89	1.074	0.162	8.561
LSCMO	0.4	10.92	12.98	2.92E-09	2.54	0.193	0.136	3.174
LSCMO	0.8	16.97	19.62	7.06E-09	2.22	0.303	0.113	3.192
LSCMO	1.2	17.49	20.72	7.50E-09	2.48	0.372	0.159	3.807
LSCMO	1.6	17.69	20.89	7.67E-09	2.25	0.500	0.208	5.063
LSCMO	2.0	17.91	20.86	7.85E-09	1.94	0.678	0.254	6.776

Creep (also called cold flow) of a solid material is a proper quantity to indicate its response under persistent mechanical stress. Therefore, the creep behavior of the two samples at all loads are computed and tabulated in Table 2. The creep within material can exist under indentation loading and reveals itself as a change of the indentation depth with a fixed applied loading force [29]. It is interesting to note that while the creep of a Pr doped sample has a non-monotonous behavior, the Sm doped one has a linear response to the applied load. When we compare the creep values for the two doped samples, we observe that the Sm doped results, in general, higher creep values than the Pr doped one. The two samples encounter the same loading process and experimental conditions. The differences in the creep values as given in Table 2 is, therefore,

caused by the different doped sample with La side.

The sudden displacement discontinuity in the indentation loading and unloading curves evidences the effect of pop-in and pop-out in the materials, respectively [30]. However, the pop-in and pop-out behaviors for the LPCMO and the LSCMO samples are not obtained at any applied loads in our experiment. Therefore, we conclude that Sm or Pr substitution with La-site significantly effects the crystal structure in a way which prevents the sudden mechanical discontinuities in the indentation processes.

We have also calculated the micro-indentation hardness by using the following formula [31]:

$$H = \frac{P_{max}}{A_c} = \frac{P_{max}}{24.5 * h_c^2} \tag{2}$$

where P_{max} is the maximum value of the applied load force for each cycle and A_c is the contact area values as defined in Eq. (1). Using P_{max} values in Figs. 4 and 5, the hardness values are plotted in Fig. 6 as a function of applied loads and the numerical values are tabulated in Table 2. It is clear that the apparent hardness values significantly affected by the applied loads as well as the nature of the rare-earth element. As can be seen from Fig. 6 that the hardness values of LPCMO sample decrease with the increase in load. On the contrary, the H values for LSCMO sample increases linearly with load. The linear increase of the hardness values as a function of load is the indication of reverse indentation size effect (RISE) for Sm doped sample [32, 33]. On the other hand, the decrease of H values with the increase in applied loads shows the presence of indentation size effect (ISE) in the Pr doped sample [34]. It is recently shown that plastic, elastic and mixed plastic-elastic deformation response of the material under external loads are the prominent mechanisms that might cause ISE [35-38]. More specifically, the dislocation loops formed by indentation [35, 36] and dislocations due to strain gradients [37] are the examples of such mechanisms that result in ISE. Moreover, the indenter or specimen friction resistance

interacting with the elastic resistance of a material are another source example of the ISE [38]. On the other hand, the effect of distortion zones [39], bluntness of the indenter and clipping of the specimen around the indentation region [40] are some example mechanisms that might cause RISE behavior. We would like to mention here that a recent study [21] investigated the explicit role of the Nd and Gd doping with La site on the mechanical and structural features of $LaCaMnO_7$ compound. In this study, the apparent micro-hardness values of the considered compounds enhance with the applied load. In other words, the Nd and Gd substitution results in RISE. Our results demonstrate that the Pr doped sample, on the contrary, results in ISE.
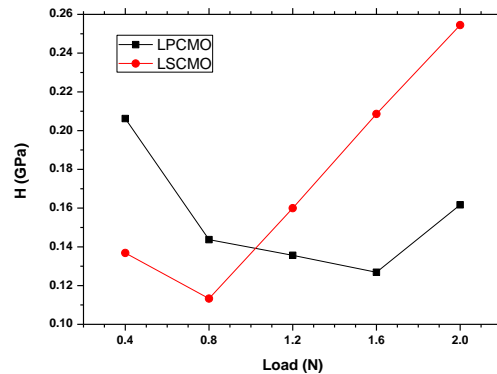
Figure 6 The apparent hardness values as a function of load for the samples LPCMO and LSCMO.

The true hardness values for our considered compounds are evaluated by using the experimental data. The methods known as indentation induced cracking (IIC) and the Hays-Kendall (HK) are appropriate to evaluate the true hardness values for the samples that exhibits RISE and ISE behaviors, respectively [39, 41]. The LSCMO sample exhibits RISE behavior as noted above. Therefore, we fit the experimental data to IIC model which is given as:

$$H_{IIC} = K(P^{5/3}/h_c^3)^m \tag{3}$$

Here m and K values are constants and independent of the type of the material and the load. In Fig. 7, we plot Ln(H) versus Ln($P^{5/3}/h_c^3$) graph for the Sm doped sample. The slope gives

the extracted m values which is calculated as 0.56 for the LSCMO sample. It explicitly proves that doping with Sm results in RISE behavior. The vertical intercept in the figure gives the true hardness value of the LSCMO sample which is approximately 2.82 GPa. We would like to mention here that the applied load (2N) shown in Fig.6 is not sufficient to approach the plateau region.
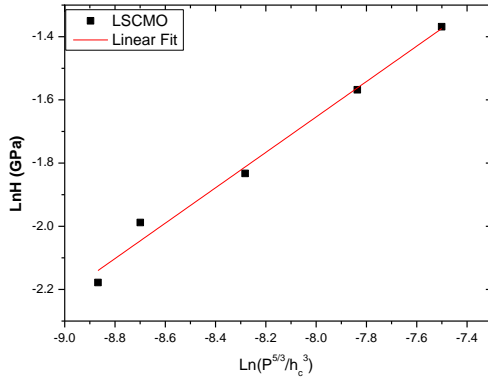
Figure 7 *Ln(H)* versus $Ln(P^{5/3}/h_c^3)$ graph for the LSCMO sample. The fitted line is obtained by using the IIC model as defined in the text.

For the LPCMO sample, we use the HK model to show the ISE behavior which is given as:

$$P\text{-}P_{0HK} = K_1 h_c^2 \qquad (4)$$

Here P_{0HK} is the value of the minimum applied load and K_1 is the hardness constant which is independent of the applied load. It is obvious from the equation that the effective indentation load (P-P_{0HK}) is directly related to the square of the indentation diagonal length. In the considered model, true hardness, H_{HK}, is calculated as

$$H_{HK} = 1854.4 K_1 \ \text{(GPa)} \qquad (5)$$

Fig. 8 shows the applied load F as a function of d^2 with the aim to examine the data using the HK model. Here we obtain a linear dependence of F on d^2 for the Pr substitution. H_{HK} and linear regression coefficient (LRC) fit parameters are calculated as 0.125 GPa and 0.9994, respectively. As can be seen from Fig. 6 that while the apparent hardness value of LPCMO sample reaches almost

the plateau region, the true hardness value is indeed in the plateau region.
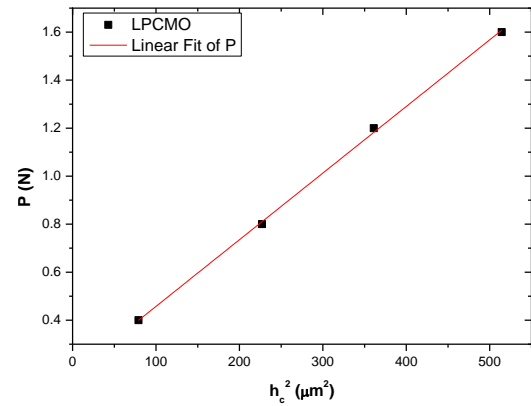
Figure 8 Load versus the squared of contact depth for the LPCMO sample. The fitted line is obtained by using the HK model.

There are several successful methods to calculate the stiffness of a sample [42-46]. A direct way to calculate the stiffness is to make a linear fit to the fraction of the highest portion of the unloading curve. The slope of the fitted line gives the stiffness of the specimen for a single load. The stiffness (S) is computed as [43]:

$$S = \left| \frac{dP}{dh} \right| = \frac{\sqrt{2}}{\pi} \cdot \frac{E_r}{\sqrt{A_c}} \qquad (6)$$

Here E_r indicates the reduced elastic modulus. The S values are tabulated in Table 2. One can note from the table that the S values depends on the load significantly. The increase in the load increases the S values for both samples. When we analyze the dopant effects, we observe that Pr doping results in higher S values than the Sr doped sample at all loads. The reduced elastic modules as a function of load can be evaluated by using the Eq. (6) and are displayed in Table 2 and Fig. 9. It is observed that the values for the considered rare-earth samples increase as a function of load.
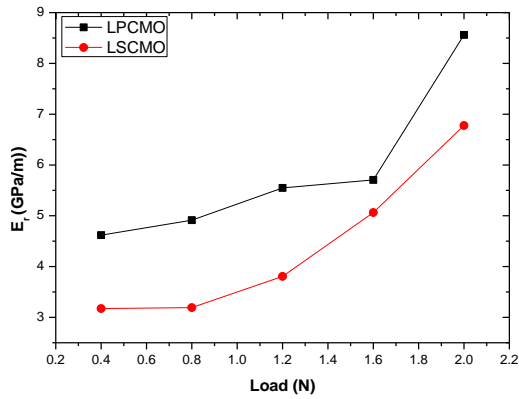
Figure 9 The elastic modulus as a function of applied load for the samples LPCMO and LSCMO.

We can calculate the percentage elastic recovery ratio (%), ERR, using the load and unload curves.

$$ERR = \frac{h_{max} - h_{min}}{h_{max}} . 100 \qquad (7)$$

The ERR provides us to quantitatively compare the elastic features of the samples. One can calculate the ERR as in Eq. 7 where h_{max} (h_{min}) values indicate the maximum (non-recovery) contact depth in the indentation stage. In Fig.10, the ERR values of the samples are shown. We observe that while the ERR values of the LPCMO are in the range 20-50%, the ERR values for LSCMO sample recover more range approximately 40-50%. This shows that the ERR values for the LSCMO sample recovers better to its original shape than that of the LPCMO one at all the considered loads. Please remark here that both samples possess the same ionic A site radius ($<r_A>\approx 1.32$ Å). However, we found here that the considered samples have different responses to the plastic deformation. Even the ionic radius of the samples is the same, the mechanical properties, such as the elastic modulus, hardness and stiffness, are quite different. The differences are due to the different microstructures and average grain sizes. From the comparison of Sm or Pr doping effects, we conclude that Sm doping leads to denser surface, better grain connectivity and smaller average grain size. Moreover, Sm doped sample has the density of voids lower than

the Pr doped one. We conclude here that the Sm doped sample has higher hardness values.
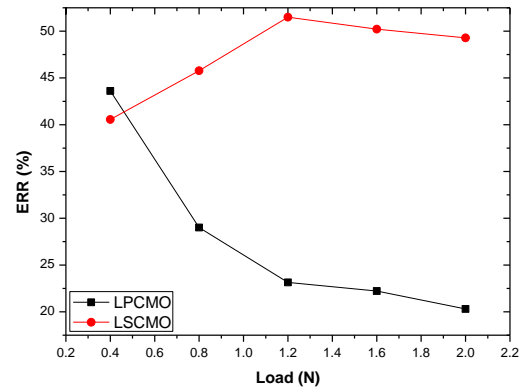
Figure 10 ERR values for LPCMO and LSCMO obtained at different loads.

4. CONCLUSIONS

We have given a comprehensive analysis on the mechanical and microstructural properties of the Ruddlesden-Popper $(La_{1-y}RE_y)_{1.4}Ca_{1.6}Mn_2O_7$ phase with RE: Pr and Sm. The explicit role of the Pr and Sm doping with La site has been revealed. The X-ray diffraction measurements demonstrate that all samples exhibit $Sr_3Ti_2O_7$-type perovskite structure with the I4/mmm space group. From the SEM micro-graphs analysis, it is found that the surface morphology and the grain size are uniform, homogenous and also dense for both samples. The dynamic Vicker micro-hardness measurements have been performed in order to study the mechanical properties. We have used the HK model for the LPCMO sample and the IIC model for the LSCMO to compute the true-hardness values. Our main conclusions can be listed as follows. The stiffness values of both samples depend on the load significantly which can increase as a function of the load. The both pop-in and pop-out behaviors for the samples are not observed at the considered loads. This is the indication that Pr and Sm doping have significance on the mechanical discontinuities. While the hardness value of the LPCMO sample decreases from 0.21 to 0.16 GPa for the load increasing from 400 to 2000 mN, the hardness value of the LSCMO sample increases from 0.14 to 0.25 GPa in the same load range. A RISE

behavior is observed for the LSCMO sample, in contrast to the LPCMO sample which exhibits ISE behavior. The true micro-hardness values of the LSCMO sample (which is 2.82 GPa) is considerably larger than that of the LPCMO (which is 0.125 GPa). The large deviation in the true micro-hardness values in the considered samples is due to the different average grain sizes and microstructures. The reduced elastic modules of the samples have been found to increase as the function of the load. The percentage elastic recovery ratio of the samples has opposite dependences on the load. While ERR values of the LSCMO sample increase as a function of the load, the values of the LPCMO decrease.

The Declaration of Conflict of Interest/ Common Interest

No conflict of interest or common interest has been declared by the author.

The Declaration of Ethics Committee Approval

This study does not require ethics committee permission or any special permission.

The Declaration of Research and Publication Ethics

The author of the paper declare that they comply with the scientific, ethical and quotation rules of SAUJS in all processes of the paper and that they do not make any falsification on the data collected. In addition, they declare that Sakarya University Journal of Science and its editorial board have no responsibility for any ethical violations that may be encountered, and that this study has not been evaluated in any academic publication environment other than Sakarya University Journal of Science.

REFERENCES

[1] F. Ben Jemaa, S. Mahmood, M. Ellouze, E.K. Hlil, F. Halouani, I. Bsoul, M. Awawdeh, "Structural, magnetic and magnetocaloric properties of $La_{0.67}Ba_{0.22}Sr_{0.11}Mn_{1−x}Fe_xO_3$ nanopowders", Solid State Sciences, vol. 37, pp. 121-130, 2014.

[2] P. Ripka and M. Janosek, "Advantages in magnetic field sensors," IEEE Sensors Journal, vol. **10**, no. 6, pp. 1108–1116, 2010.

[3] M. A. Mamun, A. Haque, A. Pelton, B. Paul and K. Ghosh, "Structural, electronic, and magnetic analysis and device characterization of ferroelectric-ferromagnetic heterostructure (BZT-BCT/LSMO/LAO)," IEEE Transactions on Magnetics., vol. 54, no. 12, pp. 1-8, 2018.

[4] S. N. Ruddlesden and P. Popper, "New compounds of the K_2NiF_4 type," Acta. Crystallographica, vol. 10, pp. 538-539, 1957.

[5] L. L. Lev, J. Krempaský, U. Staub, V. A. Rogalev, T. Schmitt, M. Shi, P. Blaha, A. S. Mishchenko, A. A. Veligzhanin, Y. V. Zubavichus, M. B. Tsetlin, H. Volfová, J. Braun, J. Minár, and V. N. Strocov, "Fermi Surface of Three-Dimensional $La_{1−x}Sr_xMnO_3$ Explored by Soft-X-Ray ARPES: Rhombohedral Lattice Distortion and Its Effect on Magnetoresistance," Physical Review Letters, vol. 114, no. 23, pp. 237601, 2015.

[6] R. Chourasia and O. P. Shrivastava, "Crystal structure and impedance study of samarium substituted perovskite: $La_{1−x}Sm_xMnO_3$ (x = 0.1–0.3)," Solid State Sciences, vol. 14, no. 3, pp. 341-348, 2012.

[7] S. Mori, C. H. Chen, and S.-W. Cheong, "Pairing of charge-ordered stripes in

(La,Ca)MnO$_3$", Nature, vol. 392, pp. 473-476, 1998.

[8] J.-S. Lee, C.-C. Kao, C. S. Nelson, H. Jang, K.-T. Ko, S. B. Kim, Y. J. Choi, S.-W. Cheong, S. Smadici, P. Abbamonte, and J.-H. Park "Fragile Magnetic Ground State in Half-Doped LaSr$_2$Mn$_2$O$_7$," Physical Review Letters, vol. 107, no. 3, pp. 037206, 2011.

[9] J.F. Mitchell, C.D. Ling, J.E. Millburn, D.N. Argyriou, A. Berger, M. Medarde, "Magnetic phase diagram of layered manganites in the highly doped regime," Journal of Applied Physics, vol. 89, no. 11, pp. 6618-6620, 2001.

[10] J. Q. Li, Y. Matsui, T. Kimura, and Y. Tokura, "Structural properties and charge-ordering transition in LaSr$_2$Mn$_2$O$_7$," Physical Review B, vol. **57**, no. 6, R3205-R3208, 1998.

[11] P. D. Battle, D. E. Cox, M. A. Green, J. E. Millburn, L. E. Spring, P. G. Radaelli, M. J. Rosseinsky, and J. F. Vente, "Antiferromagnetism, Ferromagnetism, and Phase Separation in the GMR System Sr$_{2-x}$La$_{1+x}$Mn$_2$O$_7$," Chemistry of Materials, vol. *9, no. 4*, pp. 1042-1049, **1997.**

[12] L. Vasiliu-Doloc, S. Rosenkranz, R. Osborn, S. K. Sinha, J. W. Lynn, J. Mesot, O. H. Seeck, G. Preosti, A. J. Fedro, and J. F. Mitchell, **"**Charge Melting and Polaron Collapse in La$_{1.2}$Sr$_{1.8}$Mn$_2$O$_7$," Physical Review Letters, vol. 83, no. 21, pp. 4393, 1999.

[13] M. Oumezzine, J. S. Amaral, F. J. Mompean, M. G. Hernandez, M. Oumezzine, "Structural, magnetic, magneto-transport properties and Bean-Rodbell model simulation of disorder effects in Cr^{3+} substituted La$_{0.67}$Ba$_{0.33}$MnO$_3$ nanocrystalline synthesized by modified Pechini method," RSC Advances, vol. 6, pp. 32193–32201, 2016.

[14] S. K. Mandal, T. K. Nath, and V. V. Rao, "Effect of nanometric grain size on electronic-transport, magneto-transport and magnetic properties of La$_{0.7}$Ba$_{0.3}$MnO$_3$ nanoparticles," J.

Phys.: Condens. Matter, vol. 20, pp. 385203, 2008.

[15] Y. S. Reddy, V. P. Kumar, E. Nagabhushanam, P. Kistaiah, and C. V. Reddy, "Electrical, magnetic and elastic properties of La$_{1.2}$(Sr$_{1-x}$Ca$_x$)$_{1.8}$Mn$_2$O$_7$ (0.0≤x≤0.4)," Journal of Alloys and Compounds, vol. 440, no. 1–2, pp. 6–12, 2007.

[16] Y. S. Reddy, M. V. Ramana Reddy, P. Veerasomaiah, C. Vishnuvardhan Reddy, "Elastic properties of double layered manganite La$_{1.2}$Sr$_{1.8-x}$Ca$_x$Mn$_2$O$_7$ (x=0–0.4)," Material Science (Poland), vol, 25, no. 3, pp. 619–626, 2007.

[17] Y. S. Reddy, P. Kistaiah, C. Vishnuvardhan Reddy, "Elastic properties of double layered manganites R$_{1.2}$Sr$_{1.8}$Mn$_2$O$_7$ (R = La, Pr, Nd, Sm)," Rare Metals, vol. 33, no. 2, pp. 166–170, 2014.

[18] G. Lalitha and P. Venugopal Reddy, "Elastic behavior of neodymium based manganites," Ultrasonics, vol. 52, pp. 706-711, 2012.

[19] C. Thiele, K. Dörr, O. Bilani, J. Rödel, and L. Schultz, "Influence of strain on the magnetization and magnetoelectric effect in La$_{0.7}$A$_{0.3}$MnO$_3$∕PMN−PT (001) (A = Sr , Ca)," Phys. Rev. B, vol. 75, no. 5, pp. 054408, 2007.

[20] J. J. U. Buch, G. Lalitha, T. K. Pathak, N. H. Vasoya, V. K. Lakhani, P. V. Reddy, Ravi Kumar and K. B. Modi, "Structural and elastic properties of Ca-substituted LaMnO$_3$ at 300 K," J. Phys. D: Appl. Phys., vol. 41, no. 2, pp. 025406, 2008.

[21] R. Terzioglu, "The structural and mechanical properties of Gd and Nd substituted double layered LaCaMnO$_7$ ceramics," Journal of Alloys and Compounds, vol. 797, pp. 1173–1180, 2019.

[22] V. Petříček, M. Dušek, and L. Palatinus, "Crystallographic Computing System JANA2006: General features," Zeitschrift für Kristallographie - Crystalline Materials, vol. 229, no. 5, 2014.

[23] JCPDS-International Centre for Diffraction Data Task Group on Cell Parameter Refinement," Powder Diffr., vol. 1, no. 1, pp. 66–76, 1986.

[24] De Keiyser, T. H., Langford, J. I., Mittemeijer, and Vogels, A. B. P., "Use of the Voigt function in a single-line method for the analysis of X-ray diffraction line broadening," J. Appl. Cryst., vol. 15, pp. 308- 314, 1982.

[25] P. E. Tomaszewski, "The uncertainty in the grain size calculation from X-ray diffraction data," Phase Transitions, vol. 86, no. 2–3, pp. 260–266, 2013.

[26] O. D. Neikov, Handbook of powders of non-ferrous metals. Oxford, UK; New York, NY: Elsevier, 2005.

[27] K. Higashitani, H. Makino, and S. Matsusaka, Powder Technology Handbook, 4th ed. Fourth edition. | Boca Raton, FL: Taylor & Francis Group, LLC, 2020.: CRC Press, 2019.

[28] W. C. Oliver and G. M. Pharr, "Measurement of hardness and elastic modulus by instrumented indentation: Advances in understanding and refinements to methodology," J. Mater. Res., vol. 19, no. 1, pp. 3–20, 2004.

[29] P. S. Phani and W. C. Oliver, "A direct comparison of high temperature nanoindentation creep and uniaxial creep measurements for commercial purity aluminum," Acta Materialia, vol. 111, pp. 31–38, 2016.

[30] J. E. Bradby et al., "Indentation-induced damage in GaN epilayers," Appl. Phys. Lett., vol. 80, no. 3, pp. 383–385, 2002.

[31] W. C. Oliver and G. M. Pharr, "Measurement of hardness and elastic modulus by instrumented indentation: Advances in understanding and refinements to methodology," J. Mater. Res., vol. 19, no. 1, pp. 3–20, 2004

[32] K. Sangwal, "On the reverse indentation size effect and microhardness measurement of solids," Materials Chemistry and Physics, vol. 63, no. 2, pp. 145–152, 2000.

[33] P. Feltham and R. Banerjee, "Theory and application of microindentation in studies of glide and cracking in single crystals of elemental and compound semiconductors," J Mater Sci, vol. 27, no. 6, pp. 1626–1632, 1992.

[34] W. D. Nix and H. Gao, "Indentation size effects in crystalline materials: A law for strain gradient plasticity," Journal of the Mechanics and Physics of Solids, vol. 46, no. 3, pp. 411-425, 1998.

[35] G.P. Upit, S.A. Varchenya, "Microhardness of alkali halide crystals," Physica Status Solidi B, vol. 17, no. 2, pp. 831–835, 1966.

[36] ed.) Westbrook J. H. (Jack Hall), ed.) Conrad Hans, and A. S. for Metals, "The Science of Hardness Testing and its Research Applications," ASME, Metals Park, Ohio: American Society for Metals, 1973.

[37] Q. Ma and D. R. Clarke, "Size dependent hardness of silver single crystals," J. Mater. Res., vol. 10, no. 4, pp. 853–863, 1995.

[38] H. Li and R. C. Bradt, "The microhardness indentation load/size effect in rutile and cassiterite single crystals," Journal of Materials Science, vol. 28, no. 4, pp. 917–926, 1993.

[39] K. Sangwal, "Microhardness of as-grown and annealed lead sulphide crystals," J Mater Sci, vol. 24, no. 3, pp. 1128–1132, 1989.

[40] P P. Feltham and R. Banerjee, "Theory and application of microindentation in studies of glide and cracking in single crystals of elemental and compound semiconductors," J Mater Sci, vol. 27, no. 6, pp. 1626–1632, 1992.

[41] M.L. Tarkanian, J.P. Neumann, L. Raymond, Determination of the temperature dependence of {1 0 0} and {1 1 2} slip in tungsten from Knoop hardness measurements, in: J.H. Westbrook, H. Conrad (Eds.), The Science of Hardness Testing and Its Research Applications, American Society for Metals, Metal Park, OH, pp. 187–198, 1973.

[42] J. Hay, P. Agee, and E. Herbert, "Continuous Stiffness Measurement During Instrumented

Indentation Testing," Experimental Techniques, vol. 34, no. 3, pp. 86–94, Jan. 2010.

[43] K. Zeng and C.-h Chiu, "An analysis of load–penetration curves from instrumented indentation," Acta Materialia, vol. 49, no. 17, pp. 3539–3551, 2001.

[44] W. C. Oliver and G. M. Pharr, "An improved technique for determining hardness and elastic modulus using load and displacement sensing indentation experiments," J. Mater. Res., vol. 7, no. 6, pp. 1564–1583, 1992.

[45] L. Arda, O. Ozturk, E. Asikuzun, and S. Ataoglu, "Structural and mechanical properties of transition metals doped ZnMgO nanoparticles," Powder Technology, vol. 235, pp. 479–484, 2013.

[46] M. B. Turkoz, Y. Zalaoglu, T. Turgay, O. Ozturk, B. Akkurt, and G. Yildirim, "Evaluation of key mechanical design properties and mechanical characteristic features of advanced Bi-2212 ceramic materials with homovalent Bi/Ga partial replacement: Combination of experimental and theoretical approaches," Ceramics International, vol. 45, no. 17, pp. 21183–21192, 2019.

A heuristic algorithm for workforce scheduling with synchronization constraints and ergonomic aspects at cross-dock platforms

Parmis SHAHMALEKI [*1], Alpaslan FIĞLALI [2]

Abstract

This research studied a practical scheduling problem arising in the repackaging phase of cross-dock platforms. Packaging/repackaging is one of the significant concerns in cross-dock internal operations, where most of the tasks have been done by a number limited of teams. The problem also contains many practical constraints such as synchronization between teams and ergonomic aspects, as well as several managerial constraints. These conditions make internal workforce scheduling a complex and important issue for cross-docks. Implementation of the decision support system for planning and manpower scheduling in the repackaging phase of a cross-dock is encouraged us for this research. We try to model a real-world problem from automotive industry. Due to the non-deterministic polynomial time hardness (NP-hard) of the problem, finding a good solution is difficult. Therefore a novel greedy construction heuristic algorithm is proposed. We apply this heuristic method for real problem instances. Although the current process of planning and scheduling is manually and time consuming, our proposed algorithm generates good results for real problem instances in reasonable times.

Keywords: Staff scheduling, Synchronization constraints, Ergonomics, Greedy construction heuristic, Cross-dock

* Corresponding Author: figlalia@kocaeli.edu.tr

[1] Kocaeli University, Department of Industrial Engineering ,İzmit, Turkey, ORCID: https://orcid.org/0000-0002-3863-9323

[2] Kocaeli University, Department of Industrial Engineering ,İzmit, Turkey, ORCID: https://orcid.org/0000-0002-8364-3313

Parmis SHAHMALEKI, Alpaslan FIĞLALI

A heuristic algorithm for workforce scheduling with synchronization constraints and ergonomic aspects...

1. INTRODUCTION

The automotive industry is one of the most competitive sectors in the world. Car manufacturers try to globalize their activities in order to benefit from economies of scale and maintain competitiveness. For this reason, most of them try to establish their facilities in different countries due to reducing their costs regarding the logistics and manufacturing operations. So international logistic flows significantly increase in this industry [1]. In these logistic patterns, for improving efficiency and lowering costs, reducing inventory in warehousing at every step of operations is a central concern [2].Thereby, using cross-docking platform is one of the main strategies that help carmakers to cope with their global challenges.

Cross-docking, which has applications in different sectors such as manufacturing, retail companies and logistic service providers, plays an important role in the large distribution network that has a huge variety of shipments like the automotive industry[3,4].

Cross-docking tries to reduce warehouses to trans-shipment centers where the storage of products is limited or nonexistent and its leading functions are receiving and shipping items[2].In other words, a cross-dock is an intermediate node in the supply chain that reduces the cost of storing and inventory.

In general, in a cross-dock, the working environment can be divided into three different areas. These 3 zones are inbound area, internal (treatment) area and outbound area. In Figure1 the general flow shop and operations of cross-dock has been shown. In the cross-dock, at the inbound area, large incoming loads from different suppliers are unloaded, unpacked, disaggregated, and placed. Successively, items based on the customer demands are sorted. Whenever the repackaging is needed items are transported to an intermediate area for deconsolidation, sorting, repackaging and consolidation operations, otherwise they are sent directly to the outbound zone. In this area, once the items are consolidated, the containers are

built up and finally loaded onto outbound vehicles and sent to customers.
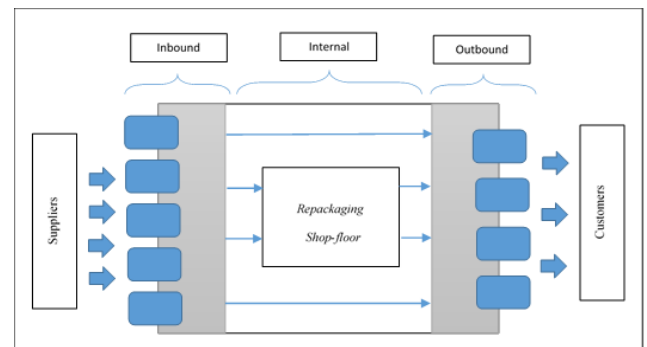
Figure 1. Cross-dock layout

This study focuses on the intermediate work area and especially on the repackaging phase.

Generally main research subjects concerning cross docking are considered as either strategical, tactical or operational level problems[1]. Using this classification, since the cross-dock platform that we consider is already active and the tactical issues are out of our scope, the problem that we address here is considered to be an operational problem. Most of the activities in the intermediate work area are heavy physical activities and done by workers, so the workforce is one of the main factors that affect the productivity of the whole system. In the repackaging stage of cross-dock, there is a limited number of worker teams that process tasks, so the efficient management of such teams in the context of manpower allocation and scheduling becomes a priority.

A simplified description of the manpower allocation problem for the repackaging phase in a cross-dock is as follows: different tasks in the shop floor demand varying number of teams. A planning center dispatches teams to satisfy this demand by considering the specified features of this real-world problem.

Furthermore, due to the customer service strategy of this cross-dock, finishing high priority tasks as early as possible is desirable in the planning period for the managers. It is noteworthy that the planning horizon is short and

Parmis SHAHMALEKI, Alpaslan FIĞLALI

A heuristic algorithm for workforce scheduling with synchronization constraints and ergonomic aspects...

daily schedules are needed. Therefore, our main goal in this research is to create a daily schedule for tasks and workers in such a way that the number of processed tasks will be maximized by taking into account the distinctive features of this real world problem.

One important feature of the considered manpower allocation is cooperation or synchronization between teams. Some of the tasks demand more than one team to be processed so cooperation will be required. Cooperation or synchronization means a temporary combination of teams joined together for a specific task [5]. These teams should start the processing of that specific task simultaneously.

Forasmuch as humans have different characteristics that distinguish them from other inanimate parts of the systems, contemplating these features lead to a more precise and realistic assessment [6].So another important feature of our problem is the ergonomic aspect. As defined by International Ergonomics Association, "ergonomics" addresses the ways and methods to optimize the worker's well-being and overall system performance via improving the interaction between humans and other elements of the system [7].

The literature frequently emphasized the significant impact of scheduling and sequencing decisions on system performance. Besides, the human factor and ergonomics literature demonstrated the important role of the sequencing of human tasks on human performance and well-being. So the interaction between scheduling and ergonomics may affect system performance positively. In their research, Carnehan et al.[8] showed that by increasing the human performance via improving workers' ergonomic criteria such as reducing stress, fatigue and work injury risk, the overall performance of the system enhanced consequently. However, typically in most scheduling problems, the effects of these human characteristics on their performance are ignored and several assumptions are used to simplify human behavior[9].

Several factors can impact human performance directly or indirectly. Some of these factors are fatigue, stress, boredom, cumulative workload, skill learning etc.[10].

Workload can be divided into physical workload and mental workload. Workload can be measured in different dimensions. Various workload assessment measures are used to assess the perceived demand of the task processed by the worker. Targeted working activities of these methods, as well as their desired level of details, provide differences in the application of them. The most frequently used ergonomic measurement methods are NLE(NOISH Lifting Equation)[11], JSI (Job Strain Index)[12], RULA (Rapid Upper Limb Assessment)[13], REBA(Rapid Entire Body Assessment)[14], EAWS(Ergonomic Assessment Worksheet)[15] and OCRA(Occupational Repetitive Actions)[16].

In this research, the focus is on physical ergonomic risks.

The works under study, which are done manually by the workforce in the repackaging section, are of the type of activities with low load and high frequency. In such situations, The International Organization for Standardization standard 11228e3 and the European Standard 1005-5 recommended using OCRA method to evaluate the risk exposure during repetitive work[17,18].So the OCRA method has been used to evaluate ergonomic scores of tasks.

To limit exposure to ergonomic risk factors and to increase safety and motivation in understudied section, two issues have been considered. First, heavy tasks (tasks with high Ergonomic Score) should not be done consecutively by a team. Second, leveling workload among teams is desired. The first issue is considered as a hard constraint in the planning process that means it should not be violated at all but for the latter issue, tolerance is acceptable so, it is applied as a soft constraint.

The main contribution of this paper, which is based on a real-world oriented case study, is twofold. These are describing a new manpower

Parmis SHAHMALEKI, Alpaslan FIĞLALI

A heuristic algorithm for workforce scheduling with synchronization constraints and ergonomic aspects...

allocation and task scheduling problem that often occurred in the interval section of cross docks and proposing a novel greedy construction heuristic to find reasonable schedules in a reasonable time. It is necessary to mention that the proposed solution algorithm alters the planning process from a subjective process to an objective one.

The rest of this paper is structured as follows. In section 2, the literature related to our work has been reviewed. We describe the model with details in section 3, and also we presented the proposed algorithm. In section 4, the computational results are provided. Finally, in section 5, we conclude our paper and suggest possible opportunities for future research.

2. LITERATURE REVIEW

The purpose of the problem is to assign a set of tasks to teams and schedule them over a planning period by considering the ergonomic fairness and synchronization features. So related literature review has been done in three directions: Synchronization workforce scheduling, ergonomics in workforce scheduling and recent publications related to the OCRA method.

Synchronization has been studied in some researches, but most of them are related to vehicle routing problems. The studies focusing on personnel scheduling and using the synchronization concept are summarized below:

Li et al.[19], for the first time, introduced the manpower allocation problem with job teaming constraints and time windows. There is a set of tasks located at different locations, and each task needs a team of workers. The objectives are to minimize a weighted sum of the total number of workers, the total traveling distances of all workers, and their total waiting time. Two heuristic algorithms are proposed which are shown to be effective for real instances in Port of Singapore.

Dohn et al.[5], introduced (m-MAPTWTC) problem. At this research, they try to assign tasks to a limited number of teams in the way that the number of assigned tasks is maximized. The studied manpower allocation problem is consisting of cooperation between teams and time windows restrictions for tasks and teams. In their model, the number of teams is limited, and the objective function is to maximize the number of assigned tasks. They introduce a branch and price approach and solve the realistic test instances from a European airport.

Ho and Leung [20]addressed a manpower scheduling problem that is motivated by airline catering operations. In their model, tight job time windows and job-skills compatibility constraints are exist. They try to form appropriate teams and assign teams to flights. The objective function is to cover the required services for as many flights as possible. The authors propose a Tabu search heuristic and a simulated annealing heuristic approach to solve the problem. The results show the effectiveness of their solving approach.

Lim et al. [21]proposed a mathematical model for the manpower allocation problem which occurs in workforce dispatching and planning in ports. In this problem, there are servicemen who are dispatched from a central point and assign to tasks in different location in the yard. In addition, there are time windows for tasks. This problem has multiple objectives. Objectives are to minimize traveling distances, traveling time, waiting times, and the number of required servicemen. Two algorithms, Tabu embedded simulated annealing and squeaky wheel optimization with local search, are proposed for solving real world data. The results confirm the effectiveness of the proposed approaches.

Luo et al.[22]considered the manpower routing problem with synchronization constraints (MRPSC). To find an exact solution, a branch and price and cut (BPC) algorithm was proposed. Experimental results show the effectiveness of this approach.

Cai et al.[23]investigated the manpower allocation problem with time windows for tasks and job teaming constraints (MAPTWTC). They

Parmis SHAHMALEKI, Alpaslan FIĞLALI

A heuristic algorithm for workforce scheduling with synchronization constraints and ergonomic aspects...

propose a tree data structure for representing solutions. A novel Tabu search algorithm with new search operators based on the tree data structure is proposed.

Nasir and Kuo[24]suggested a decision support framework for creating simultaneous schedule and route plans for caregivers and home delivery vehicles with considering synchronization between staff and vehicle's visits, multiple visits to patients, multiple routes of vehicles and pickup/delivery visits related precedence for vehicles. An MILP model was proposed and due to the complexity of the problem a hybrid genetic algorithm was developed.

The studies focusing on personnel scheduling and using the ergonomic considerations with fairness are summarized below:

Lodree, Jr. et al.[10] demonstrated the lack of collaboration between scheduling theory and human factor engineering. They proposed a framework for interdisciplinary connection between workforce assignment and scheduling with human factor engineering.

Hochdorffer et al.[25] presented a mathematical model for generating job rotation schedules. By considering the workers' qualifications, the workplace ergonomic, and workforce assignment, the complexity of the problem increases. Authors propose a linear programming based heuristic. Testing this method on real data from the assembly line of an automotive producer in Germany shows the effectivity of the approach.

Otto and Battaia [26] focused on assembly line balancing, rotation scheduling and physical ergonomic risks in their survey article. They provided a comprehensive review of articles that investigate the physical ergonomic risks for job rotation scheduling in line balancing concept. Also, they provide helpful insights and research directions for operation researchers, ergonomists, and production managers.

Yoon et al.[27] developed a mathematical model for generating job rotation schedules by considering the reduction of cumulative

workload in the automotive assembly line in Korea. Here the cumulative workload is related to successive use of the same body region. They try to reduce the variance of daily workload between workers and prevent repeated high workload exposure on the same body region. They use rapid entire body assessment (REBA) for calculating workload. Their proposed model shows good results in the ergonomic aspect, in spite of an increase in computational time.

Paulsen et al.[28] examined the inter-rater reliability of two physical exposure assessment methods of the upper extremity, the Strain Index (SI) and Occupational Repetitive Actions (OCRA) Checklist.

Rosecrance et al.[17] Conducted and compared SI (Strain Index) and OCRA checklist method for evaluating ergonomic risk of cheese processing tasks in a factory in Italy. Seven ergonomists assessed task-level physical exposures to the upper limb of workers performing 21 cheese-manufacturing tasks.

Tiacci and Mimmi [18] used the OCRA index as a method for ergonomic risk assessment for proposing an approach to design asynchronous assembly lines in compliance with ergonomic aspect at a company related to agricultural equipment. They suggested a genetic algorithm to tackle with this problem.

Reis et al.[29] analyzed the risks associated with repetitive movements of the upper limbs of workers performing meat processing tasks. The study was conducted in a slaughterhouse in Brazil. They used the OCRA checklist method.

Lasota et al.[30] used the OCRA checklist method for assessing risk measurement in the packaging operation in a factory in Poland, and their results showed the efficiency of this method for manual packaging activities

To the best of our knowledge and as can be seen from the literature review, no problem with the features discussed in this study has been investigated before.

Parmis SHAHMALEKI, Alpaslan FIĞLALI

A heuristic algorithm for workforce scheduling with synchronization constraints and ergonomic aspects...

3. PROBLEM STATEMENT OF THE STUDY

Internal operations of a cross-dock are deconsolidation, sorting, repackaging, and consolidation. This research focuses on the intermediate work area and especially on the repackaging phase. At this phase, packaging of parts is done by teams of workers and equipment. The transported parts are packed in pallets and successively in containers.

The preparation and repackage of goods is driven by international customers' orders. A schedule or daily work plan for a day is produced a day before with consideration of the rolling horizon. The domain of scheduling is 8-hour shifts.

The whole assignment and scheduling procedure consist of two main steps:

In the first step of planning and scheduling, the tasks are prioritized based on specified predetermined criteria. The higher priority means greater importance and represents the partial importance of the tasks. These given priorities act as task weights in objective function in the proposed model.

In the second step, since the number of teams is limited, some tasks can be left unassigned. We try to assign a sequential order of tasks to teams to maximize the total number of assigned tasks by considering time, ergonomic, and synchronization constraints. As a subordinate objective, during the scheduling, tasks with higher priority should be tried to schedule earlier, because depending on this cross-dock's customer service policy this approach makes advantages on service levels and in relations with international customers.

The objective function in this step is maximizing the weighted sum of selected jobs for the planning horizon.

3.1. Problem Definition

The problem is described as follows: There are N tasks to be done by M teams. A team is formed by a group of workers where the number of workers in each team is fixed and workers have the same skills and experience. Teams are homogenous and identical. Number of teams is limited. Each team can process one packing task at a time. Each task is required to be processed by one or more teams, depending on its difficulty. In some situations, all teams must collaborate to process one task. These teams should start a task at the same time, in other words there should be synchronization between teams.

The number of tasks varies daily but for the planning period (typically an 8-hour shift) it is determined. Each task has a predetermined priority (weight), deterministic processing time, due date, required number of teams and heaviness which is determined by the ergonomic score of the task.

On the other hand, as some of these tasks are ergonomically heavy, they must not be done consecutively by a team.

Transportation time is negligible compared to processing time. Therefore, the walking times for workers and transportation times for forklifts are neglected. Preemption is not allowed, which means that once a task is started, it must be finished even if a higher priority task arrives. The objective of the problem is to minimize the total weighted completion time ($\sum w_j C_j$) of the jobs. The weight (w_j) shows the relative importance of each job (j) and the C_j is the completion time of the job j.

3.2. Workload Assessment

In this research, we focus on physical ergonomic risks, and we have used the OCRA method. OCRA[16] is an observational technique that allows quick evaluation of the exposure of upper limbs in repetitive works. A higher value of the OCRA index indicates higher ergonomic risks.

The OCRA checklist method has been used in different fields, for example, in poultry slaughterhouse[29], in animal facility operators[31] and packing line operators[30].

Parmis SHAHMALEKI, Alpaslan FIĞLALI

A heuristic algorithm for workforce scheduling with synchronization constraints and ergonomic aspects...

There are two kinds of OCRA method: the OCRA index and the OCRA checklist. The OCRA checklist is a simplified version of the OCRA index [32].

We used the OCRA checklist method for assessing risk measurement for "multitask" jobs in repackaging section.

We use a five-level color system for facilitating interpretation of the overall risk scores. This system reflects the ergonomic risks in categories. Green, yellow, light red, red, and purple indicates acceptable, very low, medium-low, medium, and high risk levels, respectively [30, 33]. The OCRA checklist score is shown in Table 1.

Table 1
The OCRA checklist score

Checklist Score	Exposure Level
<= 7.5	No exposure
7.6-11.0	Very low exposure
11.1-14.0	Light exposure
14.1-22.5	Medium exposure
>=22.5	High exposure

The heaviness of each task is calculated, via the OCRA method. As can be seen from the table above, if the ergonomic score of a task is above 22, it is considered a heavy (risky) task. Besides, for each team, the cumulative ergonomic score (CES) is calculated by multiplying the OCRA score and processing time of the tasks performed by that team. As a second objective function, we try to distribute ergonomic loads fairly among the teams. This objective function is minimization and calculated as the sum of the differences from the average. 0 means all teams are evenly loaded.

3.3. Proposed Algorithm

The main goal of this research is to find a practical solution approach for real instances of the workforce scheduling problem presented in the previous section. The current approach in the cross-dock is manual, subjective, and time-consuming. We propose a greedy construction heuristic algorithm by considering all practical and ergonomic constraints.

The proposed algorithm is applied to a problem instance as follows:

A list of gaps, that is idle time interval, is determined for each team. Starting from the first task of the *Unassigned* tasks set, each task is scheduled at the earliest possible time, by considering the ergonomic and technological constraints. If possible gaps are found, the task is scheduled, relevant gaps are updated immediately, and the task is placed in the Assigned tasks set. But if the feasible gaps aren't found, then the task remains in the Unassigned tasks set.

The main flow of the algorithm is given below:

1-In the first step, tasks are sorted in decreasing order by their priorities. Sort available tasks in descending order based on their priority points that determined previously.

2-The tasks are taken from the sorted list one by one and a schedule is constructed incrementally.

3-All current intervals are searched to see if there is a sufficiently long interval for processing task$j$. Then, a set from all feasible intervals is formed.

4-Depending on the number of required teams for a task, the feasible combination of intervals is chosen and put in a $suitTj$ set. (All possible groups are collected into a $suitTj$ set.)

5-Among the feasible combinations in set $suitTj$, the one that gives the earliest start time for the task, is selected.

6-If there is no feasible interval or combination of intervals, the algorithm continues and takes the next task in the list.

7- The Algorithm continues until all possible tasks are assigned or the time is over.

The notations given below are used in the algorithm:

M total number of teams

N total number of tasks

TS planning period (typically an 8-hour shift)

Indexes

i , i' Teams i , $i' \in M$

j , j' Jobs j , $j' \in N$

$schedule$ is a $M * N$ matrix that is used to show the schedule

NRT_j refers the number of required teams to process task j.

st_j starting time of task j.

d_j is a duration of task j

In order to explain this algorithm in detail, let $gapT_i$ and $suitT_j$ be the sets of gaps for team i and suitable overlapping groups of gaps for task j, respectively.

The algorithm can be described in detail as follows:

Step1: Initialize two main sets, $Assigned\ tasks\ set = \{\}$ and $Unassigned\ tasks = \{1,2,…,N\}$, N is the total number of tasks.

Step 2: for each team i, initialize $gapT_i$ to $[0, TS]$,where TS is an available shift time and $suitT_j = \{\}$.

Step 3: for $p = 1$ to the total number of tasks until the termination criteria (all tasks are assigned or reaching maximum available time) are fulfilled do the following:

Step 3-1: consider the task j at position k in $Unassigned\ tasks\ set$

Step 3-2: determine intervals $[l, u]$ so that task j can be assigned to time slot.

Feasible intervals for task j have to be fulfilled by the time and the ergonomic criteria:

1. $u - l \geq d_j$, d_j is a duration of task j

2. If task j is heavy then tasks at position $schedule(i, u + 1)$ and position $schedule(i, l - 1)$ should be light tasks. In other words, if a task j is heavy, the tasks assigned before and after that task should be light. But if a task is light, it doesn't matter if the tasks before and after that task are heavy or light.

Step 3-3: Feasible Interval gaps for each team are arranged based on the starting time (lower bound) from earliest to the latest. (It is obvious that there is no overlap between these intervals).

Step 3-4: based on the NRT_j for a task, the feasible combination of intervals are determined and put in a $suitT_j$ set. In other words, $suitT_j$ is a set of possible groups of gaps that task j can be assigned. If $NRTj$ is 1, the $suitT_j$ consists of only feasible gaps, but when the $NRTj$ is more than 1, $suitT_j$ consists of feasible groups of gaps. It is noteworthy that the number of gaps in each group equals to the number of required team for this task. All teams in a group have a common time interval that is at least as long as the duration of the task.

Therefore, step 3-4 can be stated as follows: determine intervals $[l, u] = [l_{ik}, u_{ik}] \cap [l_{i'}, u_{i'}] … \cap [l_{i''}, u_{i''}]$ so that $u - l \geq d_j$

Step 3-5: Among the intervals determined in step 3-4, select interval or a group of intervals with minimum $[0, TS]$. If there is more than one option with minimum, assign the task to the team or teams with smallest cumulative ergonomic score.

Step 3-6: Remove interval $[stj, stj + dj]$ from related gaps.

In order to clarify the step 3-4 of the proposed algorithm, assume that $NRT_j = 1$, in this case, for each team, the feasible interval with the earliest starting time (lower bound) is selected

Parmis SHAHMALEKI, Alpaslan FIĞLALI

A heuristic algorithm for workforce scheduling with synchronization constraints and ergonomic aspects...

and moved to $suitT_j$ set. But if $1 < RNB_j \leq M$, then all possible combinations of feasible gaps are selected.

A compound is feasible if the overlap of all considered intervals is equal to or greater than the processing time of task j, in other words,

$$\min \underbrace{(u_{i,k}, u_{i'k'}, \dots, u_{i''k''})}_{\text{the number is equal to} RNB_j} - \max(l_{i,k}, l_{i'k'}, \dots, l_{i''k''}) \geq d_j$$

If a compound is feasible then it be placed in $(suitT_j)$ set of task j.

An acceleration mechanism may be useful in some cases.

If for an interval of a team a feasible combination is found then the search on next intervals of this team will be stopped and the search continues from the intervals of the next team. In other words, since we are trying to find the earliest starting time for each task, we will stop looking at the next intervals of the same team as soon as we find the first possible interval. Therefore useless searching will not be done.

If in searching the upper bound of considered interval is smaller than the lower bound of the interval then searching in intervals of this team will stop because the intervals in each team sorted based on their lower bound.

The intervals of each team is sorted based on lower bound (starting times) from earliest to the latest. In a case, where a task required more than one team, in searching process between teams to find suitable combination of intervals, if the upper bound of an interval of team i is smaller than a lower bound of an interval of team i' so the searching is stopped on the intervals of team i' and searching process continues from next team's intervals.

The flowchart of the main steps of the proposed algorithm is shown in Figure 2.

As an illustration, let us consider a small instance with 12 tasks and three teams. Priorities (weights), Processing times, number of required

teams, and ergonomic scores are given in Table 2.

The consecutive steps of the algorithm are shown in Table 3. k is a counter. The Gantt chart of the obtained solution is depicted in Figure 3.

After executing the algorithm, the tasks that remain in unassigned set, will be shifted to the next period, and obviously their priority will be changed.
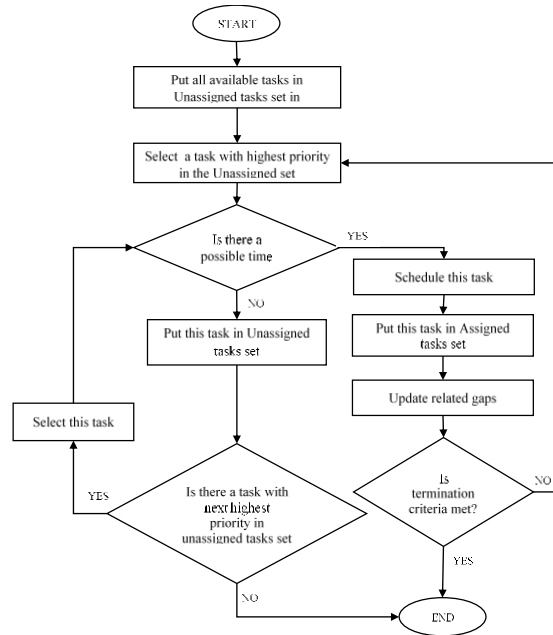
Figure 2 Flowchart of the algorithm

4. RESULTS AND DISCUSSION

Since this study's problem has not been investigated in the literature before, there is no exact or approximate solution method developed for its solution.

The method currently used in the cross-dock, where the study was conducted, is somehow inspired by dispatching rules. Dispatching rules are kinds of construction heuristic methods that are widely used in practical scheduling problems. Examples of common dispatching rules are FIFO (First In First Out), SPT (Shortest Processing Time), EDD (Earliest DueDate) [34][35]. There are also different dispatching rules explicitly developed for the problems defined in the literature [36][37].

Since there is no definitive dispatching rule that can be used directly regarding the unique features of this problem, we developed and coded the highest priority first (HPF)based dispatching rule for simulating the current method in the cross-dock. The advantage of the HPF is to serve to minimize the "total weighted completion time" objective function but its disadvantage is disregarding the ergonomic fairness.

The proposed algorithm and HPF heuristic were coded in MATLAB 2014a and the results were compared with the schedules implemented by the cross-dock. These algorithms were implemented in a personal laptop with Core i5 processor, 2.40 GHz CPU, 4 GB RAM, and Microsoft Windows 10 64-bit operating system.

The number of teams was three, and the number of jobs was between 40 and 60. To measure the efficiency of the proposed algorithm, real problems were solved using the proposed algorithm and HPF heuristic and the results were compared with the real schedules.

It takes approximately 2 hours for an employee to make a daily schedule, and a schedule is created in line with the employee's experience, in case the person responsible for scheduling is absent due to sickness, leave, etc., the schedule can be very inefficient. Since the CPU time of the heuristic method we recommend is limited to seconds, it mainly provides ease of application. In addition, when 15 charts belonging to different days are compared, it is seen that an average of 6% improvement is achieved in the total completion time of the works and 7% in the balanced distribution of the workload in terms of ergonomic scores. The most important advantage of the model is that important works are completed earlier. Also, despite the HPF heuristic CPU time being relatively smaller than the proposed heuristic, the solution values are drastically worse. The comparison of all algorithms and performance improvement of the proposed heuristic can be seen at Table 4. Based on the results, the proposed algorithm is superior to the current conventional method and HPF heuristic in terms of quality. Since the solution time of the proposed algorithm is much less than the time to solve the existing method, using this algorithm is economical in terms of time.

Table 2
Data for the example

Task j	1	2	3	4	5	6	7	8	9	10	11	12
Weight(priority)	10000	9000	7000	5500	1000	750	200	80	20	15	10	5
Processing time	10	5	15	5	5	5	10	5	15	7	5	15
Number of required team	2	1	3	1	1	3	2	2	2	1	2	1
Ergonomic Score	25	25	10	25	10	20	25	25	25	15	15	15

Parmis SHAHMALEKI, Alpaslan FIĞLALI

A heuristic algorithm for workforce scheduling with synchronization constraints and ergonomic aspects...

Table 3
Steps of the algorithm

k	Task	$[l, u]$	st	Team 1		Team 2		Team 3	
				Idle Gaps	CES*	Idle Gaps	CES	Idle Gaps	CES
1	1	[0,10]	0	GapT1[10,120]	25	GapT2[10,120]	25	GapT3[0,120]	0
2	2	[0,5]	0	GapT1[10,120]	25	GapT2[10,120]	25	GapT3[5,120]	25
3	3	[10,25]	10	GapT1[25,120]	35	GapT2[25,120]	35	GapT3[5,10]∪[25,120]	35
4	4	[25,30]	25	GapT1[30,120]	60	GapT2[25,120]	35	GapT3[5,10]∪[25,120]	35
5	5	[5,10]	5	GapT1[30,120]	60	GapT2[25,120]	35	GapT3[25,120]	45
6	6	[30,35]	30	GapT1[35,120]	80	GapT2[25,30]∪[35,120]	55	GapT3[25,30]∪[35,120]	65
7	7	[35,45]	35	GapT1[35,120]	80	GapT2[25,30]∪[45,120]	80	GapT3[25,30]∪[45,120]	90
8	8	[25,30]	25	GapT1[35,120]	80	GapT2[45,120]	105	GapT3[45,120]	115
9	10	[35,42]	35	GapT1[42,120]	95	GapT2[45,120]	105	GapT3[45,120]	115
10	11	[45,50]	45	GapT1[42,45]∪[50,120]	110	GapT2[50,120]	120	GapT3[45,120]	115
11	9	[50,65]	50	GapT1[42,45]∪[65,120]	135	GapT2[65,120]	145	GapT3[45,120]	115
12	12	[45,60]	45	GapT1[42,45]∪[65,120]	135	GapT2[65,120]	145	GapT3[60,120]	130

*CES is the abbreviation of Cumulative Ergonomic Score
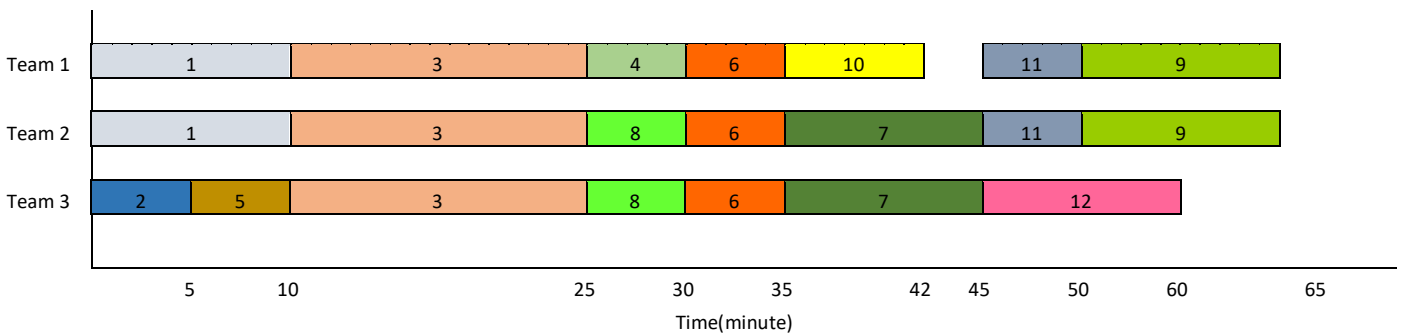
Figure 3 The Gantt chart of the obtained solution

Table 4.
Comparison of the solution methods

Instance	Proposed Heuristic			HPF Heuristic			Manual Method		Proposed Heuristic vs. Manual Method		Proposed Heuristic vs. HPF	
	$\sum wjcj$	CES	CPU time (Sec)	$\sum wjcj$	CES	CPU time (Sec)	$\sum wjcj$	CES	$\sum wjcj$	Workload Distribution	$\sum wjcj$	Workload Distribution
1	690752	313.33	0.32	777734	962.00	0.09	777872	341.67	16.02	8.29	16.33	67.43
2	742267	1302.00	0.35	787240	1624.00	0.14	807887	1418.00	4.58	8.18	5.71	19.83
3	1418647	858.00	0.19	1418653	858.00	0.10	1616997	858.00	0.71	0.00	0.71	0.00
4	1721428	1084.00	0.21	1733178	1236.00	0.15	1805598	1114.33	1.63	2.72	1.83	12.30
5	753777	684.00	0.21	763623	2702.00	0.21	798905	718.00	6.19	4.74	6.53	74.69
6	794155	550.00	0.19	971740	2446.67	0.10	803709	595.00	11.14	7.56	18.27	77.52
7	1968954	290.00	0.27	2390292	1874.67	0.12	2162847	300.33	12.99	3.44	17.63	84.53
8	1121493	905.33	0.28	1122900	1689.33	0.09	1232756	1005.67	9.02	9.98	9.03	46.41
9	966846	855.33	0.20	1064701	2160.00	0.08	1010923	964.00	6.22	11.27	9.19	60.40
10	1395727	652.00	0.21	1590251	1520.00	0.13	1437489	708.00	9.22	7.91	12.23	57.11
11	1256580	1149.33	0.18	1264311	1458.67	0.09	1269109	1211.67	1.00	5.14	1.40	21.21
12	1753390	1768.67	0.20	1796118	1918.00	0.12	1910249	1892.00	1.95	6.52	2.38	7.79
13	881664	844.67	0.23	882114	1261.33	0.11	898537	913.33	1.88	7.52	0.05	33.03
14	2011394	414.00	0.32	2013991	750.67	0.12	2149915	446.00	0.57	7.17	0.63	44.85
15	1655576	484.67	0.20	1791964	1587.33	0.10	1754871	580.67	10.05	16.53	10.40	69.47
								Average	6.21	7.13	7.49	45.10

Parmis SHAHMALEKI, Alpaslan FIĞLALI

A heuristic algorithm for workforce scheduling with synchronization constraints and ergonomic aspects...

On the other hand, due to the higher quality of the solutions produced, it is also appropriate to use the obtained schedule when it is evaluated in terms of accuracy. In addition, an exact and systematic method like the OCRA was used for evaluating risk factors of each task,which brings more accuracy in practice. This algorithm also tries to distribute workloads evenly among teams.

5. CONCLUSIONS

The distribution center links overseas industrial sites with domestic suppliers. In terms of guaranteeing a high service quality and rate, distribution, operation planning, and scheduling play an important role. In the under researched distribution center, tasks scheduling and workforce assignment in the repackaging section, are the key activities. Due to current manual process for scheduling in this section, finding an alternative algorithm has been identified as an improvement opportunity.

In this paper, the workforce scheduling problem at the repackaging section under real conditions is discussed. In this problem, some works require cooperation between more than one team simultaneously and heavy tasks shouldn't be performed consecutively. The goal is to find the best work schedule and workforce allocation to maximize the number of jobs performed in a work shift with a limited number of work teams.

Due to the high complexity of the problem, a greedy heuristic algorithm that provides appropriate schedules in a shorter time was suggested.After coding this algorithm with MATLAB and comparing its results with the available information, the efficiency of this algorithm was measured. The results show that acceptable answers are obtained in a shorter time. Therefore, it is recommended to implement this algorithm in the distribution center.

In future research, a more accurate model of the problem can be considered. Also, according to the dynamic conditions of the data, more efficient and accurate solution methods can be researched. In addition, solving the problem with multi-objective approach can be considered as one of the directions of future research.

Funding

The Declaration of Conflict of Interest/ Common Interest

No conflict of interest or common interest has been declared by the authors.

Authors' Contribution

All authors have contributed to the theory of the manuscript and the writing of the manuscript equally.

The Declaration of Ethics Committee Approval

The authors declare that this document does not require an ethics committee approval or any special permission.

The Declaration of Research and Publication Ethics

The authors of the paper declare that they comply with the scientific, ethical and quotation rules of SAUJS in all processes of the paper and that they do not make any falsification on the data collected. In addition, they declare that Sakarya University Journal of Science and its editorial board have no responsibility for any ethical violations that may be encountered, and that this study has not been evaluated in any academic publication environment other than Sakarya University Journal of Science.

REFERENCES

[1]   C. Serrano, X. Delorme, and A. Dolgui, "Distribution and operation planning at a cross-dock platform: A case of study at Renault," in *2015 4th International Conference on Advanced Logistics and Transport (ICALT)*, 2015: IEEE, pp. 193-198.

Parmis SHAHMALEKI, Alpaslan FIĞLALI

A heuristic algorithm for workforce scheduling with synchronization constraints and ergonomic aspects...

[2] M. P. Fanti, G. Stecco, and W. Ukovich, "Solving Scheduling Problems in Distribution Centers by Mixed Integer Linear Programming Formulations," *IFAC Proceedings Volumes,* vol. 44, no. 1, pp. 8205-8210, 2011/01/01/ 2011, doi: https://doi.org/10.3182/20110828-6-IT-1002.03532.

[3] Y. Li, A. Lim, and B. Rodrigues, "Crossdocking—JIT scheduling with time windows," *Journal of the Operational Research Society,* vol. 55, no. 12, pp. 1342-1351, 2004.

[4] Y. Maknoon and G. Laporte, "Vehicle routing with cross-dock selection," *Computers & Operations Research,* vol. 77, pp. 254-266, 2017.

[5] A. Dohn, E. Kolind, and J. Clausen, "The manpower allocation problem with time windows and job-teaming constraints: A branch-and-price approach," *Computers & Operations Research,* vol. 36, no. 4, pp. 1145-1157, 2009.

[6] C. D. Wickens, S. E. Gordon, and Y. Liu, "An introduction to human factors engineering," 1998.

[7] "International Ergonomics Association. Definition and Domains of Ergonomics. ." https://www.iea.cc. (2020).

[8] B. J. Carnahan, M. S. Redfern, and B. Norman, "Designing safe job rotation schedules using optimization and heuristic search," *Ergonomics,* vol. 43, no. 4, pp. 543-560, 2000.

[9] J. Boudreau, W. Hopp, J. O. McClain, and L. J. Thomas, "On the interface between operations and human resources management," *Manufacturing & Service Operations Management,* vol. 5, no. 3, pp. 179-202, 2003.

[10] E. J. Lodree Jr, C. D. Geiger, and X. Jiang, "Taxonomy for integrating scheduling theory and human factors:

Review and research opportunities," *International Journal of Industrial Ergonomics,* vol. 39, no. 1, pp. 39-51, 2009.

[11] T. R. Waters, V. Putz-Anderson, A. Garg, and L. J. Fine, "Revised NIOSH equation for the design and evaluation of manual lifting tasks," *Ergonomics,* vol. 36, no. 7, pp. 749-776, 1993.

[12] J. S. Moore and A. Garg, "The Strain Index: a proposed method to analyze jobs for risk of distal upper extremity disorders," (in eng), *Am Ind Hyg Assoc J,* vol. 56, no. 5, pp. 443-58, May 1995, doi: 10.1080/15428119591016863.

[13] L. McAtamney and E. N. Corlett, "RULA: a survey method for the investigation of work-related upper limb disorders," *Applied ergonomics,* vol. 24, no. 2, pp. 91-99, 1993.

[14] S. Hignett and L. McAtamney, "Rapid Entire Body Assessment (REBA)," *Applied Ergonomics,* vol. 31, no. 2, pp. 201-205, 2000/04/03/ 2000, doi: https://doi.org/10.1016/S0003-6870(99)00039-3.

[15] "EAWS website." www.eaws.it (2015).

[16] E. Occhipinti, "OCRA: a concise index for the assessment of exposure to repetitive movements of the upper limbs," (in eng), *Ergonomics,* vol. 41, no. 9, pp. 1290-311, Sep 1998, doi: 10.1080/001401398186315.

[17] J. Rosecrance, R. Paulsen, and L. Murgia, "Risk assessment of cheese processing tasks using the Strain Index and OCRA Checklist," *International Journal of Industrial Ergonomics,* vol. 61, pp. 142-148, 2017/09/01/ 2017, doi: https://doi.org/10.1016/j.ergon.2017.05.009.

[18] L. Tiacci and M. Mimmi, "Integrating ergonomic risks evaluation through

Parmis SHAHMALEKI, Alpaslan FIĞLALI

A heuristic algorithm for workforce scheduling with synchronization constraints and ergonomic aspects...

OCRA index and balancing/sequencing decisions for mixed model stochastic asynchronous assembly lines," *Omega,* vol. 78, pp. 112-138, 2018/07/01/ 2018, doi: https://doi.org/10.1016/j.omega.2017.08.011.

[19] Y. Li, A. Lim, and B. Rodrigues, "Manpower allocation with time windows and job-teaming constraints," *Naval Research Logistics (NRL),* vol. 52, no. 4, pp. 302-311, 2005.

[20] S. C. Ho and J. M. Leung, "Solving a manpower scheduling problem for airline catering using metaheuristics," *European Journal of Operational Research,* vol. 202, no. 3, pp. 903-921, 2010.

[21] A. Lim, B. Rodrigues, and L. Song, "Manpower allocation with time windows," *Journal of the Operational Research Society,* vol. 55, no. 11, pp. 1178-1186, 2004.

[22] Z. Luo, H. Qin, W. Zhu, and A. Lim, "Branch-and-price-and-cut for the manpower routing problem with synchronization constraints," *Naval Research Logistics (NRL),* vol. 63, no. 2, pp. 138-171, 2016.

[23] Y. Cai, Z. Zhang, S. Guo, H. Qin, and A. Lim, "A Tree-Based Tabu Search Algorithm for the Manpower Allocation Problem with TimeWindows and Job-Teaming Constraints," in *Twenty-Third International Joint Conference on Artificial Intelligence*, 2013.

[24] J. A. Nasir and Y.-H. Kuo, "A decision support framework for home health care transportation with simultaneous multi-vehicle routing and staff scheduling synchronization," *Decision Support Systems,* p. 113361, 2020/07/15/ 2020, doi: https://doi.org/10.1016/j.dss.2020.113361.

[25] J. Hochdörffer, M. Hedler, and G. Lanza, "Staff scheduling in job rotation environments considering ergonomic aspects and preservation of qualifications," *Journal of manufacturing systems,* vol. 46, pp. 103-114, 2018.

[26] A. Otto and O. Battaïa, "Reducing physical ergonomic risks at assembly lines by line balancing and job rotation: A survey," *Computers & Industrial Engineering,* vol. 111, pp. 467-480, 2017.

[27] S.-Y. Yoon, J. Ko, and M.-C. Jung, "A model for developing job rotation schedules that eliminate sequential high workloads and minimize between-worker variability in cumulative daily workloads: Application to automotive assembly lines," *Applied ergonomics,* vol. 55, pp. 8-15, 2016.

[28] R. Paulsen, T. Gallu, D. Gilkey, R. Reiser, 2nd, L. Murgia, and J. Rosecrance, "The inter-rater reliability of Strain Index and OCRA Checklist task assessments in cheese processing," (in eng), *Appl Ergon,* vol. 51, pp. 199-204, Nov 2015, doi: 10.1016/j.apergo.2015.04.019.

[29] D. Reis, A. Moro, E. Ramos, and P. Reis, "Upper Limbs Exposure to Biomechanical Overload: Occupational Risk Assessment in a Poultry Slaughterhouse," Cham, 2016: Springer International Publishing, in Advances in Physical Ergonomics and Human Factors, pp. 275-282.

[30] A. M. Lasota, "Ergonomic evaluation of physical risk for packing line operators," *Logistics and Transport,* vol. 26, 2015.

[31] V. Occhionero, R. Ghersi, L. Prandini, L. Korpinen, and F. Gobba, "The biomechanical overload of the upper limb: a neglected occupational hazard in animal facility operators," *Ergonomics,* vol. 60, no. 3, pp. 366-374, 2017/03/04

Parmis SHAHMALEKI, Alpaslan FIĞLALI

A heuristic algorithm for workforce scheduling with synchronization constraints and ergonomic aspects...

2017, doi: 10.1080/00140139.2016.1176257.

[32] E. Occhipinti and D. Colombini, "A Checklist for Evaluating Exposure to Repetitive Movements of the Upper Limbs Based on the OCRA Index," 2010.

[33] D. Colombini, E. Occhipinti, and E. Álvarez-Casado, "The revised OCRA Checklist method," *Editorial Factors Humans: Barcelona, Spain,* 2013.

[34] M. Pinedo, *Scheduling*, vol. 29. Springer, 2012.

[35] O. Holthaus and C. Rajendran, "New dispatching rules for scheduling in a job shop — An experimental study," *Int. J. Adv. Manuf. Technol.*, vol. 13, no. 2, pp. 148–153, 1997.

[36] S. Jun, S. Lee, and H. Chun, "Learning dispatching rules using random forest in flexible job shop scheduling problems," *Int. J. Prod. Res.*, vol. 57, no. 10, pp. 3290–3310, May 2019.

[37] Tsung-Che Chiang and Li-Chen Fu, "Using dispatching rules for job shop scheduling with due date-based objectives," in *Proceedings 2006 IEEE International Conference on Robotics and Automation, 2006. ICRA 2006.*, May 2006, pp. 1426–1431.

Sakarya University Journal of Science
SAUJS

Title: Investigation of Antibacterial Activity of Juglone – Poly(ε-caprolactone) - Alumina Composite Films

Authors: Ayşegül HOŞ, Uğursoy OLGUN, Kenan TUNÇ

Investigation of Antibacterial Activity of Juglone-Poly(ε-caprolactone) - Alumina Composite Films

Ayşegül HOŞ[*1], Uğursoy OLGUN[2], Kenan TUNÇ[2]

Abstract

The aim of this study was to produce the Poly(ε-caprolactone)(PCL)-Alumina (Al_2O_3) composite films impregnated with Juglone and determine their antibacterial properties. PCL-Al_2O_3 composite films containing 1% and 5% Juglone were prepared using the roll mill method. Juglone was chosen as the antibacterial agent in this study for the production of composite films due to its effective antimicrobial activity. The Juglone-Poly(ε-caprolactone)(PCL)-Alumina (Al_2O_3) composite films exhibited 100% antibacterial activity against both *Staphylococcus aureus* ATCC 29213 and *Escherichia coli* ATCC 25922. It was demonstrated that the Juglone-PCL-Al_2O_3 composite films may have various potential applications in food packaging and personal care products in order to ensure the microbial safety and extended shelf life of the foods and the personal care products.

Key words: Juglone, Poly(ε-caprolactone), Composite, Antibacterial

1. Introduction

Microbial contamination is one of the most serious problems in various fields such as medical devices, medicines, healthcare services, hygienic applications, water treatment systems, hospital and dental surgery equipment, textile, food packaging and storage. Therefore, the use of antimicrobials provides quality and safety to many materials and they draw the attention of the academic researchers and the industry [1]. It is well known that the human beings are frequently infected by the microorganisms such as bacteria, molds, yeasts and viruses in their environment. This has led to an intensive research of antibacterial materials containing various natural and inorganic substances [2]. Recently, plant based antimicrobial agents are being developed in combination with the polymeric materials because of their antibacterial, eco-friendly and body-friendly properties [3].

Phenolic compounds, which are secondary metabolites found in plants, are responsible for the defense mechanisms of plants. Naphthoquinones and flavonoids are regarded as major phenolic compounds in walnut [4]. Naphthoquinones have been preferred in the treatment of fungal, bacterial, and viral infections for centuries in folk medicines [5]. Juglone (5-

---

[*] Corresponding Author: aysegulhos@medipol.edu.tr
[1] Istanbul Medipol University, School of Pharmacy, İstanbul, Turkey.
ORCID: https://orcid.org/ 0000-0001-5605-6159
[2] Sakarya University, Faculty of Art and Sciences, Sakarya, Turkey,
E-mail: uolgun@sakarya.edu.tr ORCID: https://orcid.org/ 0000-0001-7104-9926
E- mail: ktunc@sakarya.edu.tr, ORCID: https://orcid.org/0000-0002-9888-1453

Hydroxy 1,4-naphthoquinone) draws attention among naftokinones due to its chemical reactivity [4]. It is known to have toxic effects, causes death of plants when injected into the petiole of many plants such as tomatoes and alfalfa. Another function of Juglone is that it is a seed germination inhibitor [6]. It has dark orange-brown dyeing properties and has important uses in the food and cosmetic industry as a dyeing agent [7].

Juglone is known to inhibit a broad spectrum of microorganisms including bacteria, algae, and fungi [8]. The mechanism of its action responsible for these effects are peptidyl-prolyl isomerase Pin-1 inhibition, transcription inhibition, DNA topoisomerase-II stimulation, elimination of cell membrane potential and/or formation of hydrogen peroxide [9]. Other positive properties of Juglone are the biodegradability with non-toxic degradation products, the enhancement of degradation in sunlight, and the short half-live of it ranging from a few hours to less than 2 days in natural saline waters [8]. Also, Juglone, a natural Quinone, is an electroactive molecule and has been used as a redox molecule bound to the surface in recent studies [10]. Juglone was chosen as antibacterial agent in this study for production of composite films because of its many interesting properties.

In this study, the antibacterial activities of Juglone and Alumina incorporated PCL films have been evaluated. In the first stage of this study, Juglone-Poly(ε-caprolactone) (PCL) - Alumina (Al$_2$O$_3$) composite films were produced. In the second stage, the antibacterial activities of the produced composite films were determined.

2. Material and Method

2.1. Material

The following commercially available products were used:
1. Poly(ε-caprolactone) (Mn:42500, M$_w$:65000, Sigma-Aldrich)
2. Juglone (5 - Hydroxy 1,4 Naphthoquinone C$_{10}$H$_6$O$_3$, 97%, Sigma-Aldrich)
3. Tryptic Soy Broth dehydrated medium (Merck), Nutrient Agar dehydrated medium (Acumedia) and ready-to-use Sheep Blood Agar medium (Besimik)
4. *Staphylococcus aureus* ATCC 29213 (Microbiologics) and *Escherichia coli* ATCC 25922 (Microbiologics), which were used as test microorganisms.

2.2. Preparation of Juglone-PCL-Al$_2$O$_3$ composite films

Juglone-PCL-Al$_2$O$_3$ composite films were prepared by adding the Juglone and Al$_2$O$_3$ into the PCL polymer melt at about 100°C. Then, the melted polymer composite mixtures turned into the thin film forms using the roll mill method [11]. The composite films were cut to a certain size (2 cm × 5 cm) and used in experimental studies (Figure 1).
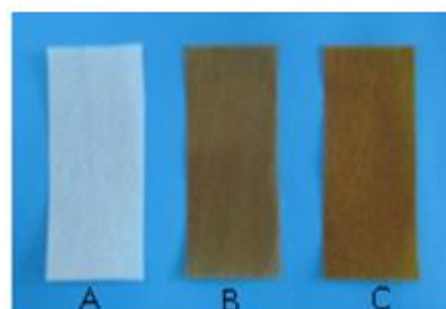
Figure 1 A) Control film (PCL-Al$_2$O$_3$), B) Juglone (1%) - PCL-Al$_2$O$_3$ composite film, C) Juglone (5%) - PCL-Al$_2$O$_3$ composite film

During the melting and stirring process, Juglone was added to PCL-Al$_2$O$_3$ at a percentage of 1% and 5%. The different amounts of Juglone and the PCL-Al$_2$O$_3$ used in this study were given in Table 1.

Table 1 Contents of Juglone-PCL-Al$_2$O$_3$ composite films

Composite Film	PCL - Al$_2$O$_3$ (30%)	Juglone
PCL-Al$_2$O$_3$ (control film)	0.8746 g	–
Juglone (1%) - PCL-Al$_2$O$_3$	0.8748 g	0.0088 g
Juglone (5%) - PCL-Al$_2$O$_3$	0.8747 g	0.0435 g

2.3. Determination of antibacterial activity of Juglone-PCL-Al₂O₃ composite films

The antibacterial activity of Juglone-PCL-Al₂O₃ composite films against *Staphylococcus aureus* ATCC 29213 and *Escherichia coli* ATCC 25922 was determined by the contact plate method [12]. Each sides of the composite films were sterilized by UV light (Philips Ultra Violet TUV 30W) for 5 minutes. Test microorganisms were cultivated in Tryptic Soy Broth medium at $37 \pm 1°C$ for 24 hours. Next, they were inoculated to Sheep Blood Agar and were incubated at $37 \pm 1°C$ for 24 hours. A bacterial suspension of 1×10^6 CFU/mL was obtained from the 24-hour bacterial culture by using the densitometer (Biosan).

30 µL of the bacterial suspension was sprayed on the surfaces of the control film and composite films. The films were placed in such a way that their sprayed surfaces contact with the Nutrient Agar medium. All microbiological studies were performed under aseptic conditions. At the end of the incubation, bacterial colonies growing on the composite film surfaces were counted and the antibacterial activity was determined using the antimicrobial activity formula given below:

$$R = [(B-C)/B] \times 100$$

R: Antimicrobial activity (%)
B: Number of bacteria in the control sample (CFU/sample)
C: Number of bacteria in the modified sample (CFU/sample)

3. Results

Juglone-PCL-Al₂O₃ composite films with 30% added alumina containing different percentages of Juglone (1% and 5%) were prepared using the roll-mill technique. The alumina and Juglone additives in the specified amounts were added into the PCL polymer melted at 100 °C and mixed. In the next step, the melted mixture was transformed into thin films using the roll-mill. The images of composite films and the chemical structure of Juglone and PCL were given in Figure 2.

Figure 2 The images of composite films and chemical structures of Juglone and poly(ε-caprolactone)

The antibacterial activities of Juglone-PCL-Al₂O₃ composite films were determined by using the contact plate method. At the end of the incubation period, the bacterial growth was observed as expected in the composite films used as the control. However, in Juglone-PCL-Al₂O₃ composite films, no bacterial growth was observed. The results of antibacterial activity (R%) calculated for the control film and the Juglone-PCL-Al₂O₃ composite films were given in Table 2.

Table 2 Antibacterial activity (R%) for Juglone-PCL-Al₂O₃ composite films

Test microorganism	Antibacterial activity (R%)		
	PCL-Al₂O₃ (control)	Juglone (1%)-PCL-Al₂O₃	Juglone (5%)-PCL-Al₂O₃
E. coli	0	100	100
S. aureus	0	100	100

4. Discussion and Conclusion

The use of antimicrobials as an additive in polymers provides great benefit in terms of both quality and microbial safety. Microorganisms such as bacteria, fungi and algae affect the aesthetic and physical properties of plastics. Antimicrobial additives are used in many areas, including food production equipment, medical devices in hospitals (catheters), external instruments (stethoscope, medical gloves), flooring and wall coverings [13].

Today, new types of biocidal materials need to be investigated because of the acquired resistance of the pathogenic microorganisms to the known antimicrobial agents. Recent studies in this area have focused on obtaining natural compounds with bactericidal and fungicidal properties from plants and using them as the antimicrobial additives. Novel materials intended to have antimicrobial effects are also expected to be harmless to the environment. In our study, we have used Juglone as a natural compound, and poly(ε-caprolactone) as a biodegradable polymer. These are suitable materials in that respect. In a study by Mirjalili *et al.*, the antibacterial activity of walnut, turmeric and henna-dyed viscose fabrics were compared with viscose fabrics treated with Ag nanoparticles. Natural dyes were demonstrated to have strong antibacterial activity against *E. coli*, similar to Ag nanoparticles [14]. In our study, Juglone-PCL-Al_2O_3 composite films showed high antibacterial effects against both *E. coli* and *S. aureus*.

The use of antibacterial composite materials in packaging, personal care products and food industry products may increase the quality of these products and extend their shelf life. Recently, the increase in the use of packages made from conventional polymers that are not biodegradable, causes serious ecological problems. Solano and Gante reported that they developed antimicrobial packaging materials by incorporating known concentrations (w/w) of essentials oils of oregano (*Origanum vulgare*) and thyme (*Thymus vulgaris*) into low-density polyethylene (LDPE). They determined the antimicrobial films developed by them showed antimicrobial activity against food pathogens such as *S. typhimurium*, *L. monocytogenes*, and *E. coli* O157:H7 [15]. Many more studies about the incorporation of antimicrobial agent into the polymeric matrix performed by the researchers [16,17]. Examples can be listed as follows: Sodium benzoate incorporated into Poly (butylene adipate-co-terephthalate) / Organoclay nanocomposite [18]; Plantaricin BM-1 incorporated into PE, LDPE and HDPE [19]; Potassium sorbate and Vanillin incorporated into Chitosan films [20]; Potassium sorbate and Oregano essential oil incorparated into Thermoplastic starch and Poly(butylene adipate-coterephthalate) [21], *Thymus kotschyanus* essential oil incorporated into starch-chitosan composite film [22].

In our literature search, no study was found about the preparation of Juglone-Poly(ε-caprolactone) (PCL)-Alumina (Al_2O_3) composite films. Also, no previous work can be found about the antibacterial activity of these PCL polymer composites. Therefore, in this present work, we have reported the first method for the preparation of and tested their antibacterial surface properties.

As shown in our study, the use of naturel antibacterial agents in polymer composites may have many advantages. For instance, the reduced toxic material properties, the decrease in production costs and no environmental contaminations can be achieved. These biodegradable polymer composites may have potential utilizations in packaging of personal care products, toys and foods due to their effective antibacterial properties. Furthermore, the medical uses of antibacterial biopolymer composite products are also well known. We are currently working on the wound healing and anti-aging properties of these composite films. These Juglone - Poly(ε-caprolactone) (PCL) - Alumina (Al_2O_3) composite films can be used also in implants and different tissue parts.

The Declaration of Conflict of Interest/ Common Interest

No potential conflict of interest was reported by the authors.

The Declaration of Ethics Committee Approval

Ethics Committee Approval is not required.

The Declaration of Research and Publicatıon Ethics

In the writing process of this study, international scientific, ethical and citation rules have been followed.

REFERENCES

[1] el-R. Kenawy, S.D. Worley, and R. Broughton, "The chemistry and applications of antimicrobial polymers: A state-of-the-art review," Biomacromolecules, vol. 8, no.5, pp. 1359-1384, 2007.

[2] A.R. Sahahverdi, A. Fakhimi, H.R. Sahahverdi, and S. Minaian, "Synthesis and effect of silver nanoparticles on the antibacterial activity of different antibiotics against *Staphylococcus aureus* and *Escherichia coli*," Nanomedicine: Nanotechnology, Biology and Medicine, vol. 3, pp. 168-171, 2007.

[3] S.K. Bhullar, D. Rana, B.K. Ozsel, R. Yadav, G. Kaur, M. Chintamaneni, H.S. Buttar, M.B.G. Jun and M. Ramalingam, "A Comparative Study of the Antibacterial Activity of Rosemary Extract Blended with Polymeric Biomaterials", Journal of Bionanoscience, vol. 10, pp. 326–330, 2016.

[4] A. Solar, M. Colarič, V. Usenik, and F. Stampar, "Seasonal variations of selected flavonoids, phenolic acids and quinones in annual shoots of common walnut (*Juglans regia* L.)," Plant Science, vol. 170, pp. 453-461, 2006.

[5] T. Zmantar, H. Miladi, B. Kouidhi, Y. Chaabouni, R.B. Slama, A. Bakhrouf, K. Mahdouani and K. Chaieb, "Use of juglone as antibacterial and potential efflux pump inhibitors in *Staphylococcus aureus* isolated from the oral cavity", Microbial Pathogenesis, vol. 101, pp. 44-49, 2016.

[6] M. Kılınç and H.G. Kutbay, "Bitki ekolojisi," Palme Publication, pp. 134-135, 2004.

[7] J. Velíšek, J. Davídek, and K. Cejpek, "Biosynthesis of food constituents: Natural pigments. Part 1-a Review," Czech J. Food Sci., vol. 25, no. 6, pp. 291-315, 2007.

[8] M.P. Strugstad and S. Despotovski., "A Summary of Extraction, Synthesis, Properties, and Potential Uses of Juglone: A Literature Review", Journal of Ecosystems and Management, vol. 13, no. 3, pp. 1–16, 2012.

[9] M.T. Paulsen and M. Ljungman, "The natural toxin juglone causes degradation of p53 and induces rapid H2AX phosphorylation and cell death in human fibroblasts," Toxicology and Applied Pharmacology, vol. 209, pp. 1-9, 2005.

[10] M. Saberian, H. Hamzeiy, A. Aghanejad and D. Asgari, "Aptamer-based nanosensors: juglone as an attached-redox molecule for detection of small molecules," BioImpacts, vol. 1, no. 1, pp. 31-36, 2011.

[11] U. Olgun, K. Tunç and V. Özaslan, "Preparation of antimicrobial polycaprolactone silica composite films with nanosilver rods and triclosan using roll-milling method," Polym. Adv. Technol., vol. 22, pp. 232–236, 2011.

[12] U. Olgun, K. Tunç and A. Hoş, "Preparation and antibacterial properties of nano biocomposite Poly(ε-caprolactone)-SiO$_2$ films with nanosilver," J Polym Res, vol. 26, no. 24, 2019.

[13] K. Simpson, "Using silver to fight microbial attack," Plastics Additives & Compounding, pp. 32-35, 2003.

[14] M. Mirjalili and M. Abbasipour, "Comparison between antibacterial activity of some natural dyes and silver nanoparticles," Journal of Nanostructure in Chemistry, vol. 3, no. 37, pp. 1-3, 2013.

[15] A.C.V. Solano and C.R. Gante "Two Different Processes to Obtain Antimicrobial Packaging Containing Natural Oils", Food Bioprocess Technol, vol. 5, pp. 2522–2528, 2012.

[16] T. Huang, Y. Qian, J. Wei and C. Zhou, "Polymeric Antimicrobial Food Packaging and Its Applications", Polymers, vol. 11, no. 560, 2019.

[17] C. Pérez-Pérez, C. Regalado-González, C.A. Rodríguez-Rodríguez, J.R. Barbosa-Rodríguez and F. Villaseñor-Ortega, Incorporation of antimicrobial agents in food packaging films and coatings, Ramón Gerardo Guevara-González and Irineo Torres-Pacheco (eds), Advances in Agricultural and Food Biotechnology, pp. 193-216, Research Signpost, Kerala, India, 2006.

[18] D. Mondal, B. Bhowmick, D. Maity, M.R. Mollick, D. Rana, V. Rangarajan, R. Sen and D. Chattopadhyay, Investigation on Sodium Benzoate Release from Poly(Butylene Adipate-Co-Terephthalate)/Organoclay/Sodium Benzoate Based Nanocomposite Film and Their Antimicrobial Activity, Journal of Food Science, vol. 80, no. 3, 2015.

[19] M. Zhang, X. Gao, H. Zhang, H. Liu, J. Jin, W. Yang and Y. Xie, "Development and antilisterial activity of PE-based biological preservative films incorporating plantaricin BM-1", FEMS Microbiology Letters, vol. 364, no. 7 2017.

[20] J. Sangsuwan, N. Rattanapanone and I. Pongsirikul, "Development of active chitosan films incorporating potassium sorbate or vanillin to extend the shelf life of butter cake" International Journal of Food Science and Technology, doi:10.1111/ijfs.12631, 2014.

[21] L. A. Cestari, R. C. Gaiotto, J. L. Antigo, M. R. S. Scapim, G. S. Madrona, F. Yamashita, M. S. S. Pozza and I. N. Prado, "Effect of active packaging on low-sodium restructured chicken steaks", J Food Sci Technol, vol. 52 no. 6, pp. 3376–3382, 2015.

[22] T. Mehdizadeh, H. Tajik, S.M.R. Rohani and A.R. Oromiehie, "Antibacterial, antioxidant and optical properties of edible starch-chitosan composite film containing *Thymus kotschyanus* essential oil", Veterinary Research Forum, vol. 3, no. 3, pp. 167-173, 2012.

Title: Investigation on the Adsorption of the Potassium Atom onto C20 Fullerene Surface

Authors: Mehmet Dinçer ERBAŞ, Ferhat DEMİRAY

INVESTIGATION ON THE ADSORPTION OF THE POTASSIUM ATOM ONTO C$_{20}$ FULLERENE SURFACE

Mehmet DinçerERBAŞ[1], Ferhat DEMİRAY[*2]

Abstract

In this study, based on the Density Functional Theory (DFT), we examined the structural and electronic properties of potassium (K) atoms doped fullerene (C$_{20}$K).Structural optimization calculations were performed without any symmetry restrictions for the three distinct formations, namely, "pentagon", "bridge" and "on-top", in which K atom can be adsorbed onto C$_{20}$ fullerene.The "pentagon" structure was obtained as the most stable structure because it has a lower total energy value compared to the other two structures.Adsorption energies were calculated as -1.52 eV in the "pentagon" structure, -1.47 eV in the "bridge" structure and -1.41 eV in the "on-top" structure. According to the computed E_{ads} values, adsorption for all of the three distinct structures is chemisorption. The GapHL value for the "pentagon" structure, which is the most stable structure, was calculated as 0.98 eV and this structure can be considered as a semiconductor material.The results obtained by the adsorption of C$_{20}$ fullerene with K atom are expected to guide future experimental and theoretical studies.

Keywords: Molecular Structures, Density Functional Theory, C$_{20}$ fullerene, Potassium, Nanotechnology.

[1]Bolu Abant İzzet Baysal University, Department of Engineering, Bolu, Turkey, Email:dincer.erbas@ibu.edu.tr, ORCID: https://orcid.org/0000-0003-1762-0428, , ORCID: https://orcid.org/0000-0002-4071-9285

[*]Corresponding Author: ferhatdemiray@ibu.edu.tr

1. INTRODUCTION

Nanotechnology, as a general definition, is a field of research aiming at the macro level production of new and different materials with manipulation activities on 1 - 100 nanometer scale material [1]. Due to the study of matter at this scale, intermolecular interactions in research on nanotechnology can be examined using Density Functional Theory (DFT) [2], [3], which is a computational quantum mechanics modeling method. Thus, it is possible to theoretically scale the structural and electronic properties of the material planned to be produced. Stability and conductivity are the main characteristics that are scaled on the newly produced material. Stable molecules with superconductivity and semiconductivity have a wide range of uses in research and development activities carried out at the nano-scale. New generation semiconductor materials have a wide range of uses, especially in the creation of nano-scale robots and the control of robot swarms consisting of these robots [4]. The main purpose of this research is to examine the structural and electronic properties of the fullerene molecule doped with potassium, which is possible to be produced at nano-scale. Structural optimization of this molecule, which has not been studied in the literature yet, has been carried out at different geometric positions. In addition, the molecule mentioned has been shown to have semi-conductor properties in a stable geometric structure.

The remainder of the article is organized as follows: In section 2, information is given on the research on fullerene. In section 3, the theoretical calculation method used for modeling is introduced. The results of the analysis made on this model and the comments on the results are presented in section 4. Finally in section 5, the research conducted was summarized and further information was given about the subjects that could be seen as a continuation of this research.

2. RELATED WORK

One of the most studied molecular structures in nano-scale manipulation is fullerenes. Fullerene is an allotrope of carbon formed by the combination of many carbon atoms. Fullerenes are defined as C_n in which n represents the number of carbon atoms contained in the molecules. All fullerenes contain even numbers of carbon atoms. The first discovered and most widely studied type of fullerene is the C_{60} molecule with its soccer ball-like geometric structure [5], [6]. Although fullerenes are mostly synthesized in a laboratory environment, they can be also found in nature [7]. Fullerenes are studied extensively in many fields such as chemistry, materials science and nanotechnology [8], [9], [10], [11].

The smallest possible fullerene type is the C_{20}dodechedral molecule [12]. The C_{20} isomers can have many different geometric shapes, such as rings, bowls, or cages. Possible stable structures obtained by functionalization of C_{20} are candidates to have both superconducting and semiconductor properties; for this reason, they have been the subject of many different studies. Due to its reactive structure, C_{20} is more difficult to be formed in the laboratory compared to C_{60} [12]. For this reason, theoretical studies have a very large place in the study of the different isomers of this molecule or the structures of complex molecules consisting of the combination of this molecule with other atoms and molecules.

Studies on potassium-doped Carbon nanotube can be found in the literature [13], [14]. These studies have shown that superconductivity is achieved by doping potassium into the fullerene C_{60} and C_{70} molecules, which are carbon allotropes [15], [16]. As far as we know, there is no study on the adsorption of potassium atom on the outer surface of C_{20} fullerene. In this theoretical study, changes in the structural properties of fullerene C_{20} upon the adsorption of K atom on the outer surface of the molecule have been investigated. The electronic properties of the most stable $C_{20}K$ molecular structure that is obtained are also presented. Our primary goal in this study is to provide a foresight for future experimental and theoretical studies on this material.

3. THEORETICAL CALCULATION METHOD

In calculations for the adsorption of potassium atom onto C_{20} fullerene, geometry optimizations and total energy calculations were performed using the generalized gradient approximation (GGA) with the help of SIESTA code [17]. In the generalized gradient approximation (GGA), for the exchange-correlation energy functional, the Perdew – Burke – Ehrenzhof (PBE) parameterization was utilized [18]; furthermore, polarized orbitals and expanded double-ζ orbitals were utilized as the base set. No symmetry constraints were used for optimized geometries and all force components on each atom were performed using the conjugate gradient algorithm until all force components were less than 0.01 eV / Å. To determine the electronic structure, the difference between the highest occupied molecular orbital (HOMO) and the lowest unoccupied molecular orbital (LUMO) was computed and the energy range for the optimized structures, HOMO - LUMO gap (GapHL), was calculated.

4. RESULTS AND DISCUSSION

As shown in Figure 1, there are three possible positions for determining the adsorption of potassium (K) atom on C_{20} fullerene. As shown in Figure 1. a, the adsorbed K atom can be placed in the center of the pentagon and this structure is called the "pentagon". Similarly, as shown in Figure 1 b and c, the K atom can be adsorbed on the C - C bond or on the C atom, and these structures are named as the "bridge" and the "on-top", respectively. Structural optimization calculations were made for all three possible adsorption positions without using any symmetry constraints. Adsorption energies of the optimized molecular structures were calculated as follows:

$$E_{ads} = E(C_{20}K) - E(C_{20}) - E(K) \qquad (1)$$

In this formula; E $(C_{20}K)$ is the total energy of the new molecular structure obtained $C_{20}K$, $E(C_{20})$ is the total energy of pure fullerene, and finally E(K) is the total energy of the potassium atom.

As it has the lowest energy in the total energy calculations we have made, we determined the "pentagon" structure as the most stable among all structures. The pentagon structure has 0.05 and 0.11 eV lower energy than the bridge and on-top structures, respectively. The C - K bond length is calculated as 2.804 Å for the "on-top" structure. In the bridge structure, C - K bond lengths show a slight asymmetry and they are obtained as 2.804 and 2.947 Å. For the "bridge" structure shown in Figure 1b, the bond angle between C - K - C atoms was obtained as 31.52° degrees. The bond lengths between carbon and potassium atoms were calculated as 3.027 Å for the "pentagon" structure. The C - K bond lengths obtained are in agreement with the previous studies [19], [20].

The C - C bond lengths for the undoped fullerene C_{20} structure vary between 1.44 - 1.51 Å. The bond lengths of the C atom, to which the potassium atom will be doped, with other carbon atoms increase slightly for the "on-top" structure and it has been obtained as 1.52 Å. The bond lengths between other C - C atoms do not change and are the same as those in pure fullerene. The C - C bond length between the C atoms bonding with the K atom in the "bridge" structure increases and it is calculated as 1.57 Å. Other bond lengths between C - C are the same as the bond lengths in pure fullerene and range between 1.44 to 1.51 Å. The C - C bond lengths obtained for the "pentagon" structure are also obtained at the same values as the C - C bond lengths in pure fullerene.

The adsorption energies for the optimized structures shown in Fig. 1 were obtained as -1.52, -1.47 and -1.41 eV for the "pentagon", "bridge" and "on-top" structures, respectively. The range of adsorption energy ranges from 0 to -0.829 eV for physisorption and -0.829 to -4.1457 eV for chemisorption [21], [22]. Considering the adsorption energies calculated for the structure shown in figure 1, the adsorption is determined as chemisorption for all of the three structures.
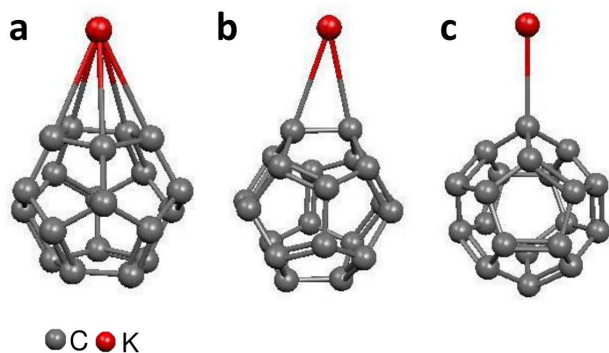
Figure 1. Adsorption positions of the K atom on C_{20}. a) "pentagon", b) "bridge", and c) "on-top" structures.

The density of states for the "pentagon" structure, which has the most stable optimized molecular structure obtained by doping potassium atom to C_{20} fullerene, is shown in Figure 2. Here, the energies are in accordance with the Fermi energy level (E_F) represented by the dashed line. In order to determine the electronic structure, the difference between the highest occupied molecular orbital (HOMO) and the lowest unoccupied molecular orbital (LUMO) was taken and the energy range HOMO - LUMO gap (GapHL) of the "pentagon" structure was calculated.
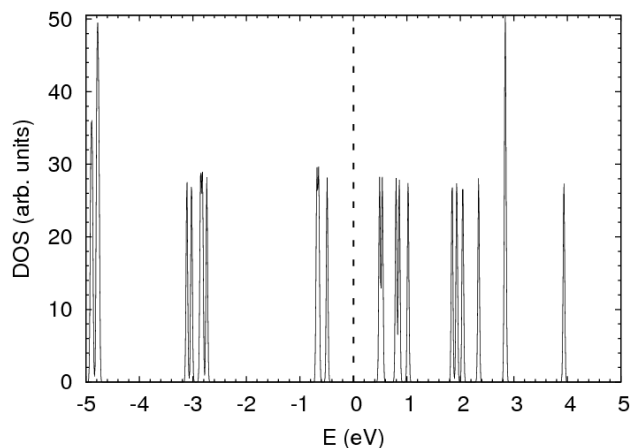
Figure 2. Density of states (DOS) for the optimized "pentagon" structure. Energies are according to the Fermi energy level (E_F), shown by the dashed line.

The GapHL value of the pure fullerene C_{20} was obtained as 0.61 eV. As seen in Figure 2, the pentagon formed by the addition of K atoms to the fullerene molecule increases the value of GapHL to 0.98 eV in the $C_{20}K$ structure and so it is a semiconductor material. No experimental or theoretical data, that we can compare the GapHL value we obtained, can be found in the literature.

5. CONCLUSION

By using Density Functional Theory (DFT), the structural and electronic properties of the new molecular structure obtained by doping potassium atom to C_{20} fullerene were investigated. Structural optimization calculations were made without any symmetry restrictions for the "pentagon", "bridge" and "on-top" positions, which are the three cases where the K atom can be doped to the fullerene C_{20}. According to the calculated total energy values, the "pentagon" structure has the lowest energy value and was obtained as the most stable structure. The adsorption energies for the "pentagon", "bridge" and "on-top" positions are computed as -1.52, -1.47 and -1.41 eV, respectively. Considering the adsorption energies obtained, adsorption is chemisorption for all three structures. GapHL for the "pentagon" structure, which was obtained as the most stable structure, was 0.98eV and so this material can be considered as a semiconductor. The results obtained in our study are expected to guide future experimental and theoretical studies.

The Declaration of Conflict of Interest/ Common Interest

No conflict of interest or common interest has been declared by the authors.

Authors' Contribution

MDE: Investigation, conceptualization, visualization, editing and finalizing the manuscript.

FD:Investigation, conceptualization, visualization, editing and finalizing the manuscript

The Declaration of Ethics Committee Approval

The authors declare that this document does not require an ethics committee approval or any special permission.

The Declaration of Research and Publication Ethics

The authors of the paper declare that they comply with the scientific, ethical and quotation rules of SAUJS in all processes of the paper and that they do not make any falsification on the data collected. In addition, they declare that Sakarya University Journal of Science and its editorial board have no responsibility for any ethical violations that may be encountered, and that this study has not been evaluated in any academic publication environment other than Sakarya University Journal of Science.

REFERENCES

[1]   D. K. Eric,"Nanosystems: molecular machinery, manufacturing, and computation," New York: John Wiley & Sons, 1992.

[2]   P. Hohenberg, and W. Kohn,"Inhomogeneous electron gas," Physical review, vol. 136, no. 3B, B864, 1964.

[3]   W. Kohn, amd L. J. Sham,"Self-consistent equations including exchange and correlation effects,"Physical review, vol. 140, no. 4A, A1133, 1965.

[4]   P. Yang, R. Yan, and M. Fardy, "Semiconductor nanowire: what's next?" Nano letters, vol. 10, no. 5, pp. 1529-1536, 2010.

[5]   W. Kratschmer, L. D. Lamb, K. Fostiropoulos and D. R.

Huffman"SolidC$_{60}$: a new form of carbon," Nature, vol. 347, pp. 354 - 358, 1990.

[6]   H. W. Kroto, J. R. Heath, S. C. O'Brien and R. E. Smalley,"C$_{60}$: Buckminster fullerene," Nature, vol. 318, pp. 162 – 163, 1985.

[7]   P. R. Buseck, S. J. Tsipurskyamd R. Hettich,"Fullerenes from the geological environment," Science, vol. 257, no: 5067, pp. 215-217, 1992.

[8]   B. J. Lynch, Y. Zhao, D. G. Truhlar, "Effectiveness of Diffuse Basis Functions for Calculating Relative Energies by Density Functional Theory,' J. Phys. Chem. A. vol. 107, pp. 1384 – 1388, 2003.

[9]   S. Grimme, M. Steinmetz and M. Korth, "How to Compute Isomerization Energies of Organic Molecules with Quantum Chemical Methods," J. Org. Chem. vol. 72, pp. 2118 – 2126, 2007.

[10]   B. C. Thompson, andJ. M. Fréchet,"Polymer–fullerene composite solar cells,"Angewandtechemie international edition, vol. 47, no. 1, pp. 58-77, 2008

[11]   F. Wudl,"Fullerene materials," Journal of Materials Chemistry, vol. 12, no. 7, pp. 1959-1963, 2002.

[12]   V. Parasuk and J. Almlöf, "C$_{20}$: the smallest fullerene?," Chemical physics letters, vol 184, no. 1-3, pp. 187-190, 1991.

[13]   A.S. Claye., N. M. Nemes., A. Jánossy and J. E. Fischer, "Structure and electronic properties of potassium-doped single-wall carbon nanotubes," Phys. Rev. B, vol. 62, pp. 4845-4848, 2000.

[14]   T. Miyake amd S. Saito, "Electronic structure of potassium-doped carbon nanotubes," Phys. Rev. B, vol. 68, Art. no. 155424, 2003.

[15]   J.E. Schirber, D. L. Overmyer, H. H. Wang, J. M. Williams, K. D. Carlson,

A.M. Kini, U. Welp and W. K. Kwok, "Pressure-dependence of the superconducting transition-temperature of potassium fullerene, KXC$_{60}$," Physica C, vol. 178, pp. 137-139, 1991.

[16] M. Kobayashi, Y. Akahama, H. Kawamura, H. Shinohara, H. Sato and Y. Saito, "Structure sequence and possible superconductivity in potassium-doped fullerene C70Kx," Phys. Rev. B, vol. 48, p. 16877, 1993.

[17] J. M. Soler, E. Artacho, J. D. Gale, A. García, J. Junquera, P. Ordejon and D. Sánchez-Portal, "The SIESTA method for ab initio order-N materials simulation," J. Phys. Condens. Matter vol. 14, pp. 2745 – 2749, 2002.

[18] J. P. Perdew, K. Burke andM. Ernzerhof, "Generalized gradient approximation made simple," Phys. Rev. Lett. vol. 77, pp. 3865–3868, 1996.

[19] D. Sankar De, J. A. Flores-Livas, S. Saha, L. Genovese and S. Goedecker, "Stable structures of exohedrally decorated C$_{60}$-fullerenes," Carbon, vol. 129, pp. 847-853, 2018.

[20] Y. F. Wang, Y. Li, Z. R. Li, F. Ma, D. Wu andC. C. Sun, "PerfluorinatedExohedral Potassium-Metallofullerene K...C(n)F(n) (n = 20 or 60): Partial Interior and Surface Excess Electron State," Theor. Chem. Acc. vol. 127, pp. 641–650, 2010.

[21] E. Çalışkan, and S. Göktürk,"Adsorption characteristics of sulfamethoxazole and metronidazole on activated carbon," Separation Science and Technology, vol. 45, no.2, pp. 244-255, 2010.

[22] G. Gereli, Y. Seki,İ. M. Kuşoğlu, and K. Yurdakoç,"Equilibrium and kinetics for the sorption of promethazine hydrochloride onto K10 montmorillonite," Journal of colloid and interface science, vol. 299, no. 1, pp. 155-162, 2006.

Title: On The Existence Conditions for New Kinds of Solutions to (3+1)-Dimensional mKDV
and mBBM Equations

Authors: Hami GÜNDOĞDU, Ömer Faruk GÖZÜKIZIL

New Kinds of Solutions to (3+1)-Dimensional mKDV and mBBM Equations

Hami GÜNDOĞDU[*1], Ömer Faruk GÖZÜKIZIL[2]

Abstract

In this work, we consider (3+1) dimensional nonlinear partial differential equations, namely modified KdV and Benjamin-Bona-Mahony equations. Different types of solutions to these equations are derived by Jacobi elliptic sine function expansion method. Besides that, we introduce new types of solutions for two more modified forms of given equations. The gained solutions include exact, singular, periodic, and kink solutions. It is stated that some conditions related to the coefficients provide us with the existence of the gained solutions.

Keywords: Elliptic sine function method, (3+1)-Dimensional mKdV equation, (3+1)-Dimensional mBBM Equation

1. INTRODUCTION

Nonlinear partial differential equations, shortly NLPDEs, have a substantial space in most branches of science and engineering. They have helped us by describing scientific problems in nonlinear optics, solid-state physics, plasma waves, fluid mechanics, chemical kinematics, plasma physics and some other areas. In these fields, a considerable amount of information can be gathered if travelling wave solutions of NLPDEs are obtained. These solutions allow us to understand distinct types of scientific events, not been explained yet. In the literature, it is generally seen that (1+1) and (2+1) dimensional NLPDEs have been studied by researchers. Moreover, many methods have been discovered to acquire the exact solutions to these kinds of NLPDEs. The tanh-coth method [1], the tanh-sech method [2], the sech-csch method [3], the modified extended tanh-function method [4], the sine-cosine method [5], generalized hyperbolic function method [6], the (G'/G) expansion method [7], the exp-function method [8], and Jacobi elliptic function expansion method [9] can be given as examples of numerical, analytical and theoretical methods. Eventually, it is possible to gain the solutions of NLPDEs by using one of these methods.

---

[*]Corresponding Author: hamigundogdu@sakarya.edu.tr
[1] Sakarya University, Department of Mathematics, 54187, Serdivan, Turkey.
ORCID: https://orcid.org/0000-0002-7042-1885
[2] Sakarya University, Department of Mathematics, 54187, Serdivan, Turkey.
E-Mail: farukg@sakarya.edu.tr ORCID: https://orcid.org/0000-0002-5975-6430

In some models, the encountered problems may not be represented by (1+1) or (2+1) dimensional NLPDEs. Yet, they may be modelled by (3+1) or higher dimensional equations. Under these circumstances, getting solutions of NLPDEs is not straightforward. There is a fact that (3+1) dimensional equations symbolize real-world problems. Therefore, it encourages scientists to pay more attention to these types of equations. In addition to (3+1) dimensional ones, higher dimensional NLPDEs is quite attractive for not only physicists but also mathematicians.

We examine, in this work, modified KdV(mKdV) and modified Benjamin-Bona-Mahony (mBBM) equations which have considerable importance in (1+1) dimensional equations. Moreover, these NLPDEs make data available and convenient to use in some substantial areas such as fluid mechanics, solitary waves, electro-dynamics and so on. The famous KdV equation was introduced in [10] as in the following:

$$u_t + uu_x + u_{xxx} = 0. \tag{1}$$

This equation has been used for modelling shallow water waves of small amplitude and large wavelength. In addition to that, some important physical, chemical and even biological events, for instance, acoustic solitons in plasma, blood pressure pulses and internal gravity waves have modelled by equation (1).

Having an important role to describe some significant scientific models lead scientists to do more works on KdV equation. That is why Benjamin, Bona and Mahony come up with the regularized long-wave equation, also called BBM equation as an alternative to equation (1). BBM equation is given in [11] by

$$u_t + u_x + uu_x - u_{xxt} = 0. \tag{2}$$

It is seen that there is a slight difference between equation (1) and (2). u_{xxx} is replaced by $-u_{xxt}$. The equation (2) has been used to analyze the surface waves of large wavelength in liquids, acoustic gravity waves, incompressible fluids and anharmonic crystals, hydromagnetic waves in cold plasma and some others.

In the literature, modified forms of the equations, mentioned above, have been given by

$$u_t + u^2 u_x + u_{xxx} = 0, \tag{3}$$

and

$$u_t + u_x + u^2 u_x - u_{xxt} = 0. \tag{4}$$

The equations given in (3) and (4) are called modified KdV (mKdV) and modified BBM (mBBM) equations, respectively. There are numerous studies on mKdV and mBBM equations. The existence of the solutions, exact solutions by many methods, new solitary solutions, approximate explicit solutions of these equations, and more examples can be found in the open literature.

(3+1) dimensional NLPDEs are of plenty improvements in most fields of modern sciences. Therefore, a great deal of equations in this dimension have been considered and analyzed. Moreover, Hereman [12] have introduced the (3+1) dimensional mKdV equation in the following form:

$$u_t + 6u^2 u_x + u_{xyz} = 0. \tag{5}$$

In the same manner, two types of mKdV equations have been given in [13] as follows:

$$u_t + 6u^2 u_y + u_{xyz} = 0, \tag{6}$$

and

$$u_t + 6u^2 u_z + u_{xyz} = 0. \tag{7}$$

Introducing new kinds of (3+1) dimensional mKdV equation has provided Wazwaz with the motivation for bringing new types of (3+1) mBBM equation. As a result,

$$u_t + u_x + u^2 u_y - u_{xzt} = 0, \tag{8}$$

$$u_t + u_z + u^2 u_x - u_{xyt} = 0, \tag{9}$$

and

$$u_t + u_y + u^2 u_z - u_{xxt} = 0 \tag{10}$$

have been presented in the same paper.

Our purpose is to derive different types of solutions to (3+1) dimensional equations given in (5) and (8) under the conditions that they exist. Jacobi elliptic sine function expansion method (sn-ns method), proposed by Liu et al. [14], is used to achieve our aim. Because, this method is one of the most respectable methods, see its efficiency [15]-[18]. This method gives the singular solution, periodic solution, exact solution and kink solution.

2. MAIN PRINCIPLES OF THE METHOD

In this chapter, the fundamental principles of the method have been given. With the help of this method, we have looked for the travelling wave solutions of (3+1) dimensional nonlinear partial differential equation given in the general form

$$P\left(u, u_t, u_x, u_y, u_z, u_{xy}, u_{xzt}, \ldots\right) = 0. \tag{11}$$

Firstly, the wave transformation for (3+1) dimension is considered as follows:

$$u(x, y, z, t) = v(\xi), \ \xi = \alpha x + \beta y + \gamma z - \omega t, \tag{12}$$

where α, β, γ are arbitrary constants and ω stands for the dispersion relation.

Then, putting the ordinary derivatives of $v(\xi)$ instead of the partial derivatives of $u(x,y,z,t)$ turns (11) into the following ordinary differential equation(ODE) with respect to the variable ξ as in the following:

$$Q(v, v', v'', \ldots) = 0, \tag{13}$$

with Q being a polynomial with respect to functions v, v', v'',...

In this method, the travelling wave solutions to (13) are investigated in the following form:

$$v(\xi) = a_0 + \sum_{j=1}^{n} a_j sn^j\left(\xi \mid m\right) + b_j ns^j\left(\xi \mid m\right) \tag{14}$$

where n, the balancing constant, is desired positive parameter, sn is the Jacobi elliptic *sine* function and ns represents the inverse of sn. In (13), equating the power of highest-order of linear and nonlinear terms to each other gives n.

Putting (14) into the equation (13) offers an equation in the power of sn and ns. All the coefficients of the same power of sn and ns in the resulting equation are collected. After that, these coefficients should be equal to zero. Therefore, it provides us with a system of algebraic equations involving the parameters, a_k, b_k, $(k = 0,\ldots,n)$ and ω. Solving the algebraic system yields the desired parameters. Then, putting these parameters into (14) gives the analytic solutions, depended in the variable ξ, in a closed-form. Then, putting the wave transformation $\xi = \alpha x + \beta y + \gamma z - \omega t$ back into the solutions in (14) gives us the desired solutions.

3. SOLUTIONS OF (3+1) MKDV AND MBBM EQUATIONS

Our purpose is to obtain the solutions of different types of (3+1) mKdV and mBBM equations given in (5)-(10) in this section. In this regard, the method mentioned above has been applied to these equations, respectively.

3.1. Solutions of mKdV Equations

We consider the mKdV equations given in (5)-(7). Firstly, we obtain the solutions of equation (5). Using the transformations in (12) turns the equation (5) into the following ODE:

$$-\omega v' + 6\alpha v^2 v' + \alpha\beta\gamma v''' = 0. \tag{15}$$

Taking integration of the equation (15) and considering the integration constant as zero yields the following equation:

$$-\omega v + 2\alpha v^3 + \alpha\beta\gamma v'' = 0. \tag{16}$$

It can be rewritten as follows:

$$v'' - (\frac{w}{\alpha\beta\gamma})v + (\frac{2}{\beta\gamma})v^3 = 0. \tag{17}$$

It has the form of Duffing Equation with $p = -\frac{w}{\alpha\beta\gamma}$, $q = \frac{2}{\beta\gamma}$ and $r = 0$.

Now, we are to determine the balancing constant n. For this purpose, we equalize the highest order of linear term and the highest power of the nonlinear term. Then, it gives $n = 1$.

Afterwards, the solution is taken in the following form:

$$v(\xi) = a_0 + \sum_{j=1}^{1} a_j sn^j\left(\xi \mid m\right) + b_j ns^j\left(\xi \mid m\right) \tag{18}$$

or

$$v(\xi) = a_0 + a_1 sn\left(\xi \mid m\right) + b_1 ns\left(\xi \mid m\right) \tag{19}$$

Inserting $v(\xi)$ into the equation (17) yields the following algebraic system:

$sn^2 : 3a_0 a^2_1 q = 0,$

$sn^1 : a^3_1 q + 2k^2 m^2 a_1 = 0,$

$sn^0 : 3a^2_1 b^2_1 q + 3a^2_0 a_1 b_1 - k^2 m^2 a_1 b_1 - k^2 a_1 b_1 + pa_1 b_1 = 0,$

$ns^1 : 6a_0 a_1 b_1 q + a^3_0 q + a_0 p = 0,$

$ns^2 : b^3_1 q + 2k^2 b_1 = 0.$

Solving this system, we obtain the following unknown parameters:

$a_0 = 0, a_1 = \pm\frac{m\sqrt{-2p}}{\sqrt{(m^2 + 6m + 1)q}}, b_1 = \pm\frac{\sqrt{-2p}}{\sqrt{(m^2 + 6m + 1)q}}, k = \frac{\sqrt{p}}{\sqrt{(m^2 + 6m + 1)}},$

$a_0 = 0, a_1 = \pm\frac{m\sqrt{-2p}}{\sqrt{(m^2 - 6m + 1)q}}, b_1 = \pm\frac{\sqrt{-2p}}{\sqrt{(m^2 - 6m + 1)q}}, k = \frac{\sqrt{p}}{\sqrt{(m^2 - 6m + 1)}},$

$a_0 = 0, a_1 = \pm\frac{m\sqrt{-2p}}{\sqrt{(m^2 + 1)q}}, b_1 = 0, k = \frac{\sqrt{p}}{\sqrt{(m^2 + 1)}},$

$a_0 = 0, a_1 = 0, b_1 = \pm\frac{m\sqrt{-2p}}{\sqrt{(m^2 + 1)q}}, k = \frac{\sqrt{p}}{\sqrt{(m^2 + 1)}}.$

Inserting these coefficients in the expansion (18) gives us the solutions in the following forms:

$$v_1(\xi) = \pm\frac{\sqrt{-2p}}{\sqrt{(m^2 + 6m + 1)q}}[msn(\frac{\sqrt{p}}{\sqrt{(m^2 + 6m + 1)}}\xi, m) + ns(\frac{\sqrt{p}}{\sqrt{(m^2 + 6m + 1)}}\xi, m)],$$

$$v_2(\xi) = \pm\frac{\sqrt{-2p}}{\sqrt{(m^2 - 6m + 1)q}}[msn(\frac{\sqrt{p}}{\sqrt{(m^2 - 6m + 1)}}\xi, m) + ns(\frac{\sqrt{p}}{\sqrt{(m^2 - 6m + 1)}}\xi, m)],$$

$$v_3(\xi) = \pm\frac{m\sqrt{-2p}}{\sqrt{(m^2 + 1)q}}sn(\frac{\sqrt{p}}{\sqrt{(m^2 + 1)}}\xi, m),$$

$$v_4(\xi) = \pm\frac{m\sqrt{-2p}}{\sqrt{(m^2 + 1)q}}ns(\frac{\sqrt{p}}{\sqrt{(m^2 + 1)}}\xi, m).$$

In order to get the exact solutions, we let $m \to 1$. We therefore have

$$v_1(\xi) = \pm\sqrt{\frac{-2p}{q}}\coth(k\xi, m), \ k = \sqrt{\frac{p}{2}},$$

$$v_2(\xi) = \pm\sqrt{\frac{2p}{q}}\text{csch}(k\xi, m), \ k = \sqrt{-p},$$

$$v_3(\xi) = \pm\sqrt{\frac{-p}{q}}\tanh(k\xi, m), \ k = \sqrt{\frac{p}{2}},$$

where $p = -\frac{w}{\alpha\beta\gamma}$ and $q = \frac{2}{\beta\gamma}$.

To be specific, we take $k = \pm 1$. Then, we have the following solutions:

$u_1(x,y,z,t) = \pm\sqrt{-\beta\gamma}\coth(\alpha x + \beta y + \gamma z + 2\alpha\beta\gamma t),$

$u_2(x,y,z,t) = \pm\sqrt{-\beta\gamma}\cot(\alpha x + \beta y + \gamma z - 2\alpha\beta\gamma t),$

$u_3(x,y,z,t) = \pm\sqrt{-\beta\gamma}\text{csch}(\alpha x + \beta y + \gamma z - \alpha\beta\gamma t),$

$u_4(x,y,z,t) = \pm \sqrt{-\beta\gamma} \csc(\alpha x + \beta y + \gamma z + \alpha\beta\gamma t),$

$u_5(x,y,z,t) = \pm \sqrt{-\beta\gamma} \tanh(\alpha x + \beta y + \gamma z + 2\alpha\beta\gamma t),$

$u_6(x,y,z,t) = \pm \sqrt{-\beta\gamma} \tan(\alpha x + \beta y + \gamma z - 2\alpha\beta\gamma t).$

Under the condition of $\beta\gamma < 0$, the above solutions exist. Furthermore, u_1, u_3 and u_4 provide us with singular solutions. u_2 is the exact solution. u_6 gives the periodic solution. Eventually, the kink solution is derived from u_5.

Here we obtain the solutions of equation (6). Using the wave transformation we have

$$-\omega v' + 6\beta v^2 v' + \alpha\beta\gamma v''' = 0. \qquad (20)$$

Integrating it and considering the integration constant as zero yields the following equation:

$$-\omega v + 2\beta v^3 + \alpha\beta\gamma v'' = 0. \qquad (21)$$

From the same process above, we gain the solutions for the equation (6) as follows:

$u_1(x,y,z,t) = \pm \sqrt{-\alpha\gamma} \coth(\alpha x + \beta y + \gamma z + 2\alpha\beta\gamma t),$

$u_2(x,y,z,t) = \pm \sqrt{-\alpha\gamma} \cot(\alpha x + \beta y + \gamma z - 2\alpha\beta\gamma t),$

$u_3(x,y,z,t) = \pm \sqrt{-\alpha\gamma} \operatorname{csch}(\alpha x + \beta y + \gamma z - \alpha\beta\gamma t),$

$u_4(x,y,z,t) = \pm \sqrt{-\alpha\gamma} \csc(\alpha x + \beta y + \gamma z + \alpha\beta\gamma t),$

$u_5(x,y,z,t) = \pm \sqrt{-\alpha\gamma} \tanh(\alpha x + \beta y + \gamma z + 2\alpha\beta\gamma t),$

$u_6(x,y,z,t) = \pm \sqrt{-\alpha\gamma} \tan(\alpha x + \beta y + \gamma z - 2\alpha\beta\gamma t).$

These solutions exist for $\alpha\gamma < 0$. For equation (6), exact solution, periodic solution, kink solution, and the singular solutions are acquired.

Now we look for the solutions to the last equation (7) of mKDV equations. Using the wave transformation we have

$$-\omega v + 2\gamma v^3 + \alpha\beta\gamma v'' = 0. \qquad (22)$$

Following the same process above gives the desired solutions for the equation (7) as follows:

$u_1(x,y,z,t) = \pm \sqrt{-\alpha\beta} \coth(\alpha x + \beta y + \gamma z + 2\alpha\beta\gamma t),$

$u_2(x,y,z,t) = \pm \sqrt{-\alpha\beta} \cot(\alpha x + \beta y + \gamma z - 2\alpha\beta\gamma t),$

$u_3(x,y,z,t) = \pm \sqrt{-\alpha\beta} \operatorname{csch}(\alpha x + \beta y + \gamma z - \alpha\beta\gamma t),$

$u_4(x,y,z,t) = \pm \sqrt{-\alpha\beta} \csc(\alpha x + \beta y + \gamma z + \alpha\beta\gamma t),$

$u_5(x,y,z,t) = \pm \sqrt{-\alpha\beta} \tanh(\alpha x + \beta y + \gamma z + 2\alpha\beta\gamma t),$

$u_6(x,y,z,t) = \pm \sqrt{-\alpha\beta} \tan(\alpha x + \beta y + \gamma z - 2\alpha\beta\gamma t).$

These solutions exist in the case of $\alpha\beta < 0$. Here we obtain different kinds of solutions to equation (7) such as exact solution, periodic solution, kink solution, and singular solutions.

3.2. Solutions of mBBM Equations

We consider the mBBM equation (8) and two more alternative forms of mBBM equation given in (9) and (10).

At first, we consider the mBBM equation (8). By using the transformation

$$-\omega v' + \alpha v' + \beta v^2 v' + \alpha\gamma\omega v''' = 0. \tag{23}$$

Integrating both sides of the equation (23) and taking the integration constant as zero satisfies the following equation:

$$-\omega v + \alpha v + (\beta/3)\, v^3 + \alpha\beta\gamma v''' = 0. \tag{24}$$

We can rewrite the equation (24) as follows:

$$v'' + \left(\frac{\alpha - w}{\alpha\gamma w}\right)v + \frac{\beta}{3\alpha\gamma w}v^3 = 0. \tag{25}$$

It is in the form of Duffing Equation with $p = \dfrac{\alpha - w}{\alpha\gamma w}$, $q = \dfrac{\beta}{3\alpha\gamma w}$, and $r = 0$.

It is seen that mKdv and mBBm equations have similar structures. As a result, the procedure given above can be certainly followed here, as well. At the end of some calculations, we gain the desired solutions of the different forms of mBBM equation (8), (9), and (10).

For the equation (8), we have the following solutions:

$$u_1(x,y,z,t) = \pm\frac{\alpha}{\beta}\sqrt{-\frac{6\beta\gamma}{1+2\alpha\gamma}}\coth(\alpha x + \beta y +$$

$$\gamma z - \frac{\alpha}{1+2\alpha\gamma}t),\ \frac{\beta\gamma}{1+2\alpha\gamma} < 0,$$

$$u_2(x,y,z,t) = \pm\frac{\alpha}{\beta}\sqrt{-\frac{6\beta\gamma}{1-2\alpha\gamma}}\cot(\alpha x + \beta y + \gamma z$$

$$-\frac{\alpha}{1-2\alpha\gamma}t),\ \frac{\beta\gamma}{1-2\alpha\gamma} < 0,$$

$$u_3(x,y,z,t) = \pm\frac{\alpha}{\beta}\sqrt{-\frac{6\beta\gamma}{1-\alpha\gamma}}\operatorname{csch}(\alpha x + \beta y + \gamma z$$

$$-\frac{\alpha}{1-\alpha\gamma}t),\ \frac{\beta\gamma}{1-\alpha\gamma} < 0,$$

$$u_4(x,y,z,t) = \pm\frac{\alpha}{\beta}\sqrt{-\frac{6\beta\gamma}{1+2\alpha\gamma}}\csc(\alpha x + \beta y + \gamma z$$

$$-\frac{\alpha}{1+2\alpha\gamma}t),\ \frac{\beta\gamma}{1+2\alpha\gamma} < 0,$$

$$u_5(x,y,z,t) = \pm\frac{\alpha}{\beta}\sqrt{-\frac{6\beta\gamma}{1+2\alpha\gamma}}\tanh(\alpha x + \beta y +$$

$$\gamma z - \frac{\alpha}{1+2\alpha\gamma}t),\ \frac{\beta\gamma}{1+2\alpha\gamma} < 0,$$

$$u_6(x,y,z,t) = \pm\frac{\alpha}{\beta}\sqrt{-\frac{6\beta\gamma}{1-2\alpha\gamma}}\tan(\alpha x + \beta y + \gamma z$$

$$-\frac{\alpha}{1-2\alpha\gamma}t),\ \frac{\beta\gamma}{1-2\alpha\gamma} < 0.$$

For the equation (9), we obtain the following solutions:

$$u_1(x,y,z,t) = \pm\sqrt{-\frac{6\beta\gamma}{1+2\alpha\gamma}}\coth(\alpha x + \beta y + \gamma z -$$

$$\frac{\gamma}{1+2\alpha\gamma}t),\ \frac{\beta\gamma}{1+2\alpha\gamma} < 0,$$

$$u_2(x,y,z,t) = \pm\sqrt{-\frac{6\beta\gamma}{1-2\alpha\gamma}}\cot(\alpha x + \beta y + \gamma z -$$

$$\frac{\gamma}{1-2\alpha\gamma}t),\ \frac{\beta\gamma}{1-2\alpha\gamma} < 0,$$

$$u_3(x,y,z,t) = \pm\sqrt{-\frac{6\beta\gamma}{1-\alpha\gamma}}\operatorname{csch}(\alpha x + \beta y + \gamma z -$$

$$\frac{\gamma}{1-\alpha\gamma}t),\ \frac{\beta\gamma}{1-\alpha\gamma} < 0,$$

$$u_4(x,y,z,t) = \pm \sqrt{-\frac{6\beta\gamma}{1+2\alpha\gamma}} \csc(\alpha x + \beta y + \gamma z - \frac{\gamma}{1+2\alpha\gamma}t), \quad \frac{\beta\gamma}{1+2\alpha\gamma} < 0,$$

$$u_5(x,y,z,t) = \pm \sqrt{-\frac{6\beta\gamma}{1+2\alpha\gamma}} \tanh(\alpha x + \beta y + \gamma z - \frac{\gamma}{1+2\alpha\gamma}t), \quad \frac{\beta\gamma}{1+2\alpha\gamma} < 0,$$

$$u_6(x,y,z,t) = \pm \sqrt{-\frac{6\beta\gamma}{1-2\alpha\gamma}} \tan(\alpha x + \beta y + \gamma z - \frac{\gamma}{1-2\alpha\gamma}t), \quad \frac{\beta\gamma}{1-2\alpha\gamma} < 0.$$

For the equation (10), we gain the following solutions:

$$u_1(x,y,z,t) = \pm \frac{\alpha}{\gamma} \sqrt{-\frac{6\beta\gamma}{1+2\alpha^2}} \coth(\alpha x + \beta y + \gamma z - \frac{\beta}{1+2\alpha^2}t), \quad \frac{\beta\gamma}{1+2\alpha^2} < 0,$$

$$u_2(x,y,z,t) = \pm \frac{\alpha}{\gamma} \sqrt{-\frac{6\beta\gamma}{1-2\alpha^2}} \cot(\alpha x + \beta y + \gamma z - \frac{\beta}{1-2\alpha^2}t), \quad \frac{\beta\gamma}{1-2\alpha^2} < 0,$$

$$u_3(x,y,z,t) = \pm \frac{\alpha}{\gamma} \sqrt{-\frac{6\beta\gamma}{1-\alpha^2}} \csch(\alpha x + \beta y + \gamma z - \frac{\beta}{1-\alpha^2}t), \quad \frac{\beta\gamma}{1-\alpha^2} < 0,$$

$$u_4(x,y,z,t) = \pm \frac{\alpha}{\gamma} \sqrt{-\frac{6\beta\gamma}{1+\alpha^2}} \csc(\alpha x + \beta y + \gamma z - \frac{\beta}{1+\alpha^2}t), \quad \frac{\beta\gamma}{1+\alpha^2} < 0,$$

$$u_5(x,y,z,t) = \pm \frac{\alpha}{\gamma} \sqrt{-\frac{6\beta\gamma}{1+2\alpha^2}} \tanh(\alpha x + \beta y + \gamma z - \frac{\beta}{1+2\alpha^2}t), \quad \frac{\beta\gamma}{1+2\alpha^2} < 0,$$

$$u_6(x,y,z,t) = \pm \frac{\alpha}{\gamma} \sqrt{-\frac{6\beta\gamma}{1-2\alpha^2}} \tan(\alpha x + \beta y + \gamma z - \frac{\beta}{1-2\alpha^2}t), \quad \frac{\beta\gamma}{1-2\alpha^2} < 0.$$

The exact, singular, periodic and kink solutions of the mBBM equations (8), (9), and (10) are obtained with the conditions in which they exist.

4. MAIN RESULTS

In our work, some other forms of modified KdV and BBM equations in addition to well-known ones have been investigated. The principal purpose is to acquire different kinds of solutions to these equations. So, we have applied to the Jacobi elliptic sine function expansion method for achieving this goal. Eventually, the solutions are obtained. It is guaranteed the existence of solutions under some conditions, related to the coefficients, α, β and γ.

In [13], Wazwaz obtained the solutions of the equations (5) and (8) by using some methods such as the sech-csch, tanh-coth, the sec-csc and the tan-coth method. For the equations (6), (7), (9) and (10), Wazwaz used the sech-csch and tanh-coth method to get the soliton and the kink solution. In this paper, we have just benefited from the sn-ns method.

In addition to one-dimensional NLPDEs, it is seen that the method is completely applicable, suitable and useful for solving higher order dimensional NLPDEs. This method allows us to get the solutions in different forms of functions such as Jacobi elliptic, hyperbolic and trigonometric functions. Because of this reason, there is no need for using a lot of distinct methods to obtain different types of solutions.

The Declaration of Conflict of Interest/ Common Interest

No conflict of interest or common interest has been declared by the authors.

Authors' Contribution

All authors have contributed to studying and writing of the manuscript equally.

The Declaration of Ethics Committee Approval

This study does not require ethics committee permission or any special permission.

The Declaration of Research and Publication Ethics

The authors of the paper declare that they comply with the scientific, ethical and quotation rules of SAUJS in all processes of the paper and that they do not make any falsification on the data collected. In addition, they declare that Sakarya University Journal of Science and its editorial board have no responsibility for any ethical violations that may be encountered and that this study has not been evaluated in any academic publication environment other than Sakarya University Journal of Science.

REFERENCES

[1] A. Wazwaz, "The extended tanh method for new solitons solutions for many forms of the fifth-order KdV equations," *Appl. Math. Comput.* Vol. 184, pp.1002-1014, 2007.

[2] A. Wazwaz, "New travelling wave solutions of different physical structures to generalized BBM equation," *Phys. Lett. A.* Vol. 355, pp.358-362, 2006.

[3] A. Wazwaz and M. A. Helal, "Non-linear variants of the BBM equation with compact and noncompact physical structures," *Chaos. Solitons. Fractals.* Vol. 26, pp.767-776, 2005.

[4] S. Elwakil, K. El-Labany, A. Zahran, and R. Sabry, "Modified extended tanh-function method for solving nonlinear partial differential equations," *Phys. Lett. A.* Vol. 299, pp.179-88, 2002.

[5] C. T. Yan, "A simple transformation for nonlinear waves," *Phys. Lett. A.* Vol. 224, pp. 77-84, 1996.

[6] T. Gao, and B. Tian, "Generalized hyperbolic-function method with computerized symbolic computation to construct the solitonic solutions to nonlinear equations of mathematical physics," *Comput. Phys. Commun.* Vol. 133, pp. 158-164, 2001.

[7] M. Wang, X. Li, and J. Zhang, "The (G'/G)- expansion method and travelling wave solutions of nonlinear evolution equations in mathematical physics," *Phys. Lett. A.* Vol. 372, pp. 417-423, 2008.

[8] J. He and L. Zhang, "Generalized solitary solution and compacton-like solution of the Jaulent-Miodek equations using the Exp-function method," *Phys. Lett. A.* Vol. 371, pp. 1044-1047, 2008.

[9] H. Gündogdu and Ö. F. Gözükızıl, "Solving Benjamin-Bona-Mahony equation by using the sn-ns method and the tanh-coth method," *Math. Morav.*, Vol. 21, pp. 95-103, 2017.

[10] D. J. Korteweg and G. De Vries, "On the change of long waves advancing in a rectangular canal and a new type of long stationary wave," *Phil. Mag.*, Vol. 39, pp. 422-443, 1835.

[11] T. B. Benjamin, J. L. Bona, and J. J. Mahony, "Model equations for long waves in nonlinear dispersive systems," *Philos. Trans. R. Soc. London. Ser. A.*, Vol. 272, pp. 47-48, 1972.

[12] W. Hereman, "Shallow water waves and solitary waves, Ecnyclopedis of Complexity and Systems Science," Springer Verlag, Heibelberg, Germany, 2009.

[13] A. Wazwaz, "Exact soliton and kink solutions for new (3+1)-dimensional nonlinear modified equations of wave propagation," *Open. Eng.*, Vol. 7, pp. 169-174, 2017.

[14] S. K. Liu, Z. T. Fu, and S. D. Liu, "Jacobi elliptic function expansion method and periodic wave solutions of nonlinear wave equations,'' *Phys. Lett. A.*, Vol. 289, pp. 69-74, 2001.

[15] H. Gündogdu and Ö. F. Gözükızıl, "On different kinds of solutions to simplified modified form of Camassa-Holm equation,'' J. Appl. Math. & Comput. Mech. Vol. 18, pp. 31-40, 2019.

[16] H. S. Alvaro, "Solving nonlinear partial differential equations by the sn-ns method," *Abstr. Appl. Analysis.*, Vol. 25, pp. 1-25, 2012.

[17] H. Zhang, "Extended Jacobi elliptic function expansion method and its applications," *Commun. Non. Sci. Numer. Simul.*, Vol. 12, pp. 627-635, 2007.

[18] H. Gündogdu and Ö. F. Gözükızıl, "On The New Type Of Solutions To Benney-Luke Equation,'' Bol. Soc. Paran. Mat. doi:10.5269/bspm.41244.

Sakarya University Journal of Science
SAUJS

Title: Solving Bigeometric Volterra Integral Equations by Using Successive Approximations Method

Authors: Nihan GÜNGÖR

Solving Bigeometric Volterra Integral Equations by Using Successive Approximations Method

Nihan GÜNGÖR*1

Abstract

In this study, the successive approximations method has been applied to investigate the solution for the linear bigeometric Volterra integral equations of the second kind in the sense of bigeometric calculus. The conditions to be taken into consideration for the bigeometric continuity and the uniqueness of the solution of linear bigeometric Volterra integral equations of the second kind are researched. Finally, some numerical examples are presented to illustrate successive approximations method.

Keywords: bigeometric calculus, bigeometric Volterra integral equations, successive approximations method.

1. INTRODUCTION

The non-Newtonian calculus comprising of the branches of geometric, harmonic, quadratic, bigeometric, biharmonic and biquadratic calculus introduced and studied by Grossman and Katz [13]. Bigeometric calculus which is one of the most popular non-Newtonian calculus is worked by many researchers. Boruah and Hazarika [2,3] named Bigeometric calculus as G -calculus and investigated basic properties of derivative and integral in the sense of bigeometric calculus and also applications in numerical analysis. Boruah et al. [4] researched solvability of bigeometric differential equations by using numerical methods. Güngör [12] defined Volterra integral equations in the bigeometric calculus and investigated the relationship between bigeometric Volterra integral equations and bigeometric differential equations. For understanding non-Newtonian calculus and especially bigeometric calculus, the reader can find more details in [1-16, 21, 22].

Integral equations have used for the solution of several problems in engineering, pure and applied mathematics and mathematical physics. Volterra integral equations which is solved by using analytical and numerical methods, have an important role in the theory of integral equations.

---

* Corresponding Author: nihangungor@gumushane.edu.tr

1 Gümüşhane University, Faculty of Engineering, Mathematical Engineering Program, Gümüşhane, Turkey. ORCID: https://orcid.org/0000-0003-1235-2700

One can find relevant terminology related to integral equations in [17-20, 23, 24] and also the details of successive approximations method can be found in [17, 19, 20, 24].

A generator is a one-to-one function α whose domain is $\mathbb{R}$ the set of real numbers and whose range is a subset of $\mathbb{R}$. The range of generator α is indicated by $\mathbb{R}_\alpha = \{\alpha(x) : x \in \mathbb{R}\}$. α-arithmetic operations are described as indicated, below:

$\alpha-$ addition $\qquad x \dot{+} y = \alpha\left[\alpha^{-1}(x) + \alpha^{-1}(y)\right]$

$\alpha-$ subtraction $\qquad x \dot{-} y = \alpha\left[\alpha^{-1}(x) - \alpha^{-1}(y)\right]$

$\alpha-$ multiplication $\quad x \dot{\times} y = \alpha\left[\alpha^{-1}(x) \times \alpha^{-1}(y)\right]$

$\alpha-$ division $\qquad x \dot{/} y = \alpha\left[\alpha^{-1}(x) / \alpha^{-1}(y)\right]$

$\alpha-$ order $\qquad x \dot{<} y \Leftrightarrow \alpha^{-1}(x) < \alpha^{-1}(y)$

for $x, y \in \mathbb{R}_\alpha$. $\left(\mathbb{R}_\alpha, \dot{+}, \dot{\times}\right)$ is complete field. In particular, the identity function I generates classical arithmetic and the exponential function generates geometric arithmetic. The numbers $x \dot{>} \dot{0}$ are α-positive numbers and the numbers $x \dot{<} \dot{0}$ are α-negative numbers in $\mathbb{R}_\alpha$. α-zero and α-one numbers are denoted by $\alpha(0) = \dot{0}$ and $\alpha(1) = \dot{1}$, respectively. α-integers are obtained by successive α-addition of $\dot{1}$ to $\dot{0}$ and successive α-subtraction of $\dot{1}$ from $\dot{0}$. Hence the α-integers are as follows:

$$\ldots, \alpha(-2), \alpha(-1), \alpha(0), \alpha(1), \alpha(2), \ldots$$

For each integer n, we set $\dot{n} = \alpha(n)$. If $\dot{n}$ is an α-positive integer, then it is n times sum of $\dot{1}$ [13].

Grosmann and Katz described the $*$-calculus with the help of two arbitrary selected generators. Let α and β are arbitrarily chosen generators and $*$ is the ordered pair of arithmetic (α-arithmetic, β-arithmetic). The following notions are used:

	$\alpha-$ arithmetic	$\beta-$ arithmetic
Realm	$A(\subseteq \mathbb{R}_\alpha)$	$B(\subseteq \mathbb{R}_\beta)$
Summation	$\dot{+}$	$\ddot{+}$
Subtraction	$\dot{-}$	$\ddot{-}$
Multiplication	$\dot{\times}$	$\ddot{\times}$
Division	$\dot{/}$ (or $-\alpha$)	$\ddot{/}$ (or $-\beta$)
Order	$\dot{<}$	$\ddot{<}$

If the generators α and β are chosen as one of I and $\exp$, the following special calculus are obtained:

Calculus	α	β
Classic	I	I
Geometric	I	$\exp$
Anageometric	$\exp$	I
Bigeometric	$\exp$	$\exp$.

The ι (iota) which is an isomorphism from α-arithmetic to β-arithmetic uniquely satisfying the following three properties:

(1) ι is one to one,
(2) ι is on A and onto B,
(3) For any numbers x and y in A,

$$\iota(x \dot{+} y) = \iota(x) \ddot{+} \iota(y),$$
$$\iota(x \dot{-} y) = \iota(x) \ddot{-} \iota(y),$$
$$\iota(x \dot{\times} y) = \iota(x) \ddot{\times} \iota(y),$$
$$\iota(x \dot{/} y) = \iota(x) \ddot{/} \iota(y), \; y \neq \dot{0},$$
$$x \dot{<} y \Leftrightarrow \iota(x) \ddot{<} \iota(y).$$

It turns out that $\iota(x) = \beta\{\alpha^{-1}(x)\}$ for every x in A [13].

2. BIGEOMETRIC CALCULUS

Throughout this study, we will deal with Bigeometric calculus which is the $*$-calculus for which $\alpha = \beta = \exp$ as specified above. In other words, one uses geometric arithmetic on function arguments and values in the bigeometric calculus.

Thereby, we will start by giving the geometric arithmetic and its necessary properties.

If the function exp from $\mathbb{R}$ to $\mathbb{R}^+$ which gives $\alpha^{-1}(x) = \ln x$ is selected as a generator, that is to say that α-arithmetic turns into geometric arithmetic. The range of generator exp is denoted by $\mathbb{R}_{\exp} = \{e^x : x \in \mathbb{R}\}$. The following notions are used:

geometric addition $\quad x \oplus y = \alpha\left[\alpha^{-1}(x) + \alpha^{-1}(y)\right] = e^{(\ln x + \ln y)} = x.y$

geometric subtraction $\quad x \ominus y = \alpha\left[\alpha^{-1}(x) - \alpha^{-1}(y)\right] = e^{(\ln x - \ln y)} = x/y, \ y \neq 0$

geometric multiplication $\quad x \odot y = \alpha\left[\alpha^{-1}(x) \times \alpha^{-1}(y)\right] = e^{(\ln x \times \ln y)} = x^{\ln y}$

geometric division $\quad x \oslash y = \alpha\left[\alpha^{-1}(x) / \alpha^{-1}(y)\right] = e^{(\ln x \div \ln y)} = x^{\frac{1}{\ln y}}, \ y \neq 1$

geometric order $\quad x <_{\exp} y \Leftrightarrow \alpha^{-1}(x) = \ln x < \alpha^{-1}(y) = \ln y$

$\left(\mathbb{R}_{\exp}, \oplus, \odot\right)$ is a field with geometric zero 1 and geometric identity e. The geometric positive real numbers and geometric negative real numbers are denoted by $\mathbb{R}_{\exp}^+ = \{x \in \mathbb{R}_{\exp} : x > 1\}$ and $\mathbb{R}_{\exp}^- = \{x \in \mathbb{R}_{\exp} : x < 1\}$, respectively. Now, we will give some useful and necessary relations between geometric and classical arithmetic operations. The geometric absolute valued of $x \in \mathbb{R}_{\exp}$ defined by

$$|x|_{\exp} = \begin{cases} x & , \ x > 1 \\ 1 & , \ x = 1 \\ 1/x & , \ x < 1. \end{cases}$$

Thus $|x|_{\exp} \geq 1$. For all $x, y \in \mathbb{R}_{\exp}$, the following relations hold:

$x^{2_{\exp}} = x \odot x = x^{\ln x}$ $\qquad \sqrt{x^{2_{\exp}}}^{\exp} = |x|_{\exp}$

$\sqrt{x}^{\exp} = e^{(\ln x)^{1/2}}$ $\qquad x^{p_{\exp}} = x^{\ln^{p-1} x}$

$x^{-1_{\exp}} = e^{\frac{1}{\ln x}}$ $\qquad e^n \odot x = x^n$

$x \odot e = x, \ x \oplus 1 = x \qquad 1 \ominus e \odot (x \ominus y) = y \ominus x$

$|e^x|_{\exp} = e^{|x|}$

$|x \oplus y|_{\exp} \leq_{\exp} |x|_{\exp} \oplus |y|_{\exp} \quad |x \odot y|_{\exp} = |x|_{\exp} \odot |y|_{\exp}$

$|x \ominus y|_{\exp} \geq_{\exp} |x|_{\exp} \ominus |y|_{\exp} \quad |x \oslash y|_{\exp} = |x|_{\exp} \oslash |y|_{\exp}$

[2-4, 13, 15]. The geometric factorial notation $!_{\exp}$ denoted by

$n!_{\exp} = e^n \odot e^{n-1} \odot \ldots \odot e^2 \odot e = e^{n!}$ [2].

Definition 1. Let (x_n) be sequence and x be a point in metric space $\left(\mathbb{R}_{\exp}, |.|_{\exp}\right)$. If for every $\varepsilon >_{\exp} 1$, there exits $n_0 = n_0(\varepsilon) \in \mathbb{N}$ such that $|x_n \ominus x|_{\exp} <_{\exp} \varepsilon$ for all $n \geq n_0$, then it is said that the sequence (x_n) exp-convergent and denoted by $\exp\lim_{n \to \infty} x_n = x$ [22].

Definition 2. Let $f : A \subset \mathbb{R}_{\exp} \to \mathbb{R}_{\exp}$ be a function and $a \in A'^{\exp}$, $b \in \mathbb{R}_{\exp}$. If for every $\varepsilon >_{\exp} 1$ there is a number $\delta = \delta(\varepsilon) >_{\exp} 1$ such that $|f(x) \ominus b|_{\exp} <_{\exp} \varepsilon$ for all $x \in A$ whenever $1 <_{\exp} |x \ominus a|_{\exp} <_{\exp} \delta$, then it is said that the BG-limit function f at the point a is b and it is indicate by $_{BG}\lim_{x \to a} f(x) = b$ or $f(x) \overset{BG}{\to} b$. Here

$$1 <_{\exp} |x \ominus a|_{\exp} <_{\exp} \delta \Rightarrow \frac{a}{\delta} < x < a\delta \qquad \text{and}$$

$$|f(x) \ominus b|_{\exp} <_{\exp} \varepsilon \Rightarrow \frac{b}{\varepsilon} < f(x) < b\varepsilon \ [2,13,15].$$

Definition 3. Let $a \in A$ and $f : A \subset \mathbb{R}_{\exp} \to \mathbb{R}_{\exp}$ be a function. If for every $\varepsilon >_{\exp} 1$ there is a number $\delta = \delta(\varepsilon) >_{\exp} 1$ such that $|f(x) \ominus f(a)|_{\exp} <_{\exp} \varepsilon$ for all $x \in A$ whenever $1 <_{\exp} |x \ominus a|_{\exp} <_{\exp} \delta$, then it is said that f is BG-continuous at point $a \in A$. The function f is BG-continuous at the point $a \in A$ iff this point a is an element of domain of the function f and $_{BG}\lim_{x \to a} f(x) = f(a)$ [2, 13, 15].

Theorem 1. If the function $f : [r, s] \subset \mathbb{R}_{\exp} \to \mathbb{R}_{\exp}$ be BG-continuous, then f is exp-bounded on $[r, s] \subset \mathbb{R}_{\exp}$ [10].

Definition 4. Let $f:(r,s) \subset \mathbb{R}_{\exp} \to \mathbb{R}_{\exp}$ be a function and $a \in (r,s)$. If the following limit

$$_{BG}\lim_{x \to a} \frac{f(x) \ominus f(a)}{x \ominus a} \bigg|_{\exp} = \lim_{x \to a} \left[\frac{f(x)}{f(a)} \right]^{\frac{1}{\ln x - \ln a}}$$

exists, it is indicated by $f^{BG}(a)$ and called the BG-derivative of f at a and say that f is BG-differentiable. If the function f is BG-differentiable at all points of the $\exp$-open interval (r,s), then f is BG-differentiable on (r,s) and BG-derivative of f identified as

$$_{BG}\lim_{h \to 1} \frac{f(x \oplus h) \ominus f(x)}{h} \bigg|_{\exp} = \lim_{h \to 1} \left[\frac{f(hx)}{f(x)} \right]^{\frac{1}{\ln h}}$$

for $h \in \mathbb{R}_{\exp}$ and denoted by f^{BG} or $\dfrac{d^{BG} f}{dx^{BG}}$ [2, 13, 15].

Definition 5. The BG-average of a BG-continuous positive function f on $[r,s] \subset \mathbb{R}_{\exp}$ is defined as the $\exp$-limit of the $\exp$-convergent sequence whose n-th term is geometric average of $f(a_1), f(a_2), \ldots, f(a_n)$ where $a_1, a_2, \ldots, a_n$ is the n-fold $\exp$-partition of $[r,s]$ and denoted by $\overset{BG}{M_r^s} f$. The BG-integral of a BG-continuous function f on $[r,s]$ is the positive number

$$\left[\overset{BG}{M_r^s} f \right]^{[\ln(s) - \ln(r)]} \quad \text{and is denoted by } _{BG}\int_r^s f(x) \, dx^{BG}$$

[3, 13, 15].

Remark 1. If f is BG-continuous positive function on $[r,s] \subset \mathbb{R}_{\exp}$, then

$$_{BG}\int_r^s f(x) \, dx^{BG} = \exp\left(\int_{\ln(r)}^{\ln(s)} \ln f(e^t) \, dt \right),$$

i.e., the BG-integral of the function f is defined by

$$_{BG}\int_r^s f(x) \, dx^{BG} = e^{\int_r^s \frac{\ln f(x)}{x} dx}$$

[3, 13, 15].

Theorem 2. If f and g are BG-continuous positive functions on $[r,s] \subset \mathbb{R}_{\exp}$ and λ, μ are arbitrary constants, then

(1) $_{BG}\int_r^s \big(\lambda \odot f(x) \oplus \mu \odot g(x) \big) dx^{BG}$

$$= \lambda \odot {}_{BG}\int_r^s f(x) \, dx^{BG} \oplus \mu \odot {}_{BG}\int_r^s g(x) \, dx^{BG}$$

(2) $_{BG}\int_r^s \big(f(x) \big)^\lambda dx^{BG} = \left({}_{BG}\int_r^s f(x) \, dx^{BG} \right)^\lambda$

(3) $_{BG}\int_r^s f(x) \, dx^{BG} = {}_{BG}\int_r^t f(x) \, dx^{BG} \oplus {}_{BG}\int_t^s f(x) \, dx^{BG}$

where $r <_{\exp} t <_{\exp} s$

(4) $\left| {}_{BG}\int_r^s f(x) \, dx^{BG} \right|_{\exp} \leq_{\exp} {}_{BG}\int_r^s \big| f(x) \big|_{\exp} dx^{BG}$

[10, 13, 15].

Theorem 3. *(First fundamental theorem of BG-calculus)* If f is BG-continuous on $[r,s] \subset \mathbb{R}_{\exp}$ and $g(x) = {}_{BG}\int_r^x f(x) \, dx^{BG}$ for every $x \in [r,s]$, then $g^{BG} = f$ on $[r,s]$ [13, 15].

Theorem 4. *(Second fundamental theorem of BG-calculus)* If f^{BG} is BG-continuous on $[r,s] \subset \mathbb{R}_{\exp}$, then

$$_{BG}\int_r^s f^{BG}(x) \, dx^{BG} = f(s) \ominus f(r) \quad [13, 15].$$

Definition 6. Let A be a nonempty subset of $\mathbb{R}_{\exp}$ and let $n \in \mathbb{N}$. The sequence $(f_n) = (f_1, f_2, \ldots, f_n, \ldots)$ is called BG-function sequence for functions $f_n : A \subseteq \mathbb{R}_{\exp} \to \mathbb{R}_{\exp}$. Here all functions defined on same set. The

sequence $f_n(x_0)$ is exp-sequence in $\mathbb{R}_{\exp}$ for each $x_0 \in A$ [21].

Definition 7. Let the BG-function sequence (f_n) where $f_n : A \subseteq \mathbb{R}_{\exp} \to \mathbb{R}_{\exp}$. The BG-function sequence (f_n) BG-uniform converges to the function f on the set A, if for any given $\varepsilon >_{\exp} 1$, there exists a naturel number n_0 depends on number ε but not depend on variable x such that $\left| f_n(x) \ominus f(x) \right|_{\exp} <_{\exp} \varepsilon$ for all $n > n_0$ and each $x \in A$. We denote BG-uniform convergence by $\underset{n\to\infty}{_{BG}\lim} f_n = f$ $(BG-\text{uniform})$ or $f_n \overset{BG}{\to} f$ $(BG-\text{uniform})$ [21].

Definition 8. Let the BG-function sequence (f_n) with $f_n : A \subseteq \mathbb{R}_{\exp} \to \mathbb{R}_{\exp}$. The infinite exp-sum $\underset{\exp}{\sum_{n=1}^{\infty}} f_n = f_1 \oplus f_2 \oplus \cdots \oplus f_n \oplus \cdots$ is called BG-function series. The exp-sum $S_n = \underset{\exp}{\sum_{k=1}^{n}} f_k$ is called n-th partial exp-sum of the series $\underset{\exp}{\sum_{n=1}^{\infty}} f_n$ for $n \in \mathbb{N}$ [21].

Definition 9. Let the BG-function series $\underset{\exp}{\sum_{n=1}^{\infty}} f_n$ with $f_n : A \subseteq \mathbb{R}_{\exp} \to \mathbb{R}_{\exp}$ and the function $f : A \subseteq \mathbb{R}_{\exp} \to \mathbb{R}_{\exp}$ be given. If the partial exp-sums sequence (S_n) where $S_n = \underset{\exp}{\sum_{k=1}^{n}} f_k$ is BG-uniform convergent to the function f, then $\underset{\exp}{\sum_{n=1}^{\infty}} f_n$ is called BG-uniform convergent to the function f on the set A and $\underset{\exp}{\sum_{n=1}^{\infty}} f_n = f$ $(BG\text{-uniform})$ is written [21].

Theorem 5. *(BG-Weierstrass M-criterion)* If there exist exp-numbers M_n such that $\left| f_n(x) \right|_{\exp} <_{\exp} M_n$ for all $x \in A$ where $f : A \subseteq \mathbb{R}_{\exp} \to \mathbb{R}_{\exp}$ and the series $\underset{\exp}{\sum_{n=1}^{\infty}} M_n$ is exp-convergent, then the series $\underset{\exp}{\sum_{n=1}^{\infty}} f_n$ is BG-uniform convergent and exp-absolutely convergent [21].

Theorem 6. The functions $f_n : A \subseteq \mathbb{R}_{\exp} \to \mathbb{R}_{\exp}$ be BG-continuous and the function $f : A \subseteq \mathbb{R}_{\exp} \to \mathbb{R}_{\exp}$ be given. If $\underset{\exp}{\sum_{n=1}^{\infty}} f_n = f$ $(BG\text{-uniform})$, then the function f is BG-continuous on the set A [21].

Theorem 7. The functions $f_n : [a,b] \subseteq \mathbb{R}_{\exp} \to \mathbb{R}_{\exp}$ be BG-continuous on $[a,b] \subseteq \mathbb{R}_{\exp}$ for all $n \in \mathbb{N}$ and $f_n \overset{BG}{\to} f$ $(BG-\text{uniform})$ on $[a,b] \subseteq \mathbb{R}_{\exp}$. Then the function f is BG-continuous on $[a,b] \subseteq \mathbb{R}_{\exp}$ and $\underset{n\to\infty}{_{BG}\lim} {_{BG}\int_a^b} f_n(x) dx^{BG} = {_{BG}\int_a^b} f(x) dx^{BG}$ [21].

3. SOLVING BY SUCCESSIVE APPROXIMATIONS METHOD

From [12], we know that the equation of an unknown $\mathbb{R}_{\exp}$-valued function $v(x)$ is occurred form as

$$v(x) = f(x) \oplus \left(\lambda \odot {_{BG}\int_1^x} K(x,s) \odot v(s) ds^{BG} \right) \quad (1)$$

where $f(x)$ and $K(x,s)$ are specified $\mathbb{R}_{\exp}$-valued functions and $\lambda \in \mathbb{R}_{\exp}$, is called linear BG-Volterra integral equation of the

second kind. The function $K(x,s)$ is the kernel of BG - Volterra equation.

In this method, the zeroth approximation $v_0(x)$ is identified as

$$v_0(x) = f(x).$$

If we substitute $v_0(x)$ instead of the unknown function $v(x)$ on the right side of the equation (1), then the first approximation $v_1(x)$ is found by

$$v_1(x) = f(x) \oplus \left(\lambda \odot BG \int_1^x K(x,s) \odot v_0(s) ds^{BG} \right).$$

The second approximation is obtained as

$$v_2(x) = f(x) \oplus \left(\lambda \odot BG \int_1^x K(x,s) \odot v_1(s) ds^{BG} \right)$$

by replacing $v_1(x)$ instead of $v(x)$ on right side of the equation (1). By proceeding similarly, the n-th approximation is obtained in the following form:

$$v_n(x) = f(x) \oplus \left(\lambda \odot BG \int_1^x K(x,s) \odot v_{n-1}(s) ds^{BG} \right).$$

That is to say, the approximations can be put in a repeated scheme given by

$$v_0(x) = f(x)$$

$$v_n(x) = f(x) \oplus \left(\lambda \odot BG \int_1^x K(x,s) \odot v_{n-1}(s) ds^{BG} \right),$$
$$n \geq 1. \qquad (2)$$

The successive approximations method gives the exact solution, if it exists, by

$$BG \lim_{n \to \infty} v_n(x) = v(x).$$

Now, we will give the necessary proposition for using the proof of the theorem that answers the question the BG-convergence of $v_n(x)$.

Proposition 1. Let taken

$$\psi_0(x) = f(x)$$

$$\psi_n(x) = BG \int_1^x K(x,s) \odot \psi_{n-1}(s) ds^{BG}, \ n \geq 1. \qquad (3)$$

If $f(x)$ is BG-continuous for $1 \leq_{\exp} x \leq_{\exp} a$ and $K(x,s)$ is BG-continuous for $1 \leq_{\exp} x \leq_{\exp} a$ and $1 \leq_{\exp} s \leq_{\exp} x$, then the series

$$\exp \sum_{n=0}^{\infty} \lambda^{n_{\exp}} \odot \psi_n(x) \qquad (4)$$

is BG-uniform convergent and $\exp$-absolutely convergent.

Proof. Since $f(x)$ is BG-continuous for $1 \leq_{\exp} x \leq_{\exp} a$, there is $m \geq_{\exp} 1$ such that

$$|f(x)|_{exp} \leq_{\exp} m \qquad (5)$$

on $1 \leq_{\exp} x \leq_{\exp} a$. Because of $K(x,s)$ is BG-continuous for $1 \leq_{\exp} x \leq_{\exp} a$ and $1 \leq_{\exp} s \leq_{\exp} x$, there is $M \geq_{\exp} 1$ such that

$$|K(x,s)|_{exp} \leq_{\exp} M \qquad (6)$$

on $1 \leq_{\exp} s \leq_{\exp} x \leq_{\exp} a$. From (5) and (6), we find

$$|\psi_1(x)|_{exp} = \left| BG \int_1^x K(x,s) \odot \psi_0(s) ds^{BG} \right|_{exp}$$

$$= \left| BG \int_1^x K(x,s) \odot f(s) ds^{BG} \right|_{exp}$$

$$\leq_{\exp} BG \int_1^x |K(x,s)|_{exp} \odot |f(s)|_{exp} ds^{BG}$$

$$\leq_{\exp} {}_{BG}\int_1^x M \odot m \, ds^{BG}$$

$$= m \odot M \odot x$$

by replacing $\psi_0(x)$ right side of the equation in (3). Therefore, we obtain

$$\left|\psi_2(x)\right|_{exp} = \left|{}_{BG}\int_1^x K(x,s) \odot \psi_1(s) \, ds^{BG}\right|_{exp}$$

$$\leq_{\exp} {}_{BG}\int_1^x \left|K(x,s)\right|_{exp} \odot \left|\psi_1(s)\right|_{exp} ds^{BG}$$

$$\leq_{\exp} {}_{BG}\int_1^x m \odot M^{2_{\exp}} \odot s \, ds^{BG}$$

$$= m \odot M^{2_{\exp}} \odot \frac{x^{2_{\exp}}}{2!_{\exp}} \exp$$

by replacing $\psi_1(x)$ in (3). In a similar manner, we get

$$\left|\psi_n(x)\right|_{exp} \leq_{\exp} m \odot M^{n_{\exp}} \odot \frac{x^{n_{\exp}}}{n!_{\exp}} \exp$$

for $1 \leq_{\exp} x \leq_{\exp} a$ and $n \in \mathbb{N}$. Consequently,

$$\left|\exp\sum_{n=0}^{\infty} \lambda^{n_{\exp}} \odot \psi_n(x)\right|_{exp} \leq_{\exp} \exp\sum_{n=0}^{\infty} \left|\lambda\right|_{exp}^{n_{\exp}} \odot \left|\psi_n(x)\right|_{exp}$$

$$\leq_{\exp} \exp\sum_{n=0}^{\infty} m \odot \left|\lambda\right|_{exp}^{n_{\exp}} \odot M^{n_{\exp}} \odot \frac{x^{n_{\exp}}}{n!_{\exp}} \exp$$

$$= \exp\sum_{n=0}^{\infty} \frac{m \odot \left|\lambda\right|_{exp}^{n_{\exp}} \odot M^{n_{\exp}}}{n!_{\exp}} \exp \odot x^{n_{\exp}}$$

holds. Let consider the $\exp$-series

$$\exp\sum_{n=0}^{\infty} \frac{m}{n!_{\exp}} \exp\odot\left(\left|\lambda\right|_{\exp}\odot M\right)^{n_{\exp}}.$$

If the rate test is applied as follows

$$\exp\lim_{n\to\infty}\left|\frac{\dfrac{m}{(n+1)!_{\exp}}\exp\odot\left(\left|\lambda\right|_{\exp}\odot M\right)^{(n+1)_{\exp}}}{\dfrac{m}{n!_{\exp}}\exp\odot\left(\left|\lambda\right|_{\exp}\odot M\right)^{n_{\exp}}}\right|_{\exp}$$

$$= \exp\lim_{n\to\infty}\left|\frac{\left|\lambda\right|_{\exp}\odot M}{e^{n+1}}\right|_{\exp}$$

$$= \lim_{n\to\infty} e^{\frac{M^{|\ln\lambda|}}{n+1}} = 1 <_{\exp} e$$

then we can see that the series is $\exp$-convergent. This implies via BG-Weierstrass M-criterion, the $\exp$-series $\exp\sum_{n=0}^{\infty}\lambda^{n_{\exp}}\odot\psi_n(x)$

is BG-uniform convergent and $\exp$-absolutely convergent.

The convergence of $v_n(x)$ will be verified by the following theorem:

Theorem 8. Suppose that the following conditions are satisfied:
(i) $f(x)$ is BG-continuous for $1 \leq_{\exp} x \leq_{\exp} a$,
(ii) $K(x,s)$ is BG-continuous for $1 \leq_{\exp} x \leq_{\exp} a$ and $1 \leq_{\exp} s \leq_{\exp} x$,

then the sequence $v_n(x)$ in (2), converges to solution $v(x)$ of the equation (1), and also the solution $v(x)$ is BG-continuous function on $1 \leq_{\exp} x \leq_{\exp} a$.

Proof. Let taken $v_0(x) = f(x) = \psi_0(x)$. Hence we find

$$v_1(x) = f(x) \oplus \left(\lambda \odot {}_{BG}\int_1^x K(x,s) \odot v_0(s) \, ds^{BG}\right)$$

$$= f(x) \oplus \left(\lambda \odot {}_{BG}\int_1^x K(x,s) \odot f(s) \, ds^{BG}\right)$$

$$= f(x) \oplus \lambda \odot \psi_1(x)$$

where $\psi_1(x) = {}_{BG}\int_1^x K(x,s) \odot \psi_0(s)\,ds^{BG}$. The second approximation $v_2(x)$ is obtained as

$$v_2(x) = f(x) \oplus \left(\lambda \odot {}_{BG}\int_1^x K(x,s) \odot v_1(s)\,ds^{BG} \right)$$

$$= f(x) \oplus \left(\lambda \odot {}_{BG}\int_1^x K(x,s) \odot \left[f(s) \oplus \lambda \odot \psi_1(s) \right] ds^{BG} \right)$$

$$= f(x) \oplus \lambda \odot {}_{BG}\int_1^x K(x,s) \odot f(s)\,ds^{BG} \oplus$$

$$\oplus \lambda^{2_{exp}} \odot {}_{BG}\int_1^x K(x,s) \odot \psi_1(s)\,ds^{BG}$$

$$= f(x) \oplus \lambda \odot \psi_1(x) \oplus \lambda^{2_{exp}} \odot \psi_2(x)$$

where $\psi_2(x) = {}_{BG}\int_1^x K(x,s) \odot \psi_1(s)\,ds^{BG}$.

Proceeding this manner, we get

$$v_n(x) = {}_{exp}\sum_{k=0}^n \lambda^{k_{exp}} \odot \psi_k(x)$$

$$= f(x) \oplus {}_{exp}\sum_{k=1}^n \lambda^{k_{exp}} \odot \psi_k(x).$$

Under the hypothesis, $v_n(x)$ is BG-continuous on $1 \leq_{exp} x \leq_{exp} a$ and also the series ${}_{exp}\sum_{n=0}^\infty \lambda^{n_{exp}} \odot \psi_n(x)$ is BG-uniform convergent by Proposition 1. Therefore there exists a BG-continuous function $v(x)$ such that ${}_{BG}\lim_{n\to\infty} v_n(x) = v(x)$, i.e,

$${}_{exp}\sum_{n=0}^\infty \lambda^{n_{exp}} \odot \psi_n(x) = v(x)$$

by Theorem 6. Now, we need to show $v(x)$ is solution of the equation (1). If the expressions

$$\psi_0(x) = f(x)$$

$$\lambda^{k_{exp}} \odot \psi_k(x) = \lambda^{k_{exp}} \odot {}_{BG}\int_1^x K(x,s) \odot \psi_{k-1}(s)\,ds^{BG}$$

for $k \in \mathbb{N}$, is added side to side, we find

$$\psi_0(x) \oplus_{exp}\sum_{k=1}^n \lambda^{k_{exp}} \odot \psi_k(x) =$$

$$f(x) \oplus \lambda \odot {}_{BG}\int_1^x K(x,s) \odot_{exp}\sum_{k=1}^n \lambda^{(k-1)_{exp}} \odot \psi_{k-1}(s)\,ds^{BG}.$$

As a result of this, we can write

$${}_{exp}\sum_{k=0}^n \lambda^{k_{exp}} \odot \psi_k(x) =$$

$$f(x) \oplus \lambda \odot {}_{BG}\int_1^x K(x,s) \odot_{exp}\sum_{k=0}^{n-1} \lambda^{k_{exp}} \odot \psi_k(s)\,ds^{BG}.$$

If we take BG-limit as $n \to \infty$ on both sides of the equation, we obtain

$$v(x) = f(x) \oplus \lambda \odot$$

$${}_{BG}\int_1^x K(x,s) \odot \left({}_{BG}\lim_{n\to\infty}{}_{exp}\sum_{k=0}^{n-1} \lambda^{k_{exp}} \odot \psi_k(s) \right) ds^{BG}$$

$$= f(x) \oplus \lambda \odot {}_{BG}\int_1^x K(x,s) \odot v(s)\,ds^{BG}$$

by Theorem 7. This completes the proof.

Remark 2. Under the hypothesis of Theorem 8, the series in (4) BG-convergences and equals to solution $v(x)$ of the equation (1). For this reason, the solution of (1) also can be determined by aid of the system (3)-(4).

Theorem 9. Under the hypothesis of Theorem 8, the BG-Volterra integral equation (1) has an unique solution on $[1,a] \subset \mathbb{R}_{exp}$.

Proof. Assume that $v(x)$ and $u(x)$ are different solutions of the equation (1). Then, it is written

$$v(x) = f(x) \oplus \left(\lambda \odot {}_{BG}\int_1^x K(x,s) \odot v(s)\,ds^{BG} \right)$$

$$u(x) = f(x) \oplus \left(\lambda \odot {}_{BG}\int_1^x K(x,s) \odot u(s)\,ds^{BG} \right).$$

If we set $\phi(x) = v(x) \ominus u(x)$, then

$$\left| \phi(x) \right|_{\exp} = \left| \lambda \odot {}_{BG}\int_1^x K(x,s) \odot \phi(s)\,ds^{BG} \right|_{\exp}$$

$$\leq_{\exp} \left| \lambda \right|_{\exp} \odot {}_{BG}\int_1^x \left| K(x,s) \right|_{exp} \odot \left| \phi(s) \right|_{\exp} ds^{BG}$$

$$\leq_{\exp} M \odot \left| \lambda \right|_{\exp} \odot {}_{BG}\int_1^x \left| \phi(s) \right|_{\exp} ds^{BG}$$

from (6). If it is taken

$$h(x) = {}_{BG}\int_1^x \left| \phi(s) \right|_{\exp} ds^{BG} \geq_{\exp} 1, \qquad (7)$$

then we find

$$\left| \phi(x) \right|_{\exp} \leq_{\exp} \left| \lambda \right|_{\exp} \odot M \odot h(x)$$

$$\left| \phi(x) \right|_{\exp} \ominus \left(\left| \lambda \right|_{\exp} \odot M \odot h(x) \right) \leq_{\exp} 1$$

$$h^{BG}(x) \ominus \left(\left| \lambda \right|_{\exp} \odot M \odot h(x) \right) \leq_{\exp} 1$$

from first fundamental theorem of BG-calculus. By multiplication with $e^{x^{-|\ln \lambda| \ln M}}$ both sides of this inequality

$$\left[e^{x^{-|\ln \lambda| \ln M}} \odot h(x) \right]^{BG} \leq_{\exp} 1. \qquad (8)$$

We find

$$e^{x^{-|\ln \lambda| \ln M}} \odot h(x) \leq_{\exp} 1$$

by BG-integration both sides of the inequality (8) according from 1 to x. Thereby, we write

$$h(x) \leq_{\exp} 1 \qquad (9)$$

From (7) and (9) we obtain

$$h(x) = {}_{BG}\int_1^x \left| \phi(s) \right|_{\exp} ds^{BG} = 1.$$

Hence it must be ${}_{BG}\int_1^x \left| \phi(s) \right|_{\exp} ds^{BG} = 1$. Therefore

$$e^{\int_1^x \frac{\ln |\phi(s)|_{\exp}}{s} ds} = 1$$

$$e^{\int_1^x \frac{\ln \phi(s)}{s} ds} = 1$$

$$\int_1^x \frac{\left| \ln \phi(s) \right|}{s} ds = 0.$$

Thus, we find $\dfrac{\ln |\phi(s)|}{s} = 0$ for all $s \in [1,x] \subset \mathbb{R}_{\exp}$, i.e., $\phi(s) = 1$ for all $1 \leq_{\exp} s \leq_{\exp} x$. As a result of this $v(x) = u(x)$ for all $x \in [1,a] \subset \mathbb{R}_{\exp}$.

3.1. Numerical Examples

Example 1. Find the solution of BG-Volterra integral equation

$$v(x) = e \oplus {}_{BG}\int_1^x (s \ominus x) \odot v(s)\,ds^{BG}$$

by aid of the series (4).

Solution. Proceeding with the recurrence relation in (3), that gives

$$\psi_0(x) = e$$

$$\psi_1(x) = {}_{BG}\int_1^x (s \ominus x) \odot \psi_0(s)\,ds^{BG}$$

$$= {}_{BG}\int_1^x (s \ominus x) \odot e\,ds^{BG} = e^{\int_1^x \frac{\ln s - \ln x}{s} ds}$$

$$= e^{-\frac{(\ln x)^2}{2!}} = \left[\left(\left(e^{\ln x} \right)^{\ln x} \right)^{\frac{1}{2!}} \right]^{-1}$$

$$= \left[\left((x)^{\ln x} \right)^{\frac{1}{\ln e^{2!}}} \right]^{-1} = (1 \ominus e) \odot \frac{x^{2_{\exp}}}{2!_{\exp}} \exp$$

$$\psi_2(x) = BG \int_1^x (s \ominus x) \odot \psi_1(x) \, ds^{BG}$$

$$= BG \int_1^x (s \ominus x) \odot \left((1 \ominus e) \odot \frac{s^{2_{\exp}}}{2!_{\exp}} \exp \right) ds^{BG}$$

$$= BG \int_1^x (s \ominus x) \odot e^{-\frac{(\ln s)^2}{2}} \, ds^{BG}$$

$$= e^{-\frac{1}{2} \int_1^x \frac{(\ln s)^3 - (\ln s)^2 \ln x}{s} ds}$$

$$= e^{\frac{(\ln x)^4}{4!}} = \frac{x^{4_{\exp}}}{4!_{\exp}} \exp$$

and so on. The solution of the integral equation is obtained as a series form is given by

$$v(x) = e \oplus (1 \ominus e) \odot \frac{x^{2_{\exp}}}{2!_{\exp}} \exp \oplus \frac{x^{4_{\exp}}}{4!_{\exp}} \exp \oplus$$

$$(1 \ominus e) \odot \frac{x^{6_{\exp}}}{6!_{\exp}} \oplus \frac{x^{8_{\exp}}}{8!_{\exp}} \oplus \cdots$$

$$= e \oplus {}_{\exp} \sum_{n=1}^{\infty} (1 \ominus e)^{n_{\exp}} \odot \frac{x^{(2n)_{\exp}}}{(2n)!_{\exp}} \exp$$

$$= e \oplus {}_{\exp} \sum_{n=1}^{\infty} \psi_n(x)$$

and the closed form by

$$v(x) = e^{\cos \ln x}$$

obtained upon using the geometric Taylor expansion for $e^{\cos \ln x}$.

Example 2. Solve the BG-Volterra integral equation

$$v(x) = x \oplus BG \int_1^x (s \ominus x) \odot v(s) \, ds^{BG}$$

by using successive approximations method.

Solution. Taking the zero approximation as

$$v_0(x) = x .$$

Substituting this equality into $v(x)$ under the BG-integral in the iteration formula (2), we find the first approximation as

$$v_1(x) = x \oplus BG \int_1^x (s \ominus x) \odot s \, ds^{BG}$$

$$= x \oplus e^{\int_1^x \left(\frac{\ln s \ln \frac{s}{x}}{s} \right) ds} = x \oplus e^{\int_1^x \left(\frac{\ln^2 s - \ln s \ln x}{s} \right) ds}$$

$$= x \oplus e^{-\frac{\ln^3 x}{6}} = x \ominus \frac{x^{3_{\exp}}}{3!_{\exp}} \exp .$$

Then, we find the second approximation as

$$v_2(x) = x \oplus BG \int_1^x (s \ominus x) \odot \left(s \ominus \frac{s^{3_{\exp}}}{3!_{\exp}} \exp \right) ds^{BG}$$

$$= x \oplus e^{\int_1^x \left(\frac{(\ln s - \ln x)\left(\ln s - \frac{\ln^3 s}{6} \right)}{s} \right) ds}$$

$$= x \oplus e^{\int_1^x \left(\frac{\ln^2 s - \frac{\ln^4 s}{6} - \ln x \ln s + \ln x \frac{\ln^3 s}{6}}{s} \right) ds}$$

$$= x \ominus e^{-\frac{\ln^3 x}{6} + \frac{\ln^5 x}{60}} = x \ominus e^{\frac{\ln^3 x}{3!}} \oplus e^{\frac{\ln^5 x}{5!}}$$

$$= x \ominus \frac{x^{3_{\exp}}}{3!_{\exp}} \exp \oplus \frac{x^{5_{\exp}}}{5!_{\exp}} \exp .$$

Proceeding the same manner we get the n-th approximation by

$$v_n(x) = x \ominus \frac{x^{3_{\exp}}}{3!_{\exp}} \exp \oplus \frac{x^{5_{\exp}}}{5!_{\exp}} \exp \oplus \cdots$$

$$\oplus (1 \ominus e)^{n_{\exp}} \odot \frac{x^{(2n+1)_{\exp}}}{(2n+1)!_{\exp}} \exp$$

for $n \geq 1$. Since the function $v_n(x)$ is n-th partial $\exp$-sum of the series

$$\exp \sum_{n=0}^{\infty} (1 \ominus e)^{n_{\exp}} \odot \frac{x^{(2n+1)_{\exp}}}{(2n+1)!_{\exp}} \exp = e^{\sin \ln x}$$

this implies that $_{BG}\lim_{n \to \infty} v_n(x) = e^{\sin \ln x}$. As a result, the solution is obtained by $v(x) = e^{\sin \ln x}$.

By using the relation bigeometric and classic calculus, we can find the iterations with Maple as follows:

```
>  k:=9;  lambda:=exp(1);  u0:=x->  x;
a:=1; f:=x->x;K:=(x,t)->t/x;
> for n from 1 to k do
  u||n:=f(x)*(exp(1)^(ln(lambda)*in
t((1/t)*ln(K(x,t))*ln(u||(n-
1)(t)),t=a..x)))assuming x>1;
  u||n:=unapply(f(x)*(exp(1)^(ln(la
mbda)*int((1/t)*ln(K(x,t))*ln(u||(n
-1)(t)),t=a..x))),x)assuming   x>1;
od;
```
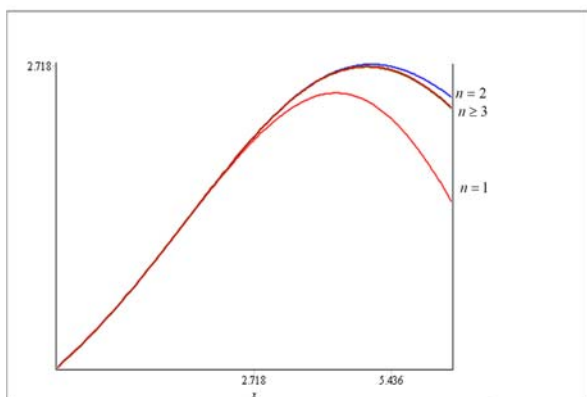

Here, we plot the successive approximations. In this figure, n is the number of iterations performed.

4. CONCLUSION

In this paper, the successive approximations method is constructed in the bigeometric calculus. The exact solution of linear bigeometric Volterra integral equations of the second kind is presented by using this analytical method. Also, we get the result that the solution of the linear bigeometric Volterra equation of the second kind can be found by aid of the series which is obtained in Proposition 1. Moreover, the necessary conditions for the bigeometric continuity and uniqueness of the solution of these equations are given. Finally, some applications are presented to explain the procedure of solutions of these equations by using these methods and how to find the approximations by using Maple are expressed.

The Declaration of Conflict of Interest/ Common Interest

No conflict of interest or common interest has been declared by the author.

The Declaration of Ethics Committee Approval

This work does not require ethics committee permission or any special permission.

The Declaration of Research and Publication Ethics

The author of the paper declares that she complies with the scientific, ethical and quotation rules of SAUJS in all processes of the paper and that she does not make any falsification on the data collected. In addition, she declares that Sakarya University Journal of Science and its editorial board have no responsibility for any ethical violations that may be encountered, and that this study has not been evaluated in any academic publication

REFERENCES

[1] D. Aniszewska and M. Rybaczuk, "Analysis of the Multiplicative Lorenz System," Chaos Solitons Fractals, vol. 25, pp. 79–90, 2005.

[2] K. Boruah and B. Hazarika, "G-Calculus," TWMS J. Pure Appl. Math., vol. 8, no. 1, pp. 94-105, 2018.

[3] K. Boruah and B. Hazarika, "Bigeometric Integral Calculus," TWMS J. Pure Appl. Math., vol. 8, no. 2, pp. 374-385, 2018.

[4] K. Boruah, B. Hazarika and A. E. Bashirov, "Solvability of Bigeometric Differential Equations by Numerical Methods," Bol. Soc. Parana. Mat., doi: 10.5269/bspm.39444, 2018.

[5] F. Córdova-Lepe, "The Multiplicative Derivative as a Measure of Elasticity in Economics," TEMAT-Theaeteto Antheniensi Mathematica, vol. 2, no.3, 2015.

[6] A.F. Çakmak and F. Başar, "On Line and Double Integrals in the Non-Newtonian Sense," AIP Conference Proceedings, 1611, pp. 415-423, 2014.

[7] A.F. Çakmak and F. Başar, "Certain Spaces of Functions over the Field of Non-Newtonian Complex Numbers," Abstr. Appl. Anal., Article ID 236124, 12 pages, doi:10.1155/2014/236124, 2014.

[8] C. Duyar and O. Oğur, "A Note on Topology of Non-Newtonian Real Numbers," IOSR Journal of Mathematics, vol. 13, no. 6, pp. 11-14, 2017.

[9] C. Duyar and B. Sağır, "Non-Newtonian Comment of Lebesgue Measure in Real Numbers," J. Math, Article ID 6507013, 2017.

[10] M. Erdoğan and C. Duyar, "Non-Newtonian Improper Integrals," Journal of Science and Arts, vol. 1, no. 42, pp. 49-74, 2018.

[11] N. Güngör, "Some Geometric of The Non-Newtonian Sequence Spaces $l_p(N)$," Math. Slovaca, vol. 70, no. 3, pp. 689-696, 2020.

[12] N. Güngör, "BG-Volterra Integral Equations and Relationship with BG-Differential Equations," GÜFBED, vol.10, no.3, pp. 814-829, 2020.

[13] M.Grosmann and R. Katz "Non-Newtonian Calculus," Lee Press, Pigeon Cove Massachussets, 1972.

[14] M. Grosmann, "An Introduction to Non-Newtonian Calculus," International Journal of Mathematical Education in Science and Technology, vol. 10, no. 4, pp. 525-528, 1979.

[15] M. Grosmann, "Bigeometric Calculus: A system with a Scale Free Derivative," 1st ed., Archimedes Foundation, Rockport Massachusetts, 1983.

[16] U. Kadak and M. Özlük, "Generalized Runge-Kutta Methods with Respect to Non-Newtonian Calculus," Abstr. Appl. Anal., Article ID 594685, 2014.

[17] M. Krasnov, K. Kiselev and G. Makarenko, "Problems and Exercises in Integral Equation," Mır Publishers, Moscow, 1971.

[18] W. V. Lovitt, "Linear Integral Equations," Dover Publications Inc., New York, 1950.

[19] M. Rahman, "Integral Equations and Their Applications"(WIT press, Boston, 2007).

[20] R. K. Saeed and K. A. Berdawood, "Solving Two-dimensional Linear Volterra-Fredholm Integral Equations of the Second Kind by Using Successive Approximation Method and Method of Successive Substitutions," ZANCO Journal of Pure and Applied Sciences, vol. 28, no.2, pp. 35-46, 2016.

[21] B. Sağır and F. Erdoğan, "On the Function Sequences and Series in the Non-Newtonian Calculus," Journal of Science and Arts, vol. 4, no. 49, pp. 915-936, 2019.

[22] C. Türkmen and F. Başar, "Some Results on the Sets of Sequences with Geometric Calculus," Commun. Fac. Sci. Univ. Ank. Sér. A1 Math. Stat., vol. 61, no. 2, pp. 17-34, 2012.

[23] V. Volterra and B. Hostinsky, "Opérations Infinitésimales linéares," Herman, Paris, 1938.

[24] A. M. Wazwaz, "Linear and Nonlinear Integral Equations Methods and Applications", Springer Verlag Berlin Heidelberg, 2011.

Title: Auto-Tuning by Using Double Extended Kalman-Bucy Filter: An Application to Dc
Motor for Controlling Speed

Authors: Hakan KIZMAZ

Auto-Tuning by Using Double Extended Kalman-Bucy Filter: An Application to Dc Motor for Controlling Speed

Hakan KIZMAZ[1*]

Abstract

In this study, a modified adaptive control algorithm is proposed and investigated. The algorithm consists of a controller, an estimator and an auxiliary model like in model reference adaptive control strategy. PID controller is used to provide controlling. The controller includes adjustable parameters. Traditional PID controller parameters are usually set to fulfil the reference behaviour criterion. In this study, minimum-time criterion is chosen. Extended Kalman-Bucy estimator is employed for estimating controller parameters to make system behave like auxiliary model. The estimator adjusts the controller parameters so that system output can catch the reference input at minimum time. The study may call as the minimization of the settling time problem. The controller and estimator of the system are operated simultaneously. The achievement of the proposed algorithm is proved by simulation results including a simple dc motor model.

Keywords: DC motor, Extended Kalman-Bucy Filter, parameter estimation, PID control, adaptive control, speed control

1. INTRODUCTION

DC motors have some advantages such as stability, linearity and controllability in point of applicability of various control algorithms. They are also able to demonstrate a high performance [1], [2]. Motion control of DC motors with high accuracy are paid attention manufacturing and industrial applications [3], [4].

Speed control is an important issue for dc and ac motors. Since DC motors could provide an easy speed or position control, they are used in many field where speed and position control are required such as industrial, robotic applications and home appliances [5]–[7].

The most used feedback control technique, PID (Proportional – Integral - Derivative) controller was defined with a formal mathematical rule by C. Minorsky a Russian American engineer in 1922[8]. PID controllers are mostly employed for industrial motor control applications due to their simplicity and efficiency [9]–[16]. However PID

---

[*] Corresponding Author: hakan.kizmaz@batman.edu.tr
[1] Batman University, Department of Engineering, Batman, Turkey, ORCID: https://orcid.org/0000-0001-7680-7191

Hakan KIZMAZ

Auto-Tuning by Using Double Extended Kalman-Bucy Filter: An Application to Dc Motor for Controlling S...

control with non-adaptive coefficient may not ensure acceptable high performance [17], [18]. In control engineering, various modern methods have been developed for dc motors, such as sliding mode control [6], [19], model reference adaptive control [20], observer based robust control [21], intelligent control [5], [22]. Each of them with their original characteristics has been implemented effectively. Adaptive control assures predefined output tracking performance and steady-state accuracy with the system uncertainties [3].

Adjusting the PID controller parameters allows the performance criterion to be maximized according to performance criterion such as minimum-time, minimum-energy etc. Although PID parameters could be adjusted manually, there exist some approaches to adjust the parameters. In [23] Ziegler-Nichols proposed a PID tuning formulation, based on time and frequency response of the system. Åström and Hägglund have a work about auto-tuning intending to simplify the applicability of Ziegler-Nichols method by relay method [24]. Schei proposed a technique for the auto-tuning of PID controllers [25]. Robust PID auto-calibration method is demonstrated in [26]. Poulin et al. presented an adaptive PID controller using an explicit identification with iterative parameter estimation [27].

Kalman filter is widely used estimation algorithm [28], [29]. The filter is able to estimate the states [30]–[32] and parameters [33] of the system by using and processing the sensor measurements. Kalman filter is capable of filtering the measurements of any sensor that may include white noise [34]. In case Kalman-Bucy filter estimates the states of any system and also the parameters of the system, the filter is called Extended Kalman-Bucy filter. The filter requires state-space model of the whole system. Including the controllable system and PID controller, can be combined as an only one system so that Extended Kalman-Bucy filter can be employed and estimate controller parameters.

In this study, an adaptive PID control algorithm is demonstrated. The adaptation of the PID controller parameter is provided by Extended

Kalman-Bucy filter with minimum-time optimization criterion. The proposed algorithm uses the Extended Kalman-Bucy filter as a parameter estimator to adjust the PID parameters. To try out the performance of the algorithm, the permanent magnet dc motor model has been used. Section 2 determine how to model of dc motor as a sample model. Section 3 demonstrates how to obtain combined system including the controller and the system in order to estimator can use. Section 4 explains how to apply the filter to the system. Section 5 includes the simulation results. Section 6 discusses the proposed algorithm in the study.

2. MODELING DC MOTOR

In this study, the dc motor is thought as a controllable object. To perform the controller system simulation, the mathematical model of the motor is required. The schematic diagram of dc motor is shown in Figure 1.
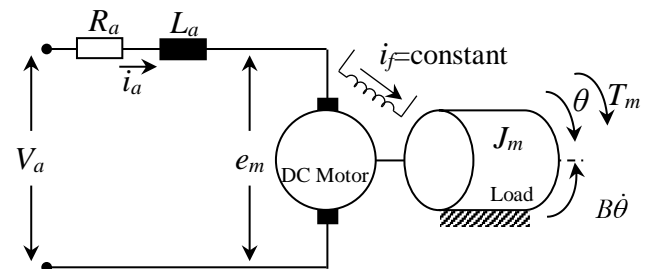
Figure 1. Schematic diagram of dc motor

Describing simulation model of dc motor requires system equations. DC motor model can be composed by following four equations.

The left side of the diagram in Figure 1 presents the armature circuit partition of dc motor. According to Kirchhoff's voltage law,

$$V_a(t) = R_a i_a(t) + L_a \frac{d}{dt} i_a(t) + e_m(t) \tag{1}$$

where V_a is applied voltage, R_a the electrical resistance of the armature circuit, i_a the armature current, L_a the electrical inductance of the armature circuit, e_m the electromotive force. The right side of the diagram presents mechanical partition of dc motor. According to Newton law,

Hakan KIZMAZ

Auto-Tuning by Using Double Extended Kalman-Bucy Filter: An Application to Dc Motor for Controlling S...

$$T_m(t) = J\frac{d}{dt}\omega_r(t) + B\omega_r(t) + T_L(t) \qquad (2)$$

where T_m the motor torque, J the moment of inertia, ω_r the rotor angular speed, B mechanical system damping ratio or the motor viscous friction constant, T_L the load moment. The motor torque T_m has a proportional relation with armature current, i_a, by a coefficient K_a.

$$T_m(t) = K_a i_a(t) \qquad (3)$$

DC motor electromotive force e_m is related to the angular speed ω_r, by coefficient K_b.

$$e_m(t) = K_b\omega_r(t) \qquad (4)$$

Substituting (3) and (4) into (1) and (2), the useful state space equations is obtained as (5) and (6)

$$\frac{d}{dt}\omega_r(t) = -\frac{B}{J}\omega_r(t) + \frac{K_a}{J}i_a(t) - \frac{1}{J}T_L(t) \qquad (5)$$

$$\frac{d}{dt}i_a(t) = -\frac{K_b}{L_a}\omega_r(t) - \frac{R_a}{L_a}i_a(t) + \frac{1}{L_a}V_a(t) \qquad (6)$$

Any linear time-invariant system is explained as follows

$$\dot{\mathbf{x}}(t) = \mathbf{A}\mathbf{x}(t) + \mathbf{B}\mathbf{u}(t) \qquad (7)$$

$$\mathbf{y}(t) = \mathbf{C}\mathbf{x}(t) \qquad (8)$$

where $\mathbf{A}$ the system matrix, $\mathbf{B}$ control input coefficient matrix and $\mathbf{C}$ observing matrix. (5) and (6) can be reformed like linear time invariant equations (7)-(8). Hence the state-space form of the dc motor system is explained as (9)-(10) [35].

$$\begin{bmatrix} \dot{\omega}_r(t) \\ \dot{i}_a(t) \end{bmatrix} = \begin{bmatrix} -\dfrac{B}{J} & \dfrac{K_a}{J} \\ -\dfrac{K_b}{L_a} & -\dfrac{R_a}{L_a} \end{bmatrix} \begin{bmatrix} \omega_r(t) \\ i_a(t) \end{bmatrix} + \begin{bmatrix} -\dfrac{1}{J} & 0 \\ 0 & \dfrac{1}{L_a} \end{bmatrix} \begin{bmatrix} T_L \\ V_a \end{bmatrix} \qquad (9)$$

$$y = \begin{bmatrix} 1 & 0 \end{bmatrix} \begin{bmatrix} \omega_r \\ i_a \end{bmatrix} \qquad (10)$$

3. COMBINED SYSTEM

PID controllers are mostly used in industrial applications due to simplicity and practicability. Here, PID controller is described for a DC motor model. The input of the DC motor is symbolized as V_a. It defines the control voltage applying to the motor and PID controller output signal as well. PID controller is then described as follows:

$$V_a = K_p e(t) + K_i \int e(t)dt + K_d \dot{e}(t) \qquad (11)$$

$$e(t) = \bar{\omega}_r(t) - \omega_r(t) \qquad (12)$$

where V_a the controller output, K_p proportional gain, K_i integral gain, K_d derivative gain, $\bar{\omega}_r$ desired or reference angular speed. ω_r is actual angular speed. $e(t)$ is the angular speed error which consists of the difference between the reference input and system output as seen in (12). Figure 2 demonstrates how to apply a PID controller to a dc motor speed control system. ω_{r_mec} is mechanical angular speed in Figure 2 [36]. The measurement of ω_r is generally performed by encoders or tachometers in practically. As a mechanical magnitude ω_{r_mec} is transformed into electrical magnitude by speed measuring block.

Figure 2. Overall, dc motor control system
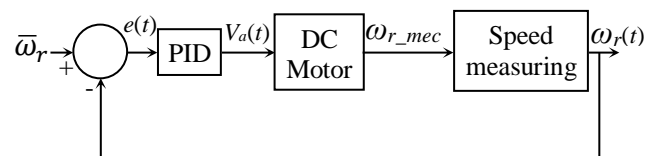
If (11) is substituted into (6), (13) is obtained,

$$\frac{d}{dt}i_a = -\frac{K_b}{L_a}\omega_r - \frac{R_a}{L_a}i_a + \frac{1}{L_a}\begin{bmatrix} K_p e(t) + \\ +K_i \int e(t)dt + \\ +K_d \frac{d}{dt}e(t) \end{bmatrix} \qquad (13)$$

Substituting (12) into (13) demonstrates the combined control system including PID controller and dc motor. The integral of the error $\int e(t)dt$ is

Hakan KIZMAZ

Auto-Tuning by Using Double Extended Kalman-Bucy Filter: An Application to Dc Motor for Controlling S...

deemed as a new state variable of the whole controlled system. Finally combined system, including PID controller and the dc motor, is described by (14)-(15) as a linear time invariant

$$
\frac{d}{dt}\begin{bmatrix} \int e(t)dt \\ \omega_r \\ i_a \end{bmatrix} = \begin{bmatrix} 0 & -1 & 0 \\ 0 & -\dfrac{B}{J} & \dfrac{K_a}{J} \\ \dfrac{K_i}{L_a} & \left[-\dfrac{K_b}{L_a} - \dfrac{K_p}{L_a} + \dfrac{K_d}{L_a}\dfrac{B}{J} \right] & \left[-\dfrac{R_a}{L_a} - \dfrac{K_d}{L_a}\dfrac{K_a}{J} \right] \end{bmatrix}\begin{bmatrix} \int e(t)dt \\ \omega_r \\ i_a \end{bmatrix} + \begin{bmatrix} 0 & 1 & 0 \\ -\dfrac{1}{J} & 0 & 0 \\ \dfrac{K_d}{L_a}\dfrac{1}{J} & \dfrac{K_p}{L_a} & \dfrac{K_d}{L_a} \end{bmatrix}\begin{bmatrix} T_L \\ \bar{\omega}_r \\ \dot{\bar{\omega}}_r \end{bmatrix} \tag{14}
$$

$$
y = \begin{bmatrix} 0 & 1 & 0 \end{bmatrix}\begin{bmatrix} \int e(t)dt \\ \omega_r \\ i_a \end{bmatrix} \tag{15}
$$

4. EXTENDED KALMAN-BUCY FILTER

Richard Bucy and et. al. developed the continuous-time Kalman filter as an unpublished work in John Hopkins Applied Physics Lab. in the late 1950s. Meantime Rudolf Kalman developed the discrete Kalman filter in 1960 [28]. Kalman and Bucy got aware of each other's work in April 1960 and cooperated to the publish of [29]. The work is sometimes called as Kalman-Bucy filter [37].

Kalman-Bucy filter is not widely used in practice owing to inapplicability in digital computers. However, the continuous-time filter provides how to make a state or parameter estimation [34]. In order to estimate the states and parameters of the system simultaneously, the whole system must be extended with parameters and linearized according to states and parameters. This kind of filter is called as Extended Kalman Filter. Here Extended Kalman Filter is going to be employed for estimating the PID parameters, K_p, K_d, K_i existing in (14) as new states of the whole system. Beside load moment T_L is needed to be estimated due to difficulty of measurement. Extended Kalman filter is presented in this study directly. The reader is referred to [28], [34], [37]–[39] for Kalman-Bucy theoretical details.

The continuous-time extended Kalman filter is written as

system. Extended Kalman-Bucy filter needs system state-space model like given below. The filter deems, K_p, K_i, K_d coefficients as system unknown parameters and estimate them.

$$
\dot{\hat{\mathbf{x}}}' = f\left(\hat{\mathbf{x}}', \mathbf{u}'\right) + \mathbf{P}(t)\mathbf{H}^T\mathbf{R}^{-1}\left(\bar{\mathbf{y}} - \mathbf{H}\hat{\mathbf{x}}'\right) \tag{16}
$$

$$
\dot{\mathbf{P}} = \begin{pmatrix} \mathbf{FP} + \mathbf{PF}^T - \\ -\mathbf{PH}^T\mathbf{R}^{-1}\mathbf{HP} + \mathbf{GQG}^T \end{pmatrix} \tag{17}
$$

where $\hat{\mathbf{x}}'$ estimated states vector, $\mathbf{H}$ observer output matrix, $\bar{\mathbf{y}}$ measurable states vector, $\mathbf{P}$ is error covariance matrix. $\mathbf{Q}$ and $\mathbf{R}$ are the system and input white noise variance matrices, respectively.

4.1. Load Moment Estimator

Measuring the load moment of dc motor has difficulties during the dc motor run. Load moment then can be estimated by using estimator. The estimator used here is Extended Kalman-Bucy filter. Unlike the indices in (16) and (17), L is used here as the load moment indice. The load moment estimator equations are then

$$
\dot{\hat{\mathbf{x}}}'_L = f\left(\hat{\mathbf{x}}'_L, \mathbf{u}'_L\right) + \mathbf{P}_L\mathbf{H}_L^T\mathbf{R}_L^{-1}\left(\bar{\mathbf{y}}_L - \mathbf{H}_L\hat{\mathbf{x}}'_L\right) \tag{18}
$$

$$
\dot{\mathbf{P}}_L(t) = \begin{pmatrix} \mathbf{F}_L\mathbf{P}_L + \mathbf{P}_L\mathbf{F}_L^T - \\ -\mathbf{P}_L\mathbf{H}_L^T\mathbf{R}_L^{-1}\mathbf{H}_L\mathbf{P}_L + \mathbf{G}_L\mathbf{Q}_L\mathbf{G}_L^T \end{pmatrix} \tag{19}
$$

Another estimator is used for estimating the PID controller coefficients. Considering the load moment, T_L, in (9) as a parameter of the dc motor, demonstrates (20) as system functions to be used for composing load moment estimator equations.

Hakan KIZMAZ

Auto-Tuning by Using Double Extended Kalman-Bucy Filter: An Application to Dc Motor for Controlling S...

$$\dot{\mathbf{x}}'_L(t) = f\left(\mathbf{x}'_L, \mathbf{u}'_L\right) = \begin{bmatrix} \dfrac{d}{dt}\omega_r(t) = -\dfrac{B}{J}\omega_r(t) + \dfrac{K_a}{J}i_a(t) - \dfrac{T_L(t)}{J} \\ \dfrac{d}{dt}i_a(t) = -\dfrac{K_b}{L_a}\omega_r(t) - \dfrac{R_a}{L_a}i_a(t) + \dfrac{1}{L_a}V_a(t) \\ \dfrac{d}{dt}T_L = w_{T_L} \end{bmatrix} \qquad (20)$$

$$\mathbf{y}_L = \mathbf{H}_L\mathbf{x}'_L + \mathbf{v}_L \qquad (21)$$

where $\mathbf{x}'_L$ the system state vector, w_{T_L} the artificial noise term added to the system so that Kalman filter can modify the estimate of T_L parameter. Moreover $\mathbf{v}_L(t) \in R^{1\times 1}$ is output white noise vector. The $\mathbf{x}'_L$ $\mathbf{u}'_L$ and $\mathbf{H}_L$ is defined as follows

$$\mathbf{x}'_L = \begin{bmatrix} \omega_r \\ i_a \\ T_L \end{bmatrix}, \quad \mathbf{u}'_L = \begin{bmatrix} V_a(t) \\ w_{T_L} \end{bmatrix}, \quad \mathbf{H}_L = \begin{bmatrix} 1 & 0 & 0 \end{bmatrix}$$

The load moment parameter is considered as the new states of the whole control system. It is required to find the partial derivative matrices, first as follows

$$F_L = \dfrac{\partial f\left(\mathbf{x}'_L, \mathbf{u}'_L\right)}{\partial \mathbf{x}'_L}\Bigg|_{\hat{\mathbf{x}}'_L, \mathbf{u}'_L} = \begin{bmatrix} -\dfrac{B}{J} & \dfrac{K_a}{J} & -\dfrac{1}{J} \\ -\dfrac{K_b}{L_a} & -\dfrac{R_a}{L_a} & 0 \\ 0 & 0 & 0 \end{bmatrix}_{\hat{\mathbf{x}}'_L, \mathbf{u}'_L} \qquad (22)$$

$$G_L = \dfrac{\partial f\left(\mathbf{x}'_L, \mathbf{u}'_L\right)}{\partial \mathbf{u}'_L}\Bigg|_{\hat{\mathbf{x}}'_L, \mathbf{u}'_L} = \begin{bmatrix} 0 & 0 \\ \dfrac{1}{L_a} & 0 \\ 0 & 1 \end{bmatrix}_{\hat{\mathbf{x}}'_L, \mathbf{u}'_L} \qquad (23)$$

(22) and (23) are substituted into (19) the equations get run in the estimator algorithm.
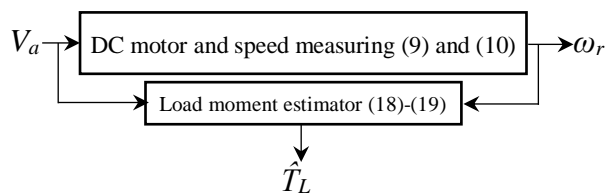
Figure 3. Load moment estimator

4.2. PID Coefficients Estimator

The extended form of the system state functions are defined as (24) - (25). Here $\mathbf{x}'$ the system state vector, w_p, w_i, w_d the artificial noise terms added to the system so that Kalman filter can modify the estimate of PID parameters. Moreover $\mathbf{v}(t) \in R^{2\times 1}$ is output white noise vector. The $\mathbf{x}'$, $\mathbf{u}'$ and $\mathbf{H}$ is defined as follows

$$\hat{\mathbf{x}}' = \begin{bmatrix} \int e(t)dt & \omega_r & i_a & K_p & K_i & K_d \end{bmatrix}$$

$$\mathbf{u}' = \begin{bmatrix} T_L & \bar{\omega}_r & \dot{\bar{\omega}}_r & w_p & w_i & w_d \end{bmatrix}^T$$

$$\mathbf{H} = \begin{bmatrix} 0 & 1 & 0 & 0 & 0 & 0 \\ 0 & 0 & 1 & 0 & 0 & 0 \end{bmatrix}$$

The PID parameters are obviously considered as the new states of the whole control system. It is required to find the partial derivative matrices first as (26) - (27). The $\mathbf{I}$ is identity cubic square matrix. The reason of using Extended Kalman filter is to estimate the controller parameters. However, controller needs a reference rule or criterion. The criterion is chosen as minimum-time criterion. Time-optimized system is used as an auxiliary reference model. The ideal transfer function of reference auxiliary model is expected as a constant. In other words, the settling time of any ideal time-optimized system is supposed to be zero.

Hakan KIZMAZ

Auto-Tuning by Using Double Extended Kalman-Bucy Filter: An Application to Dc Motor for Controlling S...

$$\dot{\mathbf{x}}'(t) = f\left(\mathbf{x}', \mathbf{u}'\right) = \begin{bmatrix} \dfrac{d}{dt}\int e(t)dt = -\omega_r + \bar{\omega}_r \\[2mm] \dfrac{d}{dt}\omega_r = -\dfrac{B}{J}\omega_r + \dfrac{K_a}{J}i_a - \dfrac{1}{J}T_L \\[2mm] \dfrac{d}{dt}i_a = \dfrac{K_i}{L_a}\int e(t)dt + \left[-\dfrac{K_b}{L_a} - \dfrac{K_p}{L_a} + \dfrac{K_d}{L_a}\dfrac{B}{J}\right]\omega_r + \left[-\dfrac{R_a}{L_a} - \dfrac{K_d}{L_a}\dfrac{K_a}{J}\right]i_a + \dfrac{K_d}{L_a}\dfrac{1}{J}T_L + \dfrac{K_p}{L_a}\bar{\omega}_r + \dfrac{K_d}{L_a}\dot{\bar{\omega}}_r \\[2mm] \dfrac{d}{dt}K_p = w_p \\[2mm] \dfrac{d}{dt}K_i = w_i \\[2mm] \dfrac{d}{dt}K_d = w_d \end{bmatrix} \quad (24)$$

$$\mathbf{y} = \mathbf{H}\mathbf{x}' + \mathbf{v} \quad (25)$$

$$\mathbf{F} = \left.\dfrac{\partial f}{\partial \mathbf{x}'}\right|_{\hat{\mathbf{x}}',\mathbf{u}'} = \begin{bmatrix} 0 & -1 & 0 & 0 & 0 & 0 \\[2mm] 0 & -\dfrac{B}{J} & \dfrac{K_a}{J} & 0 & 0 & 0 \\[2mm] \dfrac{K_i}{L_a} & \left[-\dfrac{K_b}{L_a} - \dfrac{K_p}{L_a} + \dfrac{K_d}{L_a}\dfrac{B}{J}\right] & \left[-\dfrac{R_a}{L_a} - \dfrac{K_d}{L_a}\dfrac{K_a}{J}\right] & \left[-\dfrac{1}{L_a}\omega_r + \dfrac{1}{L_a}\bar{\omega}_r\right] & \left[\dfrac{1}{L_a}\int e(t)dt\right] & \left[\dfrac{1}{L_a}\dfrac{B}{J}\omega_r - \dfrac{1}{L_a}\dfrac{K_a}{J}i_a + \dfrac{1}{L_a}\dfrac{1}{J}T_L\right] \\[2mm] 0 & 0 & 0 & 0 & 0 & 0 \\[2mm] 0 & 0 & 0 & 0 & 0 & 0 \\[2mm] 0 & 0 & 0 & 0 & 0 & 0 \end{bmatrix}_{\hat{\mathbf{x}}',\mathbf{u}} \quad (26)$$

$$\mathbf{G} = \left.\dfrac{\partial f}{\partial \mathbf{u}'}\right|_{\hat{\mathbf{x}}',\mathbf{u}'} = \begin{bmatrix} \begin{bmatrix} 0 & 1 & 0 \\[2mm] -\dfrac{1}{J} & 0 & 0 \\[2mm] \dfrac{K_d}{L_a}\dfrac{1}{J} & \dfrac{K_p}{L_a} & \dfrac{K_d}{L_a} \end{bmatrix} & [0]_{3\times3} \\[2mm] [0]_{3\times3} & \mathbf{I}_{3\times3} \end{bmatrix} \quad (27)$$

The input of the auxiliary system is reference angular speed and estimated load moment. According to the DC motor state equations (5)-(6) the derivatives of the state variables become zero when the steady state occurs. From (5) and (6), the equilibrium point elements of the system is considered as $(\bar{\omega}_r, \bar{i}_a)$. The state variables become on equilibrium point on the steady state. The derivatives of the system state vector then become zero. From (5) and (6)

$$0 = -\dfrac{B}{J}\bar{\omega}_r(t) + \dfrac{K_a}{J}\bar{i}_a(t) - \dfrac{T_L(t)}{J}$$

$$\bar{i}_a(t) = \dfrac{B\bar{\omega}_r(t) + T_L(t)}{K_a} \quad (28)$$

Hence, equilibrium point or the output vector of the auxiliary system is defined as

$$\bar{\mathbf{y}} = \left(\bar{\omega}_r, \bar{i}_a\right) = \left(\bar{\omega}_r, \dfrac{B\bar{\omega}_r(t) + T_L(t)}{K_a}\right) \quad (29)$$

(29) demonstrates the outputs of ideal reference auxiliary model. The vector is used in Kalman filter algorithm as $\bar{\mathbf{y}}$ defined before in (16). The controller coefficient estimator takes the outputs of ideal auxiliary model as if they are the measured outputs of system. Thus, the estimator will estimate the controller coefficients based on the behaviour of the reference model. Figure 4 demonstrates the auto-tuning block diagram about how to apply all equations to the control system. The block diagram in the figure includes dc motor model, PID controller, load estimator, auxiliary ideal reference model and Extended Kalman-Bucy controller parameters estimator.
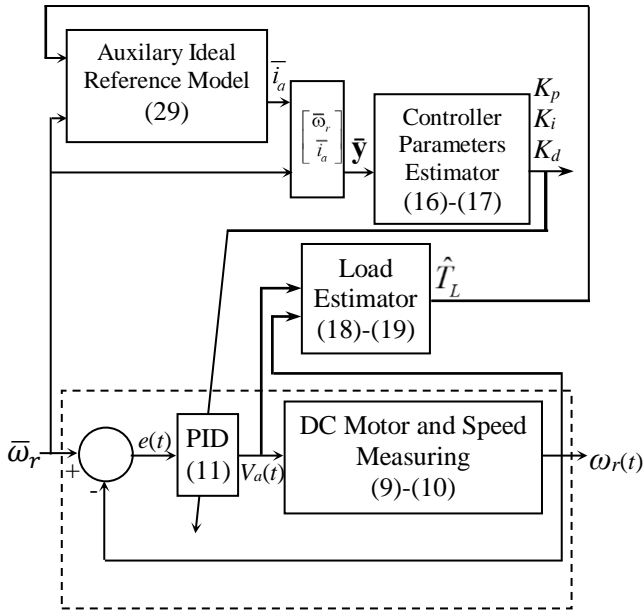
Hakan KIZMAZ

Auto-Tuning by Using Double Extended Kalman-Bucy Filter: An Application to Dc Motor for Controlling S...

Figure 4. Auto-Tuning block diagram using Extended Kalman-Bucy Filter

5. SIMULATION RESULTS

Some illustrative results are presented here related to auto-tuning using Kalman-Bucy algorithm explained in the previous section. Motor model parameters and initial conditions are chosen as below [11].

Voltage supply=110 V	Rated current=10 A
J=0.002215 kg·m^2	B=0.002953 N·m·s
K_b=1.28 V/(rad/s)	K_a=1.28 N·m/A
R_a=11.2 Ω	L_a=0.1215 H

Figure 5 demonstrates the step response of the dc motor. V_a=1 V is applied to motor as an input signal. It seems uncontrolled dc motor does not have an appropriate settling time. The speed of dc motor could be controlled by any controller such as traditional PID controller. The adjustment of PID controller parameters determines how the speed of DC motor behaves until the actual speed reaches the reference speed. Ziegler-Nichols [23] Åström-Hägglund [24] intended to find optimal PID parameters by using the time and frequency response of the system. This study intends to optimize PID parameters online, using extended

Kalman-Bucy filter at the minimum settling time of the speed of DC motor.
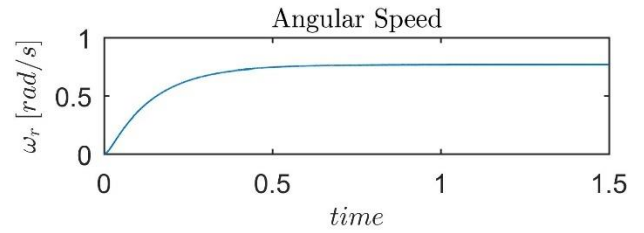
Figure 5. Dc motor step response

DC motor control system in Figure 4 has been simulated in Matlab. The initial conditions and parameters of the Kalman-Bucy filter are given as follows.

$$\hat{\mathbf{x}}'_L(0) = \begin{bmatrix} 0 & 0 & 0 \end{bmatrix}^T,$$

$$\mathbf{Q}_L=\text{diag}([1\ 1]),$$

$$\mathbf{R}_L=1,$$

$$\mathbf{P}_L(0)=\text{diag}([1\ 1\ 10^6]),$$

$$\hat{\mathbf{x}}'(0) = \begin{bmatrix} 0 & 0 & 0 & 0 & 0 & 0 \end{bmatrix}^T,$$

$$\mathbf{Q}=\text{diag}([1\ 1\ 1\ 1\ 1]), \mathbf{R}=\text{diag}([1\ 1]),$$

$$\mathbf{P(0)}= \text{diag}([1\ 1\ 1\ 10^6\ 10^6\ 10^6])$$

The initial states of all controller parameters are in estimate vector $\hat{\mathbf{x}}'(0)$ and chosen as zero.

Step response simulation results of the whole control system is demonstrated in Figure 6. The reference speed $\bar{\omega}_r$ has been chosen as 1 rad/s and applied to the control system at 0.5th second. The actual speed ω_r seems to be settled about in 1 second. Angular speed error graph demonstrates the error between reference speed and actual angular speed. Reference speed and load moment is applied to the rotor simultaneously. The load moment has been chosen as 1 Nm. The algorithm estimates the load moment as well about in 0.5 second. The PID parameters are estimated simultaneously once the algorithm runs.

Hakan KIZMAZ

Auto-Tuning by Using Double Extended Kalman-Bucy Filter: An Application to Dc Motor for Controlling S...

Figure 6. The step response simulation results of dc motor control system for load moment test (T_L= 1 Nm)
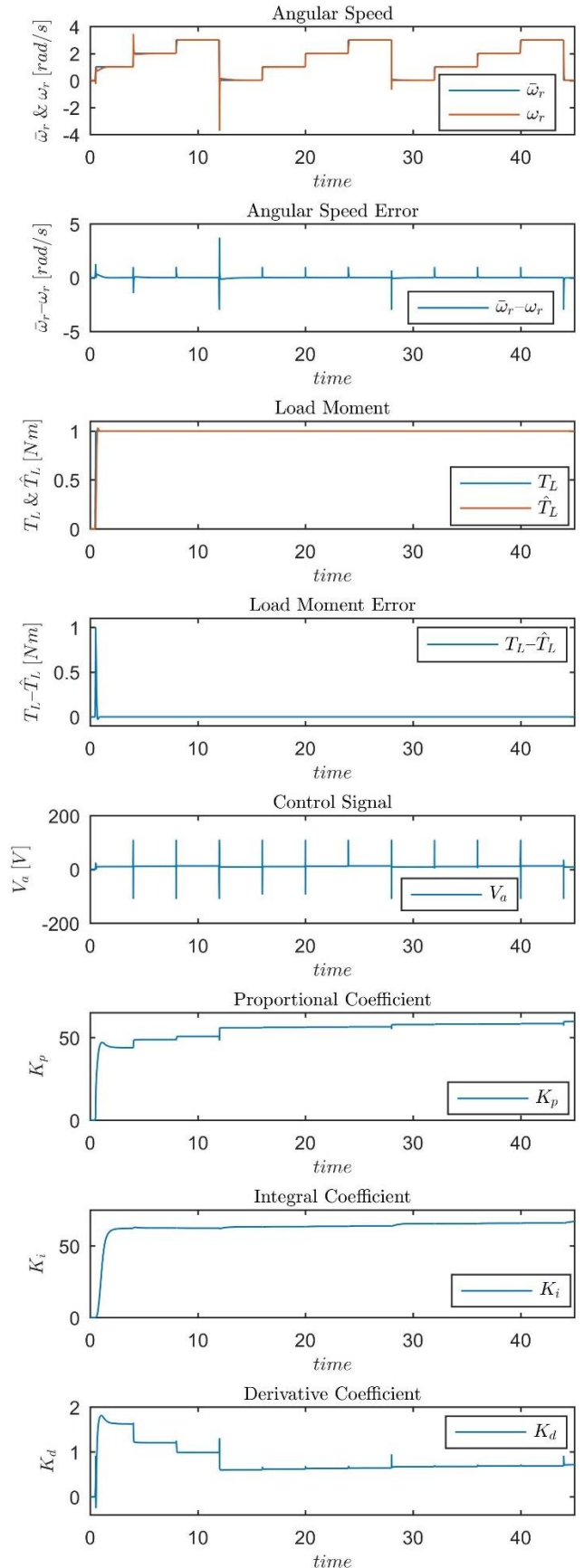
Figure 7. The simulation results with load for varying reference speed in different time intervals

Hakan KIZMAZ

Auto-Tuning by Using Double Extended Kalman-Bucy Filter: An Application to Dc Motor for Controlling S...

Figure 8. The simulation results with constant reference speed in different time intervals

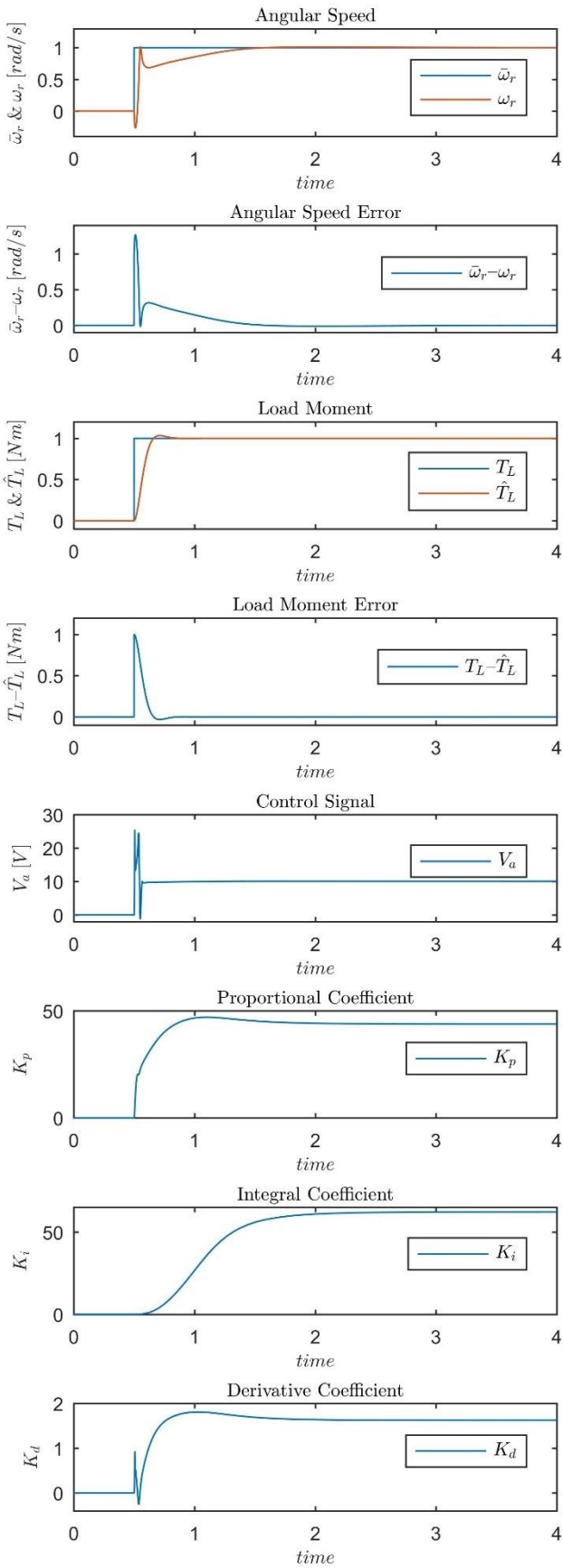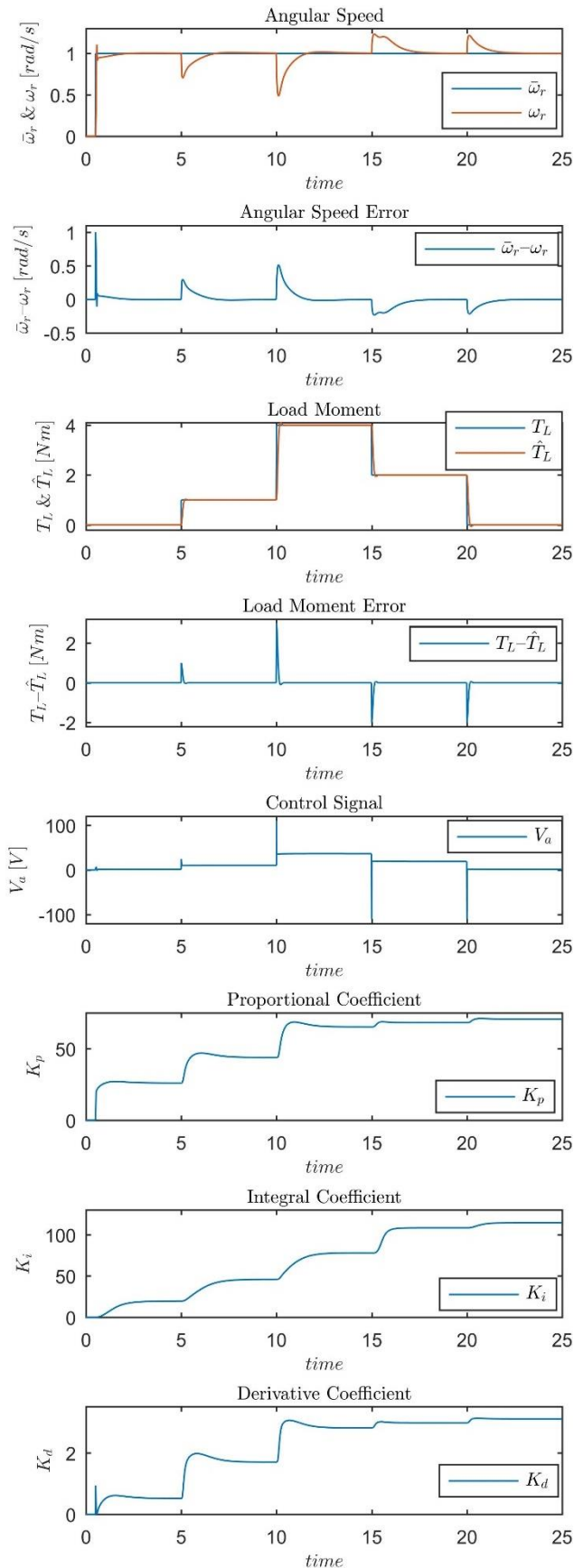Figure 7 demonstrates the simulation results that the reference speed $\bar{\omega}_r$ is taken as different values for different time intervals to examine the robustness of the algorithm. Reference speed $\bar{\omega}_r = 1$ rad/s is applied to the system at the beginning. The reference speed is then changed for every 4 second. The actual speed ω_r seems to be able to converge on the reference speed $\bar{\omega}_r$. Angular speed error graph demonstrates that error decreases over time.

Figure 8 includes the step response results of the control system with applying varying load moment to the rotor. The load moment is T_L=0 Nm at the beginning. Load moment is then increased to 1 Nm at the fifth second. Rotor speed seems to be affected and decreased at that time suddenly. However, the speed then increases to reference speed. After load moment increased, the PID parameters are being adjusted by the Extended Kalman-Bucy algorithm as well. According to error graphs, angular speed and load moment errors decrease over time.

6. CONCLUSION

Traditional PID controllers do not include adaptive parameters. The parameters are tuned by some traditional auto-tuning methods such as aforementioned above. In order the tune the controller, the step response or frequency response of the system which is desired to be controlled, is required. However, in this study, the PID controller is tuned by Extended Kalman-Bucy filter according to optimal time criterion. The estimator does not need the step or frequency response etc. except the system model. The effectiveness of the whole control algorithm showed up in the illustrative simulation results.

The controller may need high power to reach the reference speed in minimum-time according to optimal-time criterion. In such a situation, the auxiliary reference model can be chosen as a simple first order transfer function instead of a constant model. The controller can imitate the behaviour of chosen first order system. The study guides how to employ Extended-Kalman-Bucy filter to obtain model reference adaptive control system.

Hakan KIZMAZ

Auto-Tuning by Using Double Extended Kalman-Bucy Filter: An Application to Dc Motor for Controlling S...

In this paper, as a sample model, DC motor, has been used to test the algorithm. Alternatively, any linear or nonlinear system which is desired to be controlled could be chosen to analysis the algorithm. Especially, Expanded Kalman-Bucy filter is useful for non-linear system control due to linearizable. The technique in this paper, can be applied to another type control techniques such as sliding mode control etc. In addition, it is believed that the method will be more useful in systems with short time constant.

The Declaration of Conflict of Interest/ Common Interest

No conflict of interest or common interest has been declared by the author.

Author's Contribution

The author H.K. contributed 100% to the study about data processing, analysis and interpretation, intellectual/critical arrangements regarding content of the study draft, preparation the work for publication.

The Declaration of Ethics Committee Approval

This study does not require ethics committee permission or any special permission.

The Declaration of Research and Publication Ethics

The author of the paper declares that he complies with the scientific, ethical and quotation rules of SAUJS in all processes of the paper and that he does not make any falsification on the data collected. In addition, he declares that Sakarya University Journal of Science and its editorial board have no responsibility for any ethical violations that may be encountered, and that this study has not been evaluated in any academic publication environment other than Sakarya University Journal of Science.

REFERENCES

[1]   K. V. C. R. V Rajasekhar, "Design and Analysis of DC Motor With PID Controller - A State Space Approach," *ITSI Trans. Electr. Electron. Eng.*, vol. 1, no. 3, pp. 11–14, 2013.

[2]   P. M. Meshram and R. G. Kanojiya, "Tuning of PID Controller using Ziegler-Nichols Method for Speed Control of DC Motor," in *2013 IEEE International Conference on Control Applications (CCA)*, 2012, pp. 117–122.

[3]   Y. Yang, Y. Wang, and P. Jia, "Adaptive robust control with extended disturbance observer for motion control of DC motors," *Electron. Lett.*, vol. 51, no. 22, pp. 1761–1763, 2015, doi: 10.1049/el.2015.1009.

[4]   H. Chu, B. Gao, W. Gu, and H. Chen, "Low-Speed Control for Permanent-Magnet DC Torque Motor Using Observer-Based Nonlinear Triple-Step Controller," *IEEE Trans. Ind. Electron.*, vol. 64, no. 4, pp. 3286–3296, 2017, doi: 10.1109/TIE.2016.2598298.

[5]   O. Prem, "Intelligent Speed Control of DC Servo Motor Drive," pp. 3029–3033, 2018.

[6]   S. Rakhonde and V. Kulkarni, "Sliding mode controller (SMC) governed speed control of DC motor," *2018 3rd IEEE Int. Conf. Recent Trends Electron. Inf. Commun. Technol. RTEICT 2018 - Proc.*, pp. 1657–1662, 2018, doi: 10.1109/RTEICT42901.2018.9012572.

[7]   M. Mallareddy, "Application of Bio

geography based Fractional order PID controller in DC motor drive speed control," 2020.

[8] L. Samir, G. Said, and S. Youcef, "PID Control of DC Servo Motor using a Single Memory Neuron," no. October, pp. 25–27, 2018.

[9] W. G. M. Elnaim and S. F. Babiker, "Comparative study on the speed of DC motor using PID and FLC," in *Proceedings of 2016 Conference of Basic Sciences and Engineering Studies, SGCAC 2016*, 2016, pp. 24–29, doi: 10.1109/SGCAC.2016.7458001.

[10] Y. Ma, Y. Liu, and C. Wang, "Design of parameters self-tuning fuzzy PID control for DC motor," 2010, vol. 2, pp. 345–348, doi: 10.1109/ICINDMA.2010.5538300.

[11] S. K. Suman and V. K. Giri, "Speed Control of DC Motor Using Different Optimization Techniques Based PID Controller," *IEEE Int. Conf. Eng. Technol.*, vol. 2, no. 7, pp. 6488–6494, 2012.

[12] P. A. Adewuyi, "DC Motor Speed Control: A Case between PID Controller and Fuzzy Logic Controller," *Int. J. Multidiscip. Sci. Eng.*, vol. 4, no. 4, pp. 36–40, 2013.

[13] M. Jaiswal and M. P. H. O. D. Ex, "Speed Control of DC Motor Using Genetic Algorithm Based PID Controller," vol. 3, no. 7, pp. 247–253, 2013.

[14] M. D. Amanullah, M. Jain, P. Tiwari, S. Gupta, and G. Kumari, "Optimization of PID Parameter for Position Control of DC-Motor using Multi-Objective Genetic Algorithm," *Int. J. Innov. Res. Electr. Instrum. Control Eng.*, vol. 2, no. 6, pp. 1644–1650, 2014.

[15] B. Hekimoglu, "Optimal Tuning of Fractional Order PID Controller for DC Motor Speed Control via Chaotic Atom Search Optimization Algorithm," *IEEE Access*, vol. 7, pp. 38100–38114, 2019,

doi: 10.1109/ACCESS.2019.2905961.

[16] S. Ekinci, D. Izci, and B. Hekimoğlu, "PID Speed Control of DC Motor Using Harris Hawks Optimization Algorithm," *2020 Int. Conf. Electr. Commun. Comput. Eng.*, vol. 2, no. June, pp. 3–8, 2020, doi: 10.1109/ICECCE49384.2020.9179308.

[17] L. Harnefors, S. E. Saarakkala, and M. Hinkkanen, "Speed control of electrical drives using classical control methods," *IEEE Trans. Ind. Appl.*, vol. 49, no. 2, pp. 889–898, 2013, doi: 10.1109/TIA.2013.2244194.

[18] J. Han, "From PID to active disturbance rejection control," *IEEE Trans. Ind. Electron.*, vol. 56, no. 3, pp. 900–906, 2009, doi: 10.1109/TIE.2008.2011621.

[19] A. Damiano, G. L. Gatto, I. Marongiu, and A. Pisano, "Second-order sliding-mode control of dc drives," *IEEE Trans. Ind. Electron.*, vol. 51, no. 2, pp. 364–373, 2004, doi: 10.1109/TIE.2004.825268.

[20] Y. Shao and J. Li, "Modeling and Switching Tracking Control for a Class of Cart-Pendulum Systems Driven by DC Motor," *IEEE Access*, vol. 8, pp. 44858–44866, 2020, doi: 10.1109/ACCESS.2020.2978269.

[21] J. Yao, Z. Jiao, and D. Ma, "Adaptive robust control of dc motors with extended state observer," *IEEE Trans. Ind. Electron.*, vol. 61, no. 7, pp. 3630–3637, 2014, doi: 10.1109/TIE.2013.2281165.

[22] S. A. Hamoodi, I. I. Sheet, and R. A. Mohammed, "A Comparison between PID controller and ANN controller for speed control of DC Motor," *2nd Int. Conf. Electr. Commun. Comput. Power Control Eng. ICECCPCE 2019*, pp. 221–224, 2019, doi: 10.1109/ICECCPCE46549.2019.203777.

[23] N. Y. R. J.G. Ziegler, N.B. Nichols, "Optimum Settings for Automatic

Controller," *Trans. A.S.M.E*, pp. 759–768, 1942, doi: 10.1115/1.2899060.

[24]   K. J. Åström and T. Hägglund, "Automatic Tuning of Simple Regulators with Specificaiotns on Phase and Amplitude Margins," *Automatica*, vol. 20, no. 5, pp. 645–651, 1984.

[25]   T. S. Schei, "A method for closed loop automatic tuning of PID controllers," *Automatica*, vol. 28, no. 3, pp. 587–591, 1992, doi: 10.1016/0005-1098(92)90182-F.

[26]   A. A. Voda and I. D. Landau, "A method for the auto-calibration of PID controllers," *Automatica*, vol. 31, no. 1, pp. 41–53, 1995, doi: 10.1016/0005-1098(94)00067-S.

[27]   É. Poulin, A. Pomerleau, A. Desbiens, and D. Hodouin, "Development and evaluation of an auto-tuning and adaptive PID controller," *Automatica*, vol. 32, no. 1, pp. 71–82, 1996, doi: 10.1016/0005-1098(95)00105-0.

[28]   R. E. Kalman, "A new approach to linear filtering and prediction problems," *Trans. ASME-Journal Basic Eng.*, vol. 82, no. Series D, pp. 35–45, 1960, doi: 10.1115/1.3662552.

[29]   R. E. Kalman and R. S. Bucy, "New results in linear filtering and prediction theory," *J. Basic Eng.*, vol. 83, no. 1, pp. 95–108, 1961, doi: 10.1115/1.3658902.

[30]   P. Deshpande and A. Deshpande, "Inferential control of DC motor using Kalman Filter," *2012 2nd Int. Conf. Power, Control Embed. Syst.*, pp. 1–5, 2012, doi: 10.1109/ICPCES.2012.6508056.

[31]   A. Khalid and A. Nawaz, "Sensor less control of DC motor using Kalman filter for low cost CNC machine," *2014 Int. Conf. Robot. Emerg. Allied Technol. Eng.*, pp. 180–185, 2014, doi: 10.1109/iCREATE.2014.6828362.

[32]   Z. Aydogmus and O. Aydogmus, "A comparison of artificial neural network and extended Kalman filter based sensorless speed estimation," *Measurement*, vol. 63, pp. 152–158, 2015, doi: 10.1016/j.measurement.2014.12.010.

[33]   A. H. Z. Farnaz, H. S. Sajith, P. J. Binduhewa, M. P. B. Ekanayake, and B. G. L. T. Samaranayake, "Low cost torque estimator for DC servo motors," *2015 IEEE 10th Int. Conf. Ind. Inf. Syst. ICIIS 2015 - Conf. Proc.*, pp. 187–192, 2016, doi: 10.1109/ICIINFS.2015.7399008.

[34]   G. M. Siouris, *An Engineering Approach to Optimal Control and Estimation Theory*. New York: John Wiley & Sons, 1996.

[35]   P. C. Krause, O. Wasynczuk, and S. D. Sudhoff, *Analysis of Electric Machinery and Drive Systems*, 2nd ed. New York: John Wiley & Sons, 2002.

[36]   A. A. A. El-Gammal and A. A. El-Samahy, "Adaptive Tuning of a PID Speed Controller for DC Motor Drives Using Multi-Objective Particle Swarm Optimization," in *Uksim 2009: Eleventh International Conference on Computer Modelling and Simulation*, 2009, pp. 398–404.

[37]   D. Simon, *Optimal State Estimation: Kalman, H∞, and Nonlinear Approaches*. New Jersey, 2006.

[38]   R. F. Stengel, *Optimal control and estimation*. New York: Dover Publications, 1994.

[39]   J. L. Crassidis and J. L. Junkins, *Optimal estimation of dynamic systems*. New York: CRC Press, 2004.

Sakarya University Journal of Science
SAUJS

Title: Comparison of Polyol and Hydrothermal Methods for Synthesis of Zinc Oxide Nanoparticles

Authors: Elif ERÇARIKCI, Murat ALANYALIOĞLU

Comparison of Polyol and Hydrothermal Methods for Synthesis of Zinc Oxide Nanoparticles

Elif ERÇARIKCI[1], Murat ALANYALIOĞLU[*2]

Abstract

Zinc oxide (ZnO) is an inorganic semiconductor compound with a direct band gap of 3.3 eV and is mainly used as additive in many technological applications such as cosmetic, food, and cement. The functionality of ZnO strongly depends on the particle size, crystallinity, and shape. In this work, ZnO nanoparticles (ZnONPs) were prepared using two different routes: polyol and hydrothermal processes. The products were compared using scanning electron microscopy, transmission electron microscopy, X-Ray diffraction, Fourier transform infrared spectroscopy, and UV-Vis. absorption spectroscopy techniques. Additionally, hydrothermal method was performed at three temperature values of 100, 120, and 150 ºC and the effect of temperature on the hydrothermal synthesis of ZnONPs was also discussed in this study.

Keywords: ZnO, polyol method, hydrothermal method.

1. INTRODUCTION

Metal oxide nanoparticles are important materials for many technological applications like cement, cosmetic, food, and dyeing. Because the most of metal oxides demonstrate a semiconductor property, they are preferred as dopant to produce batteries [1-3], supercapacitors [4,5], sensors [6,7], solar cells [8,9], membranes [7,10] and so on.

Zinc oxide (ZnO) absorbs sunlight efficiently and it is especially preferred for solar cell applications [8,9] as well as TiO_2. The quality parameters such as crystallinity, particle size, and shape of ZnO are required to be controlled for such applications. There are various techniques to synthesize zinc oxide nanoparticles (ZnONPs) in the literature

e.g. atomic layer deposition [3,11], electrodeposition [12], thermal evaporation [13], sol-gel [14], and precipitation [15] methods.

Complicated devices and specialty are not essential for precipitation method. Hence, this method is in prevalent use. To adjust the physical, optical, and electrical properties of ZnONPs, precipitation can be applied using various approaches such as polyol [16] and hydrothermal [17] procedures, in which high temperature is applied using reducing agents and stabilizers.

In this study, ZnONPs were synthesized using both polyol and hydrothermal procedures and their morphological, crystallographic, chemical, and optical properties were compared as well as

[1] Ataturk University, Faculty of Science, Erzurum, Turkey.
ORCID: https://orcid.org/0000-0002-8490-1644 E-Mail: elif.ercarikci@atauni.edu.tr
[*]Corresponding Author: malanya@atauni.edu.tr
[2] Ataturk University, Faculty of Science, Erzurum, Turkey. ORCID: https://orcid.org/0000-0002-2223-7303

the influence of temperature on the hydrothermal process.

2. EXPERIMENTAL SECTION

All reagents were of analytical grade and all synthetic procedures were applied in aqueous solutions using ultrapure water. For the synthesis of ZnONPs by polyol method, 30 mL of diethylene glycol (DEG) solution including 4.0 mM poly(vinyl)pyrrolidone (PVP) was prepared at room temperature. $Zn(CH_3COO)_2 \cdot 6H_2O$ was added into this solution to a final concentration of 0.1 M and heated to 180 °C. Distilled water was injected into the solution at a constant rate of 1 ml/s. The mixture has started to become milky due to precipitation of ZnONPs. The precipitation was supplied for 30 min while temperature was kept constant at 180 ºC. Thus, the suspension was allowed to reach room temperature, ZnONPs were filtrated, cleaned with ethanol and distilled water, respectively, and then dried overnight at room temperature [16]. This product was quoted as ZnONPs-po

Hydrothermal synthesis of ZnONPs was accomplished by the following procedure [17]. 5 mL of 1.0 M KOH solution was added to 25 mL of DEG under magnetic stirring. 10 mL of 0.4 M $Zn(NO_3)_2 \cdot 6H_2O$ and 0.59 g of hexadecyl trimethylammonium bromide (CTAB) was also inserted into this solution and then stirred for 10 min. This dispersion was placed into autoclave and heated at different constant temperature values of 100, 120 and 150 °C for 3 h to investigate the effect of temperature on the formation of ZnONPs. When the precipitation reactions were finished, the suspensions were cooled at room temperature. The white ZnONPs powders were separated by filtration, cleaned with ethanol and distilled water, respectively, and dried overnight at room temperature. These precipitates were named as ZnONPs-ht

In these synthesis procedures, DEG was used as reducing agent, while PVP and CTAB were serving as stabilizer role to confine the particle size of ZnO. For the characterization of produced ZnONPs, morphological, optical, chemical, and crystallographic analyses were performed.

Morphological information was collected using Zeiss scanning electron microscopy(SEM) and Hitachi transmission electron microscopy (TEM). Optical and chemical analysis of the ZnONPs were provided by Shimadzu UV-Vis. spectrophotometer and Perkin-Elmer Fourier transform infrared (FTIR) system. The samples were prepared as KBr pellets for FTIR analysis. Crystallographic information of the samples were collected using Rigaku brand X-ray diffraction instrument.

3. RESULTS AND DISCUSSION

Morphological characterization of the synthesized ZnONPs was performed using SEM and TEM techniques. Fig. 1.a shows SEM image of ZnONPs-po with a very large ball-shaped view. The particle size of ZnONPs-po ranges between 400 nm and 2 µm.
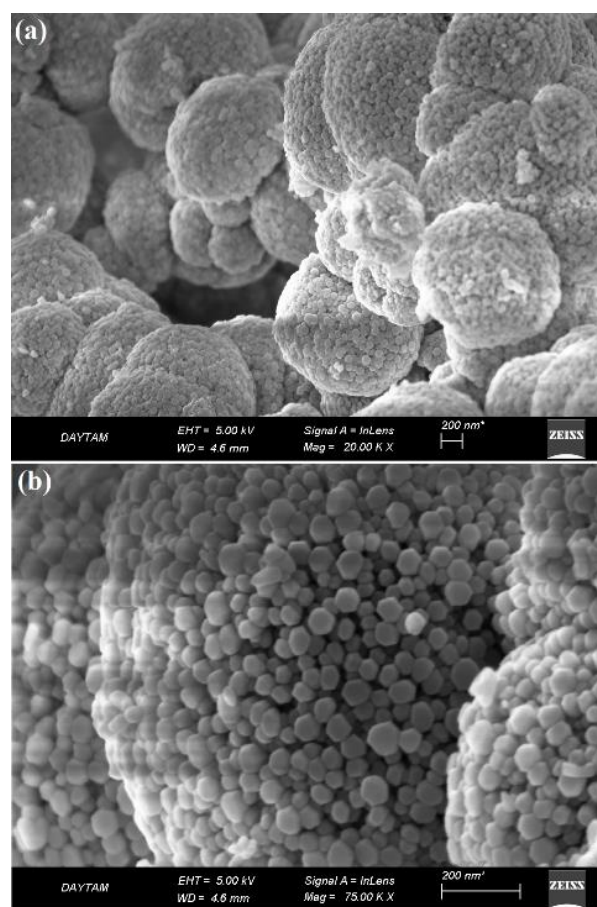
Figure 1 Low (a) and high (b) magnification SEM images of ZnONPs-po

When we focus on these large particles, it is obvious that there are many highly ordered sub-crystals as illustrated in Fig. 1.b. These hexagonal shaped sub-units are distributed so homogeneously and mean particle size is around 70 nm.
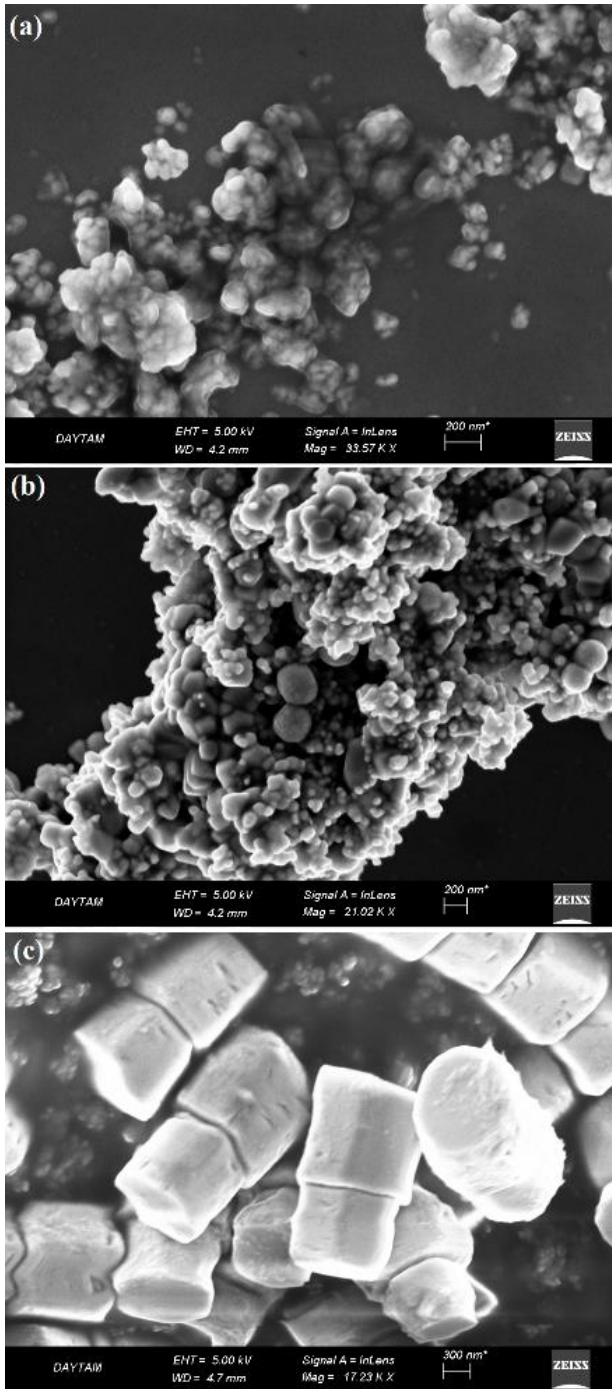
Figure 2 SEM images of ZnONPs-ht prepared at 100 ^{o}C (a), 120 ^{o}C (b), and 150 ^{o}C (c).

Fig. 2 demonstrates SEM images of ZnONPs-ht structures synthesized at 100, 120, and 150 ^{o}C. This figure indicates that ZnONPs-ht reveal a totally distinct surface structure at all of the studied temperature values. It should also be noted from Fig. 2 that surface appearance of ZnONPs-ht changes depending on the applied temperature. At 100 and 120 ^{o}C, SEM images of ZnONPs-ht reflect aggregated particles with lower crystalline view when compared to ZnONPs-po. Particle size of ZnONPs-ht was calculated as 50 nm for 100 ^{o}C (Fig. 2.a). It is observed in Fig. 2.b that more aggregated particles are seen for 120 ^{o}C and some larger particles arise on the surface. Hydrothermal synthesis at 150 ^{o}C results in a totally divergent formation. Interestingly, very large screw-like crystals with a few μm particle size constitute on the aggregated small particles.
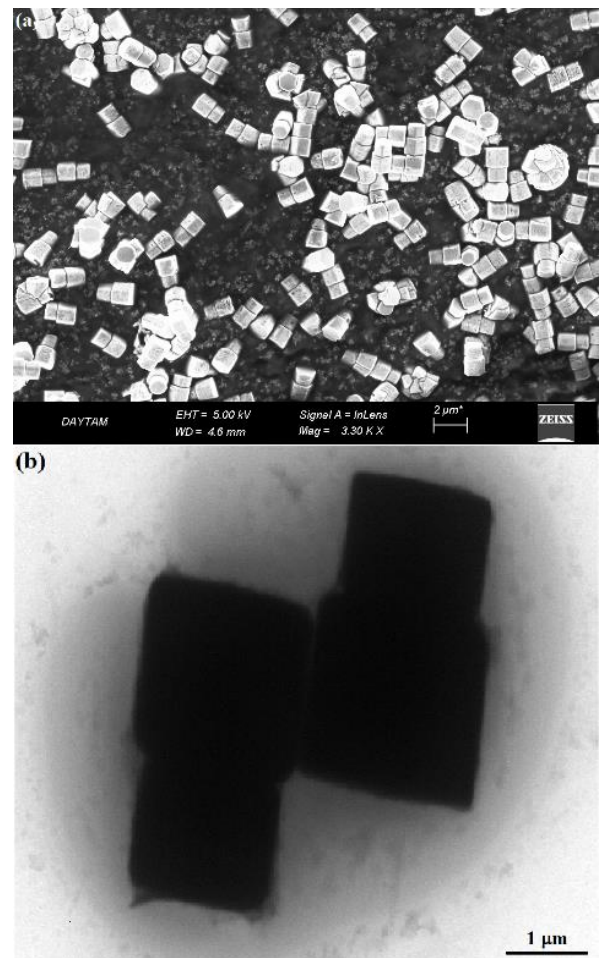
Figure 3 SEM (a) and TEM (b) images of ZnONPs-ht prepared at 150 ^{o}C.

Fig. 3.a represents a low magnification SEM image of these ZnONPs-ht crystals, in which screw-like crystals are homogenously distributed on the surface. Fig. 3.b also shows a TEM image of ZnONPs-ht synthesized at 150 ºC. This figure implies that large crystals reveal a very low transparency and the dimensions of these shapes are approximately 2.5 μm × 4.0 μm.

To investigate crystallographic properties of the prepared ZnONPs, powder XRD analysis was carried out as represented in Fig. 4. XRD spectrum of ZnONPs-po contains different peaks at 2θ values of 31.8º, 34.5º, 36.3º, 47.6º, 56.5º, 62.7º, and 67.8º for the diffractions of 100, 002, 101, 102, 110, 103, and 200 depending on the joint committee on powder diffraction standards (JCPDS) card number of 36-1451 [18]. In Fig. 4, same peaks are observed for ZnONPs-ht samples prepared at different temperatures.
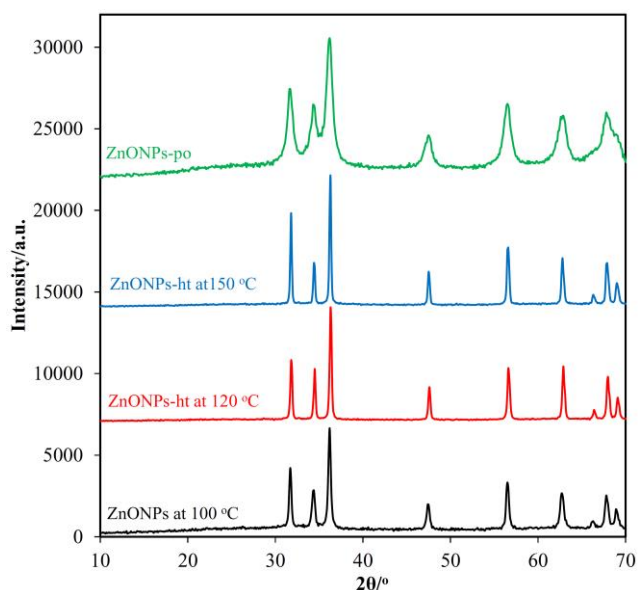
Figure 4 XRD data of ZnONPs prepared by polyol and hydrothermal methods

SEM analysis supplied visible particle size of the samples but it is clear that particle sizes for all samples are not uniform. XRD data provides mean particle size information depending on the Scherrer equation [19]. Using the most intensive peak, we have calculated particle size of ZnONPs-

po as 120 nm, while particles sizes of ZnONPs-ht samples are 345, 415, and 520 nm for 100, 120, and 150 ºC, respectively. It can be concluded from both SEM and XRD results that polyol process provides lower particle size and particle size increases by rising the applied temperature for hydrothermal process.

Fig. 5 displays FTIR spectra of ZnONPs-po and ZnO-NPs-ht. ZnONPs-po spectrum is very close to that of previous publications [20-22] and includes individual peaks at 507, 1049, 1388, 1607, 2978, and 3398 cm^{-1}, corresponding to vibration of Zn-O, C-N, C-H, C=O, C-H, and –OH groups, respectively. It is obvious that ZnONPs-po are covered with PVP molecules, those are immobilized to ZnONPs-po during the synthesis step. The FTIR spectrum of ZnONPs-ht exhibits almost similar peaks of spectrum of ZnONPs-po but two differences should be remarked. First difference is the arising of an intensive peak at 550 cm^{-1}, which is assigned to vibration of C-Br of CTAB [23], which is used as stabilizer. Second discrepancy is the diminishing the intensity of C=O bond, which is due to the absence of carbonyl group in the CTAB structure. The FTIR results ratify the successful synthesis of both ZnONPs structures by applied synthetic procedures.
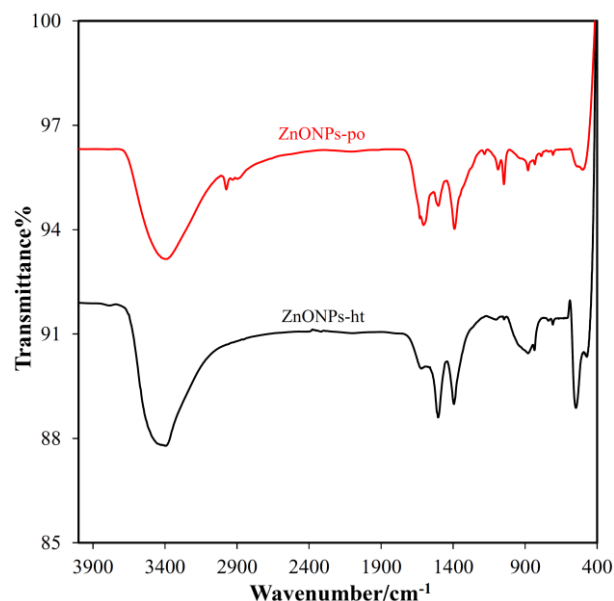
Figure 5 FTIR spectra of ZnONPs prepared by polyol and hydrothermal (150 ºC) methods

Optical properties of ZnONPs were analyzed using UV-Vis. absorption spectroscopy (Fig. 6). For ZnONPs-po and ZnONPs-ht dispersions, absorption maxima were observed at 376 and 371 nm corresponding to band gap values of 3.30 and 3.34 eV, respectively based on the following equation.

$$E = \frac{h\,c}{\lambda_{abs}}$$

where h is Planck constant (6.62×10^{-34} J.s), c is the velocity of light (3×10^{8} m.s^{-1}) and λ_{abs} is the absorption wavelength [22,24]. Calculated band gap values of both samples show that applied synthesis procedures yielded the bulk structure of ZnONPs.
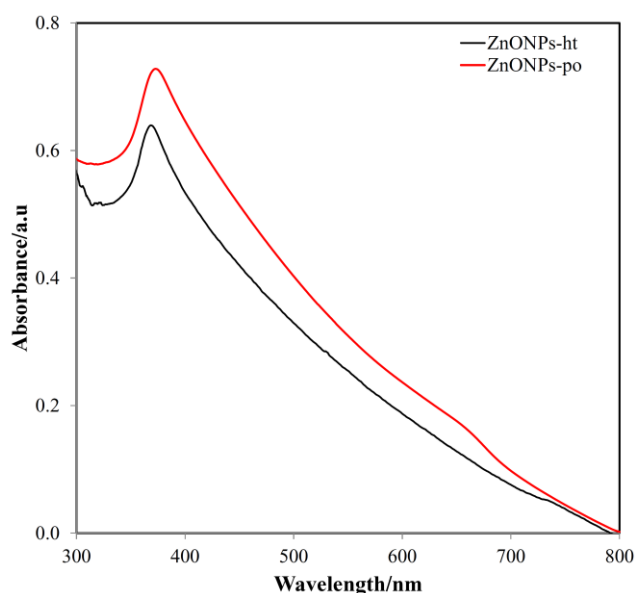
Figure 6 UV-Vis. absorption spectra of aqueous ZnONPs dispersions prepared by polyol and hydrothermal (150 ºC) methods

4. CONCLUSIONS

ZnONPs were successfully synthesized by using polyol and hydrothermal procedures. Hydrothermal synthesis was investigated for three different temperatures. SEM results revealed that polyol method presented formation of ball-shaped large particles including highly crystalline hexagonal sub-units. Hydrothermal method produced small particles with aggregation at 100 and 120 ºC but 150 ºC exhibited screw-like large crystallites rather than small particles. The XRD analysis implied that polyol process yielded lower particle size than hydrothermal approach and particle size increased by rising the temperature of exposure for hydrothermal process. Band gap values of the ZnONPs products were calculated from UV-Vis. absorption data and found same as the bulk band gap value of 3.3 eV.

Funding

The Declaration of Conflict of Interest/ Common Interest

No conflict of interest or common interest has been declared by the authors.

Authors' Contribution

The authors contributed equally to the study

The Declaration of Ethics Committee Approval

The author declares that this document does not require an ethics committee approval or any special permission

The Declaration of Research and Publication Ethics

The authors of the paper declare that they comply with the scientific, ethical and quotation rules of SAUJS in all processes of the paper and that they do not make any falsification on the data collected. In addition, they declare that Sakarya University Journal of Science and its editorial board have no responsibility for any ethical violations that may be encountered, and that this study has not been evaluated in any academic

publication environment other than Sakarya University Journal of Science.

REFERENCES

[1] S. Kasap, İ. İ. Kaya, S. Repp, and E. Erdem, "Superbat: battery-like supercapacitor utilized by graphene foam and zinc oxide (ZnO) electrodes induced by structural defects," Nanoscale Advances, vol. 1, pp. 2586-2597, 2019.

[2] M. M. Abutalib, and A.Rajeh, "Structural, thermal, optical and conductivity studies of Co/ZnO nanoparticles doped CMC polymer for solid state battery applications," Polymer Testing, vol. 91, pp. 106803, 2020.

[3] B. Zhao, F. Mattelaer, J. Kint, A. Werbrouck, L. Henderick, M. Minjauw, J. Dendooven, and C. Detavernier, "Atomic layer deposition of $ZnO-SnO_2$ composite thin film: The influence of structure, composition and crystallinity on lithium-ion battery performance," Electrochimica Acta, vol. 320, pp. 134604, 2019.

[4] A. Ali, M. Ammar, M. Ali, Z. Yahya, M. Y. Javaid, S. Hassan, and T. Ahmed, "Mo-doped ZnO nanoflakes on Ni-foam for asymmetric supercapacitor applications," RSC Advances, vol. 9, pp. 27432-27438, 2019.

[5] S. Najib, F. Bakan, N. Abdullayeva, R. Bahariqushchi, S. Kasap, G. Franzò, M. Sankir, N. D. Sankir, S. Mirabella, and E. Erdem, "Tailoring morphology to control defect structures in ZnO electrodes for high-performance supercapacitor devices," Nanoscale, vol. 12, pp. 16162-16172, 2020.

[6] N. P.Shetti, S. J. Malode, D. S. Nayak, G. B. Bagihalli, S. S. Kalanur, R. S. Malladi, C. V. Reddy, T. M. Aminabhavi, and K. R. Reddy, "Fabrication of ZnO nanoparticles modified sensor for electrochemical oxidation of methdilazine," Applied Surface Science, vol. 496, pp. 143656, 2019.

[7] E. Erçarıkcı, and Murat Alanyalıoğlu, "Dual-functional Graphene-based flexible material for membrane filtration and electrochemical sensing of heavy metal ions", IEEE Sensors Journal, DOI 10.1109/JSEN.2020.3021988, 2020.

[8] İ. Şişman, O. Tekir, and H. Karaca, "Role of ZnO photoanode nanostructures and sensitizer deposition approaches on the photovoltaic properties of CdS/CdSe and $CdS_{1-x}Se_x$ quantum dot-sensitized solar cells," Journal of Power Sources, vol. 340, pp. 192-200, 2017.

[9] İ. Şişman, M. Can, B. Ergezen, and M. Biçer, "One-step anion-assisted electrodeposition of ZnO nanofibrous networks as photoanodes for dye sensitized solar cells," RSC Advances, vol. 5, pp. 73692–73698, 2015.

[10] X. Chen, G. Huang, C. An, R. Feng, Y. Wu, and C. Huang, "Plasma-induced PAA-ZnO coated PVDF membrane for oily wastewater treatment: preparation, optimization, and characterization through Taguchi OA design and synchrotron-based X-ray analysis," Journal of Membrane Science, vol. 582, pp. 70-82, 2019.

[11] F. Naeem, S. Naeem, Z. Zhao, G. Shu, J. Zhang, Y. Mei, and G. Huang, "Atomic layer deposition synthesized ZnO nanomembranes: A facile route towards stable supercapacitor electrode for high capacitance," Journal of Power Sources, vol. 451, pp. 227740, 2020.

[12] A. M. Qadir, I. Y. Erdogan, "Structural properties and enhanced photoelectrochemical performance of ZnO films decorated with Cu_2O nanocubes," International Journal of Hydrogen Energy, vol. 44, pp. 18694-18702, 2019.

[13] G. Utlu, "Structural investigation of ZnO thin films obtained by annealing after thermal evaporation," Sakarya University Journal of Science, vol. 23, pp. 650-656, 2019.

[14] R. Mahdavi, and S. S. A. Talesh, "The effect of ultrasonic irradiation on the structure, morphology and photocatalytic performance of ZnO nanoparticles by sol-gel method," Ultrasonics Sonochemistry, vol. 39, pp. 504-510, 2017.

[15] S. M. Li, L. X. Zhang, M. Y. Zhu, G. J. Ji, L. X. Zhao, J. Yin, and L. J. Bie, "Acetone sensing of ZnO nanosheets synthesized using room-temperature precipitation," Sensors and Actuators B: Chemical, vol. 249, pp. 611-623, 2017.

[16] S. Lee, S. Jeong, D. Kim, S. Hwang, M. Jeon, and J. Moon, "ZnO nanoparticles with controlled shapes and sizes prepared using a simple polyol synthesis," Superlattices and Microstructures, vol. 43, pp. 330–339, 2008.

[17] S. M. Saleh, A. M. Soliman, M. A. Sharaf, V. Kale, and B. Gadgil, "Influence of solvent in the synthesis of nano-structured ZnO by hydrothermal method and their application in solar-still," Journal of Environmental Chemical Engineering, vol. 5, pp. 1219–1226, 2017.

[18] P. Kaur, S. Rani, and B. Lal, "Excitation dependent photoluminescence properties of ZnO nanophosphor," Optik, vol. 192, pp. 162929, 2019.

[19] Ü. Ç. Üst, Ş. B. Demir, K. Dağcı, and M. Alanyalıoğlu, "Fabrication of free-standing graphene paper decorated with flower-like PbSe$_{0.5}$S$_{0.5}$ structures," RSC Advances, vol. 6, pp. 9453-9460, 2016.

[20] S. H. Largani, M. A. Pasha, "The effect of concentration ratio and type of functional group on synthesis of CNT–ZnO hybrid nanomaterial by an in situ sol–gel process," International Nano Letters, vol. 7, pp. 25–33, 2017.

[21] T. Gutul, E. Rusu, N. Condur, V. Ursaki, E. Goncearenco, and P. Vlazan, "Preparation of poly(N-vinylpyrrolidone)-stabilized ZnO colloid nanoparticles," Beilstein Journal of Nanotechnoogy, vol. 5, pp. 402–406, 2014.

[22] J. Singh, S. Kaur, G. Kaur, S. Basu, and M. Rawat, "Biogenic ZnO nanoparticles: a study of blueshift of optical band gap and photocatalytic degradation of reactive yellow 186 dye under direct sunlight," Green Processing and Synthesis, vol. 8, pp. 272–280, 2019.

[23] T. Kasilingam, C. Thangavelu, and V. Palanivel, "Nano Analyses of Adsorbed Film onto Carbon Steel," Portugaliae Electrochimica Acta, vol. 32, pp. 259-270, 2014.

[24] M. K. Debanath, S. Karmakar, "Study of blueshift of optical band gap in Zinc Oxide (ZnO) nanoparticles prepared by low temperature wet chemical method," Materials Letters, vol. 111, pp. 116-119, 2013.

Title: Fabrication of Reduced Graphene Oxide Paper Doped with Zinc Oxide Nanoparticles as Flexible Electrode Material

Authors: Elif ERÇARIKCI, Murat ALANYALIOĞLU

Fabrication of Reduced Graphene Oxide Paper Doped with Zinc Oxide Nanoparticles as Flexible Electrode Material

Elif ERÇARIKCI[1], Murat ALANYALIOĞLU[*2]

Abstract

The conventional electrodes like glassy carbon electrode and graphite are restricted for large-scale electrochemical production and in-vivo applications. Therefore, flexible electrodes are beginning to replace with such electrodes. This work reports a simple preparation of flexible paper-like electrode material (FPEM) including reduced graphene oxide (rGO) and zinc oxide nanoparticles (ZnONPs) for possible electrochemical applications. For this purpose, graphene oxide dispersion was interacted with ZnONPs, filtered under vacuum effect through a membrane, peeled off the membrane and then reduced by hydrothermal reduction process. This FPEM was performed as working electrode for some redox processes and results revealed that rGO/ZnONPs paper allows a large potential region in acidic, basic, and neutral media for electrochemical processes.

Keywords: Reduced graphene oxide, zinc oxide nanoparticles, flexible electrode

1. INTRODUCTION

Electrochemical applications are performed on electrically conductive, inert and stable materials such as glassy carbon electrode, graphite, and noble metals. However, these conventional electrodes are not suitable for large-scale electrochemical production, in-vivo and in-situ applications due to fragile, solid, and inflexible character. In recent years, flexible paper-like electrode materials (FPEMs) have been developed using graphene skeleton by different fabrication routes such as vacuum filtration [1,2], mold-casting [3], and printing [4].

Up to now, many electrochemical applications e.g. supercapacitors [5,6], electrochemical sensors [1,2,7,8], Li-ion batteries [9] have been successfully executed using graphene-based FPEMs. For more intensive electrode applications, stability, flexibility, and potential region of FPEMs need to be further improved. To prepare graphene-based FPEMs, usually graphene oxide (GO) flakes are used as main material and converted to reduced graphene oxide (rGO) structure to increase the electrical conductivity. The rGO based paper is generally

---

[1] Ataturk University, Faculty of Science, Erzurum, Turkey.
ORCID: https://orcid.org/0000-0002-8490-1644 E-Mail: elif.ercarikci@atauni.edu.tr
[*]Corresponding Author: malanya@atauni.edu.tr
[2] Ataturk University, Faculty of Science, Erzurum, Turkey. ORCID: https://orcid.org/0000-0002-2223-7303

Elif ERÇARIKCI, Murat ALANYALIOĞLU

Fabrication of Reduced Graphene Oxide Paper Doped with Zinc Oxide Nanoparticles as Flexible Electrode...

doped with different substances like metal nanoparticles [1], metal oxide nanoparticles [5,6], polymers [8], and dyes [2,7] to adjust the conductivity and functionality. Zinc oxide (ZnO), a semiconductor substance with a direct bandgap of 3.37 eV [10-13], is a useful material for the electrode designation because of electrochemical stability, basic and economic synthesis.

This work reports the fabrication of graphene based paper-like electrode doped with zinc oxide nanoparticles (ZnONPs) using vacuum-filtration method. Characterization results revealed that ZnONPs were successfully inserted to rGO paper structure and cyclic voltammetry (CV) experiments illustrated that this paper-like material provides a flexible character and a large electrode potential region in a large pH scale.

2. EXPERIMENTAL SECTION

All of the synthesis procedures and experiments were performed in aqueous media using ultrapure water and the reagents were of analytical grade. Synthesis of GO sheets were achieved using modified Hummers method as described in our previous publications [2,7,14], in which high degree chemical oxidation of graphite resulted in formation of one-atom thick GO layers.

To prepare ZnONPs, 5 mL of 1.0 M KOH solution was added to 25 mL of diethylene glycol while stirring. A 10 mL of 0.4 M $Zn(NO_3)_2.6H_2O$ solution and 0.59 g of hexadecyl trimethylammonium bromide solution was added and stirred for 10 min. This dispersion was placed into a suitable autoclave and heated at 180 °C for 3 h. The produced ZnONPs were filtered, rinsed and dried [10].

A 100 mL of 1.0 mg mL^{-1} GO dispersion was prepared, 20 mg of ZnO-NPs was added and ultrasonic treatment was applied for 1 h to supply adsorption of ZnONPs onto GO sheets. This suspension was placed to a membrane-filtration system under vacuum effect, and then peeled from membrane to obtain freestanding GO/ZnONPs paper-like material. To improve the electrical conductivity of this paper, hydrothermal reduction was performed by sealing into ultrapure water and heating at 180 °C for 4 h in autoclave system. This paper-like material was quoted as

RZOP. We have also prepared another paper-like material without addition of ZnONPs and labeled it as RGP.

CV experiments were applied with three-electrode Gamry potentiostat system using RZOP or RGP as the working electrodes. A Pt wire and an Ag/AgCl (sat. KCl) were served as counter and reference electrode, respectively. Morphological characterization of the materials was executed using Zeiss brand scanning electron microscopy (SEM) and Hitachi brand transmission electron microscopy (TEM) systems. Optical analyses of the samples were acquired by Shimadzu UV-Vis. spectrophotometer. Crystallographic information of the paper-like materials was collected using Rigaku brand powder X-ray diffraction instrument. Raman spectra of the papers were provided with WITech micro-Raman system.

3. RESULTS AND DISCUSSION
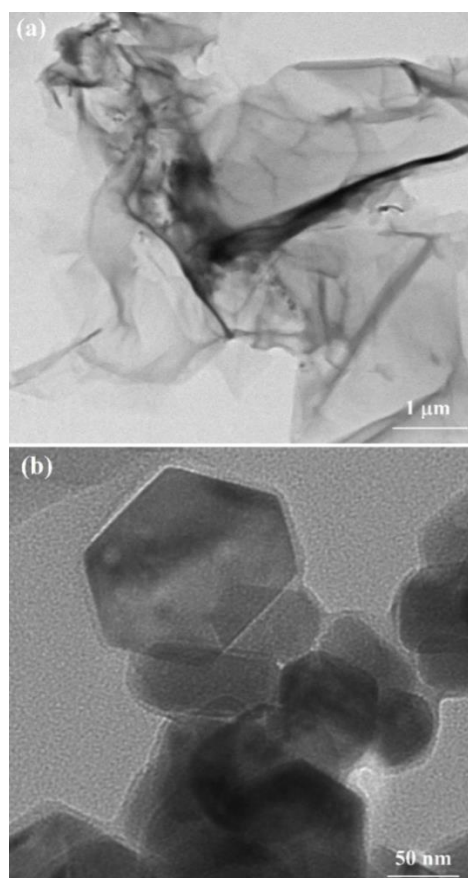
Figure 1 TEM images of GO layers (a) and ZnONPs (b)

Elif ERÇARIKCI, Murat ALANYALIOĞLU

Fabrication of Reduced Graphene Oxide Paper Doped with Zinc Oxide Nanoparticles as Flexible Electrode...

To produce a flexible graphene-based FPEM, the quality of GO layers needs to be investigated. It is clearly seen in Fig. 1.a that GO layers are so transparent and they show as large as 10 μm sheets. GO layers demonstrate characteristic wrinkled organization because of the strong one-atom thick structure and flexibility [15]. Fig. 1.b demonstrates TEM image of ZnONPs in which particle size ranges between 20 and 150 nm with a hexagonal shape and crystalline view.

To verify the attachment of ZnONPs to GO flakes, optical analysis was performed using spectrophotometric techniques. Fig. 2 illustrates UV-Vis. region absorption behavior of GO, ZnONPs, and GO/ZnONPs dispersions. GO dispersion displays a maximum at 232 nm and a shoulder at 304 nm, which are consistent with π-π and n-π transitions, respectively [14,16]. ZnONPs include two separated bands at 269 and 372 nm, which comply with previous works [12,14]. The presence of all of these observed bands at the composite dispersion verify the effective adsorption of ZnONPs to GO flakes successfully.

Figure 3 Digital photographs of RZOP

It is clear from Fig. 3 that the RZOP paper has a stable and flexible view, eventually, it can be a good nominee as a flexible working electrode in many electrochemical applications. SEM, Raman, and XRD techniques were performed to explain morphological, structural, and crystallographic, properties of the produced FPEMs.

Fig. 4.a presents SEM image of RGP and this figure indicates that rGO sheets show a wrinkled surface orientation in the paper-like material. ZnONPs demonstrate hexagonal shapes with a mean particle size of 150 nm in Fig. 4.b. Surface structure of RZOP shows that rGO layers are doped with ZnONPs as large as a few μm, in which surface scene of RZOP totally changes when compared to that of RGP. These large crystals in the RZOP structure can be attributed to aggregation of ZnONPs during the high flux vacuum-filtration process.

Raman spectrum of RGP reflects D and G bands at 1355 and 1602 cm^{-1} for defects and in-plane vibration of sp^2 carbon atoms as usual for carbon nanomaterials, respectively [17,18] (Fig. 5). These bands shift to lower energy regions, and are observed at 1313 and 1554 cm^{-1} for RZOP, indicating insertion of ZnONPs between the layers of rGO in the paper-like material. Obviously, it can be claimed from Fig. 5 that the intensity of D band diminishes when compared to the intensity of G band after doping RGP with ZnONPs, which is associated with the reduction

Figure 2 UV-Vis. absorption data of various aqueous dispersions

of defect density by patching disorders of rGO layers with ZnONPs [14].
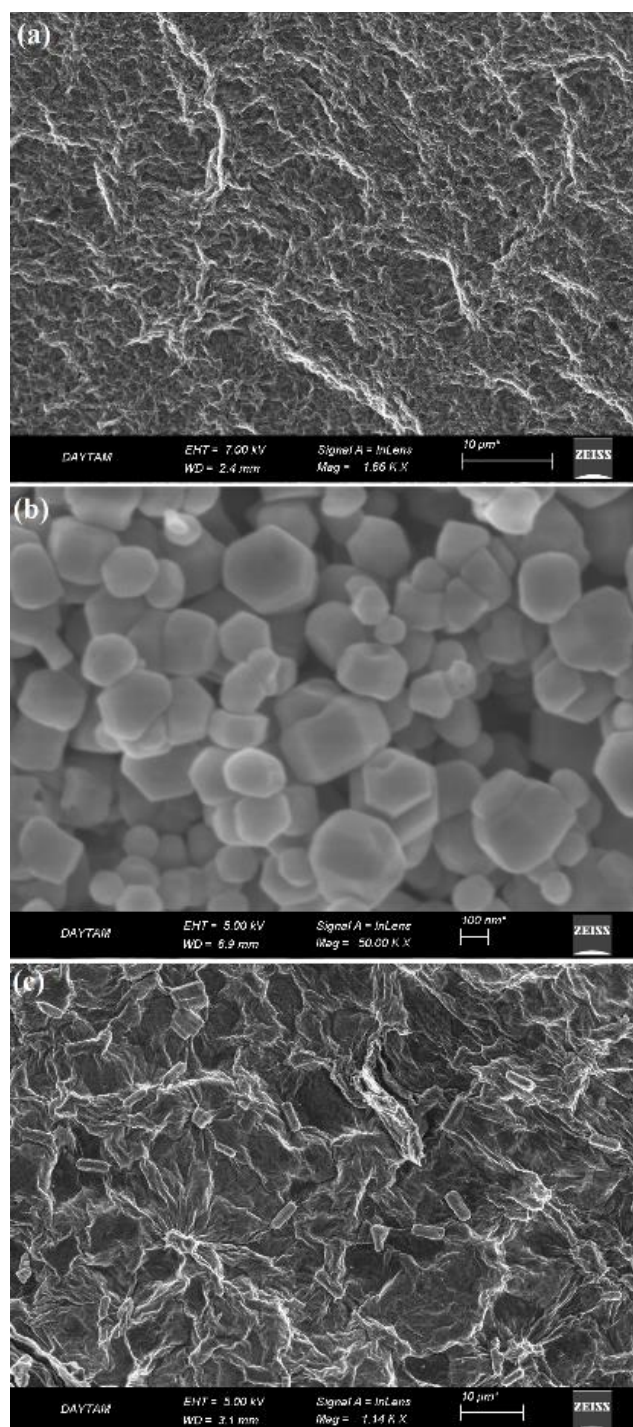
Figure 4 SEM images of RGP (a), ZnONPs (b), and RZOP (c)
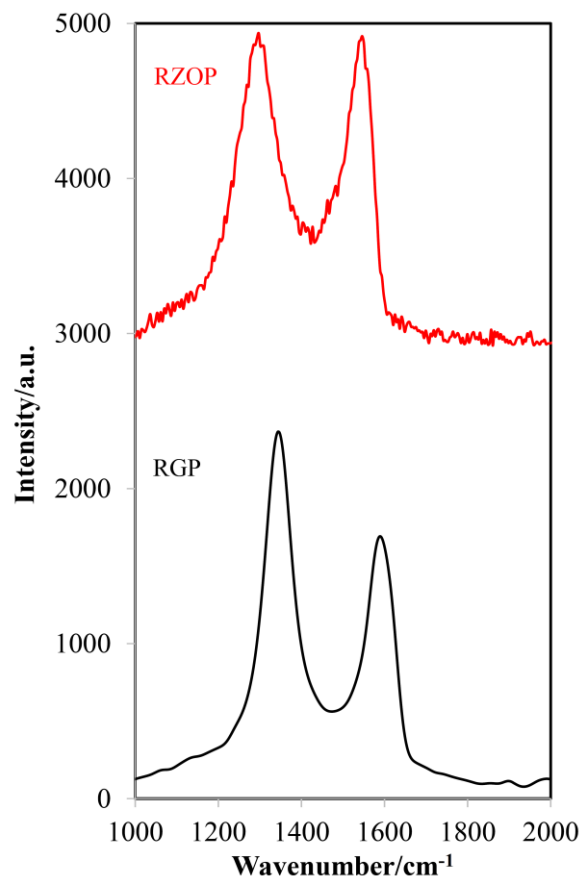
Figure 5 Raman spectra of RGP and RZOP

In Fig. 6, XRD data of ZnONPs includes the defined peaks at 31.8°, 34.5°, 36.3°, 47.5°, and 56.6° for the orientations of 100, 002, 101, 102, 110 depending on the joint committee on powder diffraction standards (JCPDS) with card number of 36-1451 [19]. RGP contains a single peak at $2\theta=24.4°$ corresponding to 002 of rGO flakes [2,7]. It is essential to mention that RZOP illustrates XRD character of both rGO and ZnONPs, affirming the success of composite formation by proposed method for FPEM.

Electrochemical performance of the prepared FPEMs can be assessed using CV experiments. CVs of both RGP and RZOP in 0.1 M KNO_3 solution containing 10 mM $K_3Fe(CN)_6$ were represented in Fig. 7. In this figure, a reversible peak pair of redox of $Fe(CN)_6^{-3/-4}$ is observed [14] for both paper-like materials as expected, which means that these materials may be performed as working electrode for many electrochemical applications. Electrochemical performance of

Elif ERÇARIKCI, Murat ALANYALIOĞLU

Fabrication of Reduced Graphene Oxide Paper Doped with Zinc Oxide Nanoparticles as Flexible Electrode...

these electrodes can be compared by calculating the potential difference between cathodic and anodic peaks (ΔEp), in which lower ΔEp value stands for a better electrochemical activity. ΔEp values for RGP and RZOP were measured as 430 mV and 340 mV. This case exhibits the contribution of ZnONPs to the electrochemical activity in the FPEM structure.
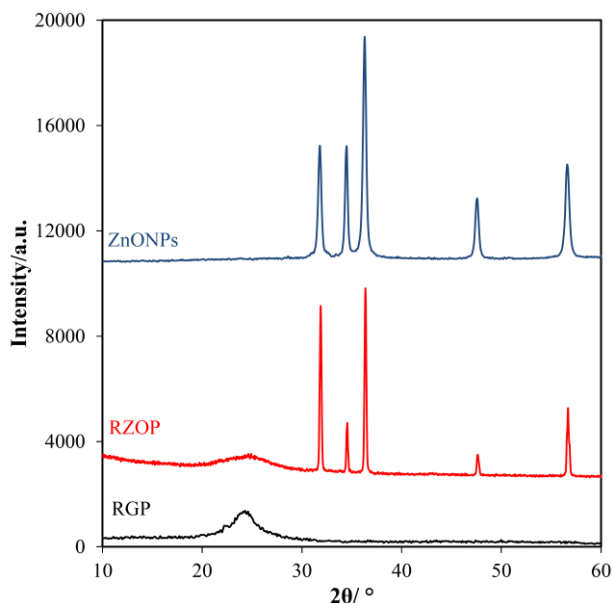
Figure 6 Powder XRD patterns of different samples

To show the available potential region of the FPEMs, CV experiment was designed in the potential range of +0.9 V and -0.9 V as shown in Fig. 8. We have employed both RGP and RZOP as working electrodes in acidic, basic and neutral phosphate buffer solutions (PBSs) and we have not observed redox peaks in neither of the working electrodes. This situation implies that RZOP can be proposed as working electrode in a large potential region for aqueous solutions at different pHs. Moreover, capacitive current of RZOP is higher than that of RGP. So, RZOP can be proposed as working electrode for flexible supercapacitor studies.
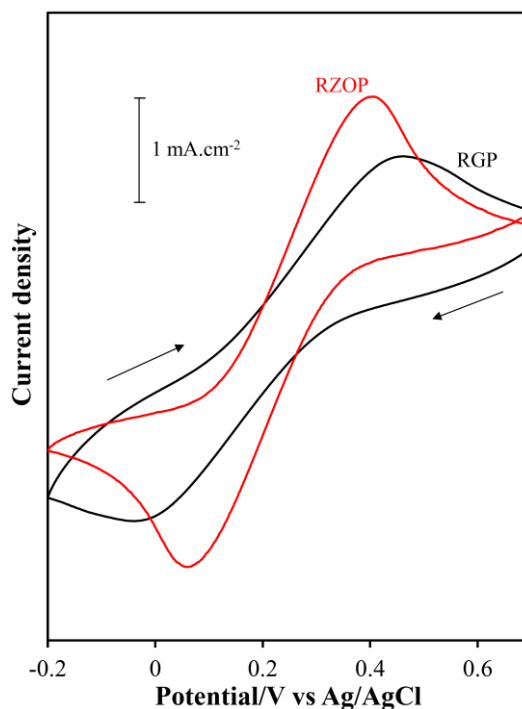
Figure 7 CVs of RGP and RZOP in 0.1 M KNO$_3$ solution containing 1.0 mM K$_3$Fe(CN)$_6$. Scan rate: 50 mV.s^{-1}
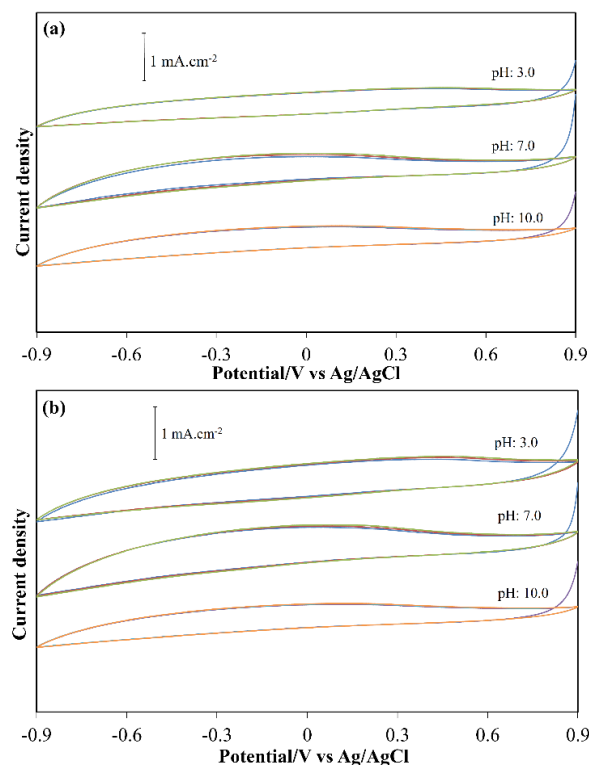
Figure 8 Successive three CV scans of RGP (a) and RZOP (b) in 0.1 M PBS at different pHs. Scan rate: 50 mV.s^{-1}

Elif ERÇARIKCI, Murat ALANYALIOĞLU

Fabrication of Reduced Graphene Oxide Paper Doped with Zinc Oxide Nanoparticles as Flexible Electrode...

4. CONCLUSIONS

Graphene-based FPEM including ZnONPs were fabricated by using a basic and affordable approach. SEM and XRD analysis results expressed the insertion of ZnONPs between rGO flakes during paper-like material formation with vacuum-filtration process. Raman spectroscopy ratified the adsorption of ZnONPs to defected places of rGO layers. Electrochemical performance of RZOP was better than that of RGP and both FPEMs exhibited utilization as working electrodes in a large potential window for acidic, basic, and neutral aqueous solutions.

Funding

The Declaration of Conflict of Interest/ Common Interest

No conflict of interest or common interest has been declared by the authors

Authors' Contribution

The authors contributed equally to the study

The Declaration of Ethics Committee Approval

The author declares that this document does not require an ethics committee approval or any special permission

The Declaration of Research and Publication Ethics

The authors of the paper declare that they comply with the scientific, ethical and quotation rules of SAUJS in all processes of the paper and that they do not make any falsification on the data collected. In addition, they declare that Sakarya University Journal of Science and its editorial board have no responsibility for any ethical violations that may be encountered, and that this study has not been evaluated in any academic publication environment other than Sakarya University Journal of Science.

REFERENCES

[1] K. D. Kıranşan, and E. Topçu, "Graphene paper with sharp-edged nanorods of Fe−CuMOF as an excellent electrode for the simultaneous detection of catechol and resorcinol," Electroanalysis, vol. 31, pp. 2518-2529, 2019.

[2] Z. Aksu, and M. Alanyalıoğlu, "Fabrication of free-standing reduced graphene oxide composite papers doped with different dyes and comparison of their electrochemical performance for electrocatalytical oxidation of nitrite," Electrochimica Acta, vol. 258, pp. 1376-1386, 2017

[3] L. Wu, M. Liu, S. Huo, X. Zang, M. Xu, W. Ni, Z. Yang, and Y. M. Yan, "Mold-casting prepared free-standing activated carbon electrodes for capacitive deionization," Carbon, vol. 149, pp. 627-636, 2019.

[4] P. He, J. Cao, H. Ding, C. Liu, J. Neilson, Z. Li, I. A. Kinloch, and B. Derby, "Screen-printing of a highly conductive graphene ink for flexible printed electronics," ACS Applied Materials and Interfaces, vol. 11, pp. 32225–32234, 2019.

[5] X. Du, S. Wang, Y. Liu, M. Lu, K. Wu, and M. Lu, "Self-assembly of free-standing hybrid film based on graphene and zinc oxide nanoflakes for high-performance supercapacitors", Journal of Solid State Chemistry, vol. 277, pp. 441–447, 2019.

[6] M. Ghorbani, M. R. Golobostanfard, and H. Abdizadeh, "Flexible freestanding sandwich type ZnO/rGO/ZnO electrode for wearable supercapacitor," Applied Surface Science, vol. 419, pp. 277–285, 2017.

Elif ERÇARIKCI, Murat ALANYALIOĞLU

Fabrication of Reduced Graphene Oxide Paper Doped with Zinc Oxide Nanoparticles as Flexible Electrode...

[7] O. Bayındır, and M. Alanyalıoğlu, "Azure B nanocomposites of chemically and electrochemically produced graphene oxide: comparison of amperometric sensor performance for NADH," IEEE Sensors Journal, vol. 19, pp. 812-819, 2019.

[8] W. K. Chee, H. N. Lim, and N. M. Huang, "Electrochemical properties of free-standing polypyrrole/graphene oxide/zinc oxide flexible supercapacitor," International Journal of Energy Research, vol. 39, pp. 111–119, 2015.

[9] H. Köse, A. O. Aydın, and Ş. Dombaycıoğlu, "Graphene-based architectures of tin and zinc oxide nanocomposites for free-standing binder-free Li-ion anodes," International Journal of Energy Research, vol. 42, 4710-4718, 2018.

[10] S. M. Saleh, A. M. Soliman, M. A. Sharaf, V. Kale, and B. Gadgil, "Influence of solvent in the synthesis of nano-structured ZnO by hydrothermal method and their application in solar-still," Journal of Environmental Chemical Engineering, vol. 5, pp. 1219–1226, 2017.

[11] S. Lee, S. Jeong, D. Kim, S. Hwang, M. Jeon, and J. Moon, "ZnO nanoparticles with controlled shapes and sizes prepared using a simple polyol synthesis," Superlattices and Microstructures, vol. 43, pp. 330–339, 2008.

[12] S. Aksoy, K. Görgün, Y. Çağlar, and M. Çağlar, "Effect of loading and standbye time of the organic dye N719 on the photovoltaic performance of ZnO based DSSC," Journal of Molecular Structure, vol. 1189, pp. 181-186, 2019.

[13] İ. Şişman, M. Can, B. Ergezen, and M. Biçer, "One-step anion-assisted electrodeposition of ZnO nanofibrous networks as photoanodes for dye sensitized solar cells," RSC Advances, vol. 5, pp. 73692–73698, 2015.

[14] E. Erçarıkcı, and Murat Alanyalıoğlu, "Dual-functional Graphene-based flexible material for membrane filtration and electrochemical

sensing of heavy metal ions", IEEE Sensors Journal, DOI: 10.1109/JSEN.2020.3021988, 2020.

[15] M. Şinoforoğlu, B. Gür, M. Arık, Y. Onganer, and Kadem Meral, "Graphene oxide sheets as a template for dye assembly: graphene oxide sheets induce H-aggregates of pyronin (Y) dye," RSC Advances, vol. 3, pp. 11832-11838, 2013.

[16] F. Zhao, S. Wang, Z. Zhu, S. Wang, F. Liu, and G. Liu, "Effects of oxidation degree on photo-transformation and the resulting toxicity of graphene oxide in aqueous environment," Environmental Pollution, vol. 249, pp. 1106-1114, 2019.

[17] Z. Ni, Y. Wang, T. Yu, and Z. Shen, "Raman spectroscopy and imaging of graphene," Nano Research, vol. 1, pp. 273-291, 2008.

[18] İ. Tiyek, U. Dönmez, B. Yıldırım, M. H. Alma, M. S. Ersoy, Ş. Karataş, and M. Yazıcı, "Synthesis of reduced graphene oxide by chemical method and its characterization," Sakarya University Journal of Science, vol. 2, pp. 349-357, 2016.

[19] P. Kaur, S. Rani, and B. Lal, "Excitation dependent photoluminescence properties of ZnO nanophosphor," Optik, vol. 192, pp. 162929, 2019.

Title: Method Development for the Chromatographic analysis of a Two-Component Tablet Formulation Using Chemometric Optimization Technique

Method Development for the Chromatographic analysis of a Two-Component Tablet Formulation Using Chemometric Optimization Technique

Faysal SELİMOĞLU[1], Betül SARITAŞ[2], Erdal DİNÇ[3*]

ABSTRACT

A novel chromatographic method, ultra-performance liquid chromatography (UPLC) was improved to determine sulfamethoxazole and trimethoprim in a two-component tablet formulation. In the implemented of the method, the chromatographic parameters were optimized by using the experimental design and optimization procedure. The central composite design and fitting model was applied to identify the suitable chromatographic conditions providing a desirable elution of sulfamethoxazole and trimethoprim in a chromatogram. In the central composite design, temperature, flow rate and buffer% were selected as the effective factors on the chromatographic resolution. The buffer system was the mixture of 0.1 M CH_3COOH and CH_3COONa (pH 4.75) in mobile phase system. In the optimization step, the chromatographic conditions were found to be 0.20 mL/min for flow rate, 38.0 °C for the column temperature and 66% for the acetate buffer system (v/v) in the mobile phase. Analysis of the investigated drugs was accomplished on a stationary phase based on Waters BEH C_{18} column (50 mm-2.1 mm, 1.7 mm i.d.). In the validation step, recovery study was performed by analyzing the synthetic binary mixture of sulfamethoxazole and trimethoprim. Recovery results were found as 99.12% for sulfamethoxazole and 99.44% for trimethoprim. Assay results showed that the optimized chromatographic technique was very suitable for the quantitation of sulfamethoxazole and trimethoprim in tablets.

Keywords: Chemometric optimization, ultra-performance liquid chromatography, Sulfamethoxazole, trimethoprim,

1. INTRODUCTION

Sulfamethoxazole (SMX) is a sulfonamide derivative, which is one of the well-known antibacterial substances [1]. SMX is slightly off-white in crystal form, and its chemical formula is $C_{10}H_{11}N_3O_3S$. It is poorly soluble in polar but highly soluble nonpolar solvents. SMX can commercially be synthesized by reacting acetyl sulfonyl chloride with 2-amino-4,6-dimethyl pyrimidine 3-amino-5-methylisoxazole in

* Corresponding Author: dinc@ankara.edu.tr

[1] Necmettin Erbakan University, Konya, Turkey, E-mail: fselimoglu@erbakan.edu.tr ,ORCID: https://orcid.org/0000-0003-3798-9054

[2] Ankara University ,Ankara, Turkey, E-mail: betul.saritas@saglik.gov.tr , ORCID: https://orcid.org/0000-0001-9701-2523

[3] Ankara University, Faculty of Pharmacy ,Ankara, Turkey, ORCID: https://orcid.org/0000-0001-6326-1441

SELİMOĞLU et al.

Method Development for the Chromatographic analysis of a Two-Component Tablet Formulation Using Chem...

acetone and pyridine [2]. SMX provides a broad-spectrum with a strong antibacterial effect on both gram-negative and gram-positive bacterial growth. SMX is used in the treatment of urinary tract infection, respiratory tract infection, and intestinal infection [3-4]. SMX interferes with the synthesis of bacterial dihydrofolate, which is a vital reproduction cofactor for eukaryotic and prokaryotic cells [5-6].

The SMX and TMP combination in the same formulation provides an extensive antibacterial spectrum to medicate more bacterial infections. TMP derives from trimethoxybenzyl-pyrimidine. TMP is an odorless, white powder in solid crystalline form and insoluble in water but soluble in dimethyl sulfoxide. TMS's chemical formula is $C_{14}H_{18}N_4O_3$. The chemical synthesis of TMP is done by two stepped reactions of 3,4,5-Trimethoxybenzaldehyde, 3-ethoxypropionitrile, and guanidine in acidic media [9]. TMP has a broad-spectrum antibiotic agent. TMP has the primary enzyme property that catalyzes the bacterial folic acid synthesis in the mechanism of action.

Due to the extensive and increasing use of SMX and TMP in human and veterinary medicines, it is needed to develop new analytical method for the quality control and quantitative assessment of SMX-TMP products. In the literature, there are many methods are mentioned about the quantification of SMX and TMP in pharmaceutical formulations [10]. However, these methods are not related to chemometric optimization for improving an UPLC approach for the quantification of TMP and SMX mixtures.

Most of the methods are based on HPLC [11-12], HPTLC [13], UV-VIS absorption spectrophotometry [14]. Multivariate statistical techniques such as, H-point standard additions method HPSAM [15], partial least squares PLS regression [16].

In the analytical chemistry laboratory, the design and optimization techniques allow an opportunity to find suitable experimental conditions for developing a new liquid chromatographic method with a few numbers of experiments. In literature, it is observed that central composite design CCD

is preferable than others (for example, full factorial design and Box-Behnken design) since it can provide good predictions throughout the experimental data of the variable process and their parameters [17-18].

In this study, a chemometric methodology was used to reach optimal conditions for developing a new chromatographic determination based on the UPLC technique for the simulations quantitative evaluation of SMX and TMP in commercial tablets. After the method validation, the quality control and routine analysis of the investigated drug compounds in commercial tablets were accomplished by the optimized and validated UPLC technique.

2. EXPERIMENTAL

2.1. Instrument and Software

Chromatographic recordings of the related drugs and their samples were obtained using a Waters® Acquity H-Class UPLC system equipped with cooling autosampler and an oven allowing control the chromatographic column's temperature, «photodiode array» detector (PDA), Chromatographic instrument was controlled with Empower 2 software (Waters, USA) Chromatographic separation of analytes was accomplished by using a Waters UPLC BEH C_{18} column (50 mm x 2.1mm i.d., 1.7 μm).
Calibration curve and mathematical calculations of the obtained data were made by using an m-file algorithm written in MATLAB software (MathWorks Inc.) and Microsoft Excel program.

2.2. Chromatographic Conditions of UPLC Analysis

In this study, chromatographic analyses were archived on a Waters UPLC BEH C18 (50 mm x 2.1 mmi.d., 1.7 μm) used as a stationary phase. The chromatographic elution of TMP and SMX was carried out by using a mobile phase consisting of a mixture of methanol and 0.1 M sodium acetate buffer (at pH 4.75) (34:66, v/v) containing 1.0 mL trimethylamine per liter. The flow rate of the mobile phase was 0.2 mL/min, and the sample injection volume was 1.5 μL. During the separation process, column

2

SELİMOĞLU et al.

Method Development for the Chromatographic analysis of a Two-Component Tablet Formulation Using Chem...

temperature was 38.0 C°, respectively. Quantification of analytes was performed by using a PDA detection at 270 nm and sulfadiazine was used as internal standard (IS).

2.3. Chemicals and Standard Solutions

Methanol was of HPLC grade (Merck, DE). Acetic acid and sodium acetate anhydrous, Reagent Plus®, ≥99.0%, Triethylamine ≥99.0% were obtained from Sigma-Aldrich (St. Louis, MO, U.S.). In the UPLC analysis of analytes, double distilled water was used during chromatographic experiments. Standards of SMX (99.7% purity) and TMP (99.6% purity) were kindly supplied from Santa Pharma Inc. (Istanbul, Turkey). A pharmaceutical tablet formulation (BACTRIM Forte Tablet produced by Deva Pharm. Ind., Istanbul, Turkey) containing 800 mg SMX and 160 mg TMP per tablet was bought from a local pharmacy. For the UPLC analysis of the drugs, the standard stock solutions for both SMX and TMP were individually obtained by dissolving of 10.0 mg of each analyte in 100 mL methanol. A series of the calibration solutions containing SMX and TMP in the working range of 1-36 µg/mL were prepared from the above stock solutions. For the validity of the proposed method, a set of 14 binary mixture containing SMX and TMP in different concentration levels. All solution of calibration, validation and commercial samples were prepared in methanol during this study.

2.4. Analysis Procedure of Tablet Samples

In applying the developed UPLC method to real tablet samples, ten tablets have been accurately weighed and pulverized in a mortar for sample preparation. A quantity of tablet powder equivalent to one tablet was dissolved in methanol in a 100 mL volumetric flask. The tablet solution was filtered through a 0.45 µm membrane filter. The sample solution was then diluted with methanol to the linear concentration range the resulting sample was injected into chromatographic instrument system. This analysis process of tablets was repeated ten times.

3. RESULTS and DISCUSSION

3.1. Chemomeetric Optimization Approach

Optimization of factors affecting the chromatographic elution of analytes is crucial to developing a new UPLC method. For this purpose, preliminary chromatographic studies were done to find factors affecting the resolution factor or chromatographic response. As a result of these studies, the column temperature (X_1), flow rate (X_2) and percentage (X_3) of buffer % (0.1 M acetate buffer at pH 4.75) in the mobile phase were selected as independent factor variables that affect the chromatographic response. The levels of these factors were demonstrated in this paper as (-1) low, as (0) medium, and as (+1) high (see Table 1).

Table 1
Selected factors, corresponding factor levels

Levels	Temperature $X1$	Flowrate $X2$	Buffer% $X3$
1.682	38.4	0.43	80.1
1	35.0	0.38	74.0
0	30.0	0.30	65.0
-1	25.0	0.22	56.0
-1.682	21.6	0.17	49.9

Low level (-1), medium level (0), high level (+1)

In the chemometric optimization procedure, the resolution factor (R) was used as a response function, which is given by the following expression:

$$R = 2 \ \frac{(t_2 - t_1)}{(W1 + W1)} \qquad (1)$$

where W_1 and W_2 denote the chromatographic peak widths of peak$_1$ and peak$_2$, respectively; t_1 and t_2 represents the elution times of analytes in a chromatogram.

Considering the factors and their factor levels illustrated in Table 1, the central composite design involving three factors variables (the temperature X_1, flow rate X_2 and percentage X_3 of 0.1 M acetate buffer system (pH=5.75) in the mobile phase) was planned as presented in Table 2.

3

Considering chromatographic conditions of the central composite design, the UPLC chromatograms were plotted by using the chromatographic instrument. Then, the data of the chromatographic responses were computed by using Equation (1) and presented in Table 2. The following second-order polynomial equation was obtained by using the mathematical relationship between the independent factor variables (X_1, X_2, and X_3) with factor interactions and the chromatographic response (R) as follows:

$$y = 1.3138 - 0.2118x_1 - 0.1378x_2 + 0.3932x_3 + 0.1178x_1^2 + 0.0738x_2^2 - 0.2930x_3^2 \quad (2)$$
$$+ 0.0265x_1x_2 - 0.0801x_1x_3 - 0.0609x_2x_3$$

In the calculation of Equation (2) by regression analysis, the values the predicted responses were obtained and listed in Table 2.

Table 2
Full factorial design and responses with calculated and predicted values

Experiment Number	Temp X_1	Flow X_2	Buffer % X_3	Responses Calculated	Predicted
1	-1	-1	-1	2.1030	2.0683
2	-1	-1	1	2.1635	2.1902
3	-1	1	-1	0.8709	0.9295
4	-1	1	1	1.8991	1.8774
5	1	-1	-1	0.9841	0.9948
6	1	-1	1	1.3252	1.2556
7	1	1	-1	0.6220	0.5843
8	1	1	1	1.6474	1.6711
9	-1.682	0	0	2.5577	2.5353
10	1.682	0	0	1.4209	1.4590
11	0	-1.682	0	1.9373	1.9719
12	0	1.682	0	1.3825	1.3636
13	0	0	-1.682	0.1805	0.1770
14	0	0	1.682	1.1745	1.1935
15	0	0	0	1.5160	1.5102
16	0	0	0	1.5110	1.5102
17	0	0	0	1.5068	1.5102
18	0	0	0	1.5088	1.5102
19	0	0	0	1.5083	1.5102
20	0	0	0	1.5128	1.5102

Response = Chromatographic resolution (R)

In order to estimate the model, which correspond to Equation (2), the statistical t-test for the model coefficients were applied and then the results of the statistical test were indicated in Table 3. From this table, it was reported that the calculated t-test results and p-values at the 95% confidence level were greater than t-table and lower than p=0.05. These results showed that the model coefficients were significant to explain our quadratic model. In other words, the computed polynomial

4

SELİMOĞLU et al.

Method Development for the Chromatographic analysis of a Two-Component Tablet Formulation Using Chem...

regression model is enough to quantify the suitable chromatographic conditions allowing better peak separation and shortest runtime for the analysis of SMX and TMP.

Table 3
Statistical results for the *t*- tests with p-values for the coefficients of the polynomial regression model

	Coefficients	T Stat	P-value
Intercept	1.5102	90.57	6.59E-16
X_1	-0.3199	28.92	5.69E-11
X_2	-0.1808	16.34	1.53E-08
X_3	0.3022	27.31	1.00E-10
x_1^2	0.1721	15.98	1.90E-08
X_2^2	0.0557	5.17	4.18E-04
X_3^2	-0.2916	27.08	1.09E-10
X_1*X_2	0.1821	12.60	1.85E-07
X_1*X_3	0.0347	2.40	3.73E-02
X_2*X_3	0.2065	14.29	5.58E-08

To demonstrate the factor interactions, three dimensional (3D) graphs and related contour plots were obtained by recording the chromatographic response versus the flow rate and temperature, the chromatographic response versus the acetate buffer (mixture of $CH_3COOH+CH_3COONa$ mixture) and temperature, and the chromatographic response versus the acetate buffer (mixture of CH_3COOH and CH_3COONa) and low rate as shown in Figures 1a-c, respectively. The bends on 3D axis of the surface and contour recordings clearly exhibit significant interactions of the chosen factors
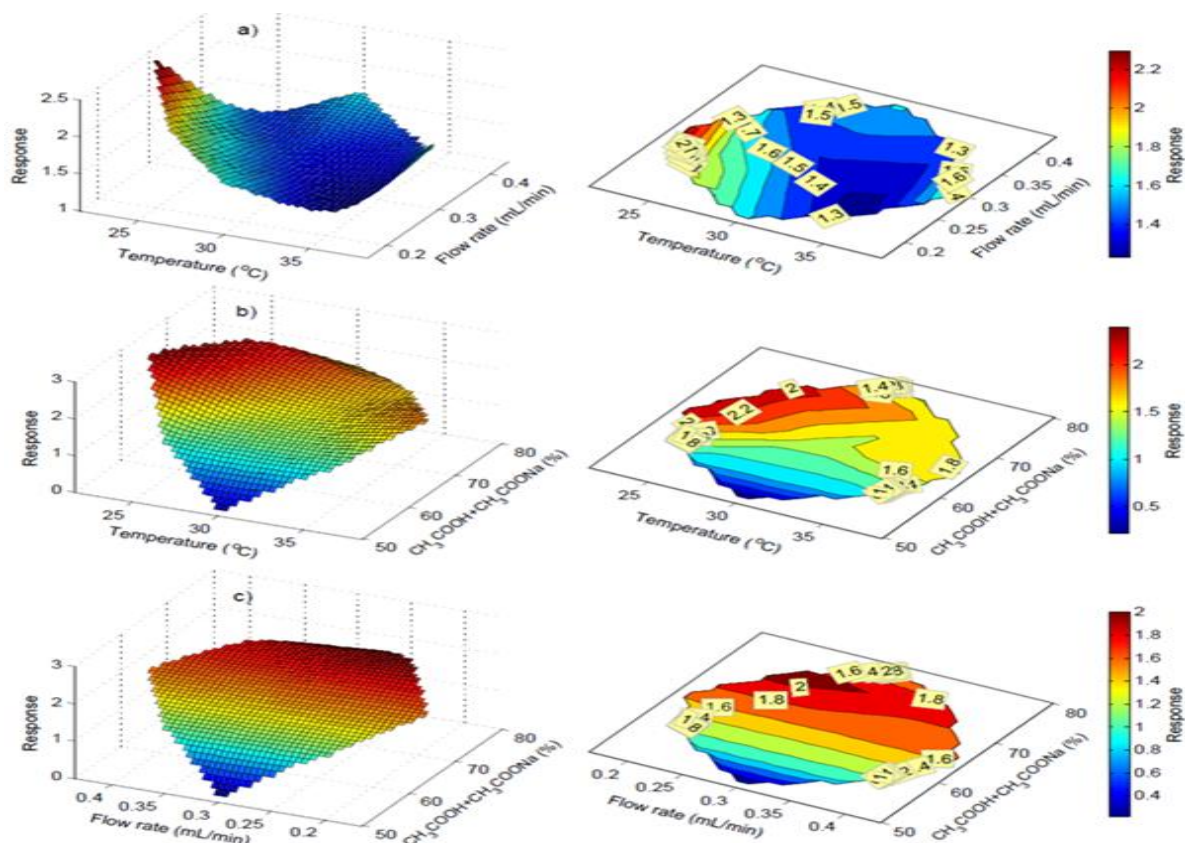
Figure 1 The plots of the surface and contour displays the relationships between flow rate-temperature and chromatographic response (a); flow rate-temperature and chromatographic response (b); flow rate and 0.1 M acetate buffer (at pH 4.75) (c).

5

Before the chemometric optimization of chromatographic conditions, Figure 2 shows a UPLC chromatogram with bad chromatographic elution of analytes and IS at the random experimental conditions. Such situation shows the necessity of chemometric optimization for chromatographic analysis of TMP and SMX in samples.
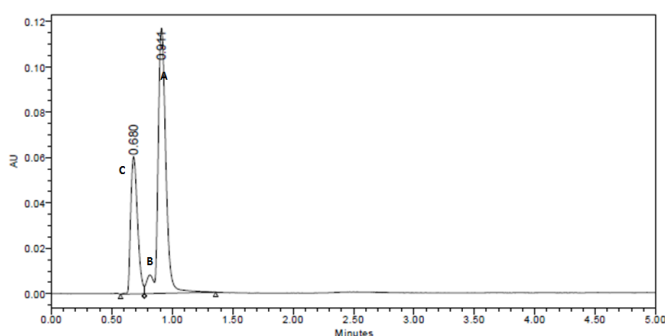
Figure 2 UPLC Chromatograms of a) 36 µg/mL SMX, b) 18 µg/mL TMP and c) 12 µg/ml IS were recorded before optimization with the detection at 270 nm.

To develop a new liquid chromatographic method, the suitable chromatographic experimental conditions for the temperature (X_1), the flow rate (X_2) and acetate buffer percentage (X_3) were computed from the mathematical solving of Equation (2) obtained by using central composite design. The calculated chromatographic parameters provided better elution of the analytes and short run time for For the preparation of calibration curves for TMP and SMX, the preparation of the calibration samples of analytes was done by mixing the standard stock solutions as depicted in the "Chemicals and Standard Solutions" section. Their chromatograms were recorded under optimized conditions, which determined as 38ºC for the column temperature, 0.2 mL/min for the flow rate of the mobile phase, 66% for the percentage for the acetate buffer at pH 4.74 in the mobile phase. Taking into account the percentage of acetate buffer defined by the optimization procedure, the mobile phase system containing a mixture of methanol and 0.1 M acetate buffer at pH 4.74 (34:66, v/v) was used.

The calibration curves were obtained by the linear regression of concentration on the chromatographic area ratio of analyte to IS.

improving a new UPLC method that enables to determine SMX and TMP in their mixture. The above optimal UPLC conditions for the elution of SMX and TMP in their mixture were found to be 38.0°C for column temperature, 0.2 mL/min for flow rate, and 66 % for the percentage of 0.1M acetate buffer at pH 4.75 in mobile phase.

Under optimized UPLC conditions, the UPLC chromatogram of a calibration sample containing 36 µg/mL SMX and 18 µg/mL TMP in the presence of 12 µg/ml IS was recorded with the PDA detection at the wavelength of 270 nm. The recorded chromatogram was illustrated in Figure 3.
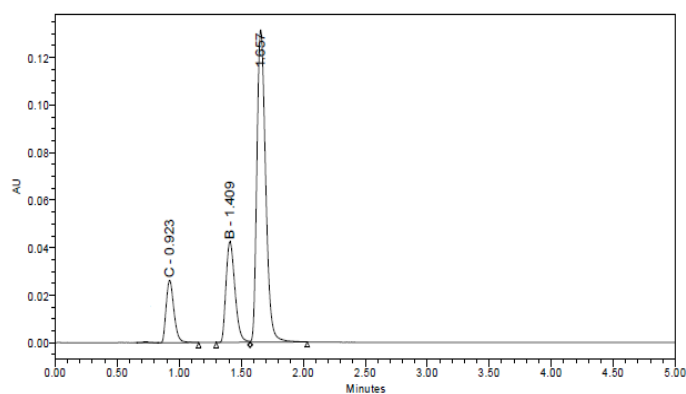
Figure 3 UPLC Chromatograms of the mixture of the standards: a) 36. µg/mL SMX, b) 18.0 µg/mL TMP and c)12.0 µg/ml IS were recorded after the central composite design and optimization procedure with the detection at 270 nm.

Regression analysis and its statistical results were given in Table 4. TMP and SMX were determined by using the calibration equations of the investigated drugs.

Table 4
Least square regression analysis and
Statistical results for the investigated drugs

Parameter	SMX	TMP
λ (nm)	270 nm	270nm
Range (µg/mL)	1.0-36.0	1.0-36.0
m	0.065117	0.021394

6

SELİMOĞLU et al.

Method Development for the Chromatographic analysis of a Two-Component Tablet Formulation Using Chem...

n	0.032512	-0.00857
r	0.99994	0.999771
SE(m)	0.00032	0.000205
SE(n)	0.002928	0.000443
SE(r)	0.009988	0.006382
LOD (µl/min)	0.36	0.16
LOQ (µl/min)	1.19	0.55

m=Slope of the regression function
n =Intercept of the linear regression function
r= Correlation coefficient of the regression function
SE (m)=Standard error of slope
SE(n)=Standard error of intercept
SE (r)= Standard error of correlation coefficients
LOD= Limit of detection
LOQ= Limit of quantitation.

3.2. Validity of the Method

The calibration curves for SMX and TMP were reported to be linear in the range of 1.0-36.0 µg/ml. High correlation coefficients were observed for the linear regression equations of TMP and SMX as shown in Table 4. A good separation of chromatographic peaks in a chromatogram with the resolution factor of 1.90 were reported as displayed in Figure 2. In the chromatogram indicated in Figure 2, the retention times for IS, TMP and SMX were reported as 0.900, 1.343 and 1.532, respectively.

The limit of detection (LOD) and the limit of quantitation (LOQ) in the dynamic concentration range were computed from the standard deviation of the intercept and slope values of calibration functions, and then their results were shown in Table 4. The developed UPLC method, which was applied in this study, supplies high chromatographic resolution with the shortest runtime for the analysis of the investigated drugs. Accuracy and precision of the newly developed UPLC method was tested by using recovery studies, including the analysis of the mixture of TMP and SMX in the presence of IS

The recovery results of the analysis were given in Table 5. As can be seen from Table 5, good accurate and precise recovery results with acceptable numerical values of the standard deviations and relative standard deviations were observed

Table 5
Recoveries of SMX and TMP in binary mixtures using the improved UPLC method

	Added (µg/ml)		Found (µg/ml)		Recovery (%)	
No.	**SMX**	**TMP**	**SMX**	**TMP**	**SMX**	**TMP**
1	1	6	0.97	6.07	96.6	101.1
2	6	6	5.68	6.02	94.6	100.3
3	12	6	12.13	6.00	101.1	100.0
4	18	6	17.78	5.62	98.8	93.7
5	24	6	24.66	5.91	102.7	98.5
6	30	6	29.66	5.80	98.9	96.7
7	36	6	35.97	5.81	99.9	96.8
8	30	1	29.81	1.05	99.4	105.0
9	30	6	30.18	5.84	100.6	97.3
10	30	12	29.68	11.74	98.9	97.8

SELİMOĞLU et al.

Method Development for the Chromatographic analysis of a Two-Component Tablet Formulation Using Chem...

11	30	18	29.34	17.75	97.8	98.6
12	30	24	29.23	24.32	97.4	101.3
13	30	30	30.76	30.19	102.5	100.6
14	30	36	29.52	37.59	98.4	104.4
				Average	99.12	99.44
				SD	2.21	3.04
				RSD	2.23	3.06

SD = Standard deviation; RSD = Relative standard deviation.

3.3. Analysis of Tablets

The optimized UPLC method was applied to the commercial tablets for the quantitative analysis of SMX and TMP amounts after the validation procedure. Under optimized chromatographic conditions, the chromatographic signals of the analytes in tablet formulation in the presence of IS were recorded as shown in Figure 4. Placing the chromatographic peak-area ratio of drug/IS to the calibration equations, SMX and TMP in tablets were computed. Tablet analysis procedure was repeated ten times.
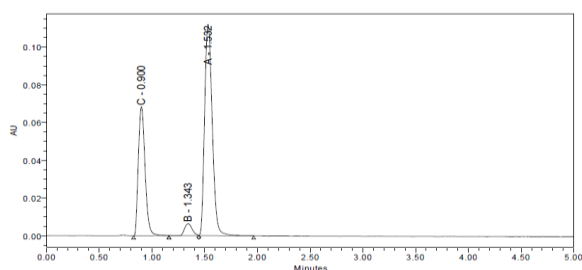
Figure 4 The UPLC Chromatograms of a) SMX b) TMP in a commercial tablet in presence of c)12 µg/ml IS with the detection at 270 nm.

The commercial tablets analysis results were listed in Table 6. These determination results were computed from the mean of a set of ten replicated experiments. The relative standard deviation values were calculated as 1.63% for SMX and 2.42 for TMP as illustrated in Table 6.

8

SELİMOĞLU et al.

Method Development for the Chromatographic analysis of a Two-Component Tablet Formulation Using Chem...

Table 6
Experimental determinations obtained by using the optimized chromatographic procedure for the analysis of the tablets.

No.	mg/tab	
	SMX	TMP
1	796.2	160.6
2	800.3	169.6
3	792.0	157.2
4	820.4	158.9
5	805.8	163.0
6	822.8	163.9
7	797.0	157.6
8	794.8	160.0
9	798.5	157.9
10	778.5	157.8
Mean	800.63	160.65
SD	13.09	3.89
RSD	1.63	2.42

SD = Standard deviation; RSD = Relative standard deviation.
Label claim is 800 mg SMX and 160 mg TMP per tablet

In conclusion, it was reported that the improved UPLC method is very appropriate for the simultaneous quantitative assessment of the related drugs in tablets.

5. CONCLUSIONS

In this paper, a chemometric methodology based on the central composite design and optimization procedure was used for finding optimal chromatographic condition for developing new UPLC method for the simultaneous quantitative assessments of SMX and TMP in binary mixtures and tablets.

This chemometric optimization approach provided the optimal chromatographic conditions giving enhanced chromatographic elution with short runtime and also economical, precise, accurate, and reliable analysis of TMP and SMX in tablets. Consequently, the improved RP-UPLC method is very suitable for the quality control and quantitative analysis of tablets containing TMP and SMX drugs.

The Declaration of Conflict of Interest/ Common Interest
No conflict of interest or common interest has been declared by the authors.

The Declaration of Ethics Committee Approval
This study does not require ethics committee permission or any special permission.

SELİMOĞLU et al.

Method Development for the Chromatographic analysis of a Two-Component Tablet Formulation Using Chem...

Authors' Contribution

The authors contributed equally to the study.

The Declaration of Research and Publication Ethics

The authors of the paper declare that they comply with the scientific, ethical and quotation rules of SAUJS in all processes of the paper and that they do not make any falsification on the data collected. In addition, they declare that Sakarya University Journal of Science and its editorial board have no responsibility for any ethical violations that may be encountered, and that this study has not been evaluated in any academic publication environment other than Sakarya University Journal of Science.

REFERENCES

[1]. U. M. Rautakorpi, T. Klaukka, P. Honkanen, M. Mäkelä, T. Nikkarinen, E. Palva, R. Roine, H. Sarkkinen, P. Huovinen "Antibiotic Use by Indication: A Basis for Active Antibiotic Policy in the Community" Journal Scandinavian Journal of Infectious Diseases vol. 33, no. 12 pp.920-936, 2009.

[2]. A.R. Gennaro, "Remington: The Science and Practice of Pharmacy", Easton, PA, Mack Publishing Co vol. II, p. 1276, 1995.

[3]. Q. Zou, H. Song, M. Tang, K. Lu "Measurements of HO2 uptake coefficient on aqueous (NH4)2SO4 aerosol using aerosol flow tube with LIF system" Chinese Chemical Letters, vol 30, no 12, pp 2236-2240, 2019.

[4]. M. J. B. Mengelers, P. E. Hougee, L. H. M. Janssen, A.S.J.P.A.M. Van Miert "Structure-activity relationships between antibacterial activities and physicochemical properties of sulfonamides" Journal of Veterinary Pharmacology and Therapeutics vol.20, pp 276-283, 1997.

[5]. Z. S. Mehdi "Analytical Method Development for the Spectrophotometric Determination of Sulfamethoxazole in Bulk Drug and Pharmaceutical Preparation" Journal of Chemistry and Biochemistry, vol. 3, no. 1, pp. 63-74, 2015.

[6]. T. Horwedel, J.C Hagopian. L.J Bowman. "W.C Chapman. PGI17-Prevention of cytomegalovirus in liver transplant recipients before and after protocol change: a cost-effectiveness analysis" Value in Health vol. 17, no. 3, pp. A38, 2014.

[7]. J. Robson, J. L. McKenzie, R. Cursons, G. M. Cook, V. L. Arcus. "The vap BC Operon from Mycobacterium smegmatis Is An Autoregulated Toxin–Antitoxin Module That Controls Growth via Inhibition of Translation" Journal of Molecular Biology, vol. 390, no. 3, pp. 339-578, 2009.

[8]. G. Geissler, E. Mutschler "Mutschler drug effects", Wissenschaftliche Verlagsgesellschaft mbH Stuttgard 9th edition 2008.

[9]. R. Vardanyan V. Hruby "Synthesis of Essential Drugs" 1st Edition Elsevier Science Published 2006.

[10]. M. Sanchez, P. F. Salinasa, M. C. Mahederoa, J.J. Aaronb. "Spectrofluorimetric determination of sulphonamides in pharmaceutical compounds and foods" Journal of Pharmaceutical and Biomedical Analysis, v. 10, no.10–12, pp. 805-808, 1992.

[11]. H. Amini, A. Ahmadiani Journal of Pharmaceutical and Biomedical Analysis v.43 pp. 1146-1150, 2007.

[12]. S. V. Temerev, "Determination of mercury in aquatic ecosystems" Journal

10

SELİMOĞLU et al.

Method Development for the Chromatographic analysis of a Two-Component Tablet Formulation Using Chem...

of Analytical Chemistry, v. 63, no.3, pp. 292-296, 2008.

[13]. D.H.Shewiyoab, E. Kaaleb, P. G .R ishab B.Dejaegherc, J. Smeyers–Verbekec Y, V. Heydenc. Journal of Chromatography A. v. 1216, no. 42, pp. 7102-7107, 2009.

[14]. P. J. Gemperlinea, J. H. Cho, B. Bakera, B. Batchelor, D. S. Walker. "Determination of multicomponent dissolution profiles of pharmaceutical products by in situ fiber-optic UV measurements" Analytica Chimica Acta, v. 345, no. 1–3, pp. 155-159, 1997.

[15]. M.H. Givianrad, M. Saber-Tehrani, P. Aberoomand-Azar, M. Mohagheghian "H-point standard additions method for simultaneous determination of sulfamethoxazole and trimethoprim in pharmaceutical formulations and biological fluids with simultaneous addition of two analytes" Spectrochimica Acta Part A: Molecular and Biomolecular

Spectroscopy, v. 78, no. 3, pp. 1196-1200, 2011.

[16]. Y. Dong, J. Li, X. Zhong, L. Cao, Q. Fan, "High-throughput prediction of tablet weight and trimethoprim content of compound sulfamethoxazole tablets for controlling the uniformity of dosage units by NIR" Spectrochimica Acta Part A: Molecular and Biomolecular Spectroscopy, v. 159, pp 78-82, 2016.

[17]. A. Glyk, D. Solle, T. Scheper, S. Beutel, "Optimization of PEG–salt aqueous two-phase systems by design of experiments" Chemometrics and Intelligent Laboratory Systems, v. 149,pp.12-21, 2015.

[18]. M. Akyüz, Ş. Ata, E. Dinç, "A chemometric optimization of method for determination of nitrosamines in gastric juices by GC–MS" Journal of Pharmaceutical and Biomedical Analysis v.117, pp. 26–36, 2016.

11

Sakarya University Journal of Science
SAUJS

Title: Synthesis and Biological Evaluation of Novel Dihydro [2,3D] Pyridine Substituted Enaminosulfonamide Compounds as Potent Human Erythrocyte Carbonic Anhydrase II (hCAII) Inhibitors

Authors: Tuna DEMİRCİ, Oğuzhan ÖZDEMİR, Mustafa Oğuzhan KAYA, Mustafa ARSLAN

Synthesis and Biological Evaluation of Novel Dihydro [2,3D] Substituted Enaminosulfonamide Compounds as Potent Human Erythrocyte Carbonic Anhydrase II (hCAII) Inhibitors

Tuna DEMİRCİ[1], Oğuzhan ÖZDEMİR[2], Mustafa Oğuzhan KAYA[3*], Mustafa ARSLAN[4]

Abstract

Dihydro [2,3D] pyridine substituted enaminosulfonamide compounds have been synthesized and their effects on carbonic anhydrase II (hCAII) have been evaluated. Pyrido [2,3 d] pyrimidines were synthesized from barbituric acid derivatives, malonanitrile, aldehyde derivatives in basic condition and then hydrolyzed with hydrochloric acid. The targeted compounds were synthesized from amino sulfanilamide, dihydro [2,3D] pyridine compounds, and triethylorthoformate. ^{1}H NMR, ^{13}C NMR, FT-IR and elemental analysis were used for the structural analysis of the compounds. The half maximal inhibitory concentration (IC_{50}) values of the compounds were determined to be between 27.03 and 104.39 μM for hCA II and 19.85-76.64 μM for K_i.

Keywords: Barbituric acid, Carbonic anhydrase II, Dihydro [2,3D] pyridine, Enaminosulfonamide

1. INTRODUCTION

Known as the first barbiturate, was synthesized by Conrad and Guthzeit in 1882 [1]. At the 1903, Fischer and von Mehring [2] made a name for themselves in the medical world by investigating hypnotic activity and phenobarbital was introduced in 1912. In fact, when this structure, which does not have physiological effect, is substituted with alkyls from the 5th position, a hypnotic effect is produced and thus numerous compounds

are prepared. Also, alkylation or aryl alkylation of position 5 has been disclosed as pharmacodynamics derivatives. This alkylation, molecular physicochemical property defining the pKa and logP value is also used as medicines against many diseases make changes accordingly. There are barbituric acid derivatives used in many treatments.

In some cases, there are many barbituric acid derivatives that do not exert a single effect but enhance the sedative-hypnotic effect when given together [3]. These compounds prevent oxidation during the biotransformation of barbiturates.

* Corresponding Author: oguzhan.kaya@kocaeli.edu.tr
[1] Duzce University, ,Duzce, Turkey, , E-mail: , ORCID: https://orcid.org/0000-0001-8933-4944
[2] Batman University, ,Batman, Turkey, , E-mail: , ORCID: https://orcid.org/ 0000-0002-9588-3285
[3] Kocaeli University, , Turkey, , E-mail: , ORCID: https://orcid.org/0000-0002-8592-1567
[4] Sakarya University, , Sakarya, Turkey, , E-mail: , ORCID: https://orcid.org/0000-0003-0796-4374

Thus, barbiturates prolong the action time and increase the depth of action.

The pharmacokinetic properties of barbituric and thiobarbituric acid derivatives are determined by enzymatic reactions against acidic and lipophilic properties [4]. These properties are based on structural and physicochemical factors. In general, lipophilic properties increased the amount of metabolization and are known to shorten the duration of action.

Dihydro [3,2-d] pyridopyrimidine compounds are nitrogen-based heterocyclic compounds that have inhibitory and activator properties for many different enzyme types. With this feature, they are compounds that have many bioactive effects. For example, diabetes[5], asthma [6], [7], cancer [8] and aids [9] are among the most important of them. Another feature is that it has shown extremely positive results against p3818 phosphoinositide 3-kinase (PI3K and Epstein-Barr virus (EBV) [10].

Sulfonamides was discovered that it could be used as diuretics in the 1940s [11] and ant diabetic in the 1950s [12]. Computer-aided drug designs that have been developing rapidly in recent years have suggested that sulfonamides may have very different biological activity. As a matter of fact, Sildenafil Citrate (Viagra) [13] was introduced in 1996 and Amprenavir [14], a protease inhibitor used in the treatment of HIV and Celecoxib, which was used for the treatment of pain relief, meniscus and rheumatism, was used in the treatment of HIV [15].

Carbonic anhydrases (CAs; EC 4.2.1.1) are zinc enzymes [16], present in both prokaryotes and eukaryotes,[17] and they catalyze the reversible hydration of CO_2 efficiently to bicarbonate [18], [19]. Abnormal increase or decrease of several CAs activities have been reported to be associated with different human disorders (Alzheimer's disease, edema, epilepsy, altitude sickness, obesity, stroke, several types of cancer) [20] due to their crucial roles in a wide range of pathophysiological processes such as in respiration, pH and CO_2 homeostasis, secretion, gluconeogenesis, and ureagenesis, [19]-[22]. The identification of hCAs in the central nervous system or the choroid plexus, hCA I is expressed in the motor neurons in the human spinal cord and plays role in edema. In contrast, hCA II, plays role in glaucoma, is located both in the choroid plexus and in oligodendrocytes, myelinated tracts, astrocytes, and myelin sheaths in the vertebrate brain [20], [23].

In the present study, we have synthesized and investigated inhibitory effects of Novel Dihydro [2,3D] Pyridine Substituted Enaminosulfonamide Compounds on hCAII.

2. MATERIALS AND METHODS

2.1. Materials and Techniques

FT-IR spectra were measured on a SHIMADZU Prestige-21 (200 VCE) spectrometer with ATR attachment. ^{1}H and ^{13}C NMR spectra were measured on spectrometer at VARIAN Infinity plus 300 and 75 Hz, respectively. ^{1}H and ^{13}C chemical shifts are referenced to the internal deuterated dimethyl sulfoxide (DMSO-$_{d6}$) solvent. The elemental analysis was carried out with a Thermo Scientific Flash 2000 instrument with tin pan. All chemical was purchased from MERCK, Alfa Easer, Sigma-Aldrich and Fluka.

2.1.1. Pyrido [2,3 d] pyrimidines synthesis

Barbituric acid derivative (1 mmol), Malonanitrile (1 mmol,) aldehyde derivates (1 mmol), and 0.1 mL of triethylamine were taken in a reaction flask and stirred in 5 mL of EtOH at rt for 3 hours. The reaction mixture was cooled to room temperature and the Ethanol removed. 3-4 ml of acetic acid was added to the crude product and poured into 50 ml of iced water. The resulting precipitate was filtered through the crucible and left to dry. The structures of the synthesis compounds were confirmed by ^{1}H NMR and ^{13}C NMR spectra.

2.1.2. Dihydro[3,2-d]pyrimidine synthesis

Pyridopyrimidines (2 mmol), 2 mL of concentrated HCl and 4 mL of water were taken up in a reaction flask and stirred overnight at 100°C. The reaction mixture was cooled to room temperature and extracted with dichloromethane (DCM). The crude product was crystallized from Ethyl acetate: Hexane (1:1). The structures of the synthesis compounds were confirmed by ^{1}H NMR and ^{13}C NMR spectra.

2.1.3. Sulfonamide substitute Dihydro[3,2-d] pyrimidine synthesis

Dihydro [3,2-d] pyrimidine (1 mmol), 5 mL of tri-ethylortaformiate and amino sulfonamide (1mmol) were taken up in a reaction flask and stirred 2h at 80°C in Ethanol. The reaction mixture was cooled to room temperature and extracted with Ethyl acetate. The crude product was crystallized from Ethyl acetate: Hexane (1: 1). The structures of the synthesis compounds were confirmed by ^{1}H NMR and ^{13}C NMR spectra.

2.1.4. Preparation of haemolysate and purification from blood red cells

Blood samples (25 ml) were taken from healthy human volunteers. They were centrifuged at 1000 g for 20 min at 4 °C and the supernatant was removed. The packed erythrocytes were washed three times with 0.9% NaCl and then hemolysis in cold water. The pH of the haemolysate was adjusted to pH 8.5 with solid Tris-base. The 25 ml haemolysate was applied to an affinity column containing Sepharose-4B-L-tyrosine-sulfonamide [24]. CA isozymes were then eluted with 0.1 M NaCl/25 mM Na_2HPO_4 (pH 6.3) and 0.1 M CH_3COONa/0.5 M $NaClO_4$ (pH 5.6), which recovered hCAII, respectively.

2.1.5. Esterase activity assay

CA activity was assayed by following the change in absorbance at 348 nm of 4-nitrophenyl-acetate (NPA) to 4-nitrophenylate ion over a period of 3 min at 25°C using a spectrophotometer (Shimadzu UV-Vis 1800) according to the method described in the literature [25]. Inhibitory effects of the compounds (1-10) on enzyme activities were tested under *in vitro* conditions.

2.1.6. *In vitro* inhibition studies

For the inhibition studies of sulfonamides, different concentrations of these compounds were added to the enzyme reaction mixture. CA enzyme activity without a synthesized compounds solution was accepted as to be 100%. Activity percentage values of CA for different concentrations of each sulfonamide were determined by regression analysis using Microsoft Office Excel programme. IC$_{50}$ values were calculated from Lineweaver–Burk [26] graphs and have been given in Table 1 .

2.1.7. Calculation of Inhibition Constants (K$_i$) by Cheng & Prusoff Equation

The inhibition constants (K$_i$) of the original synthesis sulfonamide derivatives (1→10) were calculated mathematically using the Cheng & Prusoff equation [27].

3. RESULTS AND DISCUSSION

Dihydro [2,3D] pyridine substituted enaminosulfonamide compounds which is shown in scheme 1 have been synthesized and characterized by ^{1}H NMR, ^{13}C NMR, FT-IR and elemental analysis. In the ^{1}H-NMR, Dihydro [2,3D] pyridine substituted enaminosulfonamide compounds were shown about 11.10 ppm NH peak for sulfanilamide and It can be shown a singlets relating to hydrogens of vinyl proton about 9.05 ppm. All aromatic protons were seen about 8.75 and 7.00 ppm. In addition, Sulfanilamide substituted aromatic proton signals were appeared between from 8.74 to 9.37. Barbituric acid methyl groups can be seen at about 3.50 ppm. In FTIR spectrum of compounds 1-10, it was shown about 3420 cm^{-1} NH vibration. Sulfanilamide SO$_2$ asymmetric stretching was about 1350 cm^{-1} and SO$_2$ symmetric stretching was between 1139 to 1150 cm^{-1}. Barbituric acid carbonyl group can be seen between 1520 and 1560 cm^{-1}.

Carbonic anhydrase CA (E.C:4.2.1.1) isoenzyme glaucoma [28]–[30], epilepsy [31] and certain tumor types [32]–[34] such as is one of a number of pharmacological agents designed to prevent or treat the disorder. Therefore, it is of great importance that natural phenolic compounds, which are natural and have no side effects, inhibit CA enzyme activities [35]–[37]. Many natural and synthetic substances can alter the activity of the enzyme, which can affect live metabolism even at low concentrations [38].

Synthesized human carbonic anhydrase II study the effects on enzyme activity previously studied compounds were characterized.

DEMİRCİ et al.

Synthesis and Biological Evaluation of Novel Dihydro [2,3D] Pyridine Substituted Enaminosulfonamide ...
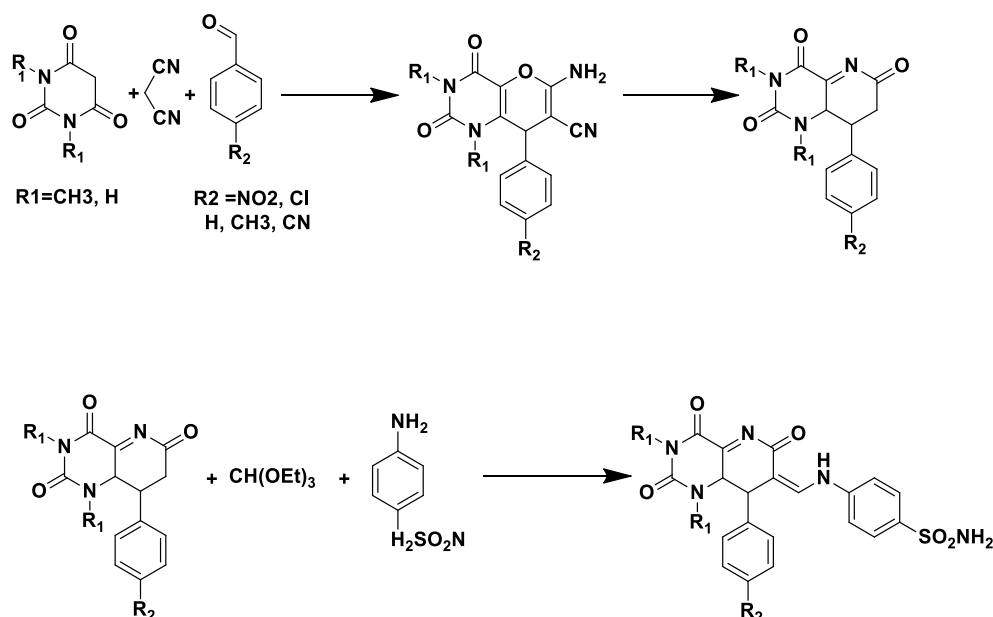
Figure 1. Synthesis of 8-(phenyl)-8,8a-dihydropyrido[3,2-d]pyrimidine-2,4,6(1H,3H,7H)-trione derivatives.
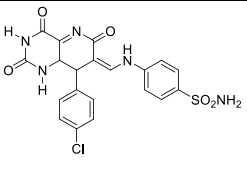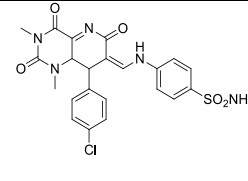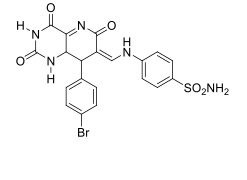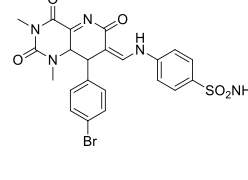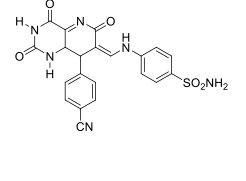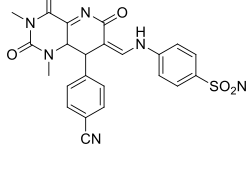
Dihydro [2,3] pyridine compound may isoenzyme activity of CAII inhibitory properties were investigated previously in the literature many times [36]. In our study, the effects of compounds 1-10 on the activity of carbonic anhydrase II isoenzyme purified from human erythrocytes were investigated (Table 1). Compounds 1 and 6 had a strong effect against carbonic anhydrase II isoenzyme activity, while compounds 3 and 8 had a lower effect on CAII activity than other compounds. The IC_{50} values of hCAII for 1 and 6 were observed as 27.03 and 28.63 µM, K_i values for 1 and 6 were 19.85 and 21.02, respectively, whereas those of 3 and 8 were found to be 100.57 and

104.39 µM for the IC_{50} values and 3 and 8 were found to be 73.84 and 76.64 µM for the K_i values (Table 1). When the data obtained are taken into consideration, the highest inhibition shows 1 and the lowest inhibition shows 8.

When looking for the inhibition mechanism with carbonic anhydrase II, it is thought to be the result of the interaction of the zinc atoms in the enzyme and the sulfonamide structure in the structure. Apart from this, the effect of functional groups on the aromatic structure has caused fundamental differences between the results due to the effect of the electron on the sulfonamide.

Table 1. Result of CAII inhibition capacity.

No	Compound	hCAII (IC$_{50}$ µM)	K$_i$ (µM)	No	Compound	hCAII (IC$_{50}$ µM)	K$_i$ (µM)
1		27.03	19.85	6		28.63	21.02
2		82.00	60.21	7		95.87	70.39

DEMİRCİ et al.

Synthesis and Biological Evaluation of Novel Dihydro [2,3D] Pyridine Substituted Enaminosulfonamide ...

3		100.57	73.84	8		104.39	76.64
4		39.95	29.33	9		45.99	33.77
5		48.85	35.87	10		57.14	41.95

4-(((2,4,7-trioxo-5-phenyl-1,2,3,4,4a,5-hexahydropyrido[2,3-d]pyrimidin-6(7H)-ylidene)methyl) amino) benzene sulfonamide 1: Yields: %88. ^{1}H NMR (300 MHz, DMSO-D_6), 11,21 (NH, s), 10,06 (1H, d, N-H), 8.78 (H, d, C=C-H), 7.98 (2H, d, Ar-H), 7.78 (2H, d, Ar-H), 7,76 (2H, s, NH$_2$), 7.60 (2H, d, Ar-H), 7.41 (2H, d, Ar-H), 7.12 (2H, d, Ar-H), 7.11 (H, t, Ar-H), 4.10 (H, s, C-H), 3.88 (H, s, C-H), ^{13}C NMR (75 MHz, DMSO-D_6), 171.16, 168.20, 155.61, 153.62, 148.76, 141.16, 140.72, 130.10, 130.09, 128.60, 127.48, 126.00, 125.72, 116.16, 45.80, 36.72. FT-IR (v, cm^{-1}): 1150,36 (O=S=O), 1256.16 (C-HN-C), 1340.53 (S-NH$_2$), 1616.86 (NH-C=O), 1645.28 (=N-C=O), 1701.22 (=N-C=O), 2191.13 (-CN),

2974.74 (Aliphatic-H), 3026.55 (C=C, Aromatic). Elemental Analysis, C$_{20}$H$_{17}$N$_5$O$_5$S, calculated: C, 54.66; H, 3.90; N, 15.94; O, 18.20; S, 7.30, Found: C, 54.52; H, 3.88; N, 15.87; O, 18.21; S, 7.52.

4-(((5-(4-nitrophenyl)-2,4,7-trioxo-1,2,3,4,4a,5-hexahydropyrido[2,3-d]pyrimidin-6(7H)-yliene) methyl) amino) benzene sulfonamide 2: Yields % 87. ^{1}H NMR (300 MHz, DMSO-D_6), 11,08 (NH, s), 10,16 (1H, d, N-H), 8.74 (H, d, C=C-H), 8,28 (2H, d, Ar-H), 8.01 (2H, d, Ar-H), 7,81 (2H, s, NH$_2$), 7.80 (2H, d, Ar-H), 7.25 (2H, d, Ar-H), 4.21 (H, s, C-H), 3.87 (H, s, C-H), ^{13}C NMR (75 MHz, DMSO-D_6), 172.06, 168.12, 156.61, 152.02, 149.70, 145.99, 140.16, 140.02, 130.88, 130.79, 128.59, 127.36, 126.12, 116.90, 45.75,

35.02. FT-IR (ν, cm-1): 1161.15 (O=S=O), 1240.23 (NO$_2$), 1288.45 (C-HN-C), 1340.53 (S-NH$_2$), 1616.35 (NH-C=O), 1645.28 (=N-C=O), 2972.31 (C=C, Aliphatic), 3026.55 (C=C, Aromatic). 3203.76 (NH), 3273.20 (NH). Elemental Analysis, C$_{20}$H$_{16}$N$_6$O$_7$S; Calculated, C,49.59; H,3.33; N,17.35; O,23.12; S,6.62. Found, C,49.29; H, 3.24; N, 17.59; O, 23.08; S, 6,80.

4-(((5-(4-chlorophenyl)-2,4,7-trioxo-1,2,3,4,4,5-hexahydropyrido[2,3-d]pyrimidin-6(7H)-ylidene) methylamino)benzenesulfonamide 3: Yields %85. ^{1}H NMR (300 MHz, DMSO-D$_6$), 11,08 (NH, s), 10,24 (1H, d, N-H), 9.06 (H, d, C=C-H), 8,18 (2H, d, Ar-H), 7,96 (2H, s, NH$_2$), 7.84 (2H, d, Ar-H), 7.44 (2H, d, Ar-H), 7.06 (2H, d, Ar-H), 4.06 (H, s, C-H), 3.82 (H, s, C-H), ^{13}C NMR (75 MHz, DMSO-D$_6$), 171.53, 167.42, 158.01, 151.88, 148.55, 141.22, 140.12, 130.82, 130.74, 128.60, 127.86, 126.13, 124.32, 116.70, 45.79, 35.48. FT-IR (ν, cm-1), 796.60 (Ar-Cl), 1143.79 (O=S=O), 1286.52 (C-HN-C), 1361.74 (S-NH$_2$), 1624.06 (NH-C=O), 2920.07 (C=C, Aliphatic), 3078.39 (C=C, Aromatic), 3213.41 (NH), 3354.21 (NH), Elemental Analysis, C$_{20}$H$_{16}$ClN$_5$O$_5$S; Calculated, C,50.69; H,3.40;

Cl,7.48; N,14.78; O,16.88; S,6.77. Found, C,50.52; H,3.44; Cl,7,76 N,14.96; O,16.56; S,6,76.

4-(((5-(4-bromophenyl)-2,4,7-trioxo-1,2,3,4,4,5-hexahydropyrido[2,3-d]pyrimidin-6(7H)-ylidene)methyl) amino) benzene sulfonamide 4: Yields: %80. ^{1}H NMR (300 MHz, DMSO-D$_6$), 12,08 (NH, s), 11,20 (NH, s), 10,64 (1H, d, N-H), 8,80 (H, d, C=C-H), 7.80 (2H, d, Ar-H), 7,66 (2H, s, NH$_2$), 7.54 (2H, d, Ar-H), 7.48 (2H, d, Ar-H), 7.16 (2H, d, Ar-H), 4.21 (H, s, C-H), 3.99 (H, s, C-H), ^{13}C NMR (75 MHz, DMSO-D$_6$), 172.63, 167.87, 158.42, 151.00, 148.75, 141.45, 140.12, 130.14, 130.01, 128.78, 127.06, 126.73, 124.32, 115.70, 45.87, 35.88. FT-IR (ν, cm^{-1}): 698.23 (Ar-Br), 1153.43 (O=S=O), 1286.52 (C-HN-C), 1338.60 (S-NH$_2$), 1593.20(NH-C=O), 1645.28 (=N-C=O), 2900.94 (C=C, Aliphatic), 3066.82 (C=C, Aromatic), 3207.62 (NH), 3361.93 (NH). Elemental Analysis, C$_{20}$H$_{16}$BrN$_5$O$_5$S; Calculated, C,46.34; H,3.11; Br, 15.42; N,13.51; O,15.43; S,6.19. Found, C,46.18; H,3.04; Br,15,66 N,14.58; O,15.68; S,4,86.

4-(((5-(4-cyanophenyl)-2,4,7-trioxo-1,2,3,4,4,5-hexahydropyrido[2,3-d]pyrimidin-6(7H)-ylidene

)methyl)amino)benzene sulfonamide 5: Yields % 81. ^{1}H NMR (300 MHz, DMSO-D$_6$), 10,57 (1H, d, N-H), 9.37 (H, d, C=C-H), 8.44 (2H, d, Ar-H), 8.21 (2H, d, Ar-H), 8,01 (2H, s, NH$_2$), 7.81 (2H, d, Ar-H), 7.41 (2H, d, Ar-H), 4.30 (H, s, C-H), 4.10 (H, s, C-H). ^{13}C NMR (75 MHz, DMSO-D$_6$), 172.99, 1680.70, 159.92, 151.80, 147.86, 145.88, 141.99, 140.78, 130.55, 130.41, 128.74, 127.86, 126.74, 116.41, 45.99, 36.02. FT-IR (v, cm^{-1}): 1166.73 (O=S=O), 1248.52 (C-HN-C), 1338.88 (S-NH$_2$), 1599.20 (NH-C=O), 1636.28 (=N-C=O), 2988.94 (C=C, Aliphatic), 3074.03 (C=C, Aromatic), 3223.20 (NH), 3388.99 (NH). Elemental Analysis, C$_{20}$H$_{16}$BrN$_5$O$_5$S; Calculated, C,46.34; H,3.11; N,13.51; O,15.43; S,6.19. Found, C,46.18; H,3.04; N,14.58; O,15.68; S,4.86.

4-(((1,3-dimethyl-2,4,7-trioxo-5-phenyl-1,2,3,4, 4,5-hexahydropyrido[2,3-d]pyrimidin-6(7H)-ylidene)methyl)amino)benzenesulfonamide 6: Yields % 81. ^{1}H NMR (300 MHz, DMSO-D$_6$), 10.62 (1H, d, N-H), 9.02 (H, d, C=C-H), 7,80 (2H, d, Ar-H), 7,81 (2H, s, NH$_2$), 7.60 (2H, d, Ar-H), 7.24 (2H, d, Ar-H), 7.01 (2H, d, Ar-H), 7.00(H, t, Ar-H), 3.98 (H, s, C-H), 3.79 (H, s, C-H), 3,40

(3H, s, CH$_3$), 3,36 (3H, s, CH$_3$), ^{13}C NMR (75 MHz, DMSO-D$_6$), 173.77, 167.70, 159.01, 150.99, 147.01 140.99, 140.58, 130.78, 130.11, 128.14, 127.75, 126.14,124.58, 115.41, 45.45, 36.99. 28.77, 26.78 FT-IR (v, cm-1): 1159.22 (O=S=O), 1253.73 (C-HN-C), 1342.46 (S-NH$_2$), 1381.03, 1548.84 (CH$_3$-N-C=O), 1589.34 (CH$_3$-N-C=O), 1641.42 (=N-C=O), 2970.38 (C=C, Aliphatic), 3080.02 (C=C, Aromatic), 3215.34 (NH). Elemental Analysis, C$_{22}$H$_{21}$N$_5$O$_5$S; Calculated, C,56.52; H,4.53; N,14.98; O,17.11; S,6.86. Found, C,56.41; H,4.54; N,14.99; O,17.05; S,7,01.

4-((((1,3-dimethyl-5-(4-nitrophenyl)-2,4,7-trioxo-1,2,3,4,4a,5-hexahydropyrido[2,3-d]pyrimidin-6 (7H)-ylidene) methyl) amino) benzene sulfonamide 7: Yields %80. ^{1}H NMR (300 MHz, DMSO-D$_6$), 10.24 (1H, d, N-H), 9.06 (H, d, C=C-H), 8.18 (2H, d, Ar-H), 8.09 (2H, d, Ar-H), 8.08 (2H, s, NH$_2$), 7.80 (2H, d, Ar-H), 7.44 (2H, d, Ar-H), 4.01 (H, s, C-H), 3.82 (H, s, C-H), 3,40 (3H, s, CH$_3$), 3,38 (3H, s, CH$_3$), ^{13}C NMR (75 MHz, DMSO-D$_6$), 174.12, 167.50, 159.99, 150.75, 147.25, 145.25, 140.98, 140.08, 130.75, 130.66, 128.72, 127.02, 126.63, 116.74, 46.52, 37.09.

DEMİRCİ et al.

Synthesis and Biological Evaluation of Novel Dihydro [2,3D] Pyridine Substituted Enaminosulfonamide ...

28.57, 26.98. FT-IR (ν, cm^{-1}), 1161.15 (O=S=O), 1257.59 (NO$_2$), 1338.60 (S-NH$_2$), 1575.84 (CH$_3$-N-C=O), 1593.20 (CH$_3$-N-C=O), 1635.64 (=N-C=O), 2927.78 (C=C, Aliphatic), 3097.98 (C=C, Aromatic), 3313.71 (NH). Elemental Analysis, C$_{22}$H$_{20}$N$_6$O$_7$S; Calculated: C,51.56; H,3.93; N,16.40; O,21.85; S,6.26. Found:C,51,71; H,4,09; N,16.29; O,21.49; S, 6,42.

4-(((5-(4-chlorophenyl)-1,3-dimethyl-2,4,7-trioxo-1,2,3,4,4a,5-hexahydropyrido[2,3-d]pyrimidin-6(7H)-ylidene)methyl)amino) benzene sulfonamide 8: Yields: % 81. ^{1}H NMR (300 MHz, DMSO-D$_6$), 10.22 (1H, d, N-H), 9.01 (H, d, C=C-H), 8.18 (2H, d, Ar-H), 7.98 (2H, s, NH$_2$), 7.89 (2H, d, Ar-H), 7.44 (2H, d, Ar-H), 7.06 (2H, d, Ar-H), 4.01 (H, s, C-H), 3.64 (H, s, C-H), 3,60 (3H, s, CH$_3$), 3,48 (3H, s, CH$_3$), ^{13}C NMR (75 MHz, DMSO-D$_6$), 171.12, 166.70, 158.89, 150.99, 147.25, 140.88, 140.08, 130.66, 130.16, 128.71, 127.12, 127,02, 126.43, 116.04, 46.33, 37.99. 28.75, 26.97. FT-IR (ν, cm^{-1}): 754.17 (Ar-Cl), 1147.65 (O=S=O), 1288.45 (C-HN-C), 1348.24 (S-NH$_2$), 1521.84 (CH$_3$-N-C=O), 1595.13(CH$_3$-N-C=O), 1668.43 (=N-C=O),

2964.59 (C=C, Aliphatic), 3009.25 (C=C, Aromatic), 3253.91 (NH). Elemental Analysis, C$_{22}$H$_{20}$ClN$_5$O$_5$S; Calculated, C, 52.64; H,4.02; Cl,7.06; N,13.95; O,15.94; S,6.39. Found, C, 52,71; H, 3.99; Cl,7.50, N,13.99; O,15.72; S, 6,09.

4-(((5-(4-bromophenyl)-1,3-dimethyl-2,4,7-trioxo-1,2,3,4,4a,5-hexahydropyrido[2,3-d] pyrimidin-6(7H)-ylidene) methyl) amino) benzene sulfonamide 9: yields: %80. ^{1}H NMR (300 MHz, DMSO-D$_6$), 10.41 (1H, d, N-H), 9.21 (H, d, C=C-H), 8.38 (2H, d, Ar-H), 8.12 (2H, s, NH$_2$), 8.01 (2H, d, Ar-H), 7.68 (2H, d, Ar-H), 7.18 (2H, d, Ar-H), 4.01 (H, s, C-H), 3.98 (H, s, C-H), 3,60 (3H, s, CH$_3$), 3,52 (3H, s, CH$_3$), ^{13}C NMR (75 MHz, DMSO-D$_6$), 172.11, 167.25, 158.78, 150.88, 147.25, 140.78, 140.18, 130.55, 130.45, 128.24, 127.14, 127,04, 126.98, 116.74, 45.73, 36.98. 28.55, 26.72. FT-IR (ν, cm^{-1}): 705.95 (Ar-Br), 1153.43 (O=S=O), 1290.38 (C-HN-C), 1363.67 (S-NH$_2$), 1489.05 (CH$_3$-N-C=O), 1556.55 (CH$_3$-N-C=O), 1579.70 (=N-C=O), 2926.01 (C=C, Aliphatic), 3032.10 (C=C, Aromatic), Elemental Analysis, C$_{22}$H$_{20}$BrN$_5$O$_5$S; Calculated, C, 48.36; H, 3.69; Br, 14.62; N,12.82; O,

DEMİRCİ et al.

Synthesis and Biological Evaluation of Novel Dihydro [2,3D] Pyridine Substituted Enaminosulfonamide ...

14.64; S, 5.87. Found, C, 48,22; H, 3.68; Br, 14.50, N, 12.95; O, 14.22; S, 6,43.

4-(((5-(4-cyanophenyl)-1,3-dimethyl-2,4,7-triox o-1,2,3,4,4a,5-hexahydropyrido[2,3-d]pyrimidin-6(7H)-ylidene) methyl) amino) benzene sulfona-mide 10: Yields: % 82. ^{1}H NMR (300 MHz, DMSO-D$_6$), 10.16 (1H, d, N-H), 9.01 (H, d, C=C-H), 8.18 (2H, d, Ar-H), 7,86 (2H, s, NH$_2$), 7.84 (2H, d, Ar-H), 7.64 (2H, d, Ar-H), 7.21 (2H, d, Ar-H), 4.11 (H, s, C-H), 3.98 (H, s, C-H), 3,52 (3H, s, CH$_3$), 3,42 (3H, s, CH$_3$), ^{13}C NMR (75 MHz, DMSO-D$_6$), 173.11, 166.25, 158.75, 150.98, 147.11, 145.99, 140.78, 140.11, 130.99, 130.44, 128.24, 127.78, 127,74, 126.00, 116.74, 45.66, 36.78. 28.65, 26.72. FT-IR (ν, cm^{-1}): 1141.86 (O=S=O), 1288.45 (C-HN-C), 1315.45 (S-NH$_2$), 1541.12 (CH$_3$-N-C=O), 1577.77 (CH$_3$-N-C=O), 1622.13 (=N-C=O), 2977.01 (C=C, Al-iphatic), 3078.39(C=C, Aromatic), 3209.55 (NH). Elemental Analysis, C$_{23}$H$_{20}$N$_6$O$_5$S; Calculated, C, 56.09; H, 4.09; N,17.06; O, 16.24, S, 6.51. Found, C, 56.21; H, 4.18; N, 16.95; O, 16.20; S, 6.67.

The Declaration of Conflict of Interest/ Common Interest

No conflict of interest or common interest has been declared by the authors.

Authors' Contribution

The authors contributed equally to the study.

The Declaration of Ethics Committee Approval

This study does not require ethics committee permission or any special permission

The Declaration of Research and Publicatıon Ethics

The authors of the paper declare that they comply with the scientific, ethical and quotation rules of SAUJS in all processes of the paper and that they do not make any falsification on the data collected. In addition, they declare that Sakarya University Journal of Science and its editorial board have no responsibility for any ethical violations that may be encountered, and that this study has not been evaluated in any academic publication environment other than Sakarya University Journal of Science.

DEMİRCİ et al.

Synthesis and Biological Evaluation of Novel Dihydro [2,3D] Pyridine Substituted Enaminosulfonamide ...

REFERENCE

[1] M. Conrad and M. Guthzeit, "Ueber Barbitursäurederivate," *Berichte der Dtsch. Chem. Gesellschaft*, vol. 15, no. 2, pp. 2844–2850, Jul. 1882.

[2] J. T. Mason, J. W. Baker, and F. Pilcher, "Sodium amytal in surgical management," *Am. J. Surg.*, vol. 9, no. 1, pp. 9–15, Jul. 1930.

[3] N. Moussier, L. Bruche, F. Viani, and M. Zanda, "Fluorinated Barbituric Acid Derivatives: Synthesis and Bio-activity," *Curr. Org. Chem.*, vol. 7, no. 11, pp. 1071–1080, Jul. 2003.

[4] A. Barakat *et al.*, "New Diethyl Ammonium Salt of Thiobarbituric Acid Derivative: Synthesis, Molecular Structure Investigations and Docking Studies," *Molecules*, vol. 20, no. 11, pp. 20642–20658, Nov. 2015.

[5] H. R. Bourne, Y. Weinstein, K. L. Melmon, L. M. Lichtenstein, C. S. Henney, and G. M. Shearer, "Modulation of Inflammation and Immunity by Cyclic AMP," *Science (80-.).*, vol. 184, no. 4132, pp. 19–28, Apr. 1974.

[6] P. M. Epstein and R. Hachisu, "Cyclic nucleotide phosphodiesterase in normal and leukemic human lymphocytes and lymphoblasts.," *Adv. Cyclic Nucleotide Protein Phosphorylation Res.*, vol. 16, pp. 303–24, 1984.

[7] M. D. Leibowitz *et al.*, "A Novel Insulin Secretagogue Is a Phosphodiesterase Inhibitor," *Diabetes*, vol. 44, pp. 68–74, 1995.

[8] E. M. Grivsky, S. Lee, C. W. Sigel, D. S. Duch, and C. A. Nichol, "Synthesis and antitumor activity of 2,4-diamino-6-(2,5-dimethoxybenzyl)-5-methylpyrido[2,3-d]pyrimidine," *J. Med. Chem.*, vol. 23, no. 3, pp. 327–329, Mar. 1980.

[9] Y. Hamamoto and N. Yamamoto, "Anti-Fas monoclonal antibody is cytocidal to human," *Proc. Nati. Acad. Sci.*, vol. 87, no. December, pp. 2–6, 1990.

[10] L. K. Wathen, "Method Of Preventing Or Treating Atherosclerosis Or Restenosis," US 2004/0067947 A1, 2004.

[11] W. B. Schwartz, "The Effect of Sulfanilamide on Salt and Water Excretion in Congestive Heart Failure," *N. Engl. J. Med.*, vol. 240, no. 5, pp. 173–177, Feb. 1949.

[12] C. C. L. Quianzon and I. E. Cheikh, "History of current non-insulin medications for diabetes mellitus," *J. Community Hosp. Intern. Med. Perspect.*, vol. 2, no. 3, pp. 19081, Jan. 2012.

[13] N. K. Terrett, A. S. Bell, D. Brown, and P. Ellis, "Sildenafil (VIAGRATM), a potent and selective inhibitor of type 5 cGMP phosphodiesterase with utility for the treatment of male erectile dysfunction," *Bioorg. Med. Chem. Lett.*, vol. 6, no. 15, pp. 1819–1824, Aug. 1996.

[14] C. R. Fischer, Jnos; Ganellin, *Analogue-based Drug Discovery□*. 2006.

[15] S. Dadiboyena and A. T. Hamme II, "Synthesis of Celecoxib and Structural Analogs- A Review," *Curr. Org. Chem.*, vol. 16, no. 11, pp. 1390–1407, May 2012.

[16] J. B. Baell, A. G. Holloway. "New Subst ructure Filters for Removal of Pan Assay Interference Compounds (PAINS) from Screening Libraries and for Their Exclu sion in Bioassays" *Journal Of Medıcınal Chemıstry*, vol. 53, no.7, pp. 2719-2740, Apr 8, 2010.

[17] S. Batra, Y. A. Sabnis, P. J. Rosenthal *et al*. "Structure-based approach to falcipain-2 inhibitors: Synthesis and biological eva luation of 1,6,7-trisubstituted dihydroi soquinolines and isoquinolines," *Bioorga*

nic&Medıcınal Chemıstry, vol.11, no.3, pp. 2293-2299, May 15, 2003.

[18] N. Berber, M. Arslan, C. Bilen *et al.* "Synthesis and evaluation of new phthala zine substituted beta-lactam derivatives as carbonic anhydrase inhibitors," *Russian Journal of Bioorganic Chemistry*, vol. 41, no. 4, pp. 414-420, Jul, 2015.

[19] M. Kalaycı, C. Türkeş, M. Arslan, Y. De mir, S. Beydemir "Novel benzoic acid de rivatives: Synthesis and biological evalua tion as multitarget acetylcholinesterase and carbonic anhydrase inhibitors," *Arch Pharm.*, e2000282, 2020. https://doi.org/10.1002/ardp.202000282

[20] B. Sever, C. Türkes, M. D. Altıntop, Y. Demir, S. Beydemir "Thiazolyl- pyrazo-line derivatives: *In vitro* and *in silico* eva luation as potential acetylcholinesterase and carbonic anhydrase inhibitors," *Inter national Journal of Biological Macromo lecules*, vol. 163, pp. 1970-1988, 2020.

[21] A. Topal, M. Atamanalp, E. Oruç, Y. De mir, S. Beydemir, A. Işık "*In vivo* changes in carbonic anhydrase activity and histo pathology of gill and liver tissues after acute exposure to chlorpyrifos in rainbow trout," *Archives of Industrial Hygiene and Toxicology*, vol. 65, no. 4, pp. 377-385, 2014.

[22] I. Gulcin, S. Beydemir "Phenolic Compo unds as Antioxidants: Carbonic Anhyd rase Isoenzymes Inhibitors," *Mini Re views in Medicinal Chemistry*, vol. 13, no. 3, pp. 408-430, 2013.

[23] M. Tugrak, H. I. Gul, Y. Demir, I. Gulcin "Synthesis of benzamide derivatives with thiourea-substituted benzenesulfonamides as carbonic anhydrase inhibitors," *Arch Pharm.*, e2000230, 2020. https://doi.org/10.1002/ardp.202000230

[24] T. Demirci, M. Arslan, Ç. Bilen, D. Demir, N. Gençer, and O. Arslan, "Synthesis and carbonic anhydrase inhibitory properties of 1,3-dicarbonyl derivatives of methylaminobenzene-sulfonamide," *J. Enzyme Inhib. Med. Chem.*, vol. 29, no. 1, pp. 132–136, 2014.

[25] J. A. Verpoorte, S. Mehta, and J. T. Edsall, "Esterase activities of human carbonic anhydrases B and C.," *J. Biol. Chem.*, vol. 242, no. 18, pp. 4221–9, Sep. 1967.

[26] H. Lineweaver and D. Burk, "The Determination of Enzyme Dissociation Constants," *J. Am. Chem. Soc.*, vol. 56, no. 3, pp. 658–666, Mar. 1934.

[27] C. Yung-Chi and W. H. Prusoff, "Relationship between the inhibition constant (K_i) and the concentration of inhibitor which causes 50 per cent inhibition (I50) of an enzymatic reaction," *Biochem. Pharmacol.*, vol. 22, no. 23, pp. 3099–3108, Dec. 1973.

[28] C. T. Supuran, A. S. A. Altamimi, and F. Carta, "Carbonic anhydrase inhibition and the management of glaucoma: a literature and patent review 2013-2019," *Expert Opin. Ther. Pat.*, vol. 29, no. 10, pp. 781–792, Oct. 2019.

[29] E. Masini, S. Sgambellone, and L. Lucarini, "Carbonic anhydrase inhibitors as ophthalmologic drugs for the treatment of glaucoma," in *Carbonic Anhydrases*, Elsevier, 2019, pp. 269–285.

[30] S. Kalinin *et al.*, "Highly hydrophilic 1,3-oxazol-5-yl benzenesulfonamide inhibitors of carbonic anhydrase II for reduction of glaucoma-related intraocular pressure," *Bioorganic Med. Chem.*, vol. 27, no. 21, p. 115086, 2019.

[31] E. Berrino and F. Carta, "Carbonic anhydrase inhibitors for the treatment of epilepsy and obesity," in *Carbonic Anhydrases*, Elsevier, 2019, pp. 311–329.

[32] C. T. Supuran, "Carbonic anhydrase inhibitors as emerging agents for the treatment and imaging of hypoxic tumors,"

Expert Opin. Investig. Drugs, vol. 27, no. 12, pp. 963–970, Dec. 2018.

[33]   C. T. Supuran, "Carbonic Anhydrase Inhibition and the Management of Hypoxic Tumors," *Metabolites*, vol. 7, no. 3, p. 48, Sep. 2017.

[34]   Y. Zhou, R. B. Mokhtari, J. Pan, E. Cutz, and H. Yeger, "Carbonic Anhydrase II Mediates Malignant Behavior of Pulmonary Neuroendocrine Tumors," *Am. J. Respir. Cell Mol. Biol.*, vol. 52, no. 2, pp. 183–192, Feb. 2015.

[35]   Z. Huyut, Ş. Beydemir, and İ. Gülçin, "Inhibition properties of some flavonoids on carbonic anhydrase I and II isoenzymes purified from human erythrocytes," *J. Biochem. Mol. Toxicol.*, vol. 31, no. 9, p. e21930, Sep. 2017.

[36]   H. Göcer, A. Akıncıoğlu, S. Göksu, and İ. Gülçin, "Carbonic anhydrase inhibitory properties of phenolic sulfonamides derived from dopamine related compounds," *Arab. J. Chem.*, vol. 10, no. 3, pp. 398–402, 2017.

[37]   T. Gokcen, M. Al, M. Topal, I. Gulcin, T. Ozturk, and A. C. Goren, "Synthesis of some natural sulphonamide derivatives as carbonic anhydrase inhibitors," *Org. Commun.*, vol. 10, no. 1, pp. 15–23, 2017.

[38]   E. Garibov *et al.*, "Synthesis of 4,5-disubstituted-2-thioxo-1,2,3,4-tetrahydropyrimidines and investigation of their acetylcholinesterase, butyrylcholinesterase, carbonic anhydrase I/II inhibitory and antioxidant activities," *J. Enzyme Inhib. Med. Chem.*, vol. 31, pp. 1–9, 2016.

Title: Removal of Acid Violet 90 Dyestuffs in Aqueous Solutions by Ozonation Method

Authors: Füsun BOYSAN

Removal of Acid Violet 90 Dyestuffs in Aqueous Solutions by Ozonation Method

Füsun BOYSAN[*1]

Abstract

Due to the colored wastewater from many industries, especially textile dyehouses, the dyestuffs that increase in variety with the developing technology, the risk of toxicity, as well as the aesthetic concerns, create a danger for human and environmental health and their treatment is becoming increasingly important. Color in wastewater can only be partially removed by conventional treatment methods. However, by treating with ozone, which is a strong oxidant, not only the color of the waste water is removed, but also the amount of organic pollution is reduced. In this study, color removal was investigated by ozonation method in synthetic water containing Acid Violet dye with an initial concentration of 50 mg/L. As a result of the study, the maximum efficiency was reached with pH 7, ozone dose 0.375 g/L.h, time 7.5 minutes, and 48.578 mg/L substance removal was achieved.

Keywords: Ozonation, Acid Violet 90, Dyestuff, Oxidation

1. INTRODUCTION

Water is considered the most effective and the leading solvent in textile production. Textile factories are the branch that consumes the most water in the industrial field, 0.2-0.5 m^3 of water is normally required to create 1 kg of finished products. The waste of textile dyeing factories generally consists of various refractory materials such as intense color, chemical oxygen demand (COD), suspended solids, heavy metals and non-ionic surfactants [1]. Also, the textile industry uses a lot of water due to the versatile washing of dyed fabrics to remove paint residues from their surfaces [2]. The presence of dyes at even very low concentrations in the effluent is undesirable as it can be highly visible [3]. Colored wastewater disrupts the clear appearance of the water and reduces the transparency of the water surface of and also disrupts the photosynthetic activity of aquatic organisms [4]. Since textile wastewaters containing toxic and potentially carcinogenic substances, they should be treated properly before discharging into water bodies [5, 6].

[*] Corresponding Author: fboysan@sakarya.edu.tr

[1] Sakarya University, Department of Environmental Engineering, Sakarya, Turkey, ORCID: https://orcid.org/0000-0003-2100-0264

It is used to process most impurities in the form of chemical and mechanical action during processing, dirt, salt, oil, grease and colors of natural fibers, used and dead dyes, chemicals, polymers and fibers. Many other industries, such as textile manufacturing and pharmaceutical, food, paper and ink manufacturing, use more than 30,000 industrial dyes with 8,000 different chemical structures and are often released into waste water [7]. Approximately 10-20% of the dyes used in textile dyehouses are directly discharged without interacting with the fabric. [8]. These potentially toxic organic and mineral compounds create wastewater that returns to the environment [9, 10].

Reactive dyes have been used more in the last decade. In addition, the wastewater treatment units of the dyehouses have started to be inadequate due to the more difficult biological degradation of these dyes, especially those containing azo groups [11]. Also, since these dyes have carcinogenic and toxic properties, more careful treatment is required before discharging [12].

Acid Violet 90 is an aromatic azo compound. Aromatic azo compounds are formed by converting the aryl diazonium cation to another aryl ring containing an electron releasing group [13]. Azo coupling reactions are carried out at cold temperatures where diazonium salts are more stable. Oxidation of hydrazines (R-NH-NH-R ') also yields azo compounds. Azo dyes derived from benzidine are carcinogens; classically their exposure to bladder cancer. Therefore, azo dye pollution is a problem to be avoided in the textile industry [14].

Since ozone is a widely used and effective oxidant, it is a treatment method used for the removal of organic and inorganic substances in water, as well as taste and color removal [15, 16]. The reaction rate of ozone is affected by both reaction kinetics and mass transfer, just like other gas absorption reactions [17]. The rate limiting step of ozone is due to a gas-liquid mass transfer rate due to its low solubility [18]. The mass transfer rate of ozone depends on the properties of the ozone mixing system, the degradation kinetics of ozone, and the size and amount of bubbles

formed [13, 19]. The efficiency of ozone can be increased with a higher ozone surface area by forming smaller bubbles [20].

In this study, the removal of Acid Violet 90 dyestuff by ozonation method was investigated and optimum removal efficiency was studied. pH, reaction time and ozone dose parameters were studied in ozone removal of Acid Violet 90 dyestuff prepared as stock. Optimum results and removal efficiency have been achieved.

2. MATERIAL AND METHOD

2.1. Acid Violet 90 measurement

The dye used in the study is CI Acid Violet 90 (I18762). An aqueous dye solution with a concentration of 50 mg/L was prepared and the absorption spectrum of the dyestuff was measured in Shimadzu UV / VIS 1700 spectrophotometer, and the wavelength at which the dyestuffs showed maximum absorbance was determined to be 525 nm. Calibration was performed between 0.1 mg/L and 50 mg/L. Line equation 1 determined as:

$$ABS = 0.0198.C - 0.0019 \qquad (1)$$

C : concentration (mg/L)

ABS : absorbance value

NaOH and HCl solutions were used for pH adjustments. A magnetic stirrer is used to make the ozonation process homogeneous. In order to find the optimum removal results, studies of pH, ozone dose and reaction time were conducted. The chemicals used in the studies are of analytical grade.
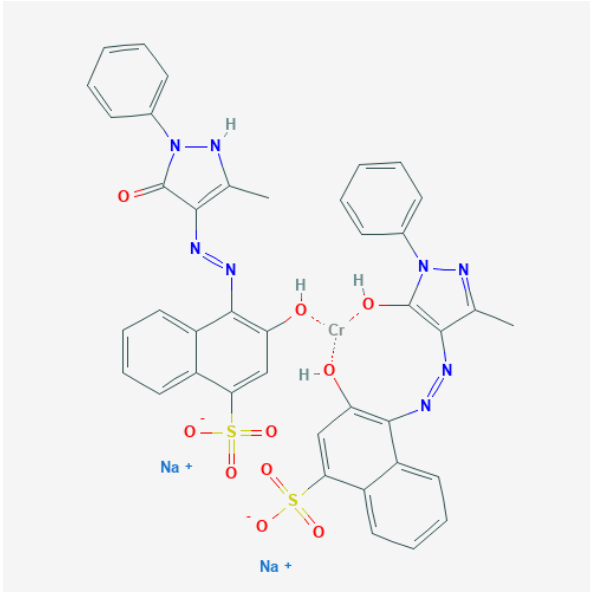
Figure 1.Acid Violet 90 molecular structure [21]

2.2. Ozonation System

Ozonation process has been done using SABO SL-10 ozone generator and its maximum capacity is 15 g/L h. In the study, 50 mL solutions were placed in 100 mL beakers as the reactor and as can be seen in Figure 2, a magnetic stirrer was used to distribute homogeneously.
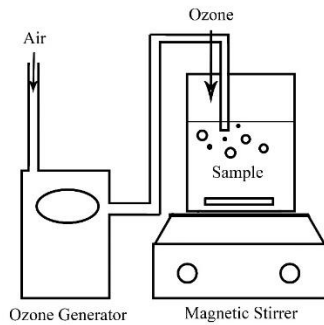
Figure 2.The diagram of the ozone purification reactor system

3. RESULT AND DISCUSSION

3.1. Effect of pH

In the study, pH adjustments were made to be 3, 5, 7, 9 and 11 and the treatment process was carried out for 5 minutes using 0.15 g/L.h ozone dose, dye concentration was 50 mg/L and the sample volume was 100 mL. As can be seen in Figure 3, while the treatment efficiency increased at neutral pH, it decreased in low and high pH. pH removal at pH 3, 5, 7, 9 and 11 respectively; 28.623, 30.804, 34.959, 30.246, 30.155 mg/L. The optimum pH result was found to be 69.91% at 7. The high removal efficiency of pH around 7 indicates that the purification process is predominantly with hydroxyl radicals [22]. In the study conducted by Chen et al., The highest color removal rate for the ozone treatment of Orange-13 dyestuff occurred at pH 10, while the highest color removal rate for Blue-19 dyestuff occurred at pH 3 [23].
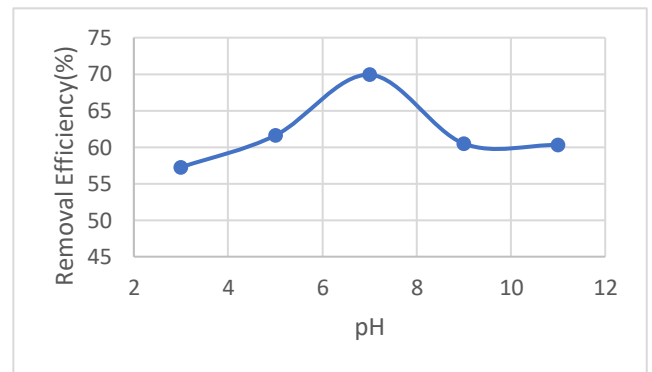
Figure 3. The effect of pH on removal efficiency (Ozone dose: 0.15 g /L.h, ,reaction time: 5 min., dye concentration: 50 mg/L, sample volume: 100 mL)

According to Chu and Ma, while ozone provides more effective oxidation at low pH, the hydroxyl radical is more effective at high pH [24]. Because of the slower decomposition rate at low pH, O_3 has a higher concentration in the aqueous phase. Ozone and OH provide a more effective reaction at high pH values, and more hydroxyl radicals are released at high pH. The effect of this on color removal is as follows:

- Hydroxyl radical provides better oxidation at high pH conditions.
- O_3 oxidation is more dominant in low pH conditions.

The oxidation capacity of the hydroxyl radical showed greater results than the oxidation capacity of the ozone molecule on dyestuffs in other studies in the literature, as in this study [25]. On

the other hand, Liu et al. also showed that the decolorization capacity of ozone is higher for some dyes at low pH [26].

3.2. Effect of Ozone Dose

In the study, at pH 7, 0.075, 0.15, 0.225, 0.3, 0.375 and 0.4 g/L.h ozone doses were treated for 5 minutes, dye concentration was 50 mg/L and the sample volume was 100 mL. As can be seen in Figure 4, as the ozone dose increases, the removal efficiency increases. While the lowest removal efficiency was found to be 59.9% at the ozone dose of 0.75 g/L.h, the highest removal efficiency should be 4.0 g/L.h, 93.5% from the ozone dose, then 93% was obtained from the 0.375 g/L.h dose. However, 0.375 g/L.h ozone dose was chosen as the optimum ozone dose with 93% efficiency in order to achieve the optimum result and the lowest cost.
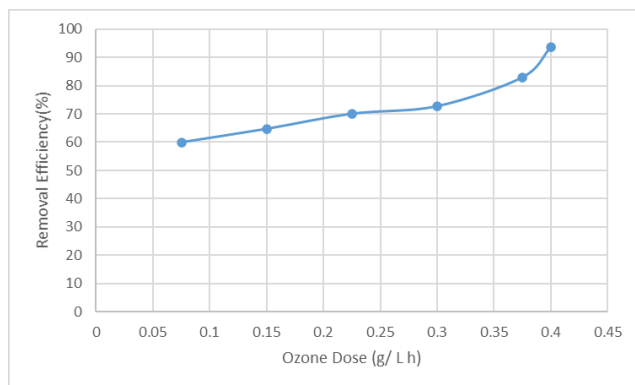
Figure 4. Effect of ozone dose on removal efficiency (pH: 7, reaction time: 5 min, dye concentration: 50 mg/L, sample volume: 100 mL)

The high ozone dose caused little increase in the color removal rate. This is because ozone passes from the gas phase to the liquid phase to form OH· radicals [24, 27, 28]. Increasing the ozone dose causes the formation of more OH· radicals and increases the removal efficiency of the dye. When the ozone concentration in the liquid phase becomes saturated, the reason why the excess ozone dose increases the color removal of dyes more is that the solubility of ozone is higher than a certain temperature and optimum dose, and it means that the hydroxyl free radicals and ozone concentrations in solution are close to unchanged [24].

3.3. Effect of Reaction Time

In the study, removal efficiencies of 1.5, 2.5, 5, 7.5, dye concentration was 50 mg/L and the sample volume was 100 mL and 10 minutes reaction time were obtained as pH 7 and ozone dose at 0.375 g/L.h. As can be seen in Figure 5, the lowest removal efficiency was 70.7% in 1.5 minutes reaction time, while the highest efficiency was reached 93% in 7.5 minutes reaction time. It was determined that 7.5 minutes was optimum because 93% yield was obtained in 10 minutes reaction time.
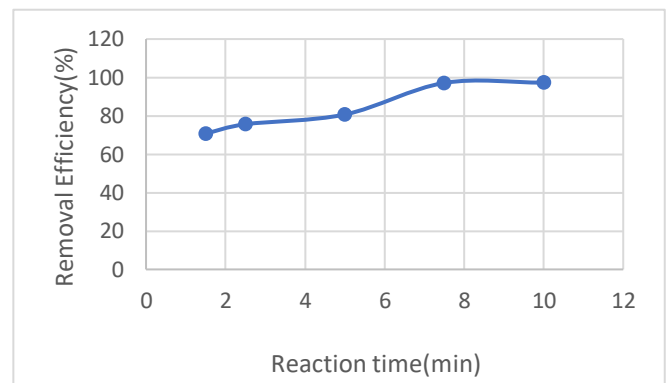
Figure 5. Effect of reaction time on removal efficiency (pH: 7, ozone dose: 0.375 g/L.h, dye concentration: 50 mg/L, sample volume: 100 mL)

As seen in the study of Öktem et al., when the reaction time increases, the curve flattens after a while and the removal almost reaches its maximum[29]. This result is consistent with mass transfer theories [30]. According to these theories, as the concentration of ozone in air bubbles increases, the driving force for transferring ozone to the paint solution increases with the increase in the ozone concentration in the solution and the dye oxidation rate.

4. CONCLUSSION

Ozonation process is an effective method for treatment and disinfection and high removal efficiencies can be achieved. From an economic point of view, advanced oxidation methods appear to be not cheap [31]. Acid Violet dye used in this study was purified using ozonation, one of

the advanced oxidation methods. High removal efficiencies were obtained in this laboratory scale dye removal study. Optimum results were measured as pH 7, ozone dose 0.375 g/L.h, reaction time 93% in 7.5 minutes. The pH value being optimum at 7 indicates that the oxidation takes place with hydroxyl ions.

Dyestuffs are very harmful to human and environmental health and therefore their purification is of great importance. In this study, very high treatment efficiency was obtained with ozonation, but more studies are needed on this subject. Efforts should be made to treat more than one dyestuff at the same time, to use more than one oxidation method together in treatment, and to ensure dye treatment from wastewater in subsequent studies. In addition, the economic aspects of these treatment methods should be considered and their costs should be compared.

Funding

The Declaration of Conflict of Interest/ Common Interest

No conflict of interest or common interest has been declared by the authors.

Authors' Contribution

All authors of the paper contributed actively to the parts of study such as experiments, analysis, writing and submission of article.

The Declaration of Ethics Committee Approval

The authors declare that this document does not require an ethics committee approval or any special permission.

The Declaration of Research and Publication Ethics

The authors of the paper declare that they comply with the scientific, ethical and quotation rules of SAUJS in all processes of the paper and that they do not make any falsification on the data collected. In addition, they declare that Sakarya University Journal of Science and its editorial board have no responsibility for any ethical violations that may be encountered, and that this study has not been evaluated in any academic publication environment other than Sakarya University Journal of Science.

REFERENCES

[1]   C. F. Gurnham, *Industrial wastewater control: A texbook and reference work*. Academic Press, 1965.

[2]   P. Pattnaik, G. S. Dangayach, and A. K. Bhardwaj, "A review on the sustainability of textile industries wastewater with and without treatment methodologies," *Rev. Environ. Health*, vol. 33, no. 2, pp. 163–203, 2018.

[3]   P. Nigam, G. Armour, I. M. Banat, D. Singh, and R. Marchant, "Physical removal of textile dyes from effluents and solid-state fermentation of dye-adsorbed agricultural residues," *Bioresour. Technol.*, vol. 72, no. 3, pp. 219–226, 2000.

[4]   D. Rawat, V. Mishra, and R. S. Sharma, "Detoxification of azo dyes in the context of environmental processes," *Chemosphere*, vol. 155, pp. 591–605, 2016.

[5]   M. W. Chang and J. M. Chern, "Decolorization of peach red azo dye, HF6 by Fenton reaction: Initial rate analysis," *J. Taiwan Inst. Chem. Eng.*, vol. 41, no. 2, pp. 221–228, 2010.

[6]   S. Khan and A. Malik, "Toxicity evaluation of textile effluents and role of native soil bacterium in biodegradation of a textile dye," *Environ. Sci. Pollut. Res.*, vol. 25, no. 5, pp. 4446–4458, 2018.

[7]   R. Molinari, F. Pirillo, M. Falco, V. Loddo, and L. Palmisano, "Photocatalytic degradation of dyes by using a membrane reactor," *Chem. Eng. Process. Process Intensif.*, vol. 43, no. 9, pp. 1103–1114, 2004.

[8]   H. Ali and S. K. Muhammad, "Biodecolorization of acid violet 19 by Alternaria solani," *African J. Biotechnol.*, vol. 7, no. 6, pp. 831–833, 2008.

[9]   R. Noyes, *Pollution prevention technology handbook*. Noyes Publications, 1993.

[10]   M. T. F. Tabrizi, D. Glasser, and D. Hildebrandt, "Wastewater treatment of reactive dyestuffs by ozonation in a semi-batch reactor," *Chem. Eng. J.*, vol. 166, no. 2, pp. 662–668, 2011.

[11]   N. H. Ince and G. Tezcanlí, "Reactive dyestuff degradation by combined sonolysis and ozonation," *Dye. Pigment.*, vol. 49, no. 3, pp. 145–153, 2001.

[12]   S. C. DeVito, "Predicting Azo Dye Toxicity," *Crit. Rev. Environ. Sci. Technol.*, vol. 23, no. 3, pp. 249–324, 1993.

[13]   R. Rojas, C. Barriga, C. P. De Pauli, and M. J. Avena, "Influence of carbonate intercalation in the surface-charging behavior of Zn-Cr layered double hydroxides," *Mater. Chem. Phys.*, vol. 119, no. 1–2, pp. 303–308, 2010.

[14]   L. Zhaoyang, S. Lili, and Zhang Quanxing, "Research development of technics and mechanism ofdye wastewater treatment by adsorption," *Ind. Water Treat. 3*, 2004.

[15]   B. Kasprzyk-Hordern, M. Ziółek, and J. Nawrocki, "Catalytic ozonation and methods of enhancing molecular ozone reactions in water treatment," *Appl. Catal. B Environ.*, vol. 46, no. 4, pp. 639–669, 2003.

[16]   S. Venkatesh, A. R. Quaff, N. D. Pandey, and K. Venkatesh, "Decolorization and mineralization of C.I. direct red 28 azo dye by ozonation," *Desalin. Water Treat.*, vol. 57, no. 9, pp. 4135–4145, 2016.

[17]   H. Zhou and D. W. Smith, "Ozone mass transfer in water and wastewater treatment: Experimental observations using a 2D laser particle dynamics analyzer," *Water Res.*, vol. 34, no. 3, pp. 909–921, 2000.

[18]   A. K. Vijh, "Potentiostat for Electrochemical Studies," vol. 117, no. 10.

[19]   W. T. Shin, A. Mirmiran, S. Yiacoumi, and C. Tsouris, "Ozonation using microbubbles formed by electric fields," *Sep. Purif. Technol.*, vol. 15, no. 3, pp. 271–282, 1999.

[20]   M. M. Mitani, A. A. Keller, O. C. Sandall, and R. G. Rinker, "Mass transfer of ozone using a microporous diffuser reactor system," *Ozone Sci. Eng.*, vol. 27, no. 1, pp. 45–51, 2005.

[21]   National Center for Biology, "PubChem Compound Summary for CID 136496748, Acid Violet 90." [Online]. Available: https://pubchem.ncbi.nlm.nih.gov/compound/Acid-Violet-90. [Accessed: 23-Oct-2020].

[22]   B. Langlais, D. A. Reckhow, and D. R. Brink, *Ozone in Water Treatment: Application and Engineering,*. Michigan: Lewis Publisher, 1991.

[23]   T. Y. Chen, C. M. Kao, A. Hong, C. E. Lin, and S. H. Liang, "Application of ozone on the decolorization of reactive dyes - Orange-13 and Blue-19," *Desalination*, vol. 249, no. 3, pp. 1238–1242, 2009.

[24]   W. Chu and C. W. Ma, "Quantitative prediction of direct and indirect dye ozonation kinetics," *Water Res.*, vol. 34, no. 12, pp. 3153–3160, 2000.

[25]   H. Y. Shu and M. C. Chang, "Decolorization effects of six azo dyes by O3, UV/O3 and UV/H2O2 processes,"

Dye. Pigment., vol. 65, no. 1, pp. 25–31, 2005.

[26] B. W. Liu, M. S. Chou, C. M. Kao, and B. J. Huang, "Evaluation of selected operational parameters for the decolorization of dye-finishing wastewater using UV/ozone," *Ozone Sci. Eng.*, vol. 26, no. 3, pp. 239–245, 2004.

[27] S. Song, Z. Liu, Z. He, Y. Li, J. Chen, and C. Li, "Degradation of the biocide 4-chloro-3,5-dimethylphenol in aqueous medium with ozone in combination with ultraviolet irradiation: Operating conditions influence and mechanism," *Chemosphere*, vol. 77, no. 8, pp. 1043–1051, 2009.

[28] F. J. Benitez, J. Beltran-Heredia, and T. Gonzalez, "Kinetics of the reaction between ozone and MCPA," *Water Res.*, vol. 25, no. 11, pp. 1345–1349, 1991.

[29] Y. A. Oktem, B. Yuzer, M. I. Aydin, H. E. Okten, S. Meric, and H. Selcuk, "Chloride or sulfate? Consequences for ozonation of textile wastewater," *J. Environ. Manage.*, vol. 247, no. March, pp. 749–755, 2019.

[30] S. P. Raghuvanshi, R. Singh, C. P. Kaushik, and A. K. Raghav, "Removal of textile basic dye from aqueous solutions using sawdust as bio-adsorbent," *Int. J. Environ. Stud.*, vol. 62, no. 3, pp. 329–339, 2005.

[31] E. Kusvuran, O. Gulnaz, S. Irmak, O. M. Atanur, H. I. Yavuz, and O. Erbatur, "Comparison of several advanced oxidation processes for the decolorization of Reactive Red 120 azo dye in aqueous solution," *J. Hazard. Mater.*, vol. 109, no. 1–3, pp. 85–93, 2004.

Sakarya University Journal of Science
SAUJS

Title: Corrigendum to "Dairesel Kesite Sahip Merkezi Çelik Çaprazların Performans Analizi" [Sakarya University Journal of Science, vol. 22, no. 2, pp. 340-349, 2018]

Authors: Zeynep YAMAN, Elif AĞCAKOCA, M. Berker ALICIOĞLU

How to cite
Zeynep YAMAN, Elif AĞCAKOCA, M. Berker ALICIOĞLU; (2021), Corrigendum to "Dairesel Kesite Sahip Merkezi Çelik Çaprazların Performans Analizi" [Sakarya University Journal of Science, vol. 22, no. 2, pp. 340-349, 2018]. Sakarya University Journal of Science, 25(1), 219-219, DOI: https://doi.org/10.16984/saufenbilder.842387
Access link
http://www.saujs.sakarya.edu.tr/en/pub/issue/58068/842387

New submission to SAUJS
https://dergipark.org.tr/en/journal/1115/submission/step/manuscript/new

Corrigendum to "Dairesel Kesite Sahip Merkezi Çelik Çaprazların Performans Analizi" [Sakarya University Journal of Science, vol. 22, no. 2, pp. 340-349, 2018]

Zeynep YAMAN[*1], Elif AĞCAKOCA[2], M. Berker ALICIOĞLU[3]

The authors regret that the junior author's name, M. Berker Alıcıoğlu, was inadvertently omitted from the article. In addition, the acknowledgment section of our article should be removed. The authors would like to apologise for any inconvenience caused.

---

[*] Corresponding Author: zdyaman@sakarya.edu.tr
[1] Sakarya University, Department of Civil Engineering, Sakarya, Turkey.
ORCID: https://orcid.org/0000-0003-0987-6685
[2] Sakarya University, Department of Civil Engineering, Sakarya, Turkey.
E-Mail: elifd@sakarya.edu.tr ORCID: https://orcid.org/0000-0001-8228-0592
[3] Celal Bayar University, Department of Civil Engineering, Manisa, Turkey.
 E-Mail: 151291001@ogr.cbu.edu.tr ORCID: https://orcid.org/0000-0003-3735-8201

Title: Investigation of Interactions of Acetylene Molecules with an Iron Nanowire and Its Effects on Mechanical Tensile Properties

Authors: Gürcan ARAL

Investigation of Interactions of Acetylene Molecules with an Iron Nanowire and Its Effects on Mechanical Tensile Properties

Gürcan ARAL[*1]

Abstract

Understanding complex atomistic-scales interactions mechanisms of reactive acetylene (C_2H_2) molecules with reactive pure iron nanowires (Fe NWs) including its effects on the tensile mechanical properties of NWs is a crucial task in nanotechnology, especially having practical significance in the mechanical reliability, durability and stability. Therefore, we performed molecular dynamics (MD) simulations based on ReaxFF reactive force field interatomic potential model to investigate the interactions of C_2H_2 molecules with surface of cylindrical pure Fe NW and its fundamental effects on the tensile mechanical deformations properties of NWs at three different strain rates. Our results reveal that the chemical energetic reactions on the free surface of cylindrical Fe NW with C_2H_2 molecules in the gas phase form $Fe_xC_yH_z$ shell layer at temperature T=300 K. The presence of $Fe_xC_yH_z$ shell layer on the free surface of NW has a significant effect on the mechanical tensile deformation mechanism of the NWs.

Keywords: acetylene, iron nanowires, molecular dynamics simulation, and reactive force field potential

---

[*] Corresponding Author: gurcanaral@iyte.edu.tr
[1] İzmir Institute of Technology, , İzmir, Turkey, ORCID: https://orcid.org/0000-0002-0800-0510

Gürcan ARAL

Investigation of Interactions of Acetylene Molecules with an Iron Nanowire and Its Effects on Mechani...

1. INTRODUCTION

Iron nano materials and their alloys are important engineering materials that are widely used in various nano-technological applications [1-4]. Although the nano-technological applications of Fe-containing materials are too many to be counted, this number is constantly increasing by the latest newly developed and more efficient techniques. Nanostructured Fe materials such as Fe NWs and nanorods are of scientific importance in nano-engineering applications, due to their interesting structural, chemical, physical and mechanical properties, that depend mostly on their surface structure, size and volume−surface ratios [1-5]. Generally, conductive Fe NWs and nanorods are synthesized by using many different chemical methods for different potential nano-engineering applications [1-3]. In particular, the properties of Fe NWs are strongly controlled with the formation of oxide shell layer on the free surface of the NW as a result of oxidation and any other reaction interactions with various reactive reactants [2,3,6]. More specifically, their relatively large surface−volume ratios and high affinities make the metallic pristine Fe NWs more sensitive and vulnerable to environmental influences [3,5]. For example, when the reactive metallic Fe NWs are exposed to different reactive media such as O_2, H_2O, CO_2, C_2H_2 C_2H_4, they are rapidly adsorbed and dissociated on the free surface of Fe NWs due to high affinity of these molecules to the metallic Fe NWs. Consequent formation of a native thin oxide shell layer with different limiting thickness, phase, stoichiometry, morphology, local atomic structures, and defects is inevitably covered the free surface of Fe NWs [2,3,6-12]. The formation of thin oxide layer on the free surface Fe NW naturally leads to change in the physical and chemical properties of Fe NW and consequently offers a wide range of functionalities, that are associated with its using in real-life applications [1,2,7,8]. Notably, various technological nano-engineering applications indicate that the resulting oxide shell layer on the free surface of Fe NWs plays critical roles on the mechanical performance, strength and durability of the pure Fe NW [3,5]

as well as the catalysis performance, compared with its surface in vacuum. Recent increasing demands of nano-engineering industry require a better and deeper understanding of the properties of nano Fe materials, such as the formation of oxide shell layer on the free surface of Fe NW and its effects on the corresponding mechanical tensile deformation mechanism and related properties [2,6].

We use atomistic MD simulation method based on reactive force field (ReaxFF) potential model to study a detailed systematic understanding of interactions of reactive acetylene (C_2H_2) gas molecules with cylindrical pure Fe NWs and the resulting formation $Fe_xC_yH_z$ shell layer on the free surface of NWs. Further, we determine the mechanical tensile deformation properties of the pure Fe and core-shell (Fe-$Fe_xC_yH_z$) structure NWs. In current literature, no information exits about the effects of the formation of $Fe_xC_yH_z$ shell layer on the mechanical tensile deformation mechanism and its related properties. In this respect, our MD simulations will play a very important role in filling the existing gap in current literature.

2. COMPUTATIONAL DETAILS

2.1 The reactive force field (ReaxFF) potential model and MD simulation method

MD is a computer simulation method based on the principle of calculating interactions between atoms in a physical system composed of N atoms via using potential energy function [13]. Namely, it is the numerical solution of the positions and velocities for each atom in a physical system via using Newtonian equations of motion. Newton's equation of motion is generally expressed as following:

$$m_i \frac{d^2 \mathbf{r}_i}{dt^2} = \mathbf{F}_i, \qquad (1)$$

in this equation, m_i is defined as the mass of the ith atom, $\mathbf{F}_i$ is the force acting on the ith atom and

Gürcan ARAL

Investigation of Interactions of Acetylene Molecules with an Iron Nanowire and Its Effects on Mechani...

V is the interaction potential energy function term between atoms. The first equation can be written as follows:

$$\mathbf{F}_i = -\frac{\partial V}{\partial \mathbf{r}_i} \tag{2}$$

Analytical potential energy function (V) describes all interactions between atoms in a physical system composed of N atoms. Therefore, it is the most important and essential input parameter for MD simulations [14]. Importantly, the quality of the simulation results produced by MD simulations depends on the precision of the potential energy function.

We carried out the MD simulations based on the ReaxFF model that was developed by van Duin et al. for Fe/C/H systems [15]. The ReaxFF interatomic potential function has successfully defined all interactions including the chemical reactions (bond formation and bond breaking) between Fe−C−H atoms in a physical system that occur during the interaction of C_2H_2 molecules with metallic Fe atoms and the mechanical deformations process [15]. This ReaxFF interatomic potential for the Fe/C/H systems includes: *i*) all ionic, covalent and metallic interactions between Fe−C−H atoms such as the core-shell ($Fe/Fe_xC_yH_z$) structure NW systems, *ii*) bond formation and breaking between Fe−C−H atoms, and also *iii*) charge variation between atoms whenever atoms change their local environment. These necessary considerations allow the MD simulations to accurately describe properties of the physical system. In other words, the realistic ReaxFF potential model allows us to accurately simulate the scientific, technological and nano-engineering problem of uniaxial mechanical tensile deformation mechanism and predict related properties of the core-shell ($Fe/Fe_xC_yH_z$) structure NWs [15].

2.2 Simulation set up and details

We begin with briefly describing the construction of [001] −oriented cylindrical pure Fe NW in the middle of a MD box. Iron atoms have a body centered cubic (BCC) unit crystal lattice structure with a unit length (a lattice constant) of 2.86 Å. First, we took 70 x 70 x 50 unit lattice cells in the x, y and z directions, respectively. As a result, a rectangular MD box consisting of only Fe atoms was created with dimensions of 20.041 x 20.041 x 14.315 nm in the x, y and z directions, respectively. Then, Fe atoms with radial distance from the middle of the MD box in the x-y plane greater than 5.0 nm that were deleted. Thus, we created a cylindrical pure Fe NW with a length of 14.315 nm and a diameter of 5.0 nm, containing 24,050 Fe atoms in vacuum, as seen in Fig. 1(a). The pure Fe NW is parallel to the z-axis. The uniaxial tensile loading is also applied in z-direction.
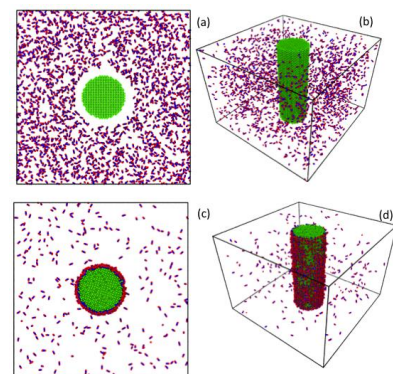
Figure 1 At the beginning of the simulation, a cylindrical pure Fe NW with a 5.0 nm diameter and 14,315 nm length was placed in the MD box. Then, 2,000 C_2H_2 molecular were dispersed randomly in the MD box, as shown in (a) sectional view and (b) side view along the z-axis. At t=3.3 ns, the formation of $Fe_xC_yH_z$ shell layer on the free surface of pure Fe NW is shown in (c) sectional view and (d) side view along the z-axis. The green, blue, and red colors indicate Fe, C and H atoms, respectively.

To study the interaction of C_2H_2 acetylene molecules with cylindrical pure Fe NW, randomly oriented 2,000 C_2H_2 molecules were inserted at a distance of 6 Å from the free surface of [001] −oriented cylindrical pure Fe NW within the MD box. The simulations were carried out using (NVT) Nose Hoover thermostats at a

Gürcan ARAL

Investigation of Interactions of Acetylene Molecules with an Iron Nanowire and Its Effects on Mechani...

temperature of 300 K [16]. The equation of motions were integrated numerically with velocity Verlet algorithm using a time step of 0.25 fs. Complex interactions processes occur instantaneously at the free surface of NW when it comes in contact with the C_2H_2 molecules at T=300K. As a result of reactive interactions, the $Fe_xC_yH_z$ shell layer was formed on the free surface of NW. Later, we deleted the C_2H_2 molecules from the MD simulation box that did not interact with the NW, that is, did not bond with the Fe atoms of NW. The snapshots in Figure 1 clearly show the initial configurations of the cylindrical pure Fe NW in the environment of C_2H_2 molecules and the final formation of the core-shell ($Fe/Fe_xC_yH_z$) structures. We used the Ovito−open visualization tool to obtain detailed atomistic level information of the formation of the core-shell ($Fe/Fe_xC_yH_z$) structures [17].

Prior to applying the uniaxial mechanical tensile load on the cylindrical pure Fe and core/shell ($Fe/Fe_xC_yH_z$) structure NWs, the configurations of all NWs were first relaxed to minimum energy positions using conjugate gradient method. Then, they were thermalized at 300 K under the Nose Hoover thermostats. Next, they were relaxed to be in equilibrium using Nosé-Hoover isothermal-isobaric (NPT) thermostats at T=300K and the zero pressure along the z-axis [18]. Finally, an external mechanical tensile load along [001] direction at three different tensile strain rates ($1x10^8$ s^{-1}, $5x10^8$ s^{-1} and $1x10^7$ s^{-1}) were applied on the well-equilibrated NWs under the canonical (NVT) ensemble at 300 K [16]. Periodic boundary conditions were applied in the loading direction while free surface was used in the x and y direction. We obtained the average engineering stress by correcting the Virial stress equation with the original volume of the NWs [13]. All uniaxial mechanical tensile loads were applied to NWs until they reached ~16% elongation. The total simulation time for the formation of $Fe_xC_yH_z$ layer on the free surface of NW and the tensile test was 3.3 and 1.5 ns, respectively. All MD simulations were performed via using LAMMPS (Large-scale Atomic/Molecular Massively Parallel Simulator) open source codes [19].

3. RESULTS AND DISCUSSIONS

3.1 Reaction of acetylene molecules with Fe NW and formation of the $Fe_xC_yH_z$ shell layer

We simulated interaction events that occurred with C_2H_2 molecules on the free surface of cylindrical pure Fe NW at temperature T=300K in the simulation of 3.3ns duration. In this reactive interaction process, 1,730 out of total 2,000 C_2H_2 molecules in the gas phase interacted with the pure Fe NW and consequently, a thin $Fe_xC_yH_z$ shell layer was formed on the free surface of NW. Namely, the pure Fe NW transforms into core/shell ($Fe/Fe_xC_yH_z$) structure, as a result of complex interaction of C_2H_2 molecules with Fe atoms a taking place on the free surface of the pure Fe NW. Snapshots as seen in the Figure 2 confirm that the initial formation of the $Fe_xC_yH_z$ shell layer around the free surface of Fe NW occurs rapidly and increases with time due to high affinity of Fe atoms to C_2H_2 molecules. Almost all C_2H_2 molecules interact directly with the Fe atoms around the reactive sites of the free surface of NW and consequently combine to form a bond between atoms. Importantly, formation and growth process of the $Fe_xC_yH_z$ shell layer on the free surface in C_2H_2 molecular environment is driven by combination of local chemical and physical reactions that occur around the free surface of reactive pure Fe NW and develop independently from each other.
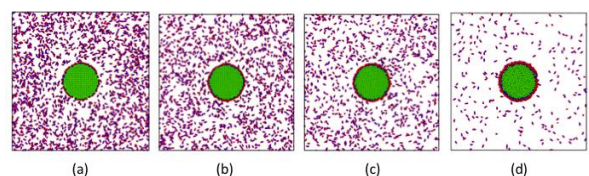

Figure 2 The pure Fe NW was initially placed in a randomly oriented and dispersed 2,000 C_2H_2 molecular environments. The formation of the $Fe_xC_yH_z$ shell layer on the surface of pristine Fe NW is shown from sectional view along the axis at (a) 0.00875 ns, (b) 0.05 ns, (c) 0.25 ns and (d) 3.3 ns. The green, blue, and red colors indicate Fe, C and H atoms, respectively.

Gürcan ARAL

Investigation of Interactions of Acetylene Molecules with an Iron Nanowire and Its Effects on Mechani...

We analyzed the bond lengths between C−H and C−C atoms in the resulting formation of $Fe_xC_yH_z$ shell layer using the radial pair distribution functions (RDF), as seen in Figure 3. During the interaction process of C_2H_2 molecules with Fe atoms, CH ions (fragments) were formed on the free surface due to C−C bond breakage within C_2H_2 molecules. Specifically, the two peaks in Figure 3 (b), which are ∼ 1.15 and ∼ 1.28 Å, indicates the C−C bond breaking between the constituent atoms of the C_2H_2 molecule. On the other hand, the bond lengths and distributions formed between C−H atoms in Figure 3 (a) indicate that some C_2H_2 molecules interact with the Fe NW to maintain their molecular structure and also to form of CH fragments. During the reaction process, CH and Fe ions partially diffuse inward and outward around the reaction region of the NW, respectively. These corresponding diffusions in tandem with the charges transfer and bonds formation between the atoms cause the formation of the $Fe_xC_yH_z$ shell layer on the free surface of NW. As time progresses during the interaction process, the resulting $Fe_xC_yH_z$ shell layer grows rapidly and becomes thicker causing the interaction kinetics to slow down. The development of $Fe_xC_yH_z$ shell layer gradually blocks diffusions paths of ions also, the interaction activity including dissociation of C_2H_2 molecules and the rate of penetration of ions decrease with the growth of the $Fe_xC_yH_z$ shell layer. In addition, the molecular pressure of C_2H_2 molecules is decreased by adsorption C_2H_2 molecules. The resulting interactions, the partial ionic diffusions and the bond formations, and the charges transfer between atoms on the free surface causes significant changes of the local atomic structure of free surface of NW leading to the formation of $Fe_xC_yH_z$ shell layer over time. As the formation of the $Fe_xC_yH_z$ shell layer thickness increases, the concentration of C and H atoms around the free surface of NW increases over time, indicating a successful formation of bonds between atoms. As a result, the pure Fe NW transforms into the core/shell ($Fe/Fe_xC_yH_z$) structure NW. Also, the developing $Fe_xC_yH_z$ shell layer on the free surfaces provides a physical separation between the pure Fe NW and reactive C_2H_2 molecules, thus the thin $Fe_xC_yH_z$

shell layer acts as a natural diffusion barrier for reactive C_2H_2 molecules over time.
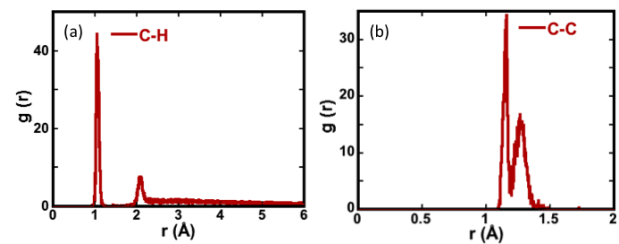
Figure 3 Radial pair distribution functions between a) C-H and b) C-C atoms are shown in the resulting formation of $Fe_xC_yH_z$ layer in the active regions close to the free surface of the cylindrical metallic Fe NW as a result of the interaction process.

Kayastha et al. observed simultaneous dissociative adsorption of C_2H_2 molecules on Fe surface, eventually leading to the formation of amorphous shell layer on the free surfaces of Fe nanoparticles that gradually prevented further contact of C_2H_2 molecules with Fe nanoparticles [11]. Also, the C_2H_2 molecules are decomposed into two CH fragments as a result of dissociative adsorption of C_2H_2 molecules on the free surface of Fe nanoparticles. In particular, they revealed that CH fragments are formed by breaking the bonds between C=C atoms in a C_2H_2 molecule. Moreover, metallic Fe atoms interact with C_2H_2 molecules to form of CH−Fe bonds, exhibiting preferentially down orientation of C atoms to the free surface. Lee et al. investigated interaction of C_2H_2 molecules on Fe [001] surface through first-principles electronic structure calculation [10]. They indicated that dissociation process involves the C−C bond breaking between constituent atoms of the C_2H_2 molecule to form CH fragments. Moreover, absorption of C_2H_2 molecules on the free surface of NW is a highly exothermic process that creates conditions for outward diffusion of Fe and inward diffusion of CH ions.

We investigated the thickness of formed $Fe_xC_yH_z$ shell layer by analyzing the atomic radial number density distribution profiles of Fe, C and H atoms per unit volume. Figure 4 highlights the total number of C_2H_2 molecules interact with pure Fe NW during the interaction process. Specifically, analysis of the atomic radial number density distribution profiles of Fe, C and

Gürcan ARAL

Investigation of Interactions of Acetylene Molecules with an Iron Nanowire and Its Effects on Mechani...

H atoms per unit volume indicates the outward diffusion of Fe ions and the inward diffusion of CH ions. Also, the positions, widths, and densities of the atomic radial number density distribution profiles of atoms reveal that the formed $Fe_xC_yH_z$ shell layer on the free surface of NW is not very uniform, and its density depends on the radial length. As a result interaction at time=3.3 ns, the average radius of the cylindrical pure Fe NW increases from r=~2.50 nm to r=~3.0 nm. Also the average thickness of the formed $Fe_xC_yH_z$ shell layer is ~0.7 nm as a result of the diffusion of CH ions, and also the attachment of the C_2H_2 molecules to the free surface of NW by making various bonds among Fe, C and H atoms. Moreover, Fe atoms diffused from the metallic core (r=~2.50 nm) to outward (r=~2.7 nm). As expected, these ionic diffusions happen along with the charges transfer between atoms. The formation of $Fe_xC_yH_z$ shell layer on the free surface of NW leads to significant local atomic structure modulation and morphology changes on the free surface of NW including the radial expansion of ~18.4% and volume expansion of ~65.0%. In other words, the bonds formed between the atoms result in the formation of the $Fe_xC_yH_z$ layer on the surface that causes significant changes in the surface chemical and physical properties of the NW including morphology and diameter of NW.
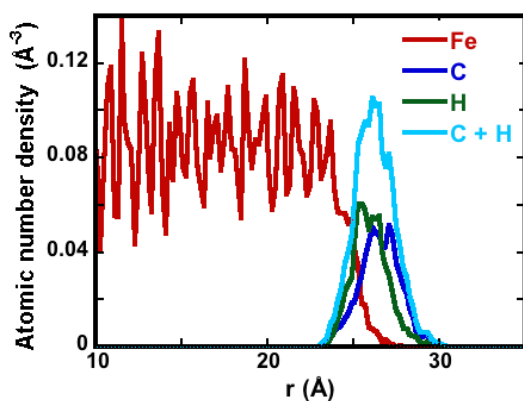
Figure 4 The atomic radial number density distribution profiles of the core/shell ($Fe/Fe_xC_yH_z$) structure are shown for C (dark blue), H (green) and C+H (blue) atoms. The atomic radial number density profiles were created by using 0.5 Å intervals along radial direction.

3.2 Formation of $Fe_xC_yH_z$ shell layer influencing the uniaxial tensile deformation properties

We performed external uniaxial mechanical tensile loading on cylindrical pure and core-shell ($Fe/Fe_xC_yH_z$) NWs at temperature T=300K and three different strain rates ($1x10^8$ s^{-1}, $5x10^8$ s^{-1} and $1x10^7$ s^{-1}). We analyzed the effects and changes of mechanical tensile deformation behaviors and corresponding properties of the pure and the layer-shell ($Fe/Fe_xC_yH_z$) NWs. Here, the pure Fe NW was taken as reference in order to compare how much the relevant properties and constants of the NW changed after the formation of $Fe_xC_yH_z$ shell layer on the free surface of NW.

As seen clearly in Figure 5, the engineering average tensile stress-strain curves of the pure and $Fe_xC_yH_z$ coated Fe NW indicate that they have notably different tensile mechanical properties and constants, depending on the external applied uniaxial tensile strain and the existence of $Fe_xC_yH_z$ shell layer. Moreover, the change of average engineering stress-strain curves show a significant reduction in strength of the $Fe_xC_yH_z$ layer-coated Fe NW as compared to the pure counterpart. But, the overall deformation trends of the average engineering stress-strain curves are very similar for all NWs [7,8,20]. Moreover, the existence of the $Fe_xC_yH_z$ shell layer leads to significantly reduce the elastic strain limit (elongation of tensile elasticity) of NW as well as the average maximum stress (yield stress) to onset of the tensile plasticity. The average engineering stress-strain curves of all NW show three different tensile deformation regimes: linear elastic, non-linear elastic and plastic deformation regime [7,8]. Specifically, the average stress profiles for all NWs, whether pure or $Fe_xC_yH_z$ shell layer coated Fe NWs, experience a sudden drop in stress after reaching their yield stress values, indicating that the NWs subsequently undergo tensile plastic deformation. Also, the average engineering stress-strain curves reveal that pure Fe NW exhibits a higher mechanical tensile resistance to onset of the tensile plasticity as

compared to the core-shell $(Fe/Fe_xC_yH_z)$ structure counterpart.
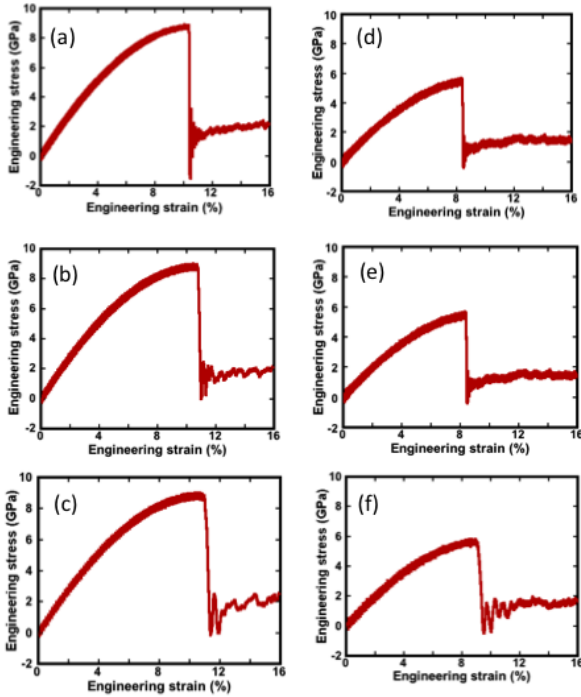
Figure 5 The average engineering tensile stress-strain curve for pure Fe NW is shown at different strain rates of: a) $1x10^8s^{-1}$, b) $5x10^8s^{-1}$ and c) $1x10^7s^{-1}$ values. On the other hand, the engineering average tensile stress-strain curve for the core-shell structure $(Fe/Fe_xC_yH_z)$ NW is shown at different strain rates of: d) $1x10^8s^{-1}$, e) $5x10^8s^{-1}$ and f) $1x10^7s^{-1}$ values.

In the non-linear elastic regime, the flow tensile stress increases gradually up to the yield stress level with increasing external applied tensile strain, and then followed by a sudden flow stress drop, indicating release of elastic energy. The tensile plastic deformation occurs a relatively low stress with fluctuating stress values around 1.0-2.0 GPa. In the meantime, the NWs beyond the yield stress continue their tensile plastic deformation with the increase of tensile stress at the partially low stress values. Specifically, twinning is a main plastic deformation mechanism. Also, it is the tensile plastic stress carrier in the plastic deformation region, leading to continued plastic deformation at partially low flow tensile stress [7,8,20]. The twinning is predominantly controlled by the relative ease of creation of defects and the propagation of displacement activities along the twin boundaries. The yield stress values for the pure Fe NWs are ~8.7 GPa for three different strain rates ($1x10^8s^{-1}$, $5x10^8s^{-1}$ and $1x10^7s^{-1}$). Corresponding to these tensile yield stress values, the yield strain values occur at ~10.4, ~10.8 and ~11.1% at the strain rates of $1x10^8s^{-1}$, $5x10^8s^{-1}$, and $1x10^7s^{-1}$, respectively. The average tensile yield stress values remain the same, but the elastic limit values depend highly on the applied external strain rates. On the other hand, the yield tensile stress values for the Fe NW covered with the $Fe_xC_yH_z$ shell layer are ~5.5 GPa and the yield strain values are ~8.4, ~9.6 and ~9.1% at three different strain rates of $1x10^8s^{-1}$, $5x10^8s^{-1}$, and $1x10^7s^{-1}$, respectively. The yield stresses for $Fe_xC_yH_z$-coated Fe NWs are approximately ~37% lower than that of their pure counterparts. Notably, our result implies that the existence of defects and interstitial impurities in the $Fe_xC_yH_z$ shell layer on the free surface of NW leads to significant decrease in the tensile yield stress value to onset tensile plasticity. The yield stress for the pure Fe NW indicates a relatively higher stress value required to initiate tensile plasticity as compared to the $Fe_xC_yH_z$-coated counterpart. Importantly, the applied external strain rates have a relatively negligible effect on the corresponding required yield tensile stress values to initiate the tensile plasticity; but it has a strong effect on the elastic elongation limits. However, variations of the engineering average stress-strain curves beyond the elastic limit, i.e. in the tensile plastic region, are only little sensitive to the existing of $Fe_xC_yH_z$ shell layer and strain rates.

The tensile yield stress and strain values depend strongly on the surface-related correlations and competitions, especially, the initial defect structures on the free surface of NWs. Here, the existence of the $Fe_xC_yH_z$ shell layer on the free surface of Fe NW leads to reduction of the tensile yield stress. This is because of the existence of defects on the free surface of NWs due to rapid formation of $Fe_xC_yH_z$ shell layer that naturally facilitates the initiation of plastic deformation in the Fe NWs. Importantly, the formed $Fe_xC_yH_z$ shell layer significantly reduces the tensile yield stress and also limit value of the elastic elongation limit, accelerating the onset of tensile plasticity.

Gürcan ARAL

Investigation of Interactions of Acetylene Molecules with an Iron Nanowire and Its Effects on Mechani...

In our literature research, there are only a few studies related to the deformation behavior of pure Fe NWs as a function of the applied external strain rates. Our results are consistent with our previous research and other's studies of tensile mechanical deformation of Fe NWs [20]. For example, Li and Han investigated tensile deformation behaviors of [001] −oriented single crystal Fe NW for different temperatures (900 K − 0.1 K) and strain rates ($1.25x10^7s^{-1}$ − $1.25x10^{10}s^{-1}$) by using MD simulations [21]. They found that Young's modulus and yield stress value were independent of the applied strain rates at the low-temperature, but these two properties decrease with increasing temperature. In addition, the Fe NWs are deformed mainly by twinning during the tensile plastic deformation region. Zhao and Liu studied the effects of strain rates ($1x10^9s^{-1}$ − $5x10^6s^{-1}$) on tensile mechanical deformation behaviors and related properties for pure copper (Cu) NWs [22]. In their study, they observed that corresponding tensile stress-strain curves in the tensile elastic regions are completely identical for all applied strain rates. However, they observed that the strain rate affects the tensile plastic deformation mechanism. Xie et al. investigated the uniaxial tensile plastic deformation mechanism of metallic [110]-oriented Fe NWs using MD simulation method [23]. Moreover, the tensile deformation of Fe NWs in the linear elastic region is completely insensitive to the strain rate. Also, they observed that the flow tensile stress drops suddenly to approximately 2.5 GPa flow stress value after reaching the yield stress value; indicating that plastic deformation starts at the same time.

In our study, we shown that the active C_2H_2 molecules interact rapidly with the Fe atoms on the free surface of NW, and consequently the pure Fe NW transforms into the core/shell ($Fe/Fe_xC_yH_z$) structure. We observed that the core/shell ($Fe/Fe_xC_yH_z$) structure NW has different tensile mechanical properties and related constant, as compared to the pure counterpart. Particularly, the onset of tensile plastic deformation of NWs is facilitated due to the existence of $Fe_xC_yH_z$ shell layer on the free surface of NW. Also, the pure Fe NWs can withstand relatively higher tensile yield stress and strain than that of the $Fe_xC_yH_z$ shell layer counterparts under externally applied mechanical tensile load. Importantly, the yield stress values are independent of the strain rates.

4. CONCLUSIONS

We investigated the tensile mechanical deformation properties of the pure and the $Fe_xC_yH_z$ layer coated Fe NWs and the related mechanical constants at T = 300 K for three different strain rates ($1x10^7s^{-1}$, $5x10^8s^{-1}$ and $1x10^8s^{-1}$). As a result; the $Fe_xC_yH_z$ layer formed on the free surface of the cylindrical pure Fe NW has a detrimental effect on tensile mechanical properties of pure Fe NW such as reduction of the mechanical tensile strength. We observed similar tensile elastic and plastic deformation behaviors under externally applied constant strain rates for all NW, except the yield stress and strain values that corresponds to the onset tensile plastic deformation. In comparison, the formed $Fe_xC_yH_z$ shell layer has a significant effect on the tensile mechanical deformation performance and related properties of the pure Fe NWs. In particular, the existence of $Fe_xC_yH_z$ shell layer on the free surface of NW significantly reduces the tensile stress and strain values required onset of the tensile plastic deformation.

In addition, it is of great importance to understand the tensile mechanical deformation mechanism of core-shell ($Fe-Fe_xC_yH_z$) NWs at different strain rates. We believe that our simulation results are very important and provide valuable contributions to many questions related to interaction of C_2H_2 molecules with pure Fe NW and its resulting effects on the tensile mechanical deformation related properties. For example, our estimation of the relevant tensile mechanical properties and constant will be of great interest in the future.

The Declaration of Conflict of Interest/Common Interest

No conflict of interest or common interest has been declared by the author.

The Declaration of Ethics Committee Approval

The author declares that this document does not require an ethics committee approval or any special permission.

The Declaration of Research and Publication Ethics

The author of the paper declares that he complies with the scientific, ethical and quotation rules of SAUJS in all processes of the article and that he does not make any falsification on the data collected. In addition, he declares that Sakarya University Journal of Science and its editorial board have no responsibility for any ethical violations that may be encountered, and that this study has not been evaluated in any academic publication environment other than Sakarya University Journal of Science.

REFERENCES

[1] A. Ali, H. Zafar, M. Zia, I.U. Haq, A.R. Phull, J.S. Ali, and A. Hussain, "Synthesis, characterization, applications, and challenges of iron oxide nanoparticles," Nanotechnology, Science and Applications, vol. 9, pp. 49–67, 2016.

[2] M. Krajewski, K. Brzozka, W.S. Lin, H.M. Lin, M. Tokarczyk, J. Borysiuk, G. Kowalskia, and D. Wasik, "High temperature oxidation of iron-iron oxide core-shell nanowires composed of iron nanoparticle," Physical Chemistry Chemical Physics, vol. 18, pp. 3900–3909, 2016.

[3] K. Gandha, J. Mohapatra, M.K Hossain, K. Elkins, N. Poudyal, K. Rajeshwarb, and J.P. Liu, "Mesoporous iron oxide nanowires: synthesis, magnetic and photo catalytic properties," RSC Advances, vol. 93, pp. 90537–90546, 2016.

[4] P. Landau, Q. Guo, P. Hosemann, Y. Wang, and J. R. Greer, "Deformation of as-fabricated and helium implanted 100 nm-diameter iron nano-pillars," Materials Science and Engineering: A, vo. 612, pp. 316–325, 2014.

[5] B. R. S. Rogne and C. Thaulow, "Strengthening mechanism of iron micro pillars," Philosophical Magazine, vol. 95, pp. 1814–1828, 2015.

[6] B. Jeon, Q. V. Overmeere, A. C. T. van Duin, and S. Ramanathan, "Nano scale oxidation and complex oxide growth on single crystal iron surfaces and external electric field effects," Physical Chemistry Chemical Physics, vol. 15, pp. 1821, 2013.

[7] G. Aral, Y. J. Wang, S. Ogata, and A. C. T. van Duin, "Effects of oxidation on tensile deformation of iron nanowires: Insights from reactive molecular dynamics simulations," Journal of Applied Physics, vol. 120, no 13, pp. 135104–1–14, 2016.

[8] G. Aral, M. M. Islam, Y. J. Wang, S. Ogata, and A. C. T. van Duin, "Oxyhydroxide of metallic nanowires in a molecular H2O and H2O2 environment and their effects on mechanical properties," Physical Chemistry Chemical Physics, vol. 20, no. 25, pp. 17289–17303, 2018.

[9] T. Pan, "Quantum chemistry-based study on iron oxidation at the iron-water interface: An X-ray analysis aided study,"

Gürcan ARAL

Investigation of Interactions of Acetylene Molecules with an Iron Nanowire and Its Effects on Mechani...

Chemical Physics Letters, vol. 511, pp. 315–321, 2011.

[10] G. D. Lee, S. Han, J. Yu, and J. Ihm, "Catalytic decomposition of acetylene on Fe [001]: A first-principles study," Physical Review B, vol. 66, pp. 081403–081407, 2002.

[11] V. Kayastha, Y. K. Yap, S. Dimovski, and Y. Gogots, "Controlling dissociative adsorption for effective growth of carbon nanotubes," Applied Physics Letters, vol. 85, no. 15, pp. 3265–3267, 2004.

[12] F. G. Sen, A. T. Alpas, A. C. T van Duin, and Y. Qi, "Oxidation-assisted ductility of aluminum nanowires," Nature Communications, vol. 5, pp. 3959–3968, 2014.

[13] M. P. Allen and L. J. Tildesley, Computer Simulation of Liquids. New York, USA, Oxford University Press, 1987.

[14] K. I. Nomuro, R. K. Kalia, A. Nakano, and P. Vashishta, "A scalable parallel algorithm for large-scale reactive force field-field molecular dynamics simulations," Computer Physics Communications, vol. 178, pp. 73–87, 2008.

[15] M. M. Islam, C. Zou, A. C. T. van Duin, and S. Raman, "Interactions of hydrogen with the iron and iron carbide interfaces: a ReaxFF molecular dynamics Study," Physical Chemistry Chemical Physics, vol. 18, pp. 761–771, 2016.

[16] G. J. Martyna, M. L. Klein and M. Tuckerman, "Nose-Hoover chains: the canonical ensemble via continuous Dynamics," Journal of Chemical Physics, vol. 97, pp. 2635–2643, 1992.

[17] A. Stukowski, "Visualization and analysis of atomistic simulation data with OVITO– the Open Visualization Tool," Modeling and Simulation in Materials Science and Engineering, vol. 18, pp. 015012, 2010.

[18] G. J. Martyna, D. J. Tobias and M. L. Klein, "Constant pressure molecular dynamics algorithms," Journal of Chemical Physics, vol. 101, no. 5, pp. 4177–4189, 1994.

[19] S. Plimpton, "Fast Parallel Algorithms for short-Range Molecular Dynamics," Journal of Computational Physics, vol. 117, pp. 1–19, 1995.

[20] C. J. Healy, and G. J. Ackland, "Molecular dynamics simulations of compression-tension asymmetry in plasticity of Fe nanopillars," Acta Materialia, vol. 70, pp. 105–112, 2014.

[21] L. Li, and M. Han, "Molecular dynamics simulations on tensile behaviors of single-crystal bcc Fe nanowire: effects of strain rates and thermal environment," Applied Physics A, Materials Science & Processing, vol. 123, no 450, pp. 1–7, 2017.

[22] L. Y. Zhao, and Y. Liu, "The influence mechanism of the strain rate on the tensile behavior of copper nanowire," Science China Technological Sciences, vol. 62, pp. 2014–2020, 2019.

[23] H. Xie, T. Yu, W. Fang, F. Yin and D. F. Khan, "Strain-rate-induced bcc-to-hcp phase transformation of Fe nanowires," Chinese Physics B, vol. 25, no. 12, pp. 126201–126207, 2016

Title: Morphological, Anatomical and Ecological Features of Ajuga salicifolia (L.)
Schreber (Lamiaceae) with Natural Spreading

Authors: Sibel ULCAY

How to cite
Sibel ULCAY; (2021), Morphological, Anatomical and Ecological Features of Ajuga
salicifolia (L.) Schreber (Lamiaceae) with Natural Spreading. Sakarya University
Journal of Science, 25(1), 230-239, DOI:
https://doi.org/10.16984/saufenbilder.796651
Access link
http://www.saujs.sakarya.edu.tr/en/pub/issue/58068/796651

New submission to SAUJS
https://dergipark.org.tr/en/journal/1115/submission/step/manuscript/new

Morphological, Anatomical and Ecological Features of *Ajuga salicifolia* (L.) Schreber (Lamiaceae) with Natural Spreading

Sibel ULCAY [*1]

Abstract

The aim of this study was to determine the morphological, anatomical and ecological characteristics of *Ajuga salicifolia* (L.) Schreber plant belonging to Lamiaceae family. The plant was collected between April and June 2019 from the open fields of Bağbaşı location in Kırşehir province. The collected samples were placed in 70% alcohol and fixed. Transverse sections were taken from the root, stem and leaf of the plant for anatomical research. In addition, superficial sections were taken from both the lower and upper parts of the leaf. According to the morphological examination, the stem of the plant is upright and occasionally accumbent. The stem is red from the basal to the middle and has hispid hairs on it. Leaves are usually oblong-lanceolate. The corolla is yellow and 1-2 very prominent red spots are seen at the far end. In the root cross section of the plant, the periderm is 1-2 layers, rectangular. Phloem is 7-8 rows and xylem are evident. Pith region is observed in the root. According to the stem cross section, the epidermis cells are circular and square shaped and covered with capitate glandular hairs and 1-3 cell eglandular hairs. The vascular bundles are in a continuous ring. Sclerenchyma also continues around the vascular bundles. Collenchyma cells are seen in the corners of the stem. The leaf of the *A. salicifolia* plant is bifacial. Stomata are anomocytic. The soils in which it grows of *A. salicifolia* are clayey, slightly alkaline, salt-free, poor in phosphorus, and rich in potassium and organic matter. As a result, the examination of the species in terms of morphology and anatomical aspects provides important benefits in the systematic of plants. For this reason, it is expected that our study will benefit the studies to be carried out on the *Ajuga* genus.

Keywords: *Ajuga*, Lamiaceae, morphology, anatomy, ecology

1. INTRODUCTION

The Lamiacaeae family is distributed in the world with 400 genera and 3200 species [1]. In Turkey, it is represented by 46 genera and 580 species. Of these species, 260 species are endemic and the rate of endemism is about 44% [2, 3]. 23 taxa of *Ajuga*, a genus in Lamiaceae family, are spread in our country [4].

* Corresponding Author: sibelulcay@gmail.com
1 Ahi Evran University, Faculty of Science and Letters, Kırşehir, Turkey, ORCID: https://orcid.org/ 0000-0002-2878-1721

Sibel ULCAY

Morphological, Anatomical and Ecological Features of Ajuga salicifolia (L.) Schreber (Lamiaceae) with...

Since secondary metabolites of family members are rich, most of them have medical and aromatic value [5]. Essential oil and phenolic compounds are also rich in flavonoids [6], and have antioxidant features [7, 8]. Species of the genus *Ajuga* include medicinal and pharmacological chemical compounds such as flavonoid, triglyceride, essential oil phytosteroid, diterpene [9, 10, 11, 12]. *Ajuga salicifolia* (L.) Schreber in Turkey "Sivrimayasıl" is known as [13]. Some species of the genus *Ajuga* are also valuable ethnoboatanically. *Ajuga* types are used in [14], treatment of sore throat [15], jaundice, gout, joint pain, Fever, asthma, gut, hemorrhoids [16] and diabetes [17], as vasoconstrictor, blood thinner and blood purifier [18].

Morphological and anatomical features of some species of the genus *Ajuga* were examined [19, 20, 21, 22]. There are also studies on petiole anatomy and trichome morphology of some *Ajuga* taxa [23]. Pfeiffer revealed the morpho-ecological characteristics of the species *Ajuga reptans* L. and performed molecular analysis of this species [24].

In species with similar morphological features, significant differences may occur in the anatomical structures of vegetative organs such as roots, stems, leaves. Accordingly, anatomical characters have been used in taxonomy in recent years [25]. In our study, it is aimed to determine the morphological, anatomical and ecological features of *Ajuga salicifolia* (L.) Schreber plant, which was not examined morphologically, anatomically and ecologically, and to compare it with other species. We believe that the findings we obtain will also be a source for the studies to be conducted on other *Ajuga* species.

2. MATERIALS AND METHODS

The samples of *A. salicifolia* species, which is our research topic, were collected from Kırşehir province and its surroundings in June 2019 (Locality: Bağbaşı district, herbarium number: Sulcay361). The diagnoses of 15 samples collected were made according to Flora of Turkey [3]. Plant samples were taken in 70% alcohol and fixed. For anatomical examinations, the cross-section from the root, stem, and leaf were by hand (Figure 2, figure 3A). In addition, superficial sections were taken from the leaf (Figure 3B, C) The sections taken were made into a permanent preparation by the glycerin-gelatin method [26]. In anatomical examinations, epidermis, collenchyma, parenchyma, in root, stem and leaf sections, and trachea and phloem elements were measured. Photographs were taken with the Nikon Eclipse Ni-U microscope and imaging system from the anatomical sections of the species. The number of stomata and epidermis cells in plants was calculated from the area of 1mm² on the lower and upper surfaces of the same age leaves of the plant [27].

For ecological studies, soil samples have been taken from the area where plant samples were collected. During the fieldwork, after removing the upper surface of the soil, a section of approximately 1 kg was taken with depth and diameter in the range of 0-20 cm. After these samples were dried in air and passed through a 2 mm sieve, they were made ready for analysis [28]. Soil analyzes have been conducted in two replications. Saturation percentage was obtained by saturating the colloid surface areas with water [29]. The pH and total salinity determinations were made in the saturation sludge [30,31]. Organic material has been classified by using modified Walkey-Black wet burning method [32]. Total lime was made with Scheibler calcimeter [33] and it was classified according to Ülgen and Yurtsever [34]. Useful phosphorus determination was made by extracting soils with sodium bicarbonate (pH: 8.5, 0.5 N NaHCO3) [35]. Changeable potassium was determined ([36] by extracting it with ammonium acetate (pH: 7, 1 N NH4OAc). Among the elements passing into the solution phase, concentration of phosphorus was determined by using the UV-VIS Spectrometer device, while the concentration of potassium was determined by using the Flame Spectrometer device.

3. RESULTS AND DISCUSSION

3.1. Morphological Results

The stem is upright, simple and occasionally accumbent. The stem is colored red from the basal part to the middle and is covered with hispid hairs. The stem is cylindrical in shape and branches from the base part. The leaves are oblong-lanceolate, oblong-elliptical in shape, opposite order, short petiole.

Figure 1 General view of *A. salicifolia*, ca: calyx, fr: fruit, lf: leaf, p: petal, st: stem

The terminal of the leaf is acute. Base of floral leaves is truncate. There are pilose hairs on the leaf. The flowers are verticillate and two flowered. Corolla is yellow and and forms a tube on the base of the corolla. The number of petals is 4. 3 of the petals are reduced. One of these petals are reduced more than the other two. The outside of the petals has velutinous hairs. The long petal has two gears and there are red spots on it (one or two). The style is bifurcated, and has the same length or shorter than the pistil corolla. The number of stamens is four. The calyx is green in color and consists of four sepals. Calyx takes the form of a tube towards the base. The fruit is nutlet (Figure 1).

Table 1 Morphological measurement results of *A. salicifolia* plant

Parts of plant	Length Min. (mm)	Length Mak (mm)	Length Mean- SD. (mm)	Breadth Min.(mm)	Breadth Max. (mm)	Breadth Mean – SD. (mm)
Stem	135	170	150,83±5,23	0,4	3,0	1,51±0,23
Root	3,5	9,0	6,900±0,88	4	13	9,33±1,30
Petiole	2	7	5,50±,56			
Leaf	12,0	40,0	25.17±4.96	7	20	13.5±4.66
Sepal	6,0	13,0	8,518±0.78			
Petal	12	30	22,00±2,22			
Pistil	12	25	17,78±1,234			
Fruit	1,5	3,0	2,15±0,15	-	-	

Sibel ULCAY

Morphological, Anatomical and Ecological Features of Ajuga salicifolia (L.) Schreber (Lamiaceae) with...

Anatomical Results

Periderm consists of 1-2 rows of rectangular shaped cells in the root cross-section of *A. salicifolia*. The cortex consists of polygonal shaped large cells. Phloem cells are 7-8 rows. Xylem is evident. Cells irregularly arranged in the pith region are circular and parenchymatic (Figure 2A).

Epidermis cells are 1-2 rows on the outer part of the stem cross-section of the plant, they are circular, square shaped, and the stem is slightly angular. Capitate glandular (Figure 2D) and 1-3 cell eglandular hairs (Figure 2C) are seen on the epidermis. The vascular bundles are in a continuous ring. Phloem is 3-4 rows and circular shape. There is sclerenchyma with 1-2 row and continuous ring on the phloem. The cortex consists of 4-6 layer cells. The cortex cells are circular and polygonal in shape. There are collenchyma cells in the corners of the cortex towards the epidermis. There are 3-4 rows of cambium (Figure 2B).

Epidermis cells are circular and rectangular in *A. salicifolia* leaf cross-section and its walls are wavy. Papillae (Figure 3D) and simple eglandular (Figure 3F) with 1-4 cells are seen on the epidermis. In addition, short-stem glandular hair are present on the epidermis (Figure 3E). There are 3-4 rows of palisade parenchyma and 2-3 rows of spongy parenchyma in the cross-section of *A. salcifolia* leaf and is mesophyll bifacial.
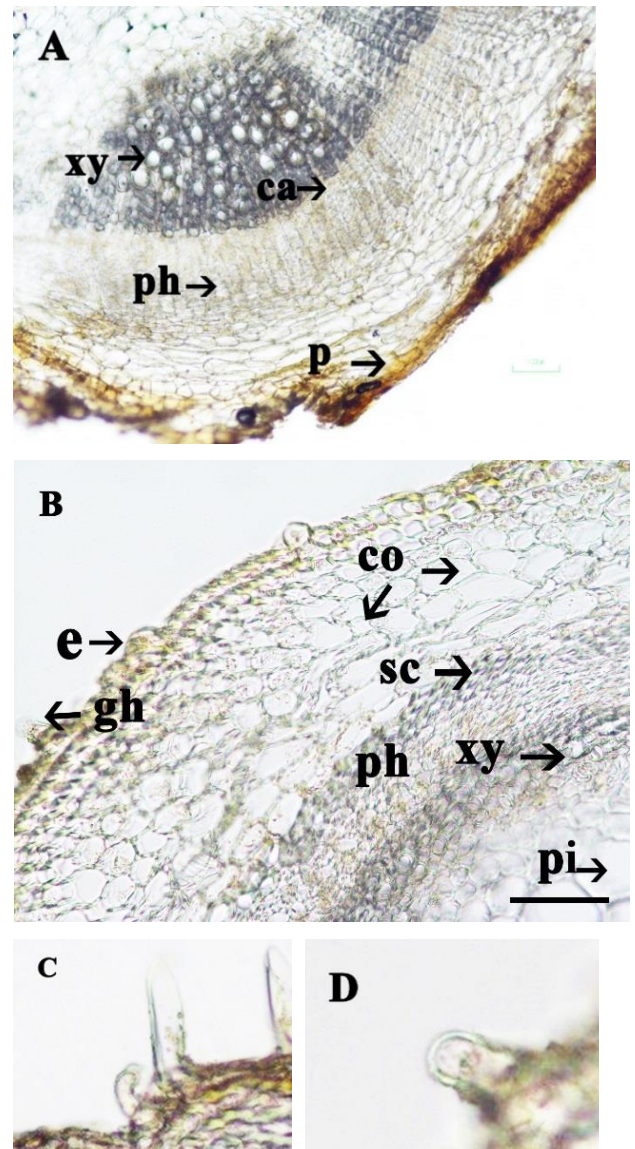
Figure 2 A Root cross section of *A. salicifolia,* B Stem cross section of *A. salicifolia*, C eglandular hair, D glandular hair, ca: cambium, co: cortex, e: epidermis, gh: glandular hair, p: periderm, ph: phloem, pi: pith, xy: xylem (Scala bar 100 mμ)

Sibel ULCAY

Morphological, Anatomical and Ecological Features of Ajuga salicifolia (L.) Schreber (Lamiaceae) with...

Table 2 Anatomical measurement results of *A. salicifolia*

		Width (μm) Mean ± SD.	Length (μm)-Mean± SD.
Root	Periderm	17.30 ±0.64	32.00±2.43
	Diameter of cortex cells	72.77±5.54	
	Diameter of phloem	12.95±	20.5687±1.08
	Diameter of xylem	24,69±1,69	
	Cell of pith	45.12±2.34	75.51±3.83
Stem	Epidermis cells	17.31±1.28	26,00±0,88
	Diameter of collenchyma cells	15..49±1.62	
	Diameter of cortex cells	30.91±2.49	
	Diameter of pith cells	79.71±7.33	
	Diameter sclerenchyma cells	7.3789±0.36	
	Diameter of phloem	9.17±1.40	
	Diameter of xylem	28.22±2.75	
Leaf	Upper epidermis	39.70±0.68	36.74±6.17
	Lower epidermis	16.19±1.08	15.68±1.34
	Palisade parenchyma	21.78±0.42	23.04±2.06
	Diameter of spongy parenchyma	9.08±0.69	
	Diameter of xylem	6.71±0.60	

Table 3 The stoma features on the upper and lower epidermis of *A. salicifolia*

	Lower surface mean/SD.	Upper surface mean/SD.
Stomata width (μm)	22.09±0.65	21.36±0.77
Stomata length (μm)	29.69±1,11	28.71±1.02
Number of stomata (1 mm^2)	82	36
Number of epidermis cells (1 mm^2)	187	267
Stomata index	30.4	11.88
Type of stomata	Anomocytic	Anomocytic

There is one vascular bundle in the median vein. Stomata on the lower epidermis is more numerous. There are 82 stomata in 1 mm^2 area and the stomata index is 30.4. On the upper surface, the number of stomata is 36 and the stomata index is 11.88. There are anomocytic stomata on both surfaces.

3.3. Ecological Results

The habitat of the *A. salicifolia* open areas, field edges and slopes areas. Species has been recorded from 1078 m. Saturation percentage of soil where the species grow is 107.8% and the soil texture is clayey. It has a pH value of 8.23 and it is slightly alkaline. Total amount of water-soluble salt of the soil is 0.02% and it is classified salt-free soil. It is 22.71% in terms of lime and it is considered as very calcareous soils. With respect to chemical features, available phosphorus amount of the soil is 0.8 kg/da and it is classified among very low phosphorus

soils. Amount of potassium that can be obtained is 233.7 kg/da and it is classified as high. Amount of organic matter is 0.4% and it is classified in the group of high hummus soils (Table 4).

Sibel ULCAY

Morphological, Anatomical and Ecological Features of Ajuga salicifolia (L.) Schreber (Lamiaceae) with...

Table 4 Soil characteristics of *A. salicifolia*

Physical properties					
Saturation (%)			Texture		
107.8			Clayey		
Chemical properties					
Total Salt Soluble in Water (%)	pH	Lime (%)	Organic Matter (%)	Phosphorus (kg/da)	Potassium (kg/da)
0.02	8.23	22.71	0.4	0.8	233.7
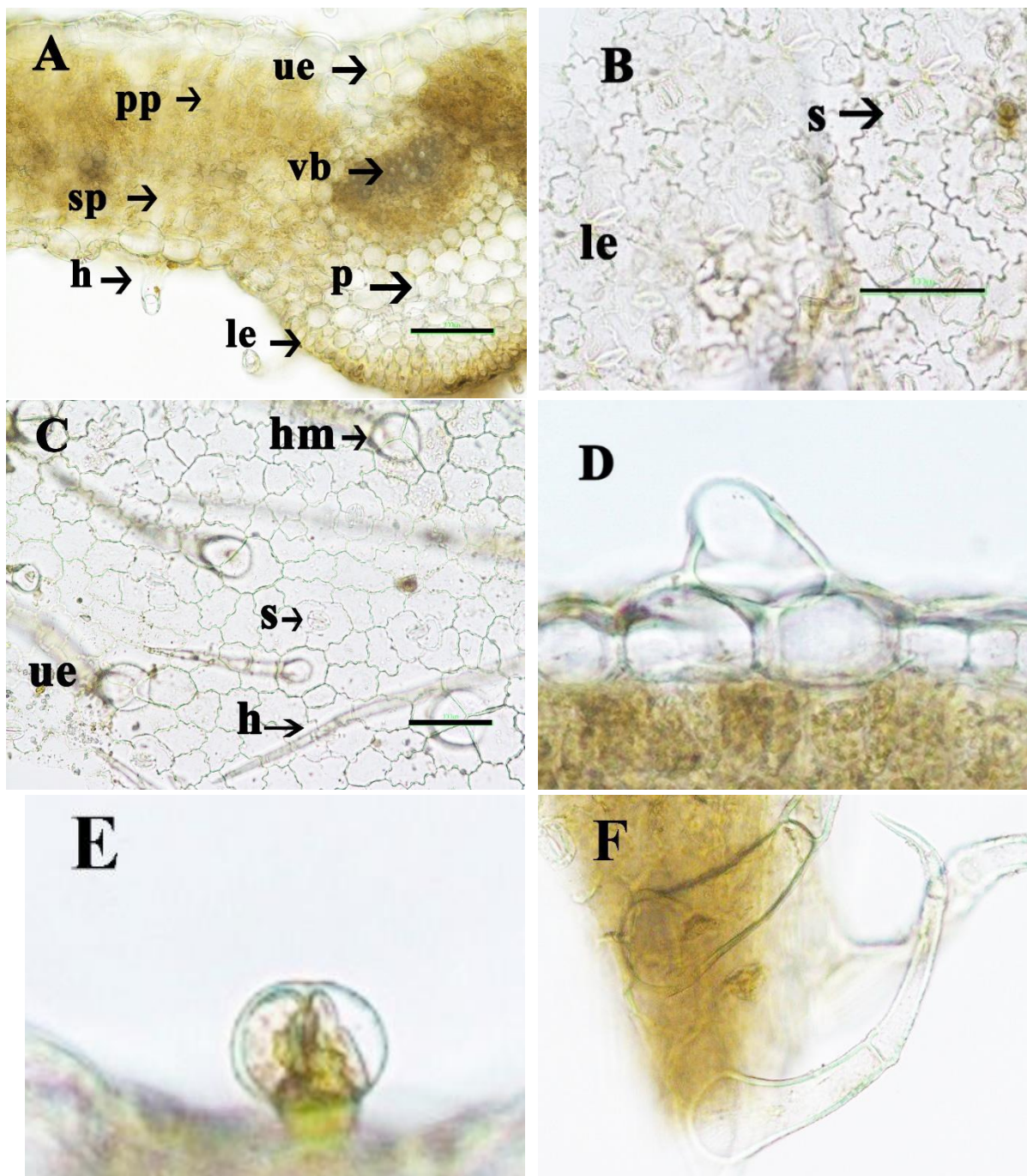
Figure 3. A Leaf cross section of *A. salicifolia*, B lower surface section of leaf, C upper surface section of leaf, D appearance of the papillae, E glandular hair, F eglandular hair, le: lower epidermis, h: hair, hm: main hair cell, p: parenchyma, pp: palisade parenchyma, s: stomata, sp: spongy parenchyma, ue: upper epidermis, vb: vascular bundle (Scala bar 100 mμ)

Sibel ULCAY

Morphological, Anatomical and Ecological Features of Ajuga salicifolia (L.) Schreber (Lamiaceae) with...

With this study, the morphological and anatomical features of the species of *A. salicifolia*, which belongs to the naturally distributed Lamiaceae family, are revealed.

Stem of *A. salicifolia* with pilose hair is about 15 cm in length. The stem length of *A. chamaepitys* (L.) Schreber subsp. *chia* (Schreber) Arcangeli *var.chia* has been reported to be 7-15 cm [19]. The shape of the leaves is usually oblong-lanceolate. The length of the petals is 12-30 mm. The petal length of *A. reptans* is 9-16 m [19]. One or two red spots are visible on the top of the petals. There are 2-3 rows of periderm outside the root of *A. salicifolia*. Epidermis is seen in the outmost part of the root of the species of *A. reptans* [19] While parenchymatic cells are present in the *A. salicifolia* pith region, the root pith area is covered with secondary xylem elements in *Ajuga relicta* P.H. Davis taxon [22].

There are 1-2 rows of epidermis at the outermost part of the stem of *A. salicifolia*, and the stem is noticeably cylindrical. Metcalfe and Chalk state that the characteristic feature of the Lamiaceae family is the rectangle stem [37]. *A. salicifolia* stem shape complies with the general feature of the family. Collenchyma cells are seen just below the corner parts of the species that is our research topic. In the family's *Ajuga postii* Briq. and *A. relicta* species and *Lycopus europaeus* L. species, collenchyma cells were sequenced in the same way [22; 38]. Capitate glandular and 1-3 cell eglandular hair is seen in the stem cross-section of the *A. salicifolia* plant. Similar hairs are seen in *A. reptans* L. and *A. chamaepitys* subsp. *chia* var. *chia* [19]. Metcalfe and Chalk state that glandular hairs are diagnostic for the Lamiaceae family [39]. In the cross section of the stem of *A. salicifolia*, a continuous ring-shaped sclerenchyma cells are seen just below the phloem. Erkara and Koyuncu mention about the presence of sclerenchyma in a small area above the xylem in the stem of the *A. reptans* species [20].

There are 3-4 rows of palisade parenchyma and 2-3 rows of spongy parenchyma in the cross section of *A. salicifolia* leaf, and is mesophyll bifacial. Sonmez and Kose state that *A. postii* leaf has a bifacial type and diacytic stomata [22]. The number of stomata on the lower leaf surface of *A. chamaepitys* subsp. *chia* var. *chia* is higher than the number of stomata on the upper surface [19]. This feature is similar to *A. salcifolia* species.

As a result, in *A. salcifolia*, the redness on the stem and petal, the leaves being generally oblong-lanceolate, the hair on the petal and stem were observed morphologically. The presence of 7-8 layered phloem and pith on the root, the presence of glandular and eglandular hairs on the stem, the formation of a continuous ring of vascular bundles, the presence of a continuous ring-shaped sclerenchyma on the phloem, the waviness of the epidermis walls on the leaf, the number of palisade and spongy parenchyma layers, hair condition and types, are important features for *A. salcifolia*. The plant, which is our subject of study, spreads in open areas, field edges, and slopes. The soils in which it grows are clayey, slightly alkaline, salt-free, poor in phosphorus, and rich in potassium and organic matter.

The Declaration of Conflict of Interest/ Common Interest

No conflict of interest or common interest has been declared by the author.

The Declaration of Ethics Committee Approval

The author declares that this document does not

Sibel ULCAY

Morphological, Anatomical and Ecological Features of Ajuga salicifolia (L.) Schreber (Lamiaceae) with...

require an ethics committee approval or any special permission.

The Declaration of Research and Publication Ethics

The author of the paper declares that he complies with the scientific, ethical and quotation rules of SAUJS in all processes of the paper and that he does not make any falsification on the data collected. In addition, he declares that Sakarya University Journal of Science and its editorial board have no responsibility for any ethical violations that may be encountered, and that this study has not been evaluated in any academic publication environment other than Sakarya University Journal of Science.

REFERENCES

[1] B. Bazarragchaa, L. S., Myoung and L. H. Yuon, "Pollen morphology of the family Lamiaceae in Mongolia," Journal of Korean Nature, vol: 5, no. 2 pp 169-179, 2012.

[2] P. H. Davis, "Flora of Turkey and the East Aegean Islands," Edinburgh, England, University Press. 1982.

[3] A. Güner, N. Özhatay, T. Ekim, K. H. C. Baser, "Flora of Turkey and the East Aegean Islands (Supplement 2)," Edinburgh, England: University Press, 2000.

[4] A. Güner, S. Aslan, T. Ekim, M. Vural, M. Babaç, "Turkey Plant List (Vascular Plants)," Istanbul: Nezahat Gökyiğit Flora Botanic Garden and Research Association Publications, 2012.

[5] Baydar, H. "Medicinal, aromatic and delightful plants: science and technology," Nobel Publications, 7th Edition, Ankara, pp. 285-304, 2019.

[6] F. Bucar, T. Kartnig, G. Paschek, E. Winkler and M. Schubert-Zsilavecz, "Flavonoid glycosides from *Lycopus europaeus*," Planta Med., vol. 61, no. 5, pp. 489, 1995.

[7] S. Dogan, M. E. Diken and M. Dogan, "Antioxidant, phenolic and protein contents of some medicinal plants," Journal of Medicinal Plants Research, vol. 4, no. 23, pp. 2566-2572, 2010.

[8] S. Senhaji, F. Lamchouri, K. Bouabid, N. Assem, M. El Haouari, K. Bargach and H. Toufik, "Phenolic contents and antioxidant properties of aqueous and organic extracts of a moroccan *Ajuga* iva subsp. *pseudoiva*," Journal of Herbs, Spices & Medicinal Plants, vol. 1 pp. 19, 2020.

[9] G. Kökdil, T. Gülaçtı, A. C. Gören, V. Wolfgang, "Steroids and terpenoids from *Ajuga relicta*," Zeitschrift für Naturforschung B Journal of Chemisty, vol. 57 (b), pp. 957-960, 2002.

[10] A. Castro, J. Coll, Y. A. Tandron, A. K. Pant and C.S. Mathela, "Phytoecdy steroids from *Ajuga macro sperma* var, *brevi* flora roots," J. Nat. Prod, vol. 71 pp. 1294-1296, 2008.

[11] Z. H. Israili and B. Lyoussi, "Ethnopharmacology of the plants of genus *Ajuga*," Pak. J. Pharm. Sci, vol. 22, no. 4, pp. 425-462, 2009.

[12] N. Haşimi, "Determination of some biological activities of petroleum ether, acetone and methanol extracts of Ajuga vestita and *Ajuga xylorrhiza* plants," Doctorate Thesis, Diyarbakır, 2012.

[13] Y. B. Köse, "sivrimayasıl," 2012. On the following site: Bizimbitkiler (2013). <http://www.bizimbitkiler.org.tr>, date of access 09.11.2020.

[14] M. Ibrar, and F. Hussain, "Ethnobotanical studies of plants of Charkotli hills, Batkhela district, Malakand, Pakistan, " Frontiers of Biology in China, vol. 4 no.4, pp. 539, 2009.

Sibel ULCAY

Morphological, Anatomical and Ecological Features of Ajuga salicifolia (L.) Schreber (Lamiaceae) with...

[15] Q, Zabihullah, A. Rashid and N, Akhtar, Ethnobotanical survey in kot Manzaray Baba valley Malakand agency, Pakistan. Pak J Plant Sci., vol. 12 no. 2, pp. 115-121, 2006.

[16] F. Güneş and N. Özhatay, "An ethnobotanical study from Kars (eastern) Turkey," Biological Diversity and Conservation, vol. 4, no. 1, pp. 30-41, 2011.

[17] R. Polat, "Ethnobotanical study on medicinal plants in Bingöl (City center) (Turkey)," Journal of Herbal Medicine, vol. 16, no. 100211, 2019.

[18] F. Naghibi, M. Mosadegh, M. S. Mohammadi, and A. B. Ghorbani, "Labiatae family in folk medicine in Iran: from ethnobotany to pharmacology," Iranian Journal of Pharmaceutical Research vol. 2, pp. 63-79, 2005.

[19] Ö. E. Akçın, G. Şenel, Y. Akcin, "The morphological and anatomical properties of *Ajuga reptans* L. and *Ajuga chamaepitys* (L.) Schreber subsp. *chia* (Schreber) *arcangeli* var. *chia* (Lamiaceae) taxa," Pakistan Journal of Biological Sciences, vol. 9, no.2, 2006.

[20] İ. P, Erkara and O. Koyuncu, "The anatomical and palynological properties of *Ajuga reptans* L.(Lamiaceae) at Risk," Anadolu University Journal of Science and Technology, vol.10, no. 2, pp. 593-601, 2009.

[21] Ö. E. Akçin, M. S. Özyurt and G. Şenel, "Petiole anatomy of some Lamiaceae taxa" Pak. J. Bot., vol. 43, no. 3, pp. 1437-1443, 2011.

[22] E. Sönmez and Y. B. Köse, "Morpho-anatomical investigations on Ajuga postii Briq and *Ajuga relicta* P.H. Davis," Biological Diversity and Conservation, vol.10, no. 1, 39-49, 2017.

[23] I. Ö. Çalı, A. Cansaran and C. Yıldırım, "Trichome morphology of *Ajuga orientalis* L. (Lamiaceae) from Turkey," Bangladesh J. Bot., vol. 43, no. 1, pp. 91-95, 2014.

[24] T. Pfeiffer, "Sexual or clonal origin? A morpho-ecological and molecular analysis in a patch of Ajuga reptans L.(Lamiaceae)," Feddes Repertorium: Zeitschrift für botanische Taxonomie und Geobotanik, vol. 116 no. 3-4, pp. 183-190. 2005.

[25] N. Kharazian, "The taxonomy and variation of leaf anatomical characters in the genus *Aegilops* L. (Poaceae) in Iran," Turk. J. Bot., vol. 31, pp. 1-9, 2007.

[26] Y. Vardar, "Botanikte Preparasyon Teknikleri," Ege Üniversitesi Fen Fakültesi Baskı İşleri, İzmir, No 1. 1987.

[27] H. Meidner, and T. A. Mansfield, "Physiology of stomata. McGraw- Hill, London," 1968.

[28] M. L. Jackson, "Soil chemical analysis," Prentice-Hall Inc., pp. 183, 1962.

[29] I. Demiralay, "Soil physical analysis," Atatürk University, Faculty of Agriculture Publications, Erzurum, no. 143, pp. 131, 1993.

[30] C.A. Black, "Methods of soil analysis, Agronomy," Agr., Madison, Wisc., no. 9, Part: 1 and 2. pp. 1572, 1965.

[31] A. Tüzüner, "Soil and water analysis laboratories handbook," T.C. Ministry of Agriculture, Forestry and Rural Affairs General Directorate of Rural Services, pp. 21-27, 1990.

[32] D. W. Nelson and L.E. Sommers, "Total carbon, organic carbon, and organic matter," P: 9611011. In D.L. Sparks (ed) Method of Soil Analysis: Chemical Methods. Part 3. SSSA, Madison, WI., 1996.

[33] F. Gülçur, "Physical and chemical analysis methods of soil," Istanbul University Faculty of Forestry Publications, İ. Ü.

Publication No: 1970, O. F. Publication no. 201, Kutulmus Printing House, Istanbul, 1974.

[34] N. Ülgen, and N. Yurtsever, "Turkey Fertilizer and Manure Guide," Soil and Fertilizer Research Institute publications. General Publication no. 209, Technical Publications no. T.66. Ankara, 1995.

[35] S. R. Olsen, V. Cole, F. S. Watanabe, and L. A. Dean, "Estimation of available phosphorus in soils by extraction with sodium bicarbonate," U.S.A., 1954.

[36] P. A. Helmke, and D.L. Sparks, "Lithium, sodium, potassium, rubidium, and calcium, in Sparks, D.L., (Ed) Methods of Soil Analysis," Part 3, Chemical Methods, SSSA Book Series no. 5, SSSA., Madison, WI, pp. 551-574, 1996.

[37] C. R. Metcalfe and L. Chalk, "Anatomy of Dicotyledon," Clarendon Press, Oxford. pp.502-535, 1972.

[38] S. Ulcay and G. Şenel, "An anatomical study on *Lycopus europaeus* l. species of family Lamiaceae," Sinop University Journal of Science, vol. 3, no. 1, pp. 45-52, 2018.

[39] C. R. Metcalfe and L. Chalk, "Anatomy of the dicotyledons," Oxford: Oxford University Press, 1950.

Title: The Effect of Hydrothermal Aging Time and Temperature on the Structural
Properties of KIT-6 Material

Authors: Dilşad Dolunay ESLEK KOYUNCU

The Effect of Hydrothermal Aging Time and Temperature on the Structural Properties of KIT-6 Material

Dilşad Dolunay ESLEK KOYUNCU [*1]

Abstract

The combined effect of hydrothermal treatment temperature and aging time on the structural properties of ordered mesoporous KIT-6 material were investigated. A series of KIT-6 materials were prepared by hydrothermal synthesis procedure. In the first step, experiments were performed at 90ºC and at different aging times (0-72 h) to understand the effect of hydrothermal aging time. It was concluded that the aging time positively affect the formation of ordered mesoporous structure and uniform pore structure occurs after 18 h. In addition, long hydrothermal treatment time favored the pore enlargement. In the second step, to understand which parameter (time or temperature) is more important in the synthesis of highly uniform material, KIT-6 materials were prepared at different temperatures ranging between 60-150ºC and at different aging times (24 h and 72 h). The experiments showed that at elevated temperatures (>90ºC) long aging times negatively affect the structural properties of the mesoporous KIT-6 structure. Highly uniform mesoporous KIT-6 material having high crystallinity, narrow pore size distribution, high BET surface area (726 cm^3/g) and high pore volume (1.5 cm^3/g) was prepared at 120ºC with an aging time of 24 h. However, it was determined that 60ºC is not a suitable temperature to obtain KIT-6 material having good structural properties and the uniform crystal structure deteriorated at 150ºC.

Keywords: KIT-6, Mesoporous silica, Aging time, Hydrothermal synthesis, Temperature effect

1. INTRODUCTION

Porous materials are divided into three basic groups in terms of their pore sizes according to IUPAC (International Union of Pure and Applied Chemistry) classification. In this context, the materials having pores widths larger than 50 nm are called macroporous; those with pores widths between 2 nm and 50 nm are called mesoporous and those with pores widths smaller than 2 nm are called microporous [1]. Mesoporous materials with superior properties have attracted great attention due to their potential use in many areas since M41S family was firstly reported by Mobil Oil Corporation [2]. MCM-41, MCM-48 and MCM-50 which are the most well-known materials of this class are ordered in hexagonal (space group p6mm), cubic (space group Ia3d)

---

* Corresponding Author: deslek@gazi.edu.tr
[1] Gazi University, ORCID: https://orcid.org/0000-0001-8092-6740

and lamellar (space group p2) arrays, respectively [3]. These mesoporous materials have high surface areas (higher than 700 m^2/g), pore volume (greater than 1.7 cm^3/g) and ordered framework [4]. In 1998, Zhao et al. (1998) prepared the highly ordered mesoporous SBA (Santa Barbara Amorphous) family under acidic conditions using non-ionic surfactant as a directing agent [5]. SBA-15 is one of the most important material of this family. SBA-15 is synthesized in an acidic medium using the non-ionic triblock copolymer Pluronic P123 as a surfactant. Similar to the MCM-41 structure, SBA-15 has a hexagonal structure with a spatial group of p6mm. However, it shows greater hydrothermal stability although it has thicker silica walls (3.1 to 6.4 nm) and larger pores (4.6 to 30 nm) than MCM-41 material [6].

KIT-6 material, which is a cubic Ia3d form of mesoporous silica, firstly synthesized by Korea Advanced Institute of Science and Technology (KAIST). Similar to MCM-48 structure, it has interpenetrating bi-continuous pore system with three dimensional cubic Ia3d symmetric structure but with larger pore diameter [7-8]. Bi-continuous channel structure of KIT-6 materials provides more active area and resistance to agglomeration [9]. In addition, the tunable pore size of this material makes the material more advantageous in terms of active metal dispersion and reactant accessibility especially in catalytic applications. By changing the synthesis conditions, such as hydrothermal treatment temperature, surfactant

type and surfactant concentration, the pore size of KIT-6 material can be tuned from 4 to 12 nm [8,10]. In the literature, KIT-6 materials have been studied for various applications as adsorbent [11], catalyst support [12,13], nano-casting template for the synthesis of Si-free mesoporous materials, such as carbon [14], TiO_2 [15], C_3N_4 [16], α-Fe_2O_3 [17], Au [18], MnO_2 [19], RuO_2 [20]. The most important reason of using KIT-6 material as a support material is the unique 3D interpenetrating pore structure which allows direct and open access of guest molecules without pore blocking [7,21,22]. In the literature, KIT-6 is used as support material in the dehydrogenation of propane [23,24], CO_2 removal [25], CO_2 reforming of methane [26], methane production via hydrogenation of CO_2 [27], hydrogenation of CO [28] etc.

Figure 1 shows the typical hydrothermal synthesis of KIT-6 material. The hydrothermal method was reported as a very important method as it enables high quality crystal formation [29]. The synthesis is performed in acidic medium of HCl. Triblock co-polymer P123 (PEO-PPO-PEO) and tetraethyl orthosilicate (TEOS) are used as surfactant and silica source, respectively. Different from the synthesis of SBA-15 material, butanol is added as co-solvent and co-surfactant [30]. It has been reported that butanol provides phase transformation and low amounts of butanol (butanol / P123 < 0.9 by weight) cause the formation of 2D hexagonal mesophase [10].
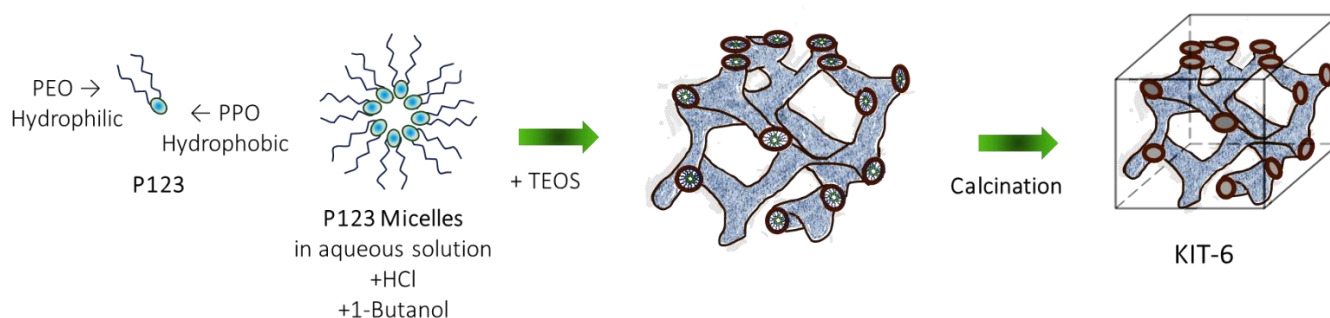

Figure 1. Typical hydrothermal synthesis mechanism of KIT-6 material

In this study, the effect of hydrothermal treatment parameters on the structural properties of mesoporous KIT-6 materials was investigated. A

series of KIT-6 materials were prepared by hydrothermal synthesis procedure. In the first step, the effect of hydrothermal treatment

duration on the structural properties of KIT-6 materials was studied at hydrothermal treatment temperature of 90ºC. In the second step, to understand which parameter (time or temperature) is more important in the synthesis of highly uniform material, KIT-6 materials were prepared at different temperatures ranging between 60-150ºC and at selected aging times at which the mesopore structure can be obtained. Structural changes in the KIT-6 materials were determined by characterization studies. There is no study present in the literature that investigate the combined effect of hydrothermal treatment duration and temperature on the structural properties of mesoporous KIT-6 material.

2. MATERIAL AND METHOD

2.1. Synthesis of Mesoporous KIT-6 Material

In this study, a series of KIT-6 materials were prepared by hydrothermal synthesis procedure as reported in the literature [31]. Firstly, until reaching complete dissolution 6 g of surfactant, Triblock copolymer Pluronic P123 (poly(ethylene oxide) - poly(propylene oxide) - poly(ethylene oxide), Sigma-Aldrich, molecular weight≈5800), 220 ml of deionized water and 12 g of co-solvent concentrated HCl (Sigma-Aldrich, 37%) were stirred at 35ºC. Then, 6 g of co-surfactant 1-Butanol (Alfa Aesar, 99 %) was added to this mixture. After 1 hour mixing at the same temperature, 12.4 g of Tetraethyl orthosilicate, TEOS (Sigma-Aldrich, 98%), was added as silica source. Mixing was carried out for 24 hours at the same temperature. The resulting mixture was transferred into a Teflon lined autoclave and hydrothermal treatment was performed under static conditions at different times (h=0-12-18-24-48-72 hours) and at different temperatures (t=60-90-120-150ºC). The solid product was recovered by vacuum filtration and washed with deionized water several times until the pH of the filtrate remained constant. The solids were oven dried at 90ºC and calcined at 750ºC for 6 hours with a heating rate of 10°C/min in air flow. The materials obtained via this procedure were named as KITt-h, where "t" stands for hydrothermal

treatment temperature and "h" represents the duration of the hydrothermal treatment.

2.2. Characterization Studies

Crystalline phases of the KIT-6 samples were determined by the low-angle powder X-ray diffraction (XRD) analysis, using a Rigaku Ultima-IV diffractometer with Cu Kα radiation (40 kV and 30 mA) at a scanning rate of $0.2º min^{-1}$. The N_2 adsorption/desorption isotherms were obtained with Quantachrome Autosorb-1C model equipment, at 77 K and the samples were vacuum dried at 250ºC for 3 h before the experiments. The specific surface areas of KIT-6 samples were calculated using the desorption points within the N_2 relative pressure range of 0.05-0.30 using Brunauer-Emmett-Teller (BET) method. The pore size distributions of the samples were obtained from the analysis of the desorption values by using the Barrett-Joyner-Halenda (BJH) method. The functional groups present in the structure were investigated by Fourier-Transform Infrared spectroscopy (FT-IR) in the medium infrared region of 4000-400 cm^{-1} with 4 cm^{-1} resolutions in a Jasco 4700 ATR/FT-IR spectrophotometer.

3. RESULTS AND DISCUSSION

A series of KIT-6 materials were prepared via hydrothermal synthesis procedure. At the first stage, the aging time of hydrothermal treatment was varied from 12 h to 72 h at 90ºC to determine the effect of aging time on the structural properties of the resulting materials. A material without hydrothermal treatment was also prepared for the comparison. The 3D ordered mesoporous silica structure were determined by the small angle XRD patterns of the KIT-6 materials (Figure 2). As it is seen in Figure 2 that the aging time has crucial effect on the crystal structure of the final material. The peak intensity of the KIT90-24 sample is larger than other prepared materials. This might be resulted from the highly organized framework with uniformly packed silica crystals. The KIT90-24 sample exhibited three characteristic XRD peaks at 2θ=1.06°, 1.2° and 1.9°, corresponding to (211),

(220) and (332) Miller indices that are the characteristics of three-dimensional mesoporous structures with spatial group Ia3d organized in body-centered cubic array [32]. As the aging time increases to 72 h the XRD peak intensity decreases to the lower values (KIT90-72). This may be the indication of deterioration in uniform crystal structure of the KIT90-72 sample because of high aging duration. In the XRD patterns of KIT90-12 and KIT90-18 samples, only the main peak of KIT-6 structure was observed with lower intensity. In the XRD patterns of the KIT-0 sample prepared without hydrothermal treatment, no peak observed that is the indication of any crystal structure.
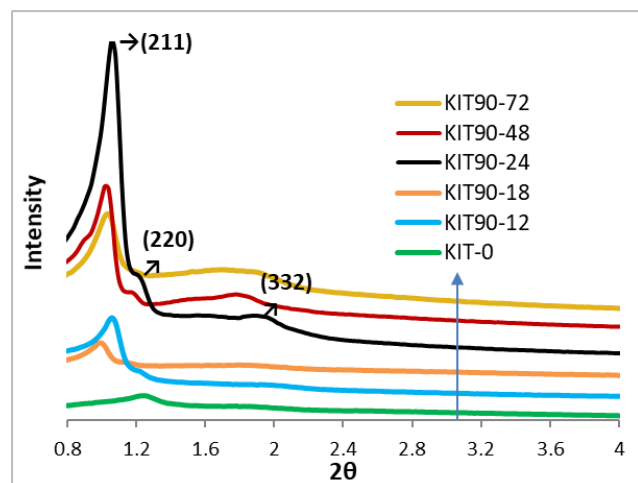
Figure 2. Small angle XRD patterns of KIT-6 materials prepared at 90°C

The interplanar spacing (d_{211}), the lattice parameter (a_0) and the wall thickness (t) values were calculated for all samples (Table 1). The interplanar spacing, which is the periodic interval of pores of KIT-6 that is the summation of the pore width and the pore wall, was calculated from Bragg's Law ($n\lambda=2d\ sin\theta$) by using the 2θ value of the (211) peak. It was observed that the wall thickness decreases slightly from 4.8 nm to 4.0 nm with the increasing aging time. Similar results were observed in the study of Merkache et al. (2015). They compared the structural changes of KIT-6 materials prepared at 100°C with aging times of 48 h and 72 h. They have reported that

the wall thickness decreases from 4.07 nm to 3.77 nm with aging time [33].

The bands related to the inorganic functional groups of KIT-6 structure were observed in the ATR/FT-IR spectra (Figure 3). It is seen that the peak intensity increases as the aging time increases. It might be due to the higher degree of TEOS silanization at longer aging times. It is known that the main bands around 1034 cm^{-1}, 800 cm^{-1} and 445 cm^{-1} are related with the structural siloxane (Si-O-Si) framework. The band at 1034 cm^{-1} and identified shoulder at 1204 cm^{-1} are the typical bands referring to asymmetric stretching of the Si-O-Si bond [33]. Bands around 810 cm^{-1} and 445 cm^{-1} could be attributed to symmetrical stretching and bending vibrations of the Si-O-Si bond, respectively [34]. A small broad peak at about ~3400 cm^{-1} are assigned to the stretching of OH^- groups of water adsorbed to the surface. Small vibrations between 1900-2400 cm^{-1} are the characteristics of ATR measurements.

The N_2 adsorption-desorption isotherms of the KIT-6 materials prepared at 90°C in different aging times are classified as Type IV according to the IUPAC classification (Figure 4). A sharp capillary condensation step at high relative pressures (nearly at P/P^0=0.6-0.8) and a final saturation plateau are the characteristics of this type of isotherms [30]. It is known that there is a correlation between the shape of observed hysteresis loop and the textural properties of the material [35]. All samples exhibit hysteresis loop at pressure ranges of P/P^0=0.5-0.8. The narrow hysteresis loop is the indication of the highly uniform pore structure. As it is seen that the regular pore structure occurs after 18 hours aging time. Non-uniform N_2 adsorption-desorption isotherm was obtained with the KIT-0 sample prepared without hydrothermal treatment. According to the IUPAC classification the samples exhibited the H1 type hysteresis loop that is related with the well-ordered three-dimensional mesopore networks of KIT-6 material [35,36]. After 24 hours of aging, adsorbed volume is decreased with increasing aging time.
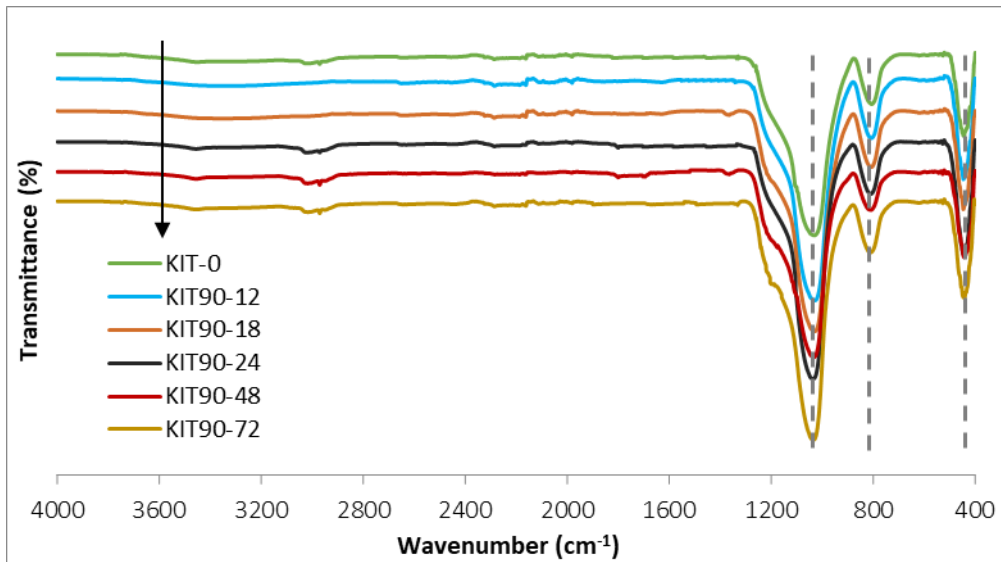
Figure 3. ATR/FT-IR spectrum of KIT-6 materials prepared at 90°C
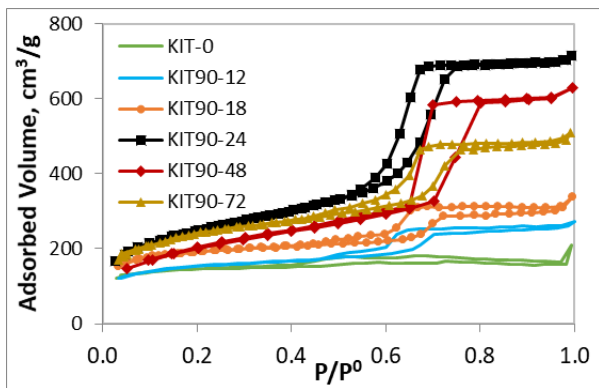
Figure 4. N$_2$ adsorption-desorption isotherms of KIT-6 materials prepared at 90°C

The pore size distribution curves determined by BJH method are given in Figure 5. KIT90-24 and KIT90-48 samples were exhibited mono-disperse pore size distribution. The pore size distribution curve of the KIT-0 sample is also given as an inner figure as a comparison. The importance of the hydrothermal treatment in the formation of mesopore structure can be seen in this graph.

Table 1 summarizes the XRD and BET results of KIT90 materials. The interplanar spacing (d$_{211}$), lattice parameter (a$_0$) and wall thickness (t) values were calculated for all samples. The interplanar spacing is the periodic interval of pores of KIT-6 that is the summation of the pore width and the pore wall. This value was calculated from Bragg's Law (nλ=2d sinθ) by using the 2θ value of the (211) peak of the samples. While there is no important change in the d$_{211}$ and a$_0$ values, the

pore diameter slightly increases with aging time. Thus, the wall thickness of the materials decreases from 4.8 nm to 4.0 nm as the aging time increases from 12 h to 72 h. This indicates that long hydrothermal treatment duration favors the pore enlargement. Similar results were obtained by Fernandes et al. (2018). They have reported that when the aging time increases from 12 h to 30 h, the pore diameter increases from 6.1 nm to 7.0 nm, respectively [30]. The KIT90-24 sample exhibited the highest BET surface area and pore volume compared to the other prepared KIT-6 supported materials.
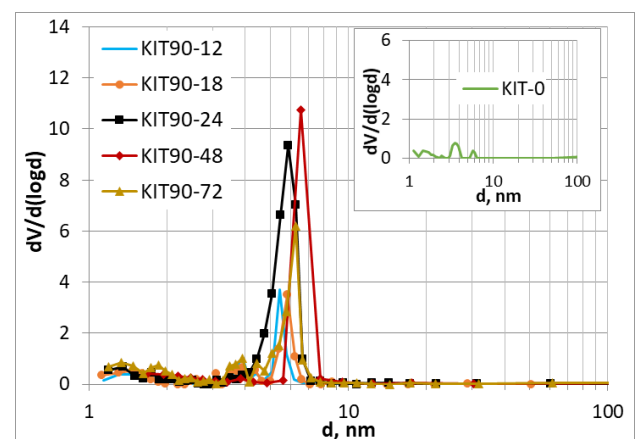
Figure 5. Pore size distribution curves of KIT-6 materials prepared at 90°C

Table 1. XRD and N_2 adsorption-desorption results at different aging times of materials prepared at 90°C

Sample	Aging temperature °C	Aging time hour	d_{211} [a] nm	a_0 [b] nm	Wall thickness [c] t, nm	Pore diameter [d] d_p, nm	Pore volume [d] V_p, cm³/g	BET surface area [d] m²/g
KIT90-0	-	0	-	-	-	1.1	0.24	470
KIT90-12		12	8.33	20.4	4.8	5.4	0.35	497
KIT90-18	90	18	8.83	21.6	5.0	5.8	0.43	615
KIT90-24		24	8.33	20.4	4.3	5.9	1.12	858
KIT90-48		48	8.65	21.2	4.1	6.5	0.93	670
KIT90-72		72	8.35	20.8	4.0	6.2	0.76	796

[a] Interplanar spacing calculated from Bragg's Law

[b] Cubic parameter, $a_0 = d_{211} * \sqrt{h^2 + l^2 + k^2}$

[c] $t = a_0/2 - d_p$

[d] Obtained from BJH desorption data

In the next stage of the study, experiments were carried out at different temperatures (60-150°C) and aging times (24 h and 72 h) to understand which parameter is more important in the synthesis of highly uniform KIT-6 materials. Aging times of 24 h and 72 h were selected at this stage. Because it is concluded in the previous stage that in the studied aging time range these treatment times are the lowest and highest temperatures at which the uniform mesoporous structure is obtained.

The XRD patterns of materials that are hydrothermally treated at different temperatures for 24 h and 72 h are given in Figure 6. Materials other than KIT120-72 and KIT150-24 exhibited all characteristic XRD peaks of mesoporous KIT-6 crystal structure. The peak intensity of the materials differs with respect to the aging temperature and aging time of the synthesis. With aging time of 24 h, it is seen that the peak intensity increases and the peaks shift to the left side with increasing temperature from 60 °C to 120°C. This results the increase in the interplanar spacing and the cubic parameter. When the temperature was raised to 150°C, the XRD peak became smaller and the other characteristic peaks of KIT-6 structure disappeared except for the main peak. This can be attributed to the deterioration of uniform crystal structure. However, in the XRD patterns of the materials with aging time of 72 h, when the temperature was increased from 60°C to 90°C the peak intensity decreases sharply and shifted to the left side. The KIT-6 material was also prepared at 150°C with an aging time of 72 h and it was observed that the material deteriorated (its result not shown in Figure). It can be concluded from these results that especially at higher temperatures long aging time causes to the

deformation of regular crystal structure of KIT-6 material.
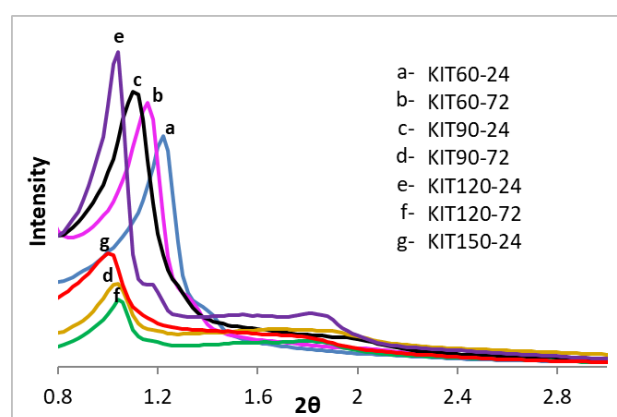
Figure 6. XRD patterns of KIT-6 materials prepared at different temperatures and at different aging times

The ATR/FT-IR spectra of KIT-6 materials prepared at different temperatures and at different aging times are given in Figure 7. As mentioned earlier, the band at 1050 cm⁻¹ and identified shoulder at about 1204 cm⁻¹ are the typical bands referring to asymmetric stretching of the Si-O-Si bond [33]. Bands around 800 cm⁻¹ and 445 cm⁻¹ could be attributed to symmetrical stretching and bending vibrations of the Si-O-Si bond, respectively [34]. It is clearly observed in the FT-IR results that peak intensities become higher when the temperature raised from 60°C to 150°C. It might be due to the higher degree of TEOS silanization at higher temperatures [37]. The hydrolysis of TEOS is the first step in the preparation of mesoporous silica materials using TEOS as a silica source. [38]. The efficiency of the hydrolysis process affects the properties of the final material. In addition to the water amount, temperature is very important parameter affecting the hydrolysis reaction efficiency. As long as water amount is sufficient and temperature is

high, TEOS is completely hydrolyzed and much Si-O-Si bond was gained. Because of the endothermic nature of the hydrolysis process high temperatures favor the formation of Si-O-Si bond [39]. The reason for getting high density FT-IR peaks at high temperatures can be explained in this way.

The N_2 adsorption-desorption isotherms of the KIT-6 samples prepared at different aging temperatures and aging times are classified as Type IV (Figure 8). It can be seen in the Figure 8

that all samples exhibit hysteresis loop at pressure ranges of P/P^0=0.5-0.8. The H1 type hysteresis loop of the samples is related with the well-ordered three-dimensional mesopore networks of KIT-6 material [35,36]. When the aging time increased from 24 hours to 72 hours, there was no significant change in the isotherm and hysteresis patterns of the samples. However, it is noteworthy that there is some shift in the isotherm and changes in the pore properties such as; pore diameter, pore volume, BET surface area, etc.
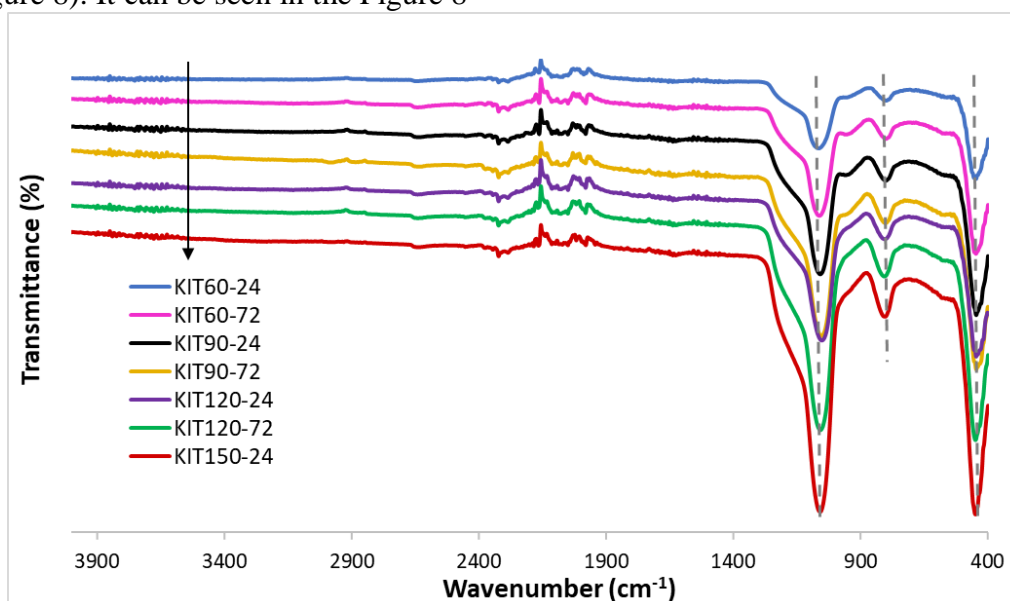
Figure 7. ATR/FT-IR spectrum of KIT-6 materials prepared at different hydrothermal treatment temperatures and at different aging times

If the temperature effect is compared for the same aging times, it is seen that at lower temperatures (especially at 60°C), the hysteresis loop shifted to the left side and the adsorbed volume decreased. The pore diameter (4.2 nm), pore volume (0.67 cm^3/g) and BET surface area (665 m^2/g) values of this sample (KIT60-24) were found to be lowest at the end of 24 h aging as compared with the other studied samples (Table 2).

It was concluded that 60°C temperature is not sufficient to obtain KIT-6 material having good mesopore structure. When the temperature raised to the 120°C, the hysteresis loop shifts to the right side and become narrower. This is the indication of the highly uniform pore structure. Interestingly, in the example of KIT150-24, it has been determined that the cubic parameter, pore volume and pore diameter are significantly increased, therefore the wall thickness and BET

surface area are also decreased. It was determined that this may be due to the deterioration in uniform mesopores of the materials because of the high synthesis temperature. If the aging time effect is compared at different temperatures it is seen that increasing aging time has positive effect on the structural properties up to 90°C. However, if the aging time increases from 24 h to 72 h at higher temperatures (>90°C), the pore size distribution becomes broader (Figure 9), pore volume and pore diameter increases thus the wall thickness and BET surface area decreases. It has been determined from these results that at elevated temperatures (120°C) long aging times negatively affect the structural properties of the mesoporous KIT-6 structure.

To determine the morphological changes in the samples, SEM analysis were performed for

KIT90-24 and KIT120-24 samples (Figure 10). Although there is not much difference between 90 ºC and 120 ºC, it is seen that there is a significant change in the morphological structure. As the hydrothermal temperature increased to 120 ºC, the rigid structure of the KIT-6 transformed into a flower-like structure with smaller particles. From the SEM images, it can be evaluated that the KIT120-24 sample has a higher pore volume and pore diameter. These results were also supported by N_2 adsorption-desorption analysis (Table 2).
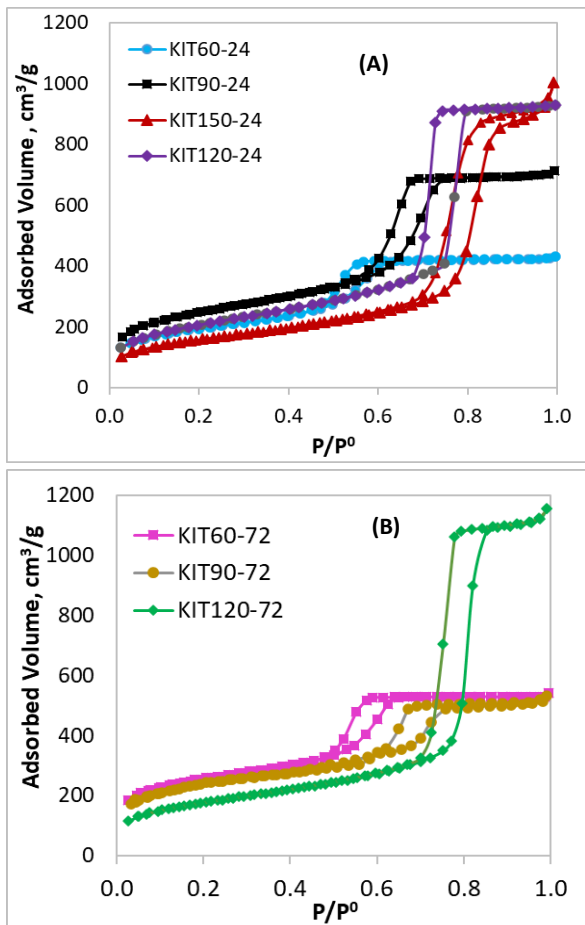
Figure 8. N_2 adsorption-desorption isotherms of KIT-6 materials prepared at different temperatures and at different aging times (A) 24 h   (B) 72 h
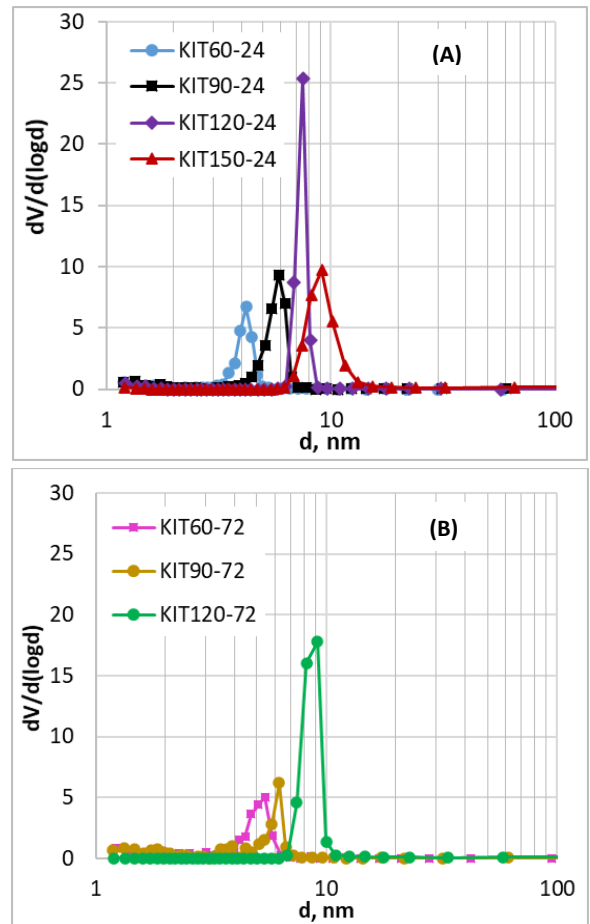
Figure 9. The pore size distribution of KIT-6 materials prepared at different temperatures and at different aging times (A) 24 h   (B) 72 h

At the end of characterization results, KIT120-24 material was determined as a suitable support material having narrow pore size distribution, high BET surface area (726 cm^3/g) and high pore volume (1.5 cm^3/g) among the other prepared samples. Results showed that this material can be used efficiently as sorbent material in many gas/liquid adsorption studies and catalyst support material in the heterogenous reaction processes.
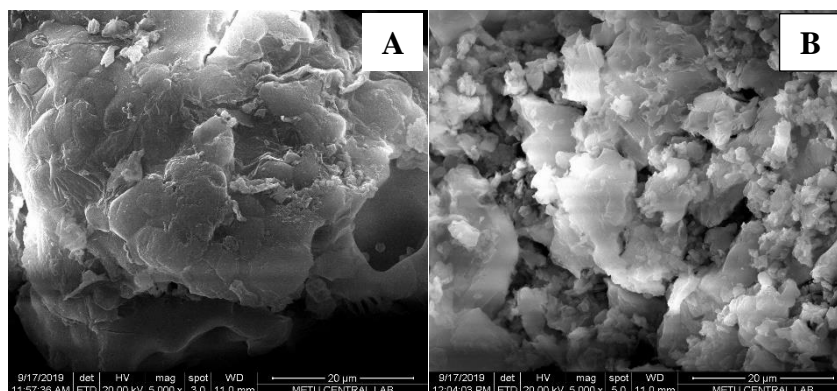
Figure 10. SEM images of (A) KIT90-24 and (B) KIT120-24 samples (x 5000)

Table 2. XRD and BET results of KIT-6 materials prepared at different hydrothermal treatment temperatures and at different aging times

Sample	Aging temperature °C	Aging time hour	d_{211}[a] nm	a_0[b] nm	Wall thickness[c] t, nm	Pore diameter[d] d_p, nm	Pore volume[d] V_p, cm^3/g	BET surface area[d] m^2/g
KIT60-24	60	24	7.24	17.7	4.7	4.2	0.67	665
KIT90-24	90		7.88	19.3	3.8	5.9	1.12	858
KIT120-24	120		8.49	20.8	2.9	7.5	1.5	726
KIT150-24	150		8.65	21.2	1.5	9.1	1.62	554
KIT60-72	60	72	7.61	18.6	4.5	4.8	0.88	817
KIT90-72	90		8.35	20.8	4.0	6.2	0.76	796
KIT120-72	120		8.49	20.8	2.2	8.2	1.97	621

[a] Interplanar spacing calculated from Bragg's Law

[b] Cubic parameter, $a_0 = d_{211} * \sqrt{h^2 + l^2 + k^2}$

[c] $t = a_0/2 - d_p$

[d] Obtained from BJH desorption data

4. CONCLUSION

In this study, the combined effects of hydrothermal treatment temperature and aging time on the structural properties of ordered mesoporous KIT-6 material were investigated. Characterization results confirmed that the temperature and aging time are the two important parameters that effect the crystal and pore structure of the material. The experiments performed at 90°C revealed that aging time positively affect the formation of ordered mesoporous structure and regular pore structure occurs after 18 hours aging time. In addition, it was concluded that long hydrothermal treatment duration favors the pore enlargement. Highly uniform mesoporous KIT-6 sample having high crystallinity, narrow pore size distribution, high BET surface area (726 cm^3/g) and high pore volume (1.5 cm^3/g) was prepared at 120°C with an aging time of 24h. However, it was reported that 60°C is not a suitable temperature to obtain KIT-6 sample having good mesopore structure and the deterioration of uniform crystal structure was observed at 150°C. The experiments conducted at different aging times showed that at elevated temperatures long aging times negatively affect the structural properties of the mesoporous KIT-6 structure.

Acknowledgement

The Declaration of Conflict of Interest/ Common Interest

No conflict of interest or common interest has been declared by the author.

The Declaration of Ethics Committee Approval

The author declares that this document does not require an ethics committee approval or any special permission.

The Declaration of Research and Publication Ethics

The author of the paper declare that they comply with the scientific, ethical and quotation rules of SAUJS in all processes of the paper and that they do not make any falsification on the data collected. In addition, they declare that Sakarya University Journal of Science and its editorial board have no responsibility for any ethical violations that may be encountered, and that this study has not been evaluated in any academic publication environment other than Sakarya University Journal of Science.

REFERENCES

[1] K.S.V. Sing, D.H. Everett, R.A.W. Haul, L. Moscou, R.A. Pierotti, J. Rououerol, and T. Siemieniewska, "Reporting physisorption data for gas/solid systems with special reference to the determination of surface area and porosity," Pure &Applied Chemistry, vol. 57, no. 4, pp. 603-619, 1985.

[2] A.M. Basso, B.P. Nicola, K. Bernardo-Gusmao, and S.B.C. Pergher, "Tunable effect of the calcination of the silanol groups of KIT-6 and SBA-15 Mesoporous Material," Applied Sciences, vol. 10, pp. 970-986, 2020.

[3] F. Hoffmann, M. Cornelius, J. Morell, and M. Froeba, "Silica-Based mesoporous organic–inorganic hybrid materials," Angewandte Chemie International Edition, vol. 45, pp. 3216–3251, 2006.

[4] D.E. Boldrini, S. Angeletti, P.M. Cervellini, and D.M. Reinoso, "Valorization of natural sediment," ACS Sustainable Chemical Engineering, vol. 7, pp. 4684−4691, 2019.

[5] D. Zhao, J. Feng, Q. Huo, N. Melosh, G.H. Fredrickson, B.F. Chmelka, and G.D. Stucky, "Triblock copolymer syntheses of mesoporous silica with periodic 50 to 300 angstrom pores," Science, vol. 279, no. 5350, pp. 548-552, 1998.

[6] R.A. Sacramento, O.M.S. Cysneiros, B.J.B Silva, and A.O.S. Silva, "Synthesis and characterization of mesoporous materials with SBA and MCM structure types," Cerâmica, vol. 65, pp. 585-591, 2019.

[7] B. Li, X. Luo, J. Huang, X. Wang, and Z. Liang, "One-pot synthesis of ordered mesoporous Cu-KIT-6 and its improved catalytic behavior for the epoxidation of styrene: Effects of the pH value of the initial gel," Chinese Journal of Catalysis, vol. 38, pp. 518–528, 2017.

[8] W. Wang, R. Qi, W. Shan, X. Wang, Q. Jia, J. Zhao, C. Zhang, and H. Ru, "Synthesis of KIT-6 type mesoporous silicas with tunable pore sizes, wall thickness and particle sizes via the partitioned cooperative self-assembly process," Microporous and Mesoporous Materials, vol. 194, pp. 167–173, 2014.

[9] L. Xu, C. Wang, and J. Guan, "Preparation of acid-base bifunctional mesoporous KIT-6 (KIT: Korea Advanced Institute of Science and Technology) and its catalytic performance in Knoevenagel reaction," Journal of Solid State Chemistry, vol. 213, pp. 250-255, 2014.

[10] F. Kleitz, S.H. Choi, and R. Ryoo, "Cubic Ia3d large mesoporous silica: synthesis and replication to platinum nanowires, carbon nanorods and carbon nanotubes," The Royal Society of Chemistry, pp. 2136–2137, 2003.

[11] R. Kishor, and A.K. Ghoshal, "APTES grafted ordered mesoporous silica KIT-6 for CO_2 adsorption," Chemical Engineering Journal, vol. 262, pp. 882–890, 2015.

[12] Q. Liu, J. Li, Z. Zhao, M. Gao, L. Kong, J. Liu and Y. Wei, "Design, synthesis and

catalytic performance of vanadium-incorporated mesoporous silica KIT-6 catalysts for the oxidative dehydrogenation of propane to propylene," Catalysis Science & Technology, vol. 6, pp. 5927-5941, 2016.

[13] F. He, J. Luo, and S. Liu, "Novel metal loaded KIT-6 catalysts and their applications in the catalytic combustion of chlorobenzene," Chemical Engineering Journal, vol. 294, pp. 362–370, 2016.

[14] D. Saikia, T.H. Wang, C.J. Chou, J. Fang, L.D. Tsai and H.M. Kao, "A comparative study of ordered mesoporous carbons with different pore structures as anode materials for lithium-ion batteries," RSC Advances, vol. 5, pp. 42922–42930, 2015.

[15] H. Tang, Y. Ren, S. Wei and G. Liu, "Preparation of 3D ordered mesoporous anatase TiO_2 and their photocatalytic activity," Rare Metals, vol. 38, pp. 453–458, 2019.

[16] S.N. Talapaneni, K. Ramadass, S.J. Ruban, M. Benzigar, K.S. Lakhi, J.H. Yang, U. Ravon, K. Albahily and A. Vinu, "3D cubic mesoporous C_3N_4 with tunable pore diameters derived from KIT-6 and their application in base catalyzed Knoevenagel reaction," Catalysis Today, vol. 324, pp. 33–38, 2019.

[17] M. Dutt, A. Kaushik, M. Tomar, V. Gupta and V. Singh, "Synthesis of mesoporous α-Fe_2O_3 nanostructures via nanocasting using MCM-41 and KIT-6 as hard templates for sensing volatile organic compounds (VOCs)," Journal of Porous Materials, vol. 27, pp. 285–294, 2020.

[18] Y. Shimasaki, M. Kitahara, M. Shoji, A. Shimojima and H. Wada, "Preparation of ordered mesoporous Au using double gyroid mesoporous silica KIT-6 via a seed-mediated growth process," Chemistry, An Asian Journal, vol. 13, no. 24, pp. 3935–3941, 2018.

[19] B. Bai, Q. Qiao, Y. Li, Y. Peng and J. Li, "Effect of pore size in mesoporous MnO_2 prepared by KIT-6 aged at different temperatures on ethanol catalytic oxidation," Chinese Journal of Catalysis, vol. 39, pp. 630–638, 2018.

[20] Y. Kim, J. Yoon, G.O. Park, S.B. Park, H. Kim, J.M. Kim and W.S. Yoon, "Enhancement of the interfacial reaction on mesoporous RuO_2 for next generation Li batteries," Journal of Power Sources, vol. 396, pp. 749–753, 2018.

[21] M. Taghizadeh, H. Akhoundzadeh and A. Rezayan, "Excellent catalytic performance of 3D-mesoporous KIT-6 supported Cu and Ce nanoparticles in methanol steam reforming," International Journal of Hydrogen Energy, vol. 43, pp. 10926–10937, 2018.

[22] S. Chirra, S. Siliveri, A. Kumar, A. Srinath, G. Sripal and R. Gujjula, "KIT-6: synthesis of a novel three-dimensional mesoporous catalyst and studies on its enhanced catalytic applications," Journal of Porous Materials, vol. 26, pp. 1667–1677, 2019.

[23] J.P. Ruelas-Leyva, A. Mata-Martinez, A. Talavera-López, S.A. Gómez, S.A. Jimenez-Lam and G.A. Fuentes, "Dehydrogenation of propane to propylene with highly stable catalysts of pt-sn supported over mesoporous silica KIT-6," International Journal of Chemical Reactor Engineering, vol. 16, no. 10, pp. 1-9, 2018.

[24] A. Mata-Martinez, S.A. Jimenez-Lam, A. Talavera-López, S.A. Gómez, G.A. Fuentes, L.A. Picos-Corrales, J.C. Piña-Victoria, J.P. Ruelas-Leyva, "The effect of Sn content in a Pt/KIT-6 catalyst over its performance in the dehydrogenation of propane," International Journal of Chemical Reactor Engineering, vol. 16, no. 10, pp. 1-9, 2018.

[25] H. Sun, C.M. Parlett, M.A. Isaacs, X. Liu, G. Adwek, J. Wang, B. Shen, J. Huang and J. Wu, "Development of Ca/KIT-6 adsorbents for high temperature CO_2 capture," Fuel, vol. 235, pp. 1070-1076, 2019.

[26] D. Xia, Y. Chen, C. Li, C. Liu and G. Zhou, "Carbon dioxide reforming of methane to syngas over ordered mesoporous Ni/KIT-6 catalysts," International Journal of Hydrogen Energy, vol. 43, no. 45, pp. 20488-20499, 2018.

[27] H. Liu, S. Xu, G. Zhou, K. Xiong, Z. Jiao, S. Wang, "CO_2 hydrogenation to methane over Co/KIT-6 catalysts: Effect of Co content," Fuel, vol. 217, pp. 570-576, 2018.

[28] J.M. Cho, G.Y. Han, H-K. Jeong, H-S. Roh and J.W. Bae, "Effects of ordered

mesoporous bimodal structures of Fe/KIT-6 for CO hydrogenation activity to hydrocarbons," Chemical Engineering Journal, vol. 354, pp. 197-207, 2018.

[29] C. Tuncer, "Hydrothermal synthesis and sol-gel methods for CdS particle production in different morphologies and their use in wastewater applications," Sakarya University Journal of Science, vol. 22, no. 3, pp. 888-897, 2018.

[30] F.R.D. Fernandes, F.G.H.S. Pinto, E.L.F. Lima, L.D. Souza, V.P.S. Caldeira and A.G.D. Santos, "Influence of synthesis parameters in obtaining KIT-6 mesoporous material," Applied Sciences, vol. 8, pp. 725-742, 2018.

[31] M.M. Ayad, N.A. Salahuddin, A.A. El-nasr and N.L. Torad, "Amine-functionalized mesoporous silica KIT-6 as a controlled release drug delivery carrier," Microporous Mesoporous Materials, vol. 229, pp. 166–177, 2016.

[32] G.G. Karthikeyan, G. Boopathi and A. Pandurangan, "Facile synthesis of mesoporous carbon spheres using 3D cubic Fe-KIT-6 by CVD technique for the application of active electrode materials in supercapacitors," ACS Omega, vol. 3, pp. 16658–16671, 2018.

[33] R. Merkache, I. Fechete, M. Maamache, M. Bernard, P. Turek, K. Al-dalama and F. Garin, "3D ordered mesoporous Fe-KIT-6 catalysts for methylcyclopentane (MCP) conversion and carbon dioxide (CO_2) hydrogenation for energy and environmental applications," Applied Catalysis A : General, vol. 504, pp. 672–681, 2015.

[34] J. Xu, Y. Hong, M.J. Cheng, B. Xue and Y.X. Li, "Vanadyl acetylacetonate grafted on ordered mesoporous silica KIT-6 and its enhanced catalytic performance for direct hydroxylation of benzene to phenol," Microporous and Mesoporous Materials, vol. 285, pp. 223–230, 2019.

[35] K.A. Cychosz and M. Thommes, "Progress in the physisorption characterization of nanoporous gas storage materials," Engineering, vol. 4, pp. 559–566, 2018.

[36] T.N. Phan, M.K. Gong, R. Thangavel, Y.S. Lee and C.H. Ko, "Enhanced electrochemical performance for EDLC using ordered mesoporous carbons (CMK-3 and CMK-8): Role of mesopores and mesopore structures," Journal of Alloys Compounds, vol. 780, pp. 90–97, 2019.

[37] R. Kishor and A.K. Ghoshal, "Understanding the hydrothermal, thermal, mechanical and hydrolytic stability of mesoporous KIT-6: A comprehensive study," Microporous and Mesoporous Materials, vol. 242, pp. 127–135, 2017.

[38] A. H. Elhaj Yousif, O. Y. Omer Alhussein and M. S. Ali Eltoum, "Characterization of hydrolyzed products of tera ethoxy silane prepared by sol-gel method," International Journal of Multidisciplinary Sciences and Engineering, vol. 6, pp. 19-24, 2015.

[39] X. Shen, Y. Zhai, Y. Sun and H. Gu, "Preparation of monodisperse spherical SiO_2 by microwave hydrothermal method and kinetics of dehydrated hydroxyl," Journal of Material Science and Technology, vol. 26, no. 8, pp. 711-714, 2010.

Title: Flora of Acarlar Longoz (Floodplain) (Sakarya) and its Surroundings

Authors: Didem KARADUMAN, Mehmet SAĞIROĞLU

FLORA OF ACARLAR LONGOZ (FLOODPLAIN) (SAKARYA) AND ITS SURROUNDINGS

Didem KARADUMAN[*1], Mehmet SAĞIROĞLU[1]

Abstract

In this study, one of the Turkey's Wetlands of International Importance Grounds, declared as Wildlife Protection Area and Grade 1 Natural Protected Area called Acar Longoz (Sakarya) and its surroundings' floristic features were studied. The study area is on the A3 square according to Davis's Grid Frame System. As a result of the studies carried out in the Acarlar floodplain, there were 360 genera, 654 species and subspecies taxa belonging to 97 families. Of the taxa identified in the area, 8 belong to Pteridophyta, 646 to Spermatophyta, 5 of which belong to Gymnospermae and 641 to Angiospermae subdivision. The endemism rate of the area was determined to be 2,137 % with 14 taxa. The number of taxa belonging to the European-Siberian phytogeographical region is in the first place with 21.47%. Additional information was also given about the remarkable plants in the research area.

Keywords: Acarlar, flora, floodplain, Sakarya, Turkey

---

[*] Corresponding Author: didemsinem@gmail.com

[1] Sakarya University, Faculty of Science and Letters, Sakarya, Turkey, ORCID: https://orcid.org/ 0000-0003-2742-4885, E-mail: msagiroglu@sakarya.edu.tr, ORCID: https://orcid.org/ 0000-0001-8654-3361

1. INTRODUCTION

The word longoz (floodplain) means flooded forest and they are riverside forests that contain woody and herbaceous climbing plants and are considered to be the equivalent of the tropical belt Mangrove forests.

Our field of study, Acarlar Longoz, is in the northeast of the Marmara region, in the province of Sakarya, on the Black Sea border, between Kaynarca and Karasu districts.

The narrowest part of the floodplain, which is approximately 14 km in length, is 300 m in the dry period, while the widest part can reach 2,5 km in width during rainy periods.

It is possible to explain the formation of Acarlar Longoz as the obstruction of the front of the streams by the coastal dunes in time, thus forming a ponding behind. Acarlar Longoz also has the character of a lagoon [1]. Small streams in the southern lands, which reach a height of approximately 100 m, are the main water sources of the floodplain lake, and the excess of the lake water flows into the Sakarya River in the east.

Acarlar Floodplain Lake and its surroundings are very difficult to pass through as it is covered with dense forest formation. Its parts outside the forest area are used by the people living in the surrounding villages as settlement and agricultural land.
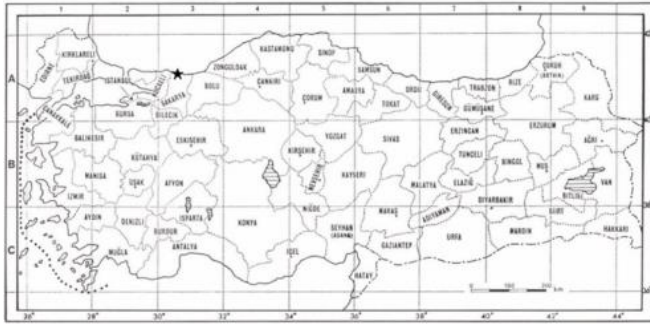
Figure 1 The Square that has Study Area According to Davis' Grid System

The northern part of the area is completely covered with coastal sand dunes. Alluvial coastal swamps and colluvial soils are located in the north of the area. Acarlar Lake and its coastal surroundings consist of hydromorphic alluvial soils and alluvial soils. As one moves west and south from the lake, there is densely lime-free brown forest soils, though less colluvial soils. In the east, there are alluvial soils and lime-free brown forest soil.

The study area stays in the Black Sea region and it has a rainy Mediterranean bioclimate floor feature [2].

Acarlar Longoz is located on one of the two important migration routes passing through Anatolia and it is one of the Turkey's Wetlands of International Importance Grounds. It was declared as a Wildlife Development Area in 1976 and as a First Degree Natural Protected Area in 1998 and was taken under absolute protection.

2. MATERIAL AND METHODS

We conducted studies in Acarlar Longoz and its surroundings, which is the current research area, between 2011-2020. 38 field studies were carried out at 29 stations in different vegetation periods and 1200 plant samples were collected during the field studies. Plant samples were collected with their flowers, fruits, roots and etc as much as possible, that are very crucial in the determination and diagnosis processes, and many of them were photographed in the field and pressed in accordance with the rules and turned into herbarium material. Flora of Turkey and East Aegean Islands [3], [4], [5], is used during diagnosis and floristic list is based on the Turkey Plant List [6] [7]. In addition, Bolu'nun Endemik ve Nadir Bitkileri [8], Bolu Abant İzzet Baysal Üniversitesi Kampüs Florası [9] and Petaloid Monocotyledonous Flora of Bolu Province, Including Annotations on Critical Petaloid Geophytes of Turkey [10] have been used in plant identification. Plant names and author names have been checked from the IPNI and The Plant List web site. [11], [12].

While the list of plants is given, first the family, then the species and, if any, subspecies taxa are written with their authors. While the sample features are given, information is give in the following order, the station number, date, collector number, wide distribution,

phytogeographic region, life form and finally whether it is endemic.

3. ABBREVIATIONS

The abbreviations used in the article are; **%:** percent, **':** minute, **°:** hour, **":** Second, **all.:** all others, **Chmp.:** Chamaeophyte, **Cltr.:** Culture, **Crp.:** Criptophyte, **D.K.:** Didem Karaduman, **E.:** East, **E.S.E.:** European-Siberian element, **Hmcp.:** hemicryptophyte, **Ir.-Tur El.:** Iran-Turan element, **km.:** Kilometer, **M.E.:** Mediterranean element, **m:** meter, **N.:** North, **Phnp.:** Phanerophyte, **sp.:** species, **subsp.:** subspecies, **Trp.:** therophytes, **W.s.:** Widespread, **var.:** variety, **V.p.:** vascular parasite

4. FINDINGS

4.1. Stations

Figure 2 General view of the area and working stations

The stations where we have collected the plant samples during the current study are; **(Station number):** Settlement, Latitude-longitude, Habitat. **(1);** Ortaköy, 41°07'43,71"-30°23'54,14", Lakeside, swamp, agricultural, forest land, **(2);** Başoğlu, 41°08'47,53"-30°23'04,68", Roadside, under forest, **(3);** Başoğlu, 41°08'28,36"-30°23'02,85", Woodland, **(4);** Başoğlu, 41°08'53,25"-30°25'20,92", Near the settlement area, in the field, **(5);** Başoğlu, 41°08'51,94"-30°23'56,99", Under forest ,field edge, roadside, **(6);** Denizköy, 41°07'06,70"-30°33'02,76", Lakeside, cultivated area, **(7);** İhsaniye, 41° 07'28,25"-30°35'70,04", Dune, lakeside, **(8);** Ihsaniye, 41°07'37,47"-30°37'08,25", Settlement area, dune, lakeside, cultivated area, **(9);**

Ortaköy, 41°07'53,37"-30°23'23,41" Forest, swamp, open land, field, **(10);** Ortaköy, 41°7'29.30"-30°23'22.22", Forest, cultivated and open fields**, (11);** Başoğlu, 41°09'59,12"-30°22'40,06", Moving dune, lakeside, village roadside, **(12);** Başoğlu, 41°09'44,97"-30°23'24,19", Dune, lakeside, under forest, **(13);** Ihsaniye, 41°07'14,62"-30°36'26,10", Dune, field, roadside cultivated, wetland, scrub areas, **(14);** Denizköy, 41°07'43,99"-30°31'32,81", Forest edge, dune**, (15);** Camitepe, 41°08'16,59"-30°27'22,37", Dune, lakeside**, (16);** Camitepe, 41°08'05,24"-30°26'24,32", Forest edge, settlement area, water edge, field edge, **(17);** Üçoluk, 41°06'42,24"-30°30'55,44", Lakeside, swamp, agricultural land, forestland, **(18);** Ortaköy, 41°7'9.35"-30°22'20.87", Settlement, Roadside, **(19);** Başoğlu, 41°08'54,34"-30°23'19,25", Settlement area, under forest, 41°08'54,34"-30°23'19,25", **(20);** Üçoluk, 41°06'09,92"-30°29'50,73", Roadside, open land, forest, **(21);** Üçoluk, 41°06'31,15"-30°31'40,04", Quercus sp. forest, 41°06'31,15"-30°31'40,04", **(22);** Karamüezzinler, 41°6'51.92"-30°32'16.28", Settlement area, cultivated areas, **(23);** Camitepe41°07'46,01"-30°28'11,32", Settlement area, cultivated areas **(24);** Denizköy, 41°07'25,07"-30°31'53,12", Roadside, **(25);** Ihsaniye, 41°06'19,13"-30°36'58,29", Forest, **(26);** Tuzla, 41°4'43.78"-30°38'34.01", Settlement area, roadside, **(27);** Turnalı, 41°7'21.01"- 30°23'51.08" Lakeside, lake, cultivated areas, **(28);** Tuzla, 41°4'0.24"-30°37'9.66", Stone pit, **(29);** Camitepe, 41°8'9.92"-30°30'12.22", Dune.

The workstations cover an area of 500 m. in radius in the center of the given coordinates.

4.2. Plant list
PTERIDOPHYTA
EQUISETIDAE
EQUISETACEAE
Equisetum arvense L., (1), 20.04.2012, D.K.1126, Crp.
Equisetum telmateia Ehrh., (14), 18.06.2018, D.K.1898, Crp.
POLYPODIIAE
ASPLENIACEAE
Asplenium scolopendrium L., (25), 18.06.2018, D.K.1900, Crp.
CYSTOPTERIDACEAE

Cystopteris fragilis (L.) Bernh., (7), 18.06.2018, D.K.1899, Crp.

DENNSTAEDTIACEAE

Pteridium aquilinum (L.) Kuhn, (6), 22.07.2012, D.K.1529, W.s., Crp.

THELYPTERIDACEAE

Thelypteris palustris (A.Gray) Schott, (7), 18.06.2018, D.K.1901, Crp.

POLYPODIACEAE

Polypodium vulgare L. subs. *vulgare,* (13), 07.04.2013, D.K.1763, Hmcp.

SALVINIACEAE

Salvinia natans (L.) All., (1), 02.09.2012, D.K.1611, Crp.

MAGNOLIOPHYTA

PINOPHYTINA

PINIDAE

CUPRESSACEAE

Cupressus sempervirens L., (15), 27.05.2012, D.K.1281, M.E., Phnp., Cltr.

Juniperus oxycedrus L. subsp. *oxycedrus*, (11), D.K.2077C, 05.08.2019, Phnp.,

PINACEAE

Pinus brutia Ten. var. *brutia*, (12), 08.04.2012, D.K.1070, M.E., Phnp.

Pinus pinaster Aiton subsp. *pinaster*, (12), 30.08.2014, D.K.1841, Phnp., Cltr.

Pinus sylvestris L., (6), 06.05.2012, D.K.1235, Phnp.

MAGNOLIOPHYTINA

MAGNOLIIDAE

ADOXACEAE

Sambucus ebulus L., (19), 16.09.2012, D.K.1655, E.S.E., Hmcp.

Sambucus nigra L., (19), 30.08.2014, D.K.1873, E.S.E., Hmcp.

Viburnum opulus L., (6), 29.04.2012, D.K.1199, E.S.E., Phnp.

ALISMATACEAE

Alisma lanceolatum With., (7), 27.6.2019,D.K.2036, Crp.

Alisma plantago-aquatica L. subsp. *plantago-aquatica*, (1), 08.07.2012, D.K.1528, E.S.E., Crp.

Sagittaria sagittifolia L., (17), 10.06.2012, D.K.1424, Crp.

AMARANTHACEAE

Amaranthus cruentus L., (9), 16.09.2012, D.K.1630, Trp.

Amaranthus retroflexus L., (22),12.10.2019, D.K.2082, Hmcp.

Atriplex hastata L., (6), 26.08.2012, D.K.1560, Hmcp.

Beta trigyna Waldst. & Kit., (9), 18.06.2018, D.K.1877, Chmp.

Chenopodium album L. subsp. *album* var. *album*, (21), 02.09.2012, D.K.1612, Trp.

Chenopodium glaucum L., (12), 25.09.2011, D.K.1008, E.S.E., Trp.

Chenopodium multifidum L., (11), 02.09.2012, D.K.1603, Hmcp.

Salsola soda L., (15), 02.07.2012, D.K.1465, Trp.

Salsola tragus subsp. *tragus*, (15), 02.09.2012, D.K.1605, Trp.

AMARYLLIDACEAE

Allium ampeloprasum L., (13), 15.06.2012, M.Sağıroğlu 3993. Widesp. [13]

Allium pallens L. subsp. *pallens,* (26), 06.2012, M.Sağıroğlu 3848. Medit. [13]

Allium scorodoprasum L. subsp. *rotundum* (L.) Stearn, (22), 10.06.2012, D.K.1414, M.E.

Allium sphaerocephalon L. subsp. *spharocephalon*,(23), 21.05.2015, D.K.1834, E.S.E., Crp.

Galanthus elwesii Hooker fil. var. *elwesii*, (8), 10.05.2013, D.K.1835, M.E.., Crp.

Galanthus gracilis Čelak., (11), 10.01.2013, D.K. 1675, M.E., Crp.

Galanthus nivalis L. subsp. *nivalis*, (12), 10.03.2013, D.K.1710, E.S.E., Crp.

Galanthus plicatus Bieb. subsp. *byzantinus* (Baker) D. A. Webb., (11), 10.05.2013, D.K.1836, E.S.E., Crp., **End.**

Leucojum aestivum L. subsp. *aestivum*, (6), 08.04.2012, D.K.1085, E.S.E.

Narcissus pseudonarcissus L., (17), 14.03.2020, D.K 2099, Crp.

Pancratium maritimum L., (8), 08.07.2012, D.K. 1527, M.E., Crp.

Sternbergia lutea (L.) Ker Gawl. ex Spreng., (4), 21.05.2015, D.K.1867, Crp.

APIACEAE

Angelica sylvestris L. var. *sylvestris* L., (16), 30.08.2014, D.K.1847, E.S.E., Hmcp.

Apium nodiflorum (L.) Lag., (9), 18.06.2018, D.K.1885, Hmcp.

Bupleurum intermedium Poiret, (6), 27.05.2012, D.K.1264, Trp.

Chaerophyllum aromaticum L., (18), 04.08.2019, D.K.2077B, Hmcp.

Chaerophyllum byzantinum Boiss., (18), 12.10.2019, D.K.2088, E.S.E., Hmcp.

Cnidium silaifolium (Jacq.) Simonk. subsp. *orientale* (Boiss.) Tutin, (20), 30.08.2014, D.K.1846, W.s., Hmcp.

Conium maculatum L., (20), 26.07.2012, D.K.1566, Hmcp.

Crithmum maritimum L., (11), 18.06.2018, D.K.1907, Hmcp.

Daucus carota L., (6), 22.07.2012, D.K.1532, Hmcp.

Daucus littoralis Sibth. & Sm., (4), 30.08.2014, D.K.1848, M.E., Hmcp.

Eryngium creticum Lam., (18), D.K.2065, 04.08.2019, Trp.

Eryngium maritimum L., (15), 26.07.2012, D.K.1565, Trp.

Lagoecia cuminoides L., (6), 25.09.2011, D.K.1015, M.E., Trp.

Oenanthe fistulosa L., (6), 27.05.2012, D.K.1239B, Hmcp.

Oenanthe pimpinelloides L., (1), 27.05.2012, D.K.1240, Chmp.

Oenanthe silaifolia Bieb., (6), 06.05.2012, D.K.1233, Chmp.

Orlaya grandiflora (L.) Hoffm. (10), 18.06.2019. D.K.1996,Trp.

Peucedanum longifolium Waldst. & Kit., (23), 27.05.2012, D.K.1323, E.S.E., Chmp.

Peucedanum obtusifolium Sibth. & Sm., (11), 18.06.2018, D.K.1908, Chmp.

Pimpinella anisum L., (6), 06.05.2012, D.K.1221, Trp.

Pseudorlaya pumila (L.) Grande, (11), 18.06.2018, D.K.1909, M.E., Hmcp.

Sium sisarum (M.Bieb.) Thell. var. *lancifolium*, (16), 18.06.2018, D.K.1876, Crp.

Torilis arvensis (Huds.) Link subsp. *arvensis*, (13), 16.09.2012, D.K.1653, Trp.

Torilis japonica (Houtt.) DC. (21), 14.07.2019, D.K.2041B, Trp.

APOCYNACEAE

Cionura erecta (L.) Griseb., (8), 27.05.2012, D.K.1364, M.E., Hmcp.

Cynanchum acutum L. subsp. *acutum*, (1), 04.08.2019, D.K.2066, W.s., Chmp.

Periploca graeca L. var. *vestita* Rohlena, (3), 02.09.2012, D.K.1570, M.E., Chmp.

Vinca major L. subsp. *majör*, (17), 10.04.2014, D.K.1829, M.E., Chmp., Cltr.

ARACEAE

Arum italicum Miller (10), 14.5.19, D.K.1920B, Hmcp.

Arum maculatum L., (3), D.K.1928B, 14.5.2019, Hmcp.

Lemna gibba L., (1), 02.09.2012, D.K.1573, W.s., Crp.

Spirodela polyrhiza (L.) Schleiden, (6), 08.07.2012, D.K.1509, Crp.

ARALIACEAE

Hedera colchica (K.Koch) K.Koch, (1), 29.04.2012, D.K.1125, E.S.E., Phnp.

Hedera helix L., (8), 05.05.2013, D.K.1811, Phnp.

ARISTOLOCHIACEAE

Aristolochia pallida Willd., (1), 30.08.2014, D.K.1863, Hmcp.

ASPARAGACEAE

Asparagus acutifolius L., (13), 07.04.2013, D.K.1762, M.E., Crp.

Asparagus aphyllus L. subsp. *orientalis* (Baker) P.H. Davis, (5), 27.05.2012, D.K.1289, M.E., Crp.

Muscari armeniacum Leichtlin ex Bakerin Gard., (6), 29.04.2012, D.K.1114, W.s., Crp.

Muscari comosum (L.) Mill., (15), 07.04.2013, D.K.1734, M.E., Crp.

Muscari neglectum Guss. ex Ten., (8), 08.04.2012, D.K.1086, W.s., Crp.

Muscari tenuiflorum Tausch, (7), 10.4.2014, D.K.1827B, Crp.

Ornithogalum montanum Cirillo. (28), 05.04.2017, M.Sağıroğlu 5740, Medit. [13]

Ornithogalum sigmoideum Freyn & Sint., (6), 26.03.2012, D.K.1028, E.S.E., Crp.

Ornithogalum wiedemannii Boiss, (6), 10.03.2013, D.K.1690, Crp.

Prospero autumnale (L.) Speta, (6), 16.09.2012, D.K.1657, M.E., Crp.

Ruscus aculeatus L. var. *aculeatus*, (3), 26.03.2012, D.K.1034, Crp.

Ruscus hypoglossum L., (2), 21.05.2015, D.K.1865, E.S.E., Crp.

Scilla bifolia L., (6), 08.04.2012, D.K.1087, M.E., Crp.

Scilla bithynica Boiss., (6), 29.04.2012, D.K.1180, E.S.E., Crp.

ASTERACEAE

Achillea maritima subsp. *maritima* (L.) Ehrend. & Y.P.Guo, (15), 26.08.2012, D.K.1568, M.E., Trp.

Anthemis arvensis L., (17), 27.05.2012, D.K.1296, E.S.E., Trp.

Anthemis cretica L. subsp. *pontica* (Willd.) Grierson, (6), 16.09.2012, D.K.1622, Hmcp.

Anthemis cotula L., (22), 08.07.2012, D.K.1524B, W.s., Hmcp.

Arctium minus (Hill) Bernh. (10), 14.7.2019., D.K.2054, E.S.E., Hmcp.

Artemisia vulgaris L., (13), 18.06.2018, D.K.1894, Chmp.

Asteriscus spinosus (L.) Sch.Bip., (14), 30.08.2014, D.K.1851, M.E., Trp.

Bellis annua L., (6), 10.01.2013, D.K.1687, M.E.., Trp.

Bellis perennis L., (22), 29.04.2012, D.K.1121, E.S.E., Hmcp.

Bellis sylvestris Cirillo, (5), 29.04.2012, D.K.1128, M.E., Hmcp.

Bidens tripartita L., (6), 25.09.2011, D.K.1009, Trp.

Bombycilaena discolor (Pers.) Lainz, (12), 10.04.2014, D.K.1826, M.E., Trp.

Carduus nutans L. subsp. *leiophyllus* (Petr.) Stoj. & Stef., (15), 08.07.2012, D.K.1520B, Hmcp.

Carduus pycnocephalus L. subsp. *albidus* (M.Bieb.) Kazmi, (4), 29.04.2012, D.K.1151, Trp.

Carduus pycnocephalus L. subsp. *arabicus* (Jacq. ex Murray) Nyman, (23), 10.06.2012, D.K.1422, M.E., Trp.

Carlina corymbosa L., (6), 02.09.2012, D.K.1584, M.E., Hmcp.

Carthamus lanatus L., (23), 08.07.2012, D.K.1519, W.s., Trp.

Centaurea iberica Trev. ex Sprengel, (15), 02.07.2012, D.K.1451, W.s.,Trp.

Centaurea kilaea Boiss., (15), 26.08.2012, D.K.1576, E.S.E., Hmcp., **End.**

Chondrilla juncea L., (4), 02.09.2012, D.K.1482, W.s., Hmcp.

Cichorium intybus L., (20), 16.09.2012, D.K.1640, W.s., Hmcp.

Cirsium arvense (L.) Scop., (21), 02.09.2012, D.K.1606, Hmcp.

Cirsium creticum (Lam.) d'Urv. subsp. *creticum,* (20), 27.05.2012, D.K.1363, M.E., Hmcp.

Cirsium hypoleucum DC, (5), 02.07.2012, D.K.1504, E.S.E.

Cirsium italicum (Savi) DC, (15), 16.09.2012, D.K.1638, M.E.., Hmcp.

Cirsium vulgare (Savi) Ten., (4), 02.09.2012, D.K.1600, Hmcp.

Conyza albida Willd. ex Spreng. (18), 4.8.2019, D.K. 2069B, Trp.

Conyza bonariensis (L.) Cronquist, (13), 07.04.2013, D.K.1760, Trp.

Conyza canadensis (L.) Cronquist, (16), 02.09.2012, D.K.1604, Trp.

Cota altissima (L.) J.Gay, (6), 21.05.2015, D.K.1567, W.s., Hmcp.

Cota austriaca (Jacq.) Sch. Bip., (9), 10.01.2013, D.K.1681, W.s., Hmcp.

Cota tinctoria (L.) J. Gay var. *tinctoria*, (17), 22.07.2012, D.K.1530, W.s., Hmcp.

Crepis reuterana Boiss. subsp. *reuterana.,* (22), 08.04.2012, D.K.1069, M.E., Hmcp.

Crepis sancta (L.) Babcock subsp. *obovata* (Boiss. & Noë) Babc., (6), 05.05.2013, D.K.1768, W.s., Trp.

Doronicum orientale Hoffm., (6), 26.03.2012, D.K.1040, Crp.

Eupatorium cannabinum L., (1), 21.05.2015, D.K.1853, E.S.E., Crp.

Glebionis segetum (L.) Fourr., (6), 21.05.2015, D.K.1286, M.E., Trp.

Hedypnois cretica (L.) Dum.-Cours., (6), 05.05.2013, D.K.1767, M.E., Hmcp.

Helianthus tuberosus L., (17), 30.08.2014, D.K.1850, Crp., Cltr.

Hypochoeris radicata L., (6), 05.05.2013, D.K.1774, E.S.E., Hmcp.

Inula germanica L., (18) 12.10.2019, D.K.2079A, E.S.E., Crp.

Jurinea kilaea Azn., (8), 08.07.2012, D.K.1574, E.S.E., Trp.

Lapsana communis L. subsp. *intermedia* (Bieb.) Hayek var. *intermedia*, (6), 10.06.2012, D.K.1379, W.s., Hmcp.

Petasites hybridus (L.) G.Gaertn., B.Mey. & Scherb., (1), 21.05.2015, D.K.1852, E.S.E.,Crp.

Pilosella x auriculoides (Láng) Arv.-Touv., (14), 02.09.2012, D.K.1620, Hmcp.

Pilosella x macrotricha (Boiss.) F.W.Schultz & Sch.Bip., (6), 02.09.2012, D.K.1660, W.s., Hmcp.

Pulicaria dysenterica (L.) Bernh. subsp. *dysenterica*, (9), 16.09.2012, D.K.1659, Crp.

Pulicaria odora (L.) Reichb., (23), 09.06.2013, D.K.1817, M.E., Trp.

Reichardia picroides (L.) Roth, (23), 16.09.2012, D.K.1663, M.E., Hmcp.

Scolymus hispanicus L. subsp. *hispanicus,* (15), 02.09.2012, D.K.1481, M.E., Chmp.

Senecio doria L. subsp. *umbrosus* (Waldst. & Kit.) Soó, (5), 16.09.2012, D.K.1649, E.S.E., Hmcp.

Senecio vulgaris L., (6), 08.04.2012, D.K.1061, Trp.

Silybum marianum (L.) Gaertn. subsp. *marianum*, (14), 02.07.2012, D.K.1479, M.E., Hmcp.

Sonchus arvensis L. subsp. *uliginosus* (M.Bieb.) Nyman, (8), 05.05.2013, D.K.1770, Hmcp.

Sonchus asper (L.) Hill subsp. *glaucescens* (Jordan) Ball, (6), 05.05.2013, D.K.1769, W.s., Hmcp.

Sonchus oleraceus L., (6), 05.05.2013, D.K.1814, Hmcp.

Taraxacum hellenicum Dahlst, (12), 05.05.2013, D.K.1744, M.E., Hmcp.

Taraxacum hybernum Stev, (2), 10.06.2012, D.K.1420, Hmcp.

Tragopogon pratensis L. subsp. *orientalis* (L.) Čelak., (9), 08.12.2018, D.K.1854, E.S.E.,

Tussilago farfara L., (12), 10.05.2013, D.K.1703, E.S.E., Crp.

Urospermum picroides (L.) Scop. ex F.W.Schmidt, (6), 23.06.2012, D.K.1408, M.E., Trp.

Xanthium orientale subsp. *italicum* (Moretti) Greuter, (3), 16.09.2012, D.K.1635, Trp.

Xanthium spinosum L., (20), 02.09.2012, D.K.1602, Trp.

Xanthium strumarium subsp. *strumarium* L., (22), 30.08.2014, D.K.1860, Trp.

BERBERIDACEAE

Berberis vulgaris L., (16), 16.09.2012, D.K.1643, Crp.

Epimedium pubigerum C.Morren & Decne, (6), 07.04.2013, D.K.1719, E.S.E., Crp.

BETULACEAE

Alnus glutinosa (L.) Gaertner. subsp. *glutinosa*, (16), 25.09.2011, D.K.1019, E.S.E., Phnp.

Carpinus betulus L., (9), 23.06.2012, D.K.1434, E.S.E., Phnp.

Carpinus orientalis Miller subsp. *orientalis,* (6), 26.03.2012, D.K.1043, Phnp.

Corylus avellana L. var. *avellana,* (6), D.K.1401A, İr.-Tur El., Phnp.

BORAGINACEAE

Anchusa leptophylla subsp. *leptophylla* Roem. & Schult. (10), D.K.2040B, 27.6.2019, Hmcp.

Anchusa officinalis L., (6), 27.05.2012, D.K.1486, E.S.E., Hmcp.

Cerinthe minor L. subsp. *auriculata* (Ten.) Domac, (20), 18.06.2018, D.K.1878, Hmcp.

Cynoglossum creticum Miller, (6), 06.05.2012, D.K.1219, Hmcp.

Echium plantagineum L., (9), 02.07.2012, D.K.1252, M.E., Hmcp.

Echium vulgare L., (6), 02.07.2012, D.K.1452, E.S.E., Hmcp.

Heliotropium europaeum L., (15), 30.08.2014, D.K.1485, Ir.-Tur El., Trp.

Heliotropium lasiocarpum Fisch. & C.A.Mey., (12), 04.08.2019, D.K.2069A, Ir.-Tur El., Chmp.

Myosotis alpestris F. W. Schmidt subsp. *alpestris*, (17), 29.04.2012, D.K.1166, W.s., Crp.

Myosotis laxa subsp. *caespitosa* (C.F.Schultz) Hyl. ex Nordh., (8), 10.06.2012, D.K.1389, Trp.

Myosotis lithospermifolia Hornem., (4), 29.04.2012, D.K.1147, Trp.

Myosotis litoralis Steven ex Fisch., (6), 08.04.2012, D.K.1052, M.E., Trp.

Myosotis ramosissima Rochel, (12), 07.04.2013, D.K.1746, M.E., Trp.

Myosotis sylvatica Ehrh. ex. Hoffm subsp. *rivularis* Vestergr., (6), 29.04.2012, D.K.1135, E.S.E., Hmcp.

Onosma taurica Wild. var. *taurica,* (2), 21.05.2015, D.K.1859, Hmcp.

Symphytum bulbosum K.F.Schimp., (3), 07.04.2013, D.K.1748, M.E., Crp.

Symphytum tuberosum L., (28), 14.03.2020, D.K.2100, E.S.E. Crp.

Trachystemon orientalis (L.) G. Don, (16), 29.04.2012, D.K.1181, E.S.E., Hmcp.

BRASSICACEAE

Alyssum dasycarpum Stephan ex Willd., (14), 29.04.2012, D.K.1153, W.s.,Trp.

Arabidopsis thaliana (L.) Heynhold, (15), 26.03.2012, D.K.1037, W.s., Trp.

Arabis sagittata (Bertol.) DC., (6), 21.05.2015, D.K.1873, M.E., Hmcp.

Arabis verna (L.) R.Br., (8), 05.05.2013, D.K.1808, W.s., Hmcp.

Cakile maritima Scop., (15), 18.06.2018, D.K.1902, Trp.

Calepina irregularis (Asso) Thell., (24), 26.03.2012, D.K.1029, Trp.

Capsella bursa-pastoris (L.) Medik, (6), 10.04.2014, D.K.1827, W.s., Trp.

Cardamine bulbifera (L.) Crantz , (1), 08.04.2012, D.K.1088, E.S.E., Crp.

Cardamine hirsuta L., (6), 10.03.2013, D.K.1692, W.s., Trp.

Cardamine pratensis L., (6), 08.04.2012, D.K.1073, W.s., E.S.E., Hmcp.

Cardamine quinquefolia (M.Bieb.) Schmalh., (9), 26.03.2012, D.K.1041, E.S.E., Crp.

Crambe tataria Sebeök var. *tataria,* (20), 08.04.2012, D.K.1062, Chmp.

Lepidium draba L. (8), 30.08.2014, D.K.1843, W.s., Hmcp.

Maresia nana (DC.) Batt, (15), 08.04.2012, D.K.1091, W.s., Trp.

Matthiola fruticulosa (L.) Maire subsp. *fruticulosa,* (15), 08.04.2012, D.K.1735, M.E., Hmcp.

Microthlaspi perfoliatum (L.) F.K.Mey., (6), 10.03.2013, D.K.1698, W.s.., Trp.

Raphanus raphanistrum L. subsp. *raphanistrum,* (20), 27.05.2012, D.K.1373, Trp.

Rapistrum rugosum (L.) All., (23), 27.05.2012, D.K.1302, Trp.

BUTOMACEAE

Butomus umbellatus L., (6), 10.06.2012, D.K.1390, W.s., E.S.E., Crp.

CACTACEAE

Opuntia ficus-barbarica A.Berger., (15), 27.05.2012, D.K.1237, Chmp.

CAMPANULACEAE

Asyneuma rigidum (Willd.) Grossh. subsp. *rigidum,* (7), 18.06.2018, D.K.1918, Ir.-Tur El., Hmcp.

Campanula persicifolia L. subsp. *persicifolia,* (6), 27.05.2012, D.K.1344, Chmp.

Jasione montana L. subsp. *montana,* (6), 18.06.2018, D.K.1910, Hmcp.

Legousia speculum-veneris (L.) Durande ex Vill., (23), 04.08.2019, D.K.2072A, M.E., Trp.

CANNABACEAE

Humulus lupulus L., (9), 30.09.2012, D.K.1672, E.S.E., Hmcp.

CAPRIFOLIACEAE

Cephalaria syriaca (L.) Schrader, (1), 02.07.2012, D.K.1454, Trp.

Cephalaria transsylvanica (L.) Schrader, (6), 27.05.2012, D.K.1251, Trp.

Dipsacus fullonum L. (10), 14.07.2019, D.K.2064B, Hmcp.

Dipsacus laciniatus L., (23), 30.09.2012, D.K.1668, W.s.., Phnp.

Knautia byzantina Fritseh (10), 04.08.2019, D.K.2056 Hmkrp, **End.**

Knautia degenii Borbás ex Formanek, (24), 10.06.2012, D.K.1409, M.E.., Hmcp., **End.**

Scabiosa argentea L. (10), 04.09.2019. D.K.2057, Trp.

Scabiosa columbaria L. subsp. *columbaria* (10), 04.09.2019, D.K.2058, Hmcp.

Valerianella pumila (L.) DC., (5), 08.04.2012, D.K.1045, Trp.

CARYOPHYLLACEAE

Arenaria serpyllifolia L. subsp. *leptoclados* (Rchb.) Nyman, (15), 29.04.2012, D.K 1100, Trp.

Arenaria serpyllifolia L. subsp. serpyllifolia, (2), 07.04.2013, D.K.1741, Trp.

Cerastium comatum Desv., (2), 07.04.2013, D.K.1742, M.E.., Trp.

Cerastium dichotomum L. subsp. *dichotumum,* (2), 08.04.2012, D.K.1046, Trp.

Cerastium dubium (Bastard) O.Schwarz, (2), 08.04.2012, D.K.1056, Trp.

Dianthus armeria L. subsp. *armeria*, (16), 02.07.2012, D.K.1475, E.S.E., Hmcp.

Minuartia anatolica (Boiss.) Woron var. *polymorpha* Mc Neill, (2), 08.04.2012, D.K.1079, Hmcp.

Myosoton aquaticum (L.) Moench, (6), 02.09.2012, D.K.1592, E.S.E., Hmcp.

Petrorhagia dubia (Raf.) G.López & Romo, (15), 27.06.2019, D.K.2030, Trp.

Petrorhagia prolifera (L.) P.W.Ball & Heywood (6), 05.05.2013, D.K.1806, Trp.

Saponaria officinalis L., (16), 23.06.2012, D.K.1447, Crp.

Scleranthus annuus L. subsp. *verticilatus* (Tausch) Arc., (8), 05.05.2013, D.K.1794, Hmcp.

Silene conoidea L., (6), 29.04.2012, D.K.1132, Hmcp.

Silene dichotoma Ehrh. Subsp. *dichotoma,* (14), 27.05.2012, D.K.1256, Hmcp.

Silene gallica L., (6), 05.05.2013, D.K.1797, Hmcp.

Silene italica (L.) Pers subsp*. italica,* (6), 05.05.2013, D.K.1799, M.E.., Hmcp.

Silene sangaria COODE & Cullen, (12), 30.08.2014, D.K.1831, Hmcp. **End.**

Silene subconica Friv., (14), 29.04.2012, D.K.1131, Trp.

Silene vulgaris (Moench) Garcke var. *macrocarpa* (Turrill) Coode &Cullen, (6), 05.05.2013, D.K.1798, Hmcp.

Spergularia marina (L.) Besser, (12), 26.07.2012, D.K.1559, Chmp.

Stellaria holostea L., (3), 06.05.2012, D.K.1039, E.S.E., Hmcp.

Stellaria media (L.) Vill., (2), 08.04.2012, D.K., Trp.

Telephium imperati L. subsp. *orientale* (Boiss.) Nyman, (15), 16.09.2012, D.K.1661, Trp.

CELASTRACEAE

Euonymus latifolius (L.) Miller, subsp. *latifolius,* (21), 26.07.2012, D.K.1561, E.S.E., Phnp.

CERATOPHYLLACEAE

Ceratophyllum demersum L., (1), 02.07.2012, D.K.1489, Crp.

CISTACEAE

Cistus creticus L., (8), 27.05.2012, D.K.1267, M.E., Chmp.

Cistus salviifolius L., (8), 05.05.2013, D.K., Chmp.

CONVOLVULACEAE

Calystegia sepium (L.) R.Br. subsp. *sepium*, (6), 02.07.2012, D.K.1484, Hmcp.

Calystegia silvatica (Kit.) Griseb., (27), D.K.1362B, 27.05.2012, Hmcp.

Convolvulus arvensis L., (5), 10.06.2012, D.K.1402, Hmcp.

Convolvulus betonicifolius Mill. subsp. *betonicifolius,* (19), D.K.2073B, 4.8.2019. M.E., Ir.-Tur El., Hmcp.

Convolvulus scammonia L., (6), 27.05.2012, D.K.1253, M.E., Hmcp.

CORNACEAE

Cornus mas L. (16), 21.05.2015, D.K.1849, E.S.E., Phnp.

Cornus sanguinea L. subsp *australis* (C. A. Meyer) Jav., (9), 06.05.2012, D.K.1185, E.S.E., Phnp.

CRASSULACEAE

Crassula tillaea Lester-Garland, (15), 08.04.2012, D.K.1071, Trp.

Sedum hispanicum L., (6), 27.05.2012, D.K.1349, W.s., Ir.-Tur El., Trp.

Sedum pallidum M.Bieb., (7), 31.05.2012, D.K.1366B, E.S.E., Trp.

CUCURBITACEAE

Ecballium elaterium (L.) A. Rich., (16), 18.06.2018, D.K.1879, M.E., Crp.

CYPERACEAE

Bolboschoenus maritimus (L.) Palla subsp. maritimus,(15), 18.06.2018, D.K 1913, W.s.,

Carex distans L. subsp. distans, (16), 06.05.2012, D.K.1230, W.s., E.S.E., Crp.

Carex divulsa Stokes, (1), 22.07.2012, D.K 1551, E.S.E., Crp.

Carex flacca Schreb. subsp. *erythrostachys* (Hoppe) Holub, (1), 06.05.2012, D.K.1231, M.E., Crp.

Carex riparia Curtis subsp. *riparia* [], D.K.1960, 14.05.2019, E.S.E., Crp.

Cyperus capitatus Vandelli, (8), 05.05.2013, D.K 1777, Trp.

Cyperus longus L. subsp. *badius* (Desf.) Bonnier & Layens, (17), 02.07.2012, D.K 1468, W.s., Trp.

Cyperus rotundus L.,(13), 27.05.2012, D.K 1332, Hmcp.

Cyperus serotinus Rottb., (17), 02.09.2012, D.K 1590, Trp.

Eleocharis palustris (L.) Roemer & Schultes subsp. *palustris,*(16), 27.05.2012, D.K 1328, W.s., Crp.

Fimbristylis bisumbellata (Forsskâl) Bubani, (9), 02.09.2012, D.K 1589, Crp.

Scirpoides holoschoenus (L.) Soják subsp. *holoschoenus*, (1), 30.09.2014, D.K 1838, Crp.

DIOSCOREACEAE

Dioscorea communis (L.) Caddick & Wilkin, (17), 21.05.2015, D.K1872, Crp.

EBENACEAE

Diospyros kaki Thunb., (20), 21.05.2015, D.K.1857, Phnp.

Diospyros lotus L., (17), 21.05.2015, D.K.1856B, Phnp.

ERICACEAE

Arbutus andrachne L., (13), 21.05.2015, D.K.1855, Phnp.

Calluna vulgaris (L.) Hull, (19), 12.02.2019, DK2090A , E.S.E., Phnp.

Erica arborea L., (2), 29.04.2012, D.K.1133, Phnp.

Rhododendron ponticum L., (3), 07.04.2013, D.K.1749, E.S.E., Phnp.

EUPHORBIACEAE

Euphorbia amygdaloides L. var. *amygdaloides,* (6), 27.05.2012, D.K.1266, E.S.E.

Euphorbia helioscopia L. subsp. *helioscopia,* (6), 29.04.2012, D.K.1177, Trp.

Euphorbia illirica Lam., (6), 27.05.2012, D.K.1369, E.S.E., Crp.

Euphorbia maculata L., (8), 02.09.2012, D.K.1582, Trp.

Euphorbia oblongata Griseb. var. *oblongata*, (3), 02.09.2012, D.K.1616, M.E., Trp.

Euphorbia paralias L., (14), 02.07.2012, D.K.1466, M.E., Trp.

Euphorbia peplis L., (15), 18.06.2018, D.K.1893 , M.E., Trp.

Euphorbia seguieriana Necker subsp. *seguieriana,* (13), 27.05.2012, D.K.1265, E.S.E., Hmcp.

Euphorbia stricta L., (3), 16.09.2012, D.K.1644, E.S.E., Trp.

FABACEAE

Acacia dealbata Link, (26), 14.3.2020, D.K.2017, Phnp.

Anthyllis hermanniae L., (14), 02.07.2012, D.K.1472, M.E., Hmcp.

Astragalus glycyphyllos L., (20), 23.06.2012, D.K.1426, E.S.E., Hmcp.

Bituminaria bituminosa (L.) C.H.Stirt., (1), 10.06.2012, D.K.1381, M.E., Hmcp.

Colutea cilicica Boiss. & Balansa, (7), 18.06.2018, D.K.1880, Phnp.

Cytisus hirsutus L., (28) ,14.03.2020, D.K. 2098, Phnp.

Dorycnium graecum (L.) Ser, (6), 06.05.2012, D.K.1226, E.S.E., Hmcp.

Galega officinalis L., (1), 10.06.2012, D.K.1388, E.S.E., Hmcp.

Genista tinctoria L., (24), 29.04.2012, D.K.1168, E.S.E., Phnp.

Gleditsia triacanthos L., (8), 26.07.2012, D.K.1562, Phnp., Cltr.

Lathyrus cicera L., (13), 05.05.2013, D.K.1783, M.E., Trp.

Lathyrus inconspicuus L. var. *inconspicuus*, (24), 29.04.2012, D.K.1105, W.s., Trp.

Lathyrus laxiflorus (Desf.) O. Kuntze subs. *laxiflorus*, (6), 10.06.2012, D.K.1383, Hmcp.

Lathyrus palustris L. subsp. *palustris,* (13), 05.05.2013, D.K.1787, E.S.E., Hmcp.

Lathyrus sativus L., (17), 23.06.2012, D.K.1438, M.E., Trp.

Lathyrus sphaericus Retz., (6), 08.04.2012, D.K.1064, M.E., Trp.

Lathyrus venetus (Miller) Wohlf., (19), 07.04.2013, D.K.1754, E.S.E., Chmp.

Lotus corniculatus L. var. *tenuifolius*, (14), 18.06.2018, D.K.1891, Hmcp.

Medicago crassipes (Boiss.) E.Small, (8), 02.07.2012, D.K.1500, Ir.-Tur E., Trp.

Medicago littoralis Rohde ex Lois. var. *littoralis*, (15), 18.06.2018, Ir.-Tur El. D.K.1892, Trp.

Medicago marina L., (8), 05.05.2013, D.K.1782, Trp.

Medicago minima (L.) Bart var. *minima*, (6), 29.04.2012, D.K.1110, Trp.

Medicago orbicularis (L.) Bart., (6), 29.04.2012, D.K.1144, Trp.

Medicago polymorpha L. var. *vulgaris* (Benth.) Shinners, (24), 29.04.2012, D.K.1162, W.s., Trp.

Melilotus albus Desr., (3), 18.06.2018, D.K.1368B, Trp.

Melilotus officinalis (L.) Desr., (17), 10.06.2012, D.K.1368B, W.s., Trp.

Ornithopus compressus L., (13), 05.05.2013, D.K.1094, M.E., Trp.

Robinia pseudoacacia L., (1), 06.05.2012, D.K.1198, Phnp.

Scorpiurus subvillosus L. var. *subvillosus,* (6), 06.05.2012, D.K.1216, Trp.

Sophora jaubertii Spach, (17), 26.07.2012, D.K.1563, E.S.E., Chmp.

Spartium junceum L., (2), 18.06.2018, D.K.1903, M.E., Phnp.

Trifolium angustifolium L. var. *angustifolium,* (6), 27.05.2012, D.K.1276, Trp.

Trifolium arvense L. var *arvense,* (6), 05.05.2013, D.K.1809, W.s., Trp.

Trifolium campestre Schreb. subsp. *campestre* var. *subsesile* (Boiss.) Keskin, (6), 29.04.2012, D.K.1143, Trp.

Trifolium cherleri L. , (6), 29.04.2012, D.K.1160, M.E., Trp.

Trifolium clusii Godr & Gren. var. *clusii,* (9), 29.04.2012, D.K.1157, M.E., Trp.

Trifolium constantinopolitanum Ser., (6), 29.04.2012, D.K.1120, Trp.

Trifolium hybridum L. var. *hybridum,* (6), 08.07.2012, D.K.1522, Hmcp.

Trifolium patens Schreb., (6), 08.04.2012, D.K.1075, Trp.

Trifolium resupinatum L. var. *resupinatum*, (16), 29.04.2012, D.K.1119, Trp.

Trifolium stellatum L. var. *stellatum*, (6), 06.05.2012, D.K.1214, Trp.

Trifolium tomentosum L. var. *tomentosum*, (6), 27.05.2012, D.K.1149, Trp.

Trifolium uniflorum L. subsp. *uniflorum*, (6), 04.07.2013. D.K.2043, M.E., Trp.

Trigonella spicata Sibth & Sm., (24), 27.05.2012, D.K.1308, M.E.., Hmcp.

Vicia hybrida L., (13), 05.05.2013, D.K.1785, W.s., Trp.

Vicia monantha Retz. subsp. *monantha*, (13), 29.04.2012, D.K.1107, Trp.

Vicia sativa L. subsp. *incisa* (Bieb) Arc. var. *incisa,* (23), 05.05.2013, D.K.1791, Trp.

Vicia sativa L. subsp. *nigra* (L.) var. *nigra,* (13), 05.05.2013, D.K.1788, Trp.

Vicia villosa Roth subsp. *eriocarpa* (Hausskn.) P.W.Ball, (6), 21.05.2015, D.K.1284, Trp.

FAGACEAE

Castanea sativa Miller, (4), 08.07.2012, D.K.1523, E.S.E., Phnp.

Fagus orientalis Lipsky, (6), 06.05.2012, D.K.1188, E.S.E., Phnp.

Quercus cerris L., (9), 09.06.2013, D.K.1823, M.E., Phnp.

Quercus frainetto Ten., (5), 29.04.2012, D.K.1163, E.S.E., Phnp.

Quercus hartwissiana Steven, (1), 08.07.2012, D.K.1513, Phnp.

Quercus infectoria Olivier subsp. *veneris* (A.Kern.) Meikle Schwarz, (21), 16.09.2012, D.K.1624, W.s., Phnp.

Quercus macranthera Fısch. & Mey. ex Hohen. subsp. *syspirensis* (C. Koch) Menıtsky, (21), 08.07.2012, D.K.1526, Phnp., **End.**

Quercus petraea (Mattuschka) Liebl subsp. *iberica* (Steven ex M.Bieb.) Krassiln., (9), 09.06.2013, D.K.1821, Phnp.

Quercus petraea (Mattuschka) Liebl subsp. *petraea*, (21), 23.06.2012, D.K.1445, Phnp.

Quercus pubescens Willd. subsp. *pubescens,* (21), 16.09.2012, D.K.1654, Phnp.

GENTIANACEAE

Blacstonia perfoliata (L.) Hudson subsp. *perfoliata*, (9), 23.06.2012, D.K.1433, Hmcp.

Centaurium erythraea Rafn subsp. *erythraea,* (9), 02.07.2012, D.K.1459, E.S.E., Hmcp.

Centaurium pulchellum (Swartz) Druce, (6), 23.06.2012, D.K.1441, Hmcp.

GERANIACEAE

Erodium acaule (L.) Becherer & Thell., (6), 10.03.2013, D.K.1700, M.E.., Trp.

Erodium ciconium (L.) L 'Hérit., (6), 08.04.2012, D.K.1068, Trp.

Erodium cicutarium (L.) L 'Hérit. subsp. *cicutarium,* (6), 29.04.2015, D.K.1101, Trp.

Geranium asphodeloides Burm subsp. *asphodeloides*, (17), 29.04.2012, D.K.1156, E.S.E., Crp.

Geranium dissectum L., (8), 05.05.2013, D.K.1804, Trp.

Geranium molle L., (23), 10.06.2012, D.K.1395, Trp.

Geranium purpureum Vill., (6), 07.04.2013, D.K.1729, Trp.

HALORAGIDACEAE

Myriophyllum spicatum L., (1), 18.06.2018, D.K.1912, Crp.

Myriophyllum verticillatum L., (1), 18.06.2018, D.K.1906, Crp.

HYDROCHARITACEAE

Hydrocharis morsus-ranae L., (1), 02.09.2012, D.K.1572, Crp.

HYPERICACEAE

Hypericum calycinum L., (9), 08.09.2013, D.K.1844, E.S.E., Crp.

Hypericum montbretii Spach, (6), 10.06.2012, D.K.1399, Hmcp.

Hypericum perforatum L. subsp. *veronense* (Schrank) H. Linb., (14), 27.05.2012, D.K.1295, Hmcp.

Hypericum tetrapterum Fries var. *tetrapterum,* (22), 02.07.2012, D.K.1460, Crp.

IRIDACEAE

Crocus pulchellus Herb., (10), 12.10.2019, D.K.2089, M.E., Crp.

Crocus speciosus subsp. *speciosus,* M..Bieb., (19), 08.12.2018, D.K1868, Crp.

Iris pseudocorus L., (6), 27.05.2012, D.K.1367, Crp.

Iris sintenisii Janka subsp. *sintenisii,* (1), 21.05.2015, D.K.1874, E.S.E., Crp.

Iris x germanica L., (17), 7.4.2013., D.K 1765, Crp.

Romulea columnae Seb. & Mauri subsp. *columnae*, (4), 10.03.2013, D.K.1704, M.E., Crp.

JUGLANDACEAE

Juglans regia L., (17), 21.05.2015, D.K.1288, Phnp.

JUNCACEAE

Juncus acutus L. subsp. *acutus*, (17), 27.05.2012, D.K 1324, Crp.

JUNCAGINACEAE

Triglochin maritima L., (11), 14.07.2019, D.K.2046A, Crp.

LAMIACEAE

Ajuga reptans L., (6), 29.04.2012, D.K.1138, E.S.E., Hmcp.

Clinopodium nepeta (L.) Kuntze subsp. *glandulosum* (Req.) Govaerts, (6) 22.07.2012, D.K.1534, Hmcp.

Clinopodium vulgare L. subsp. v*ulgare*, (17), 02.07.2012, D.K.1477, Hmcp.

Clinopodium vulgare L. subsp. *arundanum* (Boiss.) Nyman, (9), 10.06.2012, D.K.1386, W.s., Hmcp.

Lamium amplexicaule L. var. *amplexicaule*, (14), 07.04.2013 D.K.1712, W.s., E.S.E., Hmcp.

Lamium purpureum L. var. *aznavourii* Gand. ex Aznav., (14), 26.03.2012, D.K.1044, E.S.E., **End.**

Lycopus europaeus L., (8), 02.09.2012, D.K.1587, E.S.E., Hmcp.

Melissa officinalis L. subsp. *officinalis* (10), 14.7.2019, D.K.2049, E.S.E., Hmcp.

Mentha aquatica L., (17), 02.07.2012, D.K.1492, Crp.

Mentha longifolia (L.) Hudson subsp. *typhoides* (Briq) Harley, (14), 02.09.2012, D.K., W.s., Crp.

Mentha pulegium L., (22), 04.08.2019, D.K.2072B, Hmcp.

Mentha spicata L. subsp. *condensata* (Briq.) Greuter & Burdet, (6), 23.06.2012, D.K.1429, Hmcp.

Mentha suaveolens Ehrh., (6), 02.09.2012, D.K.1577, M.E., Crp.

Mentha x piperita L., (6), 02.09.2012, D.K.1613, Crp.

Prunella laciniata (L.) L., (2), 27.05.2012, D.K.1318, E.S.E., Hmcp.

Prunella vulgaris L., (23), 16.09.2012, D.K.1628, W.s., E.S.E., Hmcp.

Salvia forskahlei L., (21), 16.09.2012, D.K.1634, E.S.E., Hmcp.

Salvia sclarea L., (9), 18.06.2018, D.K.1883, Hmcp.

Salvia verbenaca L., (13), 05.05.2013, D.K.1784, M.E., Hmcp.

Scutellaria galericulata L., (9), 02.09.2012, D.K.1586, Hmcp.

Scutellaria hastifolia L., (5), 22.07.2012, D.K.1550, E.S.E., Hmcp.

Scutellaria orientalis L. subsp. *alpina* (Boiss.) O.Schwarz var. *alpina*, (18), 27.06. 2019, D.K.2028, Chmp.

Scutellaria orientalis L. subsp. *pinnatifida* J.R.Edm., (23), 27.06.2019, D.K. 2029A, W.s., Chmp.

Sideritis montana L. subsp. *montana,* (8), 05.05.2013, D.K.1803, W.s., M.E., Hmcp.

Stachys byzantina K.Koch, (15), 02.07.2012, D.K.1476, E.S.E., Hmcp.

Stachys germanica L. subsp. *heldreichii*, (12), 22.07.2012, D.K.1553, E.S.E., Hmcp.

Stachys maritima Gouan, (15), 18.06.2018, D.K.1887, E.S.E., Hmcp.

Stachys officinalis (L.) Trevisan subsp. *haussknechtii* (Nyman) Greuter & Burdet (10), 4.8.2019, D.K.2063, E.S.E., Hmcp.

Stachys setifera C.A.Mey. subsp. *lycia* (Gand.) R.Bhattacharjee, (9), 14.07. 2019, D.K.2050, Ir.-Tur El., **End.**

Stachys sylvatica L., (6), 16.09.2012, D.K.1642, E.S.E., Hmcp.

Teucrium chamaedrys L subsp. *chamaedrys*, (6), 08.07.2012, D.K.1511, E.S.E.

Teucrium polium L. subsp. *polium*, (15), 02.09.2012, D.K.1578, W.s., Chmp.

Thymus longicaulis C. Presl subsp. *longicaulis*, (13), 02.09.2012, D.K.1583, E.S.E., Chmp.

LAURACEAE

Laurus nobilis L., (17), 02.09.2012, D.K.1597, M.E., Phnp.

LENTIBULARIACEAE

Utricularia australis R. Br., (1), 02.07.2012, D.K.1490, E.S.E., Crp.

Utricularia vulgaris L., (1), 10.06.2012, D.K.1425, E.S.E., Crp.

LILIACEAE

Gagea chrysantha (Jan) Schult. & Schult.f., (1), 21.05.2015, D.K.1866, Crp.

LINACEAE

Linum bienne Miller, (6), 29.04.2012, D.K.1142, M.E., Chmp.

Linum corymbulosum Rchb., (23), 02.07.2012, D.K.1491, M.E., Trp.

Linum trigynum L., (14), 02.07.2012, D.K.1480, M.E., Trp.

LYTHRACEAE

Lythrum salicaria L., (6), 02.07.2012, D.K.1461, W.s., E.S.E., Hmcp.

Trapa natans L., (1), 18.06.2018, D.K.1884, Crp.

MALVACEAE

Abutilon theophrastii Medik., (22), 16.09.2012, D.K.1648, Trp.

Alcea biennis Winterl, (24), 16.09.2012, D.K.1656, Hmcp.

Lavatera punctata All., (10), 14.07.2019, D.K.2052, Hmcp.

Malva neglecta Wallr., (2), 27.06.2019, D.K.2029B, Trp.

Malva sylvestris L., (6), 27.05.2012, D.K.1306, Hmcp.

Tilia cordata Miller, (12), 30.08.2014, D.K.1436, Phnp.

Tilia tomentosa Moench, (6), 26.08.2012, D.K.1557, E.S.E., Phnp.

MORACEAE

Ficus carica L. subsp *carica*, (4), 08.07.2012, D.K.1521, W.s., M..E., Phnp.

Morus alba L., (17), 30.08.2014, D.K.1488, Phnp., Cltr.

Morus nigra L., (16), 18.06.2018, D.K.1886, W.s., Phnp.

Morus rubra L., (20), 18.06.2018, D.K.1917, W.s., Phnp.

NYMPHAEACEAE

Nuphar lutea (L.) Sm, (6), 02.07.2012, D.K.1506, Crp.

Nymphaea alba L., (6), 02.07.2012, D.K.1507, Crp.

OLEACEAE

Fraxinus angustifolia Vahl. Subsp. *oxycarpa* (Willd.) Franco & Rocha Afonso, (17), 02.07.2012, D.K.1473, Phnp.

Fraxinus ornus L. subsp. *ornus,* (17), 18.06.2018, D.K.1915, E.S.E., Phnp.

Ligustrum vulgare L., (13), 27.05.2012, D.K.1337, E.S.E., Phnp.

Phillyrea latifolia L., (5), 27.05.2012, D.K.1292, M.E., Phnp.

ONAGRACEAE

Circaea lutetiana L., (16), 02.07.2012, D.K.1470, Crp.

Epilobium hirsutum L., (10),14.07.2019, D.K.2055, Hmcp.

Epilobium parviflorum Schreber, (6), 30.09.2012, D.K.1666, Hmcp.

Epilobium tetragonum L. subsp. *tournefortii* (Michal.) H. Lev., (6), 10.06.2012, D.K.1397, M.E., Trp.

Ludwigia palustris (L.) Elliott., (1), 18.06.2018, D.K.1904, Crp.

Oenothera biennis L., (9), 08.07.2012, D.K.1510, Hmcp.

ORCHIDACEAE

Anacamptis pyramidalis (L.) Rich., (1), 21.05.2015, D.K 1870, W.s., Crp.

Cephalanthera epipactoides Fisch. & C.A.Mey., (9), 21.05.2015, D.K 1869, M.E., Crp.

Dactylorhiza romana (Seb.) Soó subsp. *romana*, (1), 21.05.2015, D.K 1871, M.E., Crp.

Orchis laxiflora subsp. *laxiflora* Lam., (9), 06.05.2012, D.K 1193, M.E., Crp.

Serapias cordigera L. subsp. *cordigera*, (6), 27.05.2012, D.K 1371, M.E., Crp.

Serapias vomeracea (Burm. fil.) Briq., (5), 21.05.2015, D.K 1837, M.E., Crp.

Spiranthes spiralis (L.) Chevall,(18), 12.10.2019, D.K 2079B, M.E., Crp.

OROBANCHACEAE

Orobanche nana Noë ex Reut., (13), 05.05.2013, D.K.1780B, W.s., Vas.pr.

Orobanche ramosa L., (13), 05.05.2013, D.K.1780A, Vas.pr.

Parentucellia latifolia (L.) Caruel subsp. *latifolia,* (2), 29.04.2012, D.K.1152, M.E., Trp.

OXALIDACEAE

Oxalis acetosella L., (13), 08.04.2012, D.K.1067, Crp.

Oxalis articulata Savigny, (13), 05.05.2013, D.K.1781, Crp.

Oxalis corniculata L., (13), 10.03.2013, D.K.1708, Trp.

PAPAVERACEAE

Chelidonium majus L., (1), 30.08.2014, D.K.1842, E.S.E., Hmcp.

Fumaria officinalis L. subsp. *officinalis*, (6), 08.04.2012, D.K.1083, W.s., Trp.

Glaucium flavum Crantz, (15), 31.05.2012, D.K.1366A, Hmcp.

Papaver agremone L., (6), 21.05.2015, D.K.1865B, Trp.

Papaver dubium L. subsp. *laevigatum*, (6), 14.05,2019, D.K.1935, Trp.

Papaver dubium L. subsp. *lecoqii,* (6), 14.05.2019, D.K.1962, Trp.

Papaver dubium L. subsp. *dubium*, (6), 21.05.2015, D.K.1282, Trp.

Papaver gracile Aucher ex Boiss., (6),14.05.2019, D.K.1260, M.E., Trp.

Papaver hybridum L., (6), 27.05.2012, D.K.1307, W.s., Trp.

Papaver lacerum Popov, (13), 07.04.2013, D.K.1761, W.s., Trp.

Papaver pilosum Sibth. & Sm. subsp. *pilosum*, (6), 27.05.2012, D.K.1347, Hmcp., **End.**

Papaver pilosum Sibth. & Sm. subsp. *strictum* (Boiss. & Balansa) N.Wendt ex Kadereit, (22), 21.05.2015, D.K.1856A, Hmcp., **End.**

Papaver postii Fedde, (6), 27.05.2012, D.K.1311, M.E., Trp.

Papaver rhoeas L., (6), 14.05.2019, D.K.1958, Trp.

Papaver rhoeas L., (6), 27.05.2012, D.K.1310, W.s., Trp.

Papaver somniferum L. var. *pullatum* M.A.Veselovskaya, (6), 14.05.2019, D.K.1946, Trp., **End.**

PHYTOLACCACEAE

Phytolacca americana L., (13), 08.09.2013, D.K.1832, Chmp.

PLANTAGINACEAE

Callitriche brutia Petagna, (1), 18.06.2018, D.K.1905, Crp.

Digitalis ferruginea L. subsp. *ferruginea*, (9), 4.8.2019, D.K.2061B, E.S.E., Hmcp.

Kickxia elatine (L.) Dumort subs. *crinita* (Mabille) Greuter, (12), 30.0.2014, D.K.1825, M.E., Trp.

Kickxia lanigera (Desf.) Hand.-Mazz., (13), 02.09.2012, D.K.1619, M.E., Trp.

Linaria pelisseriana (L.) Miller, (6), 08.04.2012, D.K.1092, M.E., Trp.

Linaria simplex DC., (8), 05.05.2013, D.K.1801, W.s., M.E., Trp.

Plantago bellardii All., (1), 29.04.2012, D.K.1155B, M.E., Hmcp.

Plantago cretica L., (17), 29.04.2012, D.K.1155A, M.E., Hmcp.

Plantago lagopus L., (1), 27.05.2012, D.K.1270, M.E., Hmcp.

Plantago lanceolata L., (6), 27.05.2012, D.K.1333, Hmcp.

Plantago major L. subsp. *intermedia* (Gilib.) Lange, (17), 27.05.2012, D.K.1271, W.s., Hmcp.

Plantago media L., (1), 16.09.2012, D.K.1646, Hmcp.

Plantago sempervirens Crantz, (6), 02.07.2012, D.K.1469, M.E., Hmcp.

Veronica anagallis-aquatica L., (17), 10.06.2012, D.K.1380, W.s., Hmcp.

Veronica beccabunga L., (6), 18.06.2018, D.K.1895 , W.s., Crp.

Veronica chamaedrys L., (2), 07.04.2013, D.K.1743, E.S.E., Hmcp.

Veronica crinita Kit., (6), 07.04.2013, D.K.1724, E.S.E., Hmcp.

Veronica cymbalaria Bodard, (6), 07.04.2013, D.K.1725, M.E., Trp.

Veronica persica Poir. (2), 6.3.2013, D.K.1693B, Hmcp.

Veronica serpyllifolia L., (6), 7.4.2013, D.K.1757B, Hmcp.

PLATANACEAE

Platanus orientalis L., (2), 30.08.2014, D.K.1864, Phnp.

POACEAE

Aegilops geniculata Roth, (6), 18.06.2019, D.K.2010, M.E., Trp.

Agrostis stolonifera L., (1), 27.05.2012, D.K 1305, W.s., E.S.E.,Trp.

Aira elegantissima Schur subsp. *elegantissima* (Schur), (8), 27.05.2012, D.K 1357, M.E., Trp.

Alopecurus myosuroides Huds. subsp. *myosuroides* (13), 04.08.2019,D.K.2067B, E.S.E.,Crp.

Ammophila arenaria (L.) Link subsp. *arundinacea* (Husn.) H. Lindb., (15), 18.06.2018, D.K 1916, M.E., Crp.

Arundo donax L., (17), 18.06.2018, D.K.1914, Crp.

Avena byzantina K.Koch, (6), 29.04.2012, D.K 1096, Trp., Cltr.

Avena sativa L.,(13), 05.05.2013, D.K 1778, Trp., Cltr.

Avena sterilis L. subsp. *sterilis*, (16), 27.05.2012, D.K 1356, Trp.

Bothriochloa ischaemum (L.) Keng, (20), 12.10. 2019, D.K.2083, Trp.

Brachypodium distachyon (L.) P.Beauv., (25), 08.06.2019, D.K.2011A, M.E., Trp.

Brachypodium pinnatum (L.) P.Beauv. (25), 08.06.2019, D.K.2009A, E.S.E., Trp.

Briza maxima L., (6), 06.05.2012, D. K.1234, Crp.

Briza media L., (6), 06.05.2012, D. K.1228, Crp.

Briza minor L., (8), 05.05.2013, D.K.1779, Trp.

Bromus diandrus Roth, (1), 27.05.2012, D.K 1238, Trp.

Bromus hordeaceus L. subs. *thominii* (Hardouin) Maire&Weiller, (6), 29.04.2012, D.K 1097, M.E., Trp.

Bromus japonicus Thunb. subsp. *japonicus*, (22), 27.05.2012, D.K 1249, W.s., Trp.

Bromus rigidus Roth , (1), 27.05.2012, D.K 1279, W.s., Trp.

Bromus sterilis L., (6), 27.05.2012, D.K 1314, W.s., Trp.

Catapodium marinum (L.) C.E. Hubbard, (8), 05.05.2013, D.K.1776, M.E.., Trp.

Cynodon dactylon (L.) Pers. var. *dactylon*, (1), 05.05.2013, D. K.1840, Crp.

Cynosurus cristatus L., (6), 10.06.2012, D. K.1411, E.S.E,Trp.

Cynosurus echinatus L., (16), 27.05.2012, D. K.1239, M.E., Crp.

Dactylis glomerata L. subsp *glomerata,* (6), 27.05.2012, D. K.1246, E.S.E.,Crp.

Dactylis glomerata L. subsp. *lobata* (Drejer) H.Lindb., (9), 14.05.2019 D.K.1948, E.S.E., Crp.

Echinochloa crus-galli (L.) P. Beauv., (6), 25.09.2011, D.K.1001, Trp.

Elymus elongatus (Host) Runemark subsp. *turcicus* (McGuire) Melderis, (6), 14.05.2019, D.K.1952, Hmcp.

Elymus farctus (Viv.) Runemark ex Melderis subsp. *bessarabicus* (Savul. Rayss) Melderis, (14), 27.06.2019, DK2014, Crp.

Elymus flaccidifolius (Boiss. & Heldr.) Melderis, (13), 14.05.2019, D.K.2051B, M.E., Hmcp.

Festuca drymeja Mert. & W.D.J.Koch, (6), 27.05.2012, D.K.1242, E.S.E., Crp.

Festuca valesiaca Schleich. ex Gaudin (21), 27.05.2012, D.K.1252A, Hmcp.

Holcus lanatus L., (13), 08.07.2012, D.K 1516, 20., 22.07.2012, E.S.E., Hmcp.

Hordeum bulbosum L., (17), 27.05.2012, D.K 1290, W.s., Hmcp.

Hordeum distichon L., (6), 29.04.2012, D.K 1102, Trp., Cltr.

Hordeum murinum L. subsp. *glaucum* (Steudel) Tzvelev, (14), 27.05.2012, D.K 1334, Trp.

Koeleria macrantha (Ledeb.) Schult.(14), 10.04.2014, D.K.1829B, Crp.

Lagurus ovatus L., (13), 10.06.2012, D.K 1410, M.E., Trp.

Leymus racemosus (M.Bieb.) Tzvelev subsp. *sabulosus*, (14), 22.07.2012, D.K 1839, Trp.

Lolium multiflorum Lam., (6), 27.05.2012, D.K.1277, Hmcp.

Lolium perenne L., (14)., 27.05.2012, D.K 1247, E.S.E., Hmcp.

Phalaris minor Retz., (1), 27.05.2012, D.K 1278, M.E., Trp.

Phalaris paradoxa L., (6), 29.04.2012, D. 1315, M.E., Trp.

Phalaris truncata Guss. ex Bertol., (17), 27.05.2012, D.K M.E., Trp.

Phleum pratense L., (13), 04.08.2019, D.K.2076A, E.S.E., Hmcp.

Pholiurus pannonicus (Host) Trin., (6), 02.07.2012, D.K.1503, Trp.

Phragmites australis (Cav.) Trin. ex Steudel, (12), 25.09.2011,D.K.1016, W.s., E.S.E., Crp.

Poa angustifolia L., (1), 08.04.2012, D. K.1054, W.s.., Crp.

Poa timoleontis Heldr. ex Boiss.,(13), 05.05.2013, D.K.1759, M.E., Trp.

Rostraria cristata (L.) Tzvelev var. *glabriflora* (Trautv.) Doğan, (24), 27.06.2019, D.K.2026, Trp.

Rostraria cristata (L.) Tzvelev var. *cristata* (19), 27.6.2019, D.K.2031B, Trp.

Setaria glauca (L.) P.Beauv. (1), 23.06.2012, D.K.1437, Trp.

Setaria verticillata (L.) P. Beauv. var. *ambigua* (Guss.) Pari., (6), 16.09.2012, D.K.1637, Trp.

Setaria viridis (L.) P. Beauv., (6), 02.09.2012, D.K.1585, W.s., Trp.

Tragus racemosus (L.) All. (12), 27.06.2019, D.K.2020, Trp.

Vulpia bromoides (L.) Gray, (13), 27.06.2019, D.K.2035A, E.S.E., Trp.

Vulpia myuros (L.) C. C. Gmel., (13), 27.05.2012, D.K.1241, W.s., Trp.

POLYGALACEAE

Polygala anatolica Boiss. & Heldr., (3), 02.07.2012, D.K.1875, W.s., Hmcp.

Polygala pruinosa Boiss subsp. *pruinosa* , (5), 29.04.2012, D.K.1123, W.s., Hmcp.

POLYGONACEAE

Polygonum convolvulus L., (5), 21.05.2012, D.K.1283, Hmcp.

Polygonum maritimum L., (8), 02.09.2012, D.K.1609, Trp.

Polygonum persicaria L., (1), 06.05.2012, D.K.1187, Trp.

Polygonum salicifolium Brouss. ex Willd., (6), 29.04.2012, D.K.1010, Hmcp.

Rumex acetosella L., (24), 27.05.2012, D.K.1309, Hmcp.

Rumex conglomeratus Murray, (6), 27.05.2012, D.K.1448, Hmcp.

Rumex crispus L., (6), 27.05.2012, D.K.1376, Hmcp.

Rumex obtusifolius (Schur) Celak., subsp. *subalpinus*, (6), 14.05.2019, D.K.1937, Hmcp.

POTAMOGETONACEAE

Potamogeton nodosus Poir., (27), 14.6.2019, D.K.2044B, Crp.

PRIMULACEAE

Anagallis arvensis L. var *arvensis,* (6), 27.05.2012, D.K.1300, Trp.

Anagallis arvensis L. var. *caerulea* (L.) Gouan, (13), 05.05.2013, D.K.1805B, Trp.

Anagallis arvensis L. var. *parviflora* (Hoffmanns. & Link) Ces., (13), 05.05.2013, D.K.1805A, M.E., Trp.

Anagallis minima (L.) E.H.L. Krause, (2), 08.04.2012, D.K.1080, Trp.

Androsace maxima L., (8), 05.05.2013, D.K.1796, Trp.

Cyclamen coum Miller var. *caum,* (6), 26.03.2012, D.K.1027, Crp.

Hottonia palustris L., (6), 02.07.2012, D.K.1483, E.S.E., Crp.

Lysimachia dubia Willd., (1), 29.04.2012, D.K.1139, M.E., Trp.

Lysimachia nummularia L., (1), 09.06.2013, D.K.1819, E.S.E., Hmcp.

Lysimachia punctata L., (10), 4. 8. 2019, D.K.2062, Crp.

Lysimachia verticillaris Sprengel, (20), 02.07.2012, D.K.1494, E.S.E., Hmcp.

Primula acaulis (L.) Hill subsp. *rubra* (Sm.) Greuter & Burdet, (5), 10.01.2013, D.K.1673, E.S.E., Crp.

RANUNCULACEAE

Anemone coronaria L., (16), 14.03.2020, D.K.2200, M.E., Crp.

Clematis vitalba L., (6), 16.06.2012, D.K.1651, Chmp.

Clematis viticella L., (9), 27.05.2012, D.K.1343, Chmp.

Helleborus orientalis Lam., (13), 10.03.2013, D.K.1702, E.S.E., Crp.,

Nigella arvensis L. var. *glauca* Boiss, (18), 07.07.2020, Trp.

Ranunculus arvensis L., (6), 06.05.2012, D.K.1223, W.s.,Trp.

Ranunculus constantinopolitanus (DC.) d'Urv, (1), 08.04.2012, D.K.1047, W.s., Hmcp.

Ranunculus ficaria L. subsp. *calthifolius* (Reichb.) Arc, (6), 10.03.2013, D.K.1691, Crp.

Ranunculus marginatus d' Urv., (6), 27.05.2012, D.K.1297, Trp.

Ranunculus neapolitanus Ten., (25), 08.04.2012, D.K.1072, Crp.

Ranunculus ophioglossifolius Vill., (6), 29.04.2012, D.K.1145, Crp.

Ranunculus sphaerospermus Boiss. & Blanche, (27), 14.07.2019, D.K.2045B, Crp.

Ranunculus trichophyllus Chaix ex Vill., (6), 10.04.2014, D.K.1830, W.s., Crp.

Thalictrum lucidum L., (1), 22.07.2012, D.K.1549, Crp.

RHAMNACEAE

Paliurus spina-christi Miller., (15), 29.04.2012, D.K.1172, Phnp.

Rhamnus alaternus L., (17), 30.08.2014, D.K.1845, M.E., Chmp., Cltr.

ROSACEAE

Agrimonia eupatoria L. subsp. *eupatoria*, (17), 16.09.2012, D.K.1658, Hmcp.

Crataegus microphylla C. Koch subsp. *microphylla*, (12), 07.04.2013, D.K.1745, E.S.E., Chmp.

Crataegus monogyna Jacq. var. *monogyna*, (17), 29.04.2012, D.K.1130, Phnp.

Crataegus pentagyna Waldst. & Kit. ex Willd., (8), 02.09.2012, D.K.1618, E.S.E.

Crataegus rhipidophylla Gand. var. *rhipidophylla*, (21) 23.06.2012, D.K.1443, Phnp.

Cydonia oblonga Miller, (16), 29.04.2012, D.K.1174, Phnp.

Fragaria vesca L., (17), 10.06.2012, D.K.1392, E.S.E., Hmcp.

Geum urbanum L.,(27), 14.05.2019, D.K.1922 E.S.E., Hmcp.

Laurocerasus officinalis M.Roem., (1), 29.04.2012, D.K.1113, Phnp.

Malus pumila Mill., (20), 06.05.2012, D.K.1189, Phnp., Cltr.

Malus sylvestris Miller subsp. *orientalis* (A. Uglitzkich) Browicz var. *orientalis*, (1), 08.07.2012, D.K.1524A, Phnp.

Mespilus germanica L., (9), 06.05.2012, D.K.1206, E.S.E., Phnp.

Potentilla anglica Laicharding, (6), 27.05.2012, D.K.1303, E.S.E., Hmcp.

Potentilla detommasii Ten., (6), 27.05.2012, D.K.1320, Hmcp.

Potentilla recta L., (13), 02.07.2012, D.K.1455, Hmcp.

Potentilla reptans L., (6), 27.05.2012, D.K.1244, W.s., Hmcp.

Prunus divaricata Ledeb subsp. *divaricata,* (23), 02.07.2012, D.K.1499, W.s., Phnp.

Prunus spinosa L., (16), 02.07.2012, D.K.1450, E.S.E., Phnp.

Prunus x domestica L., (8), 25.09.2011, D.K.1018, Phnp.

Pyrus communis L. subsp. *sativa* (DC.) Hegi, (21), 02.07.2012, D.K.1498, Phnp., Cltr..

Pyrus elaeagrifolia Pallas subsp. *alaeagrifolia,* (12), 09.06.2013, D.K.1816, Phnp.

Rosa canina L. (20), 16.09.2012, D.K.1626, Phnp.

Rosa gallica L., (8), 23.06.2012, D.K.1435, Phnp.

Rosa pulverulenta M.Bieb., (21), 22.07.2012, D.K.1541, Phnp.

Rosa sempervirens L., (13), 05.05.2013, D.K.1775, M.E., Phnp.

Rubus caesius L., (21), 10.06.2012, D.K.1418, W.s., Chmp.

Rubus canescens DC. var. *canescens,* (17), 08.07.2012, D.K.1514, W.s., E.S.E.

Rubus canescens DC. var. *glabratus* (Godron) Davis & Meikle, (1), 22.07.2012, D.K.1547, W.s.., E.S.E., Chmp.

Rubus hirtus Waldst & Kit., (9), 22.07.2012, D.K.1543, E.S.E., Chmp.

Rubus idaeus L. subsp. *idaeus*, (21), 02.07.2012, D.K.1508, E.S.E., Chmp., Cltr.

Rubus sanctus Schreber, (8), 22.07.2012, D.K.1554, W.s., Chmp.

Rubus tereticaulis P.J. Mueller, (9), 27.05.2012, D.K.1294, Chmp.

Sanguisorba minor (L.) subsp. *balearica* (Bourg. ex Nyman) Muñoz Garm. & C.Navarro, (6), 27.05.2012, D.K.1245, W.s., Hmcp.

Sorbus torminalis (L.) Crantz var. *torminalis,* (2), 22.07.2012, D.K.1538, W.s., E.S.E., Phnp.

RUBIACEAE

Galium debile Desv, (6), 27.05.2012, D.K.1345, M.E., Hmcp.

Galium palustre L, (6), 06.05.2012, D.K.1222, E.S.E., Hmcp.

Galium paschale Forsskâl, (6), 10.06.2012, D.K.1378, M.E., Hmcp.

Galium spurium L. subsp. *spurium,* (6), 29.04.2012, D.K.1106, E.S.E., Hmcp.

Sherardia arvensis L., (2), 07.04.2013, D.K.1739, M.E., Trp.

SALICACEAE

Populus alba var. *alba* L., (6), 18.06.2018, D.K.1888, E.S.E., Phnp.

Populus nigra (L) subsp. *nigra,* (1), 09.06.2013, D.K.1818, Phnp.

Populus tremula L. subsp. *tremula,* (6), 06.05.2012, D.K.1192, W.s., Phnp.

Salix alba L., (6), 10.06.2012, D.K.1387, W.s., E.S.E., Phnp.

Salix bornmuelleri Hausskn., (6), 29.04.2012, D.K.1176, İr.-Tur El., Phnp.

Salix caprea L., (3), 18.06.2018, D.K.1911 E.S.E., Phnp.

Salix cinerea L., (1), 06.05.2012, D.K.1194, Phnp.

Salix pseudodepressa A. Skv., (6), 08.04.2012, D.K.1049, E.S.E., Phnp.

SANTALACEAE

Osyris alba L., (3), 02.09.2012, D.K.1599, M.E., Phnp.

Viscum album L. subsp. *album*, (3), 30.08.2014, D.K.1862, Vas.pr.

SAPINDACEAE

Acer campestre L. subsp. *campestre,* (9), 06.05.2012, D.K.1197, E.S.E., Phnp.

SCROPHULARIACEAE

Scrophularia cryptophila Boiss. & Heldr., (1), 18.06.2018, D.K.1882 , M.E., Hmcp. **End.**

Scrophularia scopolii Hoppe ex Pers. var. *scopolii,* (6), 30.08.2014, D.K.1861, W.s., Hmcp.

Verbascum bithynicum Boiss., (29), 27.6.19. D.K.2024, E.S.E., Hmcp. **End.**

Verbascum degenii Halacsy., (15), 18.06.2018, D.K.1889, E.S.E., Hmcp. **End.**

Verbascum gnaphalodes M.Bieb. (15), 18.6.2019, D.K.1965, E.S.E., Hmcp.

Verbascum phlomoides L., (13), 02.09.2012, D.K.1487, E.S.E., Hmcp.

Verbascum sinuatum L. var. *sinuatum,* (15), 18.06.2018, D.K.1890, M.E., Crp.

SIMAROUBACEAE

Ailanthus altissima (Mill.) Swingle, (17), 30.08.2014, D.K.1259, Phnp.

SMILACACEAE

Smilax excelsa L., (16), 06.05.2012, D.K.1200, E.S.E., Crp.

SOLANACEAE

Datura stramonium L., (14), 30.09.2012, D.K.1669, W.s., Chmp.

Physalis alkekengi L., (16), 02.09.2012, D.K.1569, Trp.

Solanum decipiens Opiz, (16), 25.09.2011, D.K.1003, Trp.

Solanum dulcamara L., (17), 27.05.2012, D.K.1365, W.s., E.S.E., Hmcp.

Solanum luteum Mill. (10), 12.10.2019, D.K.2084B, Trp.

TAMARICACEAE

Tamarix smyrnensis Bunge, (6), 02.07.2012, D.K.1467, Phnp.

THYMELAEACEAE

Daphne pontica L. subsp. *pontica,* (3), 07.04.2013, D.K.1750, E.S.E., Phnp.

TYPHACEAE

Typha latifolia L., (11), 10.06.2012, D.K 1377, Crp.

Typha angustifolia L.(12), 14.7.2019, D.K.2042B, Crp.

Sparganium erectum L. subsp. *neglectum* (Beeby) K. Richter, (1), 25.09.2011, D.K1026, E.S.E., Crp.

ULMACEAE

Ulmus laevis Pallas, (3), 21.05.2015, D.K.1287, E.S.E., Phnp.

URTICACEAE

Parietaria judaica L. (6), 27.6.2019, D.K.2039B, Hmcp.

Urtica dioica L. subsp. *dioica* L., (19), 27.05.2012, D.K.1827, W.s., E.S.E., Hmcp.

Urtica membranacea Poiret ex Savingy, (6), 27.05.2012, D.K.1828, M.E., Trp.

VERBENACEAE

Verbena officinalis var. *officinalis,* (6), 18.06.2018, D.K.1881, W.s., Hmcp.

VIOLACEAE

Viola alba Besser subsp. *dehnhardtii* (Ten.) W.Becker, (13), 29.04.2012, D.K.1117, W.s., Hmcp.

Viola odorata L., (6), 10.03.2013, D.K.1696, W.s., Hmcp.

Viola reichenbachiana Jord. ex Boreau, (3), 07.04.2013, D.K.1751, Hmcp.

Viola tricolor L., (13), 05.05.2013, D.K.1807, W.s., Trp.

VITACEAE

Vitis vinifera L., (21), 22.07.2012, D.K.1546, Phnp.

ZYGOPHYLLACEAE

Tribulus terrestris L., (15), 02.09.2012, D.K.1588, Trp.

5. DISCUSSION-CONCLUSION

2101 samples were collected in the study which were conducted in Acarlar floodplain and its surroundings. As a result of the identification of the collected plant samples, 360 genera, 654 species and subspecies taxa belonging to 97 families were identified. 8 of the taxa determined in the field belong to the Pteridophyta division, 646 of them belong to the Spermatophyta division, 5 of them belong to the Gymnospermae and 641 of them belong to the Angiospermae subdivision. Regarding to the data that we have obtained, a comparison was made with other studies. The first 5 families with the most taxa, the first 5 genera with the most taxa, the distribution by phytogeographical regions and the endemism rates were compared, and other interesting plants in the area were also interpreted.

Some genera and taxa have been transferred to different families in the APG III [14] system that we used while creating our list. However, since the use of this system in this study did not cause a difference in the number of taxa belonging to the first 5 families and genera, there were no any problems in comparing the data.

A comparison has been made with the studies numbered 1, 2, 3, and 4 given in Table 1, since they are studies covering important wetlands and floodplain areas in Turkey. The comparison was made due to the fact that the studies of numbers 5 and 6 were conducted on the Black Sea coast, similar to our study, as well as its geographical proximity. A comparison was made with the study number 7 due to its geographical proximity to our field. Although the 4th study was carried out in an area with floodplain feature, it covers the west of the Çapraz Stream, dividing the floodplain area into two, and does not cover the entire area of the floodplain. As can be seen from the Table 1, the number of species in

Acarlar floodplain is considerably higher than other floodplain areas.

Table 1
Studies Compared with Research Area and Number of Taxa

Comparative Studies	Families	Genus	Species and subspecies taxa
I: Acarlar / Sakarya - Acarlar Longozu Florası	97	360	654
II: İğneada / Kırklareli - Flora of Igneada Floodplain Forests (Longozes) and Their Surroundings [15]	86	291	472
III: Kızılırmak Deltası /Samsun Kızılırmak Deltasi Su Ayakizinin Belirlenmesi Projesi Nihai Raporu 2018 [16]	87	338	555
IV: Karacabey/ Bursa Karadağ'ın (Karacabey/Bursa) Florası [17]	59	*	320
V: Şile / İstanbul - Şile ve civarının (İstanbul) Flora ve vejetasyonu [18]	79	256	440
VI: Akçakoca / Düzce- Flora of Akçakoca district (Düzce–Turkey) [19]	103	384	657
VII: İkramiye Valley / Sakarya- Flora of Ikramiye Valley (Sapanca) Sakarya [20]	76	258	427

As can be seen from the Table 2, the family with the most taxa in our study is the Asteraceae family with 64 taxa. When looked at other studies, the family with the most taxa is the same except for the 5th and 7th studies. However, it has been observed that the number of taxa that make up the difference is quite low. The Poaceae family, which is in the second place in our study, is in the second place in all studies, except for the 6th and 7th studies.

Table 2
Comparison of Families Containing the Most Taxa in the Research Area with Studies Made in Nearby and Similar Fields. Proportion of total number species is given in parentheses (%)

	I	II	III	IV	V	VI	VII
ASTERACEAE	64 (9,7)	47 (9,9)	63 (11,3)	36 11,2)	45 (10,2)	67 (10,2)	47 (10,8)
POACEAE	58 (8,8)	45 (9,5)	45 (8,1)	24 (7,5)	46 (10,5)	39 (5,9)	49 (11,2)
FABACEAE	49 (7,5)	32 (6,7)	43 (7,7)	14 (4,3)	59 (13,4)	61 (9,2)	43 (9,9)
ROSACEAE	34 (5,1)	19 (4)	18 (3,2)	10 (3,1)	25 (6)	22 (3,3)	20 (4,6)
LAMIACEAE	33 (5)	24 (5)	29 (5,2)	13 (4)	33 (7,5)	40 (6)	28 (6,4)

As can be seen from the Table 3, when the ratios of the genera containing the most taxa are compared with other studies, some differences are observed between them. The climates, soil structures, widths, elevation, geographic conditions of the study areas and anthropogenic effects on the area may cause these differences. While there exists a difference with the 6th study area, which does not show the characteristics of a wetland and has a high altitude, though being geographically closer, the similarity with the 5th study on the beach is somewhat more. Although there are remote areas, the number of common taxon is increasing with the areas showing the floodplain feature.

Table 3
Comparison of the Genus Containing the Most Taxa in the Research Area with Studies Made in Recent and Similar Fields. Proportion of total number species is given in parentheses (%)

	I	II	III	IV	V	VI	VII
PAPAVER	13 (1,9)	*	*	*	*	*	*
TRIFOLIUM	12 (1,8)	13 (2,7)	9 (1,6)	7 (2,2)	21 (4,8)	18 (2,7)	14 (2)

EUPHORBIA	9 (1,3)	5 (1)	13 (2,3)	4 (2,2)	7 (1,6)	11 (1,6)	*
QUERCUS	8 (1,2)	*	*	7 (2,1)	*	*	*
RANUNCULUS	8 (1,2)	8 (1,6)	9 (1,6)	*	10 (2,3)	7 (1,1)	*

If one carefully looks at the Table 4, it is clear that the 1st, 2nd, 3rd, 5th. and 6.th studies stay in the Euro-Siberian region. It is straight forward to see that the 4th study conducted in the south of the Marmara Sea is in the transition zone in terms of phytogeography.The data in the table show that the study areas have phytogeographical regions and vegetation that are compatible with each other.

Table 4
Distribution of taxa determined in the research rrea according to phytogeographic regions and comparison with other studies. Proportion of total number species is given in parentheses (%)

	I	II	III	IV	V	VI	VII
Euro-Siberian	144 (21,9)	158 (33,4)	*	52 (16,3)	76 (17,2)	163 (24,8)	110 (25,35)
Mediterranean	121 (18,4)	45 (9,5)	*	64 (19,9)	84 (19)	64 (9,7)	51 (11,5)
Irano-Turanian	10 (1,52)	1(0,2)	*	3 (0.9)	7 (1,5)	4 (0,6)	14 (3,23)

Table 5
Endemism rates. Proportion of total number species is given in parentheses (%)

	I	II	III	IV	V	VI	VII
Endemism rates	14 (2,1)	4 (0,8)	1 (0,18)	3 (0,9)	7 (1,6)	7 (1,24)	11 (2,58)

In the study area, the rate of endemism within the 14 species and the subspecies taxa is 2.13% (see Table 5). In the studies of İkramiye Valley and Şile, which are close to our study area, it has been found that the endemism rates are 1.6% (Şile) with 7 taxa and 2.58% (İkramiye Valley) with 11 taxa. In general, it is known that wetlands have low endemism rates. The other floodplain in Turkey namely İğneada Longoz has a 0.85% endemism rate with 4 taxa, whereas the Kızılırmak Delta has a 0.18% endemism rate with 1 taxon and Karacabey has 0.9% endemism rate with 3 taxa. It can be seen that the studied area has a rate of endemism similar to those of the areas which are geographically closer, it has a higher rate of endemism than other wetlands and floodplaines. One of the reason for the lower average rate of endemism is that the field worked has aquatic character. The phytogeographical region can be thought given as another reason for the low endemism rate in the study area. When looked at the distribution of endemic plants to phytogeographical regions in Turkey, Iran turan phytogeographical region has the first place, followed by Mediterranean and Euro-Siberian phytogeographical regions. As a result, our work shows that the average endemism rate is below the Turkish national rate, however it is higher than the other wetlands and swamp areas which have the similar conditions.

Endemic plants in the study area are; *Centaurea kilaea* Boiss., *Galanthus plicatus* Bieb. subsp. *byzantinus* (Baker) D. A. Webb., *Knautia byzantina* Fritseh, *Knautia degenii* Borbás ex Formanek, *Lamium purpureum* L. var. *aznavourii* Gand. ex Aznav., *Papaver pilosum* Sibth. & Sm. subsp. *pilosum, Papaver pilosum* Sibth. & Sm. subsp. *strictum* (Boiss. & Balansa) N.Wendt ex Kadereit, *Papaver somniferum* L. var. *pullatum* M.A. Veselovskaya, *Quercus macranthera* Fısch. & Mey. ex Hohen. subsp. *syspirensis* (C. Koch) Menıtsky, *Scrophularia cryptophila* Boiss. & Heldr., *Silene sangaria* Coode & Cullen , *Stachys setifera* C.A.Mey. subsp. *lycia* (Gand.) R.Bhattacharjee, *Verbascum bithynicum* Boiss., *Verbascum degenii* Halacsy.

Some plants are remarkable in our field. One of them is *Pancratium maritimum* L., which is a rare and protected species in nature. This plant is grown in costal parts and

under anthropogenic influence in Turkey. This effect has been observed in the current field studied. Some of the plants are remarkable plants that are not included in the A3 frame covering the study area according to Davis's Grid Squaring System. In the flora of Turkey, *Euphorbia maculata* L. that recorded in Hatay-Iskenderun, is collected for the first time ever outside this region. *Symphytum bulbosum* K.F.Schimp exhibit a narrow distribution in Turkey's flora (Balıkesir-Çanakkale) collected in our studied area. *G. nivalis* L. subsp. *nivalis* is one of the species whose existence is controversial in Turkey, and the Flora of Turkey identification key defines the specimen we collected as *G. nivalis* L. subsp. *nivalis* but a more detailed investigation is required in this regard.

A number of endemic plants in Acarlar floodplain exhibit a narrow distribution in Turkey's flora. *Lamium purpureum* L. var. *aznavourii* Gand. ex Aznav is only recorded in Istanbul (Turkey) on the eastern bank of flora, while *Silene sangaria* Coode & Cullen shows distribution in a narrow dune area. *Papaver somniferum* L. var. *pullatum* M.A. Veselovskaya and *Verbascum degenii* Halacsy are other endemic species in floodplain and they exhibit a narrow distribution in Turkey's flora as well.

Some of the plants have been evaluated in terms of their natural habitat altitude. It was found remarkable that *Papaver rhoeas* L (registered at 1000-1800 m.), an endemic plant *Stachys setifera* C.A.Mey. subsp. *lycia* (Gand.) R.Bhattacharjee (registered at 750-1400 m.) are grown in the area studied.

Another group of plants are not included in the A3 grid and they were not sampled from the altitude suitable for their natural habitats. Endemic plants *Papaver pilosum* Sibth. & Sm. subsp. *pilosum* and *Papaver pilosum* Sibth. & Sm. subsp. *strictum* (Boiss. & Balansa) N.Wendt ex Kadereit, *Triglochin maritima* L (registered at 1200-2000 m.) and *Scutellaria orientalis* L. subsp. *alpina* (Boiss.) O.Schwarz var. *alpina* (registered at 1000-2440 m.) are other interesting plants observed in the area.

The fact that Acarlar floodplain is on one of the two important bird migration routes passing through Anatolia is thought to be effective on flora diversity.

The northern border of Acarlar floodplain is on the coast of Karasu village where sea tourism is intense and the recognition of Acarlar floodplain lake is increasing day by day. In parallel with these situations, there is a rapid construction in the area and an increase in the number of visitors. It was observed that the swampy areas around the lake were dried and used as agricultural land, and industrial waste was left in the streams that feed the lake. Furthermore, the presence of the road which splits the foodplain lake's east and west into two at the direction of north/ south close to the village Büyükyanık block the water circulation. Similar effect has been observed from the fact that the construction in progress at the junction point of the lake and the Okçular stream has also an additional effect on that blockage process. Similar to the coastal area, the construction around the lake is increasing intensively, pesticides used in agriculture on the lake border reach the lake, the industrial wastes left in the streams feed the lake, and the lack of awareness of both the local people and the visitors to protect the floodplain cause concerns about the future of floodplain. Citizens in that region intensely use some plants for ethnobothanic reasons. For instance, *Leucojum aestivum* L. is densely collected both for ethnobothanical and trading purposes [21], [22]. This is the case for various plants, for example Asparagus, Aristolochia, Orchis, Ophyris and Aurum. This situation threatens the plant vegetation to a certain extent. Ih has been also observed that the population of some plants collect before does not exist due to the anthropogenic effects.

Acarlar floodplain has very rich flora compared to other areas with similar characteristics and is under intense anthropogenic influence.

Acknowledgements

Funding

The authors received no financial support for the research, authorship or publication of this work.

Declaration of Conflict of Interest/Common Interest

No conflict of interest or common interest has been declared by the author.

The Declaration of Ethics Committee Approval

The author declares that this document does not require an ethics committee approval or any special permission.

The Declaration of Research and Publication Ethics

The author of the paper declares that he complies with the scientific, ethical and quotation rules of SAUJS in all processes of the paper and that he does not make any falsification on the data collected. In addition, he declares that Sakarya University Journal of Science and its editorial board have no responsibility for any ethical violations that may be encountered, and that this study has not been evaluated in any academic publication environment other than Sakarya University Journal of Science.

REFERENCES

[1]   B. Gönençgil, "Tehdit Altındaki Kıyı Alanlarına Bir Örnek: Acarlar Longozu-Karasu, Sakarya", Türkiye Coğrafyası Araştırma ve Uygulama Merkezi (TÜCAM) V.Ulusal Coğrafya Sempozyumu, Ankara Üniversitesi, 2008.

[2]   Y. Akman, Iklim Ve Biyoiklim, Palme Yayın Dağıtım, Ankara. 2011.

[3]   P.H. Davis, 'Flora Of Turkey And The East Aegean Islands', Edinburgh, A.Univ. Press., Edinburgh, vol.1-9, 1965-1985.

[4]   P.H. Davis, R.R. Mill, ve K. Tan, (edlr.). Flora of Turkey and the East Aegean Islands (Supple. 1). Edinburgh University Press, Edinburgh. Vol. 10, 1988.

[5]   A. Güner, N. Özhatay, T. Ekim, K.H.C. Başer, 'Flora of Turkey and the East Aegean Islands', (supple. 2), Edinburgh Univ. Press., Edinburgh, vol. 11, 2000.

[6]   A. Güner, S. Aslan, T. Ekim, M. Vural, ve M.T. Babaç, (edlr.). Türkiye Bitkileri Listesi (Damarlı Bitkiler). Nezahat Gökyiğit Botanik Bahçesi ve Flora Araştırmaları Derneği Yayını, İstanbul, 2012.

[7]   Bizim Bitkiler, http://www.bizimbitkiler.org.tr/v2/index.php (date of access: 22.09.2020).

[8]   İ. Eker, A. Çelik , A. Kaya, & A. Aydın, Bolu'nun Endemik ve Nadir Bitkileri. Ankara. Durnat Ofset Matbaacılık San. Ve Tic. Lim. Şti., 2019. ISBN 978-605-80817-0-3.

[9]   i. Eker, A. Kaya, A. Çelik & N. Eker Bolu Abant İzzet Baysal Üniversitesi Kampüs Florası.Bolu. Kemal Matb. San. Ve Tic. Ltd. Şti., 2018. ISBN 978-605-245-222-6.

[10]   C.S. Demir, & İ. Eker, PetaloId Monocotyledonous Flora of Bolu ProvInce, IncludIng AnnotatIons on CrItIcal PetaloId Geophytes of Turkey. Pegem Akademi May Ankara, 2015. ISBN 978-605-318-145-3

[11]   The International Plant Name Index (IPNI) : http://www.ipni.org, (date of access: 25.09.2020).

[12]   The Plant List: http://www.theplantlist.org, (date of access: 27.09.2020).

[13] M. Sagıroglu, The Geophytes of Sakarya City, Sakarya University Journal of Science, 24/5, 991-1007, 2020.

[14] E. Haston, J. E. Richardson, P. F. Stevens, M. W. Chase, and D. J. Harris, "The Linear Angiosperm Phylogeny Group (LAPG) III: A Linear Sequence of The Families in APG III", Botanical Journal of the Linnean Society, 161, 128–131, 2009.

[15] A. Kavgacı, G. Özalp, N. Özhatay, Iğneada Subasar Ormanlarının (Longozes) Florası Ve Yayılışları, I.U. Orman Fakültesi Dergisi, Series;A, 57/2, 61-89, 2007.

[16] Kızılırmak Deltası /Samsun Kizilirmak Deltasi Su Ayakizinin Belirlenmesi Projesi Nihai Rapor, Ankara, 2018

[17] A. Övünç, Karadag'ın (Karacabey/Bursa) Florası, Ege Üniversitesi Fen Bilimleri Enstitüsü Yüksek Lisans Tezi, İzmir. 1997.

[18] Y. Sezer, Sile Ve Civarının (İstanbul) Flora Ve Vejetasyonu, Marmara Üniversitesi, Fen Bilimleri Enstitüsü Yüksek Lisans Tezi, İstanbul, 2016.

[19] A.D. Koca, Ş. Yıldırımlı, Flora of Akcakoca district (Düzce–Turkey), Proceedings of IV Balkan Botanical Congress, Sofia, 148-159, 2006.

[20] M. Turna, Sakarya Ikramiye Vadisi Florası, Sakarya Universitesi Fen Bilimleri Enstitüsü Yüksek Lisans Tezi, Sakarya, 2014.

[21] M. Sagıroglu, E. Olgac, B. Erturk, M. Turna, An Ethnobotanical Survey from Şile (İstanbul) and Karasu (Sakarya). Ot Sistematik Dergisi, vol.19, no.2, pp. 93-104, 2012.

[22] M. Sagıroğlu, S.T. Köseoglu, M. Turna, Medicinal Plants in Flora of Ikramiye Sapanca-Sakarya- Türkiye. Sakarya University Journal of Science, vol.2, no.3, pp. 527-539, 2017.

Title: StationNet: An Algorithm for The Extraction and Visualization of Top-n
Correlated Bike Stations in Bike Sharing Systems Big Datasets

StationNet: An Algorithm for the Extraction and Visualization of Top-n Correlated Bike Stations in Bike Sharing Systems Big Datasets

Ahmet Şakir DOKUZ[1*]

Abstract

Bike sharing systems (BSS) have emerged as an alternative and environmentally friendly transportation tool that provides short-term bike rental to city residents for their close proximity transportation purposes or sports activities. With the emergence and widespread usage of BSS, BSS operators started collecting bike user-related datasets to benefit from it and to increase service quality. Many application areas are present which use BSS big datasets, such as behavioral analyses, urban pattern discovery, and network analysis of bike stations. A bike station network can be defined as a network where bike stations are nodes and the bike trips of users from a station to another station as edges. The extraction of bike station network provides information about which stations are central, which stations have more in- or out-flows, and which regions of the cities are actively used by bike users. However, the extraction of bike station networks is challenging due to the complexity and different characteristics of bike stations, the requirement of new algorithms and new visualization techniques, and the issues related to efficient handling BSS big datasets. In this study, the concept of bike station network extraction in terms of top-n correlated stations is proposed. In particular, the extraction of a bike station network from BSS big datasets are defined and a new algorithm is proposed for extraction of bike station network, and also a new visualization approach that uses common visualization tools is utilized to represent bike station network on a map which would provide more information than a network without a background information. The proposed algorithm and visualization technique are evaluated using one year BSS big dataset. Experimental results show that the proposed algorithm could successfully extract top-n correlated bike station networks and utilized visualization technique is beneficial.

---

[*] Corresponding Author: adokuz@ohu.edu.tr
[1] Nigde Omer Halisdemir University, Department of Computer Engineering, Niğde, Turkey, ORCID: https://orcid.org/0000-0002-1775-0954

Ahmet Şakir DOKUZ

StationNet: An Algorithm for The Extraction and Visualization of Top-n Correlated Bike Stations in Bi...

1. INTRODUCTION

With the rapid increase of fuel consumption in transportation systems led to high carbon emission and the air quality issues in metropolitan cities. To reduce carbon emission and to protect the environment, the city governments and planners seek for alternative transportation systems other than traditional and fuel-based systems. Bike sharing systems (BSS) are one of the clean and environmental friendly transportation systems which both protect environment and provide physical activity for their users [1].

Bike sharing systems (BSS) are becoming one of the popular and essential part of transportation systems for city residents with their environmental friendly nature, fresh outdoor activity possibility, and carbon emissions reducing potential in comparison with traditional transportation systems [2]. BSS locate bike stations at selected parts of the cities where their users can easily reach. The users rent a bike from a station and could drop the bike to another station where the station is close to their desired destination, without requiring to return back to the rental station [3]. Some of the bike stations are highly utilized by bike users due to their central locations and high residential activities. Discovering bike station network is beneficial for BSS operators to better model user activities in terms of in-flows and out-flows for bike stations and to plan new bike stations with respect to high-demanded areas.

Bike station network can be defined as a network where bike stations are nodes and the bike trips of users from a station to another station as edges [4, 5]. Extraction of bike station networks could provide several insights into BSS operators and city planners, such as which stations are central, which stations are origin-preferred or destination-preferred, and which regions of the cities are active in terms of bike user activities.

However, extraction of bike station networks is challenging due to several reasons. First of all, bike station networks are complex and each bike station has its own characteristics. For this reason,

new algorithms and methods should be developed for bike station network extraction and visualization. Second, bike sharing big datasets are unstructured and have a high seasonality. Third, bike sharing datasets have a high velocity and are big, and thus, novel approaches should be developed to analyze bike sharing big dataset.

The literature studies related to BSS data mining can be divided into three main categories, i.e. behavioral analysis, spatial and temporal analysis, and network analysis. In behavioral analysis, bike repositioning problem [6-8], effects on bike ridership [9, 10], and trip advisor system [11] are studied. In spatial and temporal analysis, station preference analysis [12-14], urban bike activity analysis [15-17], trip duration prediction [18], and citywide bike usage prediction [19-21] are studied. In network analysis, spatio-temporal graph analysis [23, 25] community discovery [4, 26] and station characteristics extraction [5, 24, 27] are studied.

In bike station network analysis, Calafiore, et al. [22] proposed and implemented a model that is based on closed queuing networks for ToBike BSS system using stations and itineraries between stations as nodes to identify customer arrival rates for each station. Yang, et al. [23] analyzed Nanchang BSS in terms of spatio-temporal and graph-based aspects over a period of a new metro line came into operation and travel behavior changes of before and after the metro line are investigated. Lin, et al. [5] proposed a deep learning-based approach for learning correlations between stations to predict station-level hourly demand. They also performed graph network analysis and visualization to discover more knowledge about station correlations. Oppermann, et al. [24] recorded data from several hundred BSS networks and combined with other data sources and extracted characteristic network metrics from the data. They also designed an online visualization tool to make the dataset publicly available. Zaltz Austwick, et al. [25] used visualization, statistical analyses, and spatial and network analyses to explore BSS usage characteristics of five different cities to investigate features of each city and to uncover similarities between cities. Shi, et al. [26]

Ahmet Şakir DOKUZ

StationNet: An Algorithm for The Extraction and Visualization of Top-n Correlated Bike Stations in Bi...

proposed an interactive visual analytics system to detect cycling communities of BSS using different community detection algorithms to find bike station communities. Yao, et al. [4] applied detailed network analysis methods to analyze relationships between bike stations of BSS using real-time data of Nanjing public bike system and they resulted that many stations have low usage characteristics and there is a geographical division between highly utilized and low-demand stations. They also discovered top-10 and bottom-10 related stations with ranking stations based on several parameters. Liu, et al. [27] proposed a method which is able to uncover the structure of transportation network and identify bicycle infrastructures to characterize roadways based on different network centrality measures.

In this study, bike station network for BSS is extracted and visualized. For this purpose, first, network extraction algorithm of StationNet algorithm is proposed for extracting most related stations in terms of incoming and outgoing bike activities. Then, two different tools are used as complementary of each other to visualize extracted bike station network. Gephi graph visualization tool is used for construction of nodes and edges, and Google Earth Pro map tool is used for mapping the station network. The experiments are performed for analyzing performances of both StationNet algorithm and the benefit of visualization method.

Main contributions of this study are given as follows:

- The definitions related to bike station network extraction are provided.
- A novel algorithm is proposed for bike station network extraction.
- A new approach is utilized for visualization of extracted bike station network on a map to provide more information about network and background map.
- The proposed method is experimentally evaluated on real-life BSS dataset of Chicago Divvy Bikes.

The rest of this study is organized as follows. Section 2 presents BSS big dataset and preprocessing steps, bike station network

extraction and visualization method and proposed algorithm. Section 3 evaluates the experimental results and discussion of the study. Finally, Section 4 outlines the conclusions.

2. MATERIALS AND METHOD

In this section, first the dataset of this study is introduced and the preprocessing steps are explained. Second, basic concepts and definitions of proposed method are expressed. Third, the proposed station network extraction algorithm is presented. Finally, the visualization method of this study is expressed.

2.1. The BSS Dataset

In this study, Divvy Bikes [28] BSS, which operates in Chicago, data are used as a bike sharing systems big dataset. Divvy Bikes shares the bike sharing data since 2013 as a quarter-year dataset. In each quarter-year dataset, three months of BSS activity data are present. 4 quarter-year dataset from 2018 are selected for this study, and the selected dataset is from 1 January 2018 to 31 December 2018. The total number of BSS activities in selected dataset are 3.603.082 for the year of 2018. Figure 1 presents the number of BSS activities for the selected dataset. As can be seen in the figure, Q1 and Q4 have less number of activities because these quarters contain winter and autumn months, and thus bike usages decrease because of the weather conditions. The majority of the BSS activities occurred at Q2 and Q3, which are within spring and summer seasons.
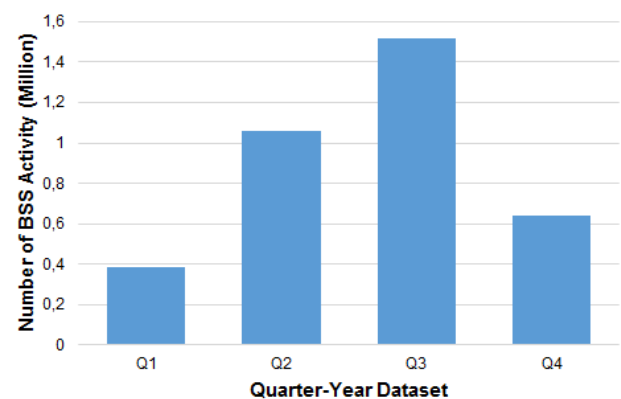

Figure 1 Number of BSS activities for each quarter-year dataset

Ahmet Şakir DOKUZ

StationNet: An Algorithm for The Extraction and Visualization of Top-n Correlated Bike Stations in Bi...
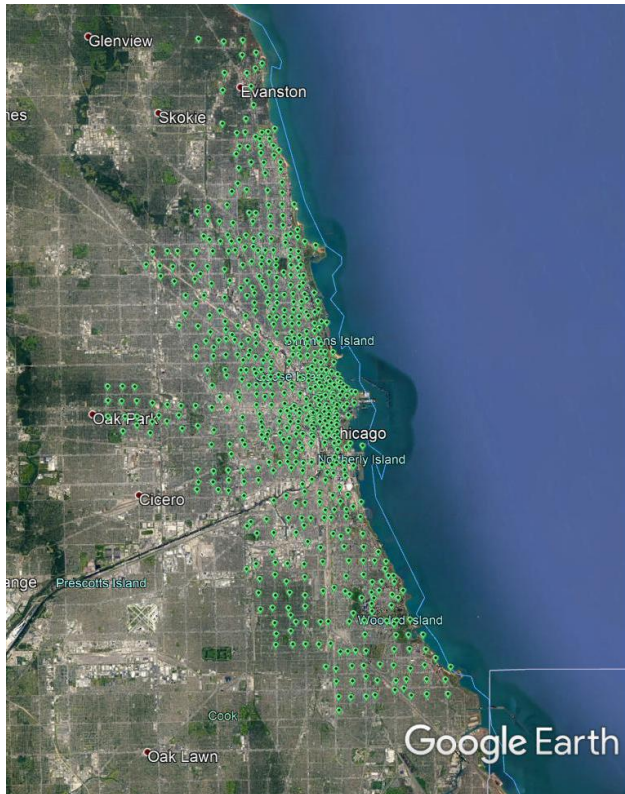
Figure 2 The distribution of all stations of Divvy Bikes [28]

There are 611 bike stations present in Divvy Bikes BSS. Figure 2 presents the distribution of all bike stations in Divvy Bikes on a map. As can be seen in Figure 2, the stations are distributed among Chicago and are clustered around the city center. Divvy Bikes [28] BSS provides latitude and longitude information of stations which are obtained as a file and used in this study.

The original dataset contains 12 columns that store information about each individual bike trips. For this study, only 3 of these columns are used, i.e., start station, end station, and trip duration.

2.1.1. Preprocessing

As preprocessing steps, first of all, quotation marks and commas in trip duration information are removed from the dataset due to achieve numerical trip duration information. Then, trip duration of each trip is checked whether the duration last more than 12 hours using a similar strategy with [4]. If the trip lasts more than 12 hours, then these trips are removed from the dataset, because no real bike trips could take such long time. After removing longer trips, the final

dataset has the number of BSS activities of 3.599.798.

2.2. Basic Concepts

In this section, basic concepts and definitions related to the proposed bike station network extraction method are presented.

Definition 1. A **bike station** *bs* is the station that a user could rent or return a bike in BSS.

Definition 2. Given two bike stations *bs1* and *bs2*, a **bike trip** *bt* is a directed trip from *bs1* to *bs2* in BSS dataset.

For example, if a user rent a bike from *bs1* and return the bike to *bs2*, then trip *bt* is constructed as *bs1→bs2*.

Definition 3. Given a bike trip *bt*, an **incoming station** is the station that *bt* started from and ended at the selected bike station.

For example, if a *bt* constructed as *bs1→bs2* and our selected bike station is *bs2*, then incoming station in *bt* is *bs1*.

Definition 4. Given a bike trip *bt*, an **outgoing station** is the station that *bt* is ended and started from the selected bike station.

For example, if a *bt* constructed as *bs1→bs2* and our selected bike station is *bs1*, then outgoing station in *bt* is *bs2*.

Definition 5. Given a list of bike trips *btlist* and a bike station *bs*, **top-n incoming station** for *bs* is the stations that have n-highest number of trips from an incoming station to *bs*.

Definition 6. Given a list of bike trips *btlist* and a bike station *bs*, **top-n outgoing station** for *bs* is the stations that have n-highest number of trips from *bs* to an outgoing station.

Definition 7. Given a list of bike stations *bslist* and top-n incoming and outgoing stations lists of each bike station *bs* in *bslist*, a **station network** of *bslist* is top-n incoming and outgoing stations for each station *bs* in *bslist*.

Ahmet Şakir DOKUZ

StationNet: An Algorithm for The Extraction and Visualization of Top-n Correlated Bike Stations in Bi...

2.3. Station Network Extraction

In this section, the proposed Station Network (StationNet) algorithm, which is developed using the basic definitions in Section 3.2, is presented. The algorithm takes BSS trip dataset as input and extracts the station network with respect to trip information in the dataset. The benefit of StationNet algorithm is that it can extract most related stations using bike trips in BSS datasets and flow of the bike users among the city bike stations could be observed. Algorithm 1 presents the pseudo code of StationNet algorithm.

Algorithm 1. StationNet Algorithm

Inputs:
D: The BSS trip dataset
S: The bike stations dataset
top-n: Top-n mostly related stations of each station in S

Output:
Network: The station network with top-n most correlated stations.

Algorithm:
1. Network = [][][][]
2. dataset = preprocess-dataset(D)
3. bsList = readDataset(S)
4. **for each** bike station bs **in** bsList
5.   incomingStation = [], outgoingStation = []
6.   **for each** bike trip bt **in** dataset
7.   **if** bs == bt.origin **and** bs == bt.destination **then**
8.   **continue**;
9.   **end if**
10.   **if** bs == bt.origin **then**
11.   outgoingStation.add(bt.destination)
12.   **else if** bs == bt.destination **then**
13.   incomingStation.add(bt.origin)
14.   **end if**
15.   **end for**
16.   [topNIncomingStations, topNIncomingWeights topNOutgoingStations, topNOutgoingWeights] = extract-top-n-stations(bsList, incomingStation, outgoingStation, *top-n*)
17.   Network.add(bs, topNIncomingStations, topNIncomingWeights, topNOutgoingStations, topNOutgoingWeights)
18. **end for**
19. **return** Network

As can be seen in Algorithm 1, the StationNet algorithm takes BSS trip and station datasets and *top-n* value as input and extracts station network for given datasets. At the first step, network matrix initialization is performed. At step 2, the dataset is preprocessed as presented in Section

2.1.1. At step 3, station dataset is read into *bsList* array. At steps between 4 and 18, the station network extraction is performed for each station. At steps between 6 and 15, each trip in the dataset is traversed and incoming and outgoing stations for selected station are extracted. At steps between 7 and 9, if selected station *bs* is at both start and end station of a bike trip, the trip is ignored, because the trip information do not add any value to station network. At steps between 10 and 14, if the trip has selected station as origin, then destination station of the trip is included in outgoing list, and if the trip has selected station as destination, then origin station of the trip is included in incoming list. At step 16, based on incoming and outgoing stations list of selected station, top-n incoming and outgoing stations are extracted. At step 17, the extracted top-n incoming and outgoing stations and their frequencies are added to the station network. Finally, at step 19, the constructed station network is returned as the output of StationNet algorithm.

Algorithm 2. *extract-top-n-stations* function

Inputs:
bsList: The bike stations list
incomingStation: Incoming stations list
outgoingStation: Outgoing stations list
top-n: Top-n mostly related stations

Output:
[topNIncomingStations, topNOutgoingStations]: The top-n most correlated stations with respect to given station.

Algorithm:
1. incomingFreqArray[], outgoingFreqArray[]
2. **for each** bike station bs **in** bsList
3.   incomingFreq = *incomingStation*.frequency(bs)
4.   outgoingFreq = *outgoingStation*.frequency(bs)
5.   incomingFreqArray.add(incomingFreq)
6.   outgoingFreqArray.add(outgoingFreq)
7. **end for**
8. *[topNIncomingStations, topNOutgoingStations]* = find-top-n-frequency(*bsList*, incomingFreqArray, outgoingFreqArray)
9. **return** *[topNIncomingStations, topNOutgoingStations]*

Algorithm 2 takes bike station list *bsList*, incoming station list *incomingStation*, outgoing station list *outgoingStation* and *top-n* value as input and returns top-n incoming and outgoing stations. At step between 2 and 7, all stations are traversed and incoming and outgoing frequencies

Ahmet Şakir DOKUZ

StationNet: An Algorithm for The Extraction and Visualization of Top-n Correlated Bike Stations in Bi...

of stations are extracted and saved to an array. Then, at step 8, the stations that have top-n highest frequencies with respect to selected station are determined. Finally, at step 9, the algorithm returns top-n incoming and outgoing stations.

2.3.1. Analysis of StationNet Algorithm

In this section, CPU utilization, RAM usage and complexity of StationNet algorithm are investigated. CPU utilizes 5 threads for running StationNet algorithm. For 4 quarter year dataset and for *top-n* value of 3, the algorithm execution time on CPU is 242 seconds. Detailed CPU time usages with respect to algorithm parameters are provided in experimental evaluation.

RAM usage of StationNet algorithm at the highest level is approximately 3.4 GB and nearly 80% of the RAM is utilized for arrays.

Algorithm complexity of StationNet algorithm is $O(n^2)$ because the algorithm contains two nested loops.

2.4. Station Network Visualization

In this section, the visualization of bike station network which is extracted by StationNet algorithm is presented. For visualization purposes, graph visualization and mapping tools are preferred which are used for visualizing and mapping complete station network.

In this study, for visualization of bike station network, open-source graph visualization tool of Gephi [29] is preferred due to its several benefits, such as geographical representation and edge weighting. Although, Gephi has geographical representation and map visualization of graphs, the map visualization ability is not sufficient at desired level. So, free version of Google Earth Pro [30] is also used for mapping the graph of the station network that is outputted from Gephi. The flow of visualization using Gephi and Google Earth Pro are presented in Figure 3.

As can be seen in Figure 3, first of all, StationNet algorithm results and station coordinate information are given to Gephi and station network is extracted as a graph. Then, station network graph is given to Google Earth Pro and Google Earth Pro maps the graph onto the earth map with the connections between each station.

At the visualization step, Gephi treated each station as nodes and each connection between stations as edges. By this way, a graph is constructed. Also, the weights of each edge are given to Gephi as the number of trips originated from a station to the other. Gephi has the ability to use geographical coordinates and locate each node in their corresponding location. For this purpose, the coordinates of each node (or station) are given as input to Gephi to correctly locate each node as shown in Figure 3.

Two different visualizations for a station network graph is presented in Figure 4. In Figure 4 (a), the default visualization is used, and there is no geographical property is used. In Figure 4 (b), geographical properties of stations are used for locating each node. As can be seen in Figure 4 (b), Gephi successfully visualizes station network, however, a map is missing at the background.
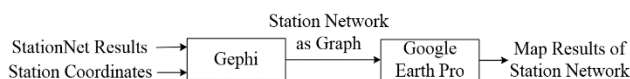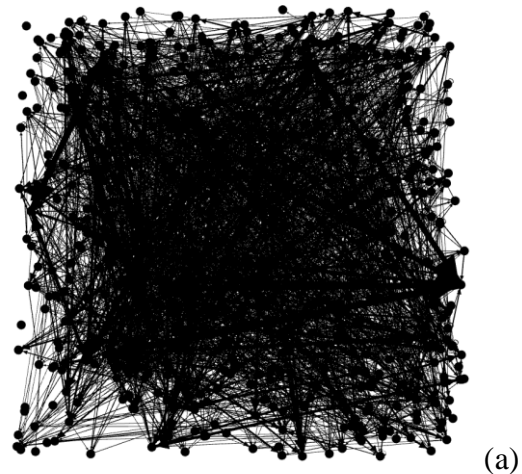

(a)

Figure 3 The visualization flow of the station network

Ahmet Şakir DOKUZ

StationNet: An Algorithm for The Extraction and Visualization of Top-n Correlated Bike Stations in Bi...

(b)

Figure 4 (a) The default and (b) geographical visualization of station network graph by Gephi

Gephi can extract the graphs to various output formats. One of these formats is KML file which is the format of Google Earth Pro. For this reason, the station network graph is extracted as KML file and given to Google Earth Pro. Figure 5 presents the output of Google Earth Pro with the station network that Gephi extracted. As can be seen in Figure 5, Google Earth Pro could construct the station network with their edges on a map at background.
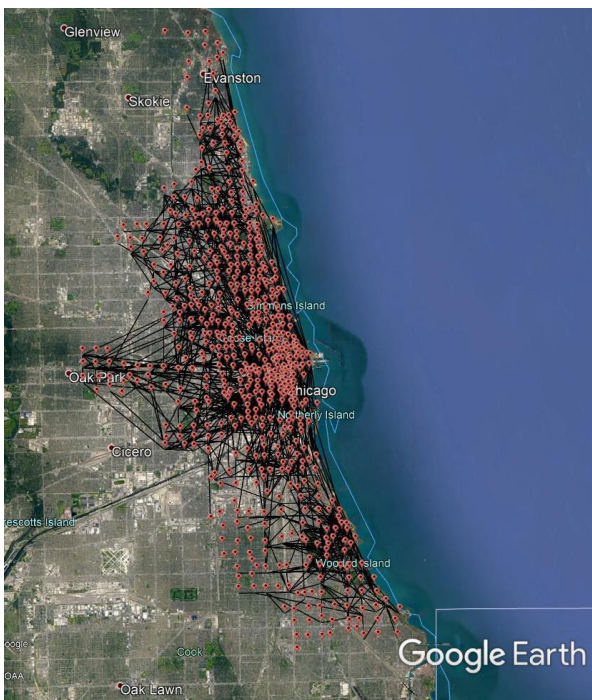

Figure 5 The mapping of station network graph by Google Earth Pro

3. RESULTS AND DISCUSSION

In this section, the experimental results of the proposed station network extraction method are presented. First, the proposed StationNet algorithm is evaluated whether it is a scalable algorithm. Then, network analysis of top-n is performed with different values that affect network results. Finally, the results of StationNet algorithm are evaluated. The experimental setup of this study is presented in Figure 6.
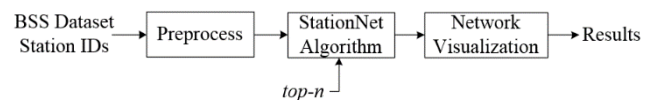

Figure 6 Experimental setup of this study

The experiments are performed on a computer with Intel Core i7 CPU with 3.40 GHz, and 8 GB of RAM. The algorithm is written in Java programming language.

3.1. Scalability Analysis

In this experiment, StationNet algorithm is evaluated whether it is scalable with the increase of the number of quarter-year dataset and the increase of the value of *top-n*. The number of quarter-year dataset is selected as 1, 2, 3, and 4 while *top-n* value is 3. The employed quarter year datasets and record counts for each number of dataset are presented in Table 1. The value of *top-n* is increased from 2 to 20, by 2 while quarter-year dataset is 2. The experimental results are presented in Figures 7 and 8.

Table 1
Dataset description

Number of Dataset	Quarters	Record Count
1	Q1	387146
2	Q1 and Q2	1446828
3	Q1, Q2 and Q3	2960399
4	Q1, Q2, Q3 and Q4	3603086

Ahmet Şakir DOKUZ

StationNet: An Algorithm for The Extraction and Visualization of Top-n Correlated Bike Stations in Bi...
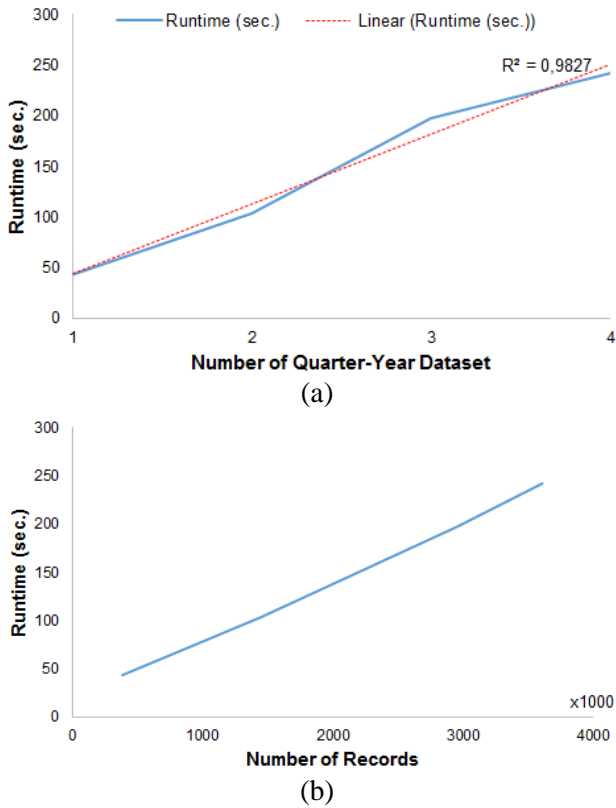
(a)

(b)

Figure 7 Runtime of StationNet algorithm for a) different number of quarter-year dataset, and b) number of records

As can be seen in Figure 7 a) and b), execution time of StationNet algorithm increases with the increase of the number of quarter-year dataset and the number of records. The increase amount is highest for 3 quarter-year dataset, because 3rd quarter contains summer months and the bike usage counts dramatically increase in this season. As can be seen in Figure 7 a), the increase trend of StationNet algorithm with respect to the number of quarter-year dataset could be seen as scalable because the execution time graphic is compatible with linear trend line with R^2 value of 0.9827.

As can be seen in Figure 8, the execution time of the StationNet algorithm increases with the increase of *top-n* value, as expected. When *top-n* value is increased, the algorithm tries to find more stations related to one station in the dataset, and thus the execution time increases. The increase trend of the algorithm with respect to *top-n* value is compatible with linear trend line with R^2 value of 0.9915, because, the execution time of the

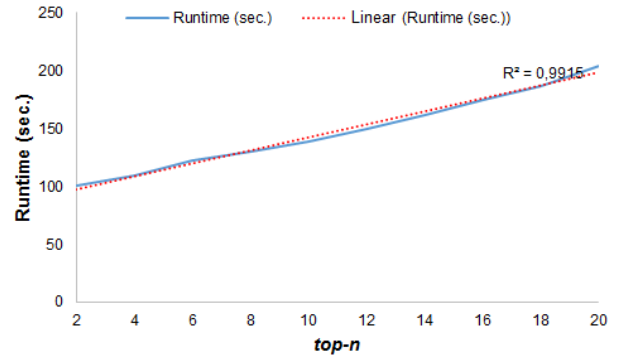algorithm increases linearly with the increase of *top-n* value.

Figure 8 Runtime of StationNet algorithm for different *top-n* value

As a result of this experiment, StationNet algorithm could be seen as a scalable and time-efficient algorithm with respect to given dataset, because it could successfully handle the increase of both the dataset and *top-n* value linearly as presented in Figures 7 and 8. Although, the algorithm complexity is $O(n^2)$, one of the nested loops is constant, the loop which traverses all stations. For this reason, the increase in the quarter year dataset leads to the linear increase of the execution time of the algorithm.

3.2. Network Analysis

In this experiment network analyses for different *top-n* values are performed. All quarters of the dataset, i.e. Q1, Q2, Q3 and Q4, are used in this experiment with a total of nearly 3,6 million records. *top-n* value is selected as 1, 2, 3, 5, 10, and 20 and the results of StationNet algorithm is evaluated for each *top-n* value. Table 2 presents statistics and network properties for each *top-n* value. Also, Figure 9 presents the station network for each *top-n* value.

Table 2
Network properties for different *top-n* values

	top-n = 1	*top-n* = 2	*top-n* = 3	*top-n* = 5	*top-n* = 10	*top-n* = 20
Number of Nodes	604	604	604	604	604	604
Number of Edges	1027	1962	2871	4673	8924	14803
Edges / Nodes	1.700	3.248	4.753	7.737	14.775	24.508

Ahmet Şakir DOKUZ

StationNet: An Algorithm for The Extraction and Visualization of Top-n Correlated Bike Stations in Bi...

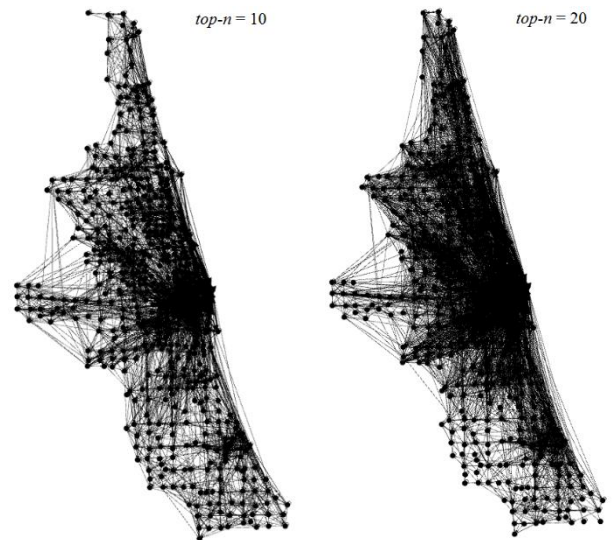| Graph Density	0.003	0.005	0.008	0.013	0.024	0.039
Modularity	0.843	0.779	0.746	0.706	0.64	0.568
Average Degree	1.681	3.206	4.692	7.635	14.581	24.031
Network Diameter	29	25	17	11	9	6
Average Path Length	9.014	8.302	5.908	4.489	3.431	2.829
Average Clustering Coefficient	0.069	0.274	0.294	0.3	0.31	0.307

Figure 9 The station network visualization for different *top-n* values

As can be seen in Table 2, the number of nodes is constant, while the number of edges increase with the increase of *top-n* value. However, the increase ratio is not linear, which can be observed in Edges / Nodes ratio, due to the reason that some stations do not have enough number of correlated stations. Graph density, average degree, and average clustering coefficient increases with the increase of *top-n* value because the network becomes more complex with the increase of *top-n* value. Contrarily, modularity, network diameter, and average path length decreases with the increase of *top-n* value, because these properties are related with connectedness of the networks.

As can be seen in Figure 9, the station network gets more complex with the increase of the *top-n* value. More edges are constructed between stations due to the increase of *top-n* value. However, when *top-n* value is increased unnecessarily, the network becomes non-functional and nearly all nodes are connected together. When all networks are investigated, the central of Chicago have high density of edges compared to other locations.

3.3. Evaluation of the Results

In this experiment, the results of StationNet algorithm are evaluated. The number of quarter-year dataset is selected as 4 and *top-n* value is selected as 5. First, the station network is

Ahmet Şakir DOKUZ

StationNet: An Algorithm for The Extraction and Visualization of Top-n Correlated Bike Stations in Bi...

visualized with the edges on a map. Second, the most central 10 stations that have highest incoming and outgoing edges are extracted and presented on a map.

As can be seen in Figure 10, the station network is clustered around the central of Chicago and near the bay area. Also, local clusters are observed near Oak Park, Ravenswood, Washington Park, and Clybourn train station.
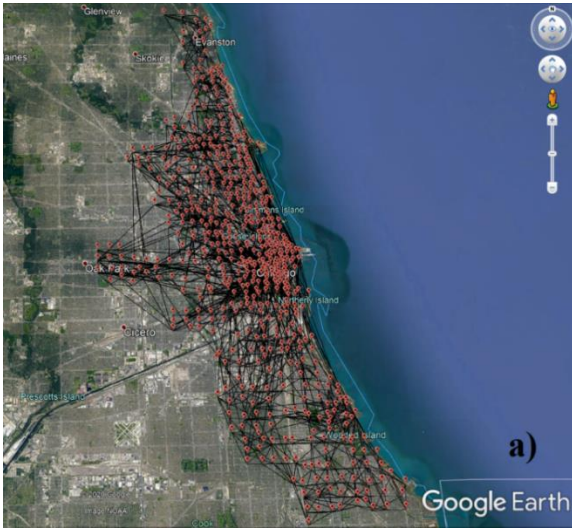

Figure 10 The station network shown on a map

Table 3 and Figure 11 presents the most central 10 stations that have highest number of edges. As can be seen in Table 3, some stations have higher outgoing edges, and other stations have higher incoming edges. For example, station 192 have 75 outgoing edges and 65 incoming edges. This means that station 192 is more preferred as an origin station. Also, the total edge counts of these 10 stations show that these stations are strongly linked with other stations in the network.

Table 3
The most central 10 stations that have the highest outgoing and incoming edges

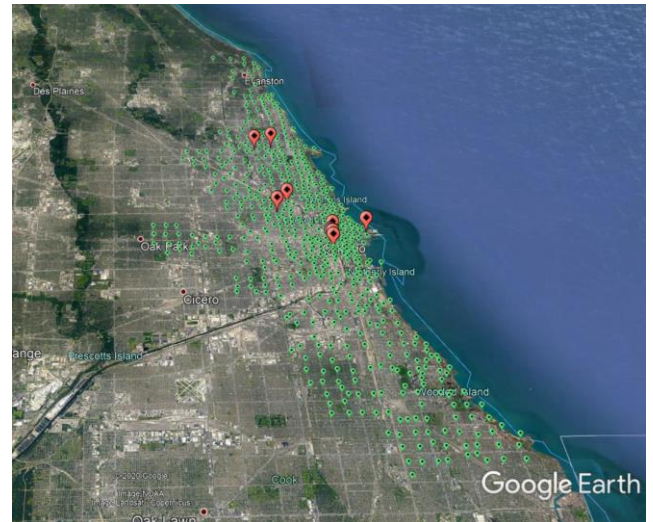| #	Station ID	Outgoing	Incoming	Total
1	192	75	65	140
2	77	65	69	134
3	91	64	67	131
4	35	46	51	97
5	344	43	43	86
6	69	36	34	70
7	133	28	39	67
8	58	36	30	66
9	239	29	31	60
10	174	26	33	59

Figure 11 The most central 10 stations (red points) and other stations (green points) on a map

In Figure 11, the most central stations are presented as red points and other stations are presented as green points. As can be seen in the figure, the most central stations are within the center of the Chicago city and these stations are in between other stations. Five of these stations are clustered at the city center. Other stations are distributed among the center and northern parts of the city. As a result, the bike users tend to visit these stations more frequent than other stations for starting or finishing their bike trips due to their various reasons.

4. CONCLUSIONS

BSS provide city residents a new transportation system while providing them a way to do sports and reach their desired destinations in the cities at the same time. The widespread use of BSS resulted a big dataset and a new knowledge platform about the citizen behavior in cities. The researchers utilized BSS datasets for various purposes, including behavioral analysis of city residents, urban pattern analysis of BSS users, and extraction of network analysis between bike stations based on the usage characteristics and utilization of these stations.

This study focuses on developing a novel algorithm for extraction of bike station networks on BSS big datasets. The proposed algorithm is designed to handle and to effectively run on BSS

Ahmet Şakir DOKUZ

StationNet: An Algorithm for The Extraction and Visualization of Top-n Correlated Bike Stations in Bi...

big datasets. Also, a new approach is utilized to visualize extracted bike station network which use Gephi and Google Earth Pro visualization and mapping tools sequentially to visualize network interaction of bike stations on a map. The proposed bike station network extraction and visualization method is experimentally evaluated on Chicago Divvy Bikes BSS big dataset. The experimental results show that the proposed bike station network extraction algorithm of StationNet algorithm is scalable with the increase of the dataset size for given BSS big dataset and the algorithm could successfully extract bike station network of given BSS big dataset. Also, visualization tools are seen as beneficial of understanding the network structure of the StationNet algorithm.

A limitation of this study is that, this study does not exclude low profile stations, which brings extra complexity to the algorithm. Also, the mapping of all station network leads to complicated visualization and each station could not be observed separately.

For the future studies, the community detection from the results of StationNet algorithm could be performed. Also, spatial and temporal analyses of bike station networks could be applied on BSS big datasets. The extraction and visualization of bike station networks in BSS datasets could be performed using big data technologies, such as Hadoop MapReduce and cloud computing resources.

The Declaration of Conflict of Interest/ Common Interest

No conflict of interest or common interest has been declared by the authors.

The Declaration of Ethics Committee Approval

This study does not require ethics committee permission or any special permission.

The Declaration of Research and Publication Ethics

The authors of the paper declare that they comply with the scientific, ethical and quotation rules of SAUJS in all processes of the paper and that they do not make any falsification on the data collected. In addition, they declare that Sakarya University Journal of Science and its editorial board have no responsibility for any ethical violations that may be encountered, and that this study has not been evaluated in any academic publication environment other than Sakarya University Journal of Science.

REFERENCES

[1] Y. Zhang and Z. Mi, "Environmental benefits of bike sharing: A big data-based analysis," Applied Energy, vol. 220, pp. 296-301, 2018/06/15/ 2018.

[2] E. Eren and V. E. Uz, "A review on bike-sharing: The factors affecting bike-sharing demand," Sustainable Cities and Society, p. 101882, 2019/10/15/ 2019.

[3] S. A. Shaheen, S. Guzman, and H. Zhang, "Bikesharing in Europe, the Americas, and Asia:Past, Present, and Future," Transportation Research Record, vol. 2143, pp. 159-167, 2010.

[4] Y. Yao, Y. Zhang, L. Tian, N. Zhou, Z. Li, and M. Wang, "Analysis of Network Structure of Urban Bike-Sharing System: A Case Study Based on Real-Time Data of a Public Bicycle System," Sustainability, vol. 11, p. 5425, 2019.

Ahmet Şakir DOKUZ

StationNet: An Algorithm for The Extraction and Visualization of Top-n Correlated Bike Stations in Bi...

[5] L. Lin, Z. He, and S. Peeta, "Predicting station-level hourly demand in a large-scale bike-sharing network: A graph convolutional neural network approach," Transportation Research Part C: Emerging Technologies, vol. 97, pp. 258-276, 2018/12/01/ 2018.

[6] M. Dell'Amico, M. Iori, S. Novellani, and A. Subramanian, "The Bike sharing Rebalancing Problem with Stochastic Demands," Transportation Research Part B: Methodological, vol. 118, pp. 362-380, 2018/12/01/ 2018.

[7] G. Erdoğan, M. Battarra, and R. Wolfler Calvo, "An exact algorithm for the static rebalancing problem arising in bicycle sharing systems," European Journal of Operational Research, vol. 245, pp. 667-679, 2015/09/16/ 2015.

[8] S. Ban and K. H. Hyun, "Curvature-based distribution algorithm: rebalancing bike sharing system with agent-based simulation," Journal of Visualization, vol. 22, pp. 587-607, 2019/06/01 2019.

[9] R. A. Rixey, "Station-Level Forecasting of Bikesharing Ridership: Station Network Effects in Three U.S. Systems," Transportation Research Record, vol. 2387, pp. 46-55, 2013/01/01 2013.

[10] Y. Xing, K. Wang, and J. J. Lu, "Exploring travel patterns and trip purposes of dockless bike-sharing by analyzing massive bike-sharing data in Shanghai, China," Journal of Transport Geography, vol. 87, p. 102787, 2020/07/01/ 2020.

[11] P. Cheng, J. Hu, Z. Yang, Y. Shu, and J. Chen, "Utilization-Aware Trip Advisor in Bike-Sharing Systems Based on User Behavior Analysis," IEEE Transactions on Knowledge and Data Engineering, vol. 31, pp. 1822-1835, 2019.

[12] A. Faghih-Imani and N. Eluru, "Analysing bicycle-sharing system user destination choice preferences: Chicago's Divvy system," Journal of Transport Geography, vol. 44, pp. 53-64, 2015/04/01/ 2015.

[13] M. Hyland, Z. Hong, H. K. R. d. F. Pinto, and Y. Chen, "Hybrid cluster-regression approach to model bikeshare station usage," Transportation Research Part A: Policy and Practice, vol. 115, pp. 71-89, 2018/09/01/ 2018.

[14] A. S. Dokuz, "Station Preference Analysis of Users in Bike Sharing Systems Big Datasets," European Journal of Science and Technology, vol. 2020 Special Issue, pp. 591-597, 1 April 2020 2020.

[15] P. Jiménez, M. Nogal, B. Caulfield, and F. Pilla, "Perceptually important points of mobility patterns to characterise bike sharing systems: The Dublin case," Journal of Transport Geography, vol. 54, pp. 228-239, 2016/06/01/ 2016.

[16] J. Wergin and R. Buehler, "Where Do Bikeshare Bikes Actually Go?: Analysis of Capital Bikeshare Trips with GPS Data," Transportation Research Record, vol. 2662, pp. 12-21, 2017/01/01 2017.

[17] W. Li, S. Wang, X. Zhang, Q. Jia, and Y. Tian, "Understanding intra-urban human mobility through an exploratory spatiotemporal analysis of bike-sharing trajectories," International Journal of Geographical Information Science, vol. 34, pp. 2451-2474, 2020/12/01 2020.

[18] V. E. Sathishkumar, J. Park, and Y. Cho, "Seoul bike trip duration prediction using data mining techniques," IET Intelligent Transport Systems, vol. 14, pp. 1465-1474, 2020.

[19] Y. Li and Y. Zheng, "Citywide Bike Usage Prediction in a Bike-Sharing System," IEEE Transactions on Knowledge and Data Engineering, pp. 1-1, 2019.

[20] X. Ma, Y. Ji, Y. Yuan, N. Van Oort, Y. Jin, and S. Hoogendoorn, "A comparison in travel patterns and determinants of user demand between docked and dockless bike-sharing systems using multi-sourced data," Transportation Research Part A: Policy and Practice, vol. 139, pp. 148-173, 2020/09/01/ 2020.

[21] N. Boufidis, A. Nikiforiadis, K. Chrysostomou, and G. Aifadopoulou, "Development of a station-level demand prediction and visualization tool to support bike-sharing systems' operators," Transportation Research Procedia, vol. 47, pp. 51-58, 2020/01/01/ 2020.

Ahmet Şakir DOKUZ

StationNet: An Algorithm for The Extraction and Visualization of Top-n Correlated Bike Stations in Bi...

[22] G. C. Calafiore, F. Portigliotti, and A. Rizzo, "A Network Model for an Urban Bike Sharing System" IFAC-PapersOnLine, vol. 50, pp. 15633-15638, 2017/07/01/ 2017.

[23] Y. Yang, A. Heppenstall, A. Turner, and A. Comber, "A spatiotemporal and graph-based analysis of dockless bike sharing patterns to understand urban flows over the last mile," Computers, Environment and Urban Systems, vol. 77, p. 101361, 2019/09/01/ 2019.

[24] M. Oppermann, T. Möller, and M. Sedlmair, "Bike Sharing Atlas: Visual Analysis of Bike-Sharing Networks," International Journal of Transportation, vol. 6, pp. 1-14, 2018.

[25] M. Zaltz Austwick, O. O'Brien, E. Strano, and M. Viana, "The Structure of Spatial Networks and Communities in Bicycle Sharing Systems," PLOS ONE, vol. 8, p. e74685, 2013.

[26] X. Shi, Y. Wang, F. Lv, W. Liu, D. Seng, and F. Lin, "Finding communities in bicycle sharing system," Journal of Visualization, vol. 22, pp. 1177-1192, 2019/12/01 2019.

[27] X. C. Liu, J. Taylor, R. J. Porter, and R. Wei, "Using trajectory data to explore roadway characterization for bikeshare network," Journal of Intelligent Transportation Systems, vol. 22, pp. 530-546, 2018/11/02 2018.

[28] D. Bikes. (2020). Divvy Bike Sharing Dataset. Available: https://www.divvybikes.com/

[29] M. Bastian, S. Heymann, and M. Jacomy, "Gephi: an open source software for exploring and manipulating networks," presented at the International AAAI Conference on Weblogs and Social Media, San Jose, California, USA, 2009.

[30] Google. (2020, 02.04.2020). Google Earth Pro. Available: https://www.google.com.tr/intl/tr/earth/